

**Endocranial anatomy of Australasian flightless  
galloanseres, with a focus on evolutionary  
transformation and the phylogenetic utility of  
the avian brain**

by

**Warren D. Handley**

BSc (Hons)

*Thesis  
Submitted to Flinders University  
for the degree of*

**Doctor of Philosophy**

College of Science & Engineering

28 February 2020

---

*I recognise the lives of my father Geoff (4/3/42–16/4/16),  
mother Doddy (27/5/43–23/7/16), and sister Belinda (17/9/61–12/8/16).*

*but this work is dedicated entirely to my wonderful partner Jan Ellis  
who will likely never concede to read it while she still draws breath*



## ***Table of Contents***

|                                | <b>Page</b>   |
|--------------------------------|---|
| <b><i>Abstract</i></b>         | iii   |
| <b><i>Declaration</i></b>      | iv  |
| <b><i>Acknowledgements</i></b> | v   |
| <b><i>List of Figures</i></b>  | vii   |
| <b><i>List of Tables</i></b>   | ix  |
| <br>                           |   |
| <b><i>Chapter 1</i></b>        | <b><i>Introduction and Aims</i></b>   |
| 1.1                            | The phylogeny of modern birds (Neornithes) 1  |
| 1.2                            | Galloanseres 2  |
| 1.3                            | Galliformes 6   |
| 1.3.10                         | The Australasian galliform fossil record 14   |
| 1.3.11                         | The modern Australian galliform fauna 19  |
| 1.4                            | Anseriformes 19   |
| 1.4.7                          | The Australasian anseriform fossil record 36  |
| 1.4.8                          | The modern Australasian anseriform fauna 39   |
| 1.5                            | The avian brain 41  |
| 1.5.1                          | Understanding the vertebrate brain 41   |
| 1.5.2                          | Nomenclature 47   |
| 1.5.3                          | Endocranial anatomy 47  |
| 1.5.4                          | Functional attributes of avian endocranial anatomy 52   |
| 1.5.5                          | The morphometric approach 56  |
| 1.6                            | Aims and objectives 58  |
| 1.7                            | Thesis structure 60   |
| <br>                           |   |
| <b><i>Chapter 2</i></b>        | <b><i>General Methods</i></b>   |
| 2.1                            | Computed Tomography data 62   |
| 2.2                            | Landmarking 63  |
| 2.3                            | Data forms 63   |
| 2.4                            | Analyses 66   |
| 2.5                            | Appendices 69   |
| <br>                           |   |
| <b><i>Chapter 3</i></b>        | <b><i>Endocranial morphological transformation concomitant with the loss of flight ability in Finsch's duck <i>Chenonetta finschi</i></i></b> |

|                  |   |     |
|------------------|---|-----|
| 3.1              | Introduction  | 74  |
| 3.2              | Methods   | 76  |
| 3.3              | Results   | 81  |
| 3.4              | Discussion  | 95  |
| 3.5              | Conclusions   | 101 |
| 3.6              | Acknowledgements  | 104 |
| 3.7              | References  | 105 |
| 3.8              | Appendices  | 113 |
| <b>Chapter 4</b> | <b><i>Dromornithid endocranial anatomy</i></b>                            |     |
| 4.1              | Introduction  | 124 |
| 4.2              | Methods   | 127 |
| 4.3              | Results   | 134 |
| 4.4              | Discussion  | 165 |
| 4.5              | Acknowledgements  | 182 |
| 4.6              | References  | 183 |
| 4.7              | Appendices  | 193 |
| <b>Chapter 5</b> | <b><i>The phylogenetic utility of Galloansere endocranial anatomy</i></b> |     |
| 5.1              | Introduction  | 209 |
| 5.2              | Methods   | 212 |
| 5.3              | Results   | 221 |
| 5.4              | Discussion  | 245 |
| 5.5              | Conclusions   | 256 |
| 5.6              | Acknowledgements  | 256 |
| 5.7              | References  | 257 |
| 5.8              | Appendices  | 269 |
| <b>Chapter 6</b> | <b><i>Summary and Conclusions</i></b>                                     |     |
| 6.1              | Limitations of, and modifications to the Modular Lm suite                 | 291 |
| 6.2              | Endocranial morphology of Finsch's duck                                   | 292 |
| 6.3              | Endocranial morphology and evolution of dromornithids                     | 293 |
| 6.4              | Brain shape, phylogeny and ecology across galloanseres                    | 296 |
| 6.5              | Evolutionary correlations of fossil and extant taxa                       | 297 |
| 6.6              | Conclusion  | 301 |
| <b>Chapter 7</b> | <b><i>General References</i></b>  | 302 |

## ABSTRACT

Endocast shape is a proxy for brain morphology in birds and has increasingly been used to infer aspects of both ecology and phylogeny. For taxa known only as fossils, model endocast shape is the only way to assess brain morphology. This project reconstructed model endocasts from Computed Tomography (CT) data of fossil and extant galloanseres (land- and waterfowl and kin), to quantify the evolution of brain shape within closely related avian taxa, and assess variation in previously unknown endocasts for fossil taxa over geological time scales. Geometric information described by anatomical landmark (Lm) coordinates, combined with univariate measurements derived from those data, were used to characterise shape distinctions between galloansere endocasts across diverse temporal scales. In a novel approach for birds, the use of discrete Lm modules to compare endocast shape and infer aspects of ecology and phylogenetic utility, allowed the quantification and assessment of endocranial morphology in a way not previously attained.

I assessed morphological changes over short time scales (~20 kys) using four Finsch's duck (*Chenonetta finschi*) endocasts sampling a dated temporal sequence, documenting the transition to flightlessness in the taxon. Assessments identified a trend of hypertrophy of the rostradorsal and dorsolateral forebrain areas, along with hypotrophy of the hindbrain across time. These endocranial changes are potentially related to increasing reliance on a visually accurate, terrestrial grazing mode of life. Novel descriptions of endocasts of several species of the giant Australian galloanseres in Dromornithidae facilitated an assessment of lineage evolution across deep time (~20–8 Ma). The oldest, an endocast reconstruction for the Oligo-Miocene (~20 Ma) *Dromornis murrayi*, was compared to the brain of the middle Miocene (~12 Ma) *D. planei*, digitally extracted from a limestone matrix, and to that of the middle Miocene (~12 Ma) *Ilbandornis woodburnei*. In addition, partial endocast reconstructions for the late Miocene (~8 Ma) *D. stirtoni*, aligned with that of *D. planei*, enabled assessment of changes associated with neurocranial foreshortening across the *Dromornis* lineage. The dromornithid two lineage hypothesis is supported by minimally five endocranial differences between *Ilbandornis* and *Dromornis*. Functional interpretations suggest dromornithids were specialised herbivores that likely possessed stereoscopic depth perception, visual proficiency, and targeted a soft browse trophic niche. The phylogenetic utility of brain morphology was assessed using a combined data set of 34 galloansere endocasts, including nine fossils of six species. The rhombencephalon and mesencephalon zones of the avian brain were shown to convey phylogenetic information. Endocranial morphological correlations suggest *C. finschi* may not belong in *Chenonetta*, and its taxonomic affinities require reinvestigation. Distinctive dromornithid eminentia sagittalis morphology supports hypotheses that dromornithids are more closely related to basal galliforms than anseriforms. Close associations noted between the European fossil *Mionetta blanchardi*, and the extant Australian *Malacorhynchus membranaceus* support the hypothesised Oligo-Miocene through Miocene basal erismaturine global radiation.

## **Declaration**

I certify that this thesis:

1. Does not incorporate without acknowledgement any material previously submitted for a degree or diploma in any university; and
2. To the best of my knowledge and belief, does not contain any material previously published or written by another person except where due reference is made in the text.

A handwritten signature in black ink that reads "Warren Handley". The signature is written in a cursive style with a large initial 'W' and 'H'.

Warren D. Handley

04 July 2019

## ACKNOWLEDGEMENTS

There is no doubt in my mind that most people are born palaeontologists, evidenced by the universal fascination kids have with fossils and imagining lost worlds. However, by the time they grow up, the fascination diminishes, and they become electricians, and lawyers, and politicians who ignore the lessons of the past. My mother went to her rest with a piece of petrified wood, of Triassic age I believe, that I apparently gifted her when I was four years old, collected in the bush somewhere in the Gokwe area of my youth. I will always remember her urging me to pursue my entirely irrational love for fossil things. I have come to appreciate that one has to irrationally love and be illogically driven to pursue the business of being a palaeontologist, for if you expect to enjoy a permanent job one day, the field is likely not for you. After all, it's all gone, and who cares, right? I suggest one of the greatest mistakes of the human condition, is to consistently ignore lessons of the past. Things have happened before that will happen again, and we must draw inference from these patterns to predict circumstances that we, and the unfortunate biological organisms sharing the contemporary biome with us, will face in the future.

I spent far too many years pursuing a 'normal' life, trained in an industry that offers plenty of opportunity for work, but I couldn't stop reading of and imagining lost worlds, in my case, populated by strange and unusual, fabulously feathered things. So, I took Mum's advice, quit everything and turned up at uni. During the course of my first year in undergrad, inquiry directed me to the School of Biological Sciences building one day, wherein I found the Palaeontology laboratory, secreted cryptically, and somewhat ironically, in the basement. For the first time, I met the men and women who would influence my life so profoundly. Things have changed a bit since then. The Palaeontology labs at Flinders now occupy almost an entire wing of the first-floor of the Biological Sciences building, and is recognised as the premier palaeontology research group in the country, arguably the Southern Hemisphere. This success has been facilitated by an unwavering love of fossil things, and the persistent pursuit of excellence by several key people to whom I am forever indebted.

I would like to extend my deep thanks and appreciation to my supervisors, and two giants of Australasian vertebrate palaeontology: **1**, Gavin Prideaux is a most capable and considerate leader. He has repeatedly presented me opportunities to learn and grow, and offered me generous support throughout the time I have been associated with the Palaeo lab. Altruism almost certainly to his disadvantage in several instances, when cash flow had been tight for him. Gavin genuinely cares about students and others within his purview, and the fact I may sit here and write this sentence, is entirely due to his support during some tough times over the last decade. **2**. I consider it the greatest privilege of my life to have had the opportunity to work with, and be patiently mentored by Trevor Worthy, perhaps the greatest avian palaeontologist of his generation. One of the reasons this is the case, is that he would insist to the contrary. As my primary supervisor, Trevor offered immediate

counsel, insightful interpretation, astute direction, and suffered many, many hours of wading through my overly dense texts without ever wavering in his commitment to make sense of it all.

It has also been my privilege to work, collaborate and associate with members of the Flinders University Palaeontology lab over the years, all of whom are exceptional in their own eccentric way. In no particular order: Rod Wells, John Long, Mike Lee, Aaron Camens, Rachel Correll, Brian Choo, Alice Clement, fellow palaeoneuroanatomist, who listens patiently whilst I wax lyrical about my 12 Million year old fossil, then turns back to her 340 Million year old one, Aidan Couzens, Sam Arman, Diana Fusco, who is consistently better at everything, Grant Gully, thanks for the Beast bro, nice one, Carey Burke, without whom nothing gets to see the light of day, Elen Shute, Kailah Thorn, Amy Tschirn, Phoebe McInerney, casual superstar and resolute hand-watcher, gentleman Jacob Blokland, Lisa Nink, Ellen Mather, Jake van Zoelen, Isaac Kerr, Cassy Petho, Arthur Crichton, Nathan Phillips, and Nim Gibbs. May the gods grant you fortuitous geo-pick (aka 'skull-finder') blows.

A special mention to Vanesa De Pietri, Paul Scofield, Alan Tennyson, and the Sykes and Dodkins families. Thanks for everything, everyone. Additionally, I thank Em Sherratt and Stig Walsh for their insightful comments which substantially improved this manuscript.

My deepest thanks go to Jan Ellis, the single most important person in my life, my partner and best friend. For unconditionally supporting me through what have been the best and worst of times, thank you my beautiful gentle girl. This is for you.

My candidature at Flinders University has been supported with fee offsets, stipends and allowances by an Australian Government Research Training Program Scholarship, for which I am much appreciative, and without which I would not have been able to attend this work full-time.

I am also grateful to the Royal Society of South Australia (RSSA) for awarding me a Small Research Grant that contributed towards the research presented here; and Flinders University for awarding me an Overseas Field Trip Grant to attend excavations at the St Bathans fossil site in Otago NZ, and two Elaine Martin International Conference Travel Grants to attend the CAVEPS conference in Queenstown NZ, and the SAPE conference in Argentina.

I acknowledge the collection managers at the South Australian Museum: Philippa Horton and Maya Penck, for allowing me unfettered access to the ornithology collection, and I thank Joseph Bevitt (ANSTO) and Mishelle Korlaet (SAHMRI) for being so interested in my work, going the extra mile on my behalf, and getting things right to the best of their ability.

| <i>List of Figures</i> |   | <b>Page</b> |
|------------------------|---|-------------|
| <b>1.5.1</b>           | External endocast morphology and innervation                                  | 49          |
| <b>2.1</b>             | Landmark modules used to capture endocast morphology for Chapters 4 & 5       | 65          |
| <b>2.2</b>             | Modular Distance, Linear Distance and Modular Surface Area data forms         | 67          |
| <b>3.1</b>             | Map of New Zealand showing South Island fossil sites                          | 77          |
| <b>3.2</b>             | Modular Lm data: PCA plot: Orbit modules                                      | 83          |
| <b>3.3</b>             | Modular Lm data: PCA plot: Eminentia sagittalis modules                       | 84          |
| <b>3.4</b>             | Modular Lm data: 2B-PLS plot: Orbits vs Eminentia sagittalis modules          | 86          |
| <b>3.5</b>             | Modular Lm data: 2B-PLS plot: Orbits vs Cerebellum modules                    | 87          |
| <b>3.6</b>             | 3D modular shape change vector plots: Orbits, Emsg and Cerebellum             | 89          |
| <b>3.7</b>             | 3D modular shape change vector plots: Mes., Telen. and Rho.                   | 91          |
| <b>3.8</b>             | TPS warpgrid plot: Endocast shape change between GYL3 and CR sites            | 94          |
| <b>A3.1</b>            | Landmark modules used to capture endocast morphology for Chapter 3            | 114         |
| <b>A3.2</b>            | Modular Distance and Linear Distance ratios plot: <i>Chenonetta</i> specimens | 121         |
| <b>A3.3</b>            | Modular Surface Area ratios plot: <i>Chenonetta</i> specimens                 | 122         |
| <b>A3.4</b>            | TPS warpgrid plot: Endocast shape change between GY, HC and CR sites          | 123         |
| <b>4.1</b>             | Time series of neurocrania for <i>Dromornis</i> taxa                          | 126         |
| <b>4.2</b>             | Australian continental map showing fossil site locations                      | 129         |
| <b>4.3</b>             | Dromornithid endocasts  | 137         |
| <b>4.4</b>             | Galloansere endocasts   | 140         |
| <b>4.5</b>             | Modular Distance and Linear Distance ratios plot: dromornithid taxa           | 143         |
| <b>4.6</b>             | Modular Surface Area ratios plot: dromornithid taxa                           | 147         |
| <b>4.7</b>             | 3D modular shape variance plots for dromornithid taxa: Emsg and Tel.c         | 151         |
| <b>4.8</b>             | 3D modular shape variance plots for dromornithid taxa: Cer. and Rho.          | 157         |
| <b>4.9</b>             | 3D modular shape variance plots for dromornithid taxa: Emsg, Tel.c, and Rho.  | 162         |
| <b>A4.1</b>            | Oligo-Miocene dromornithid fossil and digital neurocrania                     | 193         |
| <b>A4.2</b>            | Oligo-Miocene dromornithid digital neurocrania                                | 194         |
| <b>A4.3</b>            | <i>Dromornis murrayi</i> fossil and digitally reconstructed endocasts         | 195         |
| <b>A4.4</b>            | Middle Miocene dromornithid fossil and digital neurocrania                    | 196         |
| <b>A4.5</b>            | Middle Miocene dromornithid digital neurocrania                               | 197         |
| <b>A4.6</b>            | Late Miocene dromornithid fossil and digital neurocrania                      | 198         |
| <b>A4.7</b>            | Late Miocene dromornithid digital neurocrania                                 | 199         |
| <b>A4.8</b>            | 2D reconstruction of the <i>Dromornis stirtoni</i> endocasts                  | 200         |
| <b>A4.9</b>            | 3D reconstruction of the <i>Dromornis murrayi</i> endocast model              | 201         |
| <b>A4.10</b>           | Modular Distance ratios plot: Chapter 4 galloansere taxa                      | 203         |

| <i>List of Figures cont.</i> |  | <b>Page</b> |
|------------------------------|--|-------------|
| <b>A4.11</b>                 | Modular Surface Area ratios plot: Chapter 4 galloansere taxa                 | 205         |
| <b>A4.12</b>                 | Quantile boxplots of gastrolith and gizzard ratios for moa, emu and droms.   | 207         |
| <b>5.1</b>                   | Undated phylogenetic tree topology for the Complete (n=34) specimen data set | 217         |
| <b>5.2</b>                   | Quantile boxplots summarising phylogenetic signal (K) results                | 224         |
| <b>5.3</b>                   | Modular Lm data: boxplots summarising distance (D)-PGLS model results        | 226         |
| <b>5.4</b>                   | Modular Lm data: mesencephalon D-PGLS Sub-Family regression plots            | 228         |
| <b>5.5</b>                   | Modular Lm data: rhombencephalon D-PGLS Sub-Family regression plots          | 229         |
| <b>5.6</b>                   | Complete Modular Lm data: PCA of Mesencephalon modules                       | 230         |
| <b>5.7</b>                   | Complete Modular Lm data: PCA of Mes. and Rho. modules                       | 232         |
| <b>5.8</b>                   | Modular Distance data: boxplots summarising D-PGLS model results             | 235         |
| <b>5.9</b>                   | Modular Distance and Surface Area data: boxplots for cov-PGLS results        | 238         |
| <b>5.10</b>                  | Modular Surface Area data: boxplots for D-PGLS model results                 | 243         |
| <b>A5.1</b>                  | Anatine endocasts: RHS lateral and caudal views                              | 269         |
| <b>A5.2</b>                  | Anseriform endocasts: RHS lateral and caudal views                           | 270         |
| <b>A5.3</b>                  | Anseriform endocasts (cont.): RHS lateral and caudal views                   | 271         |
| <b>A5.4</b>                  | Galloansere endocasts: RHS lateral and caudal views                          | 272         |
| <b>A5.5</b>                  | Anatine endocasts: dorsal and ventral views                                  | 273         |
| <b>A5.6</b>                  | Anseriform endocasts: dorsal and ventral views                               | 274         |
| <b>A5.7</b>                  | Anseriform endocasts (cont.): dorsal and ventral views                       | 275         |
| <b>A5.8</b>                  | Galloansere endocasts: dorsal and ventral views                              | 276         |
| <b>A5.9</b>                  | Complete Modular Lm data: PCA of all modules                                 | 277         |
| <b>A5.10</b>                 | Complete Modular Lm data: PCA of Emsg, Tel.c. and Cer. modules               | 277         |
| <b>A5.11</b>                 | Complete Modular Distance data: PCA of all Distance modules                  | 278         |
| <b>A5.12</b>                 | Complete Modular Surface Area data: PCA of all Surface Area modules          | 278         |
| <b>A5.13</b>                 | Modular Lm data: Mes.+ Tri.g D-PGLS Sub-Family regression plots              | 279         |
| <b>A5.14</b>                 | Complete Modular Lm data: PCA of Mes., Tri.g and Rho. modules                | 280         |

| <i>List of Tables</i> |  | <b>Page</b> |
|-----------------------|--|-------------|
| <b>A3.1</b>           | Radiocarbon ages: Honeycomb Hill, Hodges Creek and Castle Rocks sites                | 113         |
| <b>A3.2</b>           | Modularity analysis: matrix of pairwise covariation ratios                           | 119         |
| <b>A3.3</b>           | Modular Distance, Linear Distance and Modular Surface Area data                      | 120         |
| <b>A4.1</b>           | Modular Distance data: Chapter 4 galloanseres  | 202         |
| <b>A4.2</b>           | Modular Surface Area data: Chapter 4 galloanseres                                    | 204         |
| <b>A4.3</b>           | Gastrolith size, gizzard mass and body mass data: moa, emu and droms.                | 206         |
| <b>A4.4</b>           | Cranial measurements: <i>Dromornis stirtoni</i> and <i>D. planei</i> NTM collections | 208         |
| <b>A5.1</b>           | Modular Lm data: Phylo. signal and D-PGLS model results                              | 281         |
| <b>A5.2</b>           | Modular Distance values: Complete (n=34) data set                                    | 282         |
| <b>A5.3</b>           | Modular Distance ratios: Complete (n=34) data set                                    | 283         |
| <b>A5.4</b>           | Modular Distance data: Phylo. signal and D-PGLS model results                        | 284         |
| <b>A5.5</b>           | Modular Distance data: Phylo. sig. and cov-PGLS model results                        | 285         |
| <b>A5.6</b>           | Modular Surface Area values: Complete (n=34) data set                                | 286         |
| <b>A5.7</b>           | Modular Surface Area ratios: Complete (n=34) data set                                | 287         |
| <b>A5.8</b>           | Modular Surface Area data: Phylo. sig. and cov-PGLS model fitting results            | 288         |
| <b>A5.9</b>           | Modular Surface Area data: Phylo. sig. and D-PGLS model fitting results              | 289         |

## CHAPTER 1

## INTRODUCTION

This thesis explores functional and phylogenetic transformations in endocranial structure in various fossil and extant galloanseres. To set the scene for this work, this Introduction is divided into two major sections: **1**, first, I review the taxonomic composition, phylogenetic relationships and fossil record of the taxa within the Superorder Galloanserae (Class: Aves), including the living Orders Galliformes (landfowl) and Anseriformes (waterfowl), and extinct relatives. Most fossils covered here derive from the Cenozoic Era, a geological period defined as extending from the Cretaceous-Palaeogene (K-Pg) boundary (ca. 66 Million years ago) through to the present day. The reviews have an Australasian focus and set the scene for description and interpretation of the fossil taxa that will be described, analysed and discussed in this thesis. **2**, Secondly, avian neuroanatomy, and the methodology that has enabled a detailed appreciation of the structure of the avian brain, through its reconstruction from skeletal and fossil materials is reviewed. Endocranial nomenclatural protocols, and morphological and functional attributes of the avian brain are introduced. Finally, the field of geometric morphometrics, whereby geometric information described by anatomical landmarks, may be mathematically analysed to assess variation and covariation of organismal shape is reviewed. This section sets the scene for the analyses, description and interpretation of the previously unknown endocranial anatomy of focal fossil taxa, and the identification of phylogenetically informative avian endocranial morphology. [Note: throughout this thesis, I use the terms “Paleocene” to describe the earliest Epoch of the Cenozoic Era, and “Palaeogene” to describe the earliest Period of the Cenozoic Era *sensu* Pulvertaft (1999)].

**1.1 The phylogeny of modern birds (Neornithes)**

After almost 155 years of research, the Cretaceous origin of modern birds as indicated by molecular analyses, is supported by morphological and paleontological data (see Lee et al. 2014, and references therein). The mid-Cretaceous age of ca. 113.2 Million years ago (Ma) for crown Aves suggested by those authors, is consistent with recent and comprehensive dated molecular phylogenies (see also Jetz et al. 2012). Additionally, multiple lines of evidence strongly support several clades of Neornithes as having a Cretaceous origin, and the main structures of avian higher-level phylogeny are widely accepted (see Kriegs et al. 2007; Eo et al. 2009; Mayr 2011a; Jarvis et al. 2014; Burleigh et al. 2015; Prum et al. 2015).

Although the DNA–DNA hybridization studies of Sibley & Ahlquist (1990) stimulated new research in avian systematics, aspects of their proposed phylogeny have not been supported by more recent studies (e.g. Cracraft et al. 2004; Harshman 2007; Jarvis et al. 2014), and it has proved an unreliable basis for phylogenetic inference (Mayr 2011a). More recent phylogenetic analyses provide

a more robust framework for an interpretation of fossil taxa (e.g. [Cracraft et al. 2004](#); [Ericson et al. 2006](#); [Kriegs et al. 2007](#); [Mayr 2008a](#); [Hackett et al. 2008](#)). Molecular analyses have resolved the order of early neornithine divergences, and it is now accepted that Neornithes comprise two clades: Palaeognathae, and Neognathae ([Fain & Houde 2007](#); [Harshman 2007](#); [Kriegs et al. 2007](#); [Mayr 2011a](#); [Jarvis et al. 2014](#); [Claramunt & Cracraft 2015](#); [Prum et al. 2015](#)). The palaeognath clade includes the extant volant Tinamidae, the flightless ratites (Rheidae, Struthionidae, Casuariidae, and Apterygidae), and the extinct flightless ratites (Dinornithiformes and Aepyornithidae). This clade, inclusive of the five extant ratite taxa, is supported by several cranial morphological characters (see [Bock 1963](#); [Parkes & Clark 1966](#); [Cracraft 1974](#); [Mayr & Clarke 2003](#)), and was robustly supported by new generation molecular analyses (e.g. [Hackett et al. 2008](#); [Phillips et al. 2010](#); [Mitchell et al. 2014b](#); [Burleigh et al. 2015](#); see also [Mayr 2011a](#)). Neognathous birds comprise the sister clades Galloanseres and Neoaves ([Sibley & Ahlquist 1990](#); [Livezey & Zusi 2007](#); [Kriegs et al. 2007](#); [Mayr 2011a](#); [Jarvis et al. 2014](#)), with a derived reduction in the phallus and associated structures being a neoavian apomorphy (see [Livezey & Zusi 2007](#); [Montgomerie & Briskie 2007](#); [Mayr 2008b, 2011a](#); [Brennan et al. 2008](#)). As further discussion of Neoaves and Palaeognathae falls beyond the scope of this review, the following will focus on the relationships within Galloanseres.

## 1.2 Galloanseres

Galloanseres comprises four clades having a late Cretaceous Gondwanan divergence ([Worthy et al. 2017b](#), see also [2017c](#)). The Superorder is formed by Gastornithiformes, including the giant flightless Gastornithidae (Eurasia and North America) and Dromornithidae (Australia), Galliformes (landfowl), and Anseriformes (waterfowl), and a fourth clade represented by the Cretaceous Vegaviidae, (Antarctica), which together form the sister group to Neoaves, comprising all remaining taxa ([Worthy et al. 2017b](#); [Mayr et al. 2018](#)). A possible addition, and somewhat notable current exclusion from galloanseres are the Odontopterygiformes Howard, 1957, comprising several extinct pelagornithid taxa known as “bony-toothed birds”. These were large marine taxa, which appear to have had a global distribution from the late Paleocene through to the Pliocene ([Mayr 2009](#)). A systematic appraisal of the taxon by [Bourdon \(2005\)](#), reported minimally 12 apomorphies uniting pelagornithids with anseriforms (see [1.4](#) below). However, [Mayr \(2017:124\)](#) suggests pelagornithids are likely outside of Neognathae, as they lack the derived characteristics of crown Galloanseres, thus their hypothesised position within the clade remains unresolved.

Molecular analyses including DNA–DNA hybridization, mitochondrial and nuclear gene sequences ([Sibley & Ahlquist 1990](#); [Sorenson et al. 2003](#); [Cracraft et al. 2004](#); [Fain & Houde 2004](#); [Ericson et al. 2006](#); [Kriegs et al. 2007](#); [Hackett et al. 2008](#); [Eo et al. 2009](#); [Jarvis et al. 2014](#)), and morphological character analyses ([Livezey 1997b](#); [Livezey & Zusi 2001, 2007](#); [Mayr & Clarke 2003](#)), have unequivocally supported the monophyly of Galloanseres.

A sister group relationship between Galliformes and Anseriformes within Galloanseres was previously suggested by [Beddard \(1898:304\)](#) and [Simonetta \(1963\)](#), but has only been generally accepted after compelling molecular evidence became available (e.g. [Cracraft 1981, 1985](#); [Sibley et al. 1988](#); [Sibley & Ahlquist 1990](#); [Dzerzhinsky 1995](#); [Groth & Barrowclough 1999](#); [Cracraft 2001](#); [Mayr & Clarke 2003](#); [Fain & Houde 2004, 2007](#); [Poe & Chubb 2004](#); [Cracraft et al. 2004](#); [Harrison et al. 2004](#); [Ericson et al. 2006](#); [Hackett et al. 2008](#); [Jarvis et al. 2014](#)). As with palaeognathous birds, neurocranial features form the few known morphological apomorphies of Galloanseres ([Dzerzhinsky 1995](#); [Ericson 1996](#); [Cracraft & Clarke 2001](#); [Worthy et al. 2017b](#)), including those of the basiptyergoid, quadrate and mandibular processes ([Mayr 2009, 2017](#)). Extant anseriform and galliform birds are distinct in their postcranial skeletal morphology, but some of the differences are derived from the evolution of a large crop in the landfowl, which is lacking in Palaeogene stem group galliforms ([Mayr 2006](#)).

There is general agreement regarding the relationships of the major groups of extant Galloanseres, but the evolutionary history of the clade is presently not well understood ([Mayr 2009, 2011a, 2017](#)). This is due in part to the assignment of “very disparate” ([Mayr 2011a:61](#)) fossil taxa to this taxon (e.g., the anseriform-like Presbyornithidae, and the giant Gastornithiformes; see below). If all of these taxa are assigned correctly, a dramatic late Mesozoic/early Paleocene radiation must have occurred within the clade (see [Mayr 2011a](#)).

### 1.2.1 Gastornithiformes

Dromornithid and gastornithid affinities were recently further refined, with recognition of the strongly supported clade Gastornithiformes [Stejneger, 1885](#), inclusive of both taxa. Together, the dromornithids and gastornithids comprise a clade of giant flightless birds analogous with the flightless palaeognaths, with wide distributions across the Northern and Southern Hemispheres ([Worthy et al. 2017b](#), see also [2017c](#)).

**1.2.1.1 Gastornithidae**—gastornithids are large, flightless and graviportal birds known from the Paleocene to middle Eocene of Europe, and the early Eocene of North America and Asia. The taxon *Gastornis* [Hébert, 1855](#) was named in Europe from the late Paleocene–early Eocene of France ([Martin 1992](#)). This precluded recognition of their similarity to a North American species described as *Diatryma* [Cope, 1876](#) within the taxon Diatrymidae ([Cope 1876](#); [Dollo 1883](#); [Shufeldt 1909](#); [Matthew & Granger 1917](#); see also [Mayr 2009](#)). [Martin \(1992:107\)](#) noted morphological similarities between *Diatryma* and *Gastornis*, synonymization was suggested by [Buffetaut \(1997:187\)](#), and was formalised by [Mlíkovský \(2002:94\)](#). [Buffetaut \(2008\)](#) concurred that the minor morphological differences between these taxa did not support the taxonomic separation of *Diatryma* and *Gastornis*. [Mayr \(2009\)](#) considered it sensible to subsume the North American and European species in *Gastornis*, which has taxonomic priority. This was subsequently effected, and all taxa are now assigned to *Gastornis* ([Buffetaut 2013](#); [Mayr 2017](#)).

Gastornithidae were first recorded from the Paleocene of Walbeck in Germany (Mayr 2007a). The Walbeck specimen may belong to *Gastornis russelli* Martin, 1992, described from the late Paleocene of Reims, France, which is the smallest named species (Martin 1992:102). Mayr (2009) noted it is likely conspecific with *Gastornis minor* Lemoine, 1878, also named from Reims, and considered a *nomen dubium* by Martin (1992:101). *Gastornis russelli* is a small taxon which measures less than half the size of the late Paleocene–early Eocene *G. parisiensis* Hébert, 1855 (Mayr 2009). Martin (1992) argued *G. parisiensis* and *G. russelli* are the only valid Paleocene European species of gastornithid (see also Angst & Buffetaut 2013), and that *G. parisiensis* was synonymous with “*G. edwardsi*” Lemoine, 1878 from the Paleocene of France, and “*G. klaasseni*” Newton, 1886 from the early Eocene of England (Mayr 2009). Bourdon et al. (2016) referred several fossils from La Borie in France to *G. parisiensis*, which constituted the southernmost occurrence of this taxon in Europe. Those authors argued the wide geographical and temporal distribution of *G. parisiensis* included notable intraspecific size and shape variation, implying marked sexual dimorphism within the taxon. Buffetaut (2008) reported a gastornithid tibiotarsus from the early Eocene of Saint-Papoul in France, the age of which supports earlier hypotheses that large eggs from the early Eocene of Provence (see Dughi & Sirugue 1959; Fabre-Taxy & Touraine 1960; Touraine 1960), and later from Languedoc (Villatte 1966), belong to the Gastornithidae. Gastornithids continued into the Eocene in Europe with *G.* (“*Diatryma*”) *geiselensis* (Fischer, 1978), from the middle Eocene of Messel and the Geisel Valley (Fischer 1962, 1978; Peters 1988, 1991), which Mlíkovský (2002:96) regarded as a junior synonym of *G. sarasini* (Schaub, 1929) from the early Eocene of France. According to Mayr (2009, 2017), a comprehensive revision of European taxa is required.

Andors (1992) revised North American Gastornithidae, recognising two species: *Gastornis* (“*Diatryma*”) *giganteus* (Cope, 1876), and *G.* (“*D.*”) *regens* (Marsh, 1894). Both are confined to the early Eocene Wasatch and Willwood Formations (see also Andors 1991). Cockerel (1923) described feathers from the early Eocene of Colorado, and proposed they belonged to *Gastornis* (“*Diatryma*”), an identification disputed by Wetmore (1930). Andors (1992) concluded gastornithids are sister to anseriforms and argued for a European origin, which agrees with the temporal occurrence of the known species (see also Buffetaut 1997; Angst & Buffetaut 2013). Gastornithids likely dispersed into North America from Europe in the early Eocene, and were graviportal birds which lived in forested environments (Andors 1992; Mayr 2009).

*Gastornis xichuanensis* (Hou, 1980) was originally named in *Zhongyuanus* from the early Eocene of China, but was later redescribed and subsumed into *Gastornis* by Buffetaut (2013), despite Andors (1992:113) having noted this species is morphologically dissimilar to European and North American Gastornithidae. Buffetaut (2004) commented on late Eocene footprints of giant birds from France, assigned to *Gastornis*, but which lack contemporary comparative late Eocene skeletal material of the trackmaker. Similarly, Patterson & Lockley (2004) described *Ornithoformipes controversus* from a middle Eocene bird track from Washington, and assigned it to a *Gastornis*-like bird. Mayr

(2009) questions their referral, and suggested the footprints are about five Ma younger than known North American gastornithid fossils. If, however, they were from a species of *Gastornis*, they would establish the presence of “hooflike” phalanges in this taxon (Mayr 2009), comparable with those of the Miocene dromornithid birds from Australia (see below). Gastornithids were characterized by Andors (1992) as having a large, bilaterally compressed beak, a convex culmen lacking a hooked tip, wings that are considerably reduced, and a carina-less sternum. The largest gastornithid species attained a height of approximately 2 metres (m), with an estimated mass of about 175 kilograms (kg; Mayr 2009).

Some authors have argued that gastornithids were carnivorous (see Witmer & Rose 1991:95). However, Andors (1992:117) and Angst et al. (2014) advanced the hypothesis that they were herbivores. Angst & Buffetaut (2013) described a gastornithid mandible from the Paleocene of Mont-du-Berru in France, suggesting the mandibular morphology was not indicative of a carnivorous diet for these birds. This was further supported by an herbivorous diet being compellingly argued for the Dromornithidae (Murray & Vickers-Rich 2004; see below), some of which display a similar bill shape (see Murray & Megirian 1998; Murray & Vickers-Rich 2004).

**1.2.1.2 Dromornithidae**—are reviewed comprehensively as part of the Introduction to Chapter 4 (see 4.1 below), and so shall not be here.

**1.2.1.3 Vegaviidae**—fossils from Antarctica represent the most comprehensive record of Mesozoic neognaths (Mayr 2017). The earliest vegaviid fossil derives from the Late Cretaceous López de Bertodano Formation, Vega Island, western Antarctica, and was initially reported as a presbyornithid within Anseriformes by Noriega & Tambussi (1995). The fossil was later named *Vegavis iaai* Clarke et al., 2005 and recovered in an unresolved polytomy including Anatidae + *Presbyornis*, nested within crown group Anseriformes. Clarke et al. (2005) argued *Vegavis* was more derived than Anseranatidae, and that there were differences in limb proportions compared with *Presbyornis*. Subsequently, a second, better preserved fossil of the taxon was reported by Clarke et al. (2016). The tarsometatarsus of *Vegavis* reveals a complex trisulcate hypotarsus arrangement, features of which were posited by Clarke et al. (2005) as indicative of its anseriform affinities, and reasonably so, as it does resemble those of Anatidae (see Mayr 2015:11). However, Mayr (2017:91) noted the independent evolution of such hypotarsal morphology in “several neognathous groups”, precluded *Vegavis*’ anseriform designation.

Although the taxon’s crown anseriform affinities were questioned by Mayr (2009, 2013) and later by Feduccia (2014), *Vegavis iaai* was proposed as a “vetted” fossil calibration for phylogenetic divergence time estimation analyses, due to “unambiguously optimized synapomorphies” nesting the taxon within crown Anseriformes (Ksepka & Clarke 2015:5). Subsequently, the taxon was used to temporally define the split between Anatidae and remaining Anseriformes by Jetz et al. (2012), apparently with “disastrous consequences” (see Feduccia 2014:7). The fossil had been excluded from the analyses of Ericson et al. (2006) and Prum et al. (2015) for these reasons (Mayr et al. 2018).

From the López de Bertodano Formation, a putative gaviiform *Polarornis gregorii* Chatterjee, 2002 was described from an “incomplete but beautifully preserved” partial skeleton (Chatterjee 2002:126). However, Mayr (2004:281) describes the fossil as a “very fragmentary” assemblage, for which “substantial parts” were reconstructed. Additional fragmentary post cranial material from Vega and Seymour Islands were subsequently assigned to *Polarornis* by Acosta Hospitaleche & Gelfo (2015). Although Acosta Hospitaleche & Gelfo (2015:321) state Mayr & Scofield (2014) suggested *Vegavis* was “considered to have a strong similarity with *Polarornis*”, the latter authors actually advanced that while the neognathous *Australornis lovei* Mayr & Scofield, 2014 resembles *V. iaii* in some osteological details, it was distinct in several “salient features”. In fact, Mayr & Scofield (2014) do not refer to *Polarornis* other than in their systematic comparison of the taxon with *Australornis*, wherein they describe several distinct differences between them (see also Mayr et al. 2018:179).

The comprehensive phylogenetic analyses conducted by Worthy et al. (2017b, see also 2017c) “robustly” placed *Vegavis* in Galloanseres, but excluded it from Anseriformes, reinforcing its unsuitability for calibration of molecular analyses (see below). However, Worthy et al. (2017b) did not “conclusively” resolve vegaviid affinities within galloanseres (Mayr et al. 2018).

Subsequently, several Antarctic fossils were assigned into the inclusive Vegaviidae Agnolín et al., 2017. Actions described by Mayr et al. (2018:179) as “neither justifiable nor useful”. Agnolín et al.’s (2017) erection of Vegaviidae, a clade inclusive of *Vegavis*, *Polarornis* and several other fossil taxa from the Upper Cretaceous and Paleocene of the Southern Hemisphere, found Vegaviidae as the sister taxon of crown group Anseriformes. However, Mayr et al. (2018) found multiple issues with the assignments of several taxa to the new clade by Agnolín et al. (2017).

It is beyond the scope of this review to list all taxa along with those morphological distinctions, comprehensively detailed by Mayr et al. (2018), collectively precluding each taxon’s vegaviid affinities. Aside from noting that *Vegavis* and *Polarornis* were the only fossil taxa accepted as representative of Vegaviidae by those authors. Additionally, Mayr et al. (2018:184) advised that, given the complexities inherent in the phylogenetic study of extant birds, it would be “surprising” if the phylogenetic assignment of the earliest neornithine representatives was “straightforward” when using much more limited morphological data.

### 1.3 Galliformes

Within extant Galliformes, the megapodes (Megapodiidae) are the sister group of a clade including South American guans (Cracidae), guinea fowl (Numididae), New World quails (Odontophoridae), and partridges, pheasants, turkeys and kin (Phasianidae). Within Phasianidae, turkeys, formerly listed with subfamily status as Meleagridinae, are now in tribe Tetraonini with other grouse (see Dickinson & Remsen 2013).

**1.3.1 Origins of the Galliformes**—several fragmentary fossils from the Late Cretaceous of North America have been assigned to galliform birds (see Hope 2002; Clarke 2004). Earlier authors

described *Palaeophasianus meleagroides* Shufeldt, 1913 from the lower Eocene Willford Formation, Wyoming, as cracids (e.g. [Brodkorb 1964:303](#)). However, [Mayr \(2009:101\)](#) considers this taxon to be best placed in Geranoididae, i.e., related to cranes. Similarly, species of *Filholornis*, e.g. *F. paradoxus* Milne-Edwards, 1892, *F. gravis* Milne-Edwards, 1892, and *F. debilis* Milne-Edwards, 1892 from the upper Eocene/lower Oligocene Phosphate de Caux deposits in France, were listed by [Brodkorb \(1964:302\)](#) within Cracidae. [Mlíkovský \(2002:180\)](#) listed these species under the taxon *Talantatos* within Cariamidae. [Mayr \(2009:142\)](#) listed *Filholornis* as representatives of the Cariamae taxa *Idiornithidae* and *Elaphrocnemus*. What is more, the wing bones assigned to *Filholornis* by [Milne-Edwards \(1891\)](#), and the hindlimb bones described as *Elaphrocnemus* by [Mourer-Chauviré et al. \(1983\)](#), likely belong to the same taxon ([Mayr 2009](#); see also [Olson 1985:114](#)). Whatever their true affinities, these taxa are certainly not galliforms ([Mayr 2009](#)).

The earliest undisputed and best-preserved galliforms are two species of Gallinuloididae from Europe and North America (see below). Both species are considered to be outside crown group Galliformes ([Mayr 2000, 2005](#); [Mayr & Weidig 2004](#); [Ksepka 2009](#)). Additional stem group galliforms in Paraortygidae and Quercymegapodiidae (see below), are known from the middle Eocene to upper Oligocene Quercy fissure fillings in France (see [Mourer-Chauviré 1992](#)). Crown group galliforms have no pre-Oligocene fossil record ([Mayr 2005](#)), and the evolution of a large distinctive crop may have occurred in the mid-Palaeogene, in response to competition with other herbivorous birds or mammals, after the spread of grasslands through the Oligocene and Miocene (e.g. [Jacobs et al. 1999](#); [Mayr 2006](#)). The Palaeogene record of galliform birds is comparatively extensive and provides some insights into the evolution of the clade. Importantly, there is only one Palaeogene galliform bird that has been named from Africa. *Namaortyx sperrgebietensis* Mourer-Chauviré et al., 2011 was described as a galliform, family *incertae sedis*, from the middle Eocene of Namibia ([Mourer-Chauviré et al. 2011:618](#)). In addition, there is a record of early Miocene phasianids from Namibia (see [Mourer-Chauviré 2008](#); and Phasianidae below), indicating a Northern Hemisphere diversification of the taxon ([Mayr 2009](#)).

**1.3.2 Gallinuloididae**—the earliest record of fossil galliform birds comes from the description of *Gallinuloides wyomingensis* Eastman, 1900, represented by four skeletons from the early Eocene Green River Formation in North America ([Grande 1980](#); [Mayr & Weidig 2004](#); [Weidig 2010](#)). From the early Eocene of Europe, *Paraortygoides messelensis* Mayr, 2000 was named from Messel in Germany, and *P. radagasti* Dyke and Gulas, 2002 from the London Clay ([Mayr 2000, 2006](#); [Dyke & Gulas 2002](#)). [Mayr \(2009\)](#) considered that *P. radagasti* may be a junior synonym of either *Argillipes paralectoris* Harrison & Walker, 1977, or *A. aurorum* Harrison & Walker, 1977, both described from the same locality (see [Mayr 2005:fig. 6.4](#); and **1.3.9** below). *Taoperdix pessieti* (Gervais, 1862), named from the late Oligocene of France, was considered by [Mayr & Weidig \(2004\)](#) to not be a member of the Gallinuloididae (*contra* [Brodkorb 1964](#)), but may in fact be a member of the Paraortygidae (see **1.3.4** below), specimens with which the fossil had not been compared ([Mayr &](#)

Weidig 2004). Additionally, two specimens that had been assigned to *T. pessieti* (Milne-Edwards 1867–1871; Eastman 1905) correspond to *Paraortyx brancoi* (see 1.3.4 below) in size (Mayr 2009). According to Mayr & Weidig (2004:216) and Mayr (2009:38), the fossil identified as *Taoperdix* sp. by Mourer-Chauviré (1988, 1992) from the late Eocene Quercy fissure filling in France, also needs to be restudied to clarify its affinities. *Archaelectrornis sibleyi* Crowe & Short, 1992 was described as a gallinaceous bird from the early Oligocene of Nebraska, USA (Crowe & Short 1992), but this fossil was argued by Mayr & Weidig (2004:216) and Mayr (2009:38) to have been incorrectly assigned to Gallinuloididae (see 1.3.6 below). The hind limbs of a putative galliform bird were described by Lindow & Dyke (2007) from the lower Eocene Fur Formation in Denmark. However, Mayr (2009:39) considers this specimen to be incorrectly assigned due to insufficient material.

Notably, there has been much disagreement regarding the taxonomic affinities of gallinuloidids. For example, a crown position for *Gallinuloides wyomingensis* within galliforms was initially supported by several earlier authors (e.g. Tordoff & Macdonald 1957; Brodkorb 1964; Ballmann 1969; Crowe & Short 1992), and later by Dyke (2003b), who argued the taxon was “not basal within the order” (see also Dyke et al. 2003). In fact, although Dyke & Gulas (2002) agreed *Paraortygoides* was likely a stem galliform, Mayr (2009:39) found it “difficult to understand” why van Tuinen & Dyke (2004) subsequently used *G. wyomingensis* as a crown group calibration in their molecular analysis of extant galliforms. Similarly, in their analyses of the affinities of Odontophoridae (see below), Cox et al. (2007:78) employed *G. wyomingensis* as a crown galliform calibration, along with “*Schaubortyx*” (presumably *S. keltica*—see 1.3.9), as a crown calibration of the *Gallus* + *Coturnix* clade. Crowe et al. (2006) and Pereira & Baker (2006) used both *G. wyomingensis* and the putative rallid taxon *Amitabha urbsinterdictensis* Gulas-Wroblewski & Wroblewski, 2003 (see 1.3.9 below), to calibrate their molecular assessments of galliforms. What is more, Dyke & Crowe (2008) continued to firmly advocate gallinuloidid crown group affinities. The taxon’s use as calibration has been criticised by several authors (e.g. Mayr & Weidig 2004; Mayr 2006, 2009; Ksepka 2009; Weidig 2010), the use of which has likely influenced an overestimation of galliform divergence ages (see Ksepka 2009).

In summary, gallinuloidids likely comprise only *Gallinuloides* and *Paraortygoides*, and the taxa are the only stem group galliforms represented by well-preserved skeletons (Mayr 2009). Osteological features of the humerus, amongst others (see Mayr 2009:39), show that gallinuloidids form the sister clade to all other galliform birds (Mayr 2006, 2009, 2017; Ksepka 2009; Weidig 2010).

**1.3.3 Quercymegapodiidae**—was erected for *Quercymegapodius depereti* (Gaillard, 1908) and *Q. brodkorbi* Mourer-Chauviré, 1992, named from the late Eocene Quercy fissure fillings (Mayr 2009). From the late Eocene Paris Gypsum, *Ludiortyx hoffmanni* (Gervais, 1852) was initially classified into Rallidae by Brunet (1970) and Cracraft (1973). *L. hoffmanni* was considered by Mayr (2005) to be a quercymegapodiid because of a plesiomorphic feature of the carpometacarpus shared with gallinuloidids. Similarly, *Taubacrex granivora* Alvarenga, 1988, named from the late Oligocene/early Miocene Taubaté Basin in Brazil, was originally described in Rallidae (Alvarenga

1988), but was later recognised as a quercymegapodiid by Mourer-Chauviré (2000). *Ameripodius silvasantosi* Alvarenga, 1995, was described as a quercymegapodiid from the same site, and Mourer-Chauviré (2000) supported this distinction. Specimens of *Taubacrex* provide the earliest record of gastroliths in fossil galliforms (Mayr 2009). Quercymegapodiids are recognised as stem group Galliformes (Mayr 2009), and despite initial comparisons with megapodes, their similarities to extant megapodiids are plesiomorphic (see Mourer-Chauviré 1992; Mayr 2009). Nonetheless, some studies (e.g., van Tuinen & Dyke 2004 and Crowe et al. 2006) have incorrectly calibrated molecular divergence times using this clade (see above, and Mayr & Weidig 2004; Mayr 2008a for critiques).

**1.3.4 Paraortygidae**—are stem group galliforms from middle Eocene to late Oligocene Quercy fissure fillings in France (Mourer-Chauviré 1992), and from the early Oligocene of Germany (Fischer 1990, 2003). Paraortygidae comprises three recognised species: the late Eocene and early Oligocene *Paraortyx brancoi* Gaillard, 1908, *P. lorteti* Gaillard, 1908, and *Pirortyx major* (Gaillard, 1939), described from early and late Oligocene fossil sites (Mourer-Chauviré 1992). As previously noted, *Taoperdix pessieti* although named as a paraortygid, may be representative of the Gallinuloididae (see above). Paraortygids differ from gallinuloidids and quercymegapodiids in that the carpometacarpus is shorter and more robust, and is similar in proportion to those of extant galliforms (Mayr 2009).

**1.3.5 Megapodiidae**—constitute one of five extant families within the order Galliformes (see Kriegs et al. 2007; Eo et al. 2009; Mayr 2011a). As all megapodes, extinct or extant, are restricted to the Australasian and Oceania geographic regions, descriptions of this taxon are included within the Australasian galliform fossil record below (see 1.3.10).

**1.3.6 Cracidae**—from the late Eocene and early Oligocene of North America comes *Procrax*, *Archaelectornis*, and *Palaeonossax*, which are three taxa that may be closely related and are discussed together. *Procrax brevipes* Tordoff & Macdonald, 1957 was named from the late Eocene Chadron Formation of South Dakota. Tordoff & Macdonald (1957) considered this taxon related to Cracidae and placed it into Gallinuloididae. *Procrax* was listed by Brodkorb (1964:300) in Cracidae, but Olson (1985:115) noted that the fossil was incompletely prepared, preventing a thorough evaluation of its affinities (see also Ksepka 2009). *Procrax* differs postcranially from the Gallinuloididae and the Quercymegapodiidae, but Mayr (2009) considered skeletal elements of *Procrax* to “closely resemble those of the Paraortygidae”, and it is unlike any Palaeogene phasianid. Mayr (2009) concluded that *Procrax* is closely related to *Archaelectornis sibleyi* (see above), which was not compared with *P. brevipes* in its original description, and was considered more similar to Phasianidae by Crowe & Short (1992). Additionally, Mayr (2009) argued the humeri of *Procrax* and *Archaelectornis* match that of the paraortygid *Pirortyx major*. Wetmore (1956) described *Palaeonossax senectus* Wetmore, 1956, from the early Oligocene Brule Formation of South Dakota, as a member of the Cracidae. However, *P. senectus* appears quite similar to *Procrax* and *Archaelectornis* (see Mayr 2009), thus further comparisons are required to be made between these

taxa to resolve their true familial affinities. In summary, the Cracidae have no unambiguous Palaeogene fossil record (Mayr 2009; see also Olson 1985:114-115).

*Boreortalis laesslei* Brodkorb, 1954 was named from the lower Miocene of Gilchrist County, Florida. Brodkorb (1954:181) remarked that three other cracids described by Wetmore and Miller (see below) in the genus *Ortalis*, may be referable to *Boreortalis* (contra Olson & Farrand [1974:118]; who stated Brodkorb had suggested *Boreortalis* might be referable to *Rhegminornis* [see 1.3.9]). However, Brodkorb (1954:180) was apparently in no doubt of the cracid affinities of these fossils). Brodkorb (1964:304-305) subsequently subsumed *Boreortalis phengites* (Wetmore, 1923) from the lower Pliocene of Nebraska, *B. tantala* (Wetmore, 1933) from the lower Miocene of Nebraska, and *B. pollicaris* (A. H. Miller, 1944) from the lower Miocene of South Dakota into *Boreortalis*; this action was described by Olson (1985:115) as having been “purely arbitrary” in nature.

Cracidae are currently limited to a Neotropical distribution, but they are believed to have originated in North America (Olson 1985:116). Currently there are 50 species and over 60 subspecies within eleven genera in three morphological subgroups in the clade: guans (*Aburria*, *Chamaepetes*, *Oreophasis*, *Penelope*, *Penelopina*, and *Pipile*), chachalacas (*Ortalis*) of the subfamily Penelopinae, and curassows (*Crax*, *Mitu*, *Nothocrax*, and *Pauxi*) of the subfamily Cracinae (see Pereira et al. 2002).

**1.3.7 Numididae**—from the late Eocene of Mongolia *Telecrex grangeri* Wetmore, 1934 was originally described as a rallid within Telecrecinae. Olson (1974:246; see also Olson 1985:17) assigned the specimens to Numidinae, but because this taxon is sister to all other phasianids, Mayr (2009) argued the similarities between *Telecrex* and guinea fowl may be plesiomorphic for Phasianidae. Fossils of *Telecrex* have been used for molecular clock calibration (e.g. Cooper & Penny 1997), but its assignment to Numididae is not well supported until additional material is identified (Mayr 2009; see also Mourer-Chauviré 1992:69). *Telecrex peregrinus* (Mlíkovský, 1989) was named from the late Eocene of Quercy, France, but was based on material representative of a stem group cariamid. Mourer-Chauviré (1992:89) synonymised *T. peregrinus* with *Elaphrocnemus phasianus* (Milne-Edwards, 1892), asserting that the presence of Numididae in the Eocene of France is unproved, and inference thereof “must be deleted from the paleornithological literature” (see Mourer-Chauviré 1992:90). Mlíkovský (2002:182) then synonymised *Elaphrocnemus phasianus* with *Talantatos fossilis* (Giebel, 1847) in the Family Cariamidae. Cracraft (1973:508) proposed the evolution of African numidines from a secondary phasianid radiation from the Old World, was more likely than the evolution of the taxon solely in Africa. *Numida meleagris*, the extant African guinea fowl, has been reported from several Pleistocene archaeological and cave sites in Europe (Brodkorb 1964:207). Currently, numidids are only found in Africa, represented by six species in four genera (Crowe 1978; Dickinson & Remsen 2013).

**1.3.8 Odontophoridae**—from the late Eocene of Canada *Nanortyx inexpectatus* Weigel, 1963 was described in Odontophorinae. Mayr (2009:43) argued this assignment “seems based on the fact the specimens are from very small galliform birds, and come from the New World”. For which the

same may apply to a specimen from the early Oligocene of Colorado, assigned by [Tordoff \(1951:203\)](#). [Brodkorb \(1964:310-311\)](#) listed five odontophorid species from North America: *Miortyx teres* A. H Miller, 1944 from the lower Miocene Rosebud Formation, South Dakota, *Cyrtonyx cooki* Wetmore, 1934 from the middle Miocene Sheep Creek beds of Nebraska, *Colinus hibbardi* Wetmore, 1944 from the upper Pliocene Rexford Formation, Kansas, *C. suilium* Brodkorb, 1959 and *Neortyx peninsularis* Holman, 1961, both from the middle Pleistocene Reddick beds of Florida. To which may be added *Miortyx aldeni* Howard, 1966 from the early Miocene of South Dakota ([Olson 1985:117](#)). Odontophorids may have been present in North America from the Oligocene, but better material is required to confirm this with any certainty ([Olson 1985](#)). Extant New World quail comprise ten genera and 32 temperate and tropical species, ranging from southern Canada to southern Brazil and northeastern Argentina ([Dickinson & Remsen 2013](#); [Hosner et al. 2015](#)).

**1.3.9 Phasianidae**—are a widely distributed and speciose group, occurring throughout a diversity of habitats ([Mayr 2009](#)). The monophyly of Phasianidae, including Tetraonini (see below) is supported by molecular studies (e.g. [Kriegs et al. 2007](#); [Ksepka 2009](#); [Wang et al. 2013](#)).

Several phasianid genera have been described from the early Eocene—early Oligocene of Sheppey, England including *Argillipes aurorum* Harrison & Walker, 1977 and *A. paralectoris* Harrison & Walker, 1977, but the material does not allow attribution to a distinct sub-family ([Mourer-Chauviré 1992](#)). [Mlíkovský \(2002:255-256\)](#) transferred both taxa to Aves *incertae sedis*. *Amitabha urbsinterdictensis* (see also **1.3.2** above) from the middle Eocene Bridger Formation, Wyoming was reported as the sister taxon of the Phasianidae (see [Gulas-Wroblewski & Wroblewski 2003](#)). An assignment criticized by [Mayr & Weidig \(2004\)](#), who argued the fossil lacked conclusive galliform apomorphies. In fact, [Mayr \(2009\)](#) considered this species to “show little resemblance to galliform birds, let alone Phasianidae”. [Ksepka \(2009\)](#) conducted a re-examination of *A. urbsinterdictensis*, conclusively refuted its placement in Galliformes, and supported rallid affinities for the fossil. It is notable that *A. urbsinterdictensis* has been used for the calibration of molecular clocks (see [Pereira & Baker 2006](#); [Crowe et al. 2006](#)), albeit being undoubtedly not within crown group Galliformes (see [Mayr & Weidig 2004](#); [Mayr 2008a](#); [Ksepka 2009](#) for critiques).

The first unambiguous Phasianidae are represented by specimens of *Palaeortyx* reported from Oligocene Quercy fissure fillings and Allier deposits in France ([Mourer-Chauviré 1992](#); [Mourer-Chauviré et al. 2004](#)). [Mourer-Chauviré \(2006\)](#) assigned the Quercy species to *P. brevipes* Milne-Edwards, 1869, *P. gallica* Milne-Edwards, 1869, *P. prisca* (Milne-Edwards, 1869), and *P. phasianoides* Milne-Edwards, 1869. [Mayr et al. \(2006\)](#) reported an almost complete, articulated skeleton of *Palaeortyx* cf. *gallica* from the late Oligocene maar lake deposits of Enspel, Germany. This specimen preserves gastroliths, and exhibits several postcranial plesiomorphies for Phasianidae or non-numidine Phasianidae. [Ballmann \(1969\)](#) presumed a close relationship between *Palaeortyx* and *Arborophila* from the tropical and subtropical regions of Asia. [Mayr et al. \(2006\)](#) considered the limb ratio criteria [Ballmann \(1969\)](#) used, rather supported a position of *Palaeortyx* outside crown

group Phasianinae. *Schaubortyx keltica* (Eastman, 1905) named from the late Oligocene of France (see [Eastman 1905](#); [Schaub 1945](#)), differs from *Palaeortyx* in the proportions of its femur and humerus ([Mourer-Chauviré 1992](#)), with the humerus being shorter than the femur (*contra* [Mlíkovský \[2002:153\]](#) who synonymized *Schaubortyx* and *Palaeortyx* with the extant taxon *Coturnix*). [Mayr \(2009:44\)](#) considered *Schaubortyx keltica* an early representative of Phasianidae, but argued its relationship within the group remain unresolved. Furthermore, after thoroughly reviewing the morphology of *Palaeortyx* and *Coturnix*, [Göhlich & Mourer-Chauviré \(2005:1333\)](#) did not accept the synonymy of [Mlíkovský \(2002:153\)](#). They argued *Palaeortyx* constituted a valid taxon, and recognised the four species of *Palaeortyx* (see above).

Several fossil Phasianidae were described from the Shanwang Formation in China: *Shandongornis shanwanensis* Yeh, 1977 and *Linqornis gigantis* Yeh, 1980, come from the middle Miocene, and *Diangallus mious* Hou, 1985, and *Phasianus lufengia* Hou, 1985, from the upper Miocene. [Cheneval et al. \(1991:123\)](#) reported a femur of a large phasianid from the early Miocene Li locality in Thailand, which was intermediate in size between *Gallus* and *Pavo*. It is larger than *S. shanwanensis*, *D. mious*, *P. lufengia*, and smaller than *L. gigantis*, which is similar in size to a large male *Pavo*. *Lophura wayrei* Harrison & Walker, 1982 was described in the extant genus *Lophura* from the upper Miocene of Northern Pakistan ([Harrison & Walker 1982](#)). These fossils suggest that large phasianids were already present at the end of the early Miocene in South East Asia ([Cheneval et al. 1991](#)). The earliest galliforms known from Africa are early Miocene phasianids reported from Elisabethfeld and Grillental, Northern Sperrgebiet in Namibia (see [Mourer-Chauviré 2008](#)).

Having appeared no later than the early Oligocene, phasianids became diverse in the Neogene, and some genera that are presently restricted to southeastern Asia, previously had wider ranges ([Zelenkov & Kurochkin 2009a](#)). From the middle Miocene Sharga locality, Oshin Formation, western Mongolia, the new genus and species *Tologuica aurorae* Zelenkov & Kurochkin, 2009a, and *Tologuica karhui* Zelenkov & Kurochkin, 2009a were named ([Zelenkov & Kurochkin 2009a](#)). Notably, *Tologuica* displays an apomorphic hypotarsus morphology similar to the late Pliocene genus *Plioperdix* Kretzoi, 1955, but characters of the coracoid, tarsometatarsus, and carpometacarpus conform with European species of *Palaeortyx* (see above) and *Palaeocryptonyx* Depéret, 1892 ([Zelenkov & Kurochkin 2009a:213](#); see also [Göhlich & Mourer-Chauviré 2005](#)). In a later study, [Zelenkov & Panteleyev \(2014\)](#) proposed apomorphic characters of the coracoid suggested *Plioperdix* is a sister-taxon of the extant genus *Coturnix*. The Naran Bulak locality, of the middle Miocene Oshin Formation, western Mongolia, yielded the new genus and species *Lophogallus naranbulakensis* Zelenkov & Kurochkin 2010, this was a large phasianid, similar in size to the extant *Gallus* ([Zelenkov & Kurochkin 2010](#)). In his review of the galliforms from Polgárdi, a series of late Miocene localities in central Hungary, [Zelenkov \(2016b\)](#) named the new genus and species *Mioryaba magyarica* Zelenkov, 2016b, however, its taxonomic position within Phasianidae could not be “unequivocally determined”. Additionally, he named the new genus and species *Eurobambusicola turolicus*

Zelenkov, 2016b which resembled the extant genus *Bambusicola* in several morphological features (see Zelenkov 2016b:628).

Zelenkov & Kurochkin (2009b) showed phasianids were only represented by two relatively small taxa in the late Pliocene of central Asia, as compared with the larger pheasants recognised from the Miocene and early Pliocene periods (see above). Zelenkov & Kurochkin (2010) argued this was suggestive of less densely forested habitats during the late Pliocene of central Asia.

*Gallus bravardi* Gervais, 1849 was described from Ardes, Puy-de-Dôme, France based on a distal left tarsometatarsus bearing a strong spur. This specimen is presumed lost, so a comparison cannot be made with specimens assigned by Depéret (1890) to *G. bravardi* from the Pliocene of Perpignan, France, which bear a similar spur. Mourer-Chauviré (1989:439) considered the morphology of *G. bravardi* corresponded to the genus *Pavo*, and transferred it. At the same time, she also synonymised the species *Pavo moldavicus* Bocheński & Kuročkin, 1987 with *Pavo bravardi* (Gervais, 1849). Mlíkovský (2002:164) subsequently synonymised *Phasianus etuliensis* (Bocheński & Kuročkin, 1987) with *Pavo bravardi*. The presence of peafowl has been established in Europe from the middle Miocene to the early Pleistocene (see Mourer-Chauviré 1989; Boev 2002a; 2002b; Mlíkovský 2002). All of the pre-Pliocene phasianid species have been assigned to extinct genera (see Brodkorb 1964:312), and Olson (1985:118) recommended a revision of the extant taxa and osteological comparisons made with fossils, in order to understand the relationships between extant taxa and the extensive phasianid fossil record with more certainty.

The turkeys, formerly Meleagridinae, and grouse, formerly Tetraoninae, were shown by molecular studies to be sister taxa, and so are now recognised as Tetraonini and deeply nested within Phasianidae (Kriegs et al. 2007). Turkeys have no Palaeogene fossil record and may not have diversified before the Neogene (Mayr 2009). The earliest representative of the clade Tetraonini comes from the lower Miocene of Gilchrist County, Florida, USA. This was *Rhegminornis calobates* (Wetmore, 1943), initially described in the new family Rhegminornithidae, and referred to Jacanidae. The taxon was listed by Brodkorb (1967:202) as such, but Olson & Farrand (1974) reviewed the material and assigned it to Meleagrididae (now Tetraonini). If this referral of *R. calobates* is correct, it extends the fossil record of the group into the lower Miocene. However, Steadman (1980:131) argued the fossil displays characteristics of both the Meleagridinae and Phasianinae, which is not surprising given the former is now subsumed into the latter. The oldest “certain” turkey is *Proagriocharis kimbballensis* Martin & Tate, 1970 from the upper Pliocene Kimball formation, Nebraska (Steadman 1980:131). *P. kimbballensis* was smaller than turkeys known from the Pleistocene, and *R. calobates* was an even smaller taxon (Olson & Farrand 1974). Fossil turkeys were once thought to consist of large taxa in the genera *Meleagris*, *Agriocharis*, and *Parapavo*, represented by several extinct and two extant species (Martin & Tate 1970:217). However, a comprehensive review was conducted of previously described turkeys from North America by Steadman (1980:151-152), who recognised only nine species in three genera, including the single extant species *Meleagris gallopavo*.

Phasianidae are a highly speciose taxon, comprising 178 species in 52 genera inhabiting most of the Americas, Europe, Asia, all of Africa excluding the driest deserts, and much of the east coast of Australia. The greatest diversity of species is in Southeast Asia and Africa (Dickinson & Remsen 2013).

As noted above, several galliform taxa are now accepted as stem rather than crown taxa, and anseriforms are not exempt from similar issues (see 1.4 below). In addition to those molecular analyses already noted, additional studies have used galloanserine taxa for molecular clock calibrations. Together these form a recurring theme where putative stem galloanserine taxa have been, and continue to be used, to temporally calibrate crown group divergences in molecular analyses. For example, Stein et al. (2015:161) used a combination of relaxed- and strict-clock molecular models, calibrated with *Vegavis* as a crown anseriform, *Palaeortyx* for the Numididae stem-split, *Boreortalis* as crown Cracidae, and *Rhegminornis* describing the Meleagridinae and Tetraoninae crown, and argued a diversification of crown Galliformes “well before” the K-Pg event (i.e. 83.6–108.3 Ma). In a subsequent study Wang et al. (2016:5), used maximum likelihood and Bayesian methods, *Schaubortyx* to calibrate the split between *Coturnix* and *Gallus*, and *Vegavis* as a crown anseriform, to argue a Late Cretaceous divergence between galliform and anseriform crown taxa within galloanserines (i.e. 76.1 Ma). Those authors also proposed the divergence of Numididae, Odontophoridae and Phasianidae occurred in Africa. As yet, this is not supported by any fossil evidence (see Mourer-Chauviré 2008 and above). What is more, Wang et al. (2016) argued megapodiids and cracids may have South American origins, including later dispersal to other continents. However, fossils of cracids occur only on the North American continent (see 1.3.6 above), from where they are believed to have originated (e.g. Olson 1985), and those of megapodes do not occur outside of the Indonesia-Papua-Australia-Oceania regions (see below).

### 1.3.10 The Australasian galliform fossil record.

**1.3.10.1 Megapodiidae**—the only Palaeogene megapode fossil record is *Ngawupodius minya* Boles & Ivison, 1999 from the late Oligocene Namba Formation of South Australia, and is notable for its diminutive size (Boles & Ivison 1999; Boles 2008; Mayr 2009). The tarsometatarsus of *N. minya* bears a resemblance to those of the Quercymegapodiidae (see 1.3.3 above), which is a larger form, but the assignment of *N. minya* to the stem group of the Megapodiidae is considered justified (see Mayr 2009:42). Notably, no fossils of megapodes are known from the Miocene to the Pliocene periods (Mayr 2009; Shute et al. 2017). Similarly, Miocene avifaunas from mainland Asia include several phasianids (see above), but no megapodes (Cheneval et al. 1991), indicating they were restricted to the Indonesia-Papua-Australia-Oceania region at that time (Steadman 1999; Boles & Ivison 1999).

The first megapode described from Australia was *Progura gallinacea* (De Vis, 1888) from the upper Pleistocene Ravensthorpe Darling Downs deposits, South Eastern Queensland. It was originally named in Columbidae, and thought to have affinity with the crowned-pigeon *Goura* (De

Vis 1888:130-131). A revision of De Vis' work by van Tets (1974), recognized the specimens likely belonged to a megapode larger than any extant species. In addition, De Vis described other bones of this species as a stork *Palaeopelargus nobilis* (De Vis, 1891), and as an undetermined species of bustard *Chosornis praeteritus* (De Vis, 1889). van Tets (1974) attributed these fossils to a single megapode species, for which the senior synonym *Progura gallinacea* applied (van Tets 1974; Boles 2008). At the same time, *Progura naracoortensis* van Tets, 1974 was named from the middle–late Pleistocene Henschke's Quarry, Naracoorte South Australia. To which van Tets also transferred fossils that had been previously attributed to the extant megapodiid *Alectura lathamii* (see Lydekker 1891; Longman 1945). Later, van Tets (1984, 1985) revised his initial decision, and suggested the two nominal species of *Progura* likely represented a single, sexually dimorphic species (see also Shute et al. 2017). Olson (1985) raised the possibility that *P. gallinacea* and *P. naracoortensis* formed two distinct genera. However, Boles (2008:199; see also Boles 2006:403) proposed *P. naracoortensis* be placed in the synonymy of *P. gallinacea*, and that the generic nomen *Progura* should be used for the two fossil megapode species, pending revision of the taxon. What is more, Boles (2008:205-206) argued *P. gallinacea* was a giant morph of the extant megapodiid *Leipoa ocellata*, arguing the taxa were “virtually morphologically indistinguishable”, and suggested a mechanism of “late Pleistocene dwarfing” to explain the considerable size difference between the taxa. Boles (2008:203) further advanced that *Progura* is a synonym of *Leipoa*, and that fossils of the large Pleistocene species should be referred to *Leipoa gallinacea*. This recommendation resulted in the nomen *L. gallinacea* being employed for fossils of large Pleistocene megapodes in subsequent literature (see Shute et al. 2017, and references therein).

The discovery of both large and smaller megapodiid morphs in the extensive faunas from the Thylacoleo Cave of the Nullarbor Plain in Western Australia, led Shute et al. (2017) to re-examine the evolutionary relationships between Australian Plio-Pleistocene and extant megapodes. This resulted in the re-establishment of *Progura* as a valid taxon, within which *P. gallinacea* is accompanied by the new taxon *Progura campestris* Shute et al., 2017, incorporating those fossils previously attributed to *Leipoa gallinacea* (see Shute et al. 2017:14). The new genus *Latagallina* Shute et al., 2017 was erected to incorporate the previously recognised (see Boles 2008, and above) ‘smaller’ morph of *P. gallinacea*, named *P. naracoortensis* by van Tets (1974, see above). The taxon was categorised by Shute et al. (2017:25) as being “substantially” distinct from *P. gallinacea*, supporting Olson's (1985, see above) observations. Along with *La. naracoortensis*, *Latagallina* includes a smaller morph *Latagallina olsoni* Shute et al., 2017 named from fossils derived from Leana's Breath Cave on the Nullarbor, and represents the only known occurrence of the taxon. Notably, *La. olsoni* temporally and geographically overlaps with *L. ocellata*, distribution patterns argued by Shute et al. (2017:42) as indicative of niche partitioning between similarly sized taxa. Additionally, although *La. olsoni* shares osteological similarities with the congeneric *La. naracoortensis*, their geographical occurrence in the fossil record appeared to indicate an allopatric distribution (Shute et al. 2017). From Pleistocene

deposits on the Yorke peninsula in South Australia, *Garrdimalga mcnamarai* Shute et al., 2017 represents a somewhat large megapode, approaching the size range of *P. campestris* and *La. naracoortensis*. Remains of *G. mcnamarai* are fragmentary and exceedingly rare in the fossil record, and its relationship with other Plio-Pleistocene megapodes is poorly understood (Shute et al. 2017).

Australian megapode diversity appears to have reached its peak in the Pleistocene, represented by minimally seven species in six genera, for which there exists “direct” fossil evidence for five species (i.e. *L. ocellata*, *P. gallinacea*, *P. campestris*, *La. naracoortensis*, *La. olsoni*, and *G. mcnamarai*) in four genera (*Leipoa*, *Progura*, *Latagallina*, and *Garrdimalga*). Only one extant species of Australian megapode has a fossil record: *L. ocellata* was listed among late Pleistocene fossils from Victoria Fossil Cave, Naracoorte South Australia (van Tets 1974; van Tets & Smith 1974; Boles 2008; Shute et al. 2017). The two species of megapode currently extant, but for which there is no fossil record (i.e. *Alectura lathamii* and *Megapodius reinwardti*), are presumed to have co-existed alongside the extinct taxa (Shute et al. 2017). Thus, it appears Australian megapode generic diversity has halved, and species diversity has been reduced by approximately 60% since the Pleistocene (Shute et al. 2017; see also 1.3.11 below). Likewise, megapode species diversity on Pacific Islands (see 1.3.10.1.1 below) appear to have reduced by at least 50% through the Holocene, presumably through human impact (Steadman 1999).

The fossil record of Phasianidae from Australia is dominated by occurrences of the taxon *Coturnix* from cave sites across the country (see Baird et al. 1991, and references therein). Sites from Queensland include Royal Arch Cave, and Russenden Cave. New South Wales has a single phasianid (cf. *Coturnix*) occurrence from Ashford Cave. South Australian sites with reported phasianid fossils include Seton Rock Shelter, Henschke’s Cave, and Victoria Fossil Cave, which also produced the only occurrence of an extant megapode (*Leipoa ocellata*, see above). Victoria has phasianid records including Cloggs Cave, Pyramid Cave, Harmans Cave, Amphitheatre cave, Currans Creek Cave, and McEachern’s Cave. Western Australian records of phasianids include Skull Cave, Hunter River, Koonalda Cave, and Devils Lair (see Baird et al. 1991).

**1.3.10.1.1 Oceania**—the geographic region incorporating the archipelagos and islands of the South Pacific, known collectively as Oceania, has produced many megapodiid fossils. These are discussed in the following section, and the narrative moves from West to East through the region. In order to preserve narrative continuity, species of megapode that have a fossil record but are currently extant will be included in this description. Throughout Oceania, extant megapodes comprise 18 species in four genera, including nine species in *Megapodius*, and one each in *Macrocephalon* and *Eulipoa* (Jones et al. 1995). Megapodes of the genus *Megapodius* include several taxa that have variously been considered subspecies or species. For example, Mayr (1938) subsumed numerous taxa into the *M. freycinet* complex, and accepted only three species of *Megapodius*. However, White & Bruce (1986), followed by Jones et al. (1995), reinstated many taxa to specific status, so that 13 extant species are currently recognized (Dickinson & Remsen 2013). Four species of *Megapodius* occur in

Australo-Papuan region, and most overlap in size range, except for the diminutive *M. pritchardii*, and differ marginally in plumage (Jones et al. 1995; Steadman 1999; Worthy et al. 2015).

**1.3.10.1.1.1 Palau**—*Megapodius laperouse senex* Hartlaub, 1867, is the only species of megapode known from Palau, and was recorded from a rockshelter bone deposit on Ulong Island (Steadman 1999).

**1.3.10.1.1.2 Mariana Islands**—caves, rockshelters and sand deposits on Guam, Rota, Aguiguan, and Tinian have produced bones of *Megapodius l. laperouse*. The species is no longer present on Guam or Rota, or has been observed on Tinian in recent times, but still is common on uninhabited Aguiguan (Steadman 1999).

**1.3.10.1.1.3 Caroline Islands**—a late Holocene Nan Madol archaeological site on Pohnpei produced a single tarsometatarsus of *Megapodius laperouse (sensu lato)*. Steadman (1999) considered it likely this species once occurred through Micronesia, including Yap, Chuuk, Pohnpei, Kosrae, and many of the atolls in the region.

**1.3.10.1.1.4 Bismarck Archipelago**—two species of megapodes are known from late Pleistocene archaeological sites on New Ireland (see Allen et al. 1988, 1989; Marshall & Allen 1991; White et al. 1991). Namely: *Megapodius cf. eremita* Hartlaub, 1867, and an undescribed species (see *Megapodius* “new species 1”; Steadman et al. 1999:table 1), which is larger than *Megapodius molistructor* Balouet & Olson, 1989 of New Caledonia and Tonga (see below).

**1.3.10.1.1.5 Solomon Islands**—associated with middle-late Holocene archaeological sites from the island of Tikopia, bones of a medium-sized species of *Megapodius* were reported, likely referable to the extant *M. layardi* or *M. eremita* (Steadman 1999).

**1.3.10.1.1.6 Vanuatu**—a new genus and species of megapode *Mwalau walterlinii* Worthy et al., 2015 was named from the late Holocene Teouma Site on Efate Island. *Mwalau walterlinii* was a species larger than all extant megapodes, but smaller than *Progura gallinacea* (see 1.3.10.1), and displays features similar to extant *Alectura lathamii* from Australia (Worthy et al. 2015). The only other records are of bones belonging to *Megapodius layardi*, the extant endemic Vanuatu megapode (Steadman 1999; Worthy et al. 2015).

**1.3.10.1.1.7 New Caledonia**—both species of landfowl described from New Caledonia survived until human arrival ca. 3000 years ago (Steadman 1999). The extinct flightless *Sylviornis neocaledoniae* Poplin, 1980 is currently not considered to be a megapode, but a species within a separate family of Galliformes, described here to maintain narrative continuity.

*Sylviornis neocaledoniae* was a large bird (~1.2–1.6 m; ca. 40 kg; Steadman 1999), originally named as a ratite (Poplin 1980); it was later determined that *S. neocaledoniae* was a megapode (see Poplin et al. 1983; Poplin & Mourer-Chauviré 1985). Subsequently, Balouet & Olson (1989) listed *S. neocaledoniae* as family *incertae sedis*, and proposed it be placed in its own galliform family. Accordingly, Sylviornithidae Mourer-Chauviré & Balouet, 2005 was erected for it following analysis of the skull showing the genus is highly derived, and the characters bringing *S. neocaledoniae* and

Megapodiidae together are plesiomorphic (Mourer-Chauviré & Balouet 2005:206). *Sylviornis neocaledoniae* and *Megavitiornis altirostris* Worthy, 2000 (see below), have subsequently been subsumed as sister taxa within Sylviornithidae; the family was found to be the sister group to crown Galliformes, and representative of basally diverging galloanseres (Worthy et al. 2016a). Several bones, including cranial material of *S. neocaledoniae*, have been recovered from four cave sites on Grande Terre New Caledonia (see Balouet 1984, 1987; Balouet & Olson 1989; Mourer-Chauviré & Balouet 2005). Anderson et al. (2010) described several thousand avian bones from Pindai Caves, representing over 45 taxa, including minimally 20 now-extinct taxa that were present at stratigraphic levels directly below or within the period of human occupation. Anderson et al. (2010) also presented the first radiocarbon dates based on *S. neocaledoniae* bone, indicating the species persisted into the late Holocene period. *Megapodius molistructor* is another megapode described from New Caledonia that was larger than any extant species of *Megapodius* (Balouet & Olson 1989:9; Steadman 1999).

**1.3.10.1.1.8 Fiji**—the extinct megapodes *Megapodius amissus* Worthy, 2000, and a large and highly specialised bird *Megavitiornis altirostris*, were described from late Pleistocene-early Holocene sites on Viti Levu (Worthy 2000:342; 351; see also Worthy et al. 1999:240). Worthy (2000:359) noted the bill specialisation of *M. altirostris* compared well with the morphology of the large Eocene gastornithids of the Northern Hemisphere, and the Miocene dromornithids of Australia (see 1.2.1 above). Additionally, *M. altirostris* is unique in that it parallels *Sylviornis neocaledoniae* (see above) in unique morphological specialisations associated with flightlessness (Worthy 2000:362). The only other record of Fijian megapodes is based on bones from late Holocene archaeological sites on Naigani and Lakeba. Steadman (1999:13) “tentatively” referred these Lakeba bones to *Megapodius alimentum* Steadman, 1989. Later, Worthy (2000:341) reviewed the Lakeba specimens, confirming the bones were not significantly smaller than those of *M. alimentum*, a large extinct species that is commonly found in Tongan prehistoric sites (see below). Further assessment of the avifauna from the Naigani Lapita site by Irwin et al. (2011), demonstrated that at least two individuals of *M. altirostris* (described from Viti Levu by Worthy 2000; see above), displayed patterns of bone breakage consistent with their being killed and eaten. Fijian fossil records show the archipelago once had “at least” three species of megapode (Worthy 2000:362).

**1.3.10.1.1.9 Tonga**—*Megapodius pritchardii* from the island of Niufo`ou is the smallest extant megapode, and forms the only record of any extant megapode population from Tonga or elsewhere in Polynesia (Steadman 1991). The extinct *Megapodius* “new species 2” (Steadman 1993:table 1; 1995:table 5), represents the smallest megapode known, and is present in both archaeological and prehistoric deposits on `Eua (Steadman 1999:13). The extinct *Megapodius alimentum* Steadman, 1989 was named from the Tongoleleka archaeological site. *Megapodius alimentum* is the most common megapode on `Eua, and is also known from five islands in the Ha`apai Group (Ha`ano, Foa, Lifuka, `Uiha, and Ha`afeva; see Steadman 1989). The large, extinct *Megapodius* cf. *molistructor*, is represented from Ha`ano, Foa, Lifuka, and Faleloa (Steadman 1999).

**1.3.10.1.1.10 American Samoa**—[Steadman \(1991, 1994\)](#) reported a medium-sized but undetermined species of *Megapodius* from the Toaga archaeological site on Ofu Island, Manu`a Group.

**1.3.10.1.1.11 Niue**—bones of an indeterminate species of *Megapodius*, smaller than *M. pritchardii*, and larger than *M. alimentum* of Tonga (see above), were reported from the pre-human cave site Anakuli by [Steadman \(1999\)](#). Later, [Steadman et al. \(2000:174\)](#) reassessed the material, assigning them to *M. pritchardii*, and remarked that the Niuean bones were slightly larger than extant specimens of *M. pritchardii*, but were distinctly smaller than in the extant *M. freycinet (sensu lato)*.

### 1.3.11 The modern Australian galliform fauna

The Australian galliform fauna is restricted to the endemic *Coturnix pectoralis* which is widespread in all states. *Coturnix ypsilophorus* inhabits the South Eastern Australian mainland and Tasmania, *Coturnix australis* occurs in coastal areas of South Western Australia, South Australia, Victoria and New South Wales, and includes three subspecies ([Condon 1975](#)). There are three extant species of Australian megapode: *Leipoa ocellata* inhabits semi-arid and arid inland Australia in all states except Queensland, *Alectura lathami* occurs in Eastern Australia from Cape York, Queensland to the Hawkesbury River, NSW, and *Megapodius reinwardt* is found from Cape York Peninsula south to Cooktown, Queensland, on islands in the Torres Straits and off the continental East coast ([Condon 1975](#); [Boles 2008](#)).

Extant megapodes can be grouped into two clades employing distinct breeding strategies (e.g. [Harris et al. 2014](#)). While all megapodes employ a synapomorphic exothermic strategy ([Shute et al. 2017](#)), the “brush turkey” clade build mounds of organic material, and use heat generated by microbial decomposition to incubate their eggs. “Burrow-nesters”, on the other hand, dig holes in geothermal or solar-heated soils to affect similar outcomes (see [Dekker 2007](#); [Harris et al. 2014](#)). Extant mound-building “brush turkeys” comprise several genera currently restricted to the Australo-Papuan region. Burrow-nesting is restricted to the “scrubfowl” clade, including only one Australo-Papuan genus (i.e. *Megapodius* spp.; see [Harris et al. 2014](#)). Notably, [Shute et al. \(2017:55\)](#) argued a morphological basis for previously unrecognised burrow-nesting amongst several extinct Australian “brush turkey” taxa, suggesting an independent evolution or “re-evolution” of burrow-nesting within the clade.

## 1.4 Anseriformes

Crown group Anseriformes include the Anhimidae, Anseranatidae and the globally distributed Anatidae, or ‘true waterfowl’ ([Delacour & Mayr 1945](#); [Woolfenden 1961](#); [Johnsgard 1968](#); [Olson & Feduccia 1980](#); [Olson 1985](#); [Ericson 1997](#); [Livezey 1997a](#); [Kear 2005](#); [Mayr 2009](#); [Dickinson & Remsen 2013](#)). Anhimids form the sister taxon to the other Anseriformes, and their fossil record is so far restricted to South America ([Alvarenga 1999](#)).

The first attempt to comprehensively review the diversity of fossil anseriforms was made by [Lambrecht \(1933\)](#), who described and figured all known fossil taxa in an extensive monograph. [Delacour & Mayr's \(1945\)](#) monograph on the Anatidae attempted to resolve species into related groups, and to adjust the nomenclature of species and genera. Building upon these works, in 1964 two of the most quoted and useful palaeornithological works were published: [Howard's \(1964a\)](#) chapter on fossil anseriforms in [Delacour's \(1964\)](#) 'The Waterfowl of the World' listed most taxa known in a consistent format, and [Brodkorb \(1964\)](#) published the Anseriformes section of his 'Catalogue of Fossil Birds', listing all taxa with full synonymies and age ranges, with additions in [Brodkorb \(1978\)](#). Subsequently, [Bocheński \(1997\)](#) produced a list of all European fossil bird species, indicating the current status for each. Most recently, [Mlíkovský \(2002\)](#) published an extensive work on the Cenozoic birds of Europe, listing comprehensively their distributions and synonymies. This work is particularly useful, as it affords primary publication data and any subsequent taxonomic treatments. However, it has been heavily criticised for its "somewhat cavalier" approach to higher classification, which does not follow any modern system (see [Dyke 2003a:258](#); [Mourer-Chauviré 2004](#)). Consequently, synonymies by [Mlíkovský \(2002\)](#) noted herein may not withstand scrutiny.

**1.4.1 The origin of Anseriformes**—molecular clock genetic data presented by [Cooper & Penny \(1997\)](#) and [Harrison et al. \(2004\)](#), place the galliform-anseriform split in the late Cretaceous. However, several other molecular clock analyses proposed this split occurred earlier in the Cretaceous. For example, [van Tuinen & Hedges \(2001, 2004\)](#) and [van Tuinen et al. \(2006\)](#), used calibrations based on the reptile/mammal split at 310 Ma, and [Brown et al. \(2008\)](#) used *Vegavis* (see **1.2.1.3** above) to calibrate the temporal split for crown anseriforms. All authors advocated the split occurred ~90 Ma, and posited crown representative clades were well established by the end Cretaceous (~66 Ma). Notably, [Brown et al. \(2008\)](#) argued their results were "nearly identical" whether *Vegavis* was included or not. Similarly, [Stein et al. \(2015\)](#) used both nuclear and mtDNA for their Bayesian analyses, also calibrated using *Vegavis*, and recovered an early-late Cretaceous (~76.5 Ma) crown anseriform divergence estimate.

These assessments notwithstanding, recent large scale ([Claramunt & Cracraft 2015](#)) and full-genome analyses ([Jarvis et al. 2014](#)), suggested the earliest divergence between galloansere clades occurred around the K-Pg boundary, reinforcing conclusions derived from phylogenetic assessments of morphological and molecular data (e.g. [Livezey 1997b](#); [Ericson 1997](#); [Livezey & Zusi 2001](#); [Mayr & Clarke 2003](#); [Livezey & Zusi 2007](#); [Fain & Houde 2004](#); [Ericson et al. 2006](#); see also [Cracraft et al. 2004](#), and references therein). The taxonomic topology within Anseriformes continues to be refined by analyses employing molecular data (e.g. [Donne-Goussé et al. 2002](#); [Gonzalez et al. 2009](#); [Liu et al. 2014](#)), and morphological characters (see below).

It is clear that whether anseriforms and galliforms split during the Cretaceous or not, and whether by the terminal Cretaceous there existed crown group representatives in the form of orders, or

even families (e.g. [van Tuinen et al. 2006](#); [Brown et al. 2008](#)), the earliest unequivocal fossil records of virtually all neoavian taxa are derived from Palaeogene deposits ([Mayr 2009:22](#)).

**1.4.2 Presbyornithidae**—included several abundant Paleocene and Eocene taxa from Argentina, North America, Europe, and late Oligocene-Early Miocene taxa from Australia. Presbyornithids are a complicated taxon concerning both their taxonomy and their phylogenetic assignment ([Olson 1985, 1994](#); [Dyke 2001](#); [Mayr 2009](#)). A revision of New World Presbyornithidae by [Ericson \(2000\)](#) confirmed the legitimacy of four species: the Paleocene taxon *Presbyornis isoni* Olson, 1994 (see also [Benson 1999](#)), and the early Eocene taxa *P. pervetus* Wetmore, 1926, *P. recurvirostra* (Hardy, 1959), and *Telmabates antiquus* Howard, 1955. Except for the latter taxon, all species were named from North American sites ([Mayr 2009](#)). [Ericson \(2000\)](#) excluded the poorly known *Telmabates howardae* Cracraft, 1970 from the Presbyornithidae, as he regarded the affinities of this taxon uncertain. The range of the family has been extended into the late Cretaceous with the description of *Teviornis gobiensis* Kurochkin et al., 2002 from Mongolia, but this classification needs to be confirmed with analyses of more complete material ([Kurochkin et al. 2002](#); see also [Clarke & Norell 2004](#); [Mayr 2009](#)). Presbyornithid relationships have proved controversial due to the morphologically diverse nature of their post cranial skeleton, with [Olson & Feduccia \(1980\)](#), and [Olson \(1985\)](#), considering them transitional shorebirds and near Charadriiformes. For some time, it was generally agreed that they are members of anseriforms and form the sister group to Anatidae (e.g. [Olson 1994](#); [Ericson 1997, 2000](#); [Livezey 1997a, 1997b](#); [Worthy 2009](#)). Subsequently, [Worthy et al. \(2016a\)](#), whilst investigating relationships of *Sylviornis neocaledoniae* (see **1.3.10.1.1.7** above), analysed 37 taxa including 10 outgroup anseriform taxa, along with representative galloanseres, and reported *Presbyornis* and *Anseranas semipalmata* (see **1.4.4** below) formed a clade, but for which the relationship to Anatidae was unresolved. Presbyornithid association with anseranatids extends to their feeding behaviour. By means of an assessment of bill and lamellae morphology, and the form of the quadrate, [Zelenkov & Stidham \(2018\)](#) suggested presbyornithids were poorly specialised filter-feeders, could filter only larger food items compared with extant dabbling ducks, and likely used the hook on the tip of the bill to capture larger food items from within substrate, much like the extant *A. semipalmata* does. [Mayr \(2009\)](#) reported no members of Presbyornithidae were known from Australasia. However, a more recent re-evaluation of the putative burhinid *Wilaru tedfordi* Boles et al., 2013 by [De Pietri et al. \(2016c\)](#), showed *W. tedfordi* was a presbyornithid based on several autapomorphic post cranial features. They also erected an additional Australian presbyornithid *Wilaru prideauxi* De Pietri et al., 2016 that was a larger and more robust taxon than *W. tedfordi*. These were recognised as more terrestrial birds than the Northern Hemisphere presbyornithids, having adaptations that facilitated the temporal continuance of Presbyornithidae in the Southern Hemisphere by some 25 Ma. [De Pietri et al. \(2016c\)](#) argued that the morphological similarity between species of *Wilaru* and the South American presbyornithid *T. antiquus* emphasised the possibility of a Gondwanan origin, or at very least, a Gondwanan radiation of the clade. Subsequently, the comprehensive phylogenetic

analysis of [Worthy et al. \(2017b\)](#), see also [2017c](#)) included *Wilaru* in analyses for the first time, placed all presbyornithids as more basal anseriforms than previously recognised, and as sister to anseranatids + anatids. (see also [De Pietri et al. 2016c](#); [Mayr et al. 2018](#)).

**1.4.3 *Conflicto***—recently erected in Anseriformes *Familiae incertae*, *Conflicto antarcticus* Tambussi et al., 2019 will likely prove a somewhat controversial taxon. The new genus and species was described from a partial, three dimensionally preserved skeleton derived from the López de Bertodano Formation of Seymour Island, Antarctica. The same formation that yielded the Late Cretaceous/early Palaeogene vegaviids (see **1.2.1.3** above). The morphology of *C. antarcticus* preserves “key” galloanserine cranial apomorphies, including those of the nares, quadrate, and mandible. Also, the taxon displays no less than 12 anseriform synapomorphies (four cranial, one quadrate, and eight post cranial characters). [Tambussi et al. \(2019\)](#) argued that features of the quadrate (e.g., the presence of foramen pneumaticum caudomediale on the processus oticus), two synapomorphies of the carpometacarpus, the form of the femoral sulcus patellaris, and the condition of the condylus medialis of the tibiotarsus, place *C. antarcticus* firmly within anseriforms. Additionally, those authors argued the presence of “very narrow and long” mandibular rami supported a sister relationship between *C. antarcticus* and *Anatalavis oxfordi* Olson, 1999 (see **1.4.4** below). In their phylogenetic analyses, Bremer support for the clade of *C. antarcticus* + *A. oxfordi* was tenuous, therefore [Tambussi et al. \(2019\)](#) stopped short of official nomenclatural assignment. However, their analyses place *A. oxfordi* in a more basal position within Anseriformes than is currently accepted (see below). An important outcome of this work, if the basal position of *C. antarcticus* is upheld, is the recognition that the anhimid beak (i.e., mediolaterally narrow, and with a ventrally curved premaxilla, similar to those of galliforms), is likely a secondarily derived condition within Anseriformes.

*Conflicto antarcticus* would have been a reasonably large (~2.2 kg), long legged, volant bird that was likely exploiting non-marine temperate forest, and near-shore terrestrial habitats in the Early Palaeogene of Antarctica, and the taxon is likely representative of early neornithine habitat use and niche exploitation post K-Pg extinction events.

True to nomenclatural expectation, *C. antarcticus* presents somewhat of a conundrum as to where to place it in this review. I include it prior to Anseranatidae, as discussion of the taxon and its putative sister relationship with *Anatalavis* (see below) follow consecutively. However, if [Tambussi et al.’s \(2019\)](#) hypothesis of a basal anseriform position for *Anatalavis* withstands scrutiny, and that *Conflicto* + *Anatalavis* are together sister to all other anseriforms (see **1.4.2**), among which presbyornithiforms branch next as the sister group to anhimids + Anatoidea (*Anseranas* + Anatidae) (see **1.4.5**). The sequence these taxa appear in fossil checklists, and descriptions of relationships between extinct galloanseres will require revision.

**1.4.4 Anseranatidae**—the Eocene London Clay produced *Anatalavis oxfordi* Olson, 1999 which was referred to Anseranatidae ([Olson 1999](#)). The *Anatalavis* type species is *Anatalavis rex* (Shufeldt, 1915) from the early Paleocene age Hornerstone Formation in New Jersey, USA ([Olson &](#)

Parris 1987:11; Olson 1994), which has been interpreted as latest Cretaceous age (Parris & Hope 2002). The new genus *Nettapterornis* Mlíkovský, 2002 was erected for *A. oxfordi*, putatively because the morphology of the humerus differed from the type of *Anatalavis* (Mlíkovský 2002:108). However, this action was not supported by Mourer-Chauviré (2004) or Mayr (2005). Additionally, the referral of *A. oxfordi* to Anseranatidae was challenged by Dyke (2001), who suggested it was the sister group of Presbyornithidae + Anatidae. Dyke's (2001) analysis was criticised by Mayr (2005) due to a large amount of missing data, and non-inclusion of characters indicating specific anseranatid affinity previously identified by Olson (1999). From the latest Oligocene Créchy Quarry in France, *Anserpica kiliani* Mourer-Chauviré et al., 2004 was described as an anseranatid, indicating a diversity of this group in the early Cenozoic of Europe (Mourer-Chauviré et al. 2004).

*Eoanseranas handae* Worthy & Scanlon, 2009 was named from the Oligo-Miocene Carl Creek Limestone from Riversleigh in Queensland, and constitutes the oldest record of Anseranatidae in Australia. *Eoanseranas handae* confirms the presence of anseranatids in Australia since the latest Oligocene/earliest Miocene. Worthy & Scanlon's (2009) analyses showed *E. handae* was more morphologically similar to the extant anseranatid *Anseranas semipalmata*, than it is to the Northern Hemisphere anseranatids. *Eoanseranas handae* together with *Anserpica kiliani*, suggest that Anseranatidae were present in both Australia and Europe in the late Oligocene (Mayr 2009).

**1.4.5 Anhimidae**—comprise three extant species endemic to South America. From the late Oligocene/early Miocene of the Taubaté Basin, Brazil *Chaunoides antiquus* Alvarenga, 1999 was named based on isolated post cranial bones, and constitutes the only Palaeogene record of these birds (Mayr 2009). Alvarenga (1999) also argued *Loxornis clivus* Ameghino, 1895 from the late Oligocene of Argentina may also be an anhimid. Unpublished early Eocene anhimid-like birds from the Willwood Formation, Wyoming were noted by Ericson (1997), Olson (1999), and Feduccia (1999), and a possible anhimid species also occurred in the early Eocene London Clay of Walton-on-the-Naze (see Feduccia 1999:table 4.1; Mayr 2009).

#### **1.4.6 Anatidae**

The earliest unambiguously identified taxa of duck- or goose-like birds are from late Eocene deposits of Europe. No anatid fossils are known from the Palaeogene of Africa (Mayr 2009).

**1.4.6.1 Eocene–Oligocene (55–23.8 Ma)**—*Eonessa anaticula* Wetmore, 1938 from the upper Eocene of Utah, USA was placed in the new subfamily Eonessinae in Anatidae (Wetmore 1938). This classification was disputed by Olson & Feduccia (1980:19), who after reassessment of the fossils, removed *E. anaticula* from Anatidae, ruled out a relationship with Presbyornithidae, and considered its familial affinities to be indeterminate. The description of *Romainvillia stehlini* Ledebinsky, 1927 from the upper Eocene of France, was based on several bones (Brodkorb 1964; Howard 1964a), but the taxon is now considered to be outside crown group Anatidae (Mayr 2005), and has been suggested to be an anseranatid (Olson 1999). In fact, Mlíkovský (2002:109) transferred it to Anseranatidae. However, Mayr (2005) did not agree with this action, arguing *R. stehlini* lacked the dorsal pneumatic

foramen in the sternal blade of the coracoid, apomorphic of Anseranatidae. Subsequently, [Mayr \(2008c:365\)](#) re-evaluated *R. stehlini*, argued the taxon can be “unambiguously” recognised as a stem group representative of the Anatidae, and his analysis supported the clade of Presbyornithidae + (*Romainvillia* + Anatidae). [Harrison & Walker \(1976\)](#) named the new genus and species *Petropluvialis simplex* Harrison & Walker, 1976 from the upper Eocene of England, and referred the taxon to Burhinidae. However, [Mayr & Smith \(2001\)](#) considered this specimen to be an anseriform similar to *Romainvillia*. Several fossils of anseriform birds from the lowermost Oligocene of Belgium were reported by [Mayr & Smith \(2001\)](#), who referred a right coracoid to Anatidae, and ‘cf. *Paracygnopterus*’ (see below), and another coracoid was noted to be similar to *Romainvillia*. [Mayr \(2008c:368; 374\)](#) later reported the “tentative” identification of ‘cf. *Paracygnopterus*’ was no longer upheld, and the Belgian specimens should be considered Anatidae *gen. et sp. indet.* *Howardia eous* Harrison & Walker, 1976 was referred to Anseriformes, but because the generic name was preoccupied, [Harrison & Walker \(1979\)](#) proposed the new name *Palaeopapia*, and referred a partial coracoid to *P. eous* (Harrison & Walker, 1976). Those authors also erected *Palaeopapia hamstediensis*, Harrison & Walker, 1979 and the new genus and species *Paracygnopterus scotti* Harrison & Walker, 1979, both of lower Oligocene age from the Hampstead Beds, Isle of Wight. All three taxa were regarded *Aves incertae sedis* by [Dyke \(2001:12\)](#), who argued no anseriform synapomorphies had been identified in the fossils. [Mayr \(2008c:374; 2009:54\)](#) however, considers *P. scotti* to be a valid representative of Romainvilliinae. *Saintandrea chenoides* Mayr & De Pietri, 2013 was described from the late Oligocene of Saint-Andre´, France, representing the youngest record and the largest species of Romainvilliinae known ([Mayr & De Pietri 2013:424](#)). Most recently, *Romainvillia kazakhstanensis* Zelenkov, 2018 was named in the family Romainvilliidae from the upper Eocene Taizhuzgen locality, Kustovskaya Formation, eastern Kazakhstan, representing the first member of *Romainvillia* outside of France (e.g. *S. chenoides* above), and the first “reliable” record of the group in Asia ([Zelenkov 2018:225](#)).

[Mlíkovský \(2002:112\)](#) synonymised *Palaeopapia hamstediensis* with *Cygnopterus affinis* (Van Beneden, 1883), a middle Oligocene anatid taxon from Belgium considered to have anserine affinities ([Lambrecht 1933; Brodkorb 1964; Howard 1964a; Olson 1985](#)). [Mayr \(2008c:368\)](#) considered this action incorrect, arguing elements of *P. hamstediensis* are clearly distinguished from those of *C. affinis*. *Cygnopterus* was initially considered by [Cheneval \(1984\)](#) to be a swan in Cygnini, however, [Louchart et al. \(2005:385\)](#) argued that although *Cygnopterus* was an anserine, it was not “representative” of swans. [Mayr \(2008c:367\)](#) agreed with [Louchart et al. \(2005\)](#) in that *Cygnopterus* differs from crown group Anatidae. [Mlíkovský & Švec \(1986\)](#) contended that *Cygnopterus lambrechtii* Kurochkin, 1968 was not an anseriform, but that it belonged in Phoenicopteridae, and they synonymised *C. lambrechtii* with *Agnopterus turgaiensis* Tugarinov, 1940. [Mayr & Smith \(2002\)](#) and [Mayr \(2005\)](#) noted that species of *Cygnopterus* closely resembled the smaller “*Headonornis*” *hantoniensis* (Lydekker, 1891), named from the late Eocene and early Oligocene of Hordle, England.

“*H.*” *hantoniensis* has been considered an Old World representative of the Presbyornithidae by Harrison & Walker (1976, 1979), and Dyke (2001), but was assigned to Anseranatidae by Mlíkovský (2002:108). Dyke (2001:12) concluded that the humeri referred to “*Headonornis*” *hantoniensis* actually belong to *Presbyornis isoni* (see above), a species only known from the Paleocene of North America (see Olson 1994). Mayr (2008c:368) however, found “no convincing reason to assign these bones to a species that lived some 20 million years earlier on a different continent”.

Two other ‘swans’ from the Oligocene in Europe have been described: *Guguschia nailiae* Aslanova & Burčák-Abramovič, 1968 from the upper Oligocene/lower Miocene of Azerbaijan (Aslanova & Burčák-Abramovič 1968), and *Cygnavus formosus* Kurochkin, 1968 (Mlíkovský & Švec 1986; Boev 2000). Louchart et al. (2005:386) observed that *Guguschia* had some similarities with *Cygnopterus*, but both taxa, and “probably” *Cygnavus*, were likely not Cygnini, and require “firm re-evaluation”.

Several Oligocene age fossils have been named in *Anas*, but all are now considered to belong in other genera, or are generically indeterminate. The species *Anas oligocaena* Tugarinov, 1940 from the upper Oligocene of Kazakhstan, was referred to *Dendrochen* in Dendrocygnini by Mlíkovský & Švec (1986), and followed by Cheneval (1987). *Anas creccoides* Van Beneden, 1871 from the early Oligocene of Belgium was referred to Anatidae, but as this name was preoccupied, it was replaced by the substitute name *Anas benedeni* Sharpe, 1899. Brodkorb (1962:707) considered the identification of these fossils as anseriforms inappropriate, and they were relegated to *Aves incertae sedis*. Mlíkovský (2002:70) considered *Anas basaltica* Bayer, 1883 from the early Oligocene of Czechia to be an indeterminate heron. *Anas skalicensis* Bayer, 1883 is based on bones that are indeterminate at ordinal level from the middle Oligocene, although the age was reported by Bocheński (1997) as lower Miocene of the Czech Republic (Mlíkovský 2002:251). Additionally, an anseriform of undetermined subfamilial affinity within Anatidae was described as *Cayaoa bruneti*, Tonni, 1979, from the late Oligocene/early Miocene of Argentina (Tonni 1979). Noriega et al. (2008) re-examined the holotype along with previously undescribed post cranial material of *C. bruneti*, and reported it was a foot propelled diver, exhibited “extreme” reduction in forelimb proportions, and likely represented the earliest record of flightlessness in anseriforms. A recent phylogenetic assessment of the taxon by De Mendoza (2019) recovered it as a basal erismaturine (=oxyurine; see 1.4.6.2 below).

In summary, although some are anatids and others indeterminate anseriforms, none of these Oligocene taxa are correctly attributed to *Anas*, and no crown-group members of extant families are known from pre-Oligocene deposits (Mayr 2005). The earliest unambiguously identified anseriforms are from middle to late Eocene deposits of Europe (Mayr 2009; see also Zelenkov 2012a).

**1.4.6.2 Miocene** (28.3–5.3 Ma)–lower to middle Miocene ducks of the northern Hemisphere are primitive forms that do not belong in *Anas* (Worthy et al. 2007). Of the few early-middle Miocene taxa named in *Anas*, possibly all are not *Anas sensu stricto*. *Mioquerquedula* (= *Anas*) *velox* [(Milne-Edwards, 1867-71); see also Cheneval 1987:pl.1, fig.2], and *Anas sansaniensis* Milne-Edwards, 1867-

71, both from Sansan, France, are likely incorrectly placed in *Anas* (Mlíkovský 2002:118-119; Worthy et al. 2007:30; see also discussion of these taxa below). The holotype (a left femur) figured in Cheneval (1987:pl.1; figs.7a, 7b) of *Aythya chauvirae* Cheneval, 1987 named from Sansan (see also Mlíkovský 2002:121), exhibits no features that allow referral to *Aythya* to the exclusion of other taxa (see Worthy et al. 2007:30). Subsequently, Worthy & Lee (2008:704) argued it is similar to taxa such as *Mionetta blanchardi* (Milne-Edward, 1863) that are erismaturines (=oxyurines; see below). Later, however, Zelenkov (2012a:524) proposed *A. chauvirae* may be related to “one of the primitive ducks” from the Mongolian Sharga locality (see below).

In Europe, the most abundant anatid is *Mionetta blanchardi*, originally named in the genus *Anas*; this and associated anatids from Saint-Gérard-le-Puy were recognised by Cheneval (1983, 1987) as not belonging in *Anas*, and were placed in the genus *Dendrochen*. Livezey & Martin (1988) reviewed “*Anas*” *blanchardi* and erected the genus *Mionetta* in the subfamily Dendrocheninae for it. *Mionetta blanchardi* first appeared in the upper Oligocene (Mourer-Chauviré et al. 2004), and ranges across the lower Miocene (Mlíkovský 2002). Of the two taxa contemporary with *M. blanchardi*, *M. (=Anas) consobrina* (Milne-Edward, 1867-71) was considered by Livezey & Martin (1988) to be bones of large individuals of *M. blanchardi*. *Mionetta (=Anas) natator* (Milne-Edward, 1867-71), a smaller taxon, was transferred to *Mionetta*, and has an age range of upper Oligocene (Mourer-Chauviré et al. 2004) to the lower Miocene (Mlíkovský 2002). However, according to Zelenkov & Kurochkin (2012:426), the generic assignment of *M. natator* requires revision, as features of the coracoid suggest *M. natator* may be related to the middle Miocene taxon *Mioquerquedula* Zelenkov & Kurochkin, 2012 (see below). The species *Aythya (=Fuligula) arvernensis* (Lydekker, 1891), considered by Cheneval (1987) as in need of reassessment, was included by Mlíkovský (2002:110) in the synonymy of *Mionetta blanchardi*. Although *M. blanchardi* lacks specialist diving apomorphies in its hindlimbs (*contra* Livezey & Martin 1988; see Worthy et al. 2007:12), it is now considered a basal member of the Erismaturinae (=Oxyurinae; see also Worthy & Lee 2008; Worthy 2008, 2009; and 1.4.7.2 below).

[Note: with respect to nomenclatural convention, I use Erismaturinae Eyton, 1838 for stiff-tailed duck familial grouping, because Oxyurinae Phillips, 1926 is a junior homonym of Oxyuridae Cobbold, 1864 (a nematode)].

Early Miocene waterfowl from North America are few. Of the taxa from the lower Miocene of South Dakota, Livezey & Martin (1988) made the early Miocene *Dendrochen robusta* Miller, 1944, the type genus of Dendrocheninae. Cheneval (1987) transferred the primitive anatid *Anas (=Querquedula) integra* (Miller, 1944) to *Dendrochen*. Subsequently, Zelenkov & Kurochkin (2012:426), suggested *Dendrochen integra* may belong in the middle Miocene European taxon *Mioquerquedula* (see below), based on features of the coracoid. *Paranyroca magna* A.H. Miller & Compton, 1939, a large “swan-sized diver” (see Worthy et al. 2007), was placed in the family Paranyrociidae by Miller & Compton (1939), but it was later demoted by Brodkorb (1964:229) to a

subfamily of Anatidae. [Miller \(1952\)](#) reported other unidentified duck-sized anseriforms from the upper Miocene of California.

A single humerus from the upper Miocene of Argentina constitutes the record of “Dendrocheninae” in the southern Hemisphere, and was referred by [Noriega \(1995\)](#) to this subfamily. Most recently, [Worthy & Lee’s \(2008:703\)](#) analyses found no support for Dendrocheninae, and synonymised the taxon with Erismaturinae (=Oxyurinae), which was followed by [Gill et al. \(2010\)](#).

Other than these erismaturines (=oxyurines), anserines comprise all early Miocene anatids. Lower Miocene anserines of Europe are represented by *Cygnopterus alphonsi* Cheneval, 1984 and *Cygnavus senckenbergi* Lambrecht, 1931, with both taxa originating in the Oligocene ([Lambrecht 1933](#); [Kurochkin 1968](#); [Cheneval 1987](#); [Mlíkovský 2002](#); see also [Worthy et al. 2007](#)). *Cygnopterus alphonsi* was synonymized with *Cygnavus senckenbergi* by [Mlíkovský \(2002:112\)](#), however, [Louchart et al. \(2005:385\)](#) did not accept this action. [Kessler & Hír \(2009:98\)](#) described *Cygnopterus neogradensis* from the middle Miocene localities of Mátraszőlős and Litke in Hungary. *Anas robusta* (Milne-Edward, 1867-71), was assigned to *Anserobranta?* by [Cheneval \(1987\)](#), and later transferred to *Mionetta* by [Mlíkovský \(2002:111\)](#). However, *Cygnopterus* is not like *Mionetta*, due to features of the anterior ligament attachment on the proximal humerus (see [Worthy et al. 2007:30](#)), so is best recognised as an anserine in *Anserobranta?*

*Cygnus*, the “true” swans, do not appear in Europe until the middle Miocene ([Worthy et al. 2007](#)), in the form of *Cygnus* (=Anas) *atavus* (Fraas, 1870), described along with *C.* (=Anas) *cygniformis* (Fraas, 1870), and *C.* (=Palaelodus) *steinheimensis* (Fraas, 1870), from Steinheim, Germany. [Lambrecht \(1933:369\)](#) initially transferred *Cygnus* (=Anas) *atavus* and *Cygnus* (=Anas) *cygniformis* to *Anser*. [Mlíkovský \(1992:438\)](#) considered [Lambrecht’s \(1933\)](#) transfer of *Cygnus* (=Anas) *cygniformis* to *Anser tenuis*. However, lacking appropriate comparative material [Mlíkovský \(1992\)](#) retained the taxon in *Anser*, suggesting it may not be a “valid species”. At the same time [Mlíkovský \(1992:439\)](#) transferred *A. atavus* to *Cygnus (sensu stricto)*. Thereafter, [Heizmann & Hesse \(1995:174; 176\)](#) appear to have erroneously synonymised “*Anser*” *cygniformis* and “*Palaelodus*” *steinheimensis* with *Cygnus atavus*, although *A. cygniformis* remained in *Anser* as referred by [Lambrecht \(1933:369\)](#). Subsequently, all taxa were formally subsumed into *Cygnus atavus* by [Mlíkovský \(2002:113\)](#). The description of *Cygnus herenthalsi* van Beneden, 1871 from the middle Miocene of Belgium was based on a single phalanx, and was a *nomen nudum*, but made available by [Lambrecht \(1933:383\)](#) as *Cygnus herenthalsi* Lambrecht, 1933 (note spelling; see also [Brodkorb 1964:209](#) and [Howard 1964a:260](#), who according to [Mlíkovský 2002:257](#) “just repeated incorrect data given by [Lambrecht 1933:383](#)”). With regard to the taxon description, [Howard \(1964a:261\)](#) argued a single phalanx is a “dubious” diagnostic element. [Mlíkovský \(2002:257\)](#) concurred with her, and relegated the taxon to *Aves incertae sedis*. *Cygnus* (=Cyganser) *csakvarensis* (Lambrecht, 1933) was described from the late Miocene of Hungary. Originally named *Cygnus csákvarensis* ([Lambrecht 1933:383-384](#)), it was transferred to *Cyganser* as *C. csakvarensis*

(note amended spelling) by [Brodkorb \(1964:210\)](#). Later, it was referred back to *Cygnus*, in the subgenus *Olor* by [Mlíkovský \(1992:437\)](#); see also [Mlíkovský 2002:113](#)). A treatment considered with a measure of scepticism by [Louchart et al. \(2005:385\)](#), given its limited postcranial remains. Another “swan-like” bird was described as *Megalodytes morejohni* Howard, 1992 from the Middle Miocene of California ([Howard 1992](#)). However, it is a giant diving anatid not related to swans, is more similar to the extinct diving *Chendytes*, and requires “firm” reassessment (see [Louchart et al. 2005:385-386](#)). The genus *Cygnus* was reported as first occurring in the Miocene of North America by [Wetmore \(1943\)](#), but the first named species is *Cygnus mariae* Bickart, 1990 from the late Miocene. *Afrocygnus chauvireae* Louchart et al., 2005 described in the tribe Cygnini, from the late Miocene Toros Menalla Djurab locality, Chad, represents the earliest swan named outside the eastern and Mediterranean regions of Africa. [Louchart et al. \(2005\)](#) also reported the temporal presence of an unnamed smaller taxon from the same region, and that *Afrocygnus* fossils were identified from the latest Miocene to lower Pliocene of Sahabi, Libya.

Geese first appear in the middle Miocene Nördlinger Ries of Germany, represented by an undetermined species of *Anser* ([Heizmann & Hesse 1995](#)), and occur in the late Miocene of Bulgaria with *Anser thraceiensis* Burčák-Abramovič & Nikolov, 1984 ([Mlíkovský 2002:116](#)). The first appearance of *Branta* in the late Miocene of Europe is *B. thessaliensis* Boev & Koufos, 2006 from Greece. However, the authors advance no apomorphies for *Branta* (see [Boev & Koufos 2006:21](#)). Both *Anser* and *Branta* appear in the upper middle to late Miocene of North America ([Miller 1961:401](#); [Bickart 1990](#)), these fossils are younger than *Presbychen abavus* Wetmore, 1930 from the middle Miocene Temblor Formation of California ([Brodkorb 1964:212](#); [Howard 1964a:271](#)). From the latest Miocene/early Pliocene Big Sandy Formation of Arizona, [Bickart \(1990:17–34\)](#) named *Anser arenosus* Bickart, 1990, *Anser arizonae* Bickart, 1990, and *Bonibernicla (=Branta) woolfendeni* (Bickart, 1990); he also listed two other indeterminate anserines, an *Anabernicula* sp., and three undetermined species of *Anas*. Later, in an assessment of the western Mongolian Hyargas Nuur 2 fossils (see also below), [Zelenkov \(2012b\)](#) argued *Bonibernicla (=Branta) woolfendeni* (see above), was likely a junior synonym of *Bonibernicla ponderosa* Kurochkin, 1985. Originally named as a shelduck in Tadorninae, *B. ponderosa* was recognised by [Zelenkov \(2012b\)](#) as a “relatively small” goose and transferred to Anserinae. From the Caucasian region of Europe, two “anserines” were reported from the upper middle Miocene Sarmatian Hipparion Fauna, eastern Georgia, in the form of *Anser eldaricus* Burčák-Abramovič & Gadziev, 1978, and *Anser udabnensis* Burčák-Abramovič, 1957 ([Aslanova & Burčák-Abramovič 1968](#); [Burčák-Abramovič & Gadziev 1978](#); [Mlíkovský & Švec 1986](#)). *A. eldaricus* was named from such fragmentary remains that its “generic and familial identification must be questioned” ([Worthy Pers. Obs. Unpubl.](#)), additionally, [Bickart \(1990:27\)](#) observed that *A. eldaricus* is “larger than all extant geese”. The taxon *Chenornis graculoides* Portis, 1884 is sometimes listed in Anseriformes *incertae sedis* ([Lambrecht 1933:367](#)), or Anserinae

(Brodkorb 1964:211), but Howard (1964a:322) doubted its anatid affinities. Mlíkovský (2002:256) considered it attributable to Phalacrocoracidae.

The first confirmed occurrence of tadornines in Europe is from the early Pliocene, with the appearance of the genus *Tadorna* in Bulgaria and France (Mlíkovský 2002:117). However, an earlier arrival in Europe is possible, if Mlíkovský's (2002:117) referral of the Moldavian late Miocene *Anserobranta tarabukuni* (Kuročkin & Ganea, 1972) to *Alopochen* is correct (Worthy & Lee 2008). Olson (1985:188) reported Tadornini from the middle Miocene Calvert Formation of Maryland, USA (see also Alvarez & Olson 1978:530), and also mentioned fossils similar to *Tadorna* from the middle Miocene Nördlinger Ries, Germany, which remain undescribed. *Anser scaldii* (Lambrecht, 1933) was listed incorrectly by Lambrecht (1933:368), attributing it to Van Beneden 1872, but Van Beneden (1872:288, see also 1873:372) only mentions the name, and in both cases it is a *nomen nudum* (see Mlíkovský 2002:125; Worthy et al. 2008a:228). However, a brief description of the fossil given by Lambrecht (1933:368) validated the name (see Mlíkovský 2002:125). In a reassessment of the holotype (a right humerus), Worthy et al. (2008a:232) synonymised *Anser scaldii* with *Branta bernicla* (Linnaeus, 1758) in Anserinae.

There are few additional anatids recognised from the early Miocene of Europe. Mlíkovský (2002:124) erected *Oxyura doksana* from Dolnice, Czechia (see also Mlíkovský 1998:40). However, this attribution may be in doubt as *O. doksana* is described from the cranial end of a left coracoid, and features of *Oxyura* coracoids do not differ substantially from those of many anatid genera (see Worthy et al. 2007). Heizmann & Hesse (1995) reported a species of *Mergus* from the middle Miocene Steinheimer Becken, Germany, and there is a late Miocene record of *Dendronessa* sp. from Götzendorf, Austria (see Mlíkovský 2002:118).

*Sinanas diatomas* Yeh, 1980 of middle Miocene age from Shandong Province in China, was considered by Mlíkovský & Švec (1986:261) to be poorly described, and they listed *S. diatomas* in subfamily *incertae sedis*, pending revision of the holotype, the location of which is unknown. Alvarez & Olson (1978:525) described *Mergus miscellus* Alvarez & Olson, 1978, from the middle Miocene Calvert Formation, Virginia, USA. However, this assignment was criticised by Livezey & Martin (1988:209), as no synapomorphies were identified between the fossil and extant *Mergus* taxa. *Anas luederitzensis* Lambrecht, 1929 from the lower Miocene of South-West Africa (now Namibia), exhibits proximal humerus morphology distinct from *Anas*, so does not belong in the genus (Howard 1964a:296). However, it was listed in *Anas* by Brodkorb (1964:221), thus its affinities remain unresolved.

The middle Miocene Sharga locality, Oshin Formation, western Mongolia has yielded both diving and non-diving anatids (Zelenkov 2012a; see also Zelenkov 2011, 2012b; Zelenkov & Kurochkin 2012). Medium-sized diving anatids are represented by the new genus and species *Sharganetta mongolica* Zelenkov, 2011; although distinguished as a diving duck, it was not recognised as an erismaturine (=oxyurine), and its taxonomic position remains unresolved (Zelenkov

2011). The new genus and species *Nogusunna conflictoides* Zelenkov, 2011 was also recognised as a diving duck, but assignment to Erismaturinae (=Oxyurinae) was not supported. Both taxa were argued by Zelenkov (2011) to be more advanced than the early Miocene non-diving *Mionetta blanchardi* (see above), and more primitive than Anatinae and Erismaturinae. A third new genus and species *Protomelanitta gracilis* Zelenkov, 2011, was considered to be more evolutionary advanced than *S. mongolica* and *N. conflictoides*, and a basal relative of extant Mergini (Zelenkov 2011). Later, the new genus and species *Chenoanas deserta* Zelenkov, 2012a was described as a “relatively” large duck, most closely resembling the extant South American Steamer ducks (*Tachyeres* spp.). At the same time, Zelenkov (2012a:525) considered the diving duck *Aythya shihuibas* (Hou, 1985), named from the upper Miocene of Lufeng, Yunnan, China, showed characteristics of the humerus that had not been recorded in the genus *Aythya*, and transferred it to *Protomelanitta*, a genus he considered ancestral to *Aythya*. In a reassessment of the fossils, Stidham (2015:336) saw “no clear differences” in characteristics of the humerus between *Aythya shihuibas* and the extant *A. farina*, and did not accept its transfer to *Protomelanitta*. Additionally, Stidham (2015:347) suggested the taxon was likely a distinct species outside the *Aythya* crown group. From middle Miocene Esmeralda Formation, Nye County, Nevada, USA, *Protomelanitta bakeri* Stidham & Zelenkov, 2017 was named as a putative sister-taxon of *P. gracilis* (see above), these were not specialised diving ducks, but proposed as primitive members of Erismaturinae (=Oxyurinae) or a “closely related group”, and imply waterfowl dispersal between Eurasia and North America during the middle Miocene (see Stidham & Zelenkov 2017:228).

Zelenkov (2012a:522) argued “*Anas*” *sansaniensis* (see above) may belong in *Chenoanas* or “a closely related genus”, and not in *Anas*, in agreement with Mlíkovský (2002) and Worthy et al. (2007), and regarded it “plausible” to consider *Anas sansaniensis* as a *nomen dubium* until its status was appropriately reassessed. Among extinct species, Zelenkov (2012a:525) considered *Chenoanas deserta* to most closely resemble *Matanas enrighti* Worthy et al., 2007 from New Zealand (see 1.4.7.2 below), and argued both taxa may be representative of tribe Cairinini, particularly the genus *Aix*. What is more, Zelenkov (2012a:525) did not support the assignment of the upper Oligocene taxon *Anas oligocaena* (see 1.4.6.1 above) to *Dendrochen* by Mlíkovský & Švec (1986), and suggested features of the holotype (a distal humerus) also showed affinity with *Aix*.

Additionally, from the Sharga locality, the new genus and species *Mioquerquedula minutissima* Zelenkov & Kurochkin, 2012 was erected for a fossil anatid smaller in size than all extant anseriforms, excluding *Nettapus pulchellus*. The species showed affinity with some species of *Anas*, but its morphological similarities with tribe Cairinini appeared to be plesiomorphic (Zelenkov & Kurochkin 2012). *Aix praeclara* Zelenkov & Kurochkin, 2012, was described from the cranial end of a right coracoid, and represents the oldest, and only extinct species of *Aix* named, although undescribed fossil remains of *Aix* have been noted from the late Miocene of Austria (see Zelenkov & Kurochkin 2012:423). Additionally, the taxon *Anas meyerii* (Milne-Edwards, 1867-71) of the upper

Miocene of Öhningen, Germany, which Howard (1964a:297) considered generically indeterminate, and which had been synonymized with *Anas velox* by Mlíkovský (2002:118), was subsumed into *Mioquerquedula* by Zelenkov & Kurochkin (2012). Consequently, *Mioquerquedula velox* together with *M. minutissima* describe a middle to late Miocene distribution across France and western Mongolia.

The Hyargas Nuur 2 locality, of the Great Lakes Depression in western Mongolia, is considered late Miocene or early Pliocene in age (Zelenkov 2012b; see also Zelenkov 2013), and so is described here. Zelenkov (2012b) reviewed the Hyargas Nuur anseriforms, and confirmed the validity of *Aythya magna* Kurochkin, 1985, and *Aythya spatiosa* Kurochkin, 1976 previously described from the site, but noted the taxonomic position of the fossils remains uncertain, pending assessment of additional material. Zelenkov (2012b) also listed fossils of an unidentified species of *Aix*, and three unidentified species of *Anas* which were distinguishable by size. In addition, upon revision of the holotype (a cranial fragment of a coracoid) of *Aythya* (= *Anas*) *molesta* (Kurochkin, 1985), originally described in *Anas*, Zelenkov (2012b:615) argued it conformed with that of *Aythya*.

From the late Miocene, eastern Paratethys Morskaya-2 locality of Rostov Oblast, southwestern Russia, *Anas kurochkini* Zelenkov & Panteleyev, 2014 was described as a medium-sized duck, morphologically distinct from all extant dabbling ducks, but the “uniform” morphology of the coracoid suggested it likely belonged to the lineage of mallards (Zelenkov & Panteleyev 2014).

In central Hungary, Polgárdi comprises a series of late Miocene localities that have produced one of the richest European avifaunas outside of the early Miocene sequences of Saint-Gérand-le-Puy in France (see above). In his review of the Polgárdi anseriforms, Zelenkov (2016a) transferred *Aythya* (= *Anas*) *denesi* (Kessler, 2013) to *Aythya*, as the morphology of the incisura capitis and tuberculum dorsale of the humerus differed from that in *Anas*, and was typical of *Aythya*. The taxon *Anas albae* Jánossy, 1979 from Polgárdi, was considered by Lambrecht (1933:690) to be a species of *Mergus*, was listed by Mlíkovský (2002:124) as genus *incertae sedis*, and Zelenkov & Kurochkin (2012:426) proposed it may belong in *Mioquerquedula* (see above). Later, however, based on features of the fossil carpometacarpus, which constitutes the only known specimen of the species, Zelenkov (2016a:516) argued it should be considered Mergini genus *incertae sedis*. Zelenkov & Panteleyev (2014) advanced that it was “reasonable to ascribe” all latest Miocene small ducks from the eastern Paratethys localities (see above) to *A. albae*; including the small *Anas* duck noted from the Hyargas Nuur 2 locality in eastern Mongolia (see Zelenkov 2012b, and above), and *A. pullulans* Brodkorb, 1961, described from the approximately contemporary deposits of Juntura, Oregon, USA, as these fossils may be representative of a single species (see Zelenkov & Panteleyev 2014)

There are several late Miocene species named in *Anas* that are not identifiable to genus although they are anatids. Mlíkovský (2002:124; 125) listed the following as genus *incertae sedis*: *Anas isarensis* Lambrecht, 1933, from Aumeister, Germany, *Anas eppelsheimensis* Lambrecht, 1933, from Eppelsheim, Germany, *Anas oeningensis* Meyer, 1865 from Öhningen, Germany, *Anas*

*risgoviensis* Ammon, 1918 from Lierheim, Germany, and *Anser brumeli* Milne-Edwards, 1871 from Orleanais, France.

Other than species of *Anas* in Anatinae, two anseriform genera are known from the upper Miocene of Monte Observacion, Argentina: *Eutelornis patagonica* Ameghino, 1895, and *Eoneornis australis* Ameghino, 1895, are based on limited material and were considered *incertae sedis* by Lambrecht (1933:354; 353) and Howard (1964a:320; 321).

A summary of ten late Miocene to Early Pliocene avifaunas from Florida by Becker (1987), reported 13 anatid taxa: a *Dendrocygna* sp., a *Branta* sp., three indeterminate anserines, an indeterminate tadornine, two indeterminate anatines, two indeterminate *Anas* spp., one indeterminate *Aythya* sp., an *Oxyura* cf. *dominica* (Linnaeus, 1766), and the extinct *Bucephala ossivallis* Howard, 1963. Olson & Rasmussen (2001:285) reported a single specimen of middle Miocene age possibly of ?*Anas* from the ?Pungo River Formation, North Carolina, USA which “is much smaller than any living Northern Hemisphere species of that genus”.

In conclusion, by the middle Miocene the only extant anserine genera that are undoubtedly present in the fossil record are *Cygnus* and *Anser*. By the late Miocene, *Oxyura*, *Mergus*, *Bucephala*, *Aythya* and *Aix* have made appearances. The genus *Anas* Linnaeus, as now defined (e.g. Livezey 1997a:468; 477), is now known from the middle Miocene (Zelenkov 2012a), and repeatedly reported from the latest Miocene (see Zelenkov 2012b; Zelenkov & Panteleyev 2014; and references therein), implying its evolution through the middle to late Miocene.

**1.4.6.3 Pliocene** (5.3–1.8 Ma)—a comprehensive review of Pliocene anseriforms by Howard (1964a) reported 28 species of which 18 species in three genera were extinct. Howard (1964a:254) attributed *Dendrocygna eversa* Wetmore, 1924 from Arizona, to the upper Pliocene, but Brodkorb (1964:215) placed it in the lower Pleistocene. Anserines are diverse in the Pliocene with several species, some still extant, in existing genera (number of extinct taxa in parenthesis): *Cygnus* 3(2), *Anser* 2(1), and *Branta* 3(3; see Miller, L. 1930:208, 1944:27; Miller, A. 1948:132; Howard 1964a:233; 241-242). A single extinct anserine genus and species, *Eremochen russelli* Brodkorb, 1961, is known from the lower Pliocene of Oregon (Brodkorb 1964:213; Howard 1964a:271). Brodkorb (1958a:238) described *Cygnus hibbardi* Brodkorb, 1958 from the early Pleistocene Hagerman lake beds of Idaho. Brodkorb (1964:211) listed *C. hibbardi* in *Olor* and again assigned an early Pleistocene age, but it was listed by Howard (1964a:261) as Pliocene (“lower Pleistocene?”) age. Tadornines are represented by a single extinct species *Anabernicula minuscula* (Wetmore, 1924) from the San Pedro Valley Formation, Arizona. The taxon was listed by Howard (1964a:287) as upper Pliocene, but as early Pleistocene by Brodkorb (1964:219). In addition, Howard (1964a:234; 242) listed species in the extant genera (number of extinct species in parenthesis): *Anas* 9(4), *Aythya* 4(2), *Nettapus* 1(1), and *Bucephala* 2(1). Howard (1964a:299) listed *Nettion bunkeri* Wetmore, 1944 from the upper Pliocene Rexroad fauna, Kansas in *Anas*, as she did not accept the fossil was sufficiently distinct. However, Brodkorb (1964:225) listed this specimen as *Nettion bunkeri*. He also reported *N.*

*bunkeri* from the middle Pliocene McKay Reservoir, Oregon (Brodkorb 1958b:252), and from the middle Pliocene Hemphill Formation, Texas (Brodkorb 1964:225). This taxon and two other teal, *Nettion greeni* Brodkorb, 1964 from the Ash hollow Formation, South Dakota and *Nettion ogallalae* Brodkorb, 1962 from the Ogallala Formation, Kansas were also listed from the early Pliocene by Brodkorb (1964:225). *Nettion* was subsequently used as an infragenus of *Anas* by Livezey (1997a:479). Brodkorb (1964:228) listed *Fuligula aretina* Portis, 1889 and *Fuligula sepulta* Portis, 1889, from the upper Pliocene of Italy in *Aythya*. Both taxa were considered representative of *Anas* and transferred by Cheneval (1987:150). Subsequently, Mlíkovský (2002:120) synonymized them with *Anas platyrhynchos*. In an addendum to his 1964 review, Brodkorb (1967:110) listed *Anas apscheronica* Burčák-Abramovič, 1958 from the upper Pliocene of Enikend, Azerbaijan (see also Mlíkovský & Švec 1986:260). Howard (1964a) however, did not list *A. apscheronica* in her review.

Since Brodkorb's (1964) and Howard's (1964a) reviews, many taxa have been named. From Europe, Boeuf & Mourer-Chauviré (1992) described a small avian fauna of upper Pliocene age from Chilhac, France that included: *Anser* spp., the extant shelduck *Tadorna* cf. *tadorna*, and the new species *Bucephala cereti* Boeuf & Mourer-Chauviré, 1992. They also reported that *Tadorna tadorna* is well represented in the upper Pliocene karstic fillings from Villány, Hungary. Boev (1998:53, 2002b:33; 37) reported *Balcanas pliocaenica* Boev, 1998 as "a medium sized anatine", and *Anas* spp. from the early Pliocene of Dorkovo, Bulgaria. However, *B. pliocaenica* was synonymised with *Tadorna tadorna* by Mlíkovský (2002:117), as was *Anas submajor* Jánossy, 1979, from Villány, Hungary (Mlíkovský 1982:200; see also Bocheński 1997:305; Mlíkovský 2002:117). In addition, *Nettapus anatoides* (Depéret, 1890) from the upper Pliocene of Roussillon, France was originally described by Depéret (1890) as *Anser*, but was listed as *Nettapus* due to its "close affinity" by Brodkorb (1964:227) and Howard (1964a:312). *Nettapus anatoides* was similarly included in the synonymy of *Tadorna tadorna* by Mlíkovský (2002:118). Boev (2000:186) described the swan *Cygnus verae* Boev, 2000 from the early Pliocene of Sofia, Bulgaria. Mlíkovský & Švec (1986:262) reviewed anseriforms from the middle Pliocene of Western Mongolia, and transferred *Anas soporata* Kurochkin, 1968 to *Dendrocygna* (*sensu lato*), but taxonomic comparisons were limited. Subsequently, a reinvestigation of *A. soporata* material by Zelenkov & Kurochkin (2012:421), showed that the species should not have been assigned to *Dendrocygna*, and it was retained in *Anas*. Mlíkovský & Švec (1986:263) placed *Anser* (*Chen*) *liskunae* Kurochkin, 1976 in *Olor* as a smaller relative of *Olor bewickii* (Yarrell, 1830). Zelenkov (2012b:612) reassessed the fossil, noted differences in the humerus between it and *Olor*, and reassigned it to the subgenus *Chen* within *Anser*. At the same time, *Anser* (*Chen*) *devjatkini* Kurochkin, 1971, named from the Hyargas Nuur 2 locality (see 1.4.6.2 above), and accepted in *Anser* by Mlíkovský & Švec (1986:263), was noted by Zelenkov (2012b:611) as "undoubtedly" belonging to *Chen*, and also reassigned. Mlíkovský & Švec (1986:264) synonymised *Cygnus pristinus* Kurochkin, 1971 with *Cygnus olor* (Gmelin, 1789), but this assignment was not accepted by Zelenkov (2013:158), as the fossil was "clearly separable" from *C.*

olor in “several details of almost all of the known skeletal elements”. Mlíkovský & Švec (1986) accepted the generic assignment of *Aythya spatiosa* Kurochkin, 1976, and transferred *Heteroanser* (= *Heterochen*) *vicinus* (Kurochkin, 1971) to *Anser*. However, in his reassessment of *Heteroanser vicinus*, Zelenkov (2012b:608) noted “essential differences” in tarsometatarsus morphology between it and *Anser*, and erected the new genus *Heteroanser* for it.

Several species from North America have also been named. From Nebraska, an extinct goose *Anser thompsoni* Martin & Mengel, 1980 was described from the late Pliocene Broadwater Formation (Martin & Mengel 1980:76). Short (1970:542) described *Heterochen pratensis* Short, 1970 from the early Pliocene Valentine Formation based on a goose-sized tarsometatarsus which, however, did not “permit elucidation of the tribal affinities”. Olson & Rasmussen (2001:282) described the avifauna of the Lee Creek mine site, from the early Pliocene Yorktown Formation, North Carolina, and reported at least 20 anseriform species of which only *Anabernicula minuscula* (see above) was extinct. Emslie (1992:250) reported a significant avifauna from two upper Pliocene/lower Pleistocene sites in Florida that included: *Dendrocygna* spp., extant *Branta canadensis*, the extinct *Anabernicula gracilentia* Ross, 1935, five extant species of *Anas*, two extant species of *Aythya*, one extant species of *Bucephala*, and one extant species of *Mergus*. In addition, he described the new genus and species *Helonetta brodkorbi* Emslie, 1992 and argued similarities with *Nettapus*, and the new species *Oxyura hulberti* Emslie, 1992. Alvarez (1977:215) described *Oxyura zapatanima* Alvarez, 1977 from the upper Pliocene/lower Pleistocene Lago de Chapala site, Mexico.

In summary, most extant genera of waterfowl have their first appearance in the Pliocene and many extant species have a Pliocene record.

**1.4.6.4 Pleistocene** (1.8-0.1 Ma)—as seen above, the formative period of the extant avifauna occurred during the Oligocene–Miocene (33.7–5.3 Ma), and most extant genera had evolved by the terminal Miocene (e.g. Olson 1985; Feduccia 1999; Olson & Rasmussen 2001). Many species of Pleistocene anseriforms are known (e.g. Lambrecht 1933; Delacour & Mayr 1945; Brodkorb 1964; Howard 1964a; Mlíkovský & Švec 1986; Zelenkov & Kurochkin 2014), but most are in extant genera or are extant taxa. Therefore, the evolution of Pleistocene anseriform faunas contributes little to modern faunas, except in insular circumstances.

Flightless anseriforms evolved repeatedly on islands, and constitute the majority of new Pleistocene genera. For example, the flightless Campbell Island teal *Anas nesiotis* and Auckland Island teal *A. aucklandica* were afforded specific rank following molecular (Johnson & Sorenson 1999:797; Kennedy & Spencer 2000:154), plumage and behaviour (Marchant & Higgins 1990), and morphological (Livezey 1997a:478) analyses demonstrating they were distinct taxa (Gill et al. 2010:43; see also Kear 2005:579; 581). Additionally, employing molecular analyses Mitchell et al. (2014a) showed that the Chatham duck *Pachyanas chathamica* Oliver, 1955 was the most basal member of a clade including the New Zealand (NZ) and sub-Antarctic brown teals (*A. chlorotis*, *A. aucklandica*, and *A. nesiotis*), and so synonymised *Pachyanas* with *Anas*. However, it was left to

Williams (2015:76) to make the new combination *Anas chathamica* (Oliver 1955). Livezey (1990:639) remarked “*A. aucklandica* is the only anatid in which the loss of flight was coincident with a derived decrease in body size”. To this taxon (which includes *A. nesiotis* as a subspecies; see Livezey 1990:640), must now be added *Anas marecula* Olson & Jouventin, 1996, another small flightless anatid, described from the Holocene of Amsterdam Island in the Southern Indian Ocean (see Olson & Jouventin 1996:4).

The Auckland Island merganser *Mergus australis* Hombron & Jacquinot, 1841 was a basal merganser limited to a small group of islands situated south of NZ (Livezey 1989). More recently, a new species of extinct merganser was named from the Holocene of the Chatham Islands. *Mergus milleneri* Williams et al., 2014 was described as smaller than *M. australis*. Williams et al. (2014) suggested that the vernacular name of mergansers from the Auckland Islands revert to “Auckland Islands Merganser”, as the name “New Zealand Merganser” *sensu* Gill et al. (2010) was no longer appropriate, and another unnamed form is known from mainland NZ. Finsch’s duck *Chenonetta* (=Euryanas) *finschi* (Van Beneden, 1875), was placed in *Chenonetta* following Worthy & Olson’s (2002:12) analysis showing that postcranial morphological differences between the extant *C. jubata* and extinct *C. finschi* were “phylogenetically superficial”, and related to functional adaptation to the loss of flight ability. *Chenonetta finschi* was widely distributed in the late Pleistocene and Holocene of both North and South islands (Worthy 1988; Livezey 1989; see also Introduction to Chapter 3).

Flightlessness has repeatedly led to giant waterfowl. For example, two species of *Cnemiornis* from NZ: *C. gracilis* Forbes, 1892 from the Middle Pleistocene of the North Island, and *C. calcitrans* Owen, 1865 from the late Pleistocene/early Holocene of the South Island, were large flightless geese that evolved from a *Cereopsis novaehollandiae*-like ancestor on NZ (*contra* Livezey 1989, 1997a; see Worthy et al. 1997; Worthy & Holdaway 2002). In the Hawaiian Islands, highly derived, flightless, goose-like ducks were first described from Molokai (see Olson & Wetmore 1976). Four species have now been recognised: *Thambetochen chauliodous* Olson & Wetmore, 1976, *T. xanion* Olson & James, 1991, *Chelychelynechen quassus* Olson & James, 1991, and *Ptaiochen pau* Olson & James, 1991. These giant extinct anatids, known as “Moa-nalo”, were large terrestrial herbivores that evolved flightlessness before the emergence of the youngest island Hawaii, where they were not represented (Olson & James 1991; Sorenson et al. 1999). True anserines are represented on the islands by the extant *Branta sandvicensis*, the extinct *B. hylobadistes* Olson & James, 1991, the giant Holocene *Branta* (=Geochen) *rhuax* (Wetmore, 1943), and several undescribed taxa (Olson & James 1991). Recently, Olson (2013) reassessed *B.* (=Geochen) *rhuax* and synonymised the taxon with *Branta*.

In the Mediterranean, swans evolved to form dwarf and volant *Cygnus equitum* Bate, 1916, and giant, flightless *Cygnus falconeri* Parker, 1865 terrestrial forms on Malta (see Northcote 1992, and references therein). There are two possible exceptions to the norm that flightlessness evolved in insular situations. As seen in the flightless seaducks of the genus *Chendytes*, which comprised two species: *Chendytes lawi* Miller, 1925, and the smaller *C. milleri* Howard, 1955, from the Pleistocene

and early Holocene of coastal California (Livezey 1993). Species of *Chendytes* were highly adapted flightless diving waterfowl (Miller 1925; Howard 1955, 1964b). However, distribution and eggshell data suggest *Chendytes* was breeding on the islands of coastal California (Miller 1961; Miller et al. 1961; Livezey 1993), so these were indeed insular taxa. In a morphological analysis Livezey (1993) concluded *Chendytes* was within Mergini and closest to *Somateria*, but had some similarity to *Melanitta*.

#### 1.4.7 The Australasian anseriform fossil record

**1.4.7.1 Australian anseriform fossils**—are relatively poorly represented in the Australian Palaeogene compared to the global record (Worthy & Yates 2017). For example, one of the earliest Australian anseriform representative is *Eoanseranas handae* from the Oligo-Miocene of Riversleigh (see 1.4.4 above; and Worthy & Scanlon 2009). Several Australian fossil faunas contain anseriforms (e.g. Rich & van Tets 1982; Tedford & Wells 1990; McNamara 1990; Vickers-Rich 1991; Boles & Mackness 1994; Boles 1997), but the fossil record over the last ~26 Ma is relatively “patchy” (Worthy & Yates 2017). South Australia incorporates some of the most significant sources of fossil birds (Stirton et al. 1961; Woodburne et al. 1994), particularly the inland Oligocene through Pliocene sequences located around about lakes Palankarina, Pinpa, Ngapakaldi, and Yanda (Rich & van Tets 1982; Pledge & Tedford 1990; Vickers-Rich 1991; Rich et al. 1991; Worthy 2008, 2009). For example, several taxa possibly older than *Eoanseranas handae* (see above) derive from the Oligo-Miocene fluvio-lacustrine Etadunna and Namba Formations in the Lake Eyre Basin: the erismaturines (=oxyurines) *Pinpanetta tedfordi* Worthy, 2009, *P. vickersrichae* Worthy, 2009, and *P. fromensis* Worthy, 2009 were described in the new genus *Pinpanetta* Worthy, 2009. Along with the new tadornine genus and species *Australotadorna alecwilsoni* Worthy, 2009 (see Worthy 2009:417; 422; 425; 429). These South Australian sequences provide the richest and oldest anseriform assemblages in Australia (Vickers-Rich 1991; Worthy 2009). At the same time, Worthy (2009) reported three “indeterminate” anatid bones from the late Miocene (~7–5 Ma) Waite Formation at Alcoota, Northern Territory, that differed from those of *Australotadorna* and extant species of *Tadorna*. He also noted the presence of an “indeterminate duck about the size of *Malacorhynchus*” (Worthy 2009:411). The late-middle through late Miocene (12–5 Ma) was an important period as the modern Australian anseriform biota was assembled during that time, likely due to continental Australia’s increasing proximity to northern landmasses facilitating colonisation by new taxa (Worthy & Yates 2017). A later assessment of the Alcoota anseriforms yielded the new genus and species *Awengkere magnanatis* Worthy & Yates, 2017, representing a large anatid with tarsometatarsus morphology distinct from cereopsines and all terrestrial anatids (e.g., tadornines, anserines, and *Chenonetta jubata*). The taxon is also not closely related to “modern-type anatines” e.g., species of *Anas* and *Aythya*. Worthy & Yates (2017:248) argued *A. magnanatis* was potentially a “relic” of the basal radiation of Australian waterfowl, and was likely a large and “adept” diver, exploiting a niche distinct to those occupied by

known erismaturine (=oxyurine) taxa. Additional material of the small “indeterminate duck about the size of *Malacorhynchus*” (*sensu* Worthy 2009; see above), revealed key features indicating the duck was not a terrestrial grazer, it was an aquatic taxon, but not a specialist diver, and it differed from all extant Australian taxa (Worthy & Yates 2017:232). Those authors also argue the taxon most resembles erismaturine (=oxyurine) taxa which dominate the Oligo-Miocene of Australia (see Worthy 2009 above), and NZ (see Worthy & Lee 2008 below), and may have been congeneric with *Tirarinetta kanunka* Worthy, 2008, described from the Pliocene of South Australia (see below).

No extant anseriforms are known from pre-Pliocene deposits (Vickers-Rich 1991; Worthy 2009), although taxa such as *Anseranas semipalmata* (see above), erismaturines (=oxyurines), and the anserine *Cereopsis novaehollandiae*, are all considered to be the most primitive members of the modern fauna, with a presumed long history in the region (Livezey 1986, 1989, 1996, 1997a; Worthy et al. 1997). *Tirarinetta kanunka* was described from the Pliocene Tirari Formation of the Lake Eyre Basin (Worthy 2008), accompanying a fauna including nine extant taxa: *A. semipalmata*, *C. novaehollandiae*, *Cygnus atratus*, *Tadorna tadornoides*, *Biziura lobata*, *Oxyura australis*, *Aythya australis*, and two species of *Anas* cf. *A. castanea* and cf. *A. gracilis* forming part of the diversity. Worthy (2008) argued the composition of this fauna demonstrated that in Australia, there was minimally only one extinction of a waterfowl taxon since the Pliocene. Additionally, Worthy & Pledge (2007) reported a fossil from the late Pliocene Parilla Sand location in South Australia, and referred it to the extant taxon *Tadorna*.

Extant anseriform taxa become more common in Plio-Pleistocene deposits (Tedford & Wells 1990). For example, most of the Australian fossil birds named by De Vis between 1885 and 1911 may be referred to extant taxa (see Rich & van Tets [1982:361-366] for a full list of taxa; and van Tets & Rich [1990:167-168] for a full list of De Vis’ publications), but as many as 12 species in six genera were considered by van Tets & Rich (1990:165) to be valid. In all, Olson (1977a) referred nine species of anseriforms named by De Vis to extant taxa.

As seen from the preceding review, most extant anseriform genera evolved between the middle Miocene and the Pliocene. Heizmann & Hesse (1995) and Cracraft (2001) have proposed that some taxa evolved in the southern hemisphere and spread northwards into Asia and Europe. Resolution of the composition of Australasian anseriform faunas in the Oligo-Pliocene period is required to provide substance to test these ideas, and clarify the evolution of the modern fauna.

**1.4.7.2 New Zealand anseriform fossils**—the NZ archipelago is the emergent part of a continental fragment that was once part of Gondwana, but which separated from Australia and Antarctica over the period 82–60 Ma (Cooper & Millener 1993; Sutherland 1999; Worthy et al. 2017a). The NZ terrestrial flora and fauna is highly distinct, and suggestive of a Gondwanan influence (see Fleming 1979; Worthy et al. 2007). The Holocene avifauna comprised of some 217 indigenous breeding species of birds (67% endemic), of which 54 species (25%) are now extinct (Worthy et al. 2017a:180). The terrestrial fossil record, although extensive through the Quaternary (< 2.56 Ma), is

one of the world's poorest for the pre-Quaternary period (Worthy & Holdaway 2002; Worthy et al. 2017a), and until recently a Neogene record of terrestrial and freshwater animals had been tenuous. While endemic taxa of Gondwanan origin described by Fleming (1979) imply a vicariant origin for some taxa, most birds are assumed to have dispersed from Australia (e.g. Falla 1953; Fleming 1962, 1979; Millener 1991). This may have been the case until the early Miocene, but after ~20 Ma, NZ landmasses became increasingly isolated due to rising sea levels, and such overwater dispersals may have included an Antarctic component, as the southern continent was actually closer to NZ than the Australian landmass at that time (see Worthy et al. 2017a:179).

The discovery in 1980 (see Douglas et al. 1981; Douglas 1986) and description of the St Bathans Fauna (Worthy et al. 2007), from the early to upper Miocene (19–16 Ma) Manuherikia Group sediments in Central Otago, constitutes the most important fossil bird site found in NZ (Fordyce 1991), and represents the only known window into the Neogene origins of the modern NZ avifauna (Worthy et al. 2017a). The Manuherikia Group sediments were formed in Lake Manuherikia, a large fresh-water lake >5,600 km<sup>2</sup> in area, during a period characterised by the transition from warm rainforest to cooler temperatures and defined seasonality (Douglas 1986; Pole et al. 2003). The St Bathans Fauna derives from lacustrine deposits forming the lower part of the Bannockburn Formation, and comprises the most diverse fossil waterfowl assemblage known worldwide (Worthy et al. 2017a). The avifauna is dominated by minimally nine species of anseriforms (Worthy et al. 2007, 2008b; Worthy & Lee 2008), accompanied by at least 31 other species: accipitriforms (Worthy et al. 2007), apodiforms (Worthy et al. 2007), charadriiforms (De Pietri et al. 2016a, 2016b), columbiforms (Worthy et al. 2009; De Pietri et al. 2017), ciconiiforms (Scofield et al. 2010; Worthy et al. 2013a), gruiforms (Worthy et al. 2011a; Mather et al. 2019), palaeognaths (Tennyson et al. 2010; Worthy et al. 2013b), passeriforms (Worthy et al. 2010a), phoenicopteriforms (Worthy et al. 2010b), procellariiforms (Worthy et al. 2007), and psittaciforms (Worthy et al. 2011b). Notably, the remains of a parrot an order of magnitude larger than the extant heavyweight *Strigops habroptila*, were recently described from the St Bathans Fauna (Worthy et al. 2019).

Anatid bones represent six species described in four genera, two species of erismaturines (=oxyurines) are numerous, and a tadornine is common as well (Worthy et al. 2007). The erismaturine *Manuherikia lacustrina* Worthy et al., 2007 was interpreted as a small specialist diver, similar to the non-diving Miocene duck *Mionetta blanchardi* (see 1.4.6.2 above), and *Malacorhynchus scarletti* Olson, 1977 named from the Holocene of Pyramid Valley, North Canterbury (Olson 1977b:132). *Manuherikia minuta* Worthy et al., 2007 was described as a very small, volant duck with the same postcranial proportions as the extant Australian duck *Malacorhynchus membranaceus*. *Manuherikia douglasi* Worthy et al., 2008 was described as a duck with wing bones “more modified” for diving than *M. lacustrina*, and was a somewhat larger taxon (Worthy et al. 2008b:108). More recently, the presence of an as yet undescribed species of *Manuherikia* succeeding *M. lacustrina* in younger sections of the stratigraphy has been reported (see Worthy et al. 2017a:186). *Miotadorna*

*sanctibathansi* Worthy et al., 2007 was named in the new genus *Miotadorna*, it was a shelduck similar to extant *Tadorna tadornoides*, but more similar to *Alopochen aegyptiacus* (see Worthy et al. 2007:15). *Dunstanetta johnstoneorum* Worthy et al., 2007 was named in the new genus *Dunstanetta* within ?Anatinae incertae sedis, as a combination of features suggests *D. johnstoneorum* had affinity with anatids such as *Chenonetta finschi* and *Hymenolaimus malacorhynchos* (Gmelin, 1789), however, its true affinities remain obscure (Worthy et al. 2007:19). *Matanas enrighti* Worthy et al., 2007 was described in the tribe ?Anatini and is an anatid the size of *Hymenolaimus*. Similarly, the close familial affinities of this taxon remain unresolved (Worthy et al. 2007:19). However, *M. enrighti* has been associated with *Chenoanas deserta*, named from the middle Miocene Sharga locality in western Mongolia by Zelenkov (2012a:525; see 1.4.6.2 above), who argued both taxa may be representative of the genus *Aix* in tribe Cairinini.

A phylogenetic analysis by Worthy & Lee (2008:680), using a suite of 133 morphological characters, was conducted to illuminate the affinities of *M. lacustrina*, *D. johnstoneorum* and *M. sanctibathansi*, in conjunction with *Mionetta blanchardi* from Europe. Those authors concluded that *Manuherikia* and *Dunstanetta* were basal erismaturine (=oxyurine) anatids, and also subsumed all dendrochenines into an expanded Erismaturinae (=Oxyurinae; Worthy & Lee 2008:703; see also 1.4.6.2 above). An outcome of this analysis was the recognition of a novel sister-taxon relationship of *Stictonetta naevosa* and *Malacorhynchus membranaceus*, with this clade reported as either part of an erismaturine (=oxyurine) clade, or a “distinct lineage of approximately oxyurine (=erismaturine)-grade”. They also found *Chenonetta finschi* and *C. jubata* to be sister taxa, as argued previously by Worthy & Olson (2002) and contra Livezey (1997a), and the clade was found to be of similar evolutionary grade to Tadorninae. However, *Chenonetta* was not monophyletic in these analyses, so its status remains uncertain.

Worthy et al. (2008b) remarked on the occurrence in the St Bathans Fauna, of a species of anserine that was more similar to *Cereopsis novaehollandiae* and *Cnemiornis* spp., than other anserines, but of smaller size. The taxon likely had the ability to fly well, and was only “slightly smaller” than *C. novaehollandiae*. A second, smaller anserine represented by two coracoids was also noted by Worthy et al. (2008b:109), and together these fossils likely represent a continuum of cereopsines in Australasia since the early Miocene (Worthy et al. 2008b:110). The fossils remain undescribed, as “adequate” material has yet to be identified (see Worthy et al. 2017a:186).

#### 1.4.8 The modern Australasian anseriform fauna

The modern anseriform fauna of NZ, including species that were extant until around 500 years ago, prior to human-induced extinctions, comprised 18 species in 11 genera (Holdaway 1989; Worthy 2002, 2005; Worthy & Holdaway 2002; Worthy & Olson 2002; Gill et al. 2010; Tennyson 2010; Allentoft et al. 2014), of which only two genera are endemic to NZ (*Cnemiornis* and *Hymenolaimus*). *Cnemiornis* was considered by Livezey (1989, 1997a) to be a primitive monotypic

family. However, by employing an expanded dataset of morphological characters and genetic data, [Worthy et al. \(1997\)](#) showed that it was the sister taxon to the extant Australian *Cereopsis novaehollandiae* (see also **1.4.6.4** above). The genera *Chenonetta* (=Euryanas), *Oxyura*, *Biziura*, and *Malacorhynchus* are now extinct in NZ, but each has sister taxon still extant in Australia (see below). Of the modern NZ fauna, *Tadorna variegata* and the three insular teal: *Anas chlorotis*, *A. nesiotis*, and *A. aucklandica* form a sister clade to the Australian teal *A. castanea* and *A. gracilis* ([Marchant & Higgins 1990](#); [Kear 2005](#); [Dickinson & Remsen 2013](#)). However, [Mitchell et al. \(2014a:427\)](#) argued a “much closer affinity” of NZ teal with the Madagascan teal *A. bernieri* than with the Australian teals (see also **1.4.6.4** above). Additionally, four species of *Anas* are shared with Australia: *A. gracilis*, *A. castanea*, *A. superciliosa*, and *A. rhynchotis* (see [Gill et al. 2010](#)).

In comparison, the modern native Australian waterfowl fauna comprises two families: the monotypic Anseranatidae, and 20 species in 12 genera of Anatidae ([Christidis & Boles 2008](#); [Dickinson & Remsen 2013](#)). Within these anseriforms: *Anseranas*, *Biziura*, *Stictonetta*, *Cereopsis*, *Chenonetta*, and *Malacorhynchus* are monotypic in Australia, although *Biziura*, *Chenonetta*, and *Malacorhynchus* had sister species in NZ (see above). Therefore, the evolution of the modern Australian and NZ faunas were closely associated.

Significantly, the Australian fauna comprises monotypic or low diversity genera considered comparatively basal in Anseriformes. For example, Anseranatidae is regarded as sister to Anatidae, and *Dendrocygna*, *Oxyura*, *Biziura*, and *Stictonetta* are all now considered primitive anatids ([Madsen et al. 1988](#); [Sibley & Ahlquist 1990](#); [Christidis & Boles 2008](#); [Sraml et al. 1996](#); [Livezey 1997a](#); [Johnson & Sorenson 1999](#); [Sorenson et al. 1999](#); [Donne-Goussé et al. 2002](#); [Callaghan & Harshman 2005](#); [McCracken & Sorenson 2005](#); [Worthy & Lee 2008](#); [Dickinson & Remsen 2013](#)). *Malacorhynchus membranaceus*, however, is often placed within Anatinae (see [Marchant & Higgins 1990](#); [Livezey 1997a](#); [Callaghan & Harshman 2005](#); [Dickinson & Remsen 2013](#)), although several lines of evidence, e.g., feather proteins ([Brush 1976](#)), molecular ([Sraml et al. 1996](#); [Gonzalez et al. 2009](#)), and morphological and behavioural ([Frith 1967](#); [Olson & Feduccia 1980](#)) analyses, suggest it should be classified outside of Anatinae, and placed before Tadorninae in the phylogenetic sequence. [Worthy & Lee \(2008\)](#) and [Worthy \(2009\)](#) proposed including the extant taxa *Oxyura*, *Nomonyx*, *Biziura*, *Thalassornis*, *Stictonetta*, and *Malacorhynchus* in the single expanded subfamily Erismaturinae (=Oxyurinae), and that a position below Tadorninae was appropriate. In addition, *M. membranaceus* was considered by [Kear \(2005:442\)](#) to be part of the “old endemic component of Australia’s avifauna, with no close relatives elsewhere” (see also [Sraml et al. 1996:54](#)).

In summary, significant numbers of Australasian extant taxa are relatively basal in the anseriform radiation, perhaps implying a long history of evolution in the region.

## 1.5 The Avian Brain

The following review consists of three parts: **1**, first, I broadly review the development of our understanding of vertebrate neuroanatomy, including comparative assessments conducted to better appreciate vertebrate brain evolution; **2**, second, I review avian brain nomenclature and define the terminology for the morphological divisions of the avian brain that I will use. By convention, nomenclatural and morphological protocols employed are described in Methods. However, I define in advance the language adopted for the description of avian endocranial anatomy in this thesis, so that the reader is not required to refer to subsequent thesis sections for clarification of nomenclature presented in the following texts. Anatomical divisions described are not comprehensively inclusive of all recognised brain structures, but are constrained by both the limitations of the geometric morphometric analyses employed in this work, and by the full specimen suite which contains several fossils (see below); **3**, finally, I describe the current understanding of functional attributes for morphological divisions of the avian brain relevant to the current work, and introduce concepts informing the discussion of neuroanatomical trends revealed in subsequent data Chapters.

### 1.5.1 Understanding the vertebrate brain

Much of our knowledge of neuroanatomy comes from the comparative anatomists of the early 19<sup>th</sup> through early 20<sup>th</sup> centuries, during which time initial concepts and principles of vertebrate brain evolution began to be developed by anatomists like Goethe (1749-1842), and Oken (1779-1851) amongst others. This early work culminated in the unifying ideas of Ludwig Edinger (1855-1918), who framed a theory of brain evolution based on linear stepwise progression, in the manner of Aristotle's "scala naturae", i.e., brains of extant vertebrates retained ancestral structures (reviewed comprehensively by [Northcutt \(2001\)](#); see also [Emery & Clayton 2005](#); [Jarvis et al. 2005](#); [Reiner 2009](#); and references therein). Along these lines, the nomenclature that was used to define vertebrate cerebral subdivisions was developed ([Jarvis et al. 2005](#)). Consequently, the avian cerebrum, or telencephalon, was initially considered entirely composed of basal ganglia, and involved only in instinctive behaviour. The underlying premise was that the so-called neocortex, which typifies mammalian brains, exclusively facilitated malleable behaviour ([Jarvis et al. 2005](#)). These ideas were contested by several subsequent works, epitomised by [Hodos & Campbell \(1969\)](#), who showed there existed no foundation for scala naturae concepts. In fact, it was shown by multiple studies that the morphology of the vertebrate brain does not follow phylogeny in a linear manner, and that the neural anatomy of all living animals are characterised by both primitive and derived features ([Northcutt 2001](#), and references therein).

The basic neural architecture common to both sauropsid (reptiles and birds), and synapsid (mammal) lineages, appears to have evolved from a stem-amniote ancestor, which existed prior to the divergence of these lineages some 330 Ma ([Jarvis et al. 2005](#); [Walsh & Knoll 2018](#)). However, the

organisation of pallial domains between sauropsids and synapsids is more distinct, and suggests organisation of telencephalic cortical structures (i.e., layered in mammals, and nuclear in birds; see below), evolved separately sometime after the divergence of these lineages (Jarvis et al. 2005; Reiner et al. 2005; Walsh & Knoll 2018). The sauropsid clade Archosauria includes crocodiles, non-avian dinosaurs and birds (Walsh & Knoll 2018). The composition of the basic archosaur brain Bauplan (Walsh & Knoll 2018:fig 5.2) shows brain regions are located along a relatively straight axis, and describe a characteristic elongate brain morphology. This basic brain form is displayed by non-sauropod dinosaurs and related archosaurs (see Walsh & Knoll 2011; and references therein), and is similar to that found in living crocodiles (e.g. Witmer et al. 2008:fig 6.3) and caimans (e.g. Brusatte et al. 2016:fig 4).

The brain morphology of birds, however, reflects a derived morphology that is characterised by caudal regions being “folded” under a much expanded, or hypertrophied, telencephalon, producing a “flexed” form in lateral view (Walsh & Knoll 2018:63; see also Fig. 1.5.1A below). This characteristic morphology differs little from those seen in many Neogene avian taxa, and suggests the form of the avian brain has changed little in overall structure over the last 40 Ma (see Walsh & Knoll 2011, and references therein).

It is now recognised that functions similar to those of the mammalian neocortex are performed by the large pallial territories of the avian cerebrum, which unlike those of mammals, is of a nuclear rather than a layered structure, and supports cognitive abilities more advanced in some species than those of many mammals (Emery & Clayton 2005; Jarvis et al. 2005; Reiner et al. 2005; Reiner 2009; Walsh & Knoll 2018). In fact, Emery & Clayton (2004:45; see also Balanoff et al. 2013; Walsh et al. 2016) showed that birds have evolved relatively large brains with respect to body size, and the greatest hypertrophy of the avian brain, with respect to those of mammalian lineages, occurs in the areas of the hyperpallium (see Corfield et al. 2012:fig 6). This derived cerebral hypertrophy in birds has facilitated intellectual abilities which rival those of primates, at least in some psittaciform (Pepperberg 1999, 2002) and corvid taxa (Hunt 2000; Weir et al. 2002; Emery & Clayton 2004; Mehlhorn et al. 2010; see also Lefebvre et al. 2004; Chakraborty et al. 2015; Olkowitz et al. 2016).

In the latter years of the 20<sup>th</sup> century, many comparative studies attempting to better understand the evolution of the vertebrate brain were conducted. Early approaches were limited to investigations of brain size, i.e., individual brain regions compared with body mass, brain volume or other brain regions (e.g. Jerison 1973, 1991; Stephan et al. 1981; Armstrong 1983), later studies used multivariate comparative methods (Iwaniuk & Hurd 2005). This approach to understand brain evolution was necessary for two reasons. First, among regions of the brain there are processes that result in correlated morphological changes in other regions, but not all (e.g. Barton & Harvey 2000; de Winter & Oxnard 2001; Barton et al. 2003; Whiting & Barton 2003; Iwaniuk et al. 2004a). Thus, the variation in size of an individual brain region may be a consequence of: **1**, the size of other brain

regions, or **2**, as result of differential hypertrophy of distinct regions (see **1.5.2** below). Second, the structure of the brain is likely the result of several disparate selection pressures, making it difficult to distinguish evolutionary patterns within the brain with bivariate comparisons (Iwaniuk & Hurd 2005).

**1.5.1.1 Modern taxa**—initial multivariate analyses focused upon discrimination between developmental constraints (e.g. Finlay & Darlington 1995; Finlay et al. 2001), and the identification of evolutionary change in brain composition (e.g. Barton & Harvey 2000; Clark et al. 2001; de Winter & Oxnard 2001; Iwaniuk et al. 2004a, 2004b). An important outcome of these approaches was the identification of “cerebrotypes” (*sensu* Clark et al. 2001:189), whereby a series of ‘volume fractions’ or brain ratios, are derived by dividing the volume of each of the 12 internal brain regions by the volume of the entire brain, the composition of which defines the cerebrotypic of a species (Clark et al. 2001). Several previous studies had identified specific patterns of brain composition that varied among clades and by ecological niche, and similar patterns have been recognised in mammals (see Legendre et al. 1994; Lapointe et al. 1999; Clark et al. 2001; de Winter & Oxnard 2001), amphibians (Doré et al. 2002) and fish (Huber et al. 1997; Wagner 2001a, 2001b). The extent to which the phylogeny or ecology of taxa are related to particular cerebrotypes, also varies between species investigated. For example, in mammals, cerebrotypes may describe whole lineages, and species with similar modes of life will cluster together, such as in fossorial and semi aquatic insectivores (e.g. Legendre et al. 1994; Lapointe et al. 1999; Clark et al. 2001; de Winter & Oxnard 2001). Additionally, Ridet & Bauchot (1991) demonstrated that some lineages of fish displayed cerebrotypes related to specific ecological niches, even across disparate clades. Similar results have been reported in African cichlids (Huber et al. 1997), and teleosts (Wagner 2001a, 2001b). The fact that cerebrotypic clustering has been shown to correspond to ecological niches across species, provided a potentially useful mechanism for investigating brain evolution in the context of phylogeny, ecology and behavioural ecology (Iwaniuk & Hurd 2005).

There is compelling evidence to suggest cerebrotypes are also present in birds. Emery & Clayton (2004) reported similar neural structures in corvids and psittaciforms, Carezzano & Bee de Speroni (1995) described convergent evolution in the telencephalic composition of aquatic species, and in the overall brain composition of psittaciforms and passeriforms (Iwaniuk et al. 2005). Strong correlations between developmental differences and brain size have been demonstrated in birds (see Bennett & Harvey 1985; Nealen & Ricklefs 2001; Iwaniuk & Nelson 2003; Franklin et al. 2014), and Burish et al. (2004) revealed that the evolution of a large telencephalon has been driven by social complexity. Additionally, Iwaniuk & Hurd (2005) analysed the brains of 67 species and recognised five main cerebrotypes relating to both phylogeny and ecology. More recently, migratory behaviour was shown to be correlated with brain size (Sol et al. 2010), and brain region composition in passerines (Fuchs et al. 2014). Corfield et al. (2015b) tested olfactory capabilities in 135 species of birds representing 21 orders, and reported that olfactory bulb size in birds reflected phylogeny and behaviour. The underlying premise of these studies is that acquisition of a novel or complex

behaviour, is accompanied by an enlargement of its processing area (e.g. [Mehlhorn et al. 2010](#)). Thus, the brain may vary considerably in the absolute and relative sizes of its divisions (see also [Charvet et al. 2011](#); [Ward et al. 2012](#); [Sayol et al. 2016](#)). Although, differential hypertrophy of individual brain regions, putatively driven by functional requisites, has also been shown to not necessarily affect overall brain size in anseriforms (see [Iwaniuk & Nelson 2001](#); [Iwaniuk et al. 2004b](#)). The interpretation of many results, however, have been somewhat controversial (see [Healy & Rowe 2007](#); [Iwaniuk 2004](#)).

**1.5.1.2 Fossil taxa**—the study of fossil brains also has a long history (see [Northcutt 2001](#), and references therein). It is generally accepted that the field of modern comparative palaeoneurology was founded “almost single-handedly” by Otilie ‘Tilly’ Edinger in the 1920’s ([Buchholtz & Seyfarth 1999:351](#)). Tilly Edinger (1897–1967) was the daughter of the great neuroanatomist Ludwig Edinger (see above), and after her PhD graduation in 1921, she built upon and extended the work of researchers like Cornelius Ariëns Kappers (1877–1946), and Othniel Marsh (1831–1899).

Marsh, along with L. Edinger and Ariëns Kappers, developed and promoted a series of ‘laws’ concerning brain evolution, most notably that mammalian brains were characterised by a progressive increase in size across the Cenozoic. Marsh’s “general law of brain growth” was initially accepted by Tilly Edinger, but later systematically contested in her 1929 treatise “Die fossilen Gehirne” ([Buchholtz & Seyfarth 1999](#); [Northcutt 2001](#); [Walsh & Knoll 2011](#)). Among her many significant achievements, Edinger was instrumental in recognising sequential neural innovation in the history of a taxon, identified through comparison of multiple casts of fossil brains through a geological sequence, and she documented similar trends across reptile, bird and mammal taxa across her career ([Buchholtz & Seyfarth 1999](#); [Walsh & Knoll 2011](#)). Although the work of Harry Jerison did not specifically involve fossil brains, he was a much respected friend and colleague of Tilly Edinger (see [Buchholtz & Seyfarth 1999:359](#)), and so is acknowledged here. Jerison’s extension of earlier work on the relationship between brain and body size, and his development of quantitative approaches for the assessment of brain size (e.g., encephalisation quotients), arguably influenced the extension of the mathematical approach to neuroanatomy more so than anyone else in the modern era (see [Buchholtz & Seyfarth 1999](#); [Walsh & Knoll 2011](#), and references therein). The scope of Jerison’s influence across the field cannot be overstated, and his Principle of Proper Mass (see [Jerison 1973](#); and **1.5.4** below), inspired generations of research into the functional and structural attributes of the vertebrate brain.

Information of brain shape, which may be derived from the skeletal brain cavity, varies between archosaur clades. This is due to differing thicknesses of the meningeal or dural envelope (i.e., dura mater) enveloping the brain in life, which may occupy a large measure of the endocranial space between brain and skull (e.g. [Witmer et al 2008](#); [Walsh & Knoll 2011](#); [Walsh & Knoll 2018](#)). In birds, however, the braincase is largely ossified, and the relationship between the brain, dural envelope and skull is so “intimate” that the skeletal brain cavity provides a close approximation of the actual brain

within (see [Jerison 1973](#); [Iwaniuk & Nelson 2002](#); [Franzosa 2004](#); [Striedter 2005, 2006](#); [Witmer et al. 2008](#); [Picasso et al. 2009](#); [Walsh et al. 2013](#); [Walsh & Knoll 2018](#)).

The advent of high resolution magnetic resonance imaging (MRI), and micro-computed tomography ( $\mu$ CT) scanning technologies, have allowed for the extraction of a three dimensional (3D) model cast (hereafter endocast) representative of the brain cavity of a skull (see [Witmer et al. 2008](#); [Walsh & Knoll 2011](#); [Walsh et al. 2013](#); [Walsh & Knoll 2018](#)). Model endocasts represent the only way to study the evolution of brain structure in extinct birds ([Walsh & Knoll 2018](#)), and have facilitated several studies reconstructing the brain anatomy of fossil birds and kin. For example, [Domínguez Alonso et al. \(2004\)](#) reconstructed the brain and inner ear of the early avialan *Archaeopteryx lithographica* von Meyer, 1861, and argued the taxon closely resembled modern birds in derived structural adaptations necessary for flight. *Archaeopteryx lithographica* also formed the focus of a study by [Balanoff et al. \(2013\)](#), who used volumetric partitions of endocasts sampled across theropod lineages regressed against taxon body size, and argued the brain of *A. lithographica* displayed a “more generalised” volumetric signature, smaller than those of other non-avian dinosaurs. Those authors also identified a high endocranial volumetric signature for crown birds, but failed to recover *A. lithographica* in a “uniquely transitional” position between non-avian maniraptorans, and the avian crown group. [Zelenitsky et al. \(2011\)](#) considered olfactory ratios of 20 species of non-avian theropod dinosaurs, seven species of fossil birds, and 130 species of extant birds. Testing the hypothesis that olfaction diminished through early avian evolution, they revealed the importance of olfaction actually increased.

Studies focusing on Neogene birds, include those of [Ashwell & Scofield \(2008\)](#), and [Corfield et al. \(2008\)](#), who described the external morphology and volumetric variation in relative endocast size across NZ palaeognath lineages. [Picasso et al. \(2011\)](#) employed an ontogenetic series of *Rhea americana* endocasts, and by comparisons of volumetric and anatomical differences with endocasts of other ratites, reported three distinct brain morphologies among palaeognaths. [Scofield & Ashwell \(2009\)](#) supported molecular and morphology based hypotheses of the behaviour and evolution of Haast’s eagle, by using morphological characteristics of the nervous system and sensory apparatuses derived from  $\mu$ CT scans of *Hieraaetus moorei* (Haast, 1872) fossils. [Milner & Walsh \(2009\)](#) determined the brain anatomy of the odontopterygiform *Odontopteryx toliapica* Owen, 1873 and the phaethontiform *Prophaethon shrubsolei* Andrews, 1899 from the lower Eocene London Clay, exhibited a degree of telencephalic hypertrophy comparable to living avian species, but yet the eminentia sagittalis (see **1.5.2** below) was poorly developed. [Walsh & Milner \(2011b\)](#) described the neuromorphology of *Halcyornis toliapicus* Koenig, 1825 also from the London Clay, reporting the eminentia sagittalis, in contrast to those of *O. toliapica* and *P. shrubsolei* (see above), was strongly developed and comparable to those of living species. Additionally, [Walsh & Milner \(2011b\)](#) argued the morphology of the optic foramina (i.e. type 1: *sensu* [Hall et al. 2009](#)) was consistent with [Mayr’s \(2007b\)](#) Pan-Psittaciform hypothesis for the affinities of *H. toliapicus*, as type 1 foramina are also

characteristic of extant psittaciforms (see [Hall et al. 2009](#)). [Kawabe et al. \(2010\)](#) used the endocasts of 27 species representing 12 orders of birds, and by means of regression and correlation assessments of log transformed endocast length and width metrics on endocast volume, identified correlations between brain width and overall volume. [Kawabe et al. \(2013a\)](#) demonstrated by using  $\mu$ CT scans of 55 species representing 13 orders of mammals, and 64 species representing 21 avian orders, that volumes of brain endocasts have increased over evolutionary time in a wide range of mammal and bird taxa.

Fossil penguins have formed the focal taxa for several studies of endocranial anatomy. For example, [Ksepka et al. \(2012\)](#) used endocasts for three extant species of penguin, a fossil sphenisciform and two outgroup taxa, and assessed the transition from a volant ancestor to extant forms, reporting that despite over 60 Ma of evolution, the endocasts of extant penguins retain many traits linked to flight. [Paulina-Carabajal et al. \(2014\)](#) visualised and described the endocranial morphology of the Middle Miocene penguin *Pygoscelis calderensis* [Acosta Hospitaleche et al., 2006](#), and reported the brain morphology of the fossil was similar to living species of *Pygoscelis*, implying the palaeobiology of the extinct form was likely similar to extant species. [Tambussi et al. \(2015\)](#) assessed digital endocasts of six species of extinct and extant sphenisciforms along with six outgroup taxa, reporting caudal hypertrophy of the eminentia sagittalis accompanying mediolateral hypertrophy of the telencephalon (see **1.5.2** below) in penguin taxa over time. Notably, the rostral positioning of the eminentia sagittalis in fossil penguins, and the relative reduction in size, or hypotrophy, in comparison with the size of the eminentia sagittalis of extant taxa reported by [Tambussi et al. \(2015\)](#), is similar to dorsal endocranial trends found in the Eocene London Clay taxa assessed by [Milner & Walsh \(2009\)](#); see also [Walsh et al. 2016](#), and above). [Proffitt et al. \(2016\)](#) generated an endocast of the stem sphenisciform *Waimanu* sp. along with penguin endocasts sampled by other projects (e.g. [Kawabe et al. 2014](#) below; [Ksepka et al. 2012](#); and [Tambussi et al. 2015](#) above). They coded endocast morphology, and mapped the relative positioning of the eminentia sagittalis onto a supertree of waterbird taxa derived from recent molecular analyses (e.g. [Hackett et al. 2008](#); [Jarvis et al. 2014](#); and [Prum et al. 2015](#) above). [Proffitt et al. \(2016\)](#) argued some endocranial features (e.g., laterally hypertrophied telencephalon), had appeared early in the evolution of the penguin clade, but that the dorsal eminentia sagittalis was distinctly hypotrophied in the stem taxon, and it corresponded with the condition seen in wing-propelled diving procellariiforms.

These forms of analyses employing endocast anatomy have substantially improved the understanding of fossil taxa, and using fossil remains for the assessment of ancestral avian brain shape is particularly useful in understanding palaeoneurological evolution over time (e.g. [Walsh & Knoll 2018](#)). Endocranial assessments of both fossil and extant taxa may facilitate reasonable correlations of brain region morphology with behavioural traits, and afford a secondary line of evidence within a phylogenetic framework (e.g. [Walsh & Knoll 2011](#); [Walsh & Milner 2011b](#); [Wood & De Pietri 2015](#)).

### 1.5.2 Nomenclature

I follow the nomenclature in [Baumel et al. \(1993\)](#); see Fig. 1.5.1) for osteology, innervation, and external or brain surface anatomy. Descriptions of the internal architecture of the avian brain follow [Jarvis et al. \(2005\)](#); see also [Corfield et al. 2012:fig 6](#)). At first mention, osteological, innervation, and brain surface anatomy is described using Latin nomenclature, with the anglicised equivalent bracketed, or mentioned immediately subsequent. Thereafter I use anglicised equivalents where appropriate.

Much disparate terminology has been employed for the description of surface morphology of the avian skull and brain, and in some instances with no consensus for precedence of any particular term over another (e.g., see [Baumel et al. 1993:xiv-xix](#); [Jarvis et al. 2005](#), and references therein). Furthermore, [Walsh & Knoll \(2018:61\)](#) recommended a “thorough review and standardisation” of vertebrate neurological nomenclature is conducted. Therefore, I prefer and will hereafter use the following nomenclature: eminentia sagittalis (**emsg**, Fig. 1.5.1), to describe the dorsal eminences of the hyperpallium (see [Corfield et al. 2012:fig 6](#)); cerebrum pars frontalis (rostral telencephalon; **tel.r**, Fig. 1.5.1), to describe the dorsorostralateral mesopallium and nidopallium (see [Corfield et al. 2012:fig 6](#)), rostral of the arteria cerebralis medialis (medial cerebral artery; **acm**, Fig. 1.5.1) dorsoventrolateral transition of the hemispherium telencephali (telencephalic hemisphere); cerebrum pars parietalis (caudal telencephalon; **tel.c**, Fig. 1.5.1), to describe the surface topology of the mesopallium, nidopallium and arcopallium (see [Corfield et al. 2012:fig 6](#)), forming part of the caudolateral telencephalon pallial complex, caudal of the medial cerebral artery dorsoventrolateral transition; tectum mesencephali (mesencephalon; **mes**, Fig. 1.5.1), to describe the lobus opticus or tectum opticus (optic lobe); and following the recommendation of [Baumel et al. \(1993:587\)](#), I distinguish between the membranous (duct) and osseous (canal) labyrinths of the inner ear, using ductus semicircularis anterior/posterior/lateralis, to describe the anterior/posterior/lateral/semicircular ducts of the labyrinthus vestibularis (vestibular organ).

### 1.5.3 Endocranial anatomy

The following comprises a general overview of avian brain anatomy forming the morphological structures referred to in following text. By necessity, I also refer to osseous structures forming the avian neurocranium enclosing the brain, and on occasion refer to dromornithid skulls in Chapter 4 Appendices (4.7; Figs. A4.4–A4.5), comprising the only avian skulls figured in this thesis.

For geometric morphometric assessments (see 1.5.5 below), I used discrete manipulatable patches (hereafter modules) comprising semilandmarks (Slms) placed on grid junctions in various density configurations, in a manner that captured the shape characteristics of particular zones of the brain. Modular landmark (Lm) suites are introduced in Chapter 2 General Methods (see General Methods, 2.2; Fig. 2.1), and described comprehensively in Chapter 2 Appendices (A2.1), and Chapter 3 Appendices (A3.8.1) below.

### 1.5.3.1 Innervation

**1.5.3.1.1 Nervus olfactorius**—the olfactory nerve (**I**) transmits rostrocaudally into the bulbus olfactorius (olfactory bulb; **bo**, Figs. 1.5.1A, 1.5.1C) through the bony foramen n. olfactorii (**fof**, Chapter 4 Appendices, Figs. A4.4K–L, A4.5K) of the rostrorodorsal cranium.

**1.5.3.1.2 Nervus opticus**—the optic nerve (**II**) passes through the os laterosphenoidale forming the ventromedial wall of the orbit and transmits into the endocranial cavity through the foramen opticum (**fopt**, Chapter 4 Appendices, Figs. A4.4K–L, A4.5K). The optic nerves divide rostrrolaterally at the septum interorbitale into two branches of the chiasma opticum (e.g. **II**; Figs. 1.5.1A, 1.5.1C).

**1.5.3.1.3 Nervus trigeminus**—the trigeminal nerve (**V**) is a complex nerve comprising three divisions. The medial or ophthalmic branch carries the ophthalmic nerve (n. ophthalmicus–**V**<sub>1</sub>; Fig. 1.5.1C) transmitting to the ganglion trigeminale (trigeminal ganglia) on the ventral surfaces of the mesencephalon (see below), through the foramen n. ophthalmici (**foph**, Chapter 4 Appendices, Figs. A4.4K–L; A4.5K). The foramen n. ophthalmici opens into the “lacerate (presphenoid) fossa” (*sensu* [Worthy et al. 2016b:fig 1D](#)), located ventrolaterally from the foramen opticum, between the laterosphenoid, basisphenoid, parasphenoid and septum interorbitale bones (os laterosphenoidale complex) of the caudomedial wall of the orbit. The lateral or maxillomandibular branch of the trigeminal ganglion carries the maxillary nerve (n. maxillaris–**V**<sub>2</sub>; Fig. 1.5.1C), and the mandibular nerve (n. mandibularis–**V**<sub>3</sub>; Fig. 1.5.1C). Both of which enter the skull rostroventrolaterally at the foramen n. maxillomandibularis (**fm**, Chapter 4 Appendices, Figs. A4.4K–L, A4.5K), a single opening between the prootic and laterosphenoid bones of the skull.

**1.5.3.1.4 Trigeminal ganglia**—receive the three divisions of the trigeminal nerve (see above), and insert on the ventral surfaces of the mesencephalon (**tri.g**; Figs. 1.5.1A, 1.5.1C). The medial portion carrying the ophthalmic nerve (n. ophthalmicus–**V**<sub>1</sub>) separates from the lateral branch carrying the maxillary (n. maxillaris–**V**<sub>2</sub>) and mandibular nerves (n. mandibularis–**V**<sub>3</sub>). Trigeminal ganglia exhibit a small ganglionic bridge between the two primary eminences in all galloanseres assessed, excluding the erismaturine *Biziura lobata* (see below).

**1.5.3.1.5 Nervus abducens**—the abducent nerve (**VI**; Fig. 1.5.1C) inserts on the rostroventral rhombencephalon, and is transmitted caudoventrally through the bony canalis n. abducentis, after entering the skull at the foramen n. abducentis, situated in the rostromedial os laterosphenoidale complex of the orbit.

**1.5.3.1.6 Nervus facialis**—the facial nerve (**VII**; Fig. 1.5.1A) inserts at the rostroventrolateral edge of the rhombencephalon, and shares with the vestibulocochlear nerves (**VIII**<sub>r</sub> and **VIII**<sub>c</sub>—see below) the single external ganglion vestibulare (vestibular ganglion; **gv**; Fig. 1.5.1B), within the bony fossa acustica interna, wherein the nerves diverge. The facial nerve shares the ostium canalis carotici (cranial carotid canal; **occ**, Chapter 4 Appendices, Figs. A4.4K–L, A4.5K), with several carotid

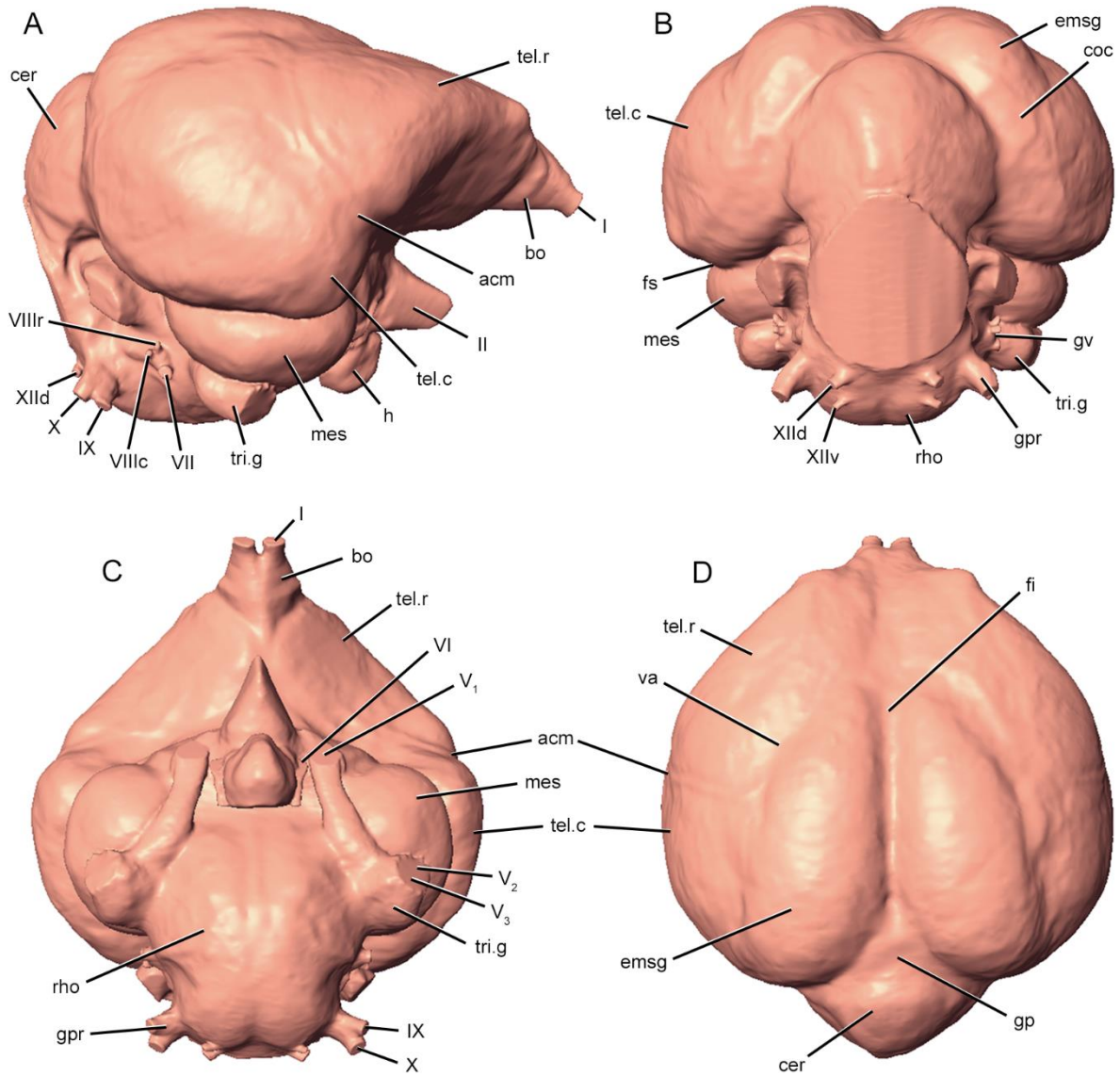


Figure 1.5.1. External endocast morphology and innervation nomenclature (see 1.5.2) used in this thesis. Illustrated using the endocast of *Aythya australis* (SAM B33108) in: RHS lateral (A); caudal (B); ventral (C); and dorsal (D) views. **Abbreviations**, **acm**, medial cerebral artery; **bo**, olfactory bulb; **cer**, cerebellum; **coc**, cerebrum pars occipitalis; **emsg**, eminentia sagittalis; **fi**, fissura interhemispherica; **fs**, fissura subhemispherica; **gp**, glandula pinealis; **gpr** proximal ganglion (ganglion of the glossopharyngeal [XI] and vagus [X] cranial nerves); **gv** vestibular ganglion (ganglion of the facial (VII), and the rostral (VIIIr) and caudal (VIIIc) vestibulocochlear nerves); **h**, hypophysis, note that the caudoventral hypophysis has been trimmed to facilitate full access to rostroventral rhombencephalon surfaces; **mes**, mesencephalon; **rho**, rhombencephalon; **RHS**, right hand side; **SAM**, South Australian Museum; **tel.c**, caudal telencephalon; **tel.r**, rostral telencephalon; **tri.g**, trigeminal ganglion (ganglion of the trigeminal [V] cranial nerve complex); **va**, vallicula telencephali; **I**, olfactory nerve (I); **II**, optic nerve (II); **V<sub>1</sub>**, ophthalmic nerve (V<sub>1</sub>); **V<sub>2</sub>**, maxillary nerve (V<sub>2</sub>); **V<sub>3</sub>**, mandibular nerve (V<sub>3</sub>); **VI**, abducent nerve (VI); **VII**, facial nerve (VII); **VIIIc**, caudal ramus of the vestibulocochlear nerve (VIII); **VIIIr**, rostral ramus of the vestibulocochlear nerve (VIII); **IX**, glossopharyngeal nerve (IX); **X**, vagus nerve (X); **XII<sub>d</sub>**, dorsal and; **XII<sub>v</sub>**, ventral rami of the hypoglossal nerve (XII).

vessels which enter the skull caudoventrolaterally of the condylus occipitalis (occipital condyle; **oc**, Chapter 4 Appendices, Figs. A4.4M–N), on the caudoventral os exoccipitale surface.

**1.5.3.1.7 Nervus vestibulocochlearis**—the vestibulocochlear nerve (**VIII**) comprises two vestibular rami. The rostral ramus (**VIIIr**; Fig. 1.5.1A) transmits alongside the facial nerve (**VII**) in the vestibular ganglion, and separates within the fossa acustica interna (see above). The caudal ramus (**VIIIc**; Fig. 1.5.1A) diverges in the fossa acustica interna, and inserts into the lateral semicircular duct of the vestibular organ.

**1.5.3.1.8 Nervus glossopharyngeus**—the glossopharyngeal nerve (**IX**; Figs. 1.5.1A, 1.5.1C) inserts caudoventrolaterally on the rhombencephalon (**rho**; Figs. 1.5.1B–C), and forms the rostral component of the combined root ganglion proximale (proximal ganglion; **gpr**; Figs. 1.5.1B–C) with n. vagus (**X**—see below). The proximal ganglion is enclosed in the fovea ganglii vagoglossopharyngealis in the lamina parasphenoidalis of the fossa cranii caudalis, between the exoccipital and opisthotic bones. The nerve enters the skull caudoventrolaterally from n. vagus (**X**) at the foramen n. glossopharyngeus (**fg**; Chapter 4 Appendices, Figs. A4.4M–N), situated in the fossa parabasalis.

**1.5.3.1.9 Nervus vagus**—the vagus nerve (**X**; Figs. 1.5.1A, 1.5.1C) forms the caudal ramus of the proximal ganglion, which it shares with the glossopharyngeal nerve (**IX**—see above). The nerves bifurcate distad to the proximal ganglion (see above), and are transmitted from the separate parabasal fossa: foramen n. vagi (**fv**), and foramen n. glossopharyngeus (**fg**) respectively, situated ventrolaterad of the occipital condyle, on the caudoventral os exoccipitale surface (Chapter 4 Appendices, Figs. A4.4M–N).

**1.5.3.1.10 Nervus hypoglossus**—the hypoglossal nerves (**XII**) comprise dorsal and ventral rami (**XIIId**; **XIIv**, respectively; Fig. 1.5.1B). The nerves enter the surface of the os exoccipitale at the foramen n. hypoglossi (**fh**, Chapter 4 Appendices, Figs. A4.4M–N), and are transmitted through canalis n. hypoglossi to insert on the caudoventrolateral brain surface.

### 1.5.3.2 Endocast surface morphology

**1.5.3.2.1 Eminentia sagittalis**—are dorsally hypertrophied, paired endocranial features incorporating the dorsal hyperpallium structures of the brain (see **H**; [Corfield et al. 2012:fig 6](#)). The eminentia sagittalis extend rostrocaudally and mediolaterally across the dorsal telencephalic hemisphere (cerebrum—see below), from the dorsomedial fissura interhemispherica (**fi**; Fig. 1.5.1D), to the dorsolateral vallecule telencephali (hereafter vallecule; **va**; Fig. 1.5.1D) transition zones delimiting the boundaries between the mediolateral eminentia sagittalis, and the dorsolateral cerebrum. Caudodorsally, the eminentia sagittalis grade into the cerebrum pars occipitalis (**coc**; Fig. 1.5.1B) of the caudomediolateral cerebrum, and into the dorsomedial transition zone rostrilaterad of the cerebellum (**cer**; Figs. 1.5.1A, 1.5.1D), in the region of the medial glandula pinealis zone (**gp**; Fig. 1.5.1D). [Note: in all Neornithes the pineal zone is much hypotrophied (*sensu* [Walsh et al. 2016](#); see also [Walsh & Knoll 2018](#)), and is not distinctly identifiable in any of the endocasts modelled for these

analyses. However, I use the terminology ‘glandula pinealis’ to identify the caudomedial zone rostrad of the medial cerebellum, where the so called “pineal trace” is evident in Archosauria].

**1.5.3.2.2 Telencephalic hemisphere**—is a general term describing the entire rostrocaudal and mediolateral telencephalon (cerebrum), incorporating the dorsorostrorocaudal mesopallium, rostrocaudolateral nidopallium, and caudoventrolateral arcopallium internal structures of the brain (see [Corfield et al. 2012:fig 6](#)). For the purposes of this study, the rostrocaudal cerebrum was segregated into two zones: the rostral and caudal telencephalon (see Fig. 2.1 and below), delimited by the dorsoventrolateral cerebral transition of the medial cerebral artery (**acm**; Figs. 1.5.1A, 1.5.1C–D).

**1.5.3.2.3 Rostral telencephalon**—is delimited from the eminentia sagittalis by the valleculla transition zone dorsolaterally (**va**; Fig. 1.5.1D). The mediolateral boundary of the rostral telencephalon begins approximately where the medial cerebral artery transitions the telencephalic hemisphere dorsoventrolaterally (**acm**; Figs. 1.5.1A, 1.5.1C–D), and extend rostrorodorsally, delimited by the dorsal rostromedial extension of the fissura interhemispherica zone (**fi**; Fig. 1.5.1D), to the caudomedial olfactory bulb (**bo**; Figs. 1.5.1A, 1.5.1C). The rostral telencephalon caudoventrolateral boundary is defined by the ventromedial endocranial contact zone with the os laterosphenoidale plate forming the caudal wall of the orbit (see **tel.r**; Fig. 1.5.1C), and incorporates this transition zone caudolaterally to meet the medial cerebral artery (**acm**; Figs. 1.5.1A, 1.5.1C–D), defining the border between the caudal and rostral telencephalon (see General Methods, Fig. 2.1 and below).

**1.5.3.2.4 Caudal telencephalon**—is delimited from the caudal eminentia sagittalis by the valleculla transition zone dorsolaterally (**va**; Fig. 1.5.1D). The mediolateral boundary of the caudal telencephalon begins approximately where the medial cerebral artery transitions the telencephalic hemisphere dorsoventrolaterally (**acm**; Figs. 1.5.1A, 1.5.1C–D). The caudal telencephalon extends ventrolaterally, and returns medially to grade into the dorsolateral mesencephalon (see below), at the fissura subhemispherica zone (**fs**; Fig. 1.5.1B). Caudally, the cerebrum pars occipitalis (**coc**; Fig. 1.5.1B), comprising part of the dorsal caudolateral caudal telencephalon, grades into the dorsorostrorolateral pons and medulla oblongata structures forming the overall hindbrain complex, rostromedial of the cerebellum (see below), in the vicinity of the glandula pinealis dorsolaterally, and medially at the rostromedial rhombencephalon (see below).

**1.5.3.2.5 Mesencephalon**—are defined by lateral expansion of the ventromedial midbrain (**mes**; Figs. 1.5.1B–C) ventrolaterad of the fissura subhemispherica, and rostrally by transition into the caudolateral chiasma opticum and tractus opticus structures, caudad of the rostral os laterosphenoidale complex. Caudomedially, the mesencephalon grade into the ventromedial pons and medulla oblongata structures forming the rhombencephalon complex (**rho**; Figs. 1.5.1B–C; see below).

**1.5.3.2.6 Cerebellum**—expands caudomedially from the transition zone of the cerebrum pars occipitalis, comprising part of the dorsolateral caudal telencephalon, and grades into the dorsorostrorolateral pons and medulla oblongata structures forming the overall mediolateral rhombencephalon complex. The cerebellum (**cer**; Figs. 1.5.1A, 1.5.1D) is delimited ventrally by the

eminence of the anterior semicircular duct of the vestibular organ, extends dorsomedially from the glandula pinealis (**gp**; Fig. 1.5.1D) region, and returns ventrally in the vicinity of the dorsolateral auricula cerebelli, to grade into the caudodorsal medulla spinalis at the osseous foramen magnum (**fm**; Chapter 4 Appendices, Figs. A4.4M–N).

**1.5.3.2.7 Rhombencephalon**—is the collective term describing the structures of the medulla oblongata and pons forming the caudoventrolateral areas of the hindbrain (**rho**; Figs. 1.5.1B–C). The rhombencephalon is delimited rostroventrally by the caudomediolateral or laterosphenoidale complex, forming the caudoventral wall of the orbits and hypophyseal structures. It is delimited rostroventrolaterally by transition into the trigeminal ganglia (**tri.g**; Fig. 1.5.1C), caudomedially by the eminence of the anterior semicircular duct of the vestibular organ, and caudoventrally by transition from the ventromediolateral medulla oblongata, into the medulla spinalis at the ventral osseous foramen magnum.

#### 1.5.4 Functional attributes of avian endocranial anatomy

[Jerison \(1973:8\)](#) proposed the “Principle of Proper Mass” which specifies particular sensory specialisations in the vertebrate brain are correlated with concomitant hypertrophy of the neural tissue controlling or processing related information, and the relative mass of functional neural tissue implies the relative importance of those functions in the species. Subsequently, comparative studies of neural systems eventuated in two primary hypotheses explaining differences seen in neural structure. [Finlay & Darlington \(1995\)](#) advanced the so called “easy” and “difficult” modes of brain evolution, where the “easy” mode proposed the likely determinant of brain size was a proportional “scaling up” of brain divisions effected by peak neurogenesis. Those authors argued the potential for differential enlargement of independent divisions of the brain, or “difficult” mode, would be “vanishingly small” ([Finlay & Darlington 1995:1583](#), see also [Finlay et al. 2001](#)). Additional studies found that overall brain size was in fact increased by independent hypertrophy of particular brain regions (see [Barton et al. 1995; 2003; Barton & Harvey 2000; Whiting & Barton 2003](#), and references therein), supporting [Jerison’s \(1973\)](#) observations, and which became to be known as the “mosaic” model of brain evolution (*sensu* [Barton & Harvey 2000](#)). The “developmental constraints theory” or “easy” mode has largely been dismissed as an adequate explanation for differences in brain architecture (see [Iwaniuk et al. 2004a](#), and references therein).

That mosaic evolution characterises some, but not all, of avian brain composition has been demonstrated by several subsequent works (see [Iwaniuk et al. 2004a; Corfield et al. 2012](#), and references therein). It is acknowledged that the brain is not strictly compartmentalised into regions that process exclusive neuronal input, but rather includes levels of interconnectivity across the whole structure ([Iwaniuk et al. 2004a](#), and references therein). It is clear that particular brain nuclei share greater levels of neuronal connectivity associated with specific functions, that a hypertrophied brain region reflects a greater level of “information-processing” power, and that these patterns are

somewhat reflective of functional specialisation (Dubbeldam 1998a; Barton & Harvey 2000; Iwaniuk et al. 2008; Corfield et al. 2012, 2015a, and references therein).

**1.5.4.1 Innervation**—characteristic mosaic correlations in the trigeminal system have previously been shown in several vertebrate taxa (see Gutiérrez-Ibáñez et al. 2009, and references therein). In birds, the trigeminal nerve system comprises the medial portion carrying the ophthalmic ( $V_1$ ) nerve which innervates the orbit and nasal cavity, the rostral palate and the tip of the upper bill, and forms a major sensory pathway for the skin of the head and maxillary rostrum. The maxillary ( $V_2$ ) branch innervates the maxillary rostrum and infraorbital regions, and the mandibular ( $V_3$ ) division innervates the entire lower bill and several mandibular and interramal regions (Dubbeldam 1980; Bubiń-Waluszewska 1981; Dubbeldam et al. 1981; Wild & Zeigler 1996). The trigeminal nucleus receives exclusively proprioceptive information from the descending tract and the principal sensory nucleus of the trigeminal system (Gutiérrez-Ibáñez et al. 2009). This includes not only projections from ophthalmic ( $V_1$ ) and maxillomandibular ( $V_2+V_3$ ) nerves described above, but taste information from the tongue is conveyed, within the lingual branch of the maxillomandibular ramus, by the facial (VII) nerve to the trigeminal principal sensory nucleus, which also receives input from glossopharyngeal (IX) and hypoglossal (XII) nerves (Dubbeldam et al. 1979; Bubiń-Waluszewska 1981; Wild & Zeigler 1980; Wild 1981, 1990; Dubbeldam 1998a, 1998b). Additionally, Dubbeldam (1992) proposed that differences in the trigeminal principal sensory nucleus were indicative of the functional demands of specific feeding behaviours. Gutiérrez-Ibáñez et al. (2009) reported hypertrophy of the trigeminal principal sensory nucleus in species that had feeding behaviours dependent on tactile input, and that beak morphology and the concentration of mechanoreceptors in the beak and tongue strongly correlate with feeding behaviour.

In summary, the trigeminal (V) nerve comprises the largest somatosensory cranial innervation complex, and transmits epicritic sensation from the entire facial region and mastication musculature (see Bubiń-Waluszewska 1981; Wild 1987; Dubbeldam 1998b).

The glossopharyngeal (IX) and vagus (X) nerves share the large proximal ganglion (see above). The glossopharyngeal components of this complex comprise somatic, “special” and visceral afferent fibres. The special fibres connect with the palatine branch of the facial (VII) nerve at the cranial cervical ganglion and are associated with sensory taste and tactile information (Dubbeldam et al. 1979; Bubiń-Waluszewska 1981; Dubbeldam 1984; Arends & Dubbeldam 1984). The general visceral efferent fibres of the glossopharyngeal (IX) nerve innervate the oesophagus and crop, exhibit size variability across taxa that show greater “distensibility” of the oesophagus (Bubiń-Waluszewska 1981), and are notably hypotrophied in taxa that have no crop (i.e., owls and hawks). The glossopharyngeal (IX) nerve complex bifurcates after separation with the vagus (X) nerve at the proximal ganglion and transmits, in two main afferent branches of the lingual and the laryngopharyngeal nerves, as the descending oesophageal nerves, innervating the tongue and the laryngeal muscles respectively.

The vagus (X) nerve complex is the most extensive of the sensory and motor cranial nerves, wherein there are two groups of motor fibres. The first consists of “general” visceral efferent fibres which innervate the muscles and glands of the thoracoabdominal viscera, including the heart and lungs etc., and is associated with circulation, respiration and digestion control (Bubień-Waluszewska 1981). The second consists of special visceral efferent fibres innervating the muscles of the pharynx and the larynx, reached via branches of the glossopharyngeal (IX) nerve (Bubień-Waluszewska 1981; for a contrary opinion, see Wild (1981) who argued that vagus projections are exclusively cardiovascular and pulmonary in function).

**1.5.4.2 Visual pathways**—there are three principal visual pathways in birds: **1**, the thalamofugal pathway transmits visual signals from the retina via the mesencephalon, to the principal optic nucleus of the dorsal thalamus, and thence to the eminentia sagittalis; **2**, the tectofugal pathway transmits via the mesencephalon, to the nucleus rotundas of the thalamus and proceeds to the entopallium of the telencephalon; and **3**, the third visual pathway transmits via the mesencephalon, through retinal recipient nuclei in the accessory optic system and pretectum, and projects to several regions of the brain, including the cerebellum (see Wylie et al. 2009; Iwaniuk et al. 2010; Wylie & Iwaniuk 2012; Corfield et al. 2012; Wylie et al. 2015, and references therein; see also Corfield et al. 2012:fig 6).

**1.5.4.2.1 Eminentia sagittalis**—are composed of two main regions, the larger ‘visual’ region located dorsally and extending caudodorsally receives retinal projections, and a smaller rostral somatosensory region, receives “substantial” somatosensory and kinesthetic input (Wild & Williams 2000; Iwaniuk et al. 2008; see also Wild 1987; Miceli et al. 1990; Deng & Wang 1992). The thalamofugal pathway incorporating the eminentia sagittalis has been shown to be primarily involved in binocular vision capability, and global stereopsis or depth perception (Pettigrew 1986; Rogers 1996; Iwaniuk & Wylie 2006; Iwaniuk et al. 2008, and references therein). Iwaniuk et al. (2008) showed the size of eminentia sagittalis were significantly correlated with more frontally orientated orbits and broader binocular fields (see also Wild et al. 2008), and argued changes in the relative size of the eminentia sagittalis suggest increases in somatosensory and motor processing capabilities (see also Wild 1997; Manger et al. 2002; Jarvis et al. 2005; Iwaniuk & Wylie 2006). Additionally, eminentia sagittalis are hypertrophied in species that forage using tactile information from the beak (Pettigrew & Frost 1985; Iwaniuk & Wylie 2006; Wylie et al. 2015; see also Martin 2009).

**1.5.4.2.2 Cerebrum** (rostral and caudal telencephalon)—the nido- and mesopallial structures of the cerebrum are recognised to form a complex with “integrative” functions (see Dubbeldam 1998a, and references therein). Thus, I describe functional interpretations for the cerebrum as a whole.

The internal structure of the dorsal and rostrocaudolateral cerebrum incorporates four main subdivisions: the hyperpallium, incorporating the eminentia sagittalis (see above), the mesopallium, incorporating the rostro- and caudodorsal telencephalon, the nidopallium, incorporating the rostro- and caudolateral telencephalon, and arcopallium incorporating the caudoventral telencephalon. The

rostromedial telencephalon incorporates the medial striatopallidal complex (striatum + pallidum) overlain rostrocaudally and dorsolaterally by the nidopallium, which is similarly overlain rostrocaudally and dorsolaterally by the mesopallium (Jarvis et al. 2005; Corfield et al. 2012). Dubbeldam & Visser (1987) showed that the caudolateral nidopallium receives arcopallial afferents sourced from the medial nidopallium, projecting mainly upon the lateral nidopallium, which contains a complex pattern of terminal fields. They identified a strong connection between the striatopallidal complex and the mediolateral nidopallium, arguing that in the mallard (*Anas platyrhynchos*) there exists two major telencephalic circuits: one relaying through the pallidum, and the other through the striatum, and that these afferent circuits play a major role in feeding behaviour.

As part of the tectofugal visual pathway (2), the telencephalon has been associated with a wide range of behaviours including: feeding, taste, tactile sense, taste discrimination, vocalisation, and with high levels of cognition and complex tasks (Corfield et al. 2012, and references therein). Furthermore, stereotyped species-specific behaviour (Reiner et al. 1984; Dubbeldam 1998a), pecking accuracy (Salzen et al. 1975), and the processing of visual information such as brightness, colour and pattern discrimination (Iwaniuk et al. 2010), have been attributed to processes within the caudolateral telencephalon. Pettigrew & Frost (1985) showed the maxillary (V<sub>2</sub>) division of the trigeminal (V) cranial nerve, which innervates the upper bill (see 1.5.4.1 above), transmits to extensive terminal fields in the region of the rostradorsal mesopallium of the cerebrum (see also Northcutt 1981). Similarly, Dubbeldam et al. (1981) showed that ascending maxillary and mandibular trigeminal projections transmitted rostradorsally via the nucleus basalis to mesopallial terminal fields (see also Wild et al. 1985). These sensorimotor projections were related to the “detection” of food particles, particularly in low-visibility feeding in anseriforms (Berkhoudt et al. 1981), and food grasping in columbiforms (Wild et al. 1984, 1985), and passerines (Wild & Farabaugh 1996).

**1.5.4.2.3 Mid- and hindbrain** (mesencephalon, cerebellum and rhombencephalon)– Hellmann et al. (2004) characterised the mesencephalon as “relay stations” for the conveyance of ascending visual output to the forebrain, projecting descending output to the premotor regions of the hindbrain, and comprise multiple cell types that are retinotopically organised and functionally specific. So called “optic flow” (*sensu* Gibson 1954) are retinal stimuli generated by self-motion through an environment (see Wylie et al. 2018, and references therein). Optic flow stimuli are analysed by recipient nuclei in the accessory optic system and the pretectum, which serves to generate optokinetic response for the control of posture and eye movement stabilisation (Simpson 1984; Simpson et al. 1988; Giolli et al. 2006; Wylie et al. 2009, 2018; Gaede et al. 2019, and references therein). The pretectal nucleus, also known as the lentiformis mesencephali, responds to “moving large-field visual stimuli” and controls posture and locomotion, including determining compensatory movement and navigation through complex environments, facilitated by processes within the cerebellum (Pakan & Wylie 2006; see also Jerison 1973). Visual signals are projected through the third (3) visual pathway via the retinal-recipient nuclei of the mesencephalon to the cerebellum (Lau

et al. 1998; Wylie 2001; Pakan & Wylie 2006; Wylie et al. 2009), where they facilitate obstacle avoidance responses. Additionally, Pakan & Wylie (2006) suggest folia VI–VIII of the cerebellum may be involved in “steering” functions, and Iwaniuk et al. (2007) showed that VI and VII folia are hypertrophied in birds they classified as “strong fliers”, and showed some evidence to support correlation of hypertrophy of the cerebellar rostral lobe with “strong hindlimbs” in birds.

### 1.5.5 The morphometric approach

Geometric morphometrics is the field of biological shape analysis, whereby geometric information described by multivariate cartesian coordinates of anatomical landmarks, may be analysed by various methods, to mathematically assess variation and covariation of organismal shape in either two or three dimensions (Zelditch et al. 2004; Adams et al. 2004; Cardini & Loy 2013).

Landmark based geometric morphometric methods start with the acquisition of Lm coordinates based on “biologically definable” morphological structures (see General Methods, 2.2). These coordinates, as variables, may not be directly analysed as the effects of variation in position, scale and orientation are still present in those raw data (Adams et al. 2004). Thus, non-shape variation is removed by superimposition methods, such as Generalised Procrustes Analyses (GPA *sensu* Gower 1975; Rohlf & Slice 1990; see General Methods, 2.4.1). Raw Lm coordinates are translated, scaled and optimally rotated to a common reference, or consensus, using least-squares estimates for translation and rotation parameters (Rohlf & Slice 1990; Bookstein 1991). GPA superimposition yields aligned Procrustes residuals, comprising correlated shape variables, along with a size variable in the form of centroid size, and differences in shape may be described by assessment of the variation between shape variables of corresponding Lms across specimens (see Zelditch et al. 2004; Adams et al. 2004, 2013; Gunz et al. 2005; Adams & Collyer 2016).

Geometric morphometric approaches have been well established (e.g. Rohlf 1990; Rohlf & Marcus 1993; Dryden & Mardia 1993, 1998; Bookstein 1997b; Zelditch et al. 2004; Adams et al. 2004, 2013; Slice 2005, 2007; Mitteroecker & Gunz 2009; Cardini & Loy 2013, and references therein). As a comprehensive description of the development of the field falls outside the scope of this review, I refer the interested reader to those references above, which collectively review the progress of the field into the modern era.

The contemporary literature abounds with geometric morphometric assessments employing Lms to quantify, assess and describe shape differences across a specimen suite. In the following, I focus on two dimensional (2D) and 3D assessments of avian skull and brain morphology published in peer reviewed literature, but exclude analyses assessing phylogenetically informative aspects of shape data, as such publications are reviewed in the Introduction to Chapter 5 below.

Three dimensional Lm analyses were preceded by, and in many cases, overlapped by 2D assessments of avian cranial anatomy. For example, Marugán-Lobón & Buscalioni (2004) sampled 93 crania representative of all neornithine orders, and along with nine theropod skulls, placed 17 2D Lms

delimiting the skull, rostrum, orbital cavity and braincase. Using Principal Component Analysis (PCA, see General Methods, **2.4.2**) and Thin Plate Splines (TPS, see General Methods, **2.4.2**) to explore anatomical trends, those authors argued the morphological diversity of the avian skull is represented by changes in the craniofacial region, likely associated with expansion of the braincase in modern birds. [Marugán-Lobón & Buscalioni \(2006\)](#) used 29 skulls representing 18 families of neognaths (i.e., the sister clades Galloanseres + Neoaves, see Introduction, **1.1**). They digitised 12 2D Lms describing the lateral cranial base, orbits, external ear and rostrum, and along with angular measurements describing head posture traits, conducted Two-Block Partial Least Squares analyses (2B-PLS *sensu* [Rohlf & Corti 2000](#); see Chapter 3 Methods, **3.2.7.3**), and Relative Warps analyses (RWA *sensu* [Bookstein 1991](#); [Rohlf 1993](#)), to explore craniofacial shape evolution. By comparing patterns of covariance with reference to angular measures of head posture, [Marugán-Lobón & Buscalioni \(2006\)](#) showed that morphological integration underlies macroevolutionary organisation of the avian skull. [Marugán-Lobón & Buscalioni \(2009\)](#) used 72 skulls of neornithine birds (i.e., the sister clades Palaeognathae + Neognathae, see Introduction, **1.1**), and digitised nine 2D Lms on the mid-sagittal (medial) plane of the endocranial cavity within the skulls. They used RWA analyses and TPS grids to show that expansion of the avian brain had affected a change in the configuration of the neurocranial base, and orientated the foramen magnum to open more ventrally than caudally. [Marugán-Lobón \(2010\)](#) used the Lm data from [Marugán-Lobón & Buscalioni \(2006](#); see above) and used 2B-PLS assessments to investigate covariation of brain size, represented by previously published avian brain mass data, and endocranial shape variation, represented by the multivariate Lm data. However, those authors found insufficient evidence for correlation between brain mass and cranial shape diversity across the assessed taxa.

Analyses using 3D data are represented by [Kulemeyer et al. \(2009\)](#), who assessed the neurocranial morphology of corvids employing a suite of 148 Lms placed on 115 skulls and bills of six species of corvid (i.e., four *Corvis*, one *Pica*, and one *Garrulus*). They used PCA, partial least squares (PLS) regression of shape variables on centroid size, and integration analyses (see Chapter 3 Methods, **3.2.7.3**), to show that covariation in corvid skull and bill morphology is associated with binocular visual fields and foraging ecology. [Kawabe et al. \(2013b\)](#) assessed covariation between the skeletal orbit and endocast size and shape in modern birds, by using 28 Lms digitised on 61 endocasts (including four on the lateral semicircular duct; see **1.5.2** below), and nine Lms describing the orbit of 58 skulls. By means of PCA, TPS grids, independent contrasts regressions of shape on centroid size, and 2B-PLS analyses, those authors showed the size and shape of the skeletal orbit was a “dominant factor” affecting avian brain shape. They also reported consistency with results of previous assessments, with respect to the orientation and inclination of the foramen magnum and brain (see [Marugán-Lobón & Buscalioni 2006, 2009](#) above). [Kawabe et al. \(2014\)](#) employed endocasts of 28 extant waterbird taxa representing five orders, along with three extinct plotopterid specimens. They used linear distance endocast measurements, volumetric estimations, and data derived from 32 3D

Lms defining endocast shape, to investigate brain morphology by means of least-squares regressions of log-transformed body size on brain volume. PCA and Canonical Variates analyses were used to visualise group shape distinctions, and they assessed size-standardised ratios derived from linear distance measurements (generated by dividing distance values by a common size metric, in this case, telencephalon width), using t-tests to ascertain any linear differences in brain form across clades. Consequently, [Kawabe et al. \(2014\)](#) argued the pterosaur brain configuration was “distinctly” similar to those of penguins, and hypothesised a possible phylogenetic relationship between the two clades. [Kawabe et al. \(2015\)](#) assessed chicken (*Gallus gallus*) brain shape and size through ontogeny. They employed 20 3D Lms to describe the shape of 43 chicken endocasts, and derived volume measures for brain regions and eyes sampled across an ontogenetic series. PCA was employed to visualise patterns of brain shape variation through development. Shape variation at different growth stages was assessed by multivariate regression of shape variables on brain volume, and growth rate was assessed by regression of logged brain/eye volumes on body size. Results showed that in precocial species like chickens, the volume ratio of brain regions and overall brain volume did not change, but the shape of brain regions changed “considerably” through ontogeny.

The studies of [Ashwell & Scofield \(2008\)](#); [Scofield & Ashwell \(2009\)](#); [Ksepka et al. \(2012\)](#); [Smith & Clarke \(2012\)](#) and [Tambussi et al. \(2015\)](#); see above) are representative of attempts to multiply sample closely related avian species, and examine endocranial morphological differences in detail across taxa. Studies such as these have shown the shape of the avian brain remains relatively consistent within clades, and illuminated trends for particular cerebrotypes of endocranial shape specific to bird lineages. Characteristics such as these have been reinforced by multiple subsequent analyses across vertebrate groups (see above).

Few studies have used endocasts derived from fossil birds to numerically quantify the evolution of brain shape within closely related avian taxa (see above; and Chapter 5, **5.1**). The characteristics of avian endocranial cerebrotypes have been demonstrated, using traditional methods, to relate to both ecology and phylogeny. Yet, the cerebrotypes concept is contingent upon the comparison of derived ratios of whole brain regions, ratios virtually impossible to recover from fossil material or from the “surface” endocast models produced from  $\mu$ CT scanned fossil skulls. However, the application of digital Lms upon the surfaces of 3D endocast models, in a manner that captures shape characteristics of particular zones, or modules of the brain, and the analysis of these multivariate shape data by means of geometric morphometric methods, may reveal functional and potentially phylogenetically informative characteristics of the avian brain.

## **1.6 Aims and objectives**

Evolution may impact the shape of the avian brain on several temporal scales, and be revealed at diverse phylogenetic depth from within species changes, to deep lineage divergences. The

following thesis aims to explore potential morphological evolution of endocranial structure across these diverse temporal scales using three examples. Thus, the Aims of the thesis are:

### **1. Assess morphological changes over short time scales associated with loss of volancy**

The extinct duck *Chenonetta finschi* was a widespread component of the Pleistocene–Holocene NZ avifauna. Previous work on fossils of *C. finschi* has shown there was a 10% reduction in the size of forelimb and pectoral girdle elements, relative to body size, based on femur length, over this period, suggesting a rapid transition to flightlessness (see Chapter 3, **3.1**). To assess the characteristics of modular endocast shape change over time concomitant with the loss of flight ability in the taxon, I use Modular Lm configurations defining the shape of the brain (see Chapter 3, **3.2.5**; Appendices, **A3.8.1**; Fig. A3.1), to investigate shape changes in *C. finschi* endocast specimens sampled across a temporal sequence of ~20 thousand years.

### **2. Characterize endocranial morphology of Dromornithidae and relate to lineage evolution through time.**

Dromornithid cranial anatomy has previously been comprehensively described (See Chapter 4, **4.1**), but there exists no information regarding the specific shape and size of the dromornithid brain across the two lineages hypothesised by [Worthy et al. \(2016b\)](#). Those authors identified that from the Oligocene through the late Miocene, the skull shape of *Dromornis* dromornithids changed with a foreshortening of the length relative to the height of the skull (see Chapter 4, Fig. 4.1). As to how the shape of the dromornithid brain changed to accommodate these temporal changes in neurocranial anatomy has yet to be appropriately assessed. Using modular Lm configurations (see General Methods, **2.2**, Fig. 2.1, Appendices **A2.1**), I assess dromornithid endocast specimens spanning the late Oligocene to the late Miocene and: **1**, describe the morphological characteristics of the dromornithid brain and its principle innervation in detail for the first time across multiple species; **2**, identify how dromornithid brains differ morphologically from those of other basal galloanseres; **3**, assess whether there exist quantifiable differences in endocast anatomy between the hypothesised *Dromornis* and *Ilbandornis* lineages; **4**, assess how the shape of the dromornithid brain accommodated significant changes in cranial anatomy across ~20–8 Ma of evolution; and **5**, consider potential functional constraints shaping the evolution of dromornithid endocranial anatomy.

### **3. Assess whether phylogenetic signal is present in a diverse avian clade, or whether adaptation to habitat is overwhelming in endocranial structure.**

The recognition of cerebrotypes-like patterns in avian brain morphology led [Walsh & Milner \(2011a\)](#) to suggest the form of the brain, or parts thereof, may be phylogenetically informative. However, whether brain morphology holds a strong phylogenetic component within galloanseres remains to be tested. As ecology is a major force driving skull and brain shape ([Lefebvre et al. 2004](#);

Iwaniuk & Hurd 2005; Paulina-Carabajal et al. 2014), identifying how endocranial structures have evolved in response to birds' adaptations to specific habitats and behaviours (such as the feeding niches accessed by diving, dabbling or browsing), may lead to a better understanding of those that may convey phylogenetic information in birds. I build upon the work of the above authors, and with an extended dataset of neurocranial material, including extant and extinct taxa sourced from across the Superorder Galloanseres, with a focus on Anseriformes. Assess whether use of modular endocast data using both univariate and multivariate methods, can discriminate phylogenetic and functional signals. Galloanseres are ideally suited to this examination, as across the phylogenetic tree members of several trophic groups, e.g., browsers or specialist divers, are grouped in both basal and deeply nested positions in the generally accepted evolutionary tree. If ecotype rules, then all members of an ecotype might be predicted to align together in analyses. Conversely, if a phylogenetic component remains, then evolutionary disparate members of the same ecotype may be separable on endocast morphology.

### 1.7 Thesis structure

This thesis has the following structure. Peer reviewed publications cited in the Introduction (Chapter 1), General Methods (Chapter 2), and Summary and Conclusions (Chapter 6), are listed in General References (Chapter 7, see below). Those references specific to data Chapters (i.e. Chapters 3–5), are included in Chapter specific Reference sections. Citations for Figures and Tables are prefixed by the Chapter number wherein they appear. For example: Introduction Figures are cited “Figs. 1.1, 1.2”, General Methods Figures are cited “Figs. 2.1, 2.2” etc. Similarly, Figures and Tables appearing in Chapter specific Appendices are cited with the prefix ‘A’ followed by the Chapter number. For example, Chapter 3 Appendices are cited “Fig. A3.1, Table A3.1”, etc. Data Chapters, (i.e. Chapters 3–5), have been formatted as stand-alone, long format papers (e.g. Journal of Vertebrate Paleontology). To save lengthy repetition of several General Methods, nomenclatural (e.g. **1.5.2**), anatomical (e.g. **1.5.3**), and functional (e.g. **1.5.4**) attributes, more comprehensive descriptions of these common aspects are included in the Introduction and General Methods Chapters (i.e., as indicated in Introduction, **1.5**), and are referred to within text by citation of the relevant thesis section, which is presented in **bold** text. For example, “functional attributes of eminentia sagittalis are known to include.. (Bloggs 2014; see Introduction, **1.5.4.2.1**)”.

**Chapter 2** – General Methods. Includes procedures for: **1**, digitally constructing 3D endocasts derived from Computed Tomography (CT) scan data; **2**, reconstruction, remeshing and processing of raw 3D endocast models; **3**, model landmarking protocols for primary multivariate shape data generation; **4**, derivation of multivariate coordinates for 3D morphometric analyses; **5**, univariate Modular Distance and Modular Surface Area data acquisition, derivation and; **6**, analyses protocols common to all data Chapters.

**Chapter 3** – Endocranial morphological transformation concomitant with the loss of flight ability in Finsch's duck *Chenonetta finschi*: The assessment of shape changes in *C. finschi* endocast specimens sampled across a temporal sequence of ~20 thousand years.

**Chapter 4** – Dromornithid endocranial anatomy: The assessment and description of dromornithid endocast specimens spanning the late Oligocene to the late Miocene periods (~20 Million years).

**Chapter 5** – The phylogenetic utility of Galloansere endocranial anatomy: The assessment of whether galloansere brain morphology holds an informative phylogenetic component.

**Chapter 6** – Summary and Conclusions. This pulls together the overall results, assesses the efficacy of the method in analyses of endocast shape, talks about the significance of key results, and outlines possible ways forward.

**Chapter 7** – General References. Including those for the Introduction (Chapter 1), General Methods (Chapter 2), and Summary and Conclusions (Chapter 6).

## CHAPTER 2

## GENERAL METHODS

The various projects in this thesis use digitally constructed endocasts derived from CT scan data, as the primary objects with which to complete morphometric analyses to address key questions. The general methods described below apply to data processing and conditioning, and data forms common to all data Chapters. However, the Modular Lm configurations illustrated here (i.e. Fig. 2.1) apply to Chapter 4 and Chapter 5 only, and exclude Chapter 3 specific modular configurations (i.e., dorsal olfactory zone, and orbits), that were not used for subsequent analyses. Chapter 3 specific Modular Lm configurations are described in Chapter 3, **3.5.1.1** and Appendices, **A3.8.1**. Similarly, Chapter specific analytical protocols are described in Chapter specific Methods sections (see **2.4** below).

**2.1 Computed Tomography data**

Three different CT technologies were employed to capture raw CT data of specimen neurocrania:

**2.1.1** Micro-CT ( $\mu$ CT) scanned using the Skyscan 1076  $\mu$ CT instrument (Bruker microCT) at Adelaide Microscopy, University of Adelaide, where neurocrania were scanned at either 17 micrometre ( $\mu$ m) or 34  $\mu$ m resolution, depending on the physical size of the specimen. Skyscan raw  $\mu$ CT acquisition data were reconstructed using NRecon v1.6.10.4 (Bruker microCT), and compressed using ImageJ v1.51w (Rasband 2018) software.

**2.1.2** Medical X-ray CT-scanning was conducted using the Siemens Somatom Force CT instrument, located at the South Australian Health and Medical Research Institute (SAHMRI) facility in Adelaide, where resolutions between 240–320  $\mu$ m were achieved. Raw X-ray CT acquisition data were reconstructed by M. Korlaet of Dr Jones & Partners, using Siemens proprietary software.

**2.1.3** Neutron CT-scanning was conducted at the Australian Nuclear Science and Technology Organisation (ANSTO) facilities in Sydney, using the DINGO neutron CT instrument located in the OPAL reactor beam hall on thermal beam HB2. Neutron CT images were captured at low-intensity mode at a resolution of  $\sim$ 95  $\mu$ m, and raw acquisition data were reconstructed by Dr. J. Bevitt of ANSTO using ImageJ, VGStudio and Octopus software.

Individual specimen  $\mu$ CT, medical CT, and neutron CT scanning parameters are all isotropic (i.e., the same value for all three axes), and are given in Chapter specific Methods sections.

**2.1.1 Three dimensional model construction**—from reconstructed CT data was conducted using Materialise Mimics v18 software in the form of 3D endocast \*.stl surface models. Surface models were exported to Mimics 3-matic v10 software for reconstruction and remeshing operations (see below).

**2.1.2 Reconstruction operations**—in many fossils, structures are often lost or damaged by the processes of being initially interred, taphonomic processes over time, or damage incurred during recovery. Where specimens are somewhat bilaterally symmetrical, as is the case of endocasts, damaged or missing structures may be digitally reconstructed based on preservation of one side, or parts of a particular endocast. During the course of this project, reconstruction procedures were conducted for: **1**, two dimensional images of the right hand side (RHS) lateral and rostral endocasts of specimens of *Dromornis stirtoni*. Reconstructions were compiled in Adobe Photoshop v20.0 from 2D images of 3D endocast models of *D. stirtoni* (NTM P5420 and NTM P3250); and **2**, a single 3D reconstructed endocast surface model was compiled from CT data of two specimens of *D. murrayi* (QM F57984 and QM F57974), using Materialise 3-matic v10 software. Specific details and reconstruction protocols are given in Chapter 4 Methods.

**2.1.3 Remeshing**—of raw 3D \*.stl surface models is required to optimise the quality of the triangles comprising the surface mesh, and to reduce the physical file size of models for landmarking operations (see below). Remeshing operations were carried out in Materialise 3-matic v10, and conversion of remeshed \*.stl format 3D objects to \*.ply format for landmarking operations (see below), was conducted in MeshLab v2016.12 (Cignoni et al. 2008) software.

## 2.2 Landmarking

Digital landmarking of 3D endocast surface models was conducted in IDAV Landmark v3.6 (Wiley 2006) using fixed (type 1) and semi- (type 3) landmarks (*sensu* Bookstein 1991). These landmarks (Lms) and semilandmarks (Slms) were assigned into modules (see Fig. 2.1) for analyses. Endocast landmarking protocols and the full Modular Lm suite used for Chapter 3 assessments, are described in Chapter 3 Appendices (A3.8.1). The amended, full Modular Lm suite used for Chapter 4 and 5 assessments, is described in Appendices (A2.1) below.

## 2.3 Data forms

General forms of data common across each data Chapter are described here in detail, and are reiterated in condensed form within Chapter specific Methods and Results sections below.

In this thesis, I used three forms of data: **1**, 3D Modular Lm data (see 2.3.1 below), comprising multivariate Lm coordinates; **2**, two forms of univariate distance data: Modular Distance (see 2.3.2 below), and Linear Distance data (see 2.3.3 below), comprising univariate modular length and width measurements, computed directly between various Lms and Slms forming the measurement vectors; and **3**, Modular Surface Area data (see 2.3.4 below), based on modular boundaries defined by the Modular Lm suite, and comprising univariate modular surface areas and modular perimeter metrics. The primary reason for this, was to assess which data form may ultimately prove most cladistically informative (i.e. Chapter 5). Thus affording additional taxonomic differentiation of avian taxa if incorporated in the form of shape matrices (i.e. Modular Lm coordinates), as continuous

characters (Modular univariate metrics, or ratios thereof), or described as traditional discrete characters, for inclusion within more comprehensive Parsimony, Maximum Likelihood, or Bayesian forms of cladistic analyses (e.g. [Ronquist et al. 2009](#); [Pennell & Harmon 2013](#); [Garamszegi 2014](#); [Lee & Palci 2015](#); [Harmon 2019](#); and references therein). Additionally, the combination of these forms of data are expected to improve the appreciation of distinctions between endocast specimens, when used together in a systematic fashion, for example, in the descriptions of Finsch's duck (Chapter 3), and dromornithid endocranial anatomy (Chapter 4). I note that these data are not independent, i.e., Modular Distance data forms are computed directly from Lms and SImS comprising the Modular Lm suite (see below). Therefore, in no instance were different data forms directly combined in any statistical analysis. The morphological trends described by each data form were assessed individually.

**2.3.1 Three dimensional Modular Lm data**—derived from the Modular Lm suite (see Fig. 2.1), were used for all analyses described below (2.4). Statistics and numerical output from each assessment are presented in Chapter specific Tables and in text.

**2.3.2 Modular Distance data**—were calculated between Lm and semilandmark (SIm) locations for each specimen employing the 'interlmkdist' function in Geomorph (see 2.4), using raw Lm coordinate data. Modular distance measurements for the length and width of each modular structure, capturing the directional 'curve' over a 3D surface (i.e., eminentia sagittalis; Figs. 2.2C–D), were calculated incorporating the distances between each SIm forming the measurement vectors. In other words, individual measurements between SImS were added together to form the total Modular Distance measurement value (see Figs. 2.2C–D). Paired structure data (i.e., eminentia sagittalis, rostral and caudal telencephalon, mesencephalon, and trigeminal ganglion modules) were combined and mean Modular Distance length and width values calculated. For intra- and interspecific comparison, size-standardised mean Modular Distance length and width ratios were calculated by dividing  $\log_{10}$  transformed mean Modular Distance length and width values by  $\log_{10}$  transformed specimen endocast volume values.

**2.3.3 Linear (vector) Distance data**—were calculated between two Lm or SIm locations describing gross endocast morphological (vector) distances (see Figs. 2.2G–I). For intra- and interspecific comparison, size-standardised Linear Distance ratio data were calculated by dividing  $\log_{10}$  transformed Linear Distance values by  $\log_{10}$  transformed endocast volume values.

**2.3.4 Modular surface areas**—for each endocast module, as defined by the Lm modules (see Appendices A2.1 below) and visualised in Figs. 2.1A–D, were computed directly from the surface of each 3D endocast model using MeshLab v2016.12 (see Figs. 2.2J–K). Three forms of raw surface data were acquired: **1**, total endocast Surface Area; **2**, Modular Surface Area values in square millimetres ( $\text{mm}^2$ ) representative of modular surface topology, for which mean Surface Area values for all paired modules (i.e., eminentia sagittalis, rostral and caudal telencephalon, mesencephalon, and trigeminal ganglion) were computed (see Figs. 2.2 J–K: **tel.r sa**, **tel.c sa**, respectively);

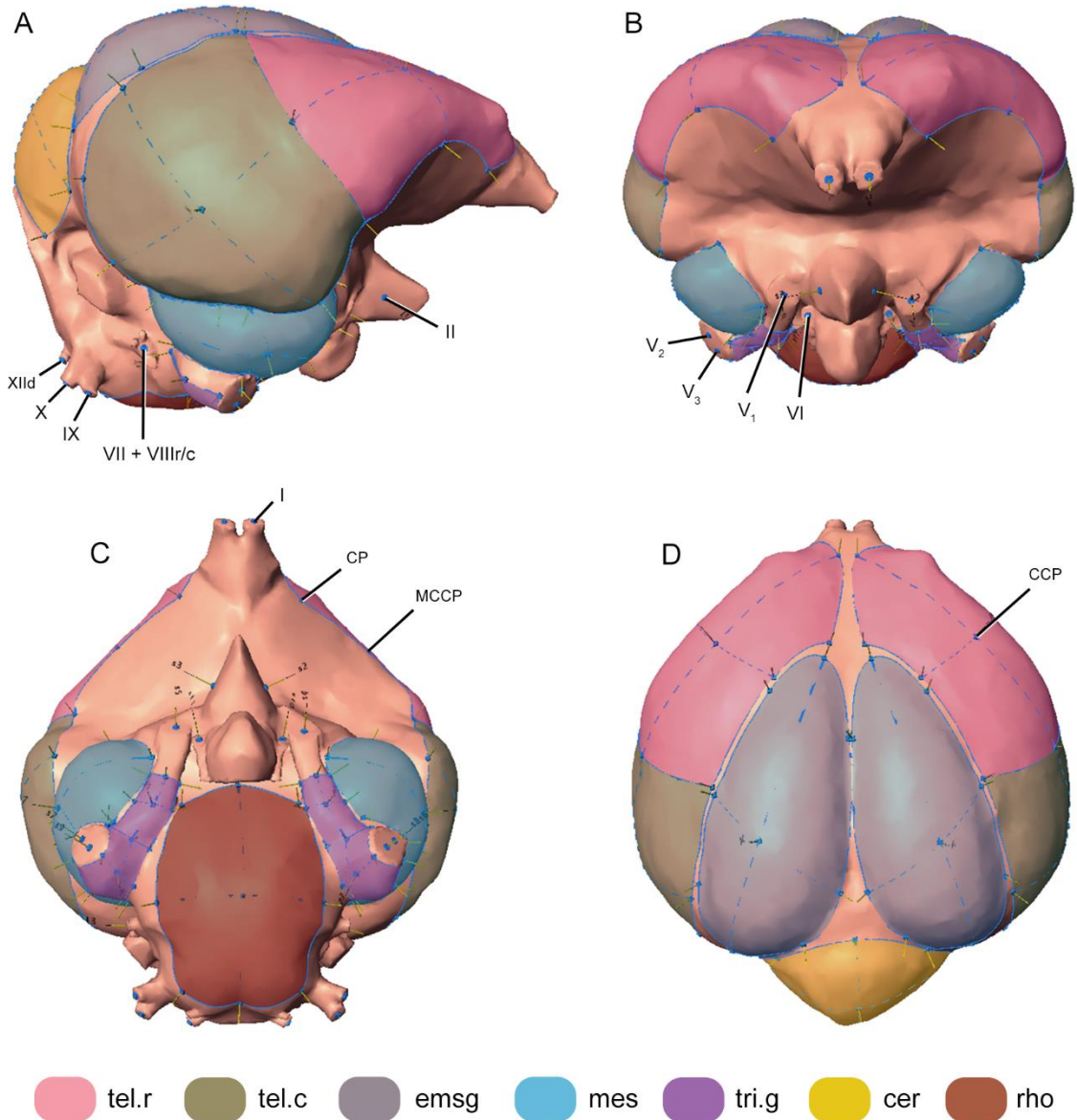


Figure 2.1. Landmark modules used to capture endocast morphology, mapped onto the endocast of *Aythya australis* (SAM B33108) and shaded to facilitate anatomical identification. **Views:** lateral RHS (A); rostral (B); ventral (C); dorsal (D). **Abbreviations,** **cer**, cerebellum; **CP**, control point; **CCP**, centre patch control point; **emsg**, eminentia sagittalis; **LHS**, left hand side; **MCCP**, mid-curve control point; **mes**, mesencephalon; **rho**, rhombencephalon; **RHS**, right hand side; **tel.c**, caudal telencephalon; **tel.r**, rostral telencephalon; **tri.g**, trigeminal ganglion; **I**, LHS olfactory nerve; **II**, RHS optic nerve; **V<sub>1</sub>**, ophthalmic nerve; **V<sub>2</sub>**, maxillary nerve; **V<sub>3</sub>**, mandibular nerve; **VI**, abducent nerve; **VII + VIIIr/c**, rami of the facial nerve (VII), and the rostral (VIIIr) and caudal (VIIIc) vestibulocochlear nerves; **IX**, glossopharyngeal nerve; **X**, vagus nerve; **XII<sub>d</sub>**, dorsal ramus of the hypoglossal nerve (see Introduction, 1.5.3).

and **3**, ‘perimeter’ data (mm) describing the total perimeter distance of the modular surface morphology computed in **2** (see Fig. 2.2K: **tel.r per**). I prefer the terminology ‘perimeter’ over ‘circumference’ to describe these metrics, as ‘circumference’ is more commonly associated with a structured, circular outline. The term ‘perimeter’ better describes the complex morphological and topological variations characteristic of the modular surfaces assessed here. These data were then size-standardised for intra- and interspecific comparison into two categories of ratio data: **1**, mean Modular Surface Area ratios were generated by dividing  $\log_{10}$  transformed mean Surface Area values by  $\log_{10}$  transformed total endocast Surface Area values; and **2**, mean Modular Perimeter ratios were generated by dividing  $\log_{10}$  transformed mean Modular Perimeter values by  $\log_{10}$  transformed total endocast Surface Area values.

## 2.4 Analyses

All data analyses and visualisations, excluding those plotted in Microsoft Excel v16, were conducted in R v3.5.2 (R Core Team 2018) using RStudio v1.1.456 (RStudio Team 2016).

Three dimensional numerical Lm and Slm data were conditioned (see **2.3.1** below) and analysed using the package Geomorph v3.0.7 (Adams et al. 2018). Geomorph is the only geometric morphometric analytical package currently capable of accommodating fixed Lm (type 1) data incorporating curve- and surface-sliding Slm (type 3) data.

General forms of analyses common across each data Chapter are described here in detail, and are reiterated in condensed form, along with detailed descriptions of Chapter specific assessments such as Modularity and Integration analyses (Chapter 3, **3.3.7**), and Phylogenetic signal and Phylogenetic Generalised Least Squares regression (PGLS) assessments (Chapter 5, **5.3.8**), which are described comprehensively in Chapter specific Analyses sections.

**2.4.1 Generalized Procrustes analysis**–GPA (Gower 1975; Rohlf & Slice 1990) is how shape variables, or coordinates, are derived from numerical landmark data. GPA is a process where all specimen numeric data are translated, scaled and optimally rotated using a least-squares criterion (Bookstein 1986; Adams et al. 2013). During superimposition, Slms on curves and surfaces were slid along tangent directions and tangent planes respectively (see Bookstein 1997a, 1997b; Gunz et al. 2005; Gunz & Mitteroecker 2013), and locations of Slms were optimised by minimising bending energy (see Bookstein 1997a, 1997b). Aligned Procrustes coordinates represent the shape of each specimen contained within a Kendall’s shape space (Kendall 1984). These are projected into a linear tangent space yielding Kendall’s tangent space coordinates (Dryden & Mardia 1993; Rohlf 1999), which are used for subsequent multivariate analyses. Aligned Procrustes residuals are correlated shape variables that describe shape differences between specimens (see Adams et al. 2004; Gunz et al. 2005; Adams et al. 2013; Adams & Collyer 2016).

**2.4.2 Principal Component Analysis**–PCA (Jolliffe 2002:7 and references therein). Principal components constitute eigenvectors of a variance-covariance matrix, and is a descriptive, dimension

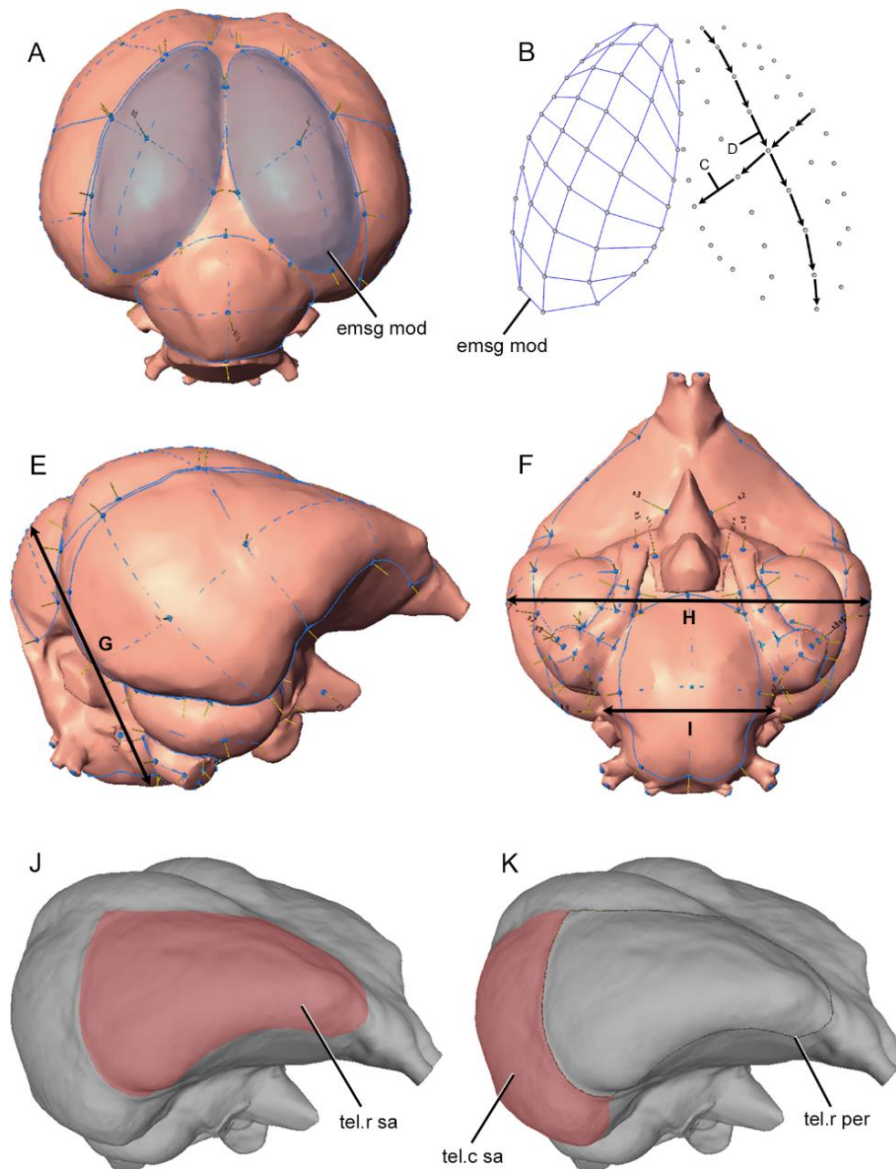


Figure 2.2. Endocast Modular Distance values (A–B), Linear Distance values (E–F), and Modular Surface Area values (J–K) illustrated using endocasts of *Aythya australis* (SAM B33108). **A**, eminentia sagittalis SIm modules viewed from the caudodorsal aspect, shaded to assist anatomical identification (see Fig. 2.1). **B**, 3D shape plot showing eminentia sagittalis SIm modules, LHS Slms (grey dots) are linked (blue) to provide perspective. Distance (vector) values were calculated between individual Slms forming the modular width (C) and modular length (D) measurement, vector values were then combined to form the total modular measurement values; **E**, *A. australis* endocast RHS lateral and **F**, ventral views; showing Linear Distance measurements for **G**, metencephalon (cerebellum + pons) total height, **H**, endocast total width; **I**, medulla oblongata total width. Endocast Surface Areas and Perimeter values for each SIm module, as visualised in Fig. 2.1, were captured directly from the surface of each 3D endocast model. **J**, endocast showing the LHS rostral telencephalon Modular Surface Area defined (**tel.r sa**–pink), for which Surface Area values were computed. **K**, showing the Modular Surface Area of the LHS caudal telencephalon module defined (**tel.c sa**–pink). The rostralateral margins of the caudal telencephalon selection closely approximate the rostral telencephalon module caudolateral boundary (**I**) delimited by the **tel.r sa** perimeter line (**tel.r per**), ensuring no overlap and allowing precise calculation of adjoining endocast modular values. For derivation of Modular Distance, Linear Distance, and Surface Area ratios from these data, see 2.3. **Abbreviations**, **emsg mod**, eminentia sagittalis module; **LHS**, left hand side; **RHS**, right hand side; **SIm**, semilandmark; **tel.c sa**, caudal telencephalon module surface area; **tel.r per**, rostral telencephalon module perimeter; **tel.r sa**, rostral telencephalon module surface area.

reducing technique (Jolliffe 2002:63). PCA is primarily employed as an ordination method to visualise patterns within data (Klingenberg 1996:31), providing valuable insight into matrix structure (Davis 2002). PCAs of all forms of data were performed. To facilitate visualisation of the multivariate shape change occurring across each axis, Thin Plate Spline (TPS *sensu* Bookstein 1989, 1991) warpgrids (see Chapter 3, 3.2.7.5), and 3D modular shape change plots (see Chapter 5, 5.2.7.2), derived from PC shape residuals describing the modular shape extremes across respective axes are given. PC Eigenvalues for each respective axis are given in parenthesis.

## 2.5 APPENDICES

**A2.1 Landmark descriptions**

A total of 20 fixed (type 1) and 460 semi (type 3) landmarks were used, for a total of 480. These landmarks were assigned into 13 modules for subsequent analyses. [Note: Modular Lm configurations described here (i.e. Fig. 2.1) apply to Chapter 4 and Chapter 5 only, and exclude Chapter 3 specific modular configurations (i.e., dorsal olfactory zone, and orbits) that were not used for subsequent analyses (see Chapter 3, **3.5.1.1**; Appendices, **A3.8.1**)].

**A2.2 Fixed landmarks (n = 20)**

**A2.2.1 Lm 1 – Lm 20:** Innervation module (Fig. 2.1; see also Introduction, **1.5.3.1**).

Innervation Lms are placed on nerve eminences truncated at the closest eminence (e.g. VIII; XII) or extension (e.g. I) of the nerve from the endocast surface. For all galloanseres, the ophthalmic ( $V_1$ ) branch of the trigeminal nerve (V), and abducent (VI) nerves were truncated where the nerves exit the os orbitosphenoidale, caudoventrolaterad of the foramen opticum (**fopt**, Chapter 4 Appendices, Figs. A4.4K–L, A4.5K), at the foramen n. ophthalmici ( $V_1$  – **foph**, Chapter 4 Appendices, Figs. A4.4K–L, A4.5K) and foramen n. abducentis (VI – **fa**, Chapter 4 Appendices, Figs. A4.4K–L, A4.5K) respectively. The rostroventral transmission of the abducent (VI) nerves were segmented out of the origin (rostroventral rhombencephalon) to facilitate full access to rostroventral rhombencephalon surfaces. The remaining two eminences of the trigeminal nerve (V) complex, i.e., maxillary ( $V_2$ ), and mandibular ( $V_3$ ) nerves, were truncated approximately where exiting the neurocranium. The glossopharyngeal (IX) and vagus (X) nerves were truncated approximately upon bifurcation from the caudoventral proximal ganglions.

**Lm 1:** Olfactory nerve (I – nervus olfactorius LHS).

**Lm 2:** Olfactory nerve (I – n. olfactorius RHS).

**Lm 3:** Optic nerve (II – n. opticus LHS).

**Lm 4:** Optic nerve (II – n. opticus RHS).

**Lm 5:** Ophthalmic nerve ( $V_1$  – n. ophthalmicus LHS).

**Lm 6:** Ophthalmic nerve ( $V_1$  – n. ophthalmicus RHS).

**Lm 7:** Maxillary nerve ( $V_2$  – n. maxillaris LHS)

**Lm 8:** Maxillary nerve ( $V_2$  – n. maxillaris RHS)

**Lm 9:** Mandibular nerve ( $V_3$  – n. mandibularis LHS)

**Lm 10:** Mandibular nerve ( $V_3$  – n. mandibularis RHS)

**Lm 11:** Abducent nerve (VI – n. abducens LHS).

**Lm 12:** Abducent nerve (VI. – n. abducens RHS).

**Lm 13:** Facial nerve (VII) (n. facialis); Vestibulocochlear nerve (VIIIr); Vestibulocochlear nerve (VIIIc) (n. vestibulocochlearis) LHS.

**Lm 14:** Facial nerve (VII) (n. facialis); Vestibulocochlear nerve (VIIIr); Vestibulocochlear nerve (VIIIc) (n. vestibulocochlearis) RHS.

**Lm 15:** Glossopharyngeal nerve (IX – n. glossopharyngeus LHS).

**Lm 16:** Glossopharyngeal nerve (IX – n. glossopharyngeus RHS).

**Lm 17:** Vagus nerve (X – n. vagus LHS).

**Lm 18:** Vagus nerve (X – n. vagus RHS).

**Lm 19:** Hypoglossal nerve (XIId – n. hypoglossus dorsal ramus) LHS.

**Lm 20:** Hypoglossal nerve (XIId – n. hypoglossus dorsal ramus) RHS.

### A2.3 Semilandmark modules

IDAV Landmark v3.6 software allows application of manipulatable rectangular ‘patches’ comprising Slms placed on grid junctions in any density configuration, i.e. 6 x 5 grid = 30 Slms. Each corner of an initially rectangular Slm patch has a control point (CP) which is used to shift the patch into position, in-between each control point is mid curve control point (MCCP), and a centre control point (CCP) allowing additional patch manipulation (see Fig. 2.1). Control points (CPs) were used to anchor each Slm patch comprising the modular suite on anatomically repeatable endocast locations. Boundaries of anatomical zones were chosen which best followed the transition zone between endocast morphology, and patch boundaries were defined as sensibly as possible within these transition zones. Once appropriately applied, mid curve control points (MCCPs) and centre control points (CCPs) were made equidistant, ensuring consistent and comparable Slm locations within each module across all specimens. For analysis, Slms on the patch periphery were treated as curve-sliding, and interior Slms were treated as surface-sliding Slms (see General Methods, 2.4.1). Descriptions for rostral telencephalon modules (see below) pertain to all taxa excluding dromornithids, as eminences of the dromornithid rostral telencephalon are either entirely engulfed by the eminentia sagittalis, and only present external morphology rostrally, or are entirely absent from the surface profile of dromornithid endocasts (see Chapter 4, 4.3.2.1). Rostral telencephalon modules were applied to dromornithid endocasts to ensure Modular Lm suite continuity across all specimens, but formed no part of subsequent analyses.

**A2.3.1 Curve and surface sliding Slms** (n = 460; Fig. 2.1); the number of Slms per module are indicated in parenthesis (n = xx).

**A2.3.1.1 Slm 21 – Slm 65:** Eminentia sagittalis module LHS (n = 45); the rostral MCCPs form the most rostradorsal eminence of the eminentia sagittalis, similarly the caudal CCPs are placed at the most caudodorsal eminence. The rostromedial MCCPs are placed in close proximity with the shared rostradorsal and caudodorsal CPs of the telencephalon modules (see below), allowing for the rostromedial CPs to be placed equidistant with the rostradorsal MCCPs and the rostromedial CPs. The

caudolateral CPs are placed equidistant with the caudodorsal MCCPs so that the caudolateral curves describe the valleculla (**va**, Introduction, Fig. 1.5.1D) transition zone between the caudolateral eminentia sagittalis and the dorsolateral caudal telencephalon. The caudodorsal MCCPs are placed equidistant with the caudodorsal CPs so that the medial curves describe the fissura interhemispherica (**fi**, Introduction, Fig. 1.5.1D) transition zones between eminentia sagittalis modules. The CCPs are then made equidistant mediolaterally between the caudolateral and caudodorsal MCCPs, and equidistant between the rostradorsal MCCPs and caudodorsal MCCPs.

**A2.3.1.2 Slm 66 – Slm 110: Eminentia sagittalis module RHS** (n = 45); see Eminentia sagittalis module LHS.

**A2.3.1.3 Slm 111 – Slm 155: Rostral telencephalon module LHS** (n = 45); the most rostral ventrolateral eminence of the telencephalon, forms the location of the rostral lateral CPs for the rostral telencephalon modules. The ventrolateral curve of the rostral telencephalon modules closely corresponds with the descending dorsolateral curve of the cerebrum fovea limbica transition. The caudoventral CPs terminate at the dorsoventral transition of the medial cerebral artery (**acm**, Introduction, Figs. 1.5.1A, 1.5.1C–D). The rostrocaudal boundary between the rostral and caudal telencephalon modules (see below) is defined by the dorsoventral transition of the medial cerebral artery. The dorsomedial CPs are situated at the point of transition into the rostral eminentia sagittalis, the MCCPs are placed equidistantly between the rostral dorsolateral CPs, and situated so as to track the medial transition zone of the rostral telencephalon into the fissura interhemispherica (**fi**, Introduction, Fig. 1.5.1D). The caudodorsal CPs are situated equidistant with respect to the dorsomedial CPs and the rostral lateral CPs, with the MCCPs situated equidistant between the former. Located so as to align the dorsolateral modular curve with the dorsolateral valleculla transition zone between the rostral telencephalon and the eminentia sagittalis. The caudal MCCPs between the caudodorsal CPs and the caudoventral CPs are made parallel and equidistant between CCPs and MCCPs.

**A2.3.1.4 Slm 156 – Slm 200: Rostral telencephalon module RHS** (n = 45); see Rostral telencephalon module LHS

**A2.3.1.5 Slm 201 – Slm 245: Caudal telencephalon module LHS** (n = 45); the dorsoventral boundary between the rostral telencephalon module and the caudal telencephalon module share five Slms that are located identically, allowing for the full Slm complement of the caudal and rostral telencephalon modules to be subset and analysed individually, or combined as a single total cerebrum module. The rostradorsal and rostroventral CPs of the caudal telencephalon modules occupy the same locations as the rostral telencephalon modules caudodorsal and caudoventral CPs respectively. The caudodorsal CPs of the caudal telencephalon module are situated at the transition zone of the dorsolateral cerebellum and the caudoventral eminence of the eminentia sagittalis (see above). The MCCPs are made equidistant, and situated to align the curve appropriately with the rostrocaudal valleculla transition zone of the dorsal caudal telencephalon into the eminentia sagittalis. The rostral

and caudal MCCPs and ventrolateral CPs are equidistantly located so as to align the curve in the transition zone between the ventrolateral caudal telencephalon, and the dorsolateral mesencephalon in the fissura subhemispherica (*fs*, Introduction, Fig. 1.5.1B) zone. The CCPs are then made dorsoventrally and rostrocaudally equidistant.

**A2.3.1.6 Slm 246 – Slm 290:** Caudal telencephalon module RHS ( $n = 45$ ); see Caudal telencephalon module LHS.

**A2.3.1.7 Slm 291 – Slm 320:** Mesencephalon modules LHS ( $n = 30$ ); the large trigeminal ganglion incorporating the three branches of the 5<sup>th</sup> cranial nerve (*V*; see **A2.2.1** above), inserting on the ventral surface of the mesencephalon, occupies a proportion of the ventromedial mesencephalon surface (see **tri.g**, Introduction, Figs. 1.5.1A–B, 1.5.1C). Thus, mesencephalon modules were arranged so as to define the margin of the trigeminal ganglion interface with the dorsolateral mesencephalon (Fig. 2.1C). Rostral MCCPs and dorsal and ventral CPs are placed where the swell of the mesencephalon transitions into the caudolateral chiasma opticum and tractus opticus structures. Caudal CPs are placed where the mesencephalon terminates into the dorsomedial pons and medulla oblongata structures (metencephalon), comprising the mediolateral rhombencephalon transition. Boundary curves are situated so that the dorsal curve describes the transition from the mesencephalon into the ventrolateral caudal telencephalon at the fissura subhemispherica zone, and the ventral curve follows the transition from the dorsal mesencephalon into the ventromediolateral rhombencephalon. MCCPs and CCPs are then made equidistant.

**A2.3.1.8 Slm 321 – Slm 350:** Mesencephalon module RHS ( $n = 30$ ); See Mesencephalon module LHS.

**A2.3.1.9 Slm 351 – Slm 380:** Trigeminal ganglion module LHS ( $n = 30$ ); the trigeminal ganglion module is constructed of two patches that are merged after fitment. The first patch captures the ophthalmic ( $V_1$ ) nerve's rostral eminence, and the second, the eminence of the maxillomandibular ( $V_2 + V_3$ ) branch. For the rostral ophthalmic ( $V_1$ ) patch, the rostral CPs are placed in rostral proximity from where the ophthalmic nerve ( $V_1$ ) eminence separates from the surface of the rhombencephalon (see below) and mesencephalon respectively. The dorsolateral curve describes the transition zone between the trigeminal ganglion and the ventral mesencephalon, and the caudal CP is placed in the junction at the eminence of the maxillomandibular ( $V_2 + V_3$ ) branch. The medial CP is aligned with the transition between the trigeminal ganglion and the rhombencephalon, and the curve follows the transition zone rostroventrally. The second (caudal) patch describes the maxillomandibular ( $V_2 + V_3$ ) branch, where the dorsolateral CP is placed in the junction at the eminence of the maxillomandibular ( $V_2 + V_3$ ) nerve, and shares the location of the rostral ( $V_1$ ) patch CP. The dorsolateral curve of the caudal patch describes the ventromedial margin of the truncated face of the maxillomandibular ( $V_2 + V_3$ ) nerve eminence, to a point approximately level with the rostral junction CP. The caudal transmission of the patch curve follows the most caudal eminence of the trigeminal ganglion, to meet the transition into the medulla oblongata, and returns following the

transition from the ventral rhombencephalon. MCCPs and CCPs are then made equidistant, and the two CPs and MCCPs forming the medial junction between the two patches are merged, forming one Slm module.

**A2.3.1.10 Slm 381 – Slm 410:** Trigeminal ganglion module RHS (n = 30). See Trigeminal ganglion module LHS.

**A2.3.1.11 Slm 411 – Slm 445:** Cerebellum module (n = 35); the rostromedial MCCP forms the most dorsal rostromedial eminence of the cerebellum module and is placed approximately in the area of the glandula pinealis (**gp**, Introduction, Fig. 1.5.1D). The caudal MCCP is placed at the most caudodorsal eminence of the cerebellum, where the medulla spinalis exits at the foramen magnum. The caudolateral CPs are placed at the most ventrolateral eminences of the cerebellum, at the transition of the auricula cerebelli into the dorsomediolateral medulla oblongata/rhombencephalon complex. The MCCPs are made equidistant with the rostromedial and rostrosagittal MCCPs, so that the ascending lateral curves describe the transition zones between the lateral mesencephalon and the caudal telencephalon, in the vicinity of the caudal cerebrum pars occipitalis dorsally, and ventrally in the area of the mediolateral rhombencephalon complex. The CCP is then made mediolaterally and rostrocaudally equidistant.

**A2.3.1.12 Slm 446 – Slm 480:** Rhombencephalon module (n = 35); the rostral MCCP forms the most rostroventromedial point of the rhombencephalon module, and is placed in the transition zone between the rhombencephalon and hypophysis (**h**, Introduction, Fig. 1.5.1A). The caudal MCCP is placed where the medulla oblongata transitions into the medulla spinalis. The rostralateral CPs are placed in the vicinity of the rostroventral mesencephalon CPs (see above). The caudolateral CPs are placed at the point where the medulla oblongata widens mediolaterally, forming a shelf between the mediolateral pons and the caudal medulla spinalis, so that the medial curves describe the transition zones between the ventrolateral mesencephalon and the dorsolateral rhombencephalon. The lateral MCCPs are then made equidistant with the lateral rostrocaudal CPs, and the CCP is made equidistant with the rostrocaudal and ventrolateral MCCPs.

## CHAPTER 3

**Endocranial morphological transformation concomitant with the loss of flight ability in Finsch's duck *Chenonetta finschi*.**

## 3.1 INTRODUCTION

New Zealand since the early Miocene period, was a land dominated by birds. The composition of the modern avifauna is representative of some taxa derived from the original Miocene fauna, thinned out by the removal of key elements through extinction, and more recent additions via dispersal (Worthy et al. 2017, and references therein). The anatid pre-human Holocene fauna of NZ had a higher diversity than in other groups, including 18 species in 11 genera, of which eight species are now extinct (Gill et al. 2010). In addition, a further four genera and eight species (including two undescribed taxa) have recently been recognised from the early Miocene of St Bathans, Otago (Worthy et al. 2017).

Finsch's duck *Chenonetta finschi* (Van Beneden, 1875), was first described in the genus *Anas* from bones discovered in Earnsclough Cave, near Alexandra in Central Otago. Van Beneden (1875) considered *C. finschi* to be comparable with the extant Plumed whistling duck *Dendrocygna eytoni*, and he noted its similarity to the extinct European *Anas blanchardi* Milne-Edwards, 1863, which is now placed in the genus *Mionetta* (Livezey & Martin 1988). Lydekker (1891:106) was first to associate fossils of *C. finschi* with the Australian wood duck *Chenonetta jubata*, when he listed bones and four crania from Earnsclough Cave as *Bernicula jubata* (Latham, 1802), but he did this without mention of *Anas finschi*. Oliver (1930:220) erected *Euryanas* to include *A. finschi*, and later Oliver (1955:403) argued that the taxon was closely related to *C. jubata*. Similarly, Falla (1953) considered *C. finschi* as the NZ counterpart of *C. jubata*. Brodkorb (1964:216-217) listed *C. finschi* within the anatid sub-family Plectropterinae (spur winged geese) with other goose-like birds, but he did not list *C. jubata*, otherwise he may have recognised the close relationship between the taxa which was accepted by Howard (1964). A systematic study of *C. finschi* conducted by Livezey (1989c:17) concluded *C. finschi* was sister to Tadorninae + Anatidae, with the taxon appearing before the divergence of these clades to form the sister group to them. Although Livezey (1989c:2) included *C. jubata* in his comparative material, he excluded the taxon from his phylogenetic analysis and proposed classification. Thus, Livezey's (1989c) assessment was limited by incomplete taxon sampling, as it included only *Tadorna* and *Anas* as representative of Tadorninae + Anatinae in a tree containing less derived, or more "primitive" species (see Worthy & Olson 2002:2). Similarly, when taxa more derived than *Stictonetta naevosa* were included in subsequent analyses (e.g. Livezey 1991, 1996; and summarised by Livezey 1997), *C. finschi* was included but *C. jubata* was not. These omissions, as argued by Worthy & Olson (2002:2), resulted in Livezey (1989c, 1991, 1996, 1997)

failing to test the relationship hypothesis forwarded by [Oliver \(1955\)](#). What is more, molecular analyses at the time (e.g. [Sraml et al. 1996](#); [Sorenson et al. 1999](#)) suggested generic relationships contradictory to those proposed by [Livezey \(1997\)](#). To address this question more comprehensively, the affinity of *C. finschi* was systematically tested against *C. jubata* and other ducks from the Australasian region by [Worthy & Olson \(2002:14\)](#), who recognised several “uniquely shared” skeletal characters between *C. finschi* and *C. jubata* and subsumed the taxon into *Chenonetta*.

*Chenonetta finschi* was a widespread and common component of the Pleistocene–Holocene NZ avifauna on both islands ([Worthy 1988a](#), and references therein). Its fossils are particularly common in pitfall accumulations (see [Worthy 1997a](#)) associated with shrubland-grassland mosaic environments distant from waterbodies ([Worthy & Holdaway 1994, 1996](#); [Worthy 1999](#); [Worthy & Holdaway 2002](#); [Worthy & Olson 2002](#); [Holdaway et al. 2002a](#)). Previous work on *C. finschi* fossils found in South Island caves has shown there was a 10% reduction in the size of forelimb and pectoral girdle elements, relative to body size, based on femur length, over a ~20 thousand year (kys) period ([Worthy 1988a, 1997b](#)), suggesting Finsch’s duck was either flightless or facultatively flightless by the late Holocene (1–2000 years ago). A more recent assessment of flight ability in *C. finschi* by [Watanabe \(2017\)](#), using linear discriminant analysis of postcranial skeletal measurements, confirmed this transition to flightlessness and suggested *C. finschi* was at least facultatively flightless by ~11 kys Before Present (BP), much earlier than previously proposed.

The large sample for *C. finschi* documenting this volant-flightless transition includes skulls for key time periods, and to my knowledge, there is no other avian lineage where fossils document such transition to flightlessness. There are several examples proposed for rapid flightlessness having occurred, i.e., in island colonising rallid taxa (see [Olson 1973](#); [Livezey 2003](#); and references therein), insular anseriform taxa in the form of Auckland and Campbell Island teals ([Livezey 1990](#)), the Auckland Island merganser ([Livezey 1989a](#)), a flightless anatine from Amsterdam Island in the Indian Ocean ([Olson & Jouventin 1996](#)), moa-nalo taxa from Hawaii ([Olson & Wetmore 1976](#); [Olson & James 1991](#)), flightless anserines from Malta in the Mediterranean ([Northcote 1992](#)), and flightless diving sea ducks from islands off the coast of California ([Livezey 1993](#), see also Introduction, **1.4.6.4**), to name a few. The ‘rate’ of transition to flightlessness in these taxa have been necessarily inferred with reference to the geological age of an island affording the temporal constraint for colonisation by volant ancestors. However, to assess a dated sequence of fossils documenting a transition to flightlessness in a single lineage affords a unique opportunity. Therefore, this project sought to identify directional changes in brain morphology along a time series of fossil specimens, and to assess changes in brain morphology concomitant with postcranial morphological changes suggesting a dramatic loss of flight capability in Finsch’s duck.

## 3.2 METHODS

**3.2.1 Nomenclature**—taxonomy of extant birds follows that in [Gill et al. \(2010\)](#) and [Dickinson & Remsen \(2013\)](#). Species authorities for extant birds are not given herein as can be found in those checklists. Those for Quaternary species from NZ are also given in full in [Gill et al. \(2010\)](#), but for other fossil taxa species, authorities are given at first mention. For anatomical nomenclature adopted in the following texts see Introduction, **1.5.2** and Introduction, Fig. 1.5.1 above.

### 3.2.2 Abbreviations

**3.2.2.1 Institutions**—NMNZ, Museum of New Zealand Te Papa Tongarewa, Wellington, New Zealand; SAM, South Australian Museum, Adelaide, Australia.

**3.2.2.2 Specimens**—Four endocasts of *Chenonetta finschi* were studied, all from sites in South Island (Fig. 3.1). NMNZ S.023702—Honeycomb Hill Cave, Graveyard, Layer 3 (GYL3) was the only specimen available from this layer, NMNZ S.023695—Honeycomb Hill Cave, Graveyard, Layer 2 (GYL2), NMNZ S.034496—Hodges Creek Cave (HC), NMNZ S.039838—Castle Rocks Fissure (CR), and one extant Australian wood duck (*Chenonetta jubata*) specimen SAM B39457 was included. Honeycomb Hill Cave and Hodge Creek Cave System are 45 km apart in northwest Nelson, but the Castle Rocks site is ~630 km distant in Southland.

### 3.2.3 Dating

A pre-existing corpus of dates (e.g. [Worthy 1993, 1997b, 1998; Holdaway et al. 2002a, 2002b; Cooper et al. 2001](#)) provides a temporal framework for the sites described below, but additional dates were obtained for the Graveyard deposits in Honeycomb Hill Cave from which my samples came. All Honeycomb Hill radiocarbon dating for this study was conducted by Rafter Radiocarbon Laboratory at the GNS Science's National Isotope Centre in Avalon, Lower Hutt, NZ. Results are reported as Conventional Radiocarbon Age defined by [Stuiver & Polach \(1977\)](#), and have not been calibrated into calendrical dates.

**3.2.3.1 Honeycomb Hill Cave**—situated in the Oparara Valley at an altitude of 300 m in north-west Nelson (Fig. 3.1). Radiocarbon ages for Layer 2 (GYL2) and Layer 3 (GYL3) in the Graveyard site have previously been reported (see [Worthy 1988a, 1993](#)) at 14–11 kys BP and 20–14 kys BP respectively. To test these earlier results, I sampled a further two Finsch's duck samples from each of GYL3 and GYL2 sites (Table A3.1, Appendices, **3.9**). Previous radiocarbon ages on moa bones from the Graveyard were recalculated from original data, and revised ages are presented here.

**3.2.3.2 Hodges Creek Cave System**—is situated on the slopes of Mt Arthur in the headwaters of Hodges Creek, at an altitude of 900 m in north-west Nelson (Fig. 3.1). The sample of *C. finschi* analysed for wing reduction derives from Takahe Tomo, one of the sites in Hodge Creek Cave System ([Worthy 1997b](#)). Two AMS radiocarbon ages were reported from this site. A left femur of a Takahe

(*Porphyrio hochstetteri*) from -5 centimetres (cm) was dated 12,210±110 yrs BP (NZA 6970) and a Finsch's duck humerus from -60 cm in the sediment deposit was dated 12,100±120 yrs BP (NZA 6971). The statistically indistinguishable ages from specimens spanning much of the deposit's depth, suggest most specimens within this deposit are likely similar in age (see [Worthy 1997b](#)).

**3.2.3.3 Castle Rocks**—is a fissure in a small limestone outcrop at an altitude of approximately 245 m at Castle Downs in Southland. Excavated in the 19<sup>th</sup> century, the thousands of bones recovered have no recorded stratigraphic relationship ([Worthy 1998](#)). This site was initially dated using a Haast's eagle (*Hieraetus moorei*) rib by [Worthy \(1998\)](#), and additional radiocarbon dating using seven *C. finschi* humeri and an *Aegothales novaezealandiae* (Scarlett, 1968) humerus was conducted by [Holdaway et al. \(2002a, 2002b\)](#), respectively). Additionally, [Cooper et al. \(2001\)](#) reported AMS dating results for an *Emeus crassus* (Owen, 1846) tibiotarsus from this site. The ten radiocarbon ages now available, reveal the Castle Rocks fauna ranges 4,829–655 yrs BP.

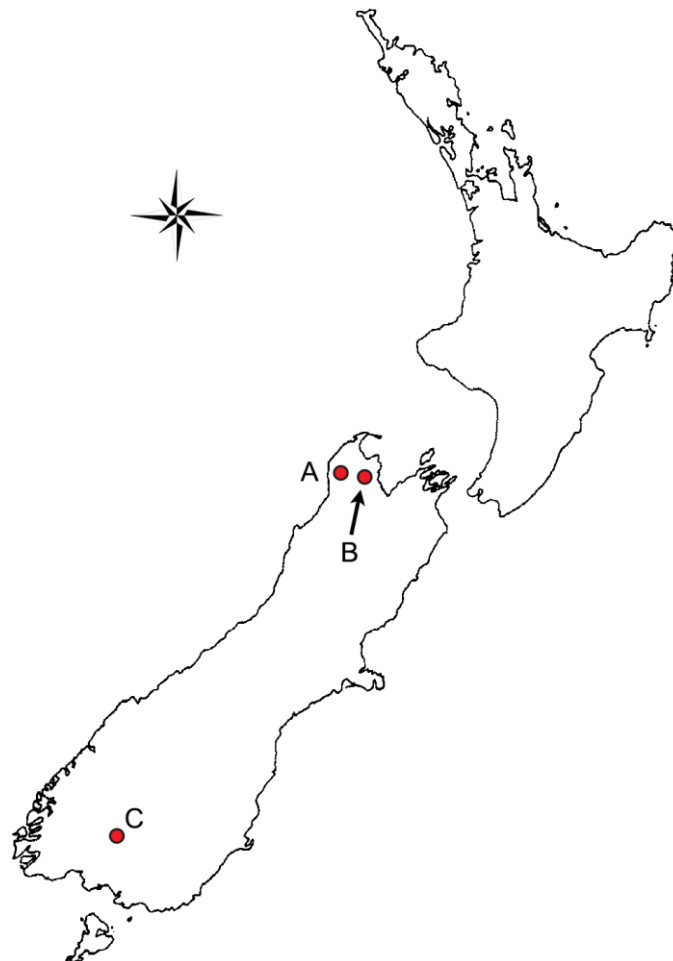


Figure 3.1. Map of New Zealand showing South Island fossil sites from where Finsch's duck specimens were sourced. **Sites:** **A**, Honeycomb Hill Cave; **B**, Hodges Creek Cave System; **C**, Castle Rocks Fissure. Adapted from [Worthy \(1988a:fig. 1\)](#).

### 3.2.4 Modelling

One of each of the following neurocrania were  $\mu$ CT scanned using the Skyscan 1076  $\mu$ CT instrument (Bruker microCT) at Adelaide Microscopy, University of Adelaide. *Chenonetta finschi*.CR was scanned at 17.0 micrometre ( $\mu$ m), at 51 kilovolts (kV) and 192 microamps ( $\mu$ A), *C. finschi*.HC was scanned at 17.0  $\mu$ m, at 70 kV and 141  $\mu$ A, *C. finschi*.GYL2 was scanned at 17.0  $\mu$ m, at 51 kV and 192  $\mu$ A, *C. finschi*.GYL3 was scanned at 17.0  $\mu$ m, at 51 kV and 192  $\mu$ A, *C. jubata* was scanned at 17.4  $\mu$ m, at 48 kV and 139  $\mu$ A. Skyscan raw  $\mu$ CT acquisition data were reconstructed using NRecon v1.6.10.4 (Bruker microCT) and compressed using ImageJ v1.51w (Rasband 2018) software.

**3.2.4.1 Three dimensional (3D) surface model construction**—was conducted using Materialise Mimics v18 software and raw 3D surface endocast \*.stl models representative of the shape of the brain were produced from reconstructed CT data. These included the base and immediate stem of the major nerves passing from the brain into the neurocranium.

**3.2.4.2 Remeshing**—of raw 3D \*.stl surface models is required to optimise the quality of the triangles comprising the surface mesh and to reduce the physical file size of models for landmarking operations (see 3.2.5 below). Remeshing operations were carried out in Materialise 3-matic v10 and conversion of remeshed \*.stl format 3D objects to \*.ply format for landmarking operations (see below), was conducted in MeshLab v2016.12 (Cignoni et al. 2008).

### 3.2.5 Landmarking

Digital landmarking of 3D endocast surface models was conducted in IDAV Landmark v3.6 (Wiley 2006), using 22 fixed (type 1) and 430 semi (type 3) landmarks (*sensu* Bookstein 1991), for a total of 452. These landmarks were assigned into 14 modules (see Fig. A3.1) for subsequent analyses. The full Lm suite used for analyses is described in Appendices (A3.8.1) below.

### 3.2.6 Data

**3.2.6.1 Modular Lm data**—three dimensional digital shape data derived from the Modular Lm suite (see 3.2.5; Fig. A3.1) were used for all analytical protocols described below (see 3.2.7). Statistics and numerical output for each assessment are presented in text, in plots (Figs. 3.2–3.5), and in Appendices (Tables A3.2, A3.3).

**3.2.6.2 Modular Distance data**—were calculated between Lm and SIm locations (hereafter Lm) for each specimen employing the ‘interlmkdist’ function in Geomorph v3.0.7 (Adams et al. 2018; see also 3.2.7 below), using raw Lm coordinate data. Modular Distance measurement values for the length and width of each modular structure, capturing the directional ‘curve’ over a 3D surface (i.e., eminentia sagittalis; see General Methods, 2.3.2, Figs. 2.2C–D), were calculated incorporating the distances between each Lm forming the measurement vectors. Then individual measurements between Lms were added together to form the total Modular Distance measurement value (see General Methods, Fig. 2.2C–D). Paired structure data (i.e., eminentia sagittalis, rostral and caudal

telencephalon, mesencephalon, and trigeminal ganglion modules) were combined and mean Modular Distance values calculated (see Table A3.3A). Size-standardised mean Modular Distance ratios were calculated by dividing  $\log_{10}$  transformed mean Modular Distance values by  $\log_{10}$  transformed specimen endocast volume values (see Table A3.3D).

**3.2.6.3 Linear (vector) Distance data**—were calculated between two Lm locations describing gross endocast morphological (vector) distances (see General Methods, Figs. 2.2G–I; Table A3.3B). Size-standardised Linear Distance ratios were calculated by dividing  $\log_{10}$  transformed Linear Distance values by  $\log_{10}$  transformed endocast volume values (see Table A3.3E).

**3.2.6.4 Modular surface areas**—for each endocast module, as defined by the Lm modules described in Appendices (A3.8.1), and shown in Fig. A3.1, were computed directly from the surface of each 3D endocast model using MeshLab (see General Methods, 2.3.4, Figs. 2.2J–K). Two forms of raw surface area data were acquired: **1**, total endocast surface area; **2**, Modular Surface Area values in square millimetres ( $\text{mm}^2$ ) representative of modular surface topology, for which mean Modular Surface Area values for all paired modules (i.e., eminentia sagittalis, rostral and caudal telencephalon, mesencephalon, and trigeminal ganglion) were computed (see Table A3.3C). Size-standardised mean Modular Surface Area ratios were calculated by dividing  $\log_{10}$  transformed mean Surface Area values by  $\log_{10}$  transformed total endocast Surface Area values (see Table, A3.3F).

### 3.2.7 Analyses

All data analyses and visualisations (Figs. 3.2–3.8, A3.4), excluding Figs. A3.2, A3.3 (Microsoft Excel v16), were conducted in R v3.5.2 (R Core Team 2018) using RStudio v1.1.456 (RStudio Team 2016). Multivariate 3D Modular Lm data were conditioned (see GPA; General Methods, 2.4.1) and analysed using Geomorph (see also General Methods, 2.4).

**3.2.7.1 Principal Component Analysis**—PCA (see General Methods, 2.4.2) were performed to assess structural patterns within data. PCAs of Modular Lm data were conducted employing the function ‘plotTangentSpace’ as implemented in Geomorph (see Figs. 3.2–3.3). To facilitate visualisation of the multivariate shape change occurring across each axis, TPS warpgrids (*sensu* Bookstein 1989, 1991) derived from PC shape residuals describing the modular shape extremes across respective axes are given (see 3.2.7.5 below). PC Eigenvalues for respective axes for all PCA plots are given in parenthesis.

As PCA is primarily a data visualisation technique, data for *C. jubata* are included in PCA plots to assess the relative positioning of the taxon in morphospace with respect to those of *C. finschi* (see Figs. 3.2–3.3). As the assessment of *C. jubata* does not form part of the intraspecific assessment of endocast shape change concomitant with the loss of flight in *C. finschi*, subsequent analyses used *C. finschi* data sets only.

**3.2.7.2 Modularity analysis**—allows the determination of the degree to which traits covary between parts or zones of an organism (Klingenberg 2009; Adams 2016). Olson & Miller (1958)

recognised that levels of covariation differ between parts of an organism, with some traits showing high correlation, and others being more independent. Correlation among traits, i.e., when changes in one trait are accompanied by changes in another, is described as “morphological integration” (Adams & Felice 2014; Adams 2016; and references therein). Assessment of morphological integration can describe correlation among traits that may be affected by factors such as functional adaptation or common developmental pathways (Adams 2016). Testing hypotheses of modularity in morphometric data previously used the RV coefficient (e.g. Klingenberg 2009), where the extent of covariation patterns are evaluated with permutation tests. However, RV-based patterns of covariation in data are compromised by sample size and the number of variables, and can have the effect of producing uninformative RV trends (see Adams & Felice 2014; Adams 2016). As an alternative, a covariance ratio (CovR) for quantifying modular structure, which is insensitive to such effects, was proposed by Adams (2016). I implemented the CovR protocol for modularity analysis (*sensu* Adams 2016) in Geomorph using 999 iterations of the permutation procedure. CovR coefficients ranging from zero to one (1) describe data where the degree of covariation between modules is less than that found within modules, and therefore characterise a more modular structure, where the modules vary independently of one another. CovR values larger than one (1) describe greater covariation between modules relative to within modules (Adams 2016). CovR coefficients are presented in Table A3.2, wherein modular CovR values are highlighted in the fashion of a ‘heat map’ and ‘hotter’ colours describe higher levels of morphological integration between modules.

**3.2.7.3 Integration analyses**—quantifies the degree of morphological integration between modular partitions of shape data. The pairwise partial least squares (PLS—see below) correlation is used as the test statistic, where the observed test value is compared to a distribution of values obtained by randomly permuting the individuals (rows) in one module, relative to those in the other. The result is significant when the observed PLS correlation is large relative to this distribution, and implies that the modular structures are integrated with one another (see Bookstein et al. 2003).

Two-block partial least squares analysis (2B-PLS *sensu* Rohlf & Corti 2000), also known as singular warps analysis (e.g. Bookstein et al. 2003), is used to assess the degree of association between two modules of GPA aligned shape coordinates. The two sets of variables are treated symmetrically without assumptions that one is the cause of variation in the other, and is based on the overall trait-covariance matrix (see Adams & Felice 2014). 2B-PLS differs from modularity tests (see 3.2.7.2 above), in that it is used to identify “latent variables” (Rohlf & Corti 2000:750) accounting for the covariance between two sets of variables, with no *a-priori* hypothesised directional relationship (Adams & Felice 2014). The correlation coefficient (r-PLS) between scores of projected values of left (x) and right (y) blocks of Lms is calculated along with the corresponding p-value, and are presented in plots (Figs. 3.4–3.5) and in text. Plots include TPS warpgrids derived from shape residuals describing the modular shape extremes across respective axes (see 3.2.7.5 below).

**3.2.7.4 Three Dimensional Vector plots**—for 3D vector plots (see Figs. 3.6–3.7), a species-mean modular configuration based on all specimens of *C. finschi* was calculated, and along with modular shapes representative of the oldest (GYL3) and youngest (CR) *C. finschi* specimens respectively, were visualised by means of 3D vector plots. Where vector lines from the species-mean modular Lm positions (grey dots) to the modular Lm positions (blue links) describe the direction and magnitude of modular shape change between the oldest (GYL3) and youngest (CR) *C. finschi* specimens, with respect to the species-mean modular shape.

**3.2.7.5 Two dimensional TPS deformation grids**—or warpgrids, are an effective method to describe shape changes captured by multivariate Lm data. I used 2D TPS warpgrids of individual modular shape change (see 3.2.7.1, and 3.2.7.3 above), and gross endocranial modular shape change between specimens of *C. finschi* (see Figs. 3.2–3.5, 3.8, A3.4). Allowing appreciation of where and to what degree morphological change occurred across the Modular Lm suite, and how individual modular shape changes affected gross endocranial morphology.

### 3.3 RESULTS

#### 3.3.1 Dating

**3.3.1.1 Honeycomb Hill sites**—four new radiocarbon ages were obtained based on Finsch's duck samples. Additionally, five previous moa samples were recalculated (Table A3.1). Two specimens of Finsch's duck from Graveyard L3 gave conventional radiocarbon ages as follows: Site 1 (NMNZ S.23725.3–19349 ± 114 yrs BP; NZA 63303), and Site 3 (NMNZ S.23840.1–19125 ± 111 yrs BP; NZA 63302). Moa radiocarbon ages were recalculated from original data from Graveyard L3: top of L3 in the main channel (*Pachyornis australis* Oliver, 1949–15680 ± 209 yrs BP; NZ 6453), base of L3 Site 1 (*Megalapteryx didinus* (Owen, 1882)–19240 ± 424 yrs BP; NZ 7316), Lag site 1 (*Megalapteryx didinus*–15532 ± 253 yrs BP; NZ 7319), base of L3 Site 2 (*Pachyornis australis*–18593 ± 253 yrs BP; NZ 7323), and base of L3 Site 3 (*Pachyornis australis*–20549 ± 436 yrs BP; NZ 7292). Two specimens of *C. finschi* from Graveyard L2 were dated: Exc. 1 (NMNZ S.23695.4–14885 ± 66 yrs BP; NZA 63304; and NMNZ S.23695.5–16454 ± 80 yrs BP; NZA 63305 respectively). Moa radiocarbon ages were recalculated from original data from L2: Top L2 (-15 cm: *Megalapteryx didinus*–11183 ± 179 yrs BP; NZ 7317), and Lag Site 1 (*Pachyornis elephantopus* (Owen, 1856)–14029 ± 176 yrs BP; NZ 6586).

Together, the new dates for *C. finschi* specimens, and recalculated existing dates comprise a total of seven dates for GYL3, and four dates for GYL2. These results show the depositional period for GYL3 is approximately 20.5–16.5 kys BP, and GYL2 is approximately 16.5–11.2 kys BP. Confirming the accuracy of earlier dates reported by Worthy (1988a, 1993), but suggest the depositional period for GYL2 is older by approximately 2 kys.

**3.3.1.2 Hodges Creek Cave**—the deposit was dated using Accelerated Mass Spectrometry (AMS) methods by [Worthy \(1997b\)](#) at  $12,210 \pm 110$  yrs BP (*Porphyrio hochstetteri*, NZA 6970); and  $12,100 \pm 120$  yrs BP (*C. finschi*, NZA 6971; Table A3.1). As argued by the author, specimens from this site display the taphonomic signature of rapid burial, and most specimens within the top 60 cm of the deposit are likely similar in age. Consequently, specimens from this site are taken to be 12,040 radiocarbon years old.

**3.3.1.3 Castle Rocks Fissure**—Results from comprehensive dating of this site by [Holdaway et al. \(2002a\)](#), and additional dates presented by [Holdaway et al. \(2002b\)](#), and [Cooper et al. \(2001\)](#); see Table A3.1), show the majority of dates cluster within 2500 years BP. I therefore take the modal value of 2087 yrs BP as the radiocarbon age of the sampled *C. finschi* cranium.

### 3.3.2 Modular Lm data

**3.3.2.1 PCA**—results, when taken together, suggests a trend of directional change in the rostroventral, rostradorsal and caudodorsal regions of the brain through time in *C. finschi*. The inclusion of *C. jubata* in PCA assessments reveal greater differences between it and *C. finschi* than between specimens of *C. finschi*, which dominate the PCA plots for Modular Lm data. Suggesting the interspecific morphological trends in *C. finschi* should be assessed without the inclusion of *C. jubata*.

PCA visualisations showed the paired orbits (Fig. 3.2) and eminentia sagittalis (Fig. 3.3) modules, appear to change shape directionally through time for *C. finschi*. The PCA plot for the orbits modules (Fig. 3.2), describe a directional change in orbit shape between the oldest (GYL3) specimen to the youngest (CR) specimen (i.e., from top of y-axis to the bottom). Where the orbits appear to rotate caudomediolaterally somewhat about a rostromedial axis, i.e., the caudal margins of the orbit modules displace mediolaterally more so than the rostral margins (see also Figs. 3.6A–B, and **3.3.6.1** below). This shape change is well captured by the Modular Lm configuration and describes a modular shape change in agreement with dating results for the temporal placement of each specimen (see **3.3.1** above; and Table A3.1 below). PC1 and PC2 eigenvectors comprise 92 % of the variance. Similarly, PCA of the paired eminentia sagittalis modules show there is a correlation of modular shape change, that broadly agrees with the temporal distribution of specimens (Fig. 3.3). These data suggest there was a directional change in eminentia sagittalis shape between the oldest (GYL3) specimen, to the youngest (CR) specimen (i.e., from top of y-axis to the bottom). Where there occurs a medial narrowing of the caudal fissura interhemispherica zone, accompanying a caudolateral shift of the valleculla (**va**; Introduction, Fig. 1.5.1), forming the transition zone between the caudolateral margins of the eminentia sagittalis, and caudodorsal telencephalic surfaces. This is also shown well by the 3D vector plots for eminentia sagittalis below (see Figs. 3.6C–D, and **3.3.6.2** below).

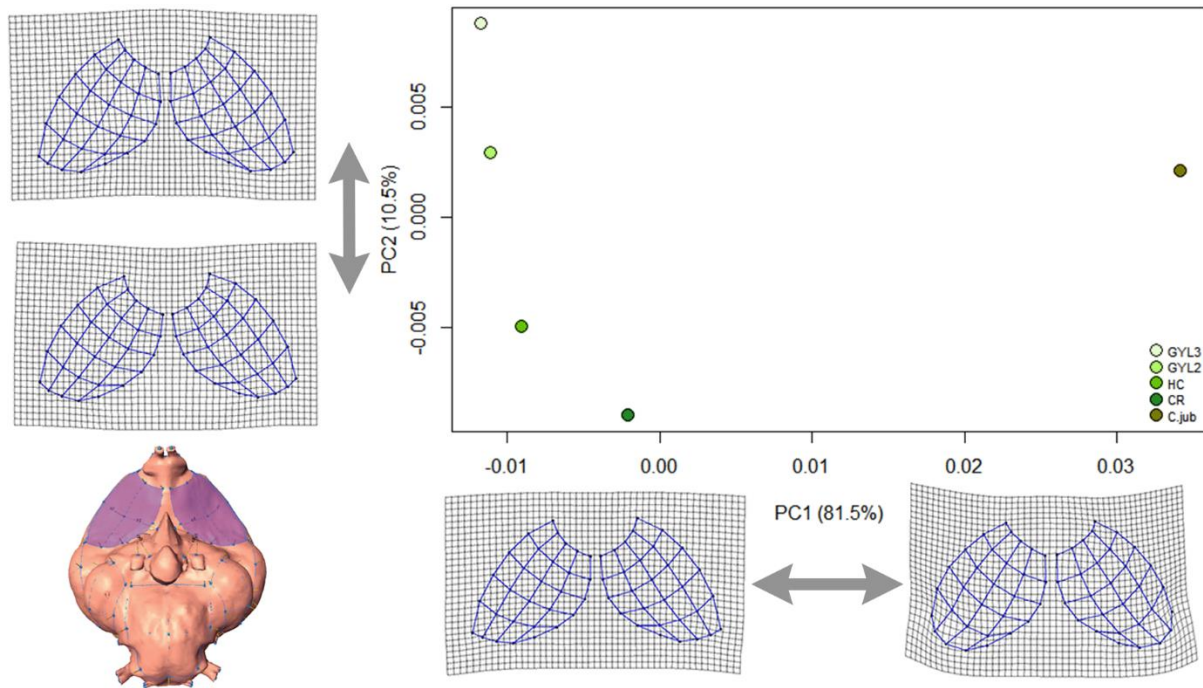


Figure 3.2. Modular Lm data, PCA plot of PC1 and PC2 for the orbit Lm modules including the Australian wood duck (*C. jubata*), describes shape change of the orbits between specimens. TPS visualisations derived from PC shape residuals for the respective PC axes are given in dorsal views describing the modular shape extremes across each axis. **Inset**, *C. finschi* (CR) endocast in ventral view showing the orbit modules on the rostroventral surface of the brain, in the same orientation as shown in both x- and y-axis TPS warpgrids. [Note, orbit TPS warpgrids (x- and y-axes) are viewed ‘through’ the endocast from the dorsal aspect, and orbit modules shown in **Inset** are viewed from the ventral aspect (i.e., rotated 180 degrees on the rostrocaudal plane)]. The eigenvalue percentage each PC contributes to an axis is given in parentheses. **Abbreviations**, **C.jub**, *C. jubata* (SAM B39457); **CR**, Castle Rocks Fissure *C. finschi* (NMNZ S.039838; ~2.1 kys); **GYL2**, Honeycomb Hill Cave Graveyard Layer 2 *C. finschi* (NMNZ S.023695; ~13.9 kys); **GYL3**, Honeycomb Hill Cave Graveyard Layer 3 *C. finschi* (NMNZ S.023702; ~18.5 kys); **HC**, Hodges Creek Cave *C. finschi* (NMNZ S.034496; ~12.2 kys).

However, temporal correlation for the eminentia sagittalis modules are not as well resolved as for the orbits modules (Fig. 3.2). PC1 and PC2 eigenvectors comprise 92.7% of the variance (Fig. 3.3).

**3.3.2.2 Modularity analysis**—results for Modular Lm data employing the complete data set of 14 morphological modules, showed the overall covariance ratio for Modular Lm data was significant (CovR = 0.88, p-value = 0.001), and suggests the degree of covariation between modules is less than that found within modules. Yet, the covariance ratio relative to this distribution, suggests there exists a degree of independence between the *a-priori* modules as defined (see Adams 2016). To identify which particular modules were displaying the greatest degree of covariation, a matrix of covariance ratios (Table A3.2) were computed for the complete Modular Lm data set. These results reveals the highest levels of covariation are between orbits and mesencephalon, orbits and eminentia sagittalis, and eminentia sagittalis and mesencephalon modules.

**3.3.2.3 Integration analyses**—results show that over the full Modular Lm suite, the integration r-PLS value approaches one, suggesting a high degree of integration between modules

overall, but the p-value is not significant ( $r$ -PLS = 0.946, p-value = 0.788). As suggested by modularity analyses results (Table A3.2; see also 3.3.2.2), some modules are clearly more closely integrated than others. Pairwise integration tests in the form of 2B-PLS analyses, assessing levels of integration between individual modules, identified the strongest integration occurred between the orbits and eminentia sagittalis modules ( $r$ -PLS = 0.984, p-value = 0.189, Fig. 3.4), and orbits and cerebellum modules ( $r$ -PLS = 0.998, p-value = 0.058, Fig. 3.5).

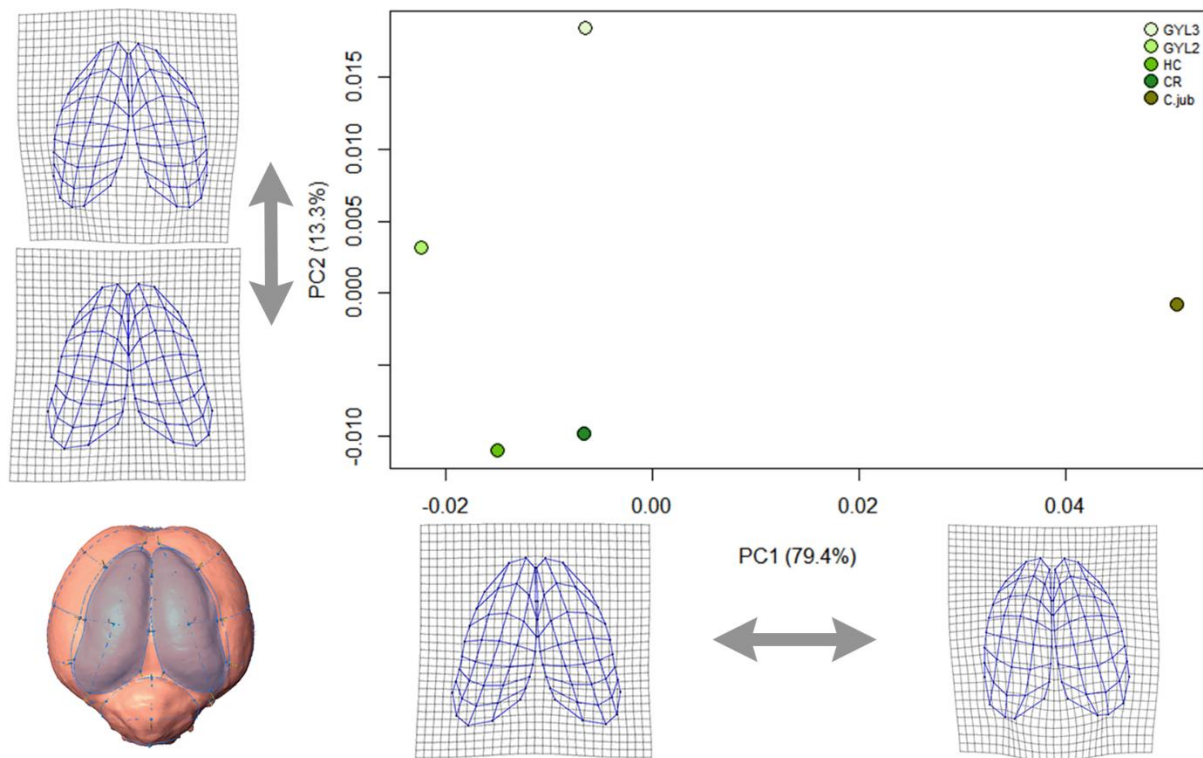


Figure 3.3. Modular Lm data, PCA plot of PC1 and PC2 for the eminentia sagittalis Lm modules including the Australian wood duck (*C. jubata*), describes shape change of the eminentia sagittalis between specimens. TPS visualisations derived from PC shape residuals for the respective PC axes are given in dorsal view describing the modular shape extremes across each axis. **Inset**, *C. finschi* (CR) endocast in dorsal view showing the eminentia sagittalis modules on the dorsal surface of the brain, in the same orientation as shown in both x- and y-axis TPS warpgrids. The percentage each PC contributes to an axis is given in parentheses. **Abbreviations**, **C.jub**, *C. jubata* (SAM B39457); **CR**, Castle Rocks Fissure *C. finschi* (NMNZ S.039838; ~2.1 kys); **GYL2**, Honeycomb Hill Cave Graveyard Layer 2 *C. finschi* (NMNZ S.023695; ~13.9 kys); **GYL3**, Honeycomb Hill Cave Graveyard Layer 3 *C. finschi* (NMNZ S.023702; ~18.5 kys); **HC**, Hodges Creek Cave *C. finschi* (NMNZ S.034496; ~12.2 kys).

The correlation of shape change between the orbits and cerebellum modules approach significance, and specimens approximate the fitted linear model with a high  $r$ -PLS value (0.998; Fig. 3.5), suggesting that shape change covariation in these modules is closely integrated. Note the positioning of specimens in Fig. 3.5 are reversed with respect to the other 2B-PLS plot presented (Fig. 3.4); this effect is likely due to cerebellum structures reducing in absolute size between the oldest (GYL3) and youngest (CR) *C. finschi* specimens over time. This trend is also captured by cerebellum

Modular Distance data (see Fig. A3.2, Table A3.3D, and **3.3.3** below), and Modular Surface Area data (see Fig. A3.3, Table A3.3F, and **3.3.5** below). Represented visually in the modular shape change plots (see Figs. 3.6E–F, and **3.3.6.5** below), which describe the overall reduction in cerebellum size between GYL3 and CR specimens. Thus, the effect of the reduction in size of cerebellum structures through time in the 2B-PLS plot (Fig. 3.5), are represented by the youngest specimen (CR) first in sequence from left to right across the x-axis, followed by the temporally correlated distribution of the other specimens. These results suggest there was a directional increase in absolute size and shape of both the orbits and eminentia sagittalis concomitant with the reduction in shape and size of the cerebellum from oldest (GYL3) to youngest (CR) specimens assessed.

**3.3.3 Modular Distance data**—Modular Distance ratio results show similar patterns as those identified by analyses of Modular Lm data. They reveal that between the oldest (GYL3) and youngest (CR) *C. finschi* specimens, overall lengths of the orbits reduce mediolaterally (0.268 vs 0.265, respectively; Table A3.3D), as orbit width increases dorsoventrally (0.245 vs 0.251; Table A3.3D, Fig. A3.2). This ‘shortening’ and ‘widening’ of the orbit modular shape, along with a concomitant ‘cupping’ of the orbits, as described by orbit TPS warpgrids for PCA and 2B-PLS plots (Figs. 3.2, 3.4–3.5), affects an increase in Modular Surface Area ratios for orbit modules between the oldest (GYL3) and youngest (CR) specimens (see **3.3.5** below). The GYL2 specimen has the largest orbit length ratio for all specimens (0.275), with an orbit width ratio that approaches that of the CR specimen (0.248 vs 0.251, respectively; Table A3.3D, Fig. A3.2). Modular Distance ratios for eminentia sagittalis modules show rostrocaudal length increases incrementally by around 5% between the oldest (GYL3) and youngest (CR) specimens (0.342 vs 0.351, respectively; Table A3.3D), but mediolateral width ratios increase to a lesser degree (0.233 vs 0.238, respectively; Table A3.3D, Fig. A3.2, but see **3.3.6.2** below). These data also show that mesencephalon length (0.287 vs 0.290, respectively; Table A3.3D), and width (0.205 vs 0.215, respectively; Table A3.3D) ratios increase somewhat between the oldest (GYL3) and youngest (CR) specimens. However, although the GYL2 specimen shows the largest mesencephalon length (0.297) and width (0.211) ratios for all specimens (Table A3.3D), the endocast volume for the GYL2 specimen is also somewhat less than those of the other specimens assessed (Table A3.3C). Results for the cerebellum show a stronger reduction in length (0.266 vs 0.254, respectively), and width (0.311 vs 0.308, respectively) ratios between the oldest (GYL3) and youngest (CR) specimens (Table A3.3D, Fig. A3.2). Modular Distance ratios for the rhombencephalon show there is a directional increase in rostrocaudal length (0.279 vs 0.282, respectively), and width (0.264 vs 0.270, respectively) ratios between the oldest (GYL3) and youngest (CR) specimens (Table A3.3D, Fig. A3.2).

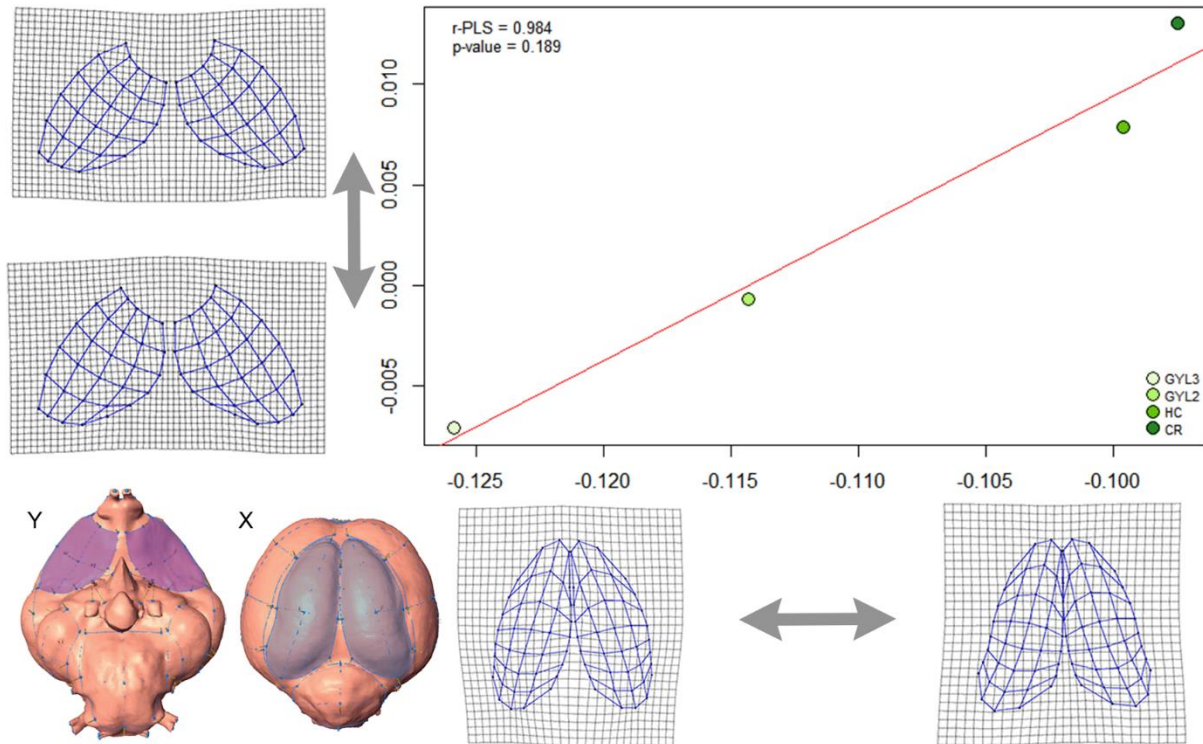


Figure 3.4. Modular Lm data. Integration analysis 2B-PLS plot of orbits vs eminentia sagittalis Lm modules, showing covariation of modular shape change between specimens of *C. finschi*. TPS warpgrids derived from PLS shape residuals for the respective axes in dorsal view, describe the modular shape extremes across each axis. **Insets**, *C. finschi* (CR) endocast in ventral (**Y**) and dorsal (**X**) views showing the orbits, and eminentia sagittalis modules in the same orientation as shown in the y-axis and x-axis TPS warpgrids respectively. [Note, orbit TPS warpgrids (y-axis) are viewed ‘through’ the endocast from the dorsal aspect, and orbit modules shown in **Y** are viewed from the ventral aspect (i.e., rotated 180 degrees on the rostrocaudal plane)]. **Abbreviations**, **CR**, Castle Rocks Fissure *C. finschi* (NMNZ S.039838; ~2.1 kys); **GYL2**, Honeycomb Hill Cave Graveyard Layer 2 *C. finschi* (NMNZ S.023695; ~13.9 kys); **GYL3**, Honeycomb Hill Cave Graveyard Layer 3 *C. finschi* (NMNZ S.023702; ~18.5 kys); **HC**, Hodges Creek Cave *C. finschi* (NMNZ S.034496; ~12.2 kys).

In summary, Modular Distance ratios describe an increase in orbit width, an increase in all ratios for eminentia sagittalis and the rhombencephalon, along with a reduction in modular length and width ratios for the cerebellum between the oldest (GYL3) and youngest (CR) *C. finschi* specimens.

**3.3.4 Linear Distance data**—ratios capturing the dorsoventral height of the hindbrain, i.e., metencephalon (cerebellum + pons) between the oldest (GYL3) and youngest (CR) specimens (0.344 vs 0.339, respectively; Table A3.3E, Fig. A3.2), shows the height of the caudal endocast decreased somewhat. The GYL2 specimen has the smallest dorsoventral hindbrain height for all specimens (0.336; Table A3.3E, Fig. A3.2). These data also show a slight decrease in total endocast length between the oldest (GYL3) and youngest (CR) specimens (0.389 vs 0.386 respectively; Table A3.3E). Linear Distance ratios reveal more substantial mediolateral hypertrophy of the caudal telencephalon between taxa, which likely occurred early in the temporal sequence between GYL3 (~18.5 kys) and GYL2/HC (~16.5~12.2 kys), as the greatest distinction in total caudal telencephalon width is found

between the GYL3 specimen and the GYL2/HC specimens (i.e. 0.362 vs 0.369/0.373 and 0.372 [CR]; Table A3.3E; see also 3.3.7 below).

**3.3.5 Modular Surface Area data**—show there is a relative increase in Modular Surface Area ratios for the orbits through time between the oldest (GYL3) and youngest (CR) specimens (0.549 vs 0.561, respectively; Table A3.3F). Although, as with the Modular Distance ratios for orbits (see 3.3.3 above), the GYL2 specimen has the largest orbit Surface Area ratio for all specimens (0.565; Table A3.3F, Fig. A3.3). The trends described by Modular Lm data (see 3.3.2 above) and Modular Distance ratios for eminentia sagittalis, are also captured by the Modular Surface Area data. Where there occurs an increase in overall Surface Area ratios between oldest (GYL3) and youngest (CR) specimens (0.615 vs 0.633, respectively; Table A3.3F).

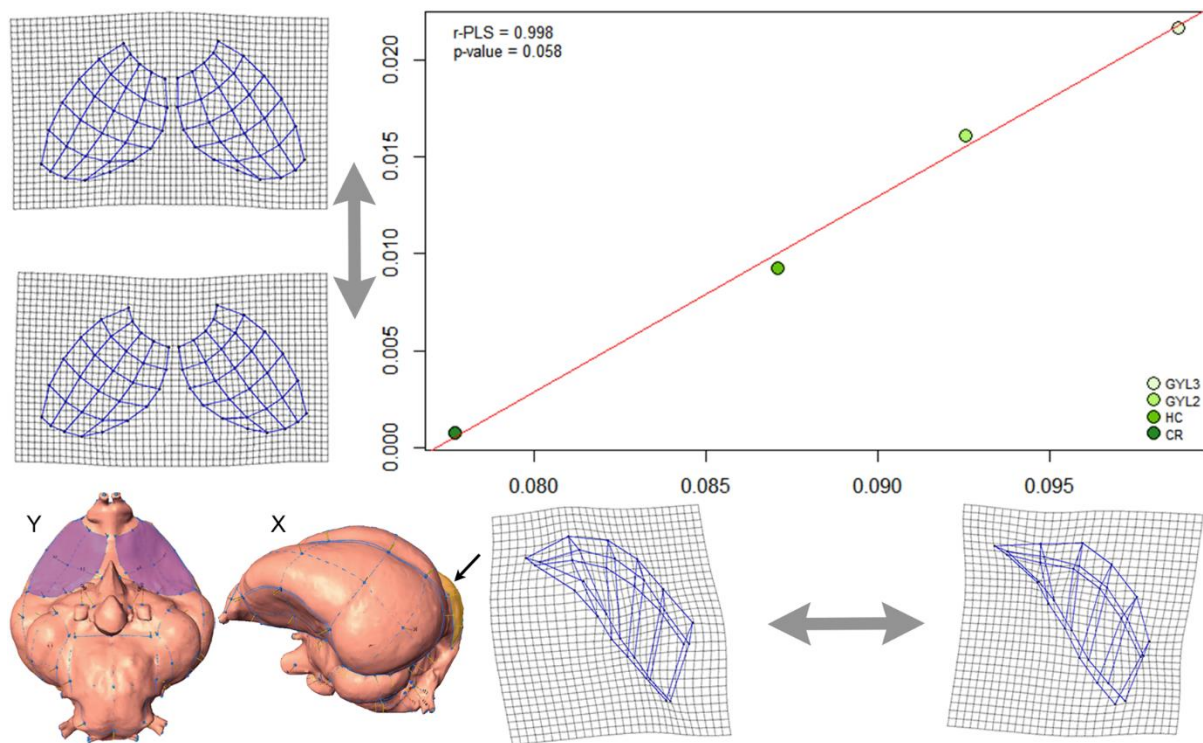


Figure 3.5. Modular Lm data. Integration analysis 2B-PLS plot for the orbits vs dorsal cerebellum Lm modules, showing covariation of modular shape change between specimens of *C. finschi*. TPS visualisations derived from PLS shape residuals for the respective axes are given in dorsal view (orbits) and lateral view (cerebellum) and describing the modular shape extremes across each axis. **Insets**, *C. finschi* (CR) endocast in ventral (**Y**) and LHS lateral (**X**) views showing the orbits, and cerebellum (arrow) modules in the same orientation as shown on the y-axis and x-axis TPS warpgrids respectively. [Note, orbit TPS warpgrids (y-axis) are viewed ‘through’ the endocast from the dorsal aspect, and orbit modules shown in **Y** are viewed from the ventral aspect (i.e., rotated 180 degrees on the rostrocaudal plane)]. **Abbreviations**, **CR**, Castle Rocks Fissure *C. finschi* (NMNZ S.039838; ~2.1 kys); **GYL2**, Honeycomb Hill Cave Graveyard Layer 2 *C. finschi* (NMNZ S.023695; ~13.9 kys); **GYL3**, Honeycomb Hill Cave Graveyard Layer 3 *C. finschi* (NMNZ S.023702; ~18.5 kys); **HC**, Hodges Creek Cave *C. finschi* (NMNZ S.034496; ~12.2 kys).

Results for the rostral telencephalon show similar patterns for an increase in Surface Area ratios between the oldest (GYL3) and youngest (CR) specimens (0.635 vs 0.654, respectively; Table A3.3F). However, GYL2 again appears to have the largest rostral telencephalon Surface Area ratio for all specimens (0.660; Table A3.3F, Fig. A3.3). Results for the caudal telencephalon show trends of an increase in Surface Area ratios between the oldest (GYL3) and youngest (CR) specimens too (0.627 vs 0.645, respectively; Table A3.3F). Taken together with results presented above for the rostral telencephalon, this suggest there was a general increase in the Modular Surface Area of the entire cerebrum between specimens over time (Table A3.3F, Fig. A3.3). However, such directional changes in the cerebrum were not particularly well captured by either the Modular Lm data or the Modular Distance ratios (see Table A3.3D), and thus should be considered with caution. There was a temporally correlated increase in the Modular Surface Area ratios for the mesencephalon between the oldest (GYL3) and youngest (CR) specimens (0.530 vs 0.553, respectively; Table A3.3F, Fig. A3.3). Notably, there occurs progressive reduction in Modular Surface Area of the cerebellum between specimens (0.630 vs 0.622, respectively; Table A3.3F, Fig. A3.3). Although, the cerebellum of GYL2 has a distinctly smaller Surface Area ratio than those of other *C. finschi* specimens (0.602; Table A3.3F, Fig. A3.3). Results for the rhombencephalon show there is a directional increase in the overall Surface Area for this module (0.573 vs 0.583, respectively; Table A3.3F, Fig. A3.3), between the oldest (GYL3) and youngest (CR) specimens.

In summary, between the oldest (GYL3) and youngest (CR) *C. finschi* specimens, these results describe directional increases in orbit Modular Surface Area ratios, ratios for eminentia sagittalis and mesencephalon, and an increase in ratios for the rhombencephalon. As was seen in the Modular Distance data above, there was a concomitant reduction in Surface Area ratios for the cerebellum between the oldest (GYL3) and youngest (CR) *C. finschi* specimens, and the GYL2 specimen showed the smallest Modular Surface Area ratio for all *C. finschi* specimens.

**3.3.6 Three Dimensional Vector plots**—afford visualisation of the displacement of modular Lm configurations with respect to a species-mean modular shape (grey dots; see **3.2.7.4** above), and allow appraisal of modular distinctions represented by Modular data forms (see **3.3.2–3.3.5** above).

**3.3.6.1 Orbits**—modular shapes representing the oldest (GYL3; Fig. 3.6A) and youngest (CR; Fig. 3.6B) specimens in Figs. 3.6A–B (blue links), show there occurred a caudolateral rotation of the orbit margins, accompanying an increase in width, and compression in length of the orbits between GYL3 and CR specimens. These trends agree with results for Modular Distance ratios and Surface Area ratios described above (Tables A3.3D, A3.3F, Figs. A3.2, A3.3). The caudolateral orbit Lms rotate mediolaterally to a greater degree than the rotation of the rostromedial Lms. Effectively the orbits rotate caudolaterally about a rostromedial axis, likely in accommodation of other changes in endocast shape, such as the mediolateral hypertrophy of the caudal telencephalon, and compression of total endocast length, between oldest (GYL3) and youngest (CR) specimens described above.

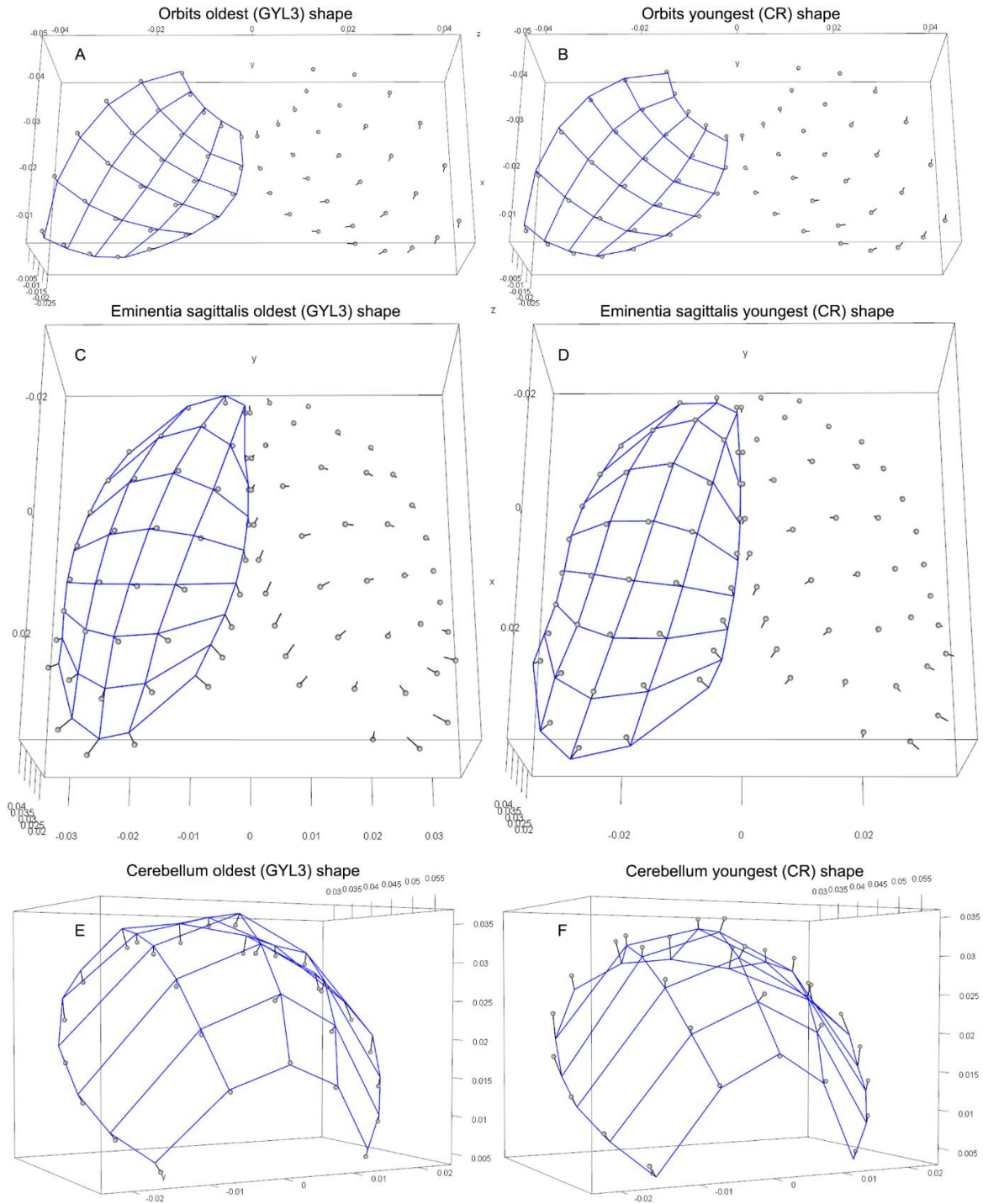


Figure 3.6. Three dimensional modular shape change vector plots. Grey circles represent the species-mean shape calculated using Modular Lm data for all *C. finschi* specimens. Vector lines from the species-mean shape (grey circles) to the oldest (GYL3) and youngest (CR) modular shapes, visualised by blue links, describe the magnitude and direction of shape change within each module between GYL3 and CR *C. finschi* specimens (see 3.2.7.4). Blue links visualise only LHS Lm locations for paired A–D modules, providing morphological perspective and allowing appreciation of vector magnitude and direction in the unlinked RHS Lm configuration. **A**, orbits, oldest (GYL3) shape; **B**, orbits, youngest (CR) shape; **C**, eminentia sagittalis oldest (GYL3) shape; **D**, eminentia sagittalis youngest (CR) shape; **E**, cerebellum oldest (GYL3) shape, **F**, cerebellum youngest (CR) shape. Modules A–D are presented in rostradorsal view, modules E–F are presented in LHS caudolateral view. **Abbreviations**, **CR**, Castle Rocks Fissure *C. finschi* (NMNZ S.039838; ~2.1 kys); **GYL3**, Honeycomb Hill Cave Graveyard Layer 3 *C. finschi* (NMNZ S.023702; ~18.5 kys).

**3.3.6.2 Eminentia sagittalis**—the changes observed in eminentia sagittalis modules are greater than those of the orbits, but are not well complemented by Modular Distance ratio results for eminentia sagittalis width (Table A3.3, Fig. A3.2; but see below). Eminentia sagittalis modular shapes representing the oldest (GYL3; Fig. 3.6C) and youngest (CR; Fig. 3.6D) specimens in Figs. 3.6C–D (blue links), allow appreciation that while there is a moderate increase in overall rostrocaudal length (Table A3.3D, Fig. A3.2), as described by Modular Distance ratios (see **3.3.3** above). The caudal Lms shift mediolaterally and caudally to a greater degree than the rostral Lms do, with respect to the species-mean. This suggests the caudal zones of the eminentia sagittalis are where most of the modular shape change had occurred, and explains why the Modular Distance width ratios do not capture well the full extent of the mediolateral hypertrophy of the eminentia sagittalis directly. Likely because distance measurements were computed rostrad to where the bulk of the mediolateral shape change occurred between the oldest (GYL3) and youngest (CR) specimens (Figs. 3.6C–D; see also General Method Fig. 2.2C). Essentially, the positioning of the rostralateral through mediolateral Lms remain more or less uniform across specimens, and changes occurring in the eminentia sagittalis are mostly caudomedially and caudolaterally orientated. The caudolateral changes are confined within a smaller rostrocaudolateral zone compared with the caudomedial shape changes.

**3.3.6.3 Cerebrum**—(complete telencephalon) vector plots allow additional insight into the trends described by the TPS warpgrids (Figs. 3.8, A3.4; see also **3.3.7** below). The rostral and caudal telencephalon Lm modules were combined and visualised together for vector plot assessments, so that shape changes occurring across the whole cerebral hemisphere could be assessed together with respect to the species-mean shape. Cerebral modular shapes representing the oldest (GYL3; Fig. 3.7C) and youngest (CR; Figs. 3.7D) specimens in Figs. 3.7C–D (blue links), show hypertrophy of the cerebrum is centred primarily in caudal telencephalic regions, and reflect mediolateral hypertrophy to a much larger degree than that observed in the rostral telencephalon. Dorsolaterally, the displacement of the caudal Lms, with respect to the species-mean configuration, is more extensive than those seen in the rostral configurations too, with the rostralateral displacement becoming more pronounced caudally of the modular median (Figs. 3.7C–D). Additionally, the caudal telencephalon rotate and expand rostralaterally, with the caudomedial Lms displaced more caudolaterally than the lateral Lms, which are displaced more laterally and rostralaterally. The effects of this caudal telencephalon hypertrophy between the oldest (GYL3) and youngest (CR) specimens, are visible in the dorsolateral Lms of the mesencephalon (Figs. 3.7A–B), which mirror the displacement of the caudoventral telencephalon Lms, with a sympathetic rostralateral Lm displacement in the fissura subhemispherica zones (**fs**, see Introduction, Fig. 1.5.1, and **3.3.6.4** below). The rostral telencephalon shows a subtle rostralateral hypertrophy, with a somewhat more pronounced rostromedial dorsal compression (Fig. 3.7D). The location of the rostromedial and rostralateral Lms, show only marginal displacement from the species-mean configuration. However, these small changes in the rostral telencephalon are notably accompanied by strong caudomediolateral hypertrophy in the caudal telencephalon, caudad of the

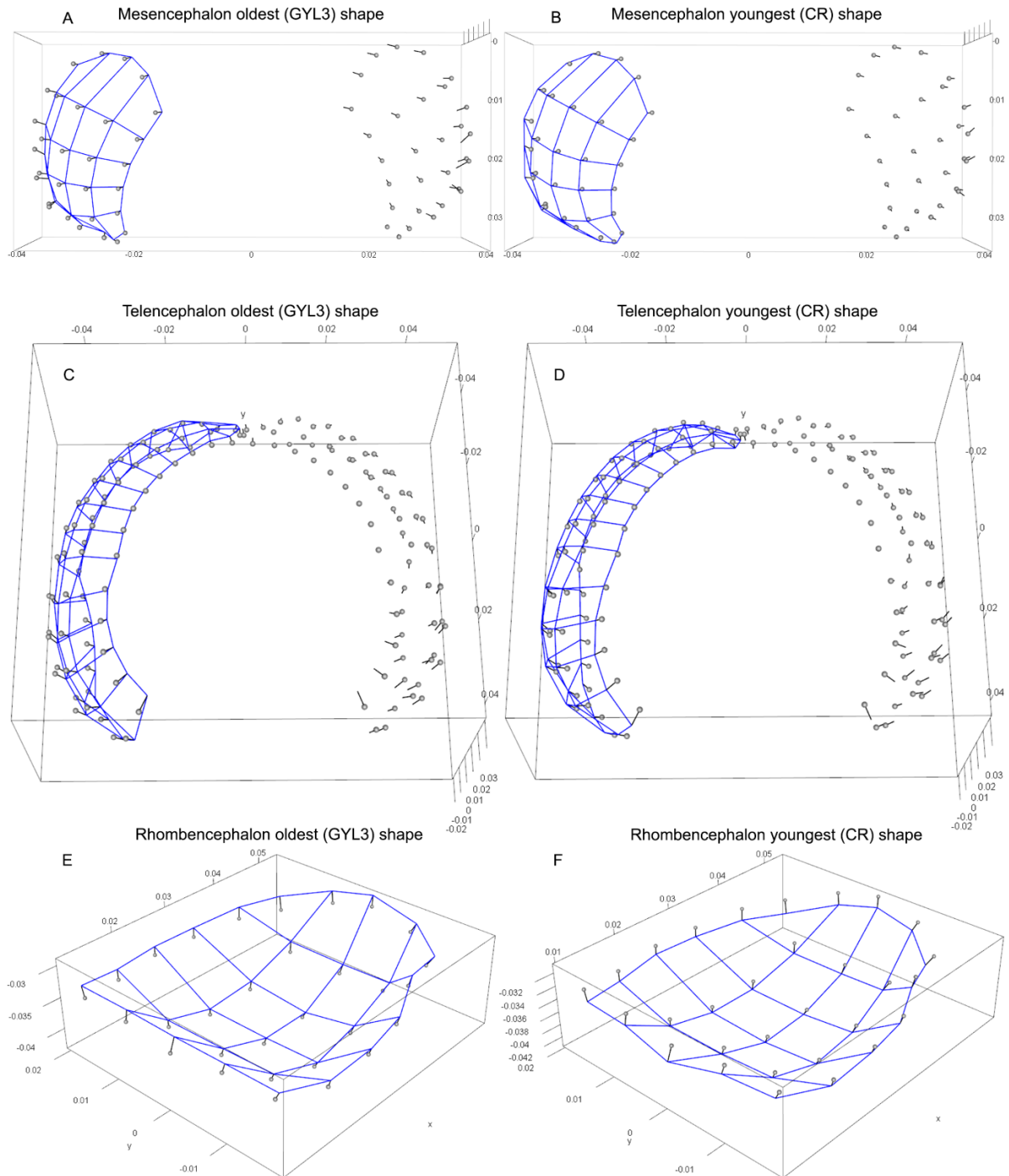


Figure 3.7. Three dimensional modular shape change vector plots. Grey circles represent the species-mean shape calculated using Modular Lm data for all *C. finschi* specimens. Vector lines from the species-mean shape (grey circles) to the oldest (GYL3) and youngest (CR) modular shapes, visualised by blue links, describe the magnitude and direction of shape change within each module between GYL3 and CR *C. finschi* specimens (see 3.2.7.4). Blue links visualise only LHS Lm locations for paired A–D modules, providing morphological perspective and allowing appreciation of vector magnitude and direction in the unlinked RHS Lm configuration. **A**, mesencephalon oldest (GYL3) shape; **B**, mesencephalon, youngest (CR) shape; **C**, complete telencephalon oldest (GYL3) shape; **D**, complete telencephalon youngest (CR) shape; **E**, rhombencephalon oldest (GYL3) shape; **F**, rhombencephalon youngest (CR) shape. Modules A–B are presented in ventral view, modules C–D are presented in rostrorodorsal view and modules E–F are presented in rostrorodorsal views. **Abbreviations**, **CR**, Castle Rocks Fissure *C. finschi* (NMNZ S.039838; ~2.1 kys); **GYL3**, Honeycomb Hill Cave Graveyard Layer 3 *C. finschi* (NMNZ S.023702; ~18.5 kys).

median cerebrum. Effectively, the shape of the dorsolateral cerebrum expands and rotates strongly rostromedially about the caudolateral median between the oldest (GYL3) and youngest (CR) specimens. These changes are well visualised by the dorsal caudolateral areas of the TPS warpgrid plots (Figs. 3.8C–D). Linear Distance ratios (see **3.3.4** above; Table A3.3E) suggest the caudolateral hypertrophy of the caudal telencephalon likely occurred early in the temporal sequence between GYL3 (~18.5 kys) and GYL2/HC (~16.5–12.2 kys). This is illustrated well by the sequential TPS warpgrid visualisations (Fig. A3.4), revealing the degree of warpgrid distortion in the caudal telencephalon areas of GYL3–GYL2 (Figs. A3.4C–D), is more pronounced than subsequent warpgrid distortions for temporally younger specimens (Figs. A3.4E–H).

**3.3.6.4 Mesencephalon**—modular shapes representing the oldest (GYL3; Fig. 3.7A) and youngest (CR; Fig. 3.7B) specimens in Figs. 3.7A–B (blue links), show shape changes across the temporal sequence. As described above, the most prominent shape change between the oldest (GYL3) and youngest (CR) specimens, occurs in the rostromedial and mediolateral displacement of Lms in the lateral rostrocaudal fissura subhemispherica region, between the caudoventral telencephalon, and the dorsolateral mesencephalon (Figs. 3.7A–B). There occurs a general caudoventral hypertrophy of the mesencephalon, accompanied by a slight rostromedial shift, which is more pronounced rostrally than caudally. Relatively minor changes in Modular Distance width and length ratios (Table A3.3D, Fig. A3.2), are accompanied by more substantial directional changes in Modular Surface Area ratios for the mesencephalon (Table A3.3F, Fig. A3.3). Suggesting a similar modular perimeter is maintained between the oldest (GYL3) and youngest (CR) specimens, but that lateral hypertrophy of the mesencephalon through time affects a progressive increase in Modular Surface Area ratios between the specimens. These trends are well visualised by the vector plots (Figs. 3.7A–B), which show a strong displacement of the lateral Lms with respect to the species-mean modular configuration, and more so in dorsal areas in the vicinity of the fissura subhemispherica zones (**fs** see **3.3.6.3** above). Additionally, overall Modular Distance length ratios for the mesencephalon remain more or less constant between the oldest (GYL3) and youngest (CR) specimens, but the entire structure shifts somewhat caudally with respect to the species-mean across the temporal period sampled (Table A3.3D, Figs. 3.7A–B).

**3.3.6.5 Cerebellum**—modular shapes representing the oldest (GYL3; Fig. 3.6E) and youngest (CR; Figs. 3.6F) specimens in Figs. 3.6E–F (blue links) describe an uncharacteristic trend in this shape analysis. The modular shape associated with the oldest (GYL3) specimen shows hypertrophy with respect to the species-mean modular shape, and the shape of the cerebellum associated with the youngest (CR) specimen shows hypotrophy with respect to the species-mean shape. The vector plots (Figs. 3.6E–F) describe directional hypotrophy of the cerebellum between the oldest (GYL3) and youngest (CR) specimens. Similar trends were captured by the Modular Distance ratios (Table A3.3D, Fig A3.2), Modular Surface Area ratios (Table A3.3F, Fig. A3.3), and Integration assessments of Modular Lm data (Fig. 3.5). The greatest dorsoventral displacement of modular Lms occurs in the

rostradorsal zone of the cerebellum, in the vicinity of the dorsomedial glandula pinealis (**gp**; see Introduction, Fig. 1.5.1, and **3.3.7** below). This is accompanied by caudolateral displacement of the caudal eminentia sagittalis (see **3.3.6.2** above), effectively ‘tucking’ the rostradorsomedial eminence of the cerebellum behind the caudodorsolateral eminence of the eminentia sagittalis, when viewed from the lateral aspect. This is clearly evident in TPS warpgrids (Figs. 3.8D, A3.4D, A3.4F, A3.4H), and is similar in direction and magnitude to the caudolateral hypertrophy shown in the caudal telencephalon (see **3.3.6.3** above). These changes to caudal endocranial morphology appear to have occurred early in the temporal series (see above, and Figs. A3.4C–H).

**3.3.6.6 Rhombencephalon**—modular shapes representing the oldest (GYL3; Fig. 3.7E) and youngest (CR; Figs. 3.7F) specimens in Figs. 3.7E–F (blue links), show a slight increase in the overall dorsoventral depth between the oldest (GYL3) and the youngest (CR) specimens. The rostroventral and caudoventral Lms shift dorsoventrally, relative to the species-mean, somewhat more than the Lms in medial zones of the rhombencephalon modules. This affords a ‘steeper’ rostroventral and caudoventral structural profile in the oldest (GYL3) specimen, when viewed from the lateral aspect. The Linear Distance ratio capturing the dorsoventral height of the hindbrain between the oldest (GYL3) and youngest (CR) specimens (see **3.3.4** above; Table A3.3E, Fig. A3.2), shows the height of the hindbrain decreased through the temporal series. This may be due to the reduction in the overall dorsal eminence of the cerebellum in the youngest (CR) taxon (see Fig. 3.6F, Table A3.3E, Fig A3.2; and above), which occurred along with increases in rhombencephalon modular length and width ratios (Table A3.3D, Fig. A3.2), and Modular Surface Area ratios (Table A3.3F, Fig. A3.3) between the oldest (GYL3) and youngest (CR) specimen.

**3.3.7 Warpgrids**—the TPS warpgrid plot (Fig. 3.8) affords visualisation of gross endocast morphological changes between the oldest (GYL3; Figs. 3.8A–B) and youngest (CR; Figs. 3.8C–D) specimens, as described by the full Modular Lm suite.

The increase in width of the orbit (purple) modules between the oldest (GYL3) and youngest (CR) specimens is evident from the lateral aspect (Figs. 3.8B, 3.8D). Where the caudodorsal expansion (i.e., increase in Modular Distance width ratios; see **3.3.4**) of the orbit margins have affected a somewhat rostradorsomedial rotation of the rostral telencephalon (pink). This is evident rostralaterally in Fig. 3.8C, and also in rostral areas of Fig. 3.8D. Viewed from the dorsal aspect (see Figs. 3.8A, 3.8C), the integrated increases in Modular Surface Area and Distance ratios, overall hypertrophy of eminentia sagittalis (grey), and hypotrophy of the cerebellum (yellow; see Fig. A3.1), are evident in the distortion of the warpgrids between the oldest (GYL3) and youngest (CR) specimens. Particularly where the cerebellum (yellow) narrows mediolaterally, and ‘tucks in’ more closely between the caudolateral eminences of the eminentia sagittalis. This ‘tucking in’ of the cerebellum, has the effect of displacing the most caudal eminence of the eminentia sagittalis laterally,

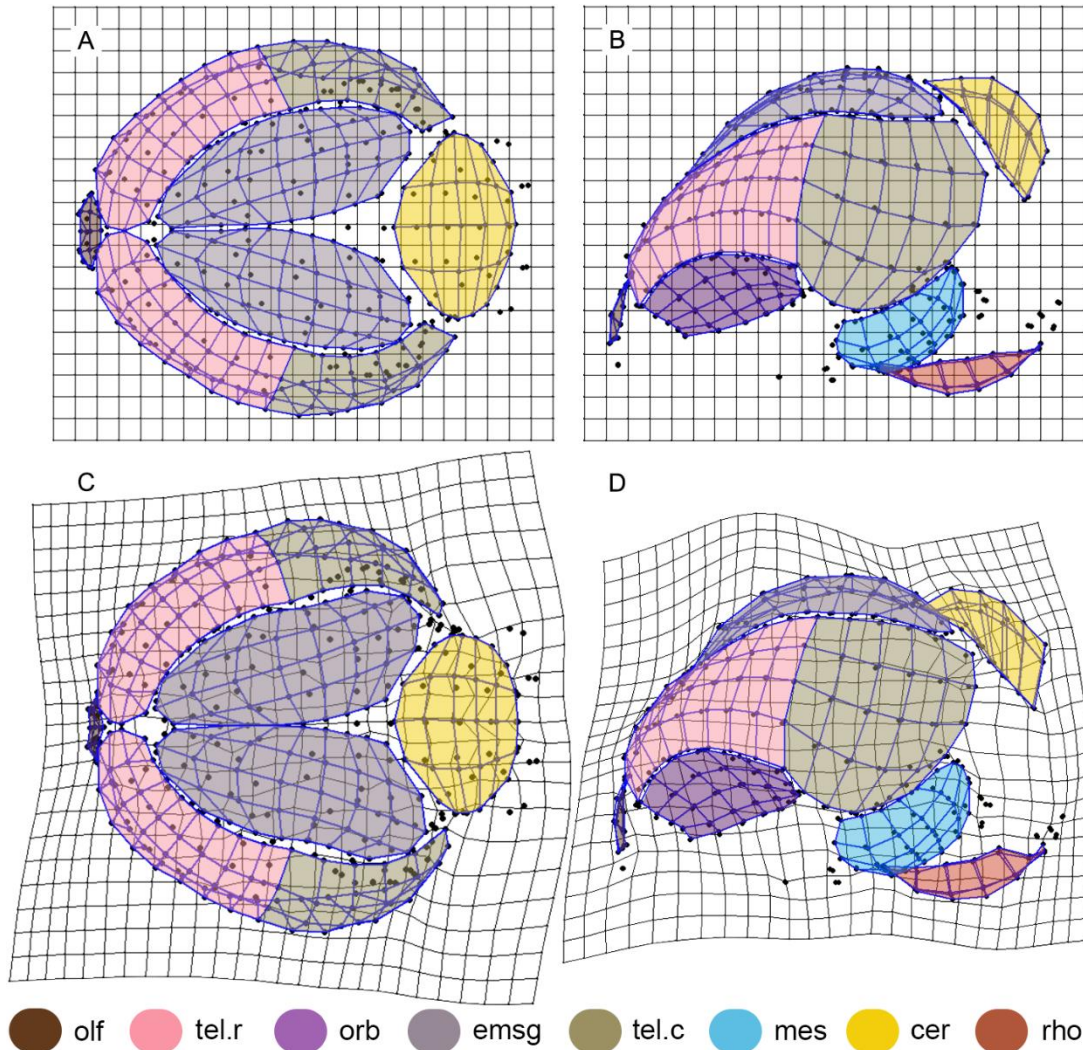


Figure 3.8. TPS warpgrid visualisations of the endocast shape change between the **A–B**, Honeycomb Hill Cave Graveyard Layer 3 *C. finschi* (NMNZ S.023702; ~18.5 kys) and the **C–D**, Castle Rocks Fissure *C. finschi* (NMNZ S.039838; ~2.1 kys) specimens. Blue links visualise target specimen shapes and are shaded to assist identification of Modular Lm configurations (see Fig. A3.1). **Views**, dorsal (**A–C**), LHS lateral (**C–D**). **Abbreviations**, **cer**, cerebellum; **emsg**, eminentia sagittalis, **mes**, mesencephalon; **olf**, olfactory; **orb**, orbit; **rho**, Rhombencephalon; **tel.c**, caudal telencephalon; **tel.r**, rostral telencephalon.

and affecting a caudomediolateral shift of eminentia sagittalis structures (see **3.3.6.2** above), with respect to those of the oldest (GYL3) specimen (Fig. 3.8A). The ‘tucking’ of the dorsal cerebellum is also well described in the caudodorsal warpgrid regions of Fig. 3.8D, where the rostradorsal margin of the cerebellum is masked by the caudal eminence of the eminentia sagittalis modules, when viewed from the lateral aspect (see also Figs. A3.4D, A3.4F, A3.4H, and above). These shifts in endocast morphology between oldest (GYL3) and youngest (CR) specimens were likely in accommodation for the slight decrease in total endocast length, and more substantial increase in overall cerebrum width between specimens (see Table A3.3E, Fig. A3.2, and **3.3.4** above). The somewhat substantial increase in overall endocast width ratios (see Table A3.3E) between oldest (GYL3) and youngest (CR)

specimens reported here, is shown well by Fig. 3.8D, where the warpgrid is distorted ‘towards’ the observer, i.e., the lateral surface of the caudal telencephalon (green) is moving out of the page, and effectively ‘tenting’ the warpgrid. These combined traits of endocast shortening and widening, along with the increase in directional size and surface areas of the orbits and eminentia sagittalis modular regions, affected the ‘tucking’ of the cerebellum in the region of the dorsomedial glandula pinealis region (**gp**; see **3.3.6.5** above), and displacing the eminentia sagittalis somewhat caudolaterally in accommodation.

### 3.4 DISCUSSION

Previous work on fossils of *Chenonetta finschi* has shown there was a 10% reduction in the size of forelimb and pectoral girdle elements, relative to body size, based on femur length, over a ~20 kys period, suggesting a rapid transition to flightlessness in the taxon (Worthy 1988a, 1997b; Watanabe 2017). I used four *C. finschi* endocasts sourced from dated, key time periods across the temporal sequence documenting the transition to flightlessness, and compared these to the endocast of its putative sister taxon *C. jubata*. I employed Modular Lm configurations defining endocast shape, along with Modular Distance and Surface Area data forms, to investigate shape change in *C. finschi* endocasts concomitant with the loss of flight ability.

In this study I have confirmed earlier dates (Conventional Radiocarbon Ages) presented by Worthy (1988a, 1993) for the Graveyard site, Honeycomb Hill Cave, and the new dates allow refining of the depositional history, placing the boundary of L3 and L2 at about 16.5 kys BP, so extending the depositional period for GYL2 by about 2 kys (and continuing to ~11.2 kys BP). This is accommodated easily by reinterpreting NZ 6453, from the top of Layer 3 in the Main Channel deposit (Worthy 1993) with an age of  $15,680 \pm 210$ , as better representing the base of Layer 2. Thus, deposition period of GYL3 is better defined as between 20.5 and 16.5 kys BP.

PCA plots of Modular Lm data describe a directional change in orbit and eminentia sagittalis shape between the older (GYL3 [~20.5~16.5 kys BP]) specimen to the younger (CR [~2.2 kys BP]) specimen. However, temporal correlation for the eminentia sagittalis modules are not as well resolved in PCA morphospace as for the orbit modules. Modularity assessments show the Lm modules used to capture brain morphology were robustly defined, and covariance ratios showed correlations between the orbits, eminentia sagittalis, and to a lesser degree, the mesencephalon and cerebellum regions of the brain. Integration analyses showed that shape change covariation between orbits, eminentia sagittalis, and cerebellum modular regions had the strongest correlation with time.

Modular Distance data describe an increase in orbit width and reduction in orbit length ratios, accompany small increases in ratios for eminentia sagittalis, mesencephalon, and rhombencephalon modules, along with a notable reduction in cerebellum Modular Distance ratios between the oldest (GYL3 [~20.5~16.5 kys BP]) and youngest (CR [~2.2 kys BP]) *C. finschi* specimens.

Linear Distance ratios show the height of the hindbrain decreased between GYL3 and CR specimens, and suggest caudolateral hypertrophy of the caudal telencephalon likely occurred early in the temporal sequence between GYL3 (~18.5 kys BP) and GYL2/HC (~16.5~12.2 kys BP).

Similarly, Modular Surface Area data show an increase in orbit Surface Area ratios, along with smaller increases in ratios for the eminentia sagittalis, mesencephalon, and rhombencephalon modules. Similar to results for all data forms, Modular Surface Area ratios for the cerebellum display an overall reduction between the oldest (GYL3 [~20.5~16.5 kys BP]) and youngest (CR [~2.2 kys BP]) *C. finschi* specimens.

Notably, both Modular Distance and Surface Area ratio values for the anomalous GYL2 (~16.5~11.2 kys BP) specimen, were the largest for orbit modules across the data set. The endocast volume for this specimen is somewhat less than for the other *C. finschi* specimens, it displays the largest rostral telencephalon Surface Area ratios, and a distinctly smaller cerebellum dorsoventral Linear Distance height and Modular Surface Area ratios, than all other specimens. Additionally, although the GYL2 (16.5–11.2 kys BP) specimen shows the largest mesencephalon Modular Distance length and width ratios across the data set, the Surface Area ratio for the mesencephalon was less than that of the CR (~2.2 kys BP) *C. finschi* specimen. This trend of a comparatively long endocast, and relatively smaller endocast volume, accompanying larger Modular Surface Area ratios for cerebrum and mesencephalon structures, strongly suggest GYL2 may be representative of the outer extremes of intrapopulation variation during the 16.5–12.1 kys BP period. Due to the small sample size, the extent of this was unable to be adequately assessed in this study.

However, if the sampled specimens reflect the mean attributes of the source populations for *C. finschi*, then these data strongly suggest there occurred shape and size changes in the *C. finschi* brain over the time period ~18.5 to ~2.2 kys BP, during which the species transitioned from a facultatively volant bird to a flightless one (see [Worthy 1988a, 1997b](#)). These changes can be broadly summarised as a directional hypertrophy of orbits, eminentia sagittalis, mesencephalon, and caudal telencephalon, accompanied by hypotrophy of the cerebellum between the oldest (GYL3 [~20.5~16.5 kys BP]) and youngest (CR [~2.2 kys BP]) *C. finschi* specimens. Additionally, results show that the most substantial changes to the *C. finschi* caudal telencephalon and hindbrain, likely occurred early in the temporal sequence (i.e. ~18.5~12.2 kys BP). Observations which align well with the hypothesis that the taxon was facultatively flightlessness by at least ~11 kys BP (see [Watanabe 2017](#)).

The evolution of disparate postcranial morphology in the transition to flightlessness is recognised to have taken place in several avian taxa, relatively rapidly in geological terms, after colonisation of isolated, predator free environments. For example, a propensity for swift transition to flightlessness in island rails was identified early by [Olson \(1973:34; see also Livezey 2003\)](#), and [McNab \(1994:629\)](#) argued many volant birds have flightless island-based subspecies (as interpreted under the biological species paradigm), and that the transition had occurred rapidly. In the case of *C. finschi*, [Worthy \(1988a:625\)](#) recognised a “considerable loss of flight ability in just 10,000 years”.

Although, for other insular (in a broad sense) taxa, [Livezey \(1990:665\)](#) suggested the volant-flightless transition may be more “protracted”, as his work on Rolland’s grebe ([Livezey 1989b](#)), Auckland Islands merganser ([Livezey 1989a](#)), and Auckland Islands teal ([Livezey 1990](#)) suggested these taxa were “evidently in transition to flightlessness”. However, as noted above, the ‘rate’ of transition to flightlessness in these taxa has been necessarily inferred by geological age constraints (see also [3.1](#)), and may be imprecise. Fossils of Finsch’s duck, however, comprise the only example for a succession of radiocarbon dated populations documenting this volant-flightless transition.

Indeed, it appears some taxa transition to flightlessness more rapidly than others, and given the marked changes identified in postcranial elements of *C. finschi* by [Worthy \(1988a, 1997b\)](#), it is likely this taxon transitioned into a flightless terrestrial grazing niche remarkably rapidly in the post-glacial Holocene period. This may have been facilitated by an absence of terrestrial predation, and release from aerial predation (e.g. Haast’s eagle [*H. moorei*] and Eyles’ harrier [*Circus teauteensis* Forbes, 1892]), accompanied by the increase of more abundant shrubland and increasingly stable food resources at the time (see [Worthy 1988a:625](#)). Furthermore, it is notable that while there are large changes in postcranial ratios, especially of relative proportions of pectoral elements, describing this transition, there are only comparatively small changes in the brains of *C. finschi* over the same period. This is not unusual, or unexpected, as similar patterns of the brain ‘lagging behind’ the body were recognised in *H. moorei* by [Scofield & Ashwell \(2009\)](#), who showed the eagle’s “ten-fold” increase in body size was only accompanied by a “doubling or tripling” of endocranium volume. This demonstrated lag of neuroanatomical hypertrophy accompanying rapid postcranial anatomical changes, is likely also reflected in the morphology of Finsch’s duck.

### **3.4.1 Functional implications of avian endocranial morphology**

The mosaic model of brain evolution suggests motor and sensory requisites associated with behaviour and ecology can lead to differential change in the size of individual brain regions (e.g. [Barton & Harvey 2000](#); [Iwaniuk & Nelson 2001](#); [Iwaniuk & Hurd 2005](#); [Corfield et al. 2012](#); [Gutiérrez-Ibáñez et al. 2014](#), and references therein; see also Introduction, [1.5.4](#)). Similarly, such patterns in the composition of the brain can be reflective of functional specialisation (e.g. [Dubbeldam 1998a](#); [Barton & Harvey 2000](#); [Iwaniuk et al. 2008](#); [Corfield et al. 2012, 2015a](#); and references therein). For example, [Iwaniuk & Nelson \(2001\)](#) proposed the size of individual brain regions in anseriforms may be indicative of specific behavioural traits, observations supported by [Corfield et al. \(2012\)](#) who found that a hypertrophied brain region conferred a greater level of “information-processing” power. Thus, conservative consideration of potential drivers of brain shape evolution in extinct species may allow for informed hypotheses of their mode of life to be assessed. Consequently, the specific changes identified in the orbits, eminentia sagittalis, cerebrum, mesencephalon, and cerebellum identified here, potentially relate to adaptive and functional trait evolution in Finsch’s

duck. The evaluation of which may potentially shed light on potential ecological and behavioural traits of the taxon, concomitant with the loss of flight.

While it is recognised that the brain is not strictly compartmentalised into regions that process exclusive neuronal input, but rather includes levels of interconnectivity across the whole structure (e.g. [Iwaniuk et al. 2004a](#)). It is clear that particular brain nuclei share greater levels of neuronal connectivity associated with specific functions (e.g. [Dubbeldam 1998a](#); [Barton & Harvey 2000](#); [Iwaniuk et al. 2008](#); [Corfield et al. 2012, 2015a](#)). In order to accommodate for the interconnectivity between individual brain regions, I summarise below the current understanding of avian visual pathways, and the functional attributes of the eminentia sagittalis, cerebrum, mesencephalon, and cerebellum as integrated units, prior to framing any functional hypotheses for Finsch's duck.

### 3.4.2 Visual pathways

There are three principal visual pathways in birds: **1**, the thalamofugal pathway transmits visual signals from the retina via the mesencephalon, to the principal optic nucleus of the dorsal thalamus, and thence to the eminentia sagittalis; **2**, the tectofugal pathway transmits via the mesencephalon to the nucleus rotundas of the thalamus and proceeds to the entopallium of the telencephalon; and **3**, the third visual pathway transmits via the mesencephalon through retinal recipient nuclei in the accessory optic system and pretectum, and projects to several regions of the brain, including the cerebellum (see [Wylie et al. 2009](#); [Iwaniuk et al. 2010](#); [Wylie & Iwaniuk 2012](#); [Corfield et al. 2012](#); [Wylie et al. 2015](#); and references therein; see also Introduction, **1.5.4.2**).

**3.4.2.1 Eminentia sagittalis**—are composed of two main regions, the larger “visual” region located dorsally and extending caudodorsally which receives retinal projections, and a smaller rostral somatosensory region, receiving “substantial” somatosensory and kinesthetic input ([Wild & Williams 2000](#); [Iwaniuk et al. 2008](#); see also [Wild 1987](#); [Miceli et al. 1990](#); [Deng & Wang 1992](#)). The thalamofugal pathway incorporating the eminentia sagittalis has been shown to be primarily involved in binocular vision capability, and global stereopsis or depth perception ([Pettigrew 1986](#); [Iwaniuk & Wylie 2006](#); [Iwaniuk et al. 2008](#), and references therein). [Iwaniuk et al. \(2008\)](#) showed the size of eminentia sagittalis were significantly correlated with more frontally orientated orbits and broader binocular fields (see also [Wild et al. 2008](#)), and argued changes in the relative size of the eminentia sagittalis also suggest increases in somatosensory and motor processing capabilities (see also [Wild 1997](#); [Manger et al. 2002](#); [Jarvis et al. 2005](#); [Iwaniuk & Wylie 2006](#)). Additionally, eminentia sagittalis are hypertrophied in species that forage using tactile information from the beak ([Pettigrew & Frost 1985](#); [Iwaniuk & Wylie 2006](#); [Wylie et al. 2015](#); see also [Martin 2009](#); and **3.4.2.2** below).

**3.4.2.2 Cerebrum**—as part of the tectofugal visual pathway (**2**), the cerebrum incorporates the modular divisions of the rostral and caudal telencephalon, which have been associated with a wide range of behaviours including: feeding, taste, tactile sense, taste discrimination, vocalisation, and with high levels of cognition and complex tasks ([Corfield et al. 2012](#), and references therein). Furthermore,

stereotyped species-specific behaviour (Reiner et al. 1984; Dubbeldam 1998a), pecking accuracy (Salzen et al. 1975), and the processing of visual information such as brightness, colour and pattern discrimination (Iwaniuk et al. 2010), have been attributed to processes within the caudolateral telencephalon. Pettigrew & Frost (1985) showed the maxillary (V<sub>2</sub>) division of the trigeminal (V) cranial nerve, which innervates the upper bill (see Introduction, 1.5.4.1; and 3.5.1.1 below), transmits to extensive terminal fields in the region of the rostradorsal mesopallium of the cerebrum (see also Northcutt 1981). Similarly, Dubbeldam et al. (1981) showed that ascending maxillary and mandibular trigeminal projections transmitted rostradorsally via the nucleus basalis to mesopallial terminal fields (see also Wild et al. 1985). These sensorimotor projections were related to the “detection” of food particles, particularly in low-visibility feeding in anseriforms (Berkhoudt et al. 1981), and food grasping in columbiforms (Wild et al. 1984, 1985), and passeriforms (Wild & Farabaugh 1996).

**3.4.2.3 Mesencephalon**—forms part of the visual pathway system. Hellmann et al. (2004) characterised the mesencephalon as “relay stations” for the conveyance of ascending visual output to the forebrain, projecting descending output to the premotor regions of the hindbrain (see 3.4.2.4 below), and comprise multiple cell types that are retinotopically organised and functionally specific. So called “optic flow” (*sensu* Gibson 1954) are retinal stimuli generated by self-motion through an environment (see Wylie et al. 2018, and references therein). Optic flow stimuli are analysed by recipient nuclei in the accessory optic system and the pretectum, which serves to generate optokinetic response for the control of posture and eye movement stabilisation (Simpson 1984; Simpson et al. 1988; Giolli et al. 2006; Wylie et al. 2009, 2018; Gaede et al. 2019; and references therein). The lentiformis mesencephali, or pretectal nucleus, responds to “moving large-field visual stimuli” and controls posture and locomotion, including determining compensatory movement and navigation through complex environments, facilitated by processes within the cerebellum (Pakan & Wylie 2006; see also Jerison 1973).

**3.4.2.4 Cerebellum**—the cerebellum has long been associated with motor integration and posture control in birds (Jerison 1973). Visual signals are projected through the third visual pathway via the retinal-recipient nuclei of the mesencephalon (see 3.4.2.3 above) to the cerebellum (Lau et al. 1998; Wylie 2001; Pakan & Wylie 2006; Wylie et al. 2009), where they facilitate obstacle avoidance responses. Additionally, Pakan & Wylie (2006) suggest folia VI–VIII of the cerebellum may be involved in “steering” functions, and Iwaniuk et al. (2007) showed that VI and VII folia are hypertrophied in birds they classified as “strong fliers”, and showed some evidence to support correlation of hypertrophy of the cerebellar rostral lobe with “strong hindlimbs” in birds.

### 3.4.3 Functional attributes of Finsch’s duck

The directional hypertrophy of orbits; eminentia sagittalis, caudal cerebrum, and mesencephalon, accompanying the hypotrophy of the cerebellum identified in *C. finschi* across the temporal sequence assessed here, suggest that in the transition to a terrestrial grazing niche, areas of

the brain involved in processing retinal projections related to global stereopsis and depth perception are somewhat hypertrophied (i.e., caudal eminentia sagittalis). Also, those playing a major role in tactile feeding behaviours and pecking accuracy (i.e., rostrocaudal cerebrum [nidopallium]) are hypertrophied. Similarly, the relative hypotrophy of the cerebellum identified here, suggests processes related to spatial awareness and obstacle avoidance responses, crucial in flighted taxa, were becoming less important for a bird transitioning from a flighted to flightless mode of life.

Hypotrophied cerebellum structures appear characteristic of flightless birds, for example, a reduced cerebellum, relative to the rest of the brain, are evident in flightless ratites (e.g. [Craigie 1939:fig 2](#); [Martin et al. 2007:fig. 2a-b](#); [Ashwell & Scofield 2008:fig 6g-l](#); [Corfield et al. 2008:fig. 1bA-E](#); [Peng et al. 2010:figs. 1, 3](#); [Picasso et al. 2011:fig 1](#); [Walsh & Knoll 2018:fig. 5.3\[1-6\]](#)), but not in their flighted relatives (see [Corfield et al. 2008:fig. 1bF-J](#); [Krabichler et al. 2015:fig. 5](#)). What is more, taxa that use nocturnal ambush predation, i.e., pouncing or swooping prey from perch, like barn owls (*Tyto alba*) and the frogmouth (*Podargus strigoides*), have much hypotrophied cerebellum morphology too (e.g. [Stingelin 1957:pl. 26](#); [Iwaniuk & Wylie 2006:fig 2](#); [Martin et al. 2007:fig. 2c](#); [Corfield et al. 2008:fig. 1bK](#); [Wylie et al. 2015:fig. 3A-B](#); [Walsh & Knoll 2018:fig. 5.3\[34-35\]](#)). It has been proposed that terrestrial birds have a relatively smaller cerebellum than arboreal ones (see [Bennet & Harvey 1985a, 1985b](#)). Similarly, an apparently hypotrophied cerebellum, relative to the rest of the brain, are evident in the giant flightless dromornithids (see Chapter 5, Figs. A5.4A–F). However, galliforms like the phasianid *Gallus gallus* and several megapodiids, have a distinctly hypertrophied cerebellum, relative to the rest of the brain (e.g., see Chapter 5, Figs. A5.4G–P; see also [Kawabe et al. 2010:fig 1XI](#)). These taxa are predominantly terrestrial omnivores, but are volant birds that will take flight when provoked. It appears then, that there does exist trends towards a hypotrophied cerebellum in flightless taxa, or those that use less large-field visual stimuli in their habitus than volant birds do. It is also notable, that the mesencephalon of the terrestrial galliform omnivores (see Chapter 5, Figs. A5.4G–P), and those of terrestrial grazers i.e. *C. jubata* (Tables A3.3D, A3.3F, Fig. A3.3; see also Chapter 5, Figs. A5.2A–B), are somewhat hypertrophied relative to the rest of the brain. However, the mesencephalon of other terrestrial grazers do not show the same pattern. For example; *Tadorna tadornoides* (Chapter 5, Figs. A5.2C–D), *Branta canadensis* (Chapter 5, Figs. A5.2E–F), *Anser caerulescens* (Chapter 5, Figs. A5.2G–H), *Cygnus atratus* (Chapter 5, Figs. A5.2I–J), *Cereopsis novaehollandiae* (Chapter 5, Figs. A5.2I–J), and *Dendrocygna bicolor* (Chapter 5, Figs. A5.3I–J), all show relatively hypotrophied mesencephalon structures with respect to the rest of the brain. Hypertrophy of the mesencephalon is evident in other taxa. For example, the fossil taxon *Mionetta blanchardi* shows hypertrophied mesencephalon structures (Chapter 5, Figs. A5.3E–H), as does the highly aquatic taxon *Nettapus pulchellus* (Chapter 5, Figs. A5.1K–L), and several other dabbling and diving anatines (see Chapter 5, Figs. A5.1A–J). The directional hypertrophy recognised here in the *C. finschi* mesencephalon may relate to increasing mesencephalon projections involved with functional adaptation during this species' expansion into a novel terrestrial grazing niche.

However, hypo- vs hypertrophy of mesencephalon structures in other dabbling, grazing and diving anatines, show variation which does not appear to follow trophic patterns. Thus, I hesitate to ascribe the directional mesencephalon hypertrophy identified in these assessments for Finch's duck, to functional trophic requisites, and further research is required to clarify these patterns.

### 3.5 CONCLUSIONS

In these assessments, I used four *Chenonetta finschi* endocasts sourced from key time periods across a radiocarbon dated temporal sequence, documenting the transition to flightlessness. I employed multivariate Modular Lm configurations to define endocast shape, and along with univariate Modular Distance and Surface Area data forms, investigated endocranial shape change in *C. finschi* concomitant with the loss of flight ability. The morphological trends described by all data forms assessed here, identify similar patterns of hypertrophy of the orbits, eminentia sagittalis, and mediolateral caudal telencephalon, along with hypotrophy of the hindbrain in Finsch's duck across the temporal sequence. These endocranial changes are potentially related to increasing reliance on a visually accurate, tactile, terrestrial grazing mode of life, and to the diminishing requisites of 3D spatial awareness in a progressively flightless taxon.

However, the only multivariate modular interactions approaching statistical significance were shape covariation between the rostroventral forebrain and the dorsal hindbrain. This is due to the low sample size, and may be improved with wider sampling of populations assessed here, with the exception of the pivotal GYL3 sample, as only one skull is known (see **3.5.1.2** below). As my sample was derived from within a relatively short (~19 kys) evolutionary period, it was not unexpected that the most strongly correlated covariation of modular shape changes identified, were relatively small. Nevertheless, I consider the Modular Lm analyses results useful quantifiers of functional shape change within and between morphological modules. Modular Distance and Modular Surface Area results support shape analyses results, and together are indicative of a trend of functional transition toward flightlessness in Finsch's duck.

#### 3.5.1 Limitations and Future directions

**3.5.1.1 Limitations**—the multivariate Modular Lm data, and the univariate Modular Distance and Surface Area data derived from, and based on modular Lm configurations, have shown the methodology I have developed here, works well to capture morphological changes occurring over time in the brains of Finsch's duck. It is clear that the quality of data derived from such a modular Lm suite, is dependent entirely on the careful and consistent placement of modular Lm patches on surfaces that do not include particularly well-defined boundaries between different brain structures. I argue that those modules having margins better delimited, can be most consistently defined, and so more reliably detect trends in morphological shape change. These include: **1**, the eminentia sagittalis,

which are bounded medially by the fissura interhemispherica zone (**fi**; Introduction, Fig. 1.5.1D), and dorsolaterally by the vallecule transition zone (**va**; Introduction, Fig. 1.5.1D) between the caudolateral eminentia sagittalis and the dorsolateral cerebrum; **2**, the rostral telencephalon, bounded caudally by the dorsoventral transition of the medial cerebral artery (**acm**; Introduction, Figs. 1.5.1A, 1.5.1C–D) across the medial cerebrum, dorsolaterally at the lateral vallecule transition between the eminentia sagittalis and the rostral extension of the fissura interhemispherica, and rostromedially at the ventrolateral transition between the rostroventral cerebrum to the ventrolateral medial cerebral artery; **3**, the caudal telencephalon, bounded rostrally by the dorsoventral transition of the medial cerebral artery across the medial cerebrum, dorsolaterally at the lateral vallecule transition between the eminentia sagittalis, and the caudally by the extension of the vallecule transition to meet the extension of the fissura subhemispherica; **4**, the mesencephalon, which are bounded by the ventrolateral caudal telencephalon at the fissura subhemispherica (**fs**; Introduction, Fig. 1.5.1B), bounded rostrally by the transition into the caudolateral chiasma opticum and tractus opticus structures, and caudally by the transition from the dorsal mesencephalon into the ventrolateral rhombencephalon; **5**, the rhombencephalon, bounded rostrally by the transition into the medial and mediolateral hypophysis, laterally by transition into the mesencephalon, and ventrolaterally where the medulla oblongata widens mediolaterally, and forms a shelf between the mediolateral pons and the caudal medulla spinalis; **6**, the cerebellum, bounded dorsomedially and dorsomediolaterally in the vicinity of the glandula pinealis (**gp**; Introduction, Fig. 1.5.1D), by the transition between the caudal eminentia sagittalis, and ventrally by the transition of the cerebrum pars occipitalis, returning caudolaterally to describe the transition between the most dorsolateral eminence of the auricula cerebelli, to the dorsal medulla spinalis transition into the caudodorsal cerebellum. (for complete descriptions see Appendices **A3.8.3**).

With careful application, appropriately located ‘control point’ Lms, which form the Lms to-which and from-which module boundary Lms are slid during superimposition (see General Methods, **2.5.1**), a comparable modular suite is able to be reliably generated from surfaces that do not necessarily comprise the recommended combination of ‘type 1’ and ‘type 3’ Lms as defined by [Bookstein \(1991\)](#). These methods will no doubt become less effective if there are many specimens being independently landmarked by several operators. I recommend that if such analyses are attempted, a single operator must apply all modular Lm patches to all specimens. This will minimise inter-operator variability, as a single operator will arguably follow a similar protocol with regard to the location of modular patch boundaries, and better allow for morphologically comparable Lm locations across the full specimen suite.

The orbits modules employed here, in retrospect, comprise the least consistently definable modular unit, as the rostradorsal borders with the rostroventral telencephalon modules are, quite frankly, susceptible to operator error regarding the placement of the boundaries in the transition zones between modules. Similarly, there is also an ill-defined rostroventromedial boundary between LHS

and RHS orbit modules. These factors together, afford only one boundary to be reliably defined for the orbit modules. Namely, the transition from the orbit zone into the tractus opticus, mediolaterad of the rostral mesencephalon, following the transition zone of the chiasma opticum ventromedially. Therefore, I will not be employing these modules for subsequent assessments (e.g. Chapters 4–5).

Furthermore, I am unconvinced that the orbit modules as used, are well-representative of the shape and size of the actual eye. While shape data derived from these modules capture well the rostroventral surface of the cerebrum, and are usefully descriptive of morphological change in these regions of the brain. How representative those data are of the actual eye is essentially debateable, as in reality, the eye would have maintained only a percentage of area contact with the assessed surface. Results for the orbits Modular Surface Area ratios suggest there occurs a progressive increase in surface area in these zones over time (see above), but in order to assess whether this is reflective of actual eye size change, I suggest additional orbit data using neurocrania will better resolve the question. For example, it is well established that linear dimensions of the skeletal avian orbit are closely representative of eye size (e.g. [Hall & Ross 2007](#); [Hall 2008](#)). The collection of additional orbit linear data from *C. finschi* neurocrania, would allow for more robust assessment and interpretation of potential eye size across the temporal sequence, facilitating more informed inference of any changes in eye size, and potential visual capability through time in Finsch's duck.

Additionally, I believe it was an oversight to remove, or 'segment out' of the final models employed for these assessments, the trigeminal ganglion (V) complexes inserting on the ventral surfaces of the mesencephalon (see **tri.g**, Introduction, Fig. 1.5.1C). In birds, the trigeminal nerve system comprises the medial portion carrying the ophthalmic (V<sub>1</sub>) nerve which innervates the orbit and nasal cavity, the rostral palate and the tip of the upper bill, and forms a major sensory pathway for the skin of the head and maxillary rostrum. The maxillary (V<sub>2</sub>) branch innervates the maxillary rostrum and infraorbital regions, and the mandibular (V<sub>3</sub>) division innervates the entire lower bill and several mandibular and interramal regions ([Dubbeldam 1980](#); [Bubień-Waluszewska 1981](#); [Dubbeldam et al. 1981](#); [Wild & Zeigler 1996](#)). The trigeminal nucleus receives exclusively proprioceptive information from the descending tract and the principal sensory nucleus of the trigeminal system ([Gutiérrez-Ibáñez et al. 2009](#)). This includes not only projections from ophthalmic (V<sub>1</sub>) and maxillomandibular (V<sub>2</sub>+V<sub>3</sub>) nerves described above, but taste information from the tongue is conveyed, within the lingual branch of the maxillomandibular ramus, by the facial (VII) nerve to the trigeminal principal sensory nucleus, which also receives input from glossopharyngeal (IX) and hypoglossal (XII) nerves ([Dubbeldam et al. 1979](#); [Bubień-Waluszewska 1981](#); [Wild & Zeigler 1980](#); [Wild 1981, 1990](#); [Dubbeldam 1998a, 1998b](#)). The glossopharyngeal (IX) and vagus (X) nerves share the large proximal ganglion, and the glossopharyngeal components of this complex comprise somatic, "special" and visceral afferent fibres. The "special" fibres connect with the palatine branch of the facial (VII) nerve at the cranial cervical ganglion, and are associated with sensory taste and tactile information ([Dubbeldam et al. 1979](#); [Bubień-Waluszewska 1981](#); [Dubbeldam 1984](#); [Arends &](#)

Dubbeldam 1984). Additionally, Dubbeldam (1992) proposed that differences in the trigeminal principal sensory nucleus were indicative of the functional demands of specific feeding behaviours. Gutiérrez-Ibáñez et al. (2009) reported hypertrophy of the trigeminal principal sensory nucleus in species that had feeding behaviours dependent on tactile input, and that beak morphology and the concentration of mechanoreceptors in the beak and tongue strongly correlate with feeding behaviour. In summary, the trigeminal (V) nerve comprises the largest somatosensory cranial innervation complex, and transmits epicritic sensation from the entire facial region and mastication musculature (see Bubień-Waluszewska 1981; Wild 1987; Dubbeldam 1998b; and Introduction, 1.5.4.1).

The assessment of this region would have likely provided additional valuable insight to the levels of sensory input from the beak, palate and tongue, allowed for assessment of distinctions in trigeminal ganglion shape, and afforded functional consideration of cerebrum afferent terminal fields associated with these nerves in Finsch's duck.

**3.5.1.2 Future directions**—my recommendations regarding the future progress of this research prior to publication, include the addition of minimally one additional specimen per dated site, (excluding the GYL3 sample, see 3.6 above). This to allow better testing of the intraspecific variation recognised in the GYL2–HC (~16.5~12.2 kys BP) sample, and better definition of the morphological differences recognised between the GYL3 (~18.5 kys BP) and CR (~2.2 kys BP) samples. Preferably this should be accompanied by linear data collected from specimen neurocranial orbits (see 3.5.1.1 above), and additional Lm modules defining the trigeminal ganglia on ventral mesencephalon surfaces (e.g. Chapter 2 Appendices, A2.3.1.9-10).

### 3.6 Acknowledgements

I thank Alan Tennyson (Museum of New Zealand Te Papa Tongarewa, Wellington, New Zealand), for providing financial assistance for two radiocarbon dates for Honeycomb Hill Cave sites, and for access to *Chenonetta finschi* specimens. Trevor Worthy (Flinders University Palaeontology, School of Science & Engineering, Adelaide) for providing financial assistance for two new radiocarbon dates for Honeycomb Hill Cave sites. The Royal Society of South Australia (RSSA) Small Research Grants Scheme for providing funding for  $\mu$ CT scanning of *Chenonetta* specimens. Adelaide Microscopy, (University of Adelaide), for access to the Skyscan  $\mu$ CT instrument. Philippa Horton and Maya Penck, (South Australian Museum, Adelaide), for access to the ornithology collection.

## 3.7 REFERENCES

- Adams, D.C., 2016. Evaluating modularity in morphometric data: challenges with the RV coefficient and a new test measure. *Methods in Ecology and Evolution* 7, 565-572. doi: 510.1111/2041-1210X.12511.
- Adams, D.C., Collyer, M.L., Kaliontzopoulou, A., 2018. *Geomorph: Software for geometric morphometric analyses*. R package version 3.0.7. <https://cran.r-project.org/package=geomorph>.
- Adams, D.C., Felice, R., 2014. Assessing phylogenetic morphological integration and trait covariation in morphometric data using evolutionary covariance matrices. *PLoS ONE* 9, e94335. doi:94310.91371/journal.pone.0094335.
- Arends, J.J.A., Dubbeldam, J.L., 1984. The subnuclei and primary afferents of the descending trigeminal system in the mallard (*Anas platyrhynchos* L.). *Neuroscience* 13, 781-795.
- Ashwell, K.W.S., Scofield, R.P., 2007. Big birds and their brains: Paleoneurology of the New Zealand moa. *Brain, Behavior and Evolution* 71, 151-166. doi:110.1159/000111461.
- Barton, R.A., Harvey, P.H., 2000. Mosaic evolution of brain structure in mammals. *Nature* 405, 1055-1058.
- Baumel, J.J., King, A.S., Breazile, J.E., Evans, H.E., Vanden Berge, J.C., 1993. *Handbook of Avian Anatomy: Nomina Anatomica Avium*. 2nd edition. Publications of the Nuttall Ornithological Club 23, Cambridge, Massachusetts, USA.
- Bennett, P.M., Harvey, P.H., 1985a. Brain size, development and metabolism in birds and mammals. *Journal of Zoology* 207, 491-509.
- Bennett, P.M., Harvey, P.H., 1985b. Relative brain size and ecology in birds. *Journal of Zoology* 207, 151-169.
- Berkhoudt, H., Dubbeldam, J.L., Zeilstra, S., 1981. Studies on the somatotopy of the trigeminal system in the mallard, *Anas platyrhynchos* L. IV. Tactile representation in the nucleus basalis. *Journal of Comparative Neurology* 196, 407-420.
- Bookstein, F.L., 1989. Principal warps: Thin-plate splines and the decomposition of deformations. *IEEE Transactions on Pattern Analysis and Machine Intelligence* 11, 567-585.
- Bookstein, F.L., 1991. *Morphometric Tools for Landmark Data: Geometry and Biology*. Cambridge University Press, Cambridge. UK. p.435.
- Bookstein, F.L., Gunz, P., Mitteroecker, P., Prossinger, H., Schaefer, K., Seidler, H., 2003. Cranial integration in *Homo*: singular warps analysis of the midsagittal plane in ontogeny and evolution. *Journal of Human Evolution* 44, 167-187. doi:110.1016/S0047-2484(1002)00201-00204.
- Brodkorb, P., 1964. Catalogue of fossil birds, Part 2 (Anseriformes through Galliformes), in: Austin Jr., O.L. (Ed.), *Bulletin of the Florida State Museum Biological Sciences* 8, University of Florida, Gainesville, pp. 201-335.
- Bubień-Waluszewska, A., 1981. The Cranial Nerves, in: King, A.S., McLelland, J. (Eds.), *Form and Function in Birds*. Vol. 2, Academic Press, London, pp. 385-438.
- Cignoni, P., Callieri, M., Corsini, M., Dellepiane, M., Ganovelli, F., Ranzuglia, G., 2008. Meshlab: an Open-Source Mesh Processing Tool, In: Scarano, V., De Chiara, R., Erra, U. (Eds.),

- Proceedings of the 2008 Eurographics Italian Chapter Conference, Salerno, Italy*, pp. 129-136. ISBN 978-123-905673-905668-905675.
- Cooper, A., Lalueza-Fox, C., Anderson, S., Rambaut, A., Austin, J., Ward, R., 2001. Complete mitochondrial genome sequences of two extinct moas clarify ratite evolution. *Nature* 409, 704-707.
- Corfield, J.R., Long, B., Krilow, J.M., Wylie, D.R.W., Iwaniuk, A.N., 2015. A unique cellular scaling rule in the avian auditory system. *Brain Structure and Function* 9, 102-120. doi:10.1007/s00429-00015-01064-00421.
- Corfield, J.R., Wild, J.M., Hauber, M.E., Parsons, S., Kubke, M.F., 2008. Evolution of brain size in the palaeognath lineage, with an emphasis on New Zealand ratites. *Brain, Behavior and Evolution* 71, 87-99. doi:10.1159/000111456.
- Corfield, J.R., Wild, J.M., Parsons, S., Kubke, M.F., 2012. Morphometric analysis of telencephalic structure in a variety of neognath and paleognath bird species reveals regional differences associated with specific behavioral traits. *Brain, Behavior and Evolution* 80, 181-195. doi:10.1159/000339828.
- Craigie, E.H., 1939. The cerebral cortex of *Rhea americana*. *Journal of Comparative Neurology* 70, 331-353.
- Deng, C., Wang, B., 1992. Overlap of somatic and visual response areas in the Wulst of pigeon. *Brain Research* 582, 320-322.
- Dickinson, E.C., Remsen Jr, J.V. (Eds.), 2013. *The Howard & Moore Complete Checklist of the Birds of the World*. 4th Edition. Aves Press, Eastbourne, U.K.
- Dubbeldam, J.L., 1980. Studies on the somatotopy of the trigeminal system in the mallard, *Anas platyrhynchos* L. II. Morphology of the principal sensory nucleus. *Journal of Comparative Neurology* 191, 557-571.
- Dubbeldam, J.L., 1984. Afferent connections of nervus facialis and nervus glossopharyngeus in the pigeon (*Columba livia*) and their role in feeding behavior. *Brain, Behavior and Evolution* 24, 47-57.
- Dubbeldam, J.L., 1992. Cranial nerves and sensory centres—a matter of definition? Hypoglossal and other afferents of the avian sensory trigeminal system. *Zoologische Jahrbücher* 122, 179-186.
- Dubbeldam, J.L., 1998a. Birds, in: Nieuwenhuys, R., ten Donkelaar, H.J., Nicholson, C. (Eds.), *The Central Nervous System of Vertebrates*, Springer-Verlag, Berlin, pp. 1525-1636.
- Dubbeldam, J.L., 1998b. The sensory trigeminal system in birds: input, organization and effects of peripheral damage. A review. *Archives of Physiology and Biochemistry* 106, 338-345. doi:10.1076/apab.1106.1075.1338.4367.
- Dubbeldam, J.L., Brauch, C.S.M., Don, A., 1981. Studies on the somatotopy of the trigeminal system in the mallard, *Anas platyrhynchos* L. III. Afferents and organization of the nucleus basalis. *Journal of Comparative Neurology* 196, 391-405.
- Dubbeldam, J.L., Brus, E.R., Menken, S.B.J., Zeilstra, S., 1979. The central projections of the glossopharyngeal and vagus ganglia in the mallard, *Anas platyrhynchos* L. *Journal of Comparative Neurology* 183, 149-168. doi:10.1002/cne.901830111.
- Falla, R.A., 1953. The Australian element in the avifauna of New Zealand. *Emu* 53, 36-46.
- Gaede, A.H., Gutierrez-Ibañez, C., Armstrong, M.S., Altshuler, D.L., Wylie, D.R.W., 2019. Pretectal projections to the oculomotor cerebellum in hummingbirds (*Calypte anna*), zebra finches

- (*Taeniopygia guttata*), and pigeons (*Columba livia*). *Journal of Comparative Neurology* xx, 1-15 (early view). doi:10.1002/cne.24697.
- Gibson, J.J., 1954. The visual perception of objective motion and subjective movement. *Psychological Review* 61, 304-314. doi:310.1037/h0061885.
- Gill, B.J., Bell, B.D., Chambers, G.K., Medway, D.G., Palma, R.L., Scofield, R.P., Tennyson, A.J.D., Worthy, T.H., 2010. *Checklist of the Birds of New Zealand, Norfolk and Macquarie Islands, and the Ross Dependency, Antarctica*. 4th Edition. Te Papa Press, Wellington, NZ.
- Giolli, R.A., Blanks, R.H.I., Lui, F., 2006. The accessory optic system: basic organization with an update on connectivity, neurochemistry, and function. *Progress in Brain Research* 151, 407-440.
- Gonzalez-Voyer, A., Winberg, S., Kolm, N., 2009. Brain structure evolution in a basal vertebrate clade: evidence from phylogenetic comparative analysis of cichlid fishes. *BMC Evolutionary Biology* 9, 238. doi:210.1186/1471-2148-1189-1238.
- Gutiérrez-Ibáñez, C., Iwaniuk, A.N., Moore, B.A., Fernández-Juricic, E., Corfield, J.R., Krilow, J.M., Kolominsky, J., Wylie, D.R.W., 2014. Mosaic and concerted evolution in the visual system of birds. *PLoS One* 9, e90102. doi:90110.91371/journal.pone.0090102.
- Gutiérrez-Ibáñez, C., Iwaniuk, A.N., Wylie, D.R.W., 2009. The independent evolution of the enlargement of the principal sensory nucleus of the trigeminal nerve in three different groups of birds. *Brain, Behavior and Evolution* 74, 280-294. doi:210.1159/000270904.
- Hall, M.I., 2008. The anatomical relationships between the avian eye, orbit and sclerotic ring: implications for inferring activity patterns in extinct birds. *Journal of Anatomy* 212, 781-794. doi:710.1111/j.1469-7580.2008.00897.x.
- Hall, M.I., Ross, C.F., 2007. Eye shape and activity pattern in birds. *Journal of Zoology* 271, 437-444. doi:410.1111/j.1469-7998.2006.00227.x.
- Hellmann, B., Güntürkün, O., Manns, M., 2004. Tectal mosaic: organization of the descending tectal projections in comparison to the ascending tectofugal pathway in the pigeon. *Journal of Comparative Neurology* 472, 395-410.
- Holdaway, R.N., Jones, M.D., Athfield, N.R.B., 2002a. Late Holocene extinction of Finsch's duck (*Chenonetta finschi*), an endemic, possibly flightless, New Zealand duck. *Journal of the Royal Society of New Zealand* 32, 629-651.
- Holdaway, R.N., Jones, M.D., Athfield, N.R.B., 2002b. Late Holocene extinction of the New Zealand owl-nightjar *Aegotheles novaezealandiae*. *Journal of The Royal Society of New Zealand* 32, 653-667.
- Howard, H., 1964. Fossil Anseriformes, in: Delacour, J. (Ed.), *The waterfowl of the world*, Country Life Ltd, London, United Kingdom., pp. 233-326.
- Iwaniuk, A.N., Dean, K.M., Nelson, J.E., 2004a. A mosaic pattern characterizes the evolution of the avian brain. *Proceedings of the Royal Society of London B: Biological Sciences* 271, S148-S151. doi:110.1098/rsbl.2003.0127.
- Iwaniuk, A.N., Gutierrez-Ibáñez, C., Pakan, J.M., Wylie, D.R.W., 2010. Allometric scaling of the tectofugal pathway in birds. *Brain, Behavior and Evolution* 75, 122-137. doi:110.1159/000311729.

- Iwaniuk, A.N., Heesy, C.P., Hall, M.I., Wylie, D.R.W., 2008. Relative Wulst volume is correlated with orbit orientation and binocular visual field in birds. *Journal of Comparative Physiology A* 194, 267-282. doi:210.1007/s00359-00007-00304-00350.
- Iwaniuk, A.N., Hurd, P.L., 2005. The evolution of cerebrotypes in birds. *Brain, Behavior and Evolution* 65, 215-230. doi:210.1159/000084313.
- Iwaniuk, A.N., Hurd, P.L., Wylie, D.R.W., 2007. Comparative morphology of the avian cerebellum: II. Size of folia. *Brain, Behavior and Evolution* 69, 196-219. doi:110.1159/000096987.
- Iwaniuk, A.N., Nelson, J.E., 2001. A comparative analysis of relative brain size in waterfowl (Anseriformes). *Brain, Behavior and Evolution* 57, 87-97.
- Iwaniuk, A.N., Wylie, D.R.W., 2006. The evolution of stereopsis and the Wulst in caprimulgiform birds: a comparative analysis. *Journal of Comparative Physiology A* 192, 1313-1326. doi:1310.1007/s00359-00006-00161-00352.
- Jarvis, E.D., Güntürkün, O., Bruce, L., Csillag, A., Karten, H., Kuenzel, W., Medina, L., Paxinos, G., Perkel, D.J., Shimizu, T., 2005. Avian brains and a new understanding of vertebrate brain evolution. *Nature Reviews Neuroscience* 6, 151-159.
- Jerison, H.J., 1973. *Evolution of the Brain and Intelligence*. Academic Press, New York.
- Kawabe, S., Shimokawa, T., Miki, H., Okamoto, T., Matsuda, S., 2010. A simple and accurate method for estimating the brain volume of birds: Possible application in paleoneurology. *Brain, Behavior and Evolution* 74, 295-301. doi:210.1159/000270906.
- Klingenberg, C.P., 2009. Morphometric integration and modularity in configurations of landmarks: tools for evaluating a priori hypotheses. *Evolution and Development* 11, 405-421.
- Krabichler, Q., Vega-Zuniga, T., Morales, C., Luksch, H., Marín, G.J., 2015. The visual system of a Palaeognathous bird: Visual field, retinal topography and retino-central connections in the Chilean Tinamou (*Nothoprocta perdicaria*). *Journal of Comparative Neurology* 523, 226-250. doi:210.1002/cne.23676.
- Lau, K.L., Glover, R.G., Linkenhoker, B., Wylie, D.R.W., 1998. Topographical organization of inferior olive cells projecting to translation and rotation zones in the vestibulocerebellum of pigeons. *Neuroscience* 85, 605-614.
- Livezey, B.C., 1989a. Phylogenetic relationships and incipient flightlessness of the extinct Auckland Islands Merganser. *Wilson Bulletin* 101, 410-435.
- Livezey, B.C., 1989b. Flightlessness in grebes (Aves, Podicipedidae): its independent evolution in three genera. *Evolution* 43, 29-54.
- Livezey, B.C., 1989c. Phylogenetic relationships of several subfossil Anseriformes of New Zealand. *Occasional papers of the Museum of Natural History of the University of Kansas* 128, 1-25.
- Livezey, B.C., 1990. Evolutionary morphology of flightlessness in the Auckland Islands Teal. *Condor*, 92, 639-673.
- Livezey, B.C., 1991. A phylogenetic analysis and classification of recent dabbling ducks (Tribe Anatini) based on comparative morphology. *Auk* 108, 471-507.
- Livezey, B.C., 1993. Morphology of flightlessness in *Chendytes*, fossil seaducks (Anatidae: Mergini) of coastal California. *Journal of Vertebrate Paleontology* 13, 185-199.
- Livezey, B.C., 1996. A phylogenetic reassessment of the tadornine-anatine divergence (Aves: Anseriformes: Anatidae). *Annals of the Carnegie Museum* 65, 27-88.

- Livezey, B.C., 1997. A phylogenetic classification of waterfowl (Aves: Anseriformes), including selected fossil species. *Annals of the Carnegie Museum* 66, 457-496.
- Livezey, B.C., 2003. Evolution of flightlessness in rails (Gruiformes, Rallidae): Phylogenetic, ecomorphological, and ontogenetic perspectives. *Ornithological Monographs* 53, 1-654.
- Livezey, B.C., Martin, L.D., 1988. The systematic position of the Miocene anatid *Anas*[?] *blanchardi* Milne-Edwards. *Journal of Vertebrate Paleontology* 8, 196-211.
- Lydekker, R., 1891. Catalogue of the Fossil Birds in the British Museum (Natural History). *British Museum of Natural History*, London.
- Manger, P.R., Elston, G.N., Pettigrew, J.D., 2002. Multiple maps and activity-dependent representational plasticity in the anterior Wulst of the adult barn owl (*Tyto alba*). *European Journal of Neuroscience* 16, 743-750. doi:710.1046/j.1460-9568.2002.02119.x.
- Martin, G.R., 2009. What is binocular vision for? A birds' eye view. *Journal of Vision* 9, 1-19. doi:10.1167/1169.1111.1114.
- Martin, G.R., Wilson, K.-J., Wild, J.M., Parsons, S., Kubke, M.F., Corfield, J., 2007. Kiwi forego vision in the guidance of their nocturnal activities. *PLoS ONE* 2, e198. doi:110.1371/journal.pone.0000198.
- McNab, B.K., 1994. Energy conservation and the evolution of flightlessness in birds. *American Naturalist* 144, 628-642.
- Miceli, D., Marchand, L., Repérant, J., Rio, J.-P., 1990. Projections of the dorsolateral anterior complex and adjacent thalamic nuclei upon the visual Wulst in the pigeon. *Brain Research* 518, 317-323.
- Milne-Edwards, A., 1863. Mémoire sur la distribution géologique des oiseaux fossils et description de quelques espèces nouvelles. *Annales des Sciences Naturelles* 4, 132-176.
- Northcote, E.M., 1992. Swans (*Cygnus*) and Cranes (*Grus*) from the Maltese Pleistocene, in: Campbell Jr., K.E. (Ed.), Papers in Avian Paleontology Honoring Pierce Brodkorb, Incorporating the Proceedings of the II International Symposium of the Society of Avian Paleontology and Evolution, Natural History Museum of Los Angeles County, 1988, *Natural History Museum of Los Angeles County Science Series* 36, pp. 285-291.
- Northcutt, R.G., 1981. Evolution of the telencephalon in nonmammals. *Annual Review of Neuroscience* 4, 301-350.
- Oliver, W.R.B., 1930. *New Zealand Birds*. 1st Edition. Fine Arts NZ, Wellington.
- Oliver, W.R.B., 1955. *New Zealand Birds*. 2nd Edition. A. H. & A. W. Reed, Wellington.
- Olson, E.C., Miller, R.L., 1958. *Morphological Integration*. University of Chicago Press, Chicago.
- Olson, S.L., 1973. Evolution of the rails of the South Atlantic islands (Aves: Rallidae). *Smithsonian Contributions to Zoology* 152, 1-53.
- Olson, S.L., James, H.F., 1991. Descriptions of Thirty-Two New Species of Birds from the Hawaiian Islands: Part I. Non-Passeriformes. *Ornithological Monographs* 45, 1-88.
- Olson, S.L., Jouventin, P., 1996. A new species of small flightless duck from Amsterdam Island, southern Indian Ocean (Anatidae: *Anas*). *Condor* 98, 1-9.
- Olson, S.L., Wetmore, A., 1976. Preliminary diagnoses of two extraordinary new genera of birds from Pleistocene deposits in the Hawaiian Islands. *Proceedings of the Biological Society of Washington* 89, 247-258.

- Pakan, J.M.P., Wylie, D.R.W., 2006. Two optic flow pathways from the pretectal nucleus lentiformis mesencephali to the cerebellum in pigeons (*Columba livia*). *Journal of Comparative Neurology* 499, 732-744. doi:10.1002/cne.21108.
- Peng, K., Feng, Y., Zhang, G., Liu, H., Song, H., 2010. Anatomical study of the brain of the African ostrich. *Turkish Journal of Veterinary and Animal Sciences* 34, 235-241. doi:10.3906/vet-0806-3919.
- Pettigrew, J.D., 1986. Evolution of Binocular Vision, in: Pettigrew, J.D., Sanderson, K.J., Levick, W.R. (Eds.), *Visual Neuroscience*, Springer, New York, pp. 208-222.
- Pettigrew, J.D., Frost, B.J., 1985. A tactile fovea in the Scolopacidae? *Brain, Behavior and Evolution* 26, 185-195. doi: 110.1159/000118775.
- Picasso, M.B.J., Tambussi, C.P., Degrange, F.J., 2011. Virtual reconstructions of the endocranial cavity of *Rhea americana* (Aves, Palaeognathae): Postnatal anatomical changes. *Brain, Behavior and Evolution* 76, 176-184. doi:110.1159/000321173.
- Rasband, W.S., 2018. *ImageJ*, U.S. National Institutes of Health, Bethesda, Maryland, USA. <https://imagej.nih.gov/ij/>.
- R Core Team, 2018. *R: A language and environment for statistical computing*. R Foundation for Statistical Computing, Vienna, Austria. URL: <https://www.R-project.org/>.
- Reiner, A., Davis, B.M., Brecha, N.C., Karten, H.J., 1984. The distribution of enkephalinlike immunoreactivity in the telencephalon of the adult and developing domestic chicken. *Journal of Comparative Neurology* 228, 245-262.
- Rohlf, F.J., Corti, M., 2000. Use of two-block partial least-squares to study covariation in shape. *Systematic Biology* 49, 740-753.
- RStudio Team, 2016. *RStudio: Integrated Development for R*, RStudio, Inc., Boston, MA URL <http://www.rstudio.com/>.
- Salzen, E.A., Parker, D.M., Williamson, A.J., 1975. A forebrain lesion preventing imprinting in domestic chicks. *Experimental Brain Research* 24, 145-157.
- Scotfield, R.P., Ashwell, K.W.S., 2009. Rapid somatic expansion causes the brain to lag behind: the case of the brain and behavior of New Zealand's Haast's Eagle (*Harpagornis moorei*). *Journal of Vertebrate Paleontology* 29, 637-649.
- Simpson, J.I., 1984. The accessory optic system. *Annual Review of Neuroscience* 7, 13-41.
- Simpson, J.I., Leonard, C.S., Soodak, R.E., 1988. The accessory optic system. Analyzer of self-motion. *Annals of the New York Academy of Sciences* 545, 170-179.
- Sorenson, M.D., Cooper, A., Paxinos, E.E., Quinn, T.W., James, H.F., Olson, S.L., Fleischer, R.C., 1999. Relationships of the extinct moa-nalos, flightless Hawaiian waterfowl, based on ancient DNA. *Proceedings of the Royal Society of London. Series B: Biological Sciences* 266, 2187-2193.
- Sraml, M., Christidis, L., Easteal, S., Horn, P., Collet, C., 1996. Molecular relationships within Australasian waterfowl (Anseriformes). *Australian Journal of Zoology* 44, 47-58.
- Stingelin, W., 1957. *Vergleichende Morphologische Untersuchungen am Vorderhirn der Vögel auf Cytologischer und Cytoarchitektonischer Grundlage*. Verlag Helbing & Lichtenhahn, Basel. p.123.
- Stuiver, M., Polach, H.A., 1977. Discussion. Reporting of 14 C data. *Radiocarbon* 19, 355-363.

- Van Beneden, P.-J., 1875. Un oiseau fossile nouveau des cavernes de la Nouvelle-Zélande. *Annales de la Société géologique de Belgique* 2, 123-130.
- Walsh, S.A., Knoll, F., 2018. The Evolution of Avian Intelligence and Sensory Capabilities: The Fossil Evidence, in: Bruner, E., Ogihara, N., Tanabe, H.C. (Eds.), *Digital Endocasts: From Skulls to Brains*, Springer Japan, Tokyo, pp. 59-69. doi:10.1007/1978-1004-1431-56582-56586.
- Watanabe, J., 2017. Quantitative discrimination of flightlessness in fossil Anatidae from skeletal proportions. *Auk* 134, 672-695.
- Wild, J.M., 1981. Identification and localization of the motor nuclei and sensory projections of the glossopharyngeal, vagus, and hypoglossal nerves of the cockatoo (*Cacatua roseicapilla*), Cacatuidae. *Journal of Comparative Neurology* 203, 351-377.
- Wild, J.M., 1987. The avian somatosensory system: connections of regions of body representation in the forebrain of the pigeon. *Brain Research* 412, 205-223.
- Wild, J.M., 1990. Peripheral and central terminations of hypoglossal afferents innervating lingual tactile mechanoreceptor complexes in Fringillidae. *Journal of Comparative Neurology* 298, 157-171.
- Wild, J.M., 1997. The avian somatosensory system: the pathway from wing to Wulst in a passerine (*Chloris chloris*). *Brain Research* 759, 122-134.
- Wild, J.M., Arends, J.J.A., Zeigler, H.P., 1984. A trigeminal sensorimotor circuit for pecking, grasping and feeding in the pigeon (*Columba livia*). *Brain Research* 300, 146-151.
- Wild, J.M., Arends, J.J.A., Zeigler, H.P., 1985. Telencephalic connections of the trigeminal system in the pigeon (*Columba livia*): a trigeminal sensorimotor circuit. *Journal of Comparative Neurology* 234, 441-464.
- Wild, J.M., Farabaugh, S.M., 1996. Organization of afferent and efferent projections of the nucleus basalis prosencephali in a passerine, *Taeniopygia guttata*. *Journal of Comparative Neurology* 365, 306-328.
- Wild, J.M., Williams, M.N., 2000. Rostral wulst in passerine birds. I. Origin, course, and terminations of an avian pyramidal tract. *Journal of Comparative Neurology* 416, 429-450.
- Wild, J.M., Zeigler, H.P., 1980. Central representation and somatotopic organization of the jaw muscles within the facial and trigeminal nuclei of the pigeon (*Columba livia*). *Journal of Comparative Neurology* 192, 175-201.
- Wild, J.M., Zeigler, H.P., 1996. Central projections and somatotopic organisation of trigeminal primary afferents in pigeon (*Columba livia*). *Journal of Comparative Neurology* 368, 136-152.
- Wiley, D.F., 2006. *Landmark Editor 3.0*. Institute for Data Analysis and Visualization, University of California, Davis. <http://graphics.idav.ucdavis.edu/research/EvoMorph>.
- Worthy, T.H., 1988a. Loss of flight ability in the extinct New Zealand duck *Euryanas finschi*. *Journal of Zoology, London* 215, 619-628.
- Worthy, T.H., 1988b. A re-examination of the moa genus *Megalapteryx*. *Notornis* 35, 99-108.
- Worthy, T.H., 1993. *Fossils of Honeycomb Hill*. Museum of New Zealand Te Papa Tongarewa, Wellington. pp 56.
- Worthy, T.H., 1997a. Quaternary fossil fauna of South Canterbury, South Island, New Zealand. *Journal of the Royal Society of New Zealand* 27, 67-162.

- Worthy, T.H., 1997b. Fossil deposits in the Hodges Creek Cave System, on the northern foothills of Mt Arthur, Nelson. South Island, New Zealand. *Notornis* 44, 111-108.
- Worthy, T.H., 1998. The Quaternary fossil avifauna of Southland, South Island, New Zealand. *Journal of the Royal Society of New Zealand* 28, 537-589.
- Worthy, T.H., 1999. The role of climate change versus human impacts-avian extinction on South Island, New Zealand. *Smithsonian Contributions to Paleobiology* 89, 111-123.
- Worthy, T.H., De Pietri, V.L., Scofield, R.P., 2017. Recent advances in avian palaeobiology in New Zealand with implications for understanding New Zealand's geological, climatic and evolutionary histories. *New Zealand Journal of Zoology* 43, 1-35.  
doi:10.1080/03014223.03012017.01307235.
- Worthy, T.H., Holdaway, R.N., 1994. Quaternary fossil faunas from caves in Takaka valley and on Takaka Hill, northwest Nelson, South Island, New Zealand. *Journal of the Royal Society of New Zealand* 24, 297-391.
- Worthy, T.H., Holdaway, R.N., 1996. Quaternary fossil faunas, overlapping taphonomies, and palaeofaunal reconstruction in North Canterbury, South Island, New Zealand. *Journal of the Royal Society of New Zealand* 26, 275-361.
- Worthy, T.H., Holdaway, R.N., 2002. *The Lost World of the Moa: Prehistoric Life of New Zealand*. Indiana University Press, Bloomington, IN. p760.
- Worthy, T.H., Olson, S.L., 2002. Relationships, adaptations, and habits of the extinct duck '*Euryanas' finschi*. *Notornis* 49, 1-17.
- Wylie, D.R.W., Gutiérrez-Ibáñez, C., Gaede, A.H., Altshuler, D.L., Iwaniuk, A.N., 2018. Visual-cerebellar pathways and their roles in the control of avian flight. *Frontiers in Neuroscience* 12, 223. doi:210.3389/fnins.2018.00223.
- Wylie, D.R.W., Gutiérrez-Ibáñez, C., Iwaniuk, A.N., 2015. Integrating brain, behavior, and phylogeny to understand the evolution of sensory systems in birds. *Frontiers in Neuroscience* 9, 281 (17 pp). doi:210.3389/fnins.2015.00281.
- Wylie, D.R.W., 2001. Projections from the nucleus of the basal optic root and nucleus lentiformis mesencephali to the inferior olive in pigeons (*Columba livia*). *Journal of Comparative Neurology* 429, 502-513.
- Wylie, D.R.W., Gutiérrez-Ibáñez, C., Pakan, J.M.P., Iwaniuk, A.N., 2009. The optic tectum of birds: mapping our way to understanding visual processing. *Canadian Journal of Experimental Psychology* 63, 328-338. doi:310.1037/a0016826.
- Wylie, D.R.W., Iwaniuk, A.N., 2012. Neural Mechanisms Underlying Visual Motion Detection in Birds, in: Lazareva, O.F., Shimizu, T., Wasserman, E.A. (Eds.), *How Animals See the World: Comparative Behavior, Biology, and Evolution of Vision*, Oxford University Press, New York, pp. 289-318.

## 3.8 APPENDICES

Table A3.1. Radiocarbon ages (Conventional ages, uncalibrated). All from Geological and Nuclear Sciences/Rafter Lab, Wellington, for Honeycomb Hill Cave and previous dating results for Hodges Creek Cave and Castle Rocks sites. **Lab Num** represents the Laboratory sample numbers, **NZ** for Gas Counting results, and **NZA** for Accelerated Mass Spectrometry (AMS) dates. **Age 2017** shows recalculated ages when paired with previously published ages and four new dates for *C. finschi*. **Abbreviations**, **BP**, before present (1950); **BT**, beyond terrace; **Cat Num**, catalogue number; **CR**, Castle Rocks Fissure; **Exc.**, excavation; **GYL2**, Honeycomb Hill Graveyard Layer 2; **GYL3**, Honeycomb Hill Graveyard Layer 3; **HC**, Hodges Creek Cave; **Hum**, humerus; **L**, left; **L2**, layer 2; **L3**, layer 3; **MC**, main channel; **NA**, not available; **NMNZ**, Museum of New Zealand Te Papa Tongarewa, Wellington, New Zealand; **Prox**, proximal; **Pt**, part; **Publ Age**, age as previously published; **Tib**, tibiotarsus; **TT**, Takahe Tomo; **yrs**, years.

| Site        | Lab Num     | Cat Num        | Taxon                             | Element    | Sample Site    | Publ Age (yrs BP)         | Age 2017 (yrs BP) |
|-------------|-------------|----------------|-----------------------------------|------------|----------------|---------------------------|-------------------|
| <b>GYL3</b> | NZ 7319     | –              | <i>Megalapteryx didinus</i>       | –          | Lag Site 1     | 10,980 ± 140 <sup>a</sup> | 15,532 ± 253      |
|             | NZ 6453     | –              | <i>Pachyornis australis</i>       | –          | Top L3 MC      | 15,680 ± 210 <sup>a</sup> | 15,680 ± 209      |
|             | NZ 7323     | –              | <i>Pachyornis australis</i>       | –          | Base L3 Site 2 | 18,600 ± 230 <sup>a</sup> | 18,593 ± 253      |
|             | NZA 63302   | NMNZ S.23840.1 | <i>Chenonetta finschi</i>         | Prox L Hum | L3 Site 3      | –                         | 19,125 ± 111      |
|             | NZ 7316     | –              | <i>Megalapteryx didinus</i>       | –          | Base L3 Site 1 | 19,300 ± 400 <sup>a</sup> | 19,240 ± 424      |
|             | NZA 63303   | NMNZ S.23725.3 | <i>Chenonetta finschi</i>         | Prox L Hum | L3 Site 1      | –                         | 19,349 ± 114      |
|             | NZ 7292     | –              | <i>Pachyornis australis</i>       | –          | Base L3 Site 3 | 20,600 ± 450 <sup>a</sup> | 20,549 ± 436      |
| <b>GYL2</b> | NZ 7317     | –              | <i>Megalapteryx didinus</i>       | –          | Top L2 (-15cm) | 11,200 ± 150 <sup>a</sup> | 11,183 ± 179      |
|             | NZ 6586     | –              | <i>Pachyornis elephantopus</i>    | –          | Lag BT, Site 1 | 14,030 ± 180 <sup>a</sup> | 14,029 ± 176      |
|             | NZA 63304   | NMNZ S.23695.4 | <i>Chenonetta finschi</i>         | Prox L Hum | L2 Exc. 1      | –                         | 14,885 ± 66       |
|             | NZA 63305   | NMNZ S.23695.5 | <i>Chenonetta finschi</i>         | Prox L Hum | L2 Exc. 1      | –                         | 16,454 ± 80       |
| <b>HC</b>   | NZA 6970    | –              | <i>Porphyrio hochstetteri</i>     | L Fem      | TT (-5 cm)     | 12,210 ± 110 <sup>b</sup> | –                 |
|             | NZA 6971    | –              | <i>Chenonetta finschi</i>         | Hum        | TT (-60 cm)    | 12,100 ± 120 <sup>b</sup> | –                 |
| <b>CR</b>   | NZA 7912    | NMNZ S2134     | <i>Hieraaetus moorei</i>          | Pt. Rib    | Fissure        | 2,096 ± 72 <sup>c</sup>   | –                 |
|             | NZA 10687   | –              | <i>Chenonetta finschi</i>         | L Hum      | Fissure        | 1,511-1,277 <sup>d</sup>  | –                 |
|             | NZA 10688   | –              | <i>Chenonetta finschi</i>         | L Hum      | Fissure        | 3,383-3,072 <sup>d</sup>  | –                 |
|             | NZA 10689   | –              | <i>Chenonetta finschi</i>         | L Hum      | Fissure        | 881-655 <sup>d</sup>      | –                 |
|             | NZA 10876   | –              | <i>Chenonetta finschi</i>         | L Hum      | Fissure        | 1,297-1,059 <sup>d</sup>  | –                 |
|             | NZA 10877   | –              | <i>Chenonetta finschi</i>         | L Hum      | Fissure        | 4,829-4,423 <sup>d</sup>  | –                 |
|             | NZA 10878   | –              | <i>Chenonetta finschi</i>         | L Hum      | Fissure        | 1,489-1,271 <sup>d</sup>  | –                 |
|             | NZA 11224   | –              | <i>Chenonetta finschi</i>         | L Hum      | Fissure        | 1,288-1,008 <sup>d</sup>  | –                 |
|             | NZA 26525/1 | NMNZ S23305    | <i>Aegothales novaezealandiae</i> | R Hum      | Fissure        | 1,014 ± 60 <sup>e</sup>   | –                 |
|             | NZA 9516    | NMNZ S91       | <i>Emeus crassus</i>              | Tib        | Fissure        | 1,330-1,160 <sup>f</sup>  | –                 |

<sup>a</sup> Worthy (1993); <sup>b</sup> Worthy (1997b); <sup>c</sup> Worthy (1998); <sup>d</sup> Holdaway et al. (2002a); <sup>e</sup> Holdaway et al. (2002b); <sup>f</sup> Cooper et al. (2001).

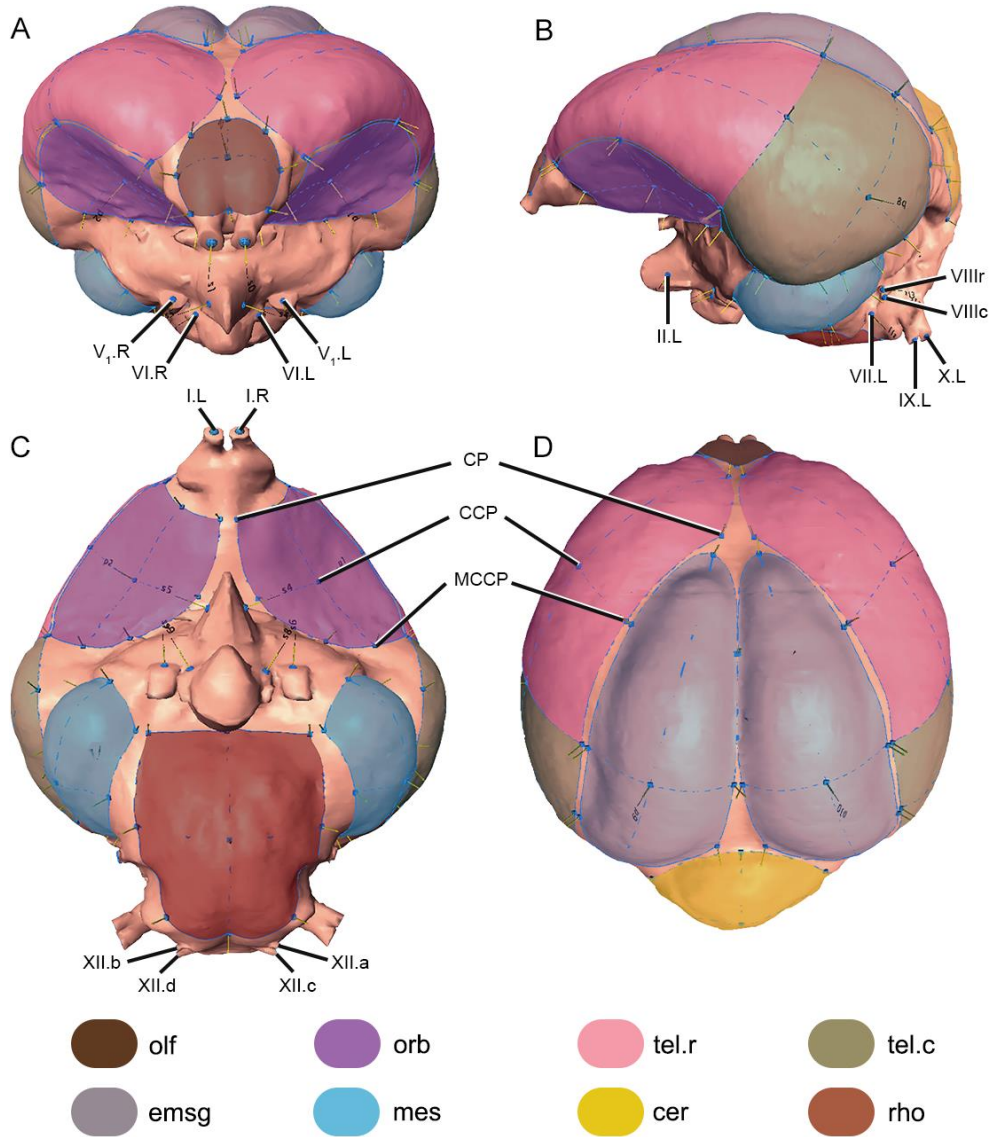


Figure A3.1. Landmark modules used to capture endocast morphology, mapped onto the endocast of *Chenonetta finschi* (NMNZ S.039838) and shaded to facilitate anatomical identification. **Views:** rostral (A); lateral LHS (B); ventral (C); dorsal (D). **Abbreviations,** **cer**, cerebellum; **CP**, control point; **CCP**, centre control point; **emsg**, eminentia sagittalis; **LHS**, left hand side; **mes**, mesencephalon; **olf**, olfactory; **orb**, orbits; **rho**, rhombencephalon; **RHS**, right hand side; **tel.c**, caudal telencephalon; **tel.r**, rostral telencephalon; **MCCCP**, mid-curve control point; **I.L**, LHS olfactory nerve; **I.R**, RHS olfactory nerve (I); **II.L**, LHS optic nerve (II); **V<sub>1</sub>.L**, LHS ophthalmic nerve (V<sub>1</sub>); **V<sub>1</sub>.R**, RHS ophthalmic nerve (V<sub>1</sub>); **VI.L**, LHS abducent nerve (VI); **VI.R**, RHS abducent nerve (VI); **VII.L**, LHS facial nerve (VII); **VIIIr**, LHS rostral ramus of the vestibulocochlear nerve (VIII); **VIIIc**, LHS caudal ramus of the vestibulocochlear nerve (VIII); **IX.L**, LHS glossopharyngeal nerve (IX); **X.L**, LHS vagus nerve (X); **XII.a**, LHS ventral eminence of the hypoglossal nerve (XII); **XII.b**, RHS ventral eminence of the hypoglossal nerve (XII), **XII.c**, LHS dorsal eminence of the hypoglossal nerve (XII); **XII.d**, RHS dorsal eminence of the hypoglossal nerve (XII; see A3.8.2.1 below).

### A3.8.1 Landmark descriptions

A total of 22 fixed (type 1) and 430 semi (type 3) landmarks were used, for a total of 452. These landmarks were assigned into 14 modules for subsequent analyses.

### A3.8.2 Fixed landmarks (n = 22)

#### A3.8.2.1 Lm 1 – Lm 22: Innervation module (see Fig. A3.1).

Innervation Lms are placed on nerve eminences truncated at the closest eminence (e.g. VIII; XII) or extension (e.g. I) of the nerve from the endocast surface. The ophthalmic ( $V_1$ ) branch of the trigeminal nerve (V), and abducent (VI) nerves were segmented out of the origin (trigeminal ganglions on the ventral mesencephalon [see also A3.8.3.1.4 below], and rostroventral rhombencephalon respectively) and truncated where the nerves exit the os orbitosphenoidale, caudoventrolaterad of the foramen opticum (**fopt**, Chapter 4 Appendices, Figs. A4.4K–L, A4.5K), at the foramen n. ophthalmici ( $V_1$  – **foph**, Chapter 4 Appendices, Figs. A4.4K–L, A4.5K) and foramen n. abducentis (VI – **fa**, Chapter 4 Appendices, Figs. A4.4K–L, A4.5K) respectively. The rostroventral transmission of the abducent (VI) nerves were segmented out of the origin (rostroventral rhombencephalon) to facilitate full access to rostroventral rhombencephalon surfaces. The glossopharyngeal (IX) and vagus (X) nerves were truncated approximately upon bifurcation from the caudoventral proximal ganglions.

**Lm 1:** Olfactory nerve (I.L – nervus olfactorius LHS).

**Lm 2:** Olfactory nerve (I.R – n. olfactorius RHS).

**Lm 3:** Optic nerve (II.L – n. opticus LHS).

**Lm 4:** Optic nerve (II.R – n. opticus RHS).

**Lm 5:** Ophthalmic nerve ( $V_1$ .L – n. ophthalmicus LHS).

**Lm 6:** Ophthalmic nerve ( $V_1$ .R – n. ophthalmicus RHS).

**Lm 7:** Abducent nerve (VI.L – n. abducens LHS).

**Lm 8:** Abducent nerve (VI.R – n. abducens RHS).

**Lm 9:** Facial nerve (VII.L – n. facialis LHS).

**Lm 10:** Facial nerve (VII.R – n. facialis RHS).

**Lm 11:** Rostral ramus of the vestibulocochlear nerve (VIII.a – n. vestibulocochlearis LHS).

**Lm 12:** Rostral ramus of the vestibulocochlear nerve (VIII.b – n. vestibulocochlearis RHS).

**Lm 13:** Caudal ramus of the vestibulocochlear nerve (VIII.c – n. vestibulocochlearis LHS).

**Lm 14:** Caudal ramus of the vestibulocochlear nerve (VIII.d – n. vestibulocochlearis RHS).

**Lm 15:** Glossopharyngeal nerve (IX.L – n. glossopharyngeus LHS).

**Lm 16:** Glossopharyngeal nerve (IX.R – n. glossopharyngeus RHS).

**Lm 17:** Vagus nerve (X.L – n. vagus LHS).

**Lm 18:** Vagus nerve (X.R – n. vagus RHS).

**Lm 19:** ventral eminence of the hypoglossal nerve (XII.a – n. hypoglossus LHS).

**Lm 20:** ventral eminence of the hypoglossal nerve (XII.b – n. hypoglossus RHS).

**Lm 21:** dorsal eminence of the hypoglossal nerve (XII.c – n. hypoglossus LHS).

**Lm 22:** dorsal eminence of the hypoglossal nerve (XII.d – n. hypoglossus RHS).

### **A3.8.3 Semilandmark modules**

IDAV Landmark v3.6 software allows application of manipulatable rectangular ‘patches’ comprising Slms placed on grid junctions in any density configuration, i.e. 6 x 5 grid = 30 Slms. Each corner of an initially rectangular Slm patch has a control point (CP) which is used to shift the patch into position. Between each control point is mid curve control point (MCCP), and a centre control point (CCP) allowing additional patch manipulation (see Fig. A3.1). Control points (CPs) were used to anchor each Slm patch comprising the modular suite on anatomically repeatable endocast locations. Boundaries of anatomical zones were chosen which best followed the transition zone between endocast morphology, and patch boundaries were defined as sensibly as possible within these transition zones. Once appropriately applied, mid curve control points (MCCPs) and centre control points (CCPs) were made equidistant, ensuring consistent and comparable Slm locations within each module across all specimens. For analysis, Slms on the patch periphery were treated as curve-sliding, and interior Slms were treated as surface-sliding Slms (see General Methods, **2.4.1**).

**A3.8.3.1 Curve and surface sliding Slms** (n = 430; Fig. A3.1), the number of Slms per module are indicated in parenthesis (n = xx).

**A3.8.3.1.1 Slm 23 – Slm 42:** Olfactory module Ventral (n = 20). On the rostradorsal surface of the endocast is a transition zone between the LHS and RHS rostral telencephalon that provide CPs for the caudal olfactory module. The caudal MCCP is placed equidistant from the caudolateral CPs in the medial depression between the rostral eminences of the telencephalon. Rostral CPs are placed in the constriction zone where the olfactory bulb transitions into the olfactory nerve foramina. The rostral MCCP is situated at the most medial rostradorsal division of the paired olfactory nerves. The CCP is located equidistantly in the medial groove between the paired lobes of the dorsal olfactory bulb.

**A3.8.3.1.2 Slm 43 – Slm 72:** Orbit module LHS (n = 30). The orbit rostradorsal CPs are placed at the most rostradorsal transition points between the orbit zone and the descending rostromedial curve of the rostral telencephalon (see below). Rostral CPs are placed as close as possible to the rostromedial transition into the ventral olfactory bulb zone. Rostral MCCPs are situated so that the dorsal curves follow the transition from the ventrolateral olfactory bulb zone into the orbit zone. Caudodorsal CPs are placed at the restriction zone where the orbit transitions into the caudal telencephalon (see below), at the point where the medial cerebral artery (**acm**, Introduction, Fig. 1.5.1) transitions ventrodorsally, forming the boundary between the rostral and caudal telencephalon. The dorsal curve between these CPs follow the ventrolateral transition into the rostral telencephalon,

along the ventral transition from the cerebrum fovea limbica. Ventral CPs are placed at the constriction zone between the transition from the orbit zone into the tractus opticus, mediolaterad of the rostral mesencephalon (see below). Situated so that the ventral curve follows the transition zone of the chiasma opticum and the tractus opticus mediodorsally to meet the ventromedial orbit CPs. All MCCPs and CCPs are then made equidistant.

**A3.8.3.1.3 Slm 73 – Slm 102:** Orbit module RHS (n = 30), see Orbit module LHS.

**A3.8.3.1.4 Slm 103 – Slm 132:** Mesencephalon module LHS (n = 30). Prior to application of the mesencephalon modules, the large trigeminal ganglia incorporating the three branches of the 5<sup>th</sup> (V) cranial nerve (ophthalmic [V<sub>1</sub>], maxillary [V<sub>2</sub>], and mandibular [V<sub>3</sub>] nerves; see Introduction, Fig. 1.5.1 above), located on the ventral surface of the mesencephalon, were segmented out of the final endocast models. This provided a continuous surface appropriate to capture the complete morphology of the mesencephalon structures (but see 3.5.1.1 above). Rostral MCCPs and dorsal and ventral CPs are placed where the swell of the mesencephalon transitions into the caudolateral chiasma opticum and tractus opticus structures. Caudal CPs are placed where the mesencephalon grades into the dorsomedial pons (metencephalon) and medulla oblongata structures comprising the mediolateral rhombencephalon transition. Boundary curves are situated so that the dorsal curve describes the transition from the mesencephalon into the ventrolateral caudal telencephalon at the fissura subhemispherica (**fs**, Introduction, Fig. 1.5.1B), and the ventral curve follows the transition from the dorsal mesencephalon into the ventrolateral rhombencephalon. MCCPs and CCPs are then made equidistant.

**A3.8.3.1.5 Slm 133 – Slm 162:** Mesencephalon module RHS (n = 30). see Mesencephalon module LHS.

**A3.8.3.1.6 Slm 163 – Slm 207:** Rostral telencephalon module LHS (n = 45). The most rostral ventrolateral eminence of the telencephalon, forms the location of the rostral lateral CPs for the rostral telencephalon modules. The ventrolateral curve of the rostral telencephalon modules closely corresponds with the dorsolateral curve of the orbit modules, and in the spacing of the MCCPs. The caudoventral CPs terminate at the dorsoventral transition of the medial cerebral artery, in proximity with the dorsolateral CPs of the orbit module, forming the boundary between the modules of the rostral telencephalon and the caudal telencephalon (see below). The dorsomedial CPs are situated at the point of transition into the rostral eminentia sagittalis, the MCCPs are placed equidistantly between the rostral dorsolateral CPs and situated so as to track the medial transition zones of the rostral telencephalon into the fissura interhemispherica. The caudodorsal CPs are situated equidistant with respect to the dorsomedial CPs and the rostral lateral CPs, with the MCCPs situated equidistant between the former, and located so as to align the dorsolateral modular curve with the dorsolateral vallicula transition zone between the rostral telencephalon and the eminentia sagittalis. The caudal MCCPs between the caudodorsal CPs and the caudoventral CPs are made parallel and equidistant between CCPs and MCCPs.

**A3.8.3.1.7 Slm 208 – Slm 237:** Caudal telencephalon module LHS (n = 30). The dorsoventral boundary between the rostral telencephalon module and the caudal telencephalon module share five Slms that are located identically, allowing for the full Slm complement of the caudal and rostral telencephalon modules to be subset and analysed individually, or combined, as a single total cerebrum module. The rostradorsal and rostroventral CPs of the caudal telencephalon modules occupy the same locations as the rostral telencephalon module caudodorsal and caudoventral CPs respectively. The caudodorsal CPs of the caudal telencephalon modules are situated at the transition zone of the dorsolateral cerebellum, and the caudoventral eminence of the eminentia sagittalis (see **A3.8.3.1.10** below), with the MCCPs made equidistant and situated to align the curve appropriately with the rostrocaudal vallecule transition of the caudodorsal telencephalon into the eminentia sagittalis. The rostral and caudal MCCPs and ventrolateral CPs are equidistantly located so as to align the curve in the transition zone between the ventrolateral caudal telencephalon, and the dorsolateral mesencephalon at the fissura subhemispherica zone. The CCPs are made dorsoventrally and rostrocaudally equidistant.

**A3.8.3.1.8 Slm 238 – Slm 282:** Rostral telencephalon module RHS (n = 45), see Rostral telencephalon module LHS

**A3.8.3.1.9 Slm 283 – Slm 312:** Caudal Telencephalon module RHS (n = 30), see Caudal Telencephalon module LHS

**A3.8.3.1.10 Slm 313 – Slm 352:** Eminentia sagittalis module LHS (n = 40). The rostral MCCPs form the most rostradorsal eminence of the eminentia sagittalis, similarly, the caudal CCPs are placed at the most caudodorsal eminence. The rostralateral MCCPs are placed in close proximity with the shared rostradorsal and caudodorsal CPs of the telencephalon modules (see above), allowing for the rostralateral CPs to be placed equidistant with the rostradorsal MCCPs and the rostromedial CPs. The caudolateral CPs are placed equidistant with the rostradorsal MCCPs so that the caudolateral curves describe the vallecule transition zone between the caudolateral eminentia sagittalis and the dorsolateral caudal telencephalon. The caudodorsal MCCPs are placed equidistant with the caudodorsal CPs, so that the medial curves describe the fissura interhemispherica transition zones between eminentia sagittalis modules. The CCPs are then made equidistant mediolaterally between the caudolateral and caudodorsal MCCPs, and equidistant between the rostradorsal MCCPs and caudodorsal MCCPs.

**A3.8.3.1.11 Slm 353 – Slm 392:** Eminentia sagittalis module RHS (n = 40), see Eminentia sagittalis module LHS.

**A3.8.3.1.12 Slm 393 – Slm 422:** Cerebellum module (n = 30). The rostromedial MCCP forms the most dorsal rostromedial eminence of the cerebellum module, and is placed approximately in the area of the glandula pinealis. The caudal MCCP is placed at the most caudodorsal eminence of the cerebellum where the medulla spinalis exits at the foramen magnum. The caudolateral CPs are placed at the most ventrolateral eminences of the cerebellum at the transition of the auricula cerebelli into the

dorsomediolateral medulla oblongata/rhombencephalon complex. The MCCPs are the made equidistant with the rostromedial MCCPs, so that the ascending lateral curves describe the transition zones between the lateral mesencephalon and the caudal cerebrum pars occipitalis dorsally, and ventrally in the area of the mediolateral rhombencephalon complex. The CCP is then made mediolaterally and rostrocaudally equidistant .

**A3.8.3.1.13 Slm 423 – Slm 452:** Rhombencephalon module (n = 30). The rostral MCCP forms the most rostroventromedial point of the rhombencephalon module, and is placed in the transition zone between the rhombencephalon and hypophysis. The caudal MCCP is placed medially where the medulla oblongata transitions into the medulla spinalis. The rostralateral CPs are placed in the vicinity of the rostroventral mesencephalon CPs (see **A3.8.3.1.4** above). The caudolateral CPs are placed at the point where the medulla oblongata widens mediolaterally, forming a shelf between the mediolateral pons and the caudal medulla spinalis, so that the medial curves describe the transition zones between the ventrolateral mesencephalon and the dorsolateral rhombencephalon. The lateral MCCPs are then made equidistant with the lateral rostrocaudal CPs, and the CCP is made equidistant with the rostrocaudal MCCPs and the ventrolateral MCCPs.

Table A3.2. Modularity analysis pairwise covariation ratio (CovR) matrix, ‘heat map’ shaded to indicate clustering of pairwise CovR values for each assessment, where ‘hotter’ colours describe higher levels of morphological integration between modules (see **3.2.7.2** above). **Abbreviations**, **Cer**, dorsal cerebellum; **EmSg Ls**, LHS eminentia sagittalis; **EmSg Rs**, RHS eminentia sagittalis; **Inerv** Innervation; **LHS**, left hand side; **Mes Ls**, LHS mesencephalon; **Mes Rs**, RHS mesencephalon; **Olf**, dorsal olfactory; **Orb Ls**, LHS Orbit; **Orb Rs**, RHS orbit; **Rho**, ventral rhombencephalon; **RHS**, right hand side; **Tel.c Ls**, LHS caudal telencephalon; **Tel.c Rs**, RHS caudal telencephalon; **Tel.r Ls**, LHS rostral telencephalon; **Tel.r Rs**, RHS rostral telencephalon.

|          | Inerv | Olf   | Orb Ls | Orb Rs | Mes Ls | Mes Rs | Tel.r Ls | Tel.c Ls | Tel.r Rs | Tel.c Rs | EmSg Ls | EmSg Rs | Cer   |
|----------|-------|-------|--------|--------|--------|--------|----------|----------|----------|----------|---------|---------|-------|
| Inerv    |       |       |        |        |        |        |          |          |          |          |         |         |       |
| Olf      | 0.946 |       |        |        |        |        |          |          |          |          |         |         |       |
| Orb Ls   | 0.899 | 0.743 |        |        |        |        |          |          |          |          |         |         |       |
| Orb Rs   | 0.891 | 0.766 | 1.005  |        |        |        |          |          |          |          |         |         |       |
| Mes Ls   | 0.829 | 0.822 | 0.896  | 0.903  |        |        |          |          |          |          |         |         |       |
| Mes Rs   | 0.845 | 0.738 | 0.954  | 0.956  | 0.998  |        |          |          |          |          |         |         |       |
| Tel.r Ls | 0.932 | 0.779 | 0.884  | 0.919  | 0.889  | 0.932  |          |          |          |          |         |         |       |
| Tel.c Ls | 0.672 | 0.588 | 0.893  | 0.944  | 0.854  | 0.901  | 0.821    |          |          |          |         |         |       |
| Tel.r Rs | 0.892 | 0.728 | 0.803  | 0.847  | 0.858  | 0.898  | 0.992    | 0.808    |          |          |         |         |       |
| Tel.c Rs | 0.639 | 0.581 | 0.861  | 0.923  | 0.884  | 0.918  | 0.846    | 1.009    | 0.838    |          |         |         |       |
| EmSg Ls  | 0.868 | 0.843 | 0.958  | 0.977  | 0.957  | 0.961  | 0.869    | 0.961    | 0.837    | 0.947    |         |         |       |
| EmSg Rs  | 0.848 | 0.845 | 0.948  | 0.956  | 0.984  | 0.974  | 0.844    | 0.93     | 0.807    | 0.923    | 1.014   |         |       |
| Cer      | 0.894 | 0.696 | 0.916  | 0.892  | 0.882  | 0.932  | 0.882    | 0.853    | 0.911    | 0.83     | 0.919   | 0.909   |       |
| Rho      | 0.889 | 0.906 | 0.851  | 0.92   | 0.919  | 0.902  | 0.946    | 0.865    | 0.899    | 0.89     | 0.932   | 0.914   | 0.768 |

Table A3.3. **A**, mean Modular Distance values calculated between modular SIm locations for each *Chenonetta* specimen (see 2.3.2; 3.2.6; Figs. 2.2C–D). Paired structure data were combined and mean Modular Distance values calculated (see 2.3.2; 3.2.6). **B**, Linear Distance values calculated between two Lm or SIm locations describing gross endocast morphological distances (see 2.3.2; 3.2.6; Figs. 2.2G–I); **C**, mean Modular Surface Area values computed directly from the endocast surfaces (see 2.3.4; Figs. 2.2J–K). **D**, size-standardised mean Modular Distance ratios calculated by dividing  $\log_{10}$  transformed mean Modular Distance values (**A**) by  $\log_{10}$  transformed specimen endocast volume. **E**, size-standardised Linear Distance ratios calculated by dividing  $\log_{10}$  transformed linear values by  $\log_{10}$  transformed specimen endocast volume; **F**, size-standardised mean Modular Surface Area ratios calculated by dividing  $\log_{10}$  transformed mean Modular Surface Area values by  $\log_{10}$  transformed specimen endocast surface area values (see 2.3; 3.2.6). **Abbreviations**, **Cer**, cerebellum; **Cer L**, cerebellum length; **Cer W**, cerebellum width; **C.jubata**, Australian wood duck *C. jubata* (SAM B39457); **CR**, Castle Rocks Fissure *C. finschi* (NMNZ S.039838; ~2.1 kys); **EmSg**, eminentia sagittalis; **EmSg L**, eminentia sagittalis length; **EmSg W**, eminentia sagittalis width; **Endo Surf**, endocast surface area; **Endo TL**, endocast total length; **Endo Vol**, endocast volume; **GYL2**, Honeycomb Hill Cave Graveyard L2 *C. finschi* (NMNZ S.023695; ~13.9 kys); **GYL3**, Honeycomb Hill Cave Graveyard L3 *C. finschi* (NMNZ S.023702; ~18.5 kys); **HC**, Hodges Creek Cave *C. finschi* (NMNZ S.034496; ~12.2 kys); **Med.Ob TW**, medulla oblongata total width; **Mes**, mesencephalon; **Mes L**, mesencephalon length; **Mes W**, mesencephalon width; **Meten.TH**, metencephalon total height; **mm**, millimetres; **mm<sup>2</sup>**, square millimetres; **mm<sup>3</sup>**, cubic millimetres; **Olf**, olfactory; **Orb**, orbits; **Rho**, rhombencephalon; **Rho L**, rhombencephalon length; **Rho W**, rhombencephalon width; **Tel.c**, caudal telencephalon; **Tel.c TW**, caudal telencephalon total width; **Tel.c L**, caudal telencephalon length; **Tel.c W**, caudal telencephalon width; **Tel.r**, rostral telencephalon; **Tel.r L**, rostral telencephalon length; **Tel.r CW**, rostral telencephalon caudal width; **Tel.r RW**, rostral telencephalon rostral width; **Tel.r TH**, rostral telencephalon total height; **Tel.r TW**, rostral telencephalon total width. For specimen details see Figs. A3.2–A3.4, and 3.2.2.2 above.

| Modular Distance             | A. Mean Modular Distance values (mm)                   |         |         |         |          | D. Mean Modular Distance ratios      |       |       |       |          |
|------------------------------|--|---------|---------|---------|----------|--------------------------------------|-------|-------|-------|----------|
|                              | GYL3   | GYL2    | HC      | CR      | C.jubata | GYL3                                 | GYL2  | HC    | CR    | C.jubata |
| Orb L                        | 9.98   | 10.50   | 10.27   | 9.77    | 9.79     | 0.268                                | 0.275 | 0.271 | 0.265 | 0.271    |
| Orb W                        | 8.17   | 8.34    | 7.89    | 8.64    | 7.73     | 0.245                                | 0.248 | 0.240 | 0.251 | 0.243    |
| Mes L                        | 11.77  | 12.66   | 11.79   | 12.13   | 13.97    | 0.287                                | 0.297 | 0.287 | 0.290 | 0.314    |
| Mes W                        | 5.82   | 6.05    | 5.79    | 6.37    | 7.29     | 0.205                                | 0.211 | 0.204 | 0.215 | 0.236    |
| Tel.r L                      | 15.81  | 16.41   | 15.29   | 16.35   | 12.36    | 0.322                                | 0.328 | 0.317 | 0.325 | 0.299    |
| Tel.r RW                     | 9.30   | 8.99    | 8.91    | 8.45    | 6.49     | 0.260                                | 0.257 | 0.254 | 0.248 | 0.223    |
| Tel.r CW                     | 10.71  | 10.89   | 10.79   | 11.13   | 8.85     | 0.276                                | 0.280 | 0.276 | 0.280 | 0.259    |
| Tel.c L                      | 12.65  | 11.87   | 12.71   | 11.94   | 13.57    | 0.296                                | 0.290 | 0.296 | 0.288 | 0.310    |
| Tel.c W                      | 13.39  | 12.94   | 13.46   | 13.41   | 13.48    | 0.302                                | 0.300 | 0.302 | 0.302 | 0.309    |
| EmSg L                       | 18.85  | 18.80   | 20.39   | 20.46   | 16.36    | 0.342                                | 0.344 | 0.350 | 0.351 | 0.332    |
| EmSg W                       | 7.35   | 7.35    | 7.26    | 7.72    | 6.07     | 0.233                                | 0.234 | 0.230 | 0.238 | 0.215    |
| Cer L                        | 9.82   | 8.75    | 9.99    | 8.89    | 10.08    | 0.266                                | 0.254 | 0.267 | 0.254 | 0.275    |
| Cer W                        | 14.37  | 14.29   | 13.58   | 14.14   | 13.50    | 0.311                                | 0.311 | 0.303 | 0.308 | 0.310    |
| Rho L                        | 10.98  | 11.39   | 11.48   | 11.36   | 11.22    | 0.279                                | 0.285 | 0.284 | 0.282 | 0.288    |
| Rho W                        | 9.60   | 10.02   | 10.45   | 10.21   | 8.72     | 0.264                                | 0.270 | 0.273 | 0.270 | 0.258    |
| Measurement                  | B. Linear Distance values (mm)                         |         |         |         |          | E. Linear Distance ratios            |       |       |       |          |
| Tel.r TW                     | 9.63   | 8.90    | 8.97    | 9.80    | 8.52     | 0.264                                | 0.256 | 0.255 | 0.265 | 0.255    |
| Tel.r TH                     | 9.74   | 9.90    | 9.65    | 9.81    | 9.38     | 0.265                                | 0.268 | 0.263 | 0.265 | 0.266    |
| Tel.c TW                     | 22.40  | 23.33   | 24.76   | 24.64   | 23.16    | 0.362                                | 0.369 | 0.373 | 0.372 | 0.374    |
| Endo TL                      | 28.18  | 28.18   | 28.92   | 27.65   | 28.69    | 0.389                                | 0.391 | 0.391 | 0.386 | 0.399    |
| Meten TH                     | 19.06  | 17.63   | 18.44   | 18.49   | 17.36    | 0.344                                | 0.336 | 0.339 | 0.339 | 0.340    |
| Med.Ob TW                    | 11.36  | 11.37   | 11.70   | 11.11   | 10.83    | 0.283                                | 0.285 | 0.286 | 0.280 | 0.283    |
| Module                       | C. Mean Modular Surface Area values (mm <sup>2</sup> ) |         |         |         |          | F. Mean Modular Surface Areas ratios |       |       |       |          |
| Olf                          | 17.84  | 15.86   | 16.26   | 16.34   | 17.52    | 0.385                                | 0.369 | 0.371 | 0.371 | 0.385    |
| Orb                          | 60.94  | 68.51   | 63.71   | 68.41   | 60.87    | 0.549                                | 0.565 | 0.552 | 0.561 | 0.553    |
| Mes                          | 52.79  | 60.46   | 55.89   | 64.12   | 81.85    | 0.530                                | 0.548 | 0.535 | 0.553 | 0.593    |
| Tel.r                        | 115.91   | 139.51  | 130.10  | 137.27  | 82.40    | 0.635                                | 0.660 | 0.647 | 0.654 | 0.594    |
| Tel.c                        | 109.20   | 118.77  | 138.46  | 128.04  | 170.72   | 0.627                                | 0.638 | 0.655 | 0.645 | 0.692    |
| EmSg                         | 100.09   | 99.52   | 103.91  | 117.31  | 79.25    | 0.615                                | 0.614 | 0.617 | 0.633 | 0.588    |
| Cer                          | 111.98   | 90.86   | 107.51  | 108.11  | 125.25   | 0.630                                | 0.602 | 0.622 | 0.622 | 0.650    |
| Rho                          | 73.07  | 81.71   | 81.72   | 80.63   | 79.07    | 0.573                                | 0.588 | 0.585 | 0.583 | 0.588    |
| Endo Surf (mm <sup>2</sup> ) | 1788.72  | 1785.12 | 1854.25 | 1858.17 | 1690.65  | 3.253                                | 3.252 | 3.268 | 3.269 | 3.228    |
| Endo Vol (mm <sup>3</sup> )  | 5308.52  | 5114.83 | 5453.94 | 5456.28 | 4477.78  | 3.725                                | 3.709 | 3.737 | 3.737 | 3.651    |

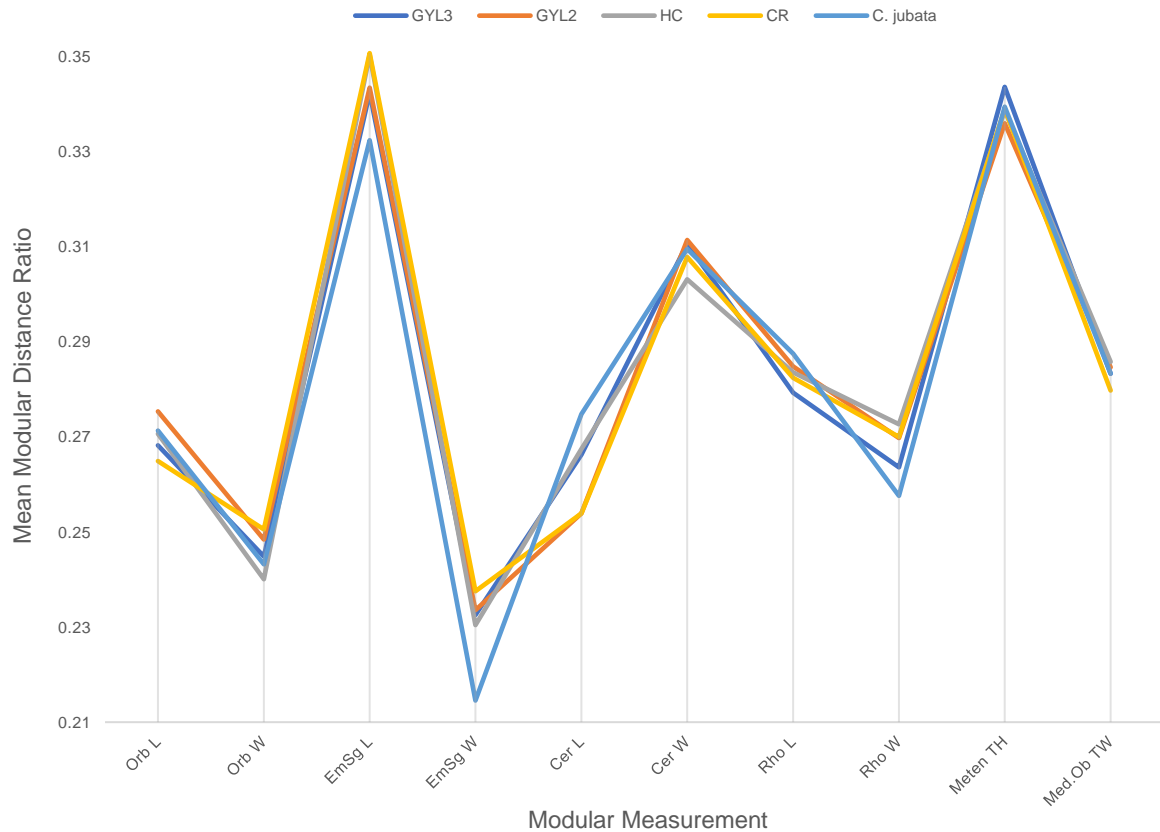


Figure A3.2. Mean Modular Distance and Linear Distance ratios plot for *Chenonetta* specimens. Ratios are size-standardised by dividing  $\log_{10}$  transformed mean Modular Distance and Linear Distance values by  $\log_{10}$  transformed specimen endocast volume (see Tables A3.3D, A3.3E; and 3.2.6.2-3, respectively). **Abbreviations**, **Cer L**, cerebellum length, **Cer W**, cerebellum width; **C. jubata**, Australian wood duck *C. jubata* (SAM B39457); **CR**, Castle Rocks Fissure *C. finschi* (NMNZ S.039838; ~2.1 kys); **EmSg L**, eminentia sagittalis length; **EmSg W**, eminentia sagittalis width; **GYL2**, Honeycomb Hill Graveyard L2 *C. finschi* (NMNZ S.023695; ~13.9 kys); **GYL3**, Honeycomb Hill Graveyard L3 *C. finschi* (NMNZ S.023702; ~18.5 kys); **HC**, Hodges Creek Cave *C. finschi* (NMNZ S.034496; ~12.2 kys); **Meten TH**, metencephalon total height; **Med.Ob TW**, medulla oblongata total width; **Orb L**, orbit length; **Orb W**, orbit width, **Rho L**, rhombencephalon length; **Rho W**, rhombencephalon width.

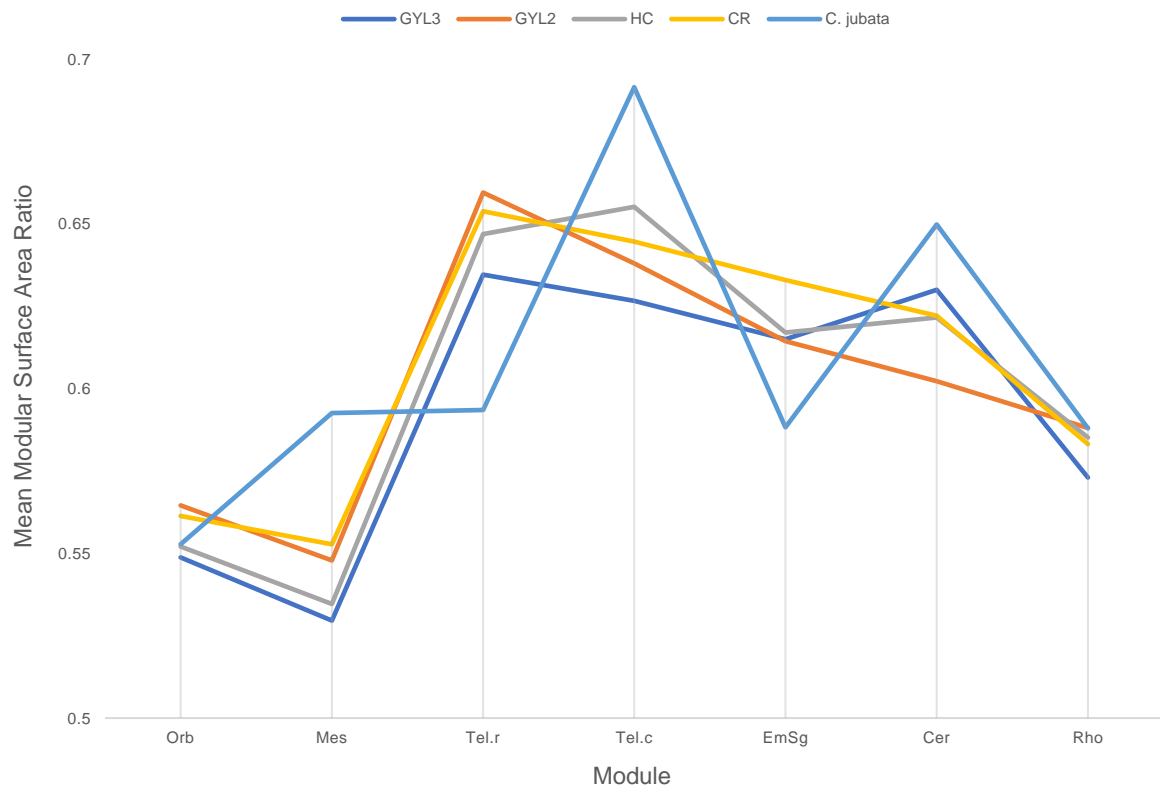


Figure A3.3. Mean Modular Surface Area ratios plot for *Chenonetta* specimens. Ratios are size-standardised by dividing  $\log_{10}$  transformed mean Modular Surface Area values by  $\log_{10}$  transformed specimen endocast Surface Area values (see Table A3.3F, 3.2.6.4). **Abbreviations**, **Cer**, cerebellum; **C. jubata**; Australian wood duck *C. jubata* (SAM B39457); **CR**, Castle Rocks Fissure *C. finschi* (NMNZ S.039838; ~2.1 kys); **EmSg**, eminentia sagittalis; **GYL2**, Honeycomb Hill Graveyard L2 *C. finschi* (NMNZ S.023695; ~13.9 kys); **GYL3**, Honeycomb Hill Graveyard L3 *C. finschi* (NMNZ S.023702; ~18.5 kys BP); **HC**, Hodges Creek Cave *C. finschi* (NMNZ S.034496; ~12.2 kys); **Mes**, mesencephalon; **Orb**, orbits; **Rho**, rhombencephalon; **Tel.c**, caudal telencephalon; **Tel.r**, rostral telencephalon.

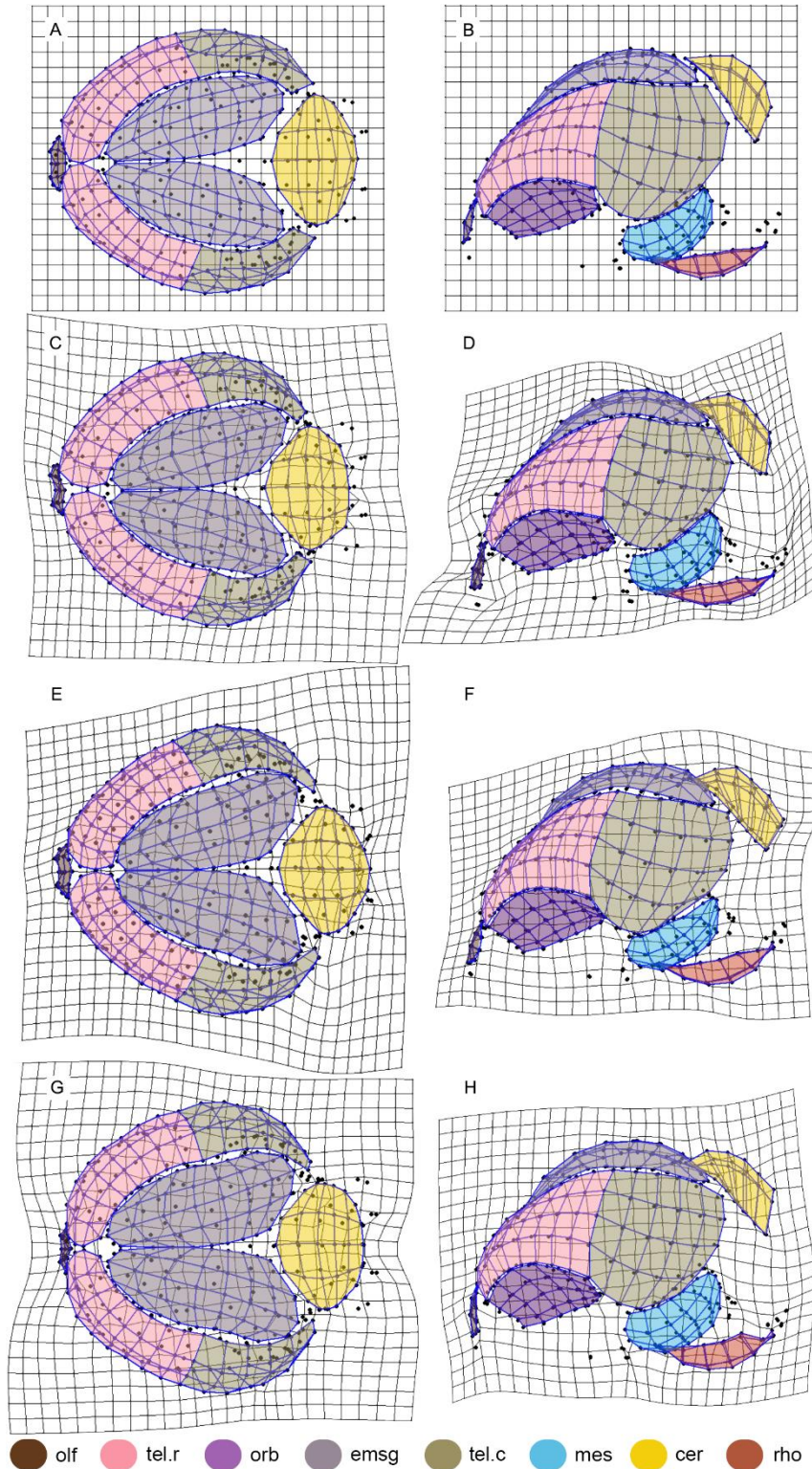


Figure A3.4. TPS warpgrid visualisations of the full endocast shape change between individual *C. finschi* specimens in: dorsal (A, C, E, G); and left lateral (B, D, F, H) views. Blue links visualise target specimen shapes and are shaded to assist identification of modular Lm configurations (see Fig. A3.1). A–B, GYL3, Honeycomb Hill Graveyard L3 *C. finschi* (NMNZ S.023702; ~18.5 kys); C–D, GYL2, Honeycomb Hill Graveyard L2 *C. finschi* (NMNZ S.023695; ~13.9 kys); E–F, HC, Hodges Creek Cave *C. finschi* (NMNZ S.034496; ~12.2 kys); G–H, CR Castle Rocks Fissure *C. finschi* (NMNZ S.039838; ~2.1 kys). **Abbreviations**, cer, cerebellum; emsg, eminentia sagittalis, GYL3, mes, mesencephalon; olf, olfactory; orb, orbit; rho, rhombencephalon; tel.c, caudal telencephalon; tel.r, rostral telencephalon.

## CHAPTER 4

**Dromornithid endocranial anatomy**

## 4.1 INTRODUCTION

The dromornithids were large flightless birds, collectively known as ‘mihirungs’, whose fossils are a distinctive component of the Cenozoic avifauna of Australia, and are comparatively abundant in the Australian Neogene fossil record (Vickers-Rich 1991; Murray & Vickers-Rich 2004). The greatest diversity of the group occurs during the Miocene (Vickers-Rich 1991; Murray & Megirian 1998, 2006; Murray & Vickers-Rich 2004; Boles 2006; Worthy et al. 2016b), but the family is known from fossils dating from the Palaeogene, with a record consisting of a fossil foot from the Eocene of Queensland (Vickers-Rich & Molnar 1996), postcranial remains from the late Oligocene Pwerte Marnte Marnte Local Fauna in the Northern Territory (Murray & Megirian 2006), and possible trackways reported from the late Oligocene of Tasmania (Vickers-Rich 1991; Mayr 2009).

The fossil record shows that the characteristic morphology of dromornithids had already evolved by the late Oligocene, and that it changed little over the next ~20 Million years (Ma), until the group became extinct in the late Pleistocene (Miller et al. 2005; Worthy et al. 2016b). Eight species in four genera of dromornithids are now recognized since *Dromornis australis* Owen, 1872 was described from undated deposits at Peak Downs, Queensland (Rich 1979; Murray & Vickers-Rich 2004; Nguyen et al. 2010; Worthy & Yates 2015; Worthy et al. 2016b). Stirling & Zietz (1896a) described *Genyornis newtoni* Stirling & Zietz, 1896 from what was originally thought to be late Pliocene/early Pleistocene (see Stirling & Zietz 1896a:177), but more recently proposed to be middle to late Pleistocene (Wells & Tedford 1995:16) deposits of Lake Callabonna, South Australia. From the late Miocene Waite Formation, Alcoota, Northern Territory, Rich (1979) described *D. stirtoni* Rich, 1979, *Ibandornis lawsoni* Rich, 1979, and *I. woodburnei* Rich, 1979, and from the late Oligocene/early Miocene Carl Creek Limestone at Riversleigh, Northern Queensland, *Barawertornis tedfordi* Rich, 1979 was described. She also named *Dromornis planei* (Rich, 1979), formerly *Bullockornis planei*, from the middle Miocene Camfield beds, Bullock Creek, Northern Territory (Rich 1979:27). Nguyen et al. (2010) suggested this species should be considered congeneric with *Dromornis* and integrated into that taxon. This was supported by Worthy et al. (2016b), upon revision of cranial material of the Bullock creek specimens, in conjunction with the description of *Dromornis murrayi* Worthy et al., 2016 from Riversleigh. At the same time, Worthy et al. (2016b) proposed the eight species of dromornithids described (see above) formed two lineages, where the *Dromornis* lineage is monotypic throughout its range, and includes *D. murrayi*, *D. planei*, *D. australis*, and *D. stirtoni*. The *Ibandornis/Barawertornis* lineage comprises the more gracile taxa *B. tedfordi*, *I. lawsoni*, *I. woodburnei*, and *G. newtoni*.

Dromornithids were long considered to be ratites (see [Stirling & Zietz 1896a, 1896b](#); [Wetmore 1960](#); [Rich 1975, 1979](#)); all ratites exhibit reduced wing morphology and are generally large terrestrial birds ([Worthy & Holdaway 2002](#); [Phillips et al. 2010](#)). These features are shared with dromornithids, but [Olson \(1985:104\)](#) succinctly opined “large size and flightlessness do not a ratite make”, and pointed out that characteristics of the dromornithid mandible, quadrate, and pelvis suggested they were likely derived from an entirely different group of birds. In more recent times, with the discovery of additional cranial elements, a phylogenetic analyses conducted by [Murray & Megirian \(1998\)](#) concluded that dromornithids were the sister-group of the Anhimidae, and so were Anseriformes. A conclusion reinforced by [Murray & Vickers-Rich \(2004\)](#), who found similarities to Anseranatidae, which are sister to anatids, and together these taxa form the sister group to anhimids within Anseriformes. In a phylogenetic study of the affinities of Pelagornithidae (bony-toothed birds), [Mayr \(2011\)](#) found dromornithids were likely stem Galloanseres, i.e., a sister group to Galliformes and Anseriformes. This hypothesis was partially supported by [Worthy et al. \(2016a\)](#), whereby with inclusion of a representative sample of extant galloanseres, along with adequate outgroup taxa comprising Neoaves and palaeognaths, and other significant fossils, *Dromornis* was found to have a stem-galliform relationship. Most recently, [Worthy et al. \(2017a, see also 2017b\)](#) conducted a phylogenetic analysis using an expanded taxon set, employing parsimony and tip-dated Bayesian approaches, and placed dromornithids along with the flightless gastornithids of Eurasia and North America in the robustly supported galloansere clade Gastornithiformes Stejneger, 1885. However, the sister relationship with galliforms within galloanseres, was weakly supported.

As with gastornithids (e.g. [Angst et al. 2014](#)), there exists convincing evidence for an herbivorous diet, as some dromornithid specimens have been preserved with gastroliths (e.g. [Archer et al. 1991:79](#), re Riversleigh D-Site specimen). Individual gizzard stones are common in Alcoota sediments (e.g. [Woodburne 1967:164](#); [Murray & Megirian 1992:fig 8A](#); [Murray & Vickers-Rich 2004:262](#); [Pers. Obs. Author](#)), and several specimens of the Pleistocene dromornithid *G. newtoni*, have complete or partial gizzard stone sets associated with skeletal remains ([Worthy Unpubl. Data](#); [Pers. Obs. Author](#)). [Handley et al. \(2016\)](#) demonstrated significant male dominated sexual dimorphism in the largest of all dromornithids, the Miocene species *D. stirtoni*, and revealed those birds identified as male had a mean mass of 528 kg based on tibiotarsi circumference metrics. Tibiotarsi were preferred for estimating body mass in large birds, especially in dromornithids, after statistical evaluations of several mass estimation algorithms, employed across a population-sized sample, showed femoral metrics likely overestimated body mass for them (see [Handley et al. 2016:13](#); see also [Grellet-Tinner et al. 2017](#)). These dromornithids, along with the giant aepyornithid morphotype *Vorombe titan* (Andrews, 1894), from the Holocene of Madagascar (see [Hansford & Turvey 2018](#)), likely comprise the largest birds to have ever evolved.

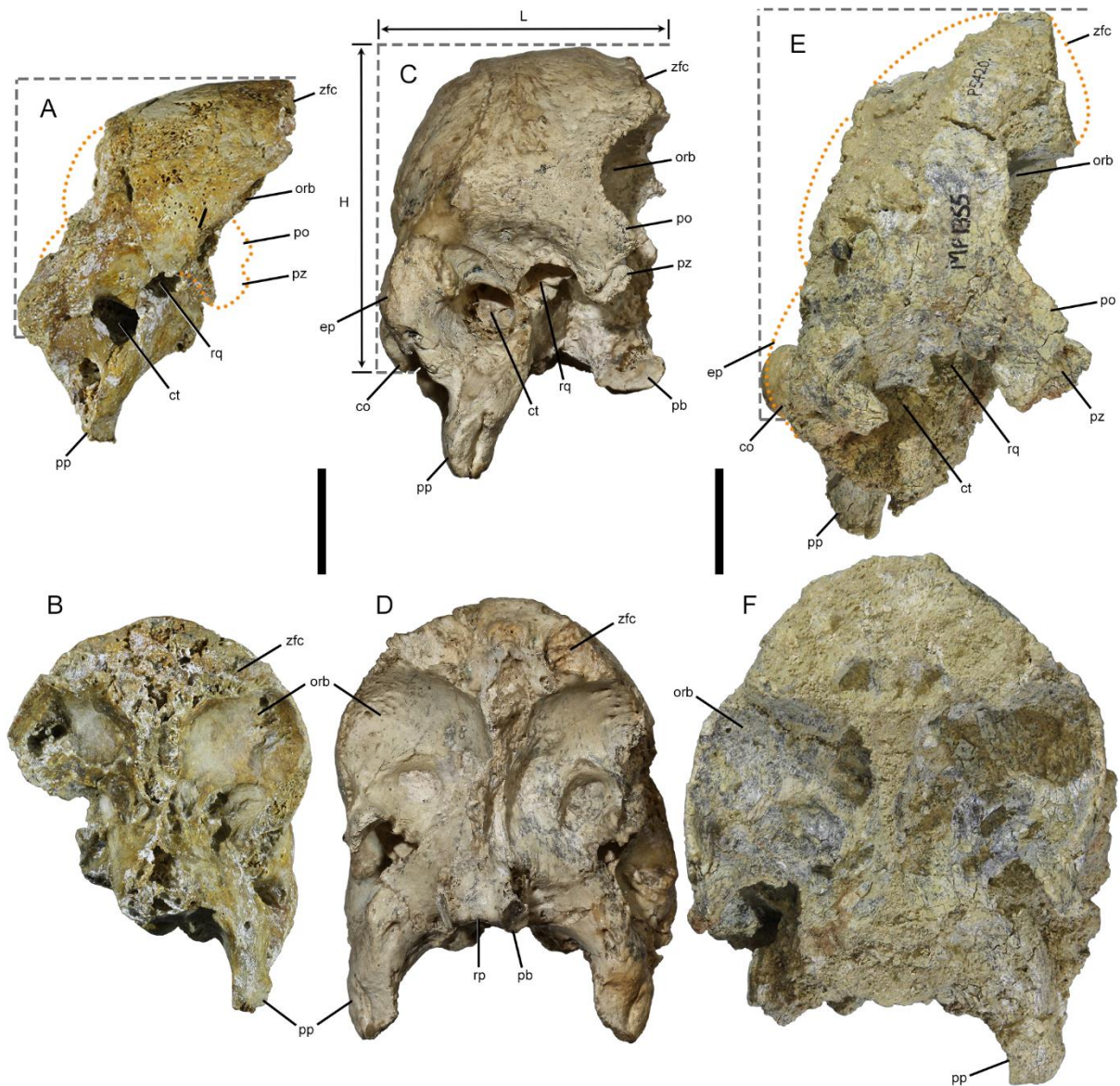


Figure 4.1. Time series of *Dromornis* taxa showing progressive increase in neurocranial height (**H**) relative to length (**L**) over ~20–8 Ma: **A–B**, *Dromornis murrayi* (QM F57984) Oligo-Miocene (25–23 Ma); **C–D**, *D. planei* (NTM P9464–106) middle Miocene (15–12 Ma); **E–F**, *D. stirtoni* (NTM P5420) Late Miocene (9–7 Ma). **Views**: RHS Lateral (**A**, **C**, **E**); Rostral, (**B**, **D**, **F**). [Note, *D. murrayi* lateral view (**A**) is the LHS of the skull which is mostly complete (see **B**) and has been flipped to RHS view]. Missing neurocranial areas are shown by orange stippled lines on **A** and **E**. **Abbreviations**, **ct**, cavum tympanicum; **ep**, exoccipital prominence; **LHS**, left hand side; **mm**, millimetres; **orb**, orbit; **pb**, processus basipterygoidei; **po**, processus postorbitalis; **pp**, processus paroccipitalis; **pz**, processus zygomaticus; **RHS**, right hand side; **rq**, recessus quadratica; **zfc**, zona flexoria craniofacialis. Scale bars equal 40 mm.

*Dromornithid* cranial anatomy has previously been comprehensively described (e.g. Murray & Megirian 1998; Murray & Vickers-Rich 2004; Worthy et al. 2016b), but there exists no information regarding the specific shape and size of the dromornithid brain across the two lineages hypothesised by Worthy et al. (2016b, see above). Those authors identified that from the Oligocene through the late Miocene, the shape of crania of dromornithids changed with a foreshortening of the length relative to the height of the skull (see Fig. 4.1). As to how the shape of the dromornithid brain changed to

accommodate these temporal changes in cranial anatomy, and whether there exists quantifiable differences in endocranial anatomy between the *Dromornis* and *Ilbandornis* lineages, has yet to be appropriately assessed.

Thus, the objectives of this chapter are to assess dromornithid endocast material spanning the late Oligocene to the late Miocene. This has important scientific implications that would: **1**, allow description of morphological characteristics of the dromornithid brain and its principle innervation for the first time; **2**, inform our understanding of how dromornithid brains differ morphologically from those of other galloanseres; **3**, allow testing of the two lineage hypothesis, by assessing whether there exists quantifiable differences in endocranial anatomy between the *Dromornis* and *Ilbandornis* lineages; **4**, assess how the shape of the brain accommodated significant changes in cranial anatomy across ~20–8 Ma of evolution, from the cassowary-sized *Dromornis murrayi* from the late Oligocene of Northern Queensland, to arguably the most massive bird that ever existed, *Dromornis stirtoni* from the late Miocene of Central Australia (Fig. 4.1E–F); **5**, allow appreciation of the potential functional constraints shaping the evolution of dromornithid endocranial anatomy across this period; and **6**, contribute to testing of the current hypothesis of dromornithids being stem-galliforms, when assessed together with an extended dataset of cranial material, including extant and extinct taxa, sourced from across the Superorder Galloanseres, forming part of an extended project including these giant enigmatic Australian birds.

## 4.2 METHODS

### 4.2.1 Abbreviations

**4.2.1.1 Institutions**—ANSTO, Australian Nuclear Science and Technology Organisation, Lucas Heights, Sydney, New South Wales, Australia, **QM**, Queensland Museum, Brisbane, Queensland, Australia, **QVM**, Queen Victoria Museum and Art Gallery, Launceston, Tasmania, **NTM**, Museum of Central Australia, Alice Springs, Northern Territory, Australia, **SAHMRI**, South Australian Medical and Health Research Institute, Adelaide, South Australia, **SAM**, South Australian Museum, Adelaide, South Australia, **MV**, Melbourne Museum, Melbourne. Australia.

**4.2.1.2 Specimens**—two neurocrania of *Dromornis murrayi* (QM F57984—Hiatus site; QM F57974—Cadbury’s Kingdom site), and a fossil endocast (QM F50412—Cadbury’s Kingdom site) from Riversleigh were studied (Figs. 4.1, 4.2, A4.1, A4.2). The fossil endocast (QM F50412) was not scanned and does not contribute to numerical analysis, but is figured for comparative purposes (see Fig. A4.3). One neurocranium respectively of *Dromornis planei* (NTM P9464-106), and *Ilbandornis woodburnei* (QVM:2000:GFV:20) from Bullock Creek LF (Figs. 4.1, 4.2, A4.4, A4.5), and two neurocrania of *Dromornis stirtoni* (NTM P5420; NTM P3250) from Alcoota LF were studied (Figs. 4.1, 4.2, A4.6, A4.7). Three neurocrania of extant basal galloansere birds were also included: an

anhimid *Anhima cornuta* (MV B12574), the anseranatid *Anseranas semipalmata* (SAM B48035), and a megapodiid *Leipoa ocellata* (SAM B11482).

#### 4.2.2 Geological and temporal data for the fossils analysed

The fossil materials used in this study were sourced from three site complexes (Fig. 4.2). Three specimens come from Riversleigh World Heritage Area in north-western Queensland, Australia: The specimen of *D. murrayi* (QM F57984—see below), is derived from the Hiatus sites (Queensland Museum Locality 941), Hals Hill, D Site Plateau, forming part of the Riversleigh Faunal Zone A deposits (e.g. ‘System A’ of Archer et al. 1989, 1997 and “Faunal Zone A” of Travouillon et al. 2006, 2011). Hiatus sites comprise “pure” limestone formed in an aquatic setting, and have proved difficult to successfully date radiometrically, due to the lack of speleothem or flowstone material often included in palaeo-cave deposits elsewhere at Riversleigh (Woodhead et al. 2016). The Hiatus fauna is considered late Oligocene–early Miocene (25–23 Ma) in age, based on biocorrelation (i.e., vertebrate stage-of-evolution (see Archer et al. 1989, 1997; Travouillon et al. 2006, 2011; Arena et al. 2016; Woodhead et al. 2016). The second specimen of *D. murrayi* (QM F57974—see below), and a fossil endocast (QM F50412—see below), come from Cadbury’s Kingdom site, considered Faunal zone B and early Miocene (~23–16 Ma) in age (Travouillon et al. 2011; Arena et al. 2016).

The second site complex is located at Bullock Creek in the Northern Territory of central Australia: One specimen of *D. planei* (NTM P9464-106—see below), and one of *I. woodburnei* (QVM:2000:GFV:20—see below), were studied from this site. The Camfield beds which crop out at Bullock Creek, are fossiliferous freshwater conglomeratic limestone deposits that contain the Bullock Creek Local Fauna (LF), which includes several aquatic and “stream-bank” species (Murray & Megirian 1992), and forms the type locality for the Camfieldian Land Mammal Age (Megirian et al. 2010). Fossils from the site are generally well preserved (Worthy et al. 2016b), and are considered to be middle Miocene (15–12 Ma) in age based on biocorrelation, specifically the stage of evolution of diprotodontid *Neohelos* spp. (Murray & Megirian 1992:198; see also Murray et al. 2000; Stirling & Zietz 1896a; Megirian et al. 2010; Woodhead et al. 2016).

The third site complex is located at Alcoota Station approximately 110 km NE of Alice Springs in the Northern Territory of central Australia (Yates 2015): Two specimens of *D. stirtoni* were studied from this site (NTM P5420 and NTM P3250—see below). The Alcoota LF derives from unconsolidated fluvial clays and silts of the Waite formation, previously interpreted as lacustrine deposits (Woodburne 1967). The sediments are now considered to be overbank silts accumulated by debris flow, wherein fossils are concentrated in extensive bonebeds with little or no association (Yates 2013, 2015; Worthy & Yates 2017). Specimens are generally poorly preserved, likely due to repeated fluctuations in moisture content of the siltstone matrix, causing fracturing and compaction of fossils over time (Murray & Megirian 1992). Alcoota LF is believed to be late Miocene (9–7 Ma) in age based on biocorrelation (Stirton et al. 1967; Murray & Megirian 1992; Murray & Vickers-Rich 2004;

Megirian et al. 2010; Worthy & Yates 2017), and is the type locality for the Waitean Land Mammal Age (Megirian et al. 2010). Alcoota LF is unique in that it preserves the only late Miocene vertebrate community known from Australia outside of Riversleigh (Murray & Megirian 1992; Murray & Vickers-Rich 2004).



Figure 4.2. Australian continental map showing fossil site locations where dromornithid neurocrania used in this study were sourced (see 4.2.2). **Abbreviations**, **Alcoota**, Alcoota Fossil Reserve, Alcoota Station, Northern Territory; **Bullock Creek**, Bullock Creek Fossil site, Camfield Station, Northern Territory; **Riversleigh**, Riversleigh World Heritage Area, north-western Queensland.

**4.2.3 Nomenclature**—for anatomical nomenclature adopted in the following texts see Introduction, 1.5.2, and Fig. 1.5.1 above.

#### 4.2.4 Modelling

One of each of the following neurocrania were  $\mu$ CT scanned using the Skyscan 1076  $\mu$ CT instrument (Bruker microCT) at Adelaide Microscopy, University of Adelaide: *L. ocellata* was scanned at 17.4 micrometre ( $\mu$ m) resolution at 48 kilovolts (kV) and 139 microamps ( $\mu$ A), *Anhima cornuta* was scanned at 34  $\mu$ m, at 100 kV and 100  $\mu$ A, and *Anseranas semipalmata* was scanned at 34.8  $\mu$ m, at 100 kV and 90  $\mu$ A. Skyscan raw  $\mu$ CT acquisition data were reconstructed using NRecon v1.6.10.4 (Bruker microCT) and compressed using ImageJ v1.51w (Rasband 2018) software (see also 2.1.1).

The neurocrania of *D. murrayi*, *D. stirtoni*, and *I. woodburnei* were medical X-ray CT-scanned using the Siemens Somatom Force CT instrument located at the SAHMRI facility in Adelaide (see 2.1.2). CT data were captured at a slice thickness of 0.4 mm, but with the application of an oversampling technique allowing the acquisition of twice the number of slices per detector row, an effective resolution of 240  $\mu\text{m}$  was achieved for all specimens, excluding *D. stirtoni* (NTM P3250) which was scanned at a resolution of 320  $\mu\text{m}$ . Raw CT acquisition data were reconstructed by M. Korlaet of Dr Jones & Partners using Siemens proprietary software.

The neurocranium of *D. planei* was scanned at the ANSTO nuclear facilities in Sydney using the DINGO neutron CT-scanning instrument, located in the OPAL reactor beam hall on thermal beam HB2. Neutron CT images were captured at low-intensity mode at  $\sim 95 \mu\text{m}$ , and raw acquisition data were reconstructed by Dr. J. Bevitt of ANSTO using ImageJ, VGStudio and Octopus software (see also General Methods, 2.1.3).

**4.2.4.1 Three dimensional (3D) surface model construction**—was conducted using Materialise Mimics v.18 software and raw 3D surface endocast \*.stl models were produced from reconstructed CT data to represent the shape of the brain. (Figs. 4.3, 4.4). These included the base and immediate stem of the major nerves passing from the brain into the neurocranium (see also General Methods, 2.1.1).

#### 4.2.4.2 Model reconstructions

The endocasts for the two fossil specimens of *D. stirtoni*: NTM P5420 and NTM P3250 were constrained by preservation. Thus, a two dimensional (2D) reconstruction representative of the species was derived using both endocast models (see 4.2.4.3 below). Similarly, endocasts for specimens of *D. murrayi* were respectively damaged and incomplete, where QM F57984 preserves only the LHS dorsolateral endocast, and QM F57974 preserves only the ventral endocast. Thus, a single 3D endocast model was compiled from CT-scan data of the two specimens of *D. murrayi* (see 4.2.4.4 below).

**4.2.4.3 Two dimensional model reconstructions**—of the right hand side (RHS) lateral and rostral endocasts of *D. stirtoni* were compiled in Adobe Photoshop v.20.0 from 2D images of the endocast models for specimen NTM P5420 (hereafter *D. stirtoni*-1), and specimen NTM P3250 (hereafter *D. stirtoni*-2).

For the lateral RHS reconstruction (Fig. A4.8J), the endocast of *D. stirtoni*-1 was not rescaled, but the more gracile endocast of *D. stirtoni*-2 was rescaled larger to fit the *D. stirtoni*-1 endocast. Models were aligned at the ventral rhombencephalon by the caudoventral descending curve of the eminentia sagittalis through the caudal telencephalon in *D. stirtoni*-2, and the ventral curve of the caudal telencephalon in *D. stirtoni*-1. This feature, in the other dromornithid taxa assessed, tends to describe a somewhat continuous dorsoventral transition curve, which was replicated here. The RHS lateral endocast of *D. planei* was rescaled larger by approximately 8%, to approximate the size of the aligned specimens of *D. stirtoni*, as judged by fit to the rostradorsal and caudodorsal eminence of the

eminentia sagittalis, and the rostroventral eminence of the hypophysis, which in *D. stirtoni*-1 is reasonably well defined. With the alignment of these structures, the angle and extent of the preserved ramus of the maxillomandibular nerves in *D. stirtoni*-1 is aligned with that of *D. planei*, and the angle of the rostradorsal cerebellum surface matches that of *D. planei*, albeit markedly more ventrally situated in *D. stirtoni*. Taken together, these morphological correlations likely represent the ‘best fit’ between taxa (Fig. A4.8J).

For the rostral endocast reconstruction (Fig. A4.8K), the RHS rostral endocast morphology of *D. stirtoni*-1 and *D. stirtoni*-2 were used to align specimens, as both models appear to have suffered a measure of left hand side (LHS) rostroventrolateral distortion. As with the RHS lateral reconstruction, the rostral model of *D. stirtoni*-1 was not rescaled, but the more gracile rostral endocast of *D. stirtoni*-2 was rescaled larger to fit the RHS rostradorsal eminence of the rostral RHS eminentia sagittalis in *D. stirtoni*-1. The eminence of the RHS caudal telencephalon and the ventral eminence of the rhombencephalon also aligns well between endocasts in this position. The rostral endocast of *D. planei* was then rescaled approximately 5% larger, aligned with the RHS eminence of the eminentia sagittalis, and with the RHS caudal telencephalon of the combined *D. stirtoni* specimens. With these features aligned, the position of the twin rostroventrolateral eminences of the rostral telencephalon, the vallecule transition zone, and the eminence of the chiasma opticum and hypophysis align well between taxa.

**4.2.4.4 Three dimensional surface model reconstruction**—a single endocast surface model was compiled from CT-scan data of the two specimens of *D. murrayi*, using Materialise 3-matic v10 software (see Fig. A4.9C). As the specimen of *D. murrayi* QM F57984 (hereafter *D. murrayi*-1) preserves only the LHS dorsolateral endocast, and the specimen of *D. murrayi* QM F57974 (hereafter *D. murrayi*-2) preserves only the ventral endocast. The LHS dorsal endocast model of *D. murrayi*-1 was mirrored and positioned to form the RHS dorsolateral endocast surfaces, producing a complete dorsal surface model (Figs. A4.9 1–4). This reconstructed dorsal surface model was then positioned, with no re-scaling modification needed, upon the ventral endocast model of *D. murrayi*-2. The two surface models were then merged, producing a single 3D \*.stl endocast surface model for further processing (Figs. A4.9 4–5).

**4.2.4.5 Remeshing**—of raw 3D \*.stl surface models is required to optimise the quality of the triangles comprising the surface mesh and to reduce the physical file size of models for landmarking operations (see below). Remeshing operations were carried out in Materialise 3-matic v10, and conversion of remeshed \*.stl format 3D objects to \*.ply format was conducted in MeshLab v2016.12 (Cignoni et al. 2008).

## 4.2.5 Landmarking

Digital landmarking of 3D endocast surface models was conducted in IDAV Landmark v3.6 (Wiley 2006), using 20 fixed (type 1) and 460 semi (type 3) landmarks (*sensu* Bookstein 1991), for a

total of 480. These landmarks were assigned into 13 modules for subsequent analyses (see General Methods, Fig. 2.1). The full Lm suite is described in General Methods Appendices (A2.1).

## 4.2.6 Data

**4.2.6.1 Modular Lm data**—three dimensional digital shape data derived from the modular Lm suite (see General Methods, A2.1, Fig. 2.1) were used for all shape assessments (see 4.2.7 below). Numerical output from each assessment are presented in text, and in Tables A4.1, A4.2.

**4.2.6.2 Modular Distance data**—were calculated between Lm and Slm locations (hereafter Lm) for each specimen employing the ‘interlmkdlist’ function in Geomorph v3.0.7 (Adams et al. 2018; see also 4.2.7 below), using raw Lm coordinate data. Modular distance measurements for the length and width of each modular structure, capturing the directional ‘curve’ over a 3D surface (i.e., *eminentia sagittalis*; see General Methods, 2.3.2, Figs. 2.2C–D), were calculated incorporating the distances between each Lm forming the measurement vectors. Then individual measurements between Lms were added together to form the total modular distance measurement value (see General Methods, Figs. 2.2C–D). Paired structure data (i.e., *eminentia sagittalis*, rostral and caudal telencephalon, mesencephalon, and trigeminal ganglion modules) were combined, and mean Modular Distance data calculated (see Table A4.1A). Size-standardised mean Modular Distance ratios were calculated by dividing  $\log_{10}$  transformed mean Modular Distance data by  $\log_{10}$  transformed specimen endocast volume values. Modular Distance ratios are presented in text, in Table A4.1C, and plotted in Figs. 4.5, A4.10.

**4.2.6.3 Linear (vector) Distance data**—were calculated between two Lm locations describing gross endocast morphological (vector) distances (see General Methods, Figs. 2.2G–I; Table A4.1B). Size-standardised Linear Distance ratio data were calculated by dividing  $\log_{10}$  transformed Linear Distance values by  $\log_{10}$  transformed specimen endocast volume values. Linear Distance ratios are presented in text, in Table A4.1D, and plotted in Figs. 4.5, A4.10.

**4.2.6.4 Modular Surface Area data**—for each endocast module, as defined by the Lm modules described in General Methods Appendices (A2.1) and shown in Fig. 2.1, were computed directly from the surface of each 3D endocast model using MeshLab (see General Methods, 2.3.4, Figs. 2.2J–K). Three forms of raw surface area data were acquired: **1**, total endocast Surface Area (see Table A4.2B); **2**, Modular Surface Area values in square millimetres ( $\text{mm}^2$ ), representative of modular surface topology, for which mean Modular Surface Area values for all paired modules (i.e., *eminentia sagittalis*, rostral and caudal telencephalon, mesencephalon, and trigeminal ganglion) were computed (see Table A4.2A); and **3**, Modular Perimeter data (mm) describing the total perimeter distance of the modular surface morphology computed in **2** (see General Methods, Fig. 2.2K: **tel.r per**; and Table A4.2B). These data were then size-standardised for intra- and interspecific comparison into two categories of ratio data: **1**, mean Modular Surface Area ratio data were generated by dividing  $\log_{10}$  transformed mean Surface Area values by  $\log_{10}$  transformed total endocast surface area values.

Modular Surface Area ratios are presented in text, in Table A4.2C, and plotted in Figs. 4.6, A4.11; and **2**, mean Modular Perimeter ratio data were generated by dividing  $\log_{10}$  transformed mean Modular Perimeter values by  $\log_{10}$  transformed total endocast surface area values. Modular Perimeter ratios are presented in text and in Table A4.2D.

**4.2.6.5 Estimated body mass data**—were computed for: Holocene NZ palaeognath moa, *Dinornis robustus* (Owen, 1846; n=5), and *Euryapteryx curtus gravis* (Owen, 1870; n=1), Australian emu (*Dromaius novaehollandiae*; n=1), and dromornithid (*Genyornis newtoni*; n=2) taxa (full specimen details are presented in Table A4.3), for which complete gizzard data are associated (see below). Body masses were calculated using [Alexander's \(1983\)](#) algorithm employing femur length (Fem L), ensuring estimated mass continuity across taxa, as no tibiotarsi circumference metrics are available for moa. However, the fossil specimen of *G. newtoni* (uncatalogued, field code CB 2018-23), lacked complete femora, therefore the mass estimation for CB 2018-23 was taken as the mean mass estimation for *G. newtoni* 'unsexed data' (n=22), from [Grellet-Tinner et al. \(2017:table A2\)](#) data, based on [Campbell & Marcus' \(1992\)](#) tibiotarsus least-shaft circumference algorithm. This value falls within the estimated mass range of [Alexander's \(1983\)](#) Fem L algorithm results for *G. newtoni* (SAM P.53833, Table A4.3).

**4.2.6.6 Gizzard data**—were compiled from the literature ([Worthy & Holdaway 2002:table 5.11](#); [Worthy Unpubl. Data](#)), and by directly measuring the complete mass and gastrolith sizes of associated gizzard contents for those fossil and extant specimens, for which body mass data were estimated (see **4.2.6.5** above). Gastrolith size is the narrowest width of two dimensions for each gastrolith measured (*sensu* [Worthy 1989](#)). Body mass, gizzard mass and gastrolith size results are presented in text and in Table A4.3A. Size-standardised gizzard mass and gastrolith ratios were calculated by dividing  $\log_{10}$  transformed gizzard mass and gastrolith size values by  $\log_{10}$  transformed specimen modal body mass values (see Table A4.3B). Estimated body mass, gizzard mass and gastrolith size ratios are presented in text, in Table A4.3B and plotted in Fig. A4.12.

#### 4.2.7 Analyses

All data analyses and visualisations (Figs. 4.7–4.9), excluding Figs. 4.5–4.6, A4.10–A4.11 (Microsoft Excel v16), were conducted in R v3.5.2 ([R Core Team 2018](#)) using RStudio v1.1.456 ([RStudio Team 2016](#)). Multivariate 3D Modular Lm data were conditioned (see GPA; General Methods, **2.4.1**) and analysed using Geomorph (see also General Methods, **2.4**).

In the following analyses, I describe: **1**, distinctions in dromornithid innervation using characteristics of dromornithid endocast morphology (see **4.3.1**, Figs. 4.3–4.4, and Appendices, Figs. A4.4–A4.5 below); **2**, dromornithid endocranial morphology using characteristics of dromornithid endocast morphology (see **4.3.2**, Figs. 4.3–4.4, and Appendices, Figs. A4.4–A4.5 below); **3**, distinctions between the endocast morphology of dromornithid taxa (see **4.3.3** below), using the morphological trends described by 3D modular shape change plots (see **4.2.7.1** and Figs. 4.7–4.9

below), along with size-standardised ratios of: Modular Distance (see **4.2.6.2** above, Fig. 4.5, and Appendices, Fig. A4.10, Table A4.1C below), and Linear Distance data (see **4.2.6.3** above, Fig. 4.5, and Appendices, Fig. A4.10, Table A4.1D below), derived directly from Modular Lm data (see General Methods, **2.3**; and **4.2.6** above), and Modular Surface Area data (see **4.2.6.4** above, Fig. 4.6, and Appendices, Fig. A4.11, Tables A4.2C–D below), to quantify distinctions between dromornithid specimens visualised by 3D modular shape change plots; **4**, distinctions between the endocast morphology of dromornithid taxa and extant galloanseres included in these analyses (see **4.3.4** below), using characteristics of dromornithid and galloansere endocast morphology (see Figs. 4.3–4.4 below), along with morphological trends described by size-standardised ratios of Modular Distance (see **4.2.6.2** above), Linear Distance (see **4.2.6.3** above), and Modular Surface Area (see **4.2.6.4** above) results (see Appendices, Figs. A4.10–A4.11; Tables A4.1C–D, A4.2C–D below); **5**, I used estimated body mass data (see **4.2.6.5** above, and Appendices, Fig. A4.12; Tables A4.3A–B below), along with Gizzard data (see **4.2.6.6** above, and Appendices, Fig. A4.12; Tables A4.3A–B below), including size-standardised ratios of gizzard mass and gizzard stone size, for complete and associated gizzard samples derived from dromornithid and ratite specimens (see **4.3.5** below), to inform the framing of trophic hypotheses for focal dromornithid taxa (see **4.4.4.1** below).

**4.2.7.1 Three dimensional modular shape variance plots**—to better understand the extent of particular morphological variation between dromornithid taxa across the modular Lm suite, I used 3D shape variance plots to visualise the modular shape variation between individual species of dromornithid. A species of dromornithid represented by black dots and blue links, is superimposed over another species of dromornithid represented by grey dots and grey links, visualising the extent and direction of modular shape variation between the two species. In this manner, modular shape variation between all dromornithid taxa were visualised (see Figs. 4.7–4.9).

## 4.3 RESULTS

### **4.3.1 Dromornithid endocranial innervation** (see Figs. 4.3–4.4, A4.4–A4.5)

**4.3.1.1 The olfactory nerve (I)**—transmits into the olfactory bulb through the bony foramen n. olfactorii (Figs. A4.4K–L). The dromornithid olfactory bulb is best described by the more complete RHS lateral view of *D. murrayi* (Fig. 4.3E). The margins of the olfactory bulb are pronounced both dorsally and ventrally, but caudodorsally masked by the rostral eminence of the eminentia sagittalis. The caudomediolateral transmission of the olfactory bulb margins are shown by the ventral view of *D. murrayi* and *D. planei* (Figs. 4.3D, 4.3H) as transitioning into the rostroventral endocast without reduction in mediolateral width, as seen in other galloansere taxa (e.g. Figs. 4.4E, 4.4H).

**4.3.1.2 The optic nerve (II)**—passes through the os laterosphenoidale forming the caudal wall of the orbit, and transmits into the endocranial cavity through the foramen opticum (Figs. A4.4K–L).

The interorbital septum rostral of the foramen opticum is robust, and the optic nerve divides rostrolaterally into two well defined branches of the chiasma opticum (e.g. Figs. 4.3A–B).

#### 4.3.1.3 The trigeminal nerve (V)—is a complex nerve comprising three divisions.

The medial or ophthalmic branch carries the ophthalmic nerve ( $V_1$ ), and passes rostrally from the trigeminal ganglion on the ventral surface of the mesencephalon (see 4.3.2.5 below), through the foramen n. ophthalmici (**foph**; Figs. A4.4K–L, A4.5K,  $V_1$ , Fig. A4.5L), to open into the ‘lacerate (presphenoid) fossa’ (*sensu* Worthy et al. 2016b:fig 1D), located ventrolaterally from the foramen opticum, between the laterosphenoid and the basisphenoid, parasphenoid, and interorbital septum on the rostromedial wall of the orbit. In dromornithids, the foramen n. ophthalmici is paired with the foramen n. abducentis, which transmits the abducent nerve rostrally ( $VI$ , see below). The lateral or maxillomandibular branch of the trigeminal ganglion, carries the maxillary nerve ( $V_2$ ) and the mandibular nerve ( $V_3$ ), both of which exit the skull rostroventrolaterally at the foramen n. maxillomandibularis (**fm**, Figs. A4.4K–L, A4.5K–L), a single opening between the prootic and laterosphenoid bones of the skull. In dromornithids, the maxillomandibular branch is distinctive in that it is markedly elongate, transmitting the  $V_2$  and  $V_3$  cranial nerves minimally 20 mm (in *Dromornis*) rostroventrolaterally, prior to exiting the skull at the foramen n. maxillomandibularis (**fm**, Figs. A4.4K–L, A4.5K,  $V_2+V_3$ , Fig. A4.5L).

4.3.1.4 The abducent nerve ( $VI$ )—inserts on the rostroventral rhombencephalon and is transmitted caudoventrally through the bony canalis n. abducentis, after entering the skull at the foramen n. abducentis, which in dromornithids is paired with the foramen n. ophthalmici, forming a single bi-lobal foramen in the rostromedial os laterosphenoidale structures of the orbit (**fa**; Figs. A4.4K–L, A4.5K,  $VI$ , Fig. 4.5L; and above).

4.3.1.5 The facial nerve ( $VII$ )—inserts at the rostroventrolateral edge of the rhombencephalon (Fig. 4.3D), and shares with the vestibulocochlear nerves ( $VIIIr$  and  $VIIIc$ , see below), the single external vestibular ganglion within the bony fossa acustica interna, wherein the nerves diverge. The divergence of these three nerves are distinct in the higher resolution *D. planei* data, but in the lower resolution *D. murrayi* and *I. woodburnei* data, the divergence was indistinguishable. Thus, a single landmark was used to capture the eminence of the vestibular ganglion incorporating the  $VII$ ,  $VIIIr$  and  $VIIIc$  cranial nerves (see General Methods, A2.1, Fig. 2.1). The facial nerve shares the ostium canalis carotici (**occ**; Figs. A4.4M–N) with several carotid vessels, which enter the skull caudoventrolaterally of the occipital condyle (**oc**; Figs. A4.4M–N) on the caudoventral os exoccipitale surface.

4.3.1.6 The vestibulocochlear nerve ( $VIII$ )—comprises two vestibular rami. The rostral ramus ( $VIIIr$ ) runs alongside the facial nerve ( $VII$ —see above) in the vestibular ganglion, and separates within the fossa acustica interna. The caudal ramus ( $VIIIc$ ) diverges in the fossa acustica interna, and inserts into the lateral semicircular duct (**lsd**, Fig. 4.4) of the vestibular organ (**vo**, Fig. 4.3A). For landmarking purposes, the vestibulocochlear ( $VIII$ ) and facial nerves ( $VII$ ), were captured with a single landmark (see above, and General Methods, A2.1, Fig. 2.1).

**4.3.1.7 The glossopharyngeal nerve (IX)**—inserts caudoventrolaterally on the rhombencephalon, and forms the rostral component of the combined root proximal ganglion (**gpr**, Fig. 4.4C) with n. vagus (X, see below). The proximal ganglion is enclosed in the fovea ganglii vagoglossopharyngealis, in the lamina parasphenoidalis of the fossa cranii caudalis between the exoccipital and opisthotic bones. The nerve enters the skull caudoventrolaterally from the vagus nerve (X) at the foramen n. glossopharyngeus (**fg**; Figs. A4.4M–N), situated in the fossa parabasalis. In dromornithids, the glossopharyngeal (IX) and vagus (X) nerves separate somewhat caudoventrolaterally from the eminence of the proximal ganglion from the rhombencephalon structure (Figs. 4.3D, 4.4C). The separation of the glossopharyngeal (IX) and vagus (X) nerves in dromornithids is similar to, but occurs to some extent further distally, than the condition seen in *A. semipalmata* (Fig. 4.4G), but is distinct to that seen in *A. cornuta* (Figs. 4.4K), and the megapodiid *L. ocellata* (Figs. 4.4O).

**4.3.1.8 The vagus nerve (X)**—forms the caudal ramus of the proximal ganglion, with which it shares with the glossopharyngeal nerve (IX—see above, Fig. 4.3D). The nerves bifurcate distad to the proximal ganglion (see above), and are transmitted from the separate parabasal fossa: foramen n. vagi (**fv**), and foramen n. glossopharyngeus (**fg**) respectively, situated ventrolaterad to the occipital condyle, on the caudoventral os exoccipitale surface (see Figs. A4.4M–N).

**4.3.1.9 The hypoglossal nerves (XII)**—comprise dorsal and ventral rami (XIId, XIIv, respectively; see Introduction, Fig. 1.5.1), which in dromornithids appear represented by one nerve eminence at either side of the caudoventrolateral medulla oblongata (Fig. 4.4C **arrow**). This condition is distinct to that seen in *A. semipalmata* (Fig. 4.4G), *A. cornuta* (Fig. 4.4K), and *L. ocellata* (Fig. 4.4O), where the hypoglossal nerve complex in these extant taxa comprise ventral (XIIv) and dorsal (XIId) rami. In dromornithids, the nerves transmit through a single canalis n. hypoglossi, and bifurcate in close proximity with the external surface of the os exoccipitale, at the paired foramen n. hypoglossi (**fh**, Figs. A4.4M–N). Thus, the hypoglossal nerve complex was captured with a single landmark at the eminence of the hypoglossal root, on either side of the caudoventrolateral medulla oblongata (see General Methods, **A2.1**, Fig. 2.1).

## 4.3.2 Characteristics of dromornithid endocranial morphology

The characteristics of the dromornithid brain is ascertained with reference to the endocast models of *Dromornis planei* (NTM P9464-106; Figs. 4.3A–D), *D. murrayi* reconstruction (QM F57984 + QM F57974, [see Fig. A4.9], Figs. 4.3E–H), and *Ibandornis woodburnei* (QVM:2000:GFV:20; Figs. 4.3I–L).

**4.3.2.1 Rostral telencephalon**—the external morphology of the rostral telencephalon as defined here (see Introduction, **1.5.3.2.3**; General Methods, Fig. 2.1, Appendices, **A2.3.1.3**), evident rostradorsally of the medial cerebral artery (**acm**, see Fig. 4.4; and Introduction, Fig. 1.5.1) in both anseriforms, and somewhat less so in galliforms, is notably absent in dromornithids. I prefer the

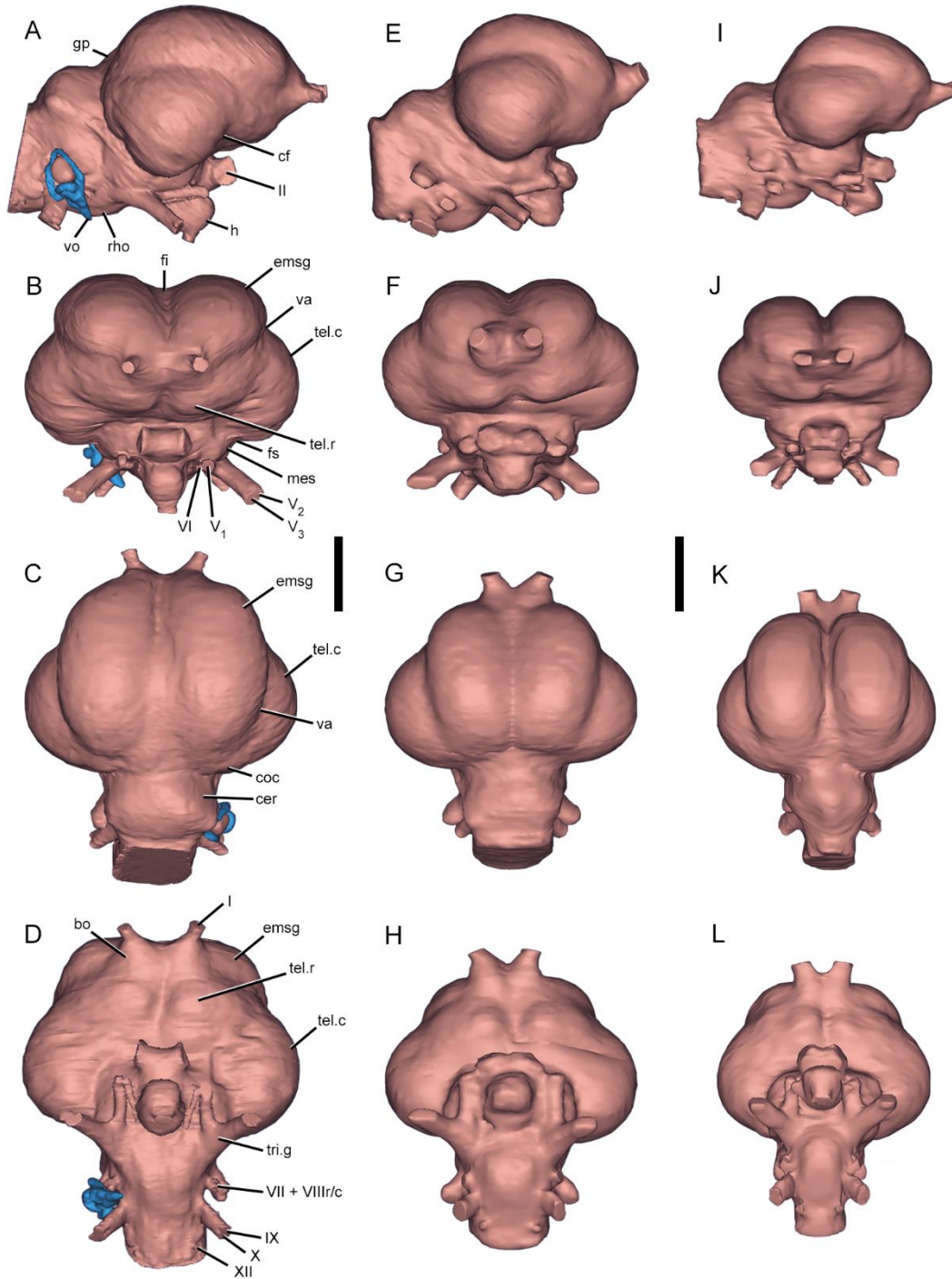


Figure 4.3. Dromornithid endocasts showing relative size differences between taxa: **A–D**, *Dromornis planei* (NTM P9464-106); **E–H**, *D. murrayi* reconstruction (QM F57984 + QM F57974—see Fig. A4.9); **I–L**, *Ibandornis woodburnei* (QVM:2000:GFV:20). **Views.** RHS lateral (**A, E, I**); rostral (**B, F, J**); dorsal (**C, G, K**); ventral (**D, H, L**). Trigeminal nerves (**V<sub>1</sub>**, **V<sub>2</sub>**, **V<sub>3</sub>**) are truncated approximately where exiting the neurocranium. **Abbreviations**, **bo**, bulbus olfactorius; **cer**, cerebellum; **cf**, cerebrum fovea limbica; **coc**, cerebrum pars occipitalis; **emsg**, eminentia sagittalis; **gp**, glandula pinealis; **h**, hypophysis; **mes**, mesencephalon; **mm**, millimetres; **fi**, fissura interhemispherica; **fs**, fissura subhemispherica; **tel.c**, caudal telencephalon; **tel.r**, rostral telencephalon; **tri.g**, trigeminal ganglion; **rho**, rhombencephalon; **RHS**, right hand side; **va**, vallecule telencephali; **vo**, vestibular organ (semicircular ducts + cochlea [blue]; see also 4.4.1.3); **I**, olfactory nerve; **II**, optic nerve; **V<sub>1</sub>**, ophthalmic nerve; **V<sub>2</sub>**, maxillary nerve; **V<sub>3</sub>**, mandibular nerve; **VI**, abducent nerve; **VII + VIIIr/c**, rami of the facial nerve (VII), and the rostral (VIIIr) and caudal (VIIIc) vestibulocochlear nerves; **IX**, glossopharyngeal nerve; **X**, vagus nerve; **XII**, hypoglossal nerve. Scale bars equal 20 mm.

explanation that these structures in dromornithids have been engulfed rostromediolaterally by hypertrophy of the eminentia sagittalis (see below), and that the external remnants of rostral telencephalon morphology are only visible rostrally as twin eminences ventromediolateral of the olfactory bulb, on either side of the rostromedial surface of the dromornithid endocast (**tel.r**; Figs. 4.3B, 4.3D).

**4.3.2.2 Eminentia sagittalis**—in dromornithids are greatly hypertrophied and dominate the entire dorsal endocast morphology (**emsg**, Fig. 4.3). The eminentia sagittalis extend rostromediolaterally to effectively engulf the olfactory bulbs (see **4.3.1.1** above), and extend rostroventrally over the most rostral eminence of the rostral telencephalon, substantially overhanging the rostroventral surface of the brain when viewed from the ventral aspect (Figs. 4.3D, 4.3H, 4.3L). The eminentia sagittalis extend rostrolaterally and engulf the rostradorsal telencephalon (see above, Fig. 4.3), effectively masking the rostradorsal endocast morphology commonly observed in galloanseres (Fig. 4.4, see also Chapter 5, Figs. A5.1–A5.8). The eminentia sagittalis extend mediolaterally across the entire dorsal forebrain to the lateral vallecule transition zones, delimiting the boundaries between the mediolateral eminentia sagittalis, and the dorsolateral caudal telencephalon (see **4.3.2.4** below). The vallecule transition zones are well defined, as the eminentia sagittalis are strongly dorsolaterally expanded in these areas (**va**; Figs. 4.3C, 4.3G, 4.3K, 4.4B, 4.4D). Caudodorsally, the eminentia sagittalis grade into the cerebrum pars occipitalis (**coc**; Fig. 4.3C) in the region of the medial glandula pinealis (**gp**; Fig. 4.3A), rostrolaterad of the dorsomedial cerebellum (Fig. 4.3C). Notably, the dromornithid eminentia sagittalis structures are located somewhat rostrally on the dorsal endocast (e.g. Figs. 4.3C, 4.3G, 4.3K, 4.4D), such that they do not overlap the rostromedial eminence of the cerebellum from the lateral aspect (e.g. Figs. 4.3A, 4.3E, 4.3I, 4.4A), similar to the condition in the anhimid *Anhima cornuta* (Figs. 4.4I, 4.4L), and megapodiid *Leipoa ocellata* (Figs. 4.4M, 4.4P), and distinct to the condition seen in the anseriform *Anseranas semipalmata* (Figs. 4.4E, 4.4H).

**4.3.2.3 Hypophysis**—appears to be primarily involved in venous and arterial blood transmission for the brain, the description and functional interpretation of which is beyond the scope of this chapter. However, it is notable that the dromornithid hypophysis is a large and well defined structure, and is distinct in that it is robust and projects further rostroventrally than in other galloanseres (**h**; Figs. 4.3A, 4.3E, 4.3I, 4.4A, 4.4E, 4.4I, 4.4M; see also Chapter 5, Figs. A5.1–A5.4).

**4.3.2.4 Caudal telencephalon**—in dromornithids are well defined, and are delimited from the eminentia sagittalis by the vallecule transition zone dorsolaterally (**va**, Figs. 4.3B–C, 4.4B, 4.4D). The mediolateral hypertrophy of the caudal telencephalon begins approximately where the medial cerebral artery transitions the telencephalic hemisphere dorsoventrolaterally (**acm**, Figs. 4.4B, 4.4D). The caudal telencephalon extends ventrolaterally, approximately level (dorsoventrally) with the fissura subhemispherica (**fs**, Figs. 4.3B, 4.4B), and return medially somewhat acutely to grade into the

ventrolateral mesencephalon (see below). Caudally, the cerebrum pars occipitalis forming part of the dorsal caudolateral caudal telencephalon, grade into the dorsorostrrolateral pons and medulla oblongata structures forming the overall metencephalon complex rostromedial of the cerebellum, in the vicinity of the glandula pinealis dorsolaterally, and medially at the rostromedialateral metencephalon.

**4.3.2.5 Mesencephalon**—in dromornithids are somewhat visually inconspicuous structures in comparison to other galloansere taxa (**mes**, Figs. 4.4B vs 4.4F, 4.4J, 4.4N; see also Chapter 5, Figs. A5.1–A5.4). They are defined by a slight lateral hypertrophy of the ventromedial endocast ventrolaterad of the fissura subhemispherica, and rostrally by transition into the caudolateral chiasma opticum and tractus opticus structures. The mesencephalon grade caudally into the ventromedialateral metencephalon complex (see below, Figs. 4.3, 4.4A–D).

**4.3.2.6 Trigeminal ganglia**—receive the three divisions of the trigeminal nerve (V, see **4.3.1.3** above) and insert on the ventral surface of the mesencephalon (**tri.g**, Figs. 4.3D, 4.3H, 4.3L, 4.4A; see also Introduction, Fig. 1.5.1). The trigeminal ganglia form part of the Modular Lm suite, therefore, are described here (see **4.2.6.1** above, General Methods, **A2.1**, Fig. 2.1). The medial portion of the trigeminal ganglion carrying the ophthalmic nerve (n. ophthalmicus–V<sub>1</sub>), separates from the lateral branch carrying the maxillary (n. maxillaris–V<sub>2</sub>), and mandibular nerves (n. mandibularis–V<sub>3</sub>), and exhibits a small ganglionic bridge between the two primary eminences (Figs. 4.3D, 4.3H, 4.3L). The characteristics of the dromornithid trigeminal ganglia are distinctive, in that the maxillomandibular branch transmits minimally 20 mm (in *Dromornis* taxa) rostroventrolaterally, prior to exiting the skull at the foramen n. maxillomandibularis (see **4.3.1.3** above).

**4.3.2.7 Cerebellum**—in dromornithids is compressed rostrocaudally and expanded mediolaterally (Figs. 4.3C, 4.3G, 4.3K, 4.4D), and more so in *Dromornis* taxa. From the lateral aspect (see Figs. 4.3A, 4.3E, 4.3I, 4.4A), the dorsal rostroventral surface forms a shelf somewhat level with the dorsal lateral semicircular duct (**lsd**, Figs. 4.4C–D) of the vestibular organ (**vo**, Fig. 4.3A), before turning sharply ventrally in the vicinity of the dorsolateral auricula cerebelli, to grade into the caudodorsal medulla spinalis at the foramen magnum. Overall, the dromornithid cerebellum and the associated ventral rhombencephalon (medulla oblongata + pons; see below), form a comparatively distinctive hind brain in these birds.

**4.3.2.8 Rhombencephalon**—is the collective term describing the structures of the medulla oblongata and pons, forming the caudoventrolateral areas of the hindbrain. In dromornithids, the ventral surface is somewhat flat rostrocaudally and mediolaterally (i.e., not as ventrally curved as in other neornithine taxa, see Figs. 4.4, see also Chapter 5, Figs. A5.1–A5.8), and extends further rostrocaudally than it does mediolaterally.

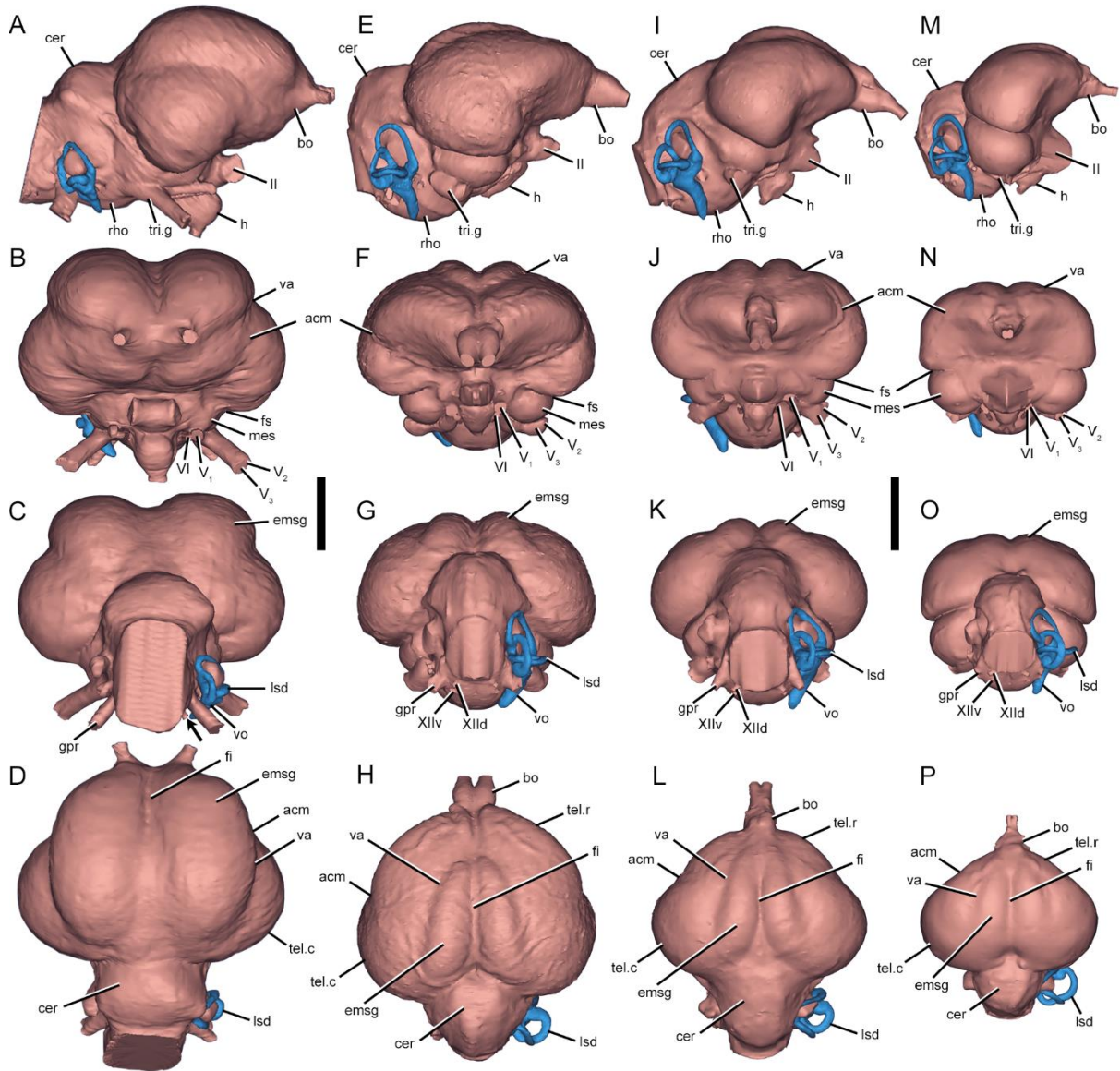


Figure 4.4. Galloansere endocasts: **A–D**, *Dromornis planei* (NTM P9464-106); **E–H**, *Anseranas semipalmata* (SAM B48035); **I–L**, *Anhima cornuta* (MV B12574); and **M–P**, *Leipoa ocellata* (SAM B11482). **Views**: RHS Lateral (**A, E, I, M**); Rostral (**B, F, J, N**); Caudal (**C, G, K, O**); Dorsal (**D, H, L, P**). Endocasts are orientated in approximate ‘alert posture’ with respect to the horizontal positioning of the lateral semicircular duct of the vestibular organ (semicircular ducts + cochlea [blue]; see also 4.4.1.3). Trigeminal nerves (**V<sub>1</sub>**, **V<sub>2</sub>**, **V<sub>3</sub>**) are truncated approximately where exiting the neurocranium. Scale bars equal 20 mm for **A–D** and 10 mm for **E–P**. **Abbreviations**, **acm**, medial cerebral artery; **bo**, olfactory bulb; **cer**, cerebellum; **emsg**, eminentia sagittalis; **fi**, fissura interhemispherica; **fs**, fissura subhemispherica; **gpr**, proximal ganglion (ganglion of the glossopharyngeal (XI) and vagus (X) nerves); **h**, hypophysis; **lsd**, lateral semicircular duct; **mes**, mesencephalon; **mm**, millimetres; **rho**, rhombencephalon; **RHS**, right hand side; **tel.c**, caudal telencephalon; **tel.r**, rostral telencephalon; **tri.g**, trigeminal ganglion; **va**, vallecule telencephali; **vo**, vestibular organ; **II**, optic nerve; **V<sub>1</sub>**, ophthalmic nerve; **V<sub>2</sub>**, maxillary nerve; **V<sub>3</sub>**, mandibular nerve; **VI**, abducent nerve; **XIIId**, dorsal and; **XIIv**, ventral rami of the hypoglossal (XII) nerve—the **arrow** (**C**) indicates the dromornithid combined dorsal and ventral ramus of the hypoglossal (XII) nerve.

### 4.3.3 Endocast comparisons between dromornithid taxa

Modular shape distinctions as described by 3D modular shape variance plots (see Figs. 4.7–4.9, and 4.2.7.1 above) accompanying Modular Distance and Surface Area ratio results (see Tables A4.1–A4.2, Figs. 4.5–4.6, A4.10–A4.11) are presented below with respect to endocast morphological distinctions between dromornithid taxa. [Note: as dromornithid rostral telencephalon structures are entirely masked by the dorsal eminentia sagittalis (see 4.3.2.1 above), landmarked comparisons of these structures were not practicable].

#### 4.3.3.1 *Dromornis* taxa—*D. murrayi* vs. *D. planei*

I first compare *Dromornis murrayi* and *D. planei* to assess the morphological transition in this genus from the Late Oligocene through the middle Miocene periods.

**4.3.3.1.1 Eminentia sagittalis modules**—3D modular shape variance plots of the eminentia sagittalis of *D. planei* and *D. murrayi* (Fig. 4.7E) show that between the ~20 Ma *D. murrayi* and the ~12 Ma *D. planei*, there occurred a rostradorsal hypertrophy of the eminentia sagittalis that has largely engulfed the full extent of the olfactory bulb still visible in *D. murrayi* (Fig. 4.3E), i.e., olfactory morphology becomes less apparent in the younger *D. planei* (Fig. 4.3A). There is no evidence to suggest the olfactory bulb has reduced in relative size over time between these taxa, as the extent of the olfactory bulb of *D. planei* is visible from the ventral aspect (Fig. 4.3D), and appears to have increased in mediolateral width compared with that observed in *D. murrayi* (Fig. 4.3H). Furthermore, the rostralateral profile of the olfactory zone in *D. planei* (Fig. 4.3A), suggests the olfactory bulb of *D. planei* is minimally of comparable volume to that of *D. murrayi*, and has likely been incorporated within the rostral hypertrophy of the eminentia sagittalis, masking it from dorsal view in *D. planei*.

Not only has the hypertrophy of the eminentia sagittalis markedly increased the rostradorsal eminence of the structures in *D. planei* compared with *D. murrayi* (Figs. 4.7E, 4.7G), but results for Modular Distance data show length (0.359 vs 0.351, respectively; Table A4.1C); and width (0.302 vs 0.288, respectively; Table A4.1C) ratios of the eminentia sagittalis has increased as well (Fig. 4.5). This trend is reflected by an increase in the overall Modular Surface Area ratios (0.778 vs 0.760, respectively; Table A4.2C, Fig. 4.6), accompanied by an increase in the Perimeter ratio for eminentia sagittalis between taxa too (0.522 vs 0.519, respectively; Table A4.2D). In addition, mediolateral hypertrophy of these structures in *D. planei* has shifted the lateral margins of the eminentia sagittalis, displacing the vallecule transition zones between the dorsolateral eminentia sagittalis, and the dorsal caudal telencephalon somewhat ventrolaterally, in comparison with that of *D. murrayi* (Figs. 4.7F, 4.7G). Notably, the ventrolateral shifting of the vallecule transition zones in *D. planei* are more pronounced in the dorsal caudolateral regions of the endocast. The caudolateral eminentia sagittalis margins appear to have shifted laterally to a greater degree, with respect to the sagittal fissura interhemispherica zone, than occurred in the rostral regions of the endocast between taxa (Figs. 4.7E, 4.7F).

In summary, results show that the overall size of eminentia sagittalis increases somewhat between the Late Oligocene through the middle Miocene *Dromornis* taxa, particularly in the rostradorsal zones. This trend of hypertrophy has shifted the lateral margins of the eminentia sagittalis in the younger taxon, displacing the vallecule transition zones between the dorsolateral eminentia sagittalis, and the dorsal caudal telencephalon ventrolaterally.

**4.3.3.1.2 Caudal telencephalon modules**—the overall hypertrophy of the eminentia sagittalis in *D. planei* compared with that of *D. murrayi*, is associated with a compensatory ventral rotation of the dorsolateral surface of the caudal telencephalon. Resulting in the dorsolateral margins, defined by the vallecule, of the caudal telencephalon in *D. planei* becoming more ventrally orientated than in *D. murrayi* (Figs. 4.7G, 4.7H). The ventrolateral shifting of the vallecule transition zones, has translated to a positional displacement of the most ventral eminence of the caudal telencephalon in the area of the fissura subhemispherica too. Yet a similar dorsoventral and rostrocaudal caudal telencephalon shape is maintained in both taxa (Figs. 4.7G, 4.7H). However, while a similar shape has been preserved, there has occurred a dorsomediolateral reduction in the dorsoventral ‘profile’ of the caudal telencephalon in *D. planei*. Modular Distance data results show that the ventral rotation of these structures in *D. planei*, have resulted in an overall reduction in the dorsoventral width ratio with respect to *D. murrayi* (0.316 vs 0.326, respectively; Table A4.1C, Fig. 4.5). Along with a commensurate reduction in rostrocaudal length ratio for *D. planei* (0.333 vs 0.335, respectively; Table A4.1C, Fig. 4.5), but to a lesser degree. This is evident in the modular shape variance plots (Figs. 4.7G, 4.7H). These temporally negative trends are accompanied by a slight decrease in the Modular Surface Area ratios between *D. planei* and *D. murrayi* (0.741 vs 0.748, respectively; Table A4.2C, Fig. 4.6), with a corresponding reduction in the Perimeter ratio for the caudal telencephalon (0.491 vs 0.493, respectively; Table A4.2D).

In summary, results show the overall size of the caudal telencephalon reduces somewhat, between the Late Oligocene through the middle Miocene *Dromornis* taxa. However, the characteristic shape of the structures in the areas of the mesopallium dorsally, and particularly in the arcopallium ventrally, are maintained within the *Dromornis* lineage.

**4.3.3.1.3 Cerebellum module**—3D modular shape variance plots of the cerebellum of *D. planei* and *D. murrayi* (Figs. 4.8E, 4.8F), are suggestive of a rostradorsal hypertrophy of this structure in *D. planei* (Figs. 4.8E, 4.8H). Although the overall modular perimeter appears similar between the taxa when viewed from the dorsal aspect (Fig. 4.8F), results for Modular Surface Area data results show that the cerebellum of *D. murrayi* has a larger Perimeter ratio than that of *D. planei* (0.496 vs 0.491 respectively; Table A4.2D). However, it appears the Surface Area ratio increased somewhat between these taxa (0.687 vs 0.693 respectively; Table A4.2C, Fig. 4.6), likely affected by rostradorsal hypertrophy of the *D. planei* cerebellum with respect to that of *D. murrayi*, occurring to a greater degree rostradorsally, than caudadorsally in the vicinity of the medulla spinalis (Figs. 4.8E, 4.8H). These observations are supported Modular Distance data results for *D. planei* and *D. murrayi*,

which show an increase in length ratios (0.259 vs 0.244, respectively; Table A4.1C, Fig. 4.5), and width ratios (0.324 vs 0.311, respectively; Table A4.1C, Fig. 4.5) between species.

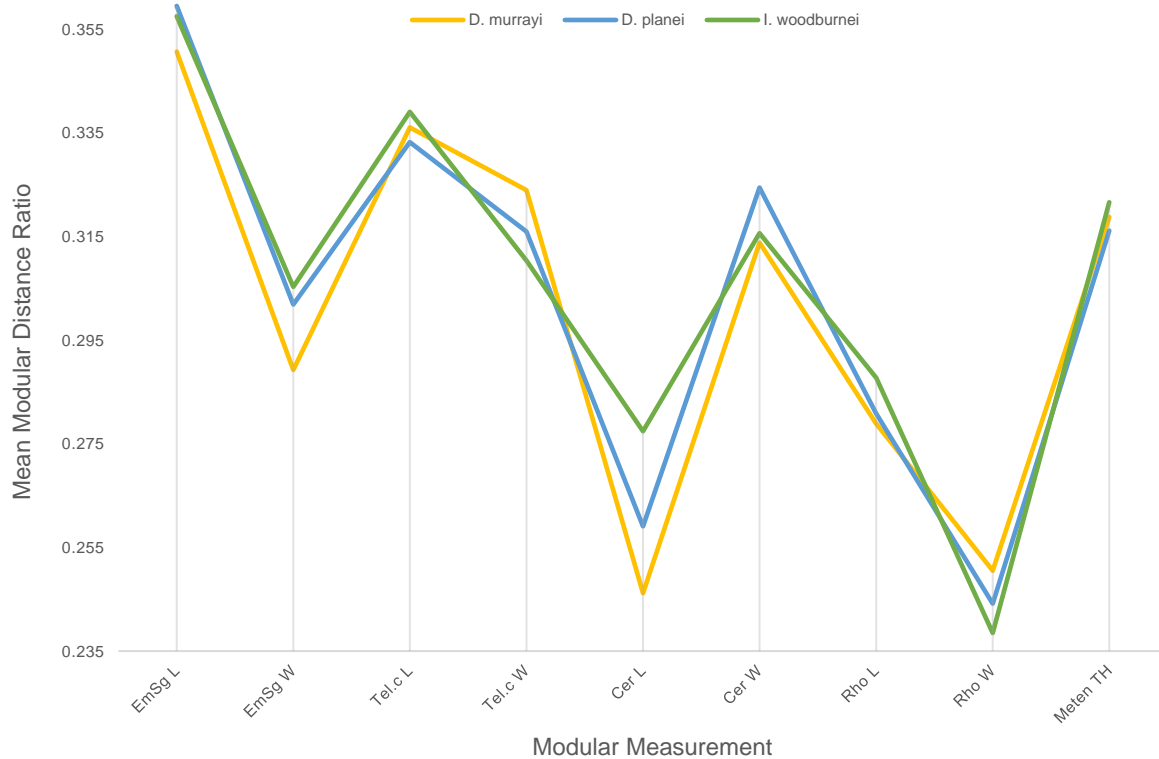


Figure 4.5. Mean Modular Distance and Linear Distance ratios plot for dromornithid taxa. Ratios are size-standardised by dividing  $\log_{10}$  transformed mean Modular Distance and Linear Distance values by  $\log_{10}$  transformed specimen endocast volume (see Tables A4.1C–D, Methods, 4.2.6.2-3).

**Abbreviations,** **Cer L**, cerebellum length; **Cer W**, cerebellum width; **D. murrayi**; *Dromornis murrayi* reconstruction (QM F57984 + QM F57974); **D. planei**; *Dromornis planei* (NTM P9464-106); **EmSg L**, eminentia sagittalis length; **EmSg W**, eminentia sagittalis width; **I. woodburnei**; *Ibandornis woodburnei* (QVM:2000:GFV:20); **Mes L**, mesencephalon length; **Mes W**, mesencephalon width; **Meten TH**, metencephalon total height; **mm**, millimetres; **Rho L**, rhombencephalon length; **Rho W**, rhombencephalon width; **Tel.c L**, caudal telencephalon length; **Tel.c W**, caudal telencephalon width.

The differences in Modular Distance ratios are likely describing the increase in cerebellum rostradorsal height between *D. murrayi* and *D. planei*. As the Modular Distance data captures the individual vectors between Lms describing the directional curve over a modular structure (see General Methods, Fig. 2.2B). These data are likely representative of the transition to a higher dorsal cerebellum surface in *D. planei*, relative to ventrolateral boundaries. Although the changes in Modular Distance length and width ratios are distinct, the differences in overall Modular Surface Area ratios between *D. planei* and *D. murrayi* are less pronounced (0.693 vs 0.687, respectively; Table A4.2C, Fig. 4.6).

In summary, results show that while there occurred rostradorsal hypertrophy in the cerebellum between the Late Oligocene through the middle Miocene taxa assessed here, these changes were not substantial. Overall, the cerebellum retains a structural form that describes distinctly similar rostrocaudal and mediolateral cerebellum characteristics for *Dromornis* taxa, trends similar to those seen in the caudal telencephalon (see **4.3.3.1.2** above).

**4.3.3.1.4 Rhombencephalon module**—results for Modular Distance data show that *D. planei* has a larger overall length ratio for the rhombencephalon than *D. murrayi* (0.281 vs 0.277, respectively; Table A4.1C, Fig. 4.5). Similarly, the width ratio for *D. planei* is smaller compared with that of *D. murrayi* (0.244 vs 0.248, respectively; Table A4.1C, Fig. 4.5). The ventral position of the rhombencephalon relative to the dorsal morphology of the endocast, has apparently shifted dorsally during this period as well (Figs. 4.8G–H). While it could be argued that the accurate placement of the rhombencephalon structure in *D. murrayi* may be compromised, due to the endocast being a reconstruction of two specimens, and thus may not be representative of the taxon. The ventral regions of the *D. murrayi* reconstruction, including the cerebellum and the rhombencephalon, were sourced from a single specimen, and only the dorsal surface of the endocast was reconstructed (see Fig. A4.9, and **4.2.4.4** above). Furthermore, the positioning of the lateral boundaries of the cerebellum (Figs. 4.8E–F, 4.8H) imply they are comparatively orientated, and that the more ventral location of the rhombencephalon in *D. murrayi* (Figs. 4.8G–H), represents an accurate morphological state for the taxon. In support of this, the form of the rhombencephalon preserved in the fossil endocast of *D. murrayi* (Fig. A4.3A), suggests the rhombencephalon in *D. murrayi* does project further ventrally than it does in *D. planei*. Therefore, the reconstructed endocast model of *D. murrayi* (Figs. 4.3E, A4.3B) likely represents the form of the rhombencephalon accurately. If this is indeed the case, then there occurred a dorsal displacement of rhombencephalon surface between *D. planei* and *D. murrayi*, accompanied with an increase in Modular Surface Area ratios (0.659 vs 0.630, respectively; Table A4.2C, Fig. 4.6), and a reduction in the mediolateral and rostrocaudal profile of the rhombencephalon in *D. planei* (Figs. 4.8G–H). This suggests that the rhombencephalon develops an overall ‘flatter’ mediolateral and rostrocaudal shape, between the Late Oligocene through the middle Miocene. The morphological changes seen in the dorsal cerebellum and ventral rhombencephalon described above, are reflected in Linear Distance ratios for the metencephalon (cerebellum + pons, see General Methods, Fig. 2.2G, and **4.2.6.3** above), between *D. planei* and *D. murrayi* (0.316 vs 0.319, respectively; Table A4.1D, Fig. 4.5). It appears the development of a ‘taller’ rostral cerebellum and shallower rhombencephalon profile in *D. planei* results in a somewhat reduced total height of the hindbrain in *D. planei*. The differences between species are not substantial, likely accommodated by the lower cerebellum dorsal height and deeper rhombencephalon ventral projection in *D. murrayi*. However, Linear Distance ratios describing the total width of the medulla oblongata are somewhat smaller between *D. planei* and *D. murrayi* (0.316 vs 0.320, respectively; Table A4.1D).

In summary, these results show a dorsal displacement of the rhombencephalon surface between *D. planei* and *D. murrayi*, and the development of an overall ‘flatter’ mediolateral and rostrocaudal rhombencephalon profile in *D. planei*. These morphological changes were accompanied by a small decrease in overall dorsoventral height of the hindbrain, a decrease in the total width of the ventromedial hindbrain, along with an increase in Modular Surface Area of the rhombencephalon between the Late Oligocene through middle Miocene *Dromornis* taxa.

#### 4.3.3.2 *Dromornis* taxa—vs *D. stirtoni*

Two specimens of *D. stirtoni* derived from the Alcoota Local Fauna were modelled to capture the shape of this, the most geologically recent species of *Dromornis*, and compare it to the older forms. Landmarking of the specimens and resultant Modular Lm, Modular Distance and Surface Area data were not possible due to the incomplete nature of the *D. stirtoni* models. However, the overall appearance of endocasts of *D. stirtoni* are distinctive, in that they appear mediolaterally wider, dorsoventrally compressed rostrally, and somewhat rostrocaudally foreshortened, compared with the other dromornithid taxa assessed. These endocast differences were expected, given the highly derived and foreshortened nature of neurocrania in the taxon (see Fig. 4.1), which likely placed structural limits on the housing of the brain.

*D. stirtoni*-1 appears to have a reasonably well preserved neurocranium (Figs. A4.6A–H, A4.7A–H). However, the endocranial capsule within suffered taphonomic degeneration of the entire caudodorsal surfaces, directly affecting those areas of the endocast (Figs. A4.8D–E). What is preserved, are primarily the rostroventral endocast surfaces, including a part of the rostradorsal eminentia sagittalis, the olfactory zone, the rostromedial eminences of the rostral telencephalon, and the mediolateral expansion of the rostroventral caudal telencephalon. The LHS rostromedial eminentia sagittalis and rostral caudal telencephalon are less well preserved than the RHS, as the specimen has experienced a somewhat rostroventrolateral ‘drift’ of cortical bone, that has distorted the LHS of the endocast more so than the RHS (Fig. A4.8E). The rostroventral eminence of the mesencephalon are preserved, but the caudal eminences in the regions of the medial medulla oblongata are less well defined (Fig. A4.8D). The RHS ramus of the maxillomandibular branch transmitting the V<sub>2</sub> and V<sub>3</sub> cranial nerves rostroventrolaterally, is relatively well captured, but the LHS is only partially preserved (Fig. A4.8F). The hypophysis and the ventral rhombencephalon including the medulla oblongata, rostroventrad of the auricula cerebelli, are preserved, but the tubae auditivae are indistinguishable in the CT data. The caudoventral rhombencephalon surface is preserved, approximately to the eminence of the hypoglossal (XII) nerves, which are not present (Fig. A4.8D). In general, the gross rostroventral morphology in the specimen *D. stirtoni*-1 is discernible, and it has not suffered much overall distortion, but all fine detail has been lost through the taphonomic processes characteristic of the unconsolidated sediments of the Alcoota site (see 4.2.2 above).

*D. stirtoni*-2 had suffered the loss of the entire rostral, and much of the caudodorsal region of the neurocranium (Figs. A4.6I–L, A4.7I–P), and consequently preserves only part of the caudodorsal

eminentia sagittalis surfaces, of which the RHS is better represented, as the LHS appears to be somewhat rostroventrolaterally distorted (Fig. A4.8H). The mediolateral eminences of the caudal telencephalon are represented, but the terminal surfaces of these structures, more so on the LHS than the RHS, were not clearly discernible in the CT data with enough consistency to facilitate accurate modelling. *D. stirtoni*-2 preserves the rostradorsal cerebellum caudally to approximately the eminences of the auricula cerebelli, and also represents the caudoventral rhombencephalon surfaces reasonably well. The endocast is truncated caudoventrally in the region of the eminence of the hypoglossal (XII) nerves, and lacks fine scale detail overall (Figs. A4.8G–H).

Collectively, the endocasts of *D. stirtoni* allow for the appreciation of parts of the rostroventral surfaces (captured by *D. stirtoni*-1, Figs. A4.8D–E), and the caudodorsal surfaces (captured by *D. stirtoni*-2, Figs. A4.8G–H). Thus, an attempt to align these endocast models and associate endocast morphology with that of *D. planei* (Fig. A4.8A) was made (see also 4.2.4.3 above), allowing appreciation as to whether there exist any fundamental differences apparent in the shape of the *D. stirtoni* endocast, with reference to that of *D. planei*.

While there appears to be a disparity in the amount of lateral RHS and rostral endocast rescaling of the *D. planei* endocast (8% and 5% respectively; see 4.2.4.3), to best fit the *D. stirtoni* composite endocasts. The capturing of precisely aligned 2D images from 3D models between taxa is intrinsically difficult, and virtually impossible to align exactly. Attempts were made to fit and align images as accurately as possible, but the variability inherent in this process likely accounts for this scaling disparity, and a better estimation of how much larger the endocast of *D. stirtoni*-1 was than that of *D. planei*, is most likely in the region of 6.5%. In addition, considerable disparity has been shown in the relative size within species of dromornithids. For example, [Handley et al. \(2016\)](#) identified ~14 % variation amongst *D. stirtoni* postcranial fossils from Alcoota, and attributed this variation to sexual dimorphism. *D. stirtoni*-1 and *D. stirtoni*-2 both comprise the largest crania known of the taxon, show considerable size differentiation, and are likely representative of a larger and smaller male, or a large male and a large female of the species.

**4.3.3.2.1 Eminentia sagittalis**—in all dromornithid taxa are much hypertrophied structures. However, these areas are least well preserved in specimens of *D. stirtoni*. Although an accurate assessment of the true extent of the eminentia sagittalis in *D. stirtoni* is not possible over the whole rostrocaudal endocast surface, several individual CT slices of raw scan data for the *D. stirtoni*-2 specimen preserve elements of the mediolateral eminentia sagittalis profile.

Fig. A4.8L shows a CT slice for *D. stirtoni*-2, where the cortical bone defining the dorsal eminentia sagittalis is caudally displaced from its original position, but maintains the shape of the dorsal mediolateral curve of the RHS eminentia sagittalis well. The slice also visualises cortical bone elements of the dorsal curve of the LHS eminentia sagittalis that have displaced into several fragments over time. Another interpretation of these fragments is that they may be calcite crust lining, formed upon the actual cortical bone of the endocranial capsule, through the wetting and drying phases the

substrate surrounding these fossils underwent over time (see 4.2.2 above). Either interpretation affords a description of the a mediolateral endocranial profile in this area of the skull, very similar to that seen in other dromornithid taxa. For example, Fig. A4.8C shows a CT slice of the mediolateral profile of the Oligo-Miocene specimen of *D. murrayi* (QM F57984), and describes dorsal margins of the

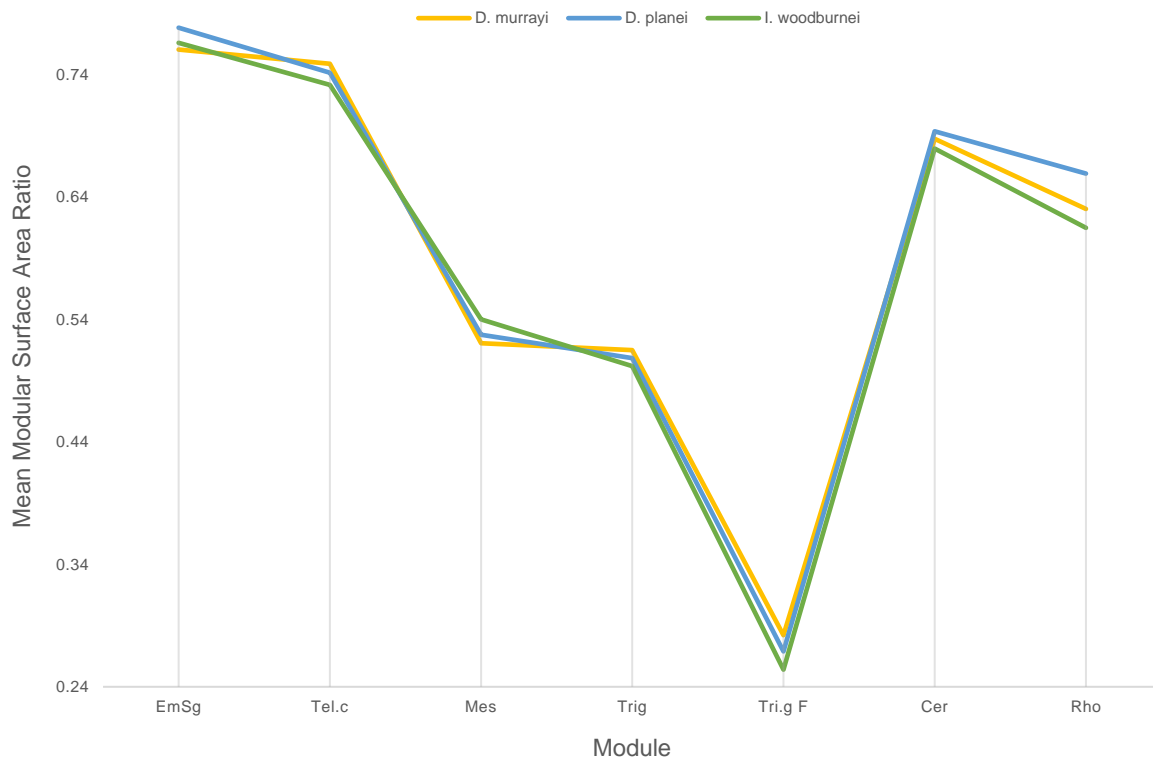


Figure 4.6. Mean Modular Surface Area ratios plot for dromornithid taxa. Ratios are size-standardised by dividing  $\log_{10}$  transformed mean Modular Surface Area values by  $\log_{10}$  transformed total endocast surface area values (see Tables A4.2C–D, Methods 4.2.6.4). **Abbreviations**, **Cer**, cerebellum; **D. murrayi**; *Dromornis murrayi* reconstruction (QM F57984 + QM F57974); **D. planei**; *Dromornis planei* (NTM P9464-106); **EmSg**, eminentia sagittalis; **I. woodburnei**; *Ibandornis woodburnei* (QVM:2000:GFV:20); **Mes**, mesencephalon; **Rho**, rhombencephalon; **Tel.c**, caudal telencephalon; **Tri.g**, trigeminal ganglion; **Tri.g F**, cross-section of the maxillomandibular ( $V_2+V_3$ ) branch of the trigeminal (V) nerve (see Fig. 4.3B).

eminentia sagittalis which are similar to those seen in the CT slice, from a similar location, of the middle-Miocene *D. planei* cranium (Fig. A4.8F). Additionally, the reconstruction of the RHS lateral profile of *D. stirtoni* (Fig. A4.8J), and the RHS of the rostral reconstruction (Fig. A4.8K), show the dorsal surfaces of the eminentia sagittalis preserved in *D. stirtoni*, closely resemble that of *D. planei*. Taken together, these images suggest the eminentia sagittalis in *D. stirtoni* likely described a comparable dorsal profile (Fig. A4.8L), and did not differ greatly from the dorsal endocast shape typical of dromornithid endocast anatomy identified here.

**4.3.3.2.2 Caudal telencephalon**—*D. stirtoni* displays the typical state of dromornithids of a clear vallecule transition zone between the dorsal eminentia sagittalis, and the mediolaterally

hypertrophied caudal telencephalon (Figs. A4.8D–E). The cerebrum fovea limbica zone preserved in the endocast of *D. stirtoni*-1, agrees with that seen in *D. planei*, and suggests the specimens share a similar transition into the dorsal caudal telencephalon. The obvious presence of the rostral telencephalon eminences on the rostroventrolateral surface of the endocast of *D. stirtoni*-1, are indicative of typical dromornithid rostroventral endocast morphology. CT slice images suggest *D. stirtoni* had mediolaterally hypertrophied caudal telencephalon (Figs. A4.8L), comparable to those seen in *D. murrayi* (Fig. A4.8C) and *D. planei* (Fig. A4.8F). Additionally, the brain of *D. stirtoni*, relative to *D. planei*, is dorsoventrally compressed, represented as an effective reduction in the most ventral eminence of the caudal telencephalon, in the area of the arcopallium (Figs. A4.8J–K). However, more complete specimens would be required to support these observations.

Notably, along with this measure of caudodorsal compression in *D. stirtoni*, there is a rostradorsal rotation of the forebrain endocast surfaces, compared with that of *D. planei*, with reference to the positioning of the olfactory zones, and the eminences of the rostral telencephalon (Figs. A4.8J–K). The hypophysis and the ramus of the maxillomandibular nerves in the ventral midbrain are well aligned between the taxa in the reconstruction (Fig. A4.8J), but rostradorsally from the tractus opticus structure in *D. stirtoni*, all forebrain structures appear rotated around the medial caudal telencephalon into a more dorsally oriented aspect. This rotation is also apparent in the rostral reconstruction (Fig. A4.8K), where the eminence of the olfactory (I) nerves appear to have shifted dorsally, to approximately the same degree as seen in the RHS lateral reconstruction (Fig. A4.8J).

In summary, these comparisons suggest *D. stirtoni* had a mediolaterally hypertrophied caudal telencephalon, comparable to those seen in other *Dromornis* taxa, but with a measure of reduction in the most ventral eminence of the caudal telencephalon in the area of the arcopallium. Additionally, rostradorsally from the tractus opticus structures, all forebrain structures in *D. stirtoni* appear rotated around the medial caudal telencephalon, into a more dorsally oriented aspect.

**4.3.3.2.3 Cerebellum**—are visible only from the RHS lateral aspect between taxa (Fig. A4.8J), and show that the dorsal surface of the cerebellum in *D. stirtoni* describes a similar rostrocaudal shape as that of *D. planei*, but the dorsal cerebellum appears more ventrally orientated. The positioning of the cerebellum dorsorostrorocaudal surface appears accurate, as the alignment of the ventral rhombencephalon, reasonably well preserved in both specimens, defined the position of the dorsal cerebellum in the process of reconstruction. Also, the position of the caudal eminentia sagittalis in *D. stirtoni* agrees with the caudal eminentia sagittalis of *D. planei*, both structures of which are derived from a single specimen (*D. stirtoni*-2). These observations suggests the apparent ventral displacement of the dorsal cerebellum surface in *D. stirtoni*, may be representative of a compensatory ventral rotation of the caudodorsal hindbrain, with respect to the rostradorsal rotation evident in the forebrain of *D. stirtoni* (see above).

**4.3.3.2.4 Rhombencephalon**—this structure in *D. stirtoni* appears to be more ventrally situated than that of *D. planei* (Fig. A4.8J). Additionally, the distance separating the location of the

rhombencephalon in *D. planei*, and those of the two specimens of *D. stirtoni*, more or less equates to the distance the dorsal surfaces of the cerebellum have displaced ventrally, and is similar to the distance the rostroventral zones of the forebrain have rotated dorsally (see above). In effect, the brain of *D. stirtoni* appears rotated about the median plane, whilst the position of the dorsomedial surfaces of the brain have been maintained, effectively foreshortening the overall rostrocaudal length of the endocast.

#### 4.3.3.3 Dromornithid taxa—*D. planei* vs. *I. woodburnei*

Fossils of these dromornithids are derived from the middle-Miocene Bullock Creek LF and are presumed similar in age. Comparison of these taxa enables assessment of morphological differences between the two contemporaneous dromornithid lineages.

**4.3.3.3.1 Eminentia sagittalis modules**—the 3D modular shape variance plots of the eminentia sagittalis of *D. planei* and *I. woodburnei* (Figs. 4.7I, 4.7J), show the rostradorsal hypertrophy of the eminentia sagittalis, that has largely engulfed the full extent of the olfactory bulb visible in *D. murrayi* (Fig. 4.3E), has similarly occurred in *I. woodburnei*, where the dorsal surface of the olfactory bulb appears entirely engulfed by the rostradorsal eminentia sagittalis in the taxon (Fig. 4.3I). Also, the differences in the rostradorsal eminentia sagittalis apparent between *D. planei* and *I. woodburnei* (Figs. 4.7I, 4.7J), are not as profound in those differences in these structures between *D. planei* and *D. murrayi* (see 4.3.3.1.1 above; Figs. 4.7E, 4.7F). The primary difference between *D. planei* and *I. woodburnei* occurs in the rostral regions of the eminentia sagittalis, where those of *D. planei* extend further rostradorsally (Figs. 4.7I, 4.7J). Results for Modular Distance data show only small differences in overall length (0.359 vs. 0.357, respectively; Table A4.1C), and width (0.302 vs. 0.305, respectively; Table A4.1C) ratios between these taxa (Fig. 4.5). The slight increase in the caudal mediolateral width ratio of the eminentia sagittalis in *Ibandornis* (Fig. 4.5), is likely due to the deeper fissura interhemispherica transition zone between the paired eminentia sagittalis structures, that effectively places the medial margins of the eminentia sagittalis in *I. woodburnei*, closer together than in species of *Dromornis* (see Figs. 4.7I, 4.7M, 4.9H, 4.9I, 4.9K, 4.9L, and 4.3.3.4.1 below). Additionally, the dorsolateral margin of the vallecule transition zones between the eminentia sagittalis and the caudal telencephalon, are more ventrolaterally located in *D. planei* (Figs. 4.7J–L, 4.9G), but the apparent ventrolateral distance differential in this zone, is offset by the dorsoventrally deeper fissura interhemispherica transition zone in *I. woodburnei* (Fig. 4.9I). This results in the mediolateral Modular Distance width ratio for eminentia sagittalis of *I. woodburnei*, being slightly larger compared to that of *D. planei* (Table A4.1C, Fig. 4.5).

Vallecule transition zones between the caudolateral eminentia sagittalis and the caudodorsal caudal telencephalon in *D. planei*, shift somewhat ventrolaterally in comparison with that of *I. woodburnei* (Figs. 4.7K, 4.9G), a shift which is more pronounced caudally than rostrally. This distinction is likely better captured by results for Modular Surface Area data, which describe a trend of a somewhat larger ratios in the *Dromornis* taxon when endocast size is accounted for. For example,

the Perimeter ratio for eminentia sagittalis of *D. planei* is greater than that of *I. woodburnei* (0.522 vs 0.520, respectively; Table A4.2D), and the Surface Area ratio is similarly greater (0.778 vs 0.765, respectively; Table A4.2C, Fig. 4.6). The disparity between a slightly larger Perimeter ratio, accompanying a greater difference in the Surface area ratio of the eminentia sagittalis between these taxa, likely reflects the greater rostradorsal hypertrophy of the structures in the *Dromornis* taxon as evidenced by the shape variation plots (Figs. 4.7I–K, 4.9G–H).

In summary, the main distinction between the eminentia sagittalis of *D. planei* and *I. woodburnei*, is in rostradorsal hypertrophy of the eminentia sagittalis. However, Modular Distance ratios show only small differences in overall length, but with a slight increase in the caudal mediolateral modular width of the eminentia sagittalis in *I. woodburnei*. This is likely due to the deeper fissura interhemispherica transition zone between the paired eminentia sagittalis structures, that places the medial margins of the eminentia sagittalis in *I. woodburnei* closer together, than in *Dromornis* taxa (see also 4.3.3.4.1 below). However, when endocast size is accounted for, *D. planei* shows somewhat larger Modular Surface Area ratios for eminentia sagittalis than *I. woodburnei*.

It is unclear whether a deeper fissura interhemispherica is characteristic of *Ilbandornis* species and more data (i.e., additional well preserved *I. woodburnei* specimens) are required to clarify this observation. However, if this is indeed the case, it likely represent a distinctive endocranial apomorphy between the two lineages.

**4.3.3.3.2 Caudal telencephalon modules**—the rostral and rostradorsal margins of the caudal telencephalon are comparable between *D. planei* and *I. woodburnei*, except for the dorsal caudolateral differences in the vallecule zone described above. However, Modular Distance data results show the caudal and ventral margins are distinctive in *I. woodburnei*, which has a greater rostrocaudal length ratio than *D. planei* (0.339 vs 0.333, respectively; Table A4.1C, Fig. 4.5), primarily occurring in the area of the cerebrum pars occipitalis (Fig. 4.7K). In addition, the dorsoventral width of the caudal telencephalon in *I. woodburnei*, is markedly less than in *D. planei*, where the most ventral eminence of the caudal telencephalon, in the area of the fissura subhemispherica, is noticeably less pronounced (Figs. 4.7K, 4.7L). Modular Distance ratios show the dorsoventral width of the caudal telencephalon of *I. woodburnei* is less than that of *D. planei* (0.310 vs 0.316, respectively; Table A4.1C, Fig. 4.5). In fact, it is less than those of both *Dromornis* taxa assessed (see 4.3.3.4.2 below). Interestingly, Modular Surface Area data results for the caudal telencephalon, show that *D. planei* has a smaller Perimeter ratio than *I. woodburnei* (0.491 vs 0.495, respectively; Table A4.2D), reflecting the rostrocaudally longer, but dorsoventrally narrower shape of the caudal telencephalon, in the *Ilbandornis* taxon.

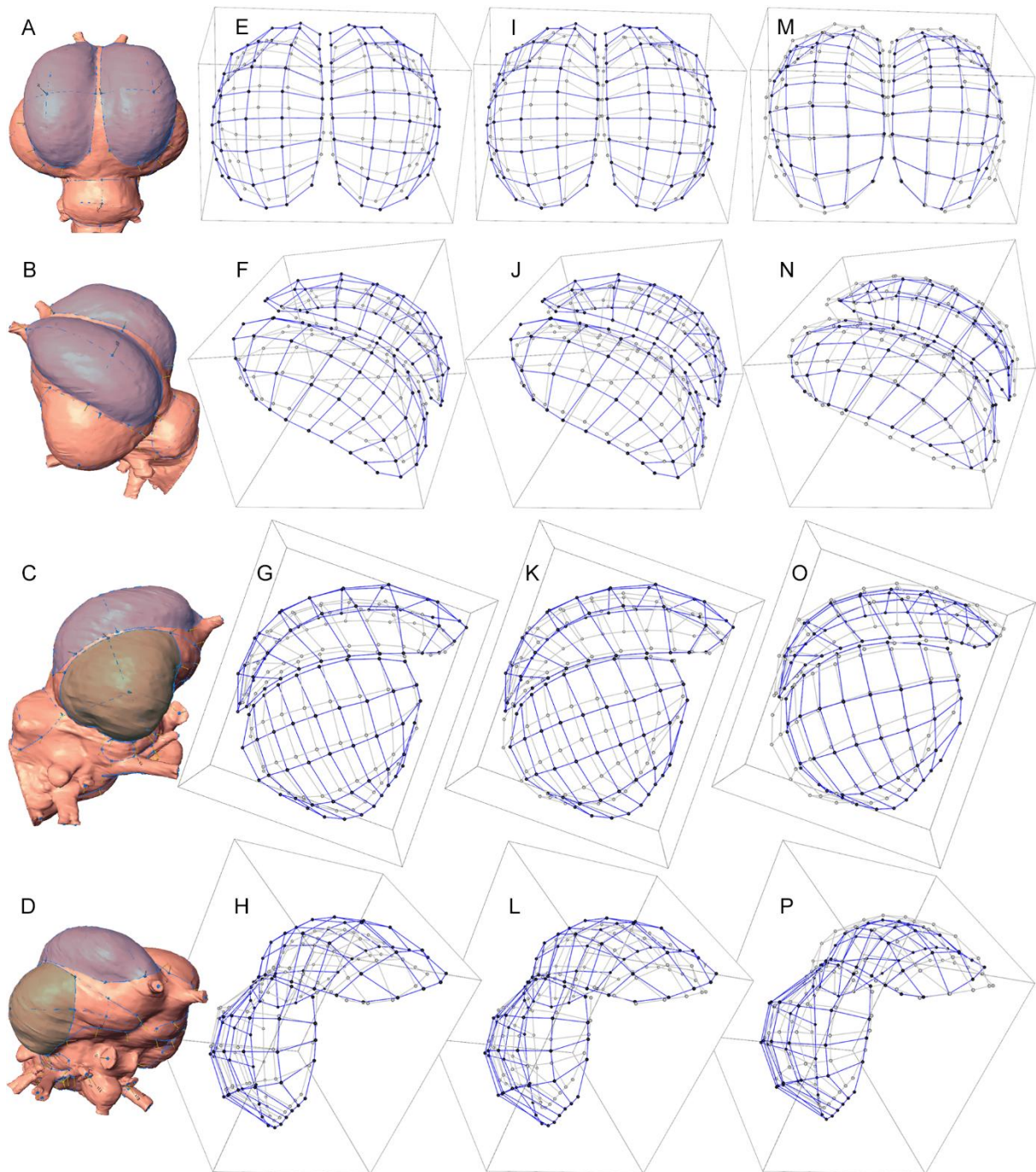


Figure 4.7. Three dimensional modular shape variance plots for dromornithid taxa (see 4.2.7.1). **A**, *Dromornis planei* (NTM P9464-106) endocast showing the caudodorsal view of the eminentia sagittalis modules represented in plots **E**, **I**, and **M**; **B**, *D. planei* endocast showing the LHS dorsolateral view of the eminentia sagittalis modules represented in plots **F**, **J** and **N**; **C**, *D. planei* endocast showing the RHS lateral view of the eminentia sagittalis and caudal telencephalon modules represented in plots **G**, **K**, and **O**; **D**, *D. planei* endocast showing the rostralateral view of the RHS eminentia sagittalis and caudal telencephalon modules represented in plots **H**, **L**, and **P**; Modules are shaded to assist anatomical identification (see General Methods, Fig. 2.1). **E–H**, *D. planei* (NTM P9464-106–blue) and *D. murrayi* (QM F57984 + QM F57974–grey); **I–L**, *D. planei* (NTM P9464-106–blue) and *Ibandornis woodburnei* (QVM:2000:GFV:20–grey); **M–P**, *D. murrayi* (QM F57984 + QM F57974–blue) and *I. woodburnei* (QVM:2000:GFV:20–grey); **Abbreviations**, **LHS** left hand side; **RHS**, right hand side. Endocasts (**A–D**) are not to scale.

However, Surface Area ratios show that the caudal telencephalon of *D. planei* is notably larger than in *I. woodburnei* (0.741 vs 0.731, respectively; Table A4.2C, Fig. 4.6). These results imply the somewhat substantial difference in surface areas of the caudal telencephalon between these taxa, include an element of mediolateral, and to a greater degree, ventrolateral hypertrophy of the caudal telencephalon in the *Dromornis* taxon.

In summary, the main distinctions between *D. planei* and *I. woodburnei* are in the caudal and ventral margins of the caudal telencephalon, where *I. woodburnei* has a greater rostrocaudal length, but a shorter dorsoventral width for the caudal telencephalon. These distinctions along with mediolateral and ventrolateral hypertrophy in the *Dromornis* taxon, affects a larger Modular Surface area for the caudal telencephalon in *D. planei*. These trends are well described by the shape variance plots (Figs. 4.7K–L, 4.9G–I), and together likely comprise distinct shape apomorphies for the caudal telencephalon between *Dromornis* and *Ilbandornis* taxa (see also 4.3.3.4.2 below).

**4.3.3.3 Cerebellum module**—the rostral cerebellum of *D. planei* and *I. woodburnei* are of comparable rostrodorsoventral height (Fig. 4.8I). Similarly, the mediolateral margins are comparable, and suggestive of a common trend in dromornithids, for a similar mediolateral cerebellum shape (Figs. 4.8I, 4.8J). However, a distinct difference between the taxa is that the rostrocaudal surface of the cerebellum in *I. woodburnei* projects further caudodorsally (Figs. 4.8I–J, 4.8L, 4.9G–I), prior to turning ventrally to grade into the dorsal medulla spinalis caudally at the foramen magnum. Results for Modular Distance data describe these characteristics well, where rostrocaudal length ratios are larger for *I. woodburnei* than for *D. planei* (0.277 vs 0.259, respectively; Table A4.1C, Fig. 4.5), but width ratios are smaller (0.315 vs 0.324, respectively; Table A4.1C, Fig. 4.5). Additionally, the rostral dorsomediolateral border of the cerebellum of *I. woodburnei*, is somewhat rostrocaudally curved as compared to that of *D. planei*, which describes a straighter dorsomediolateral margin rostrally (Fig. 4.8J). Modular Surface Area ratios are larger for *D. planei* than that of *I. woodburnei* (0.693 vs 0.679, respectively; Table A4.2C, Fig. 4.6), and implies that the increased mediolateral width of the cerebellum in *D. planei*, offsets the increased rostrocaudal length in the *Ilbandornis* taxon. Notably, Modular Surface Area data results show both taxa have identical Perimeter ratios (0.491; Table A4.2D), but the hypertrophy of the caudodorsal region of the cerebellum in *D. planei*, likely affects the larger Surface Area ratio for the *Dromornis* taxon (see above; Table A4.2C, Fig. 4.6).

In summary, there are distinct differences between *D. planei* and *I. woodburnei* in the shape of the cerebellum. The rostrocaudal surface of the cerebellum in *I. woodburnei* projects further caudodorsally, and the rostral dorsomediolateral border of the *I. woodburnei* cerebellum is somewhat rostrocaudally curved, as compared to that of *D. planei*, which describes a straighter dorsomediolateral shape. The hypertrophy of the caudodorsal region of the cerebellum results in a larger Modular Surface Area ratio for the *Dromornis* taxon. The shape of the cerebellum, both rostradorsally and caudadorsally, likely represents clear distinctions between *Ilbandornis* and *Dromornis* taxa (see also 4.3.3.4.3 below).

**4.3.3.3.4 Rhombencephalon module**—Modular shape variance plots show the mediolateral profile of the rhombencephalon in *I. woodburnei*, is noticeably more dorsoventrally curved than that of *D. planei*, which is rostrocaudally and mediolaterally less ventrally pronounced (Figs. 4.8K–L, 4.9G). Modular Distance data results show rostrocaudal length ratios are somewhat larger for *I. woodburnei* than that of *D. planei* (0.287 vs 0.281, respectively; Table A4.1C, Fig. 4.5), and mediolateral width ratios are smaller (0.238 vs 0.244, respectively; Table A4.1C, Fig. 4.5). Furthermore, the more ventral location of the rhombencephalon in *I. woodburnei*, and the position of the rhombencephalon relative to the most dorsal eminence of the cerebellum, is described well by Linear Distance ratios, suggesting the total height of the metencephalon (cerebellum + pons, see General Methods, Fig. 2.2G) is less in *D. planei* than in *I. woodburnei* (0.316 vs 0.321, respectively; Table A4.1D, Fig. 4.5). These results show that when endocast size is accounted for, the *Ilbandornis* taxon has a slightly taller hindbrain. Additionally, the Linear Distance width ratio of the medulla oblongata, describing the mediolateral width of the hindbrain, is markedly larger in *D. planei* compared to that of *I. woodburnei* (0.316 vs 0.305, respectively; Table A4.1D). The slightly greater rostrocaudal length ratio (see above) of the rhombencephalon in *I. woodburnei*, is likely due to the deeper ventromediolateral profile in the taxon, but this is offset by a wider ventral rhombencephalon in *D. planei*. Together, these characteristics result in the Modular Surface Area ratio for *D. planei* being larger overall (0.659 vs 0.615, Table A4.2C, Fig. 4.6), along with a markedly larger rhombencephalon Perimeter ratio in the *Dromornis* taxon (0.480 vs 0.450; Table A4.2D).

In summary, the flatter dorsoventral profile, and mediolaterally greater width of the *Dromornis* rhombencephalon likely comprise distinct differences in hindbrain morphology between *Dromornis* and *Ilbandornis* taxa, and accompany cerebellum distinctions described above (see also **4.3.3.4.4** below).

#### **4.3.3.4 Dromornithid taxa—*D. murrayi* vs *I. woodburnei***

In this section, I compare the Late Oligocene species of *Dromornis* with the younger, middle Miocene *Ilbandornis* lineage, to assess any distinctions between the two lineages that may reveal correlations with those identified between the middle Miocene *Dromornis* and *Ilbandornis* lineages above.

**4.3.3.4.1 Eminentia sagittalis modules**—of the middle-Miocene *I. woodburnei*, are shown by the 3D modular shape variance plots (Figs. 4.7M, 4.7N), to extend further rostradorsally, caudadorsally and mediolaterally than those of the Oligo-Miocene *D. murrayi*. Results for Modular Distance data show *I. woodburnei* has somewhat larger length (0.357 vs 0.351, respectively; Table A4.1C), and width (0.305 vs 0.288, respectively; Table A4.1C) ratios for eminentia sagittalis than *D. murrayi*. These trends suggest the modular width of *I. woodburnei* is relatively greater in comparison with *D. murrayi*, than that observed between *D. planei* and *I. woodburnei* (Table A4.1C, Fig. 4.5). This is likely due to the medial margins of the eminentia sagittalis in *I. woodburnei* tracking the rostrocaudal fissura interhemispherica zone closely, a distinctive feature of *Ilbandornis* dorsomedial

endocast morphology as described above (see **4.3.3.3.1** and Figs. 4.9I–L). As was also recognised in *D. planei*, the differences in the eminentia sagittalis of *D. murrayi* and that of *I. woodburnei* include an element of mediolateral hypertrophy, that has slightly displaced the vallecule transition zone ventrolaterally between the dorsal caudolateral eminentia sagittalis, and the dorsal caudal telencephalon in *I. woodburnei* (Figs. 4.7M, 4.7O, 4.7P, 4.9J–L). As noted above (see **4.3.3.3.1**), these shifts in the vallecule transition zones also occurred primarily in the caudolateral areas of the caudal eminentia sagittalis of *I. woodburnei*. The differences between *D. murrayi* and *I. woodburnei* in the dorsal caudal telencephalon, is comparable with those observed in the dorsal caudal telencephalon in *D. planei*, but to a lesser degree (Figs. 4.7E, 4.7G, 4.7H, 4.9D–F).

Overall, the 3D shape variance plots show the eminentia sagittalis of *D. murrayi* are more gracile than those of *I. woodburnei* (Figs. 4.7M–P, 4.9J–L). However, although *D. murrayi* has a markedly larger endocast volume (4.98 vs 4.78, respectively; Table A4.1D), and somewhat larger total endocast surface area (4.121 vs 4.01, respectively; Table A4.2D, Fig. 4.6). Results for Modular Surface Area data show the eminentia sagittalis Perimeter ratio for *D. murrayi* is quite similar to that of *I. woodburnei* (0.519 vs 0.520, respectively; Table A4.2D), but Surface Area ratios (0.760 vs 0.765, respectively; Table A4.2C, Fig. 4.6), reflect the more gracile eminentia sagittalis structures in the *Dromornis* taxon. These distinctions are well visualised by shape variance plots (Figs. 4.7M–P, 4.9J–L).

In summary, these results show that when endocast size is accounted for, the length of the eminentia sagittalis between the two taxa are somewhat similar, but *D. murrayi* has a markedly narrower eminentia sagittalis mediolateral width. These results are likely affected by the medial margins of the eminentia sagittalis in *I. woodburnei* tracking the rostrocaudal fissura interhemispherica zone more closely than in *D. murrayi*. The mediolateral hypertrophy of the eminentia sagittalis in the *Ibandornis* taxon has also affected a lateral displacement of the vallecule transition zone, but to a lesser degree than seen between *D. planei* and *I. woodburnei*.

The rostrocaudal fissura interhemispherica zone in *D. murrayi* is more similar to that seen in *D. planei*, affording additional support for the hypothesis (see **4.3.3.3.1** above) that this morphological characteristic likely represents a distinctive endocranial apomorphy between *Dromornis* and *Ibandornis* lineages.

**4.3.3.4.2 Caudal telencephalon modules**—contrary to what was observed in *D. planei*, the relatively larger overall length and width ratios for eminentia sagittalis in *I. woodburnei*, was not accompanied by a compensatory ventral rotation of the dorsolateral surface of the caudal telencephalon, so that the dorsolateral vallecule margins of the caudal telencephalon in *D. murrayi* are only marginally distinct to those of *I. woodburnei* (Figs. 4.7P, 4.9K–L; see also above). However, results for Linear Distance data suggest the total width ratio of the caudal telencephalon in *D. murrayi*, is somewhat larger than that of *I. woodburnei* (0.370 vs 0.367, respectively; Table A4.1D). The rostral and rostradorsal margins of the caudal telencephalon are comparable between the

specimens, but the caudal margins are distinct in that those of *I. woodburnei* project further caudally, in the region of the cerebrum pars occipitalis, than in the *Dromornis* specimen (Fig. 4.7O). Results for Modular Distance data show larger rostrocaudal length (0.339 vs 0.335, respectively; Table A4.1C, Fig. 4.5), but smaller dorsoventral width ratios in *I. woodburnei*, than in *D. murrayi* (0.310 vs 0.326, respectively; Table A4.1C, Fig. 4.5). Shape variance plots show the most ventral eminences of the caudal telencephalon incorporating the arcopallium, in the region of the fissura subhemispherica, are noticeably less pronounced in *I. woodburnei* (Figs. 4.7O, 4.7P, 4.9J, 4.9L). The shorter dorsoventral width ratio of the caudal telencephalon in *I. woodburnei* is offset by the increase in rostrocaudal length, and results for Modular Surface Area data show the Perimeter ratio for *I. woodburnei* is somewhat larger than for *D. murrayi* (0.495 vs 0.493, respectively; Table A4.2D). However, this does not translate to a larger caudal telencephalon Surface Area ratio for *I. woodburnei* (0.731 vs 0.748, respectively; Table A4.2C, Fig. 4.6), likely due to the somewhat larger mediolateral, and distinct ventral hypertrophy of the caudal telencephalon in *D. murrayi* (Figs. 4.7O–P, 4.9J, 4.9L).

In summary, The caudal telencephalon of *I. woodburnei* projects further caudally, in the vicinity of the cerebrum pars occipitalis, than in *D. murrayi*. Additionally, the ventral margins of the caudal telencephalon project further ventrally in the area of the arcopallium in *D. murrayi* than in *I. woodburnei*. These morphological characteristics are similar to those recognised in the comparison of the caudal and ventral projections of the caudal telencephalon between *D. planei* and *I. woodburnei* (see 4.3.3.3.2 above), and likely comprise characteristic apomorphic traits of the caudal and ventral caudal telencephalon between *Dromornis* and *Ilbandornis* lineages.

**4.3.3.4.3 Cerebellum module**—the rostradorsal eminence of the cerebellum in *I. woodburnei* projects further dorsally than in *D. murrayi*, with respect to the mediolateral margins (Fig. 4.8M). The rostradorsal cerebellum of *D. murrayi* describes a flatter dorsomediolateral margin, than that of *I. woodburnei*, which displays a more rostrally projecting mediolateral curve (Fig. 4.8N). Additionally, the caudodorsal margins in *D. murrayi* are mediolaterally flatter, and do not project as far caudally as that of *I. woodburnei* (Figs. 4.8M–N, 4.8P, 4.9J–K). These characteristics are reflected by results for Modular Distance data, showing *D. murrayi* has a smaller overall rostrocaudal length ratio than *I. woodburnei* (0.244 vs 0.277, respectively; Table A4.1C, Fig. 4.5). From the dorsal aspect, the dorsomediolateral profile of the cerebellum between taxa is quite similar (Fig. 4.8N), with the caudal width of the cerebellum appearing marginally wider in *D. murrayi*. However, the overall lateral profile of the cerebellum between these taxa, show that *I. woodburnei* displays a steeper rostrocaudal caudal profile, beginning at the medial dorsal cerebellum (Figs. 4.8M, 4.8P, 4.9J). This is likely due to the rostradorsal through dorsomedial cerebellum hypertrophy in *I. woodburnei* (Figs. 4.8M, 4.8P, 4.9J). These observations are supported by results for Modular Distance data, showing *I. woodburnei* has a somewhat larger width ratio (0.315 vs 0.311; Table A4.1C, Fig. 4.5) than *D. murrayi*. The cerebellum of *D. murrayi* appears more similar to that of *D. planei*, than it does to the cerebellum of *I. woodburnei*. What is more, the cerebellum of *Dromornis* taxa differ from that of *Ilbandornis* in

similar ways (i.e., rostradorsal and caudodorsal margins, dorsomediolateral shape viewed from the dorsal aspect etc., see **4.3.3.3.3** above and Figs. 4.8E–F, 4.8I–J, 4.8M–N). Notably, the greater cerebellum length of *I. woodburnei*, is offset by its narrower width with respect to *D. murrayi* (see above). Modular Surface Area ratios (0.679 vs 0.687, respectively; Table A4.2C, Fig. 4.6), and Perimeter ratios (0.491 vs 0.496, respectively; Table A4.2C), show *D. murrayi* had a somewhat larger cerebellum, although not as rostradorsally hypertrophied as in *I. woodburnei*.

In summary, the shapes described by the cerebellum, when viewed from the dorsal aspect, are distinct between *Dromornis* and *Ilbandornis* lineages. *Dromornis* taxa display mediolaterally wider and rostrocaudally shorter cerebellum profiles, and the *Ilbandornis* specimen displays a rostrocaudally longer and mediolaterally narrower cerebellum profile (Figs. 4.8F, 4.8J, 4.8N). Although the mediolateral cerebellum width ratio is somewhat larger in *I. woodburnei* than *D. murrayi*, this is likely due to the rostradorsally hypertrophied cerebellum of *I. woodburnei*. Taken together, these shape differences likely constitute characteristic apomorphic traits of the rostrocaudal and mediolateral cerebellum between *Dromornis* and *Ilbandornis* lineages.

It is notable, however, that there exists rostrocaudolateral profile similarities between the cerebellum of the middle Miocene *D. planei* and *I. woodburnei* specimens, that are distinct from the Late Oligocene *D. murrayi* specimen. In that both middle Miocene taxa display hypertrophy of the rostradorsal through dorsomedial cerebellum, affecting a rostrocaudally steeper caudal transition to the dorsal medulla spinalis, than in the older species of *Dromornis* (Figs. 4.8I, 4.8L, 4.9G, 4.9J).

**4.3.3.4.4 Rhombencephalon module**—The rostral margin of the rhombencephalon in *I. woodburnei*, describes a more rostrally projecting mediolateral curve (Fig. 4.8P), than those of both *Dromornis* taxa, which present flatter rostromediolateral margins (Figs. 4.8H, 4.8L). The ventral position of the rhombencephalon surface in *D. murrayi* is similar to that of *I. woodburnei* (Figs. 4.8O, 4.8P, 4.9J, 4.9L). The mediolateral profile in the *D. murrayi* and *I. woodburnei* rhombencephalon appear more ventrally curved than that of *D. planei*, which displays a flatter mediolateral shape (Figs. 4.8G, 4.8K, 4.8H, 4.8L, 4.9D, 4.9G, 4.9F, 4.9I; and above). Results for Modular Distance data show *D. murrayi* has a shorter rostrocaudal length ratio than that of *I. woodburnei* (0.277 vs 0.287, respectively; Table A4.1C, Fig. 4.5), but the width ratio of *D. murrayi* is greater (0.248 vs 0.238; Table A4.1C, Fig. 4.5). These trends are similar to what was found in the comparisons of *D. planei* and *I. woodburnei* (see **4.3.3.3.4** above). Modular Surface Area data results show that the shorter length of the *D. murrayi* rhombencephalon is offset by its greater width, and the Perimeter ratio for *D. murrayi* is marginally greater than in *I. woodburnei* (0.453 vs 0.450, respectively; Table A4.2D). The rhombencephalon in *D. murrayi* has a notably larger Surface Area ratio too (0.630 vs 0.615; Table A4.2D, Fig. 4.6), suggesting the larger width in *D. murrayi* affords a greater surface area. The Linear Distance ratio measuring the overall height of the metencephalon (cerebellum + pons), shows that *D. murrayi* has a somewhat smaller overall hindbrain height than *I. woodburnei*

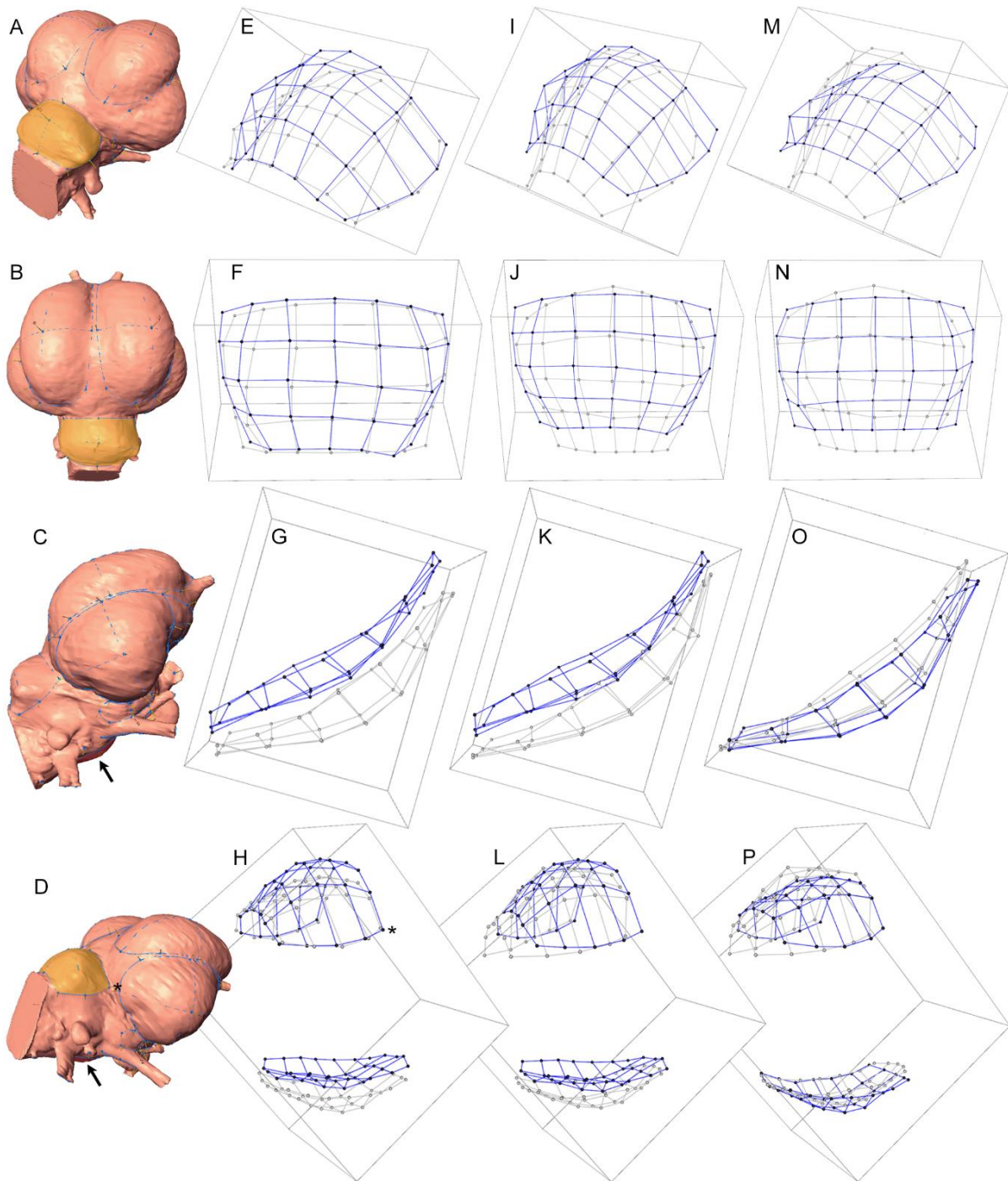


Figure 4.8. Three dimensional modular shape variance plots for dromornithid taxa (see 4.2.7.1). **A**, *Dromornis planei* (NTM P9464-106) endocast showing the RHS dorsal caudolateral view of the cerebellum module represented in plots **E**, **I**, and **M**; **B**, *D. planei* endocast showing the dorsal view of the cerebellum module represented in plots **F**, **J** and **N**; **C**, *D. planei* endocast showing the RHS lateral view of the rhombencephalon module (arrow) represented in plots **G**, **K**, and **O**; **D**, *D. planei* endocast showing the caudolateral view of the cerebellum and rhombencephalon (arrows—**C**, **D**) modules represented in plots **H**, **L**, and **P**. Asterisks (\*—**D**, **H**) indicates locations of the RHS rostralateral Lm of the cerebellum module. Modules are shaded to assist anatomical identification (see General Methods, Fig. 2.1). **E–H**, *D. planei* (NTM P9464-106—blue) and *D. murrayi* (QM F57984 + QM F57974—grey); **I–L**, *D. planei* (NTM P9464-106—blue) and *Ibandornis woodburnei* (QVM:2000:GFV:20—grey); **M–P**, *D. murrayi* (QM F57984 + QM F57974—blue) and *I. woodburnei* (QVM:2000:GFV:20—grey); **Abbreviations**, **LHS** left hand side; **Lm**, landmark; **RHS**, right hand side. Endocasts (**A–D**) are not to scale.

(0.319 vs 0.321, respectively; Table A4.1D, Fig. 4.5). As the position, in 3D space, of the rhombencephalon in *D. murrayi* is similar to that of *I. woodburnei* (Figs. 4.8O–P, 4.9J, 4.9L), the dorsoventral Linear Distance ratio reflecting the relative height of the metencephalon, is a fair indication as to how much the dorsoventral height of the overall hindbrain differs between these specimens. This likely represents the medial and rostromedial hypertrophy of the cerebellum in the *Ibandornis* specimen (see Fig. 4.8P and above). Additionally, the total Linear Distance width ratio of the medulla oblongata shows that *D. murrayi* has a notably wider hindbrain than *I. woodburnei* (0.320 vs 0.305, respectively; Table A4.1D).

In summary, these results describe a flatter dorsoventral profile, and a mediolaterally greater width of the rhombencephalon between *I. woodburnei* and *D. murrayi*, and show *I. woodburnei* has a taller overall hindbrain height than the *Dromornis* specimen. These observations compliment the characteristic hindbrain traits identified between *D. planei* and *I. woodburnei* (see 4.3.3.3.4 above), which likely represent distinct differences in hindbrain morphology between *Dromornis* and *Ibandornis* lineages.

#### 4.3.4 Dromornithid taxa vs extant Galloanseres

In this section, I compare the dromornithid condition with those of the extant galloanseres. Morphological distinctions between taxa are ascertained with reference to size-standardised ratios of: Modular Distance, Linear Distance, and Modular Surface Area results (see Appendices, Figs. A4.10–A4.11; Tables A4.1C–D, A4.2C–D), and the endocast models of *Leipoa ocellata* (SAM B11482; Figs. 4.4M–P), *Anhima cornuta* (MV B12574; Figs. 4.4I–L), *Anseranas semipalmata* (SAM B48035; Figs. 4.4E–H), *Dromornis planei* (NTM P9464-106; Figs. 4.3A–D, 4.4A–D), *D. murrayi* reconstruction (QM F57984 + QM F57974, Figs. 4.3E–H), and *Ibandornis woodburnei* (QVM:2000:GFV:20; Figs. 4.3I–L).

**4.3.4.1 Innervation**—the olfactory bulb of *A. semipalmata* displays hypertrophy in excess of that seen in *A. cornuta*, which is somewhat more than that of *L. ocellata* (Figs. 4.4E, 4.4I, 4.4M). The olfactory zones of these galloanseres appear to be wholly external to the rostral telencephalon, as the olfactory bulbs, more distinct in *A. semipalmata* and *A. cornuta*, but less so in *L. ocellata*, appear to be slightly constricted immediately anterior of the rostral telencephalon. This condition is distinct to that of dromornithids (Figs. 4.3A, 4.3E, 4.3I).

The morphologies of the trigeminal ganglia are similar between specimens, in that the ophthalmic ( $V_1$ ) branch is widely separated from the maxillomandibular ( $V_2+V_3$ ) branch, and all display a ganglionic bridge between the two nerve branches. However, the dromornithid maxillomandibular branch displays a synapomorphic morphology where it passes through the cranium. For example, the canalis n. maxillomandibularis passes minimally 20 mm (in *Dromornis*) rostroventrolaterally, prior to exiting the skull at the foramen n. maxillomandibularis (**fmx**, Figs. A4.4K–L, A4.5K;  $V_2+V_3$ , A4.5L) in all dromornithids assessed. In the extant galloanseres, this

distance is markedly shorter, and the nerves exit the skull almost directly after separation from the ventral surface of the mesencephalon (Figs. 4.4A–B, 4.4E–F, 4.4I–J, 4.4M–N; see also Chapter 5, Figs. A5.1–A5.8).

Results for Modular Distance data show length ratios of the trigeminal ganglion for *D. murrayi*, *D. planei*, and *I. woodburnei* (0.227, 0.224, 0.228, respectively; Table A4.1C) are quite similar to, but somewhat longer than those of *A. cornuta* and *A. semipalmata* (0.220; 0.223, respectively; Table A4.1C), but that of *L. ocellata* is markedly shorter than all specimens (0.168, Table A4.1C). Trigeminal ganglion width ratios show that the dromornithids *D. murrayi*, *D. planei*, and *I. woodburnei* (0.197, 0.189, 0.201, respectively; Table A4.1C) have wider trigeminal ganglion morphology than the extant galloanseres *L. ocellata*, *A. cornuta*, and *A. semipalmata* (0.127, 0.122, 0.129, respectively; Table A4.1C), with *A. cornuta* displaying the narrowest trigeminal ganglion width ratio of all specimens assessed. Similarly, Modular Surface Area data results show trigeminal ganglion Perimeter ratios for *D. murrayi*, *D. planei*, and *I. woodburnei* (0.420, 0.419, 0.420, respectively; Table A4.2D), are somewhat greater than the anhimid *A. cornuta* (0.412; Table A4.2D), and together are greater than the megapodiid *L. ocellata* (0.400; Table A4.2D). That of the anseranatid *A. semipalmata* (0.444; Table A4.2D), is the largest of all taxa assessed. Modular Surface Area ratios show that *D. murrayi*, *D. planei*, and *I. woodburnei* (0.515, 0.508, 0.502, respectively; Table A4.2C, Fig. A4.11), and *A. semipalmata* (0.462; Table A4.2C, Fig. A4.11), display the greatest trigeminal hypertrophy, followed by *A. cornuta*, and *L. ocellata* (0.398, 0.350, respectively; Table A4.2C, Fig. A4.11). Surface Area ratios of the truncated face of the maxillomandibular ( $V_2+V_3$ ) branch of the trigeminal nerve, allow inference regarding the relative importance of this nerve complex to each taxon. *D. murrayi*, *D. planei*, and *I. woodburnei* display the largest Surface Area ratios (0.282, 0.269, 0.254, respectively; Table A4.2C, Fig. A4.11), followed by *A. semipalmata* and *A. cornuta* (0.229, 0.210, respectively; Table A4.2C, Fig. A4.11). Notably, the Surface Area ratio for the megapodiid *L. ocellata* (0.039; Table A4.2C, Fig. A4.11), is the smallest of all taxa assessed. Perimeter ratios show that *A. cornuta* and *A. semipalmata* (0.289, 0.293, respectively; Table A4.2D), essentially overlap with *D. murrayi* and *D. planei* (0.292, 0.285, respectively; Table A4.2D). *Ibandornis woodburnei* (0.276; Table A4.2D) has the smallest trigeminal complex among dromornithids, and the megapodiid *L. ocellata* (0.223; Table A4.2D) has the smallest Perimeter ratio for the truncated face of the maxillomandibular nerve, for all specimens assessed.

In dromornithids, the glossopharyngeal (IX) and vagus (X) nerves separate somewhat caudoventrolaterally from the eminence of the proximal ganglion from the rhombencephalon surface (Figs. 4.3A, 4.3D–E, 4.3H–I, 4.3L, 4.4A). This condition is similar to that seen in *A. semipalmata* (Figs. 4.4E, 4.4G), but separation occurs somewhat further distally in dromornithids. The condition is, to a lesser extent, similar to that seen in *A. cornuta* (Figs. 4.4I, 4.4K), but distinct to that of *L. ocellata* (Figs. 4.4M, 4.4O). The eminence of the hypoglossal nerves (XII) which typically comprise a dorsal and ventral branch (e.g. XII<sub>d</sub>, XII<sub>v</sub>, Fig. 4.4G), is represented by one nerve root at either side of the

caudoventrolateral medulla oblongata in dromornithids (Figs. 4.3D, 4.4C). A condition distinct to those galloanseres assessed here (Figs. 4.4G, 4.4K, 4.4O).

**4.3.4.2 Eminentia sagittalis modules**—these structures in dromornithids differ from any seen in the extant galloanseres assessed (**emsg**, Figs. 4.4B–D, 4.4C–D; see also Chapter 5, Figs. A5.1–A5.8), where the eminentia sagittalis structures of *L. ocellata*, *A. cornuta*, and *A. semipalmata* appear much hypotrophied in comparison, and occupy substantially less dorsal endocast surface area, than those of all dromornithid specimens (e.g. Figs. 4.4C–D vs 4.4G–H, 4.4K–L, 4.4O–P). Modular Distance data results show length ratios for *L. ocellata*, *A. cornuta*, and *A. semipalmata* are substantially shorter (0.318, 0.331, 0.320, respectively; Table A4.1C, Fig. A4.10), and narrower (0.206, 0.210, 0.220, respectively; Table A4.1C, Fig. A4.10), than the length (0.351, 0.359, 0.357, respectively; Table A4.1C, Fig. A4.10), and width (0.288, 0.302, 0.305, respectively; Table A4.1C, Fig. A4.10) ratios for *D. murrayi*, *D. planei*, and *I. woodburnei*. Modular Surface Area data results for *L. ocellata*, *A. cornuta*, and *A. semipalmata* show that both Perimeter ratios (0.484, 0.493, 0.486, respectively; Table A4.2D), and Surface Area ratios (0.563, 0.579, 0.596, respectively; Table A4.2C, Fig. A4.11) for these specimens, are substantially less than the Perimeter (0.519, 0.522, 0.520, respectively; Table A4.2D), and Surface Area (0.760, 0.778, 0.765, respectively; Table A4.2C, Fig. A4.11) ratios of *D. murrayi*, *D. planei*, and *I. woodburnei*.

In summary, these results show that the eminentia sagittalis of extant galloanseres are much hypotrophied in comparison, and occupy substantially less dorsal endocast surface area than those of all dromornithid taxa. The megapodiid *L. ocellata* displays the most hypotrophied eminentia sagittalis, followed by the anseriforms *A. cornuta*, and *A. semipalmata* respectively. *Anseranas semipalmata* displays the most hypertrophied eminentia sagittalis of all extant galloanseres assessed.

**4.3.4.3 Rostral telencephalon modules**—evidence of the rostral telencephalon is conspicuously absent on the external morphology of dromornithid endocasts, and only present rostrally as twin eminences ventromedial of the olfactory bulb, on either side of the rostromedial surface of the endocast (**tel.r**, Figs. 4.3B, 4.3D). Consequently, detailed comparisons between dromornithid rostral telencephalon, and those of the extant galloanseres are not possible. Thus, I only present results for rostral telencephalon Modular Distance, and Surface Area data for the extant galloanseres assessed here.

Modular Distance data results show *A. semipalmata* has the largest length ratio (0.304; Table A4.1C), followed by *A. cornuta*, and *L. ocellata* (0.279, 0.274, respectively; Table A4.1C), which display somewhat similar overall length ratios for this module. Modular Distance width ratios show that *A. semipalmata* has a wider rostral telencephalon than *A. cornuta*, followed by *L. ocellata* (0.263, 0.232, 0.207, respectively; Table A4.1C), which shows a much smaller rostral telencephalon width ratio than seen in the anseriforms. Modular Surface Area data results describe similar patterns, where *A. semipalmata* displays the largest Perimeter ratio compared with those of *A. cornuta*, and *L. ocellata*

(0.515, 0.474, 0.466, respectively; Table A4.2D). *A. semipalmata* displays a larger Surface Area ratio than those of *A. cornuta*, and *L. ocellata* too (0.672, 0.567, 0.519, respectively; Table A4.2C).

In summary, these results show the megapodiid *L. ocellata* has the shortest and narrowest rostral telencephalon, followed by the anseriforms *A. cornuta*, and *A. semipalmata* respectively. *A. semipalmata* displays the most hypertrophied rostral telencephalon of the extant galloanseres assessed. (see also Fig. 4.4).

**4.3.4.4 Caudal telencephalon modules**—results for Modular Distance data show the dromornithids *D. murrayi*, *D. planei*, and *I. woodburnei* have larger rostrocaudal length ratios than all extant galloanseres assessed (0.335, 0.333, 0.339, respectively; Table A4.1C, Fig. A4.10). The length ratio for *A. cornuta* (0.324, Table A4.1C, Fig. A4.10), is more similar to dromornithids than that of *A. semipalmata*, and *L. ocellata* (0.316, 0.312, respectively; Table A4.1C, Fig. A4.10). Modular Distance dorsoventral width ratios show *A. semipalmata*, and *A. cornuta* (0.339, 0.334, respectively; Table A4.1C, Fig. A4.10), display a dorsoventrally wider caudal telencephalon than *D. murrayi*, *D. planei*, and *I. woodburnei* (0.326, 0.316, 0.310, respectively; Table A4.1C, Fig. A4.10). These results show that *L. ocellata* (0.315; Table A4.1C, Fig. A4.10) is more similar to the dromornithids in this respect. Interestingly, results for Linear Distance ratios, describing the total caudal endocast width, show the dromornithids *D. murrayi*, *D. planei*, and *I. woodburnei* (0.370, 0.366, 0.367, respectively; Table A4.1D), display comparable ratios with that of *L. ocellata* (0.367; Table A4.1D). However, the endocast total width of all dromornithids are relatively narrow, with respect to those of *A. cornuta*, and *A. semipalmata* (0.374, 0.370, respectively; Table A4.1D). Notably, *D. murrayi*, and *A. semipalmata* display identical total caudal endocast width ratios (0.370, Table A4.1D), and that of *A. cornuta* (0.374, Table A4.1D) is the largest total caudal endocast width ratio for all taxa assessed. Modular Surface Area data results show *D. murrayi*, *D. planei*, and *I. woodburnei* have smaller Perimeter ratios (0.493, 0.491, 0.495, respectively; Table A4.2D) than *L. ocellata*, *A. cornuta*, and *A. semipalmata* (0.507, 0.513, 0.518, respectively; Table A4.2D). However, *D. murrayi*, *D. planei*, and *I. woodburnei* display larger Surface Area ratios (0.748, 0.741, 0.731, respectively; Table A4.1C, Fig. A4.11) than *L. ocellata*, *A. cornuta*, and *A. semipalmata* (0.658, 0.709, 0.712, respectively; Table A4.2C, Fig. A4.11).

In summary, these results likely describe greater mediolateral hypertrophy of the dromornithid caudal telencephalon, with respect to those of the extant galloansere specimens. Notably, the relative size of the Modular Surface Area ratios for caudal telencephalon in *A. semipalmata*, and *A. cornuta* are more similar to those of dromornithids than *L. ocellata*, which displays the smallest Modular Surface Area ratio for all specimens assessed.

**4.3.4.5 Mesencephalon modules**—in dromornithids, the mesencephalon appear somewhat hypotrophied, and are not as well defined as in the other galloanseres assessed (Fig. 4.4). The megapodiid *L. ocellata* displays the most hypertrophied mesencephalon (Figs. 4.4M–O), followed by the anseranatid *A. semipalmata* (Figs. 4.4E–G). The mesencephalon of the anhimid *A. cornuta*

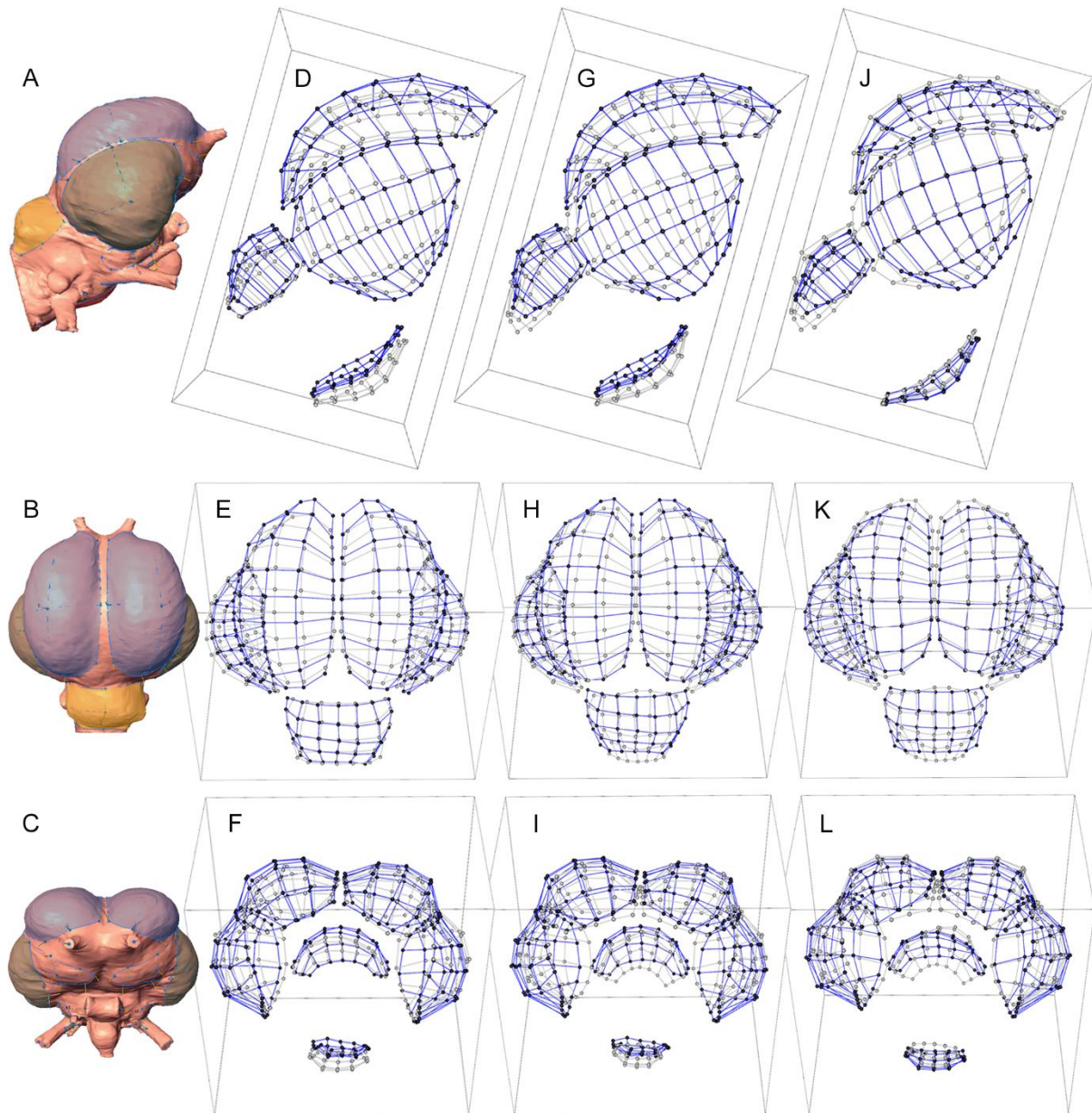


Figure 4.9. Three dimensional modular shape variance plots for dromornithid taxa (see 4.2.7.1). **A**, *Dromornis planei* (NTM P9464-106) endocast showing the RHS lateral view of the eminentia sagittalis, caudal telencephalon and cerebellum modules represented in plots **D**, **G**, and **J**; **B**, *D. planei* endocast showing the dorsal view of the eminentia sagittalis, caudal telencephalon and cerebellum modules represented in plots **E**, **H** and **K**; **C**, *D. planei* endocast showing the rostral view of the eminentia sagittalis and caudal telencephalon modules represented in plots **F**, **I** and **L**. Note: cerebellum and rhombencephalon modules presented in plots **F**, **I** and **L**, are not visible in **C**. Modules are shaded to assist anatomical identification (see General Methods, Fig. 2.1). **D–F**, *D. planei* (NTM P9464-106–blue) and *D. murrayi* (QM F57984 + QM F57974–grey); **G–I**, *D. planei* (NTM P9464-106–blue) and *Ilbandornis woodburnei* (QVM:2000:GFV:20–grey); **J–L**, *D. murrayi* (QM F57984 + QM F57974–blue) and *I. woodburnei* (QVM:2000:GFV:20–grey); **Abbreviations**, **RHS**, right hand side. Endocasts (**A–C**) are not to scale.

appears to be the most hypotrophied (Figs. 4.4I–K) among the extant taxa. Modular Distance data results show *L. ocellata* has the largest length ratio for all taxa (0.341; Table A4.1C), followed by *A. semipalmata*, and *A. cornuta* (0.290, 0.273, respectively; Table A4.1C) The anseriforms display

similar length ratios as *D. murrayi*, and *D. planei* (0.274, 0.274, respectively; Table A4.1C), but are somewhat larger than that of *I. woodburnei* (0.258; Table A4.1C). Similarly, the mesencephalon width ratio for *L. ocellata* is the largest (0.242; Table A4.1C), followed by *I. woodburnei*, *A. cornuta*, and *A. semipalmata* (0.188, 0.181, 0.153, respectively; Table A4.1C), and thereafter by *D. murrayi*, and *D. planei* (0.169, 0.161, respectively; Table A4.1C). These results show that the largest overall taxa display the smallest overall mesencephalon width ratios. Modular Surface area data results show the megapodiid *L. ocellata* has the largest Perimeter ratio of all taxa (0.516; Table A4.2D), followed by *A. semipalmata*, and *A. cornuta* (0.465, 0.453, respectively; Table A4.2D). Surface Area ratios for *L. ocellata*, *A. semipalmata*, and *A. cornuta* (0.643; 0.534, 0.508, respectively; Table A4.2C, Fig. A4.11), show that the anhimid has the smallest mesencephalon Surface Area ratio of all specimens assessed. Perimeter and Surface Area ratios for *D. murrayi* (0.424; 0.520, respectively; Tables A4.2C–D, Fig. A4.11), *D. planei* (0.444; 0.527, respectively; Tables A4.2C–D, Fig. A4.11), and *I. woodburnei* (0.432; 0.540, respectively; Tables A4.2C–D, Fig. A4.11), are interesting in that they reflect the relatively greater mesencephalon hypertrophy in *I. woodburnei* compared with species of *Dromornis*.

In Summary, these results show that the largest overall taxa, display the smallest overall mesencephalon length and width ratios. I note that although dromornithids display apparent hypotrophy of mesencephalon structures, results show both *A. semipalmata* and *A. cornuta*, while appearing to have inflated mesencephalon structures, effectively have relatively smaller mesencephalon structures than that of *I. woodburnei*. In fact, all dromornithids have larger Surface Area ratios than the anhimid *A. cornuta*. What is more, dromornithid Perimeter ratios are all smaller than those of all extant galloanseres, suggesting there occurs more hypertrophy, relative to total surface area of specimen specific endocasts, over mesencephalon surfaces in dromornithid specimens than in the extant galloanseres.

**4.3.4.6 Cerebellum module**—those of dromornithids are characteristically rostrocaudally compressed and mediolaterally expanded (see 4.3.2.7 above). From the lateral aspect, the dromornithid cerebellum forms a rostrocaudal shelf rostrally, and turns sharply ventrally in the vicinity of the dorsolateral auricula cerebelli, to meet the caudodorsal medulla spinalis at the foramen magnum. This condition is similar to that seen in *A. semipalmata*, and in *L. ocellata*, with the anseranatid showing a larger and more pronounced ventral transition (Figs. 4.4E, 4.4M). However, this characteristic is not evident in the caudodorsal cerebellum of the anhimid *A. cornuta*, which displays a comparably gradual caudoventral transitional gradient (Fig. 4.4I). In dorsal aspect, rostrad of the foramen magnum, all extant galloanseres display a rostrolateral hypertrophy of the cerebellum, prior to grading into the cerebrum pars occipitalis regions of the caudal telencephalon (Figs. 4.4H, 4.4L, 4.4P). This condition is not evident in dromornithids, which display a more abrupt dorsomediolateral expansion of cerebellum margins, after the rostral transmission of the medulla spinalis through the foramen magnum. Where after, the dorsolateral cerebellum surfaces describe a

somewhat parallel rostrocaudal transition into the cerebrum pars occipitalis regions (Figs. 4.3C, 4.3G, 4.3K, 4.4D). Modular Distance data results show cerebellum length ratios for *D. murrayi*, *D. planei*, and *I. woodburnei* (0.244, 0.259, 0.277, respectively; Table A4.1C, Fig. A4.10), are much rostrocaudally shorter than *A. cornuta*, and *A. semipalmata* (0.318, 0.296, respectively; Table A4.1C, Fig. A4.10), but the length ratio of *L. ocellata* approaches that of dromornithids (0.282; Table A4.1C, Fig. A4.10). Conversely, the mediolateral cerebellum width ratios of *D. murrayi*, *D. planei*, and *I. woodburnei* (0.311, 0.324, 0.315, respectively; Table A4.1C, Fig. A4.10), are all greater than those of *L. ocellata*, and *A. cornuta* (0.273, 0.285, respectively; Table A4.1C, Fig. A4.10), but are more similar to that of *A. semipalmata* (0.307; Table A4.1C, Fig. A4.10). Notably, results for Modular Surface Area data show *L. ocellata*, *A. cornuta*, and *A. semipalmata* have larger cerebellum Perimeter ratios (0.503, 0.523, 0.495, respectively; Table A4.2D) than *D. murrayi*, *D. planei*, and *I. woodburnei* (0.496, 0.491, 0.491, respectively; Table A4.1D), with only *A. semipalmata* comparable with that of *D. murrayi*, which displays the largest Perimeter ratios of all dromornithids. However, Surface Area ratios for *D. murrayi*, *D. planei*, and *I. woodburnei* (0.687, 0.693, 0.679, respectively; Table A4.1C, Fig. A4.11), are comparable with *A. cornuta*, are somewhat larger than that of *A. semipalmata*, and are greater than that of *L. ocellata* (0.684, 0.657, 0.625, respectively; Table A4.2C, Fig. A4.11).

In Summary, the cerebellum in dromornithids are notably shorter and wider than those of all extant galloanseres. Dromornithids display cerebellum Modular Surface Area ratios similar to that of *A. cornuta*, but greater than those of both *A. semipalmata* and *L. ocellata*. The megapodiid displays the smallest cerebellum Modular Surface Area ratio of all taxa assessed.

**4.3.4.7 Rhombencephalon module**—the rhombencephalon between taxa are distinct, with the dromornithids having somewhat flat ventral surfaces rostrocaudally and mediolaterally, and the extant galloanseres display much ventrally hypertrophied surfaces in comparison (**rho**; Figs. 4.4E, 4.4I, 4.4M). These trends are reflected by results for Modular Distance data which show length ratios for *D. murrayi*, *D. planei*, and *I. woodburnei* (0.277, 0.281, 0.287, respectively; Table A4.1C, Fig. A4.10) are similar to *L. ocellata*, *A. cornuta*, and *A. semipalmata* (0.273, 0.277, 0.288, respectively; Table A4.1C, Fig. A4.10). For the most part, all taxa overlap in ranges, excluding the length ratio for *L. ocellata*, which was the smallest of all taxa. Rhombencephalon width ratios for *L. ocellata*, *A. cornuta*, and *A. semipalmata* (0.275, 0.290, 0.255, respectively; Table A4.1C, Fig. A4.10), are all larger than those of *D. murrayi*, *D. planei*, and *I. woodburnei* (0.248, 0.244, 0.238, respectively; Table A4.1C, Fig. A4.10). Linear Distance data results for the width of the medulla oblongata, reflecting the relative width of the hindbrain, show *D. murrayi*, *D. planei*, and *I. woodburnei* (0.320, 0.316, 0.305, respectively; Table A4.1D), have greater ventral hindbrain width ratios than *L. ocellata*, *A. cornuta*, and *A. semipalmata* (0.293, 0.295, 0.295, respectively; Table A4.1D). However, the ratios describing the total height of the hindbrain in *D. murrayi*, *D. planei*, and *I. woodburnei* (0.319, 0.316, 0.321, respectively; Table A4.1D), show the depth, or ventral projection of the rhombencephalon in *L. ocellata*, *A. cornuta*, and *A. semipalmata* (0.331, 0.335, 0.333, respectively; Table A4.1D), are greater

than in dromornithids. Results for Modular Surface Area data, show rhombencephalon Perimeter ratios for *D. murrayi*, *D. planei*, and *I. woodburnei* (0.453, 0.480, 0.450, respectively; Table A4.2D) are somewhat smaller than for *L. ocellata*, *A. cornuta*, and *A. semipalmata* (0.474, 0.484, 0.476, respectively; Table A4.2D). Dromornithids display comparable results for Surface Area data, in that *A. cornuta*, *D. murrayi*, *A. semipalmata*, and *I. woodburnei* (0.632, 0.630, 0.613, 0.615, respectively; Table A4.2C, Fig. A4.11), have similar Surface Area ratios. Although *D. planei* (0.659; Table A4.2C, Fig. A4.11), has the largest Surface Area ratio of all taxa assessed, and *L. ocellata* (0.601; Table A4.2C, Fig. A4.11) the least.

In summary, rhombencephalon length ratios show all taxa, with the exception of *L. ocellata*, display somewhat similar rhombencephalon lengths. The overall width of the rhombencephalon in dromornithids are all larger than in extant galloanseres, but the overall height of the hindbrain in extant galloanseres is greater than in the dromornithids. This is likely reflective of the greater ventral hypertrophy of the structure in the extant taxa. Species of *Dromornis* have the largest rhombencephalon Surface Area ratios, but that of *I. woodburnei* overlaps with the extant galloanseres. Similarly, the overall width of the hindbrain in species of *Dromornis* are greater than in all taxa assessed, and that of *I. woodburnei* approaches those of the extant galloanseres.

#### 4.3.5 Estimated body mass, gizzard mass and gastrolith size ratios

Results for body mass data, show that *Genyornis newtoni* has the largest mean body mass for the species for which gizzard stone datasets were analysed, followed by *Dinornis robustus*, *Euryapteryx curtus gravis*, and *Dromaius novaehollandiae* (2.309, 2.133, 2.086, 1.624, respectively; Table A4.3B). The largest gizzard mass ratio, with respect to body mass, is that of *D. robustus*, followed by those of *D. novaehollandiae*, *E. c. gravis*, and *G. newtoni* (1.620, 1.465, 1.342, 1.263, respectively; Table A4.3B, Fig. A4.12). The largest gastrolith size ratio, with respect to body mass, was *D. novaehollandiae*, followed by *D. robustus*, *E. c. gravis*, and *G. newtoni* (0.817, 0.756, 0.564, 0.495, respectively; Table A4.3B, Fig. A4.12). These data show that the dromornithid *G. newtoni* was the largest taxon assessed, but when body size was accounted for, the species displays the smallest relative gizzard mass and gastrolith size ratios. Additionally, *D. novaehollandiae* had the largest gastrolith size ratio, with respect to body mass, among all taxa assessed. Notably, *G. newtoni*, and *E. c. gravis* have comparable gizzard mass and gastrolith size ratios, suggesting they potentially exploited plant foods that were similarly less fibrous.

## 4.4 DISCUSSION

Dromornithid endocranial anatomy is here described in detail for the first time, using specimens drawn from fossil sites in Australia spanning ~20–8 Ma. I have quantified changes in the shape of the dromornithid endocranium through time within and between lineages, and show the brains of

these giant extinct birds are distinctive. In the following, I describe: **1**, the morphological characteristics of the dromornithid brain, and describe these features with respect to those of other galloanseres; **2**, I review potential lineage-specific apomorphies identified in dromornithid endocranial anatomy; and **3**, comment on morphological changes observed to have occurred in the endocranial anatomy of the *Dromornis* lineage over time; **4**, finally, I assess potential functional implications of the dromornithid endocranial condition.

#### **4.4.1 Comparisons of endocranial characteristics of dromornithids and extant galloanseres**

In this section I summarise the main characteristics of the dromornithid brain, and describe dromornithid endocranial features with respect to those of other galloanseres.

##### **4.4.1.1 Innervation**

**4.4.1.1.1 Olfactory**—the olfactory bulb in dromornithids is pronounced both dorsally and ventrally in the oldest (*D. murrayi*) species. However, in middle Miocene taxa (*D. planei* and *I. woodburnei*) its dorsal morphology is masked by the rostral eminence of the eminentia sagittalis (see **4.4.1.2** below). There appears no reduction in the size of the olfactory bulb in the younger taxa, as from the ventral aspect, lateral margins of the organ transition into the rostroventral endocast without reduction in mediolateral width. In extant galloanseres, the olfactory bulb of *A. semipalmata* displays hypertrophy in excess of that seen in *A. cornuta*, which is somewhat more than that of *L. ocellata*. The olfactory zones of these galloanseres, appear wholly external to the rostral telencephalon, as the olfactory bulb margins appear to constrict somewhat, prior to grading caudally into the rostral telencephalon, a condition distinct to that of dromornithids.

Taken together, the evidence shows that the eminentia sagittalis extends rostromediolaterally to effectively engulf the olfactory bulbs (see **4.4.1.2** below), and so a first assessment may consider that dromornithids had hypotrophied olfactory bulbs. Therefore, care must be taken when interpreting the size of the olfactory bulb, where in dorsal aspect, the eminentia sagittalis and telencephalon are together very broad rostrally. For example, this condition occurs in all moa species, uniquely so among ratites, but engulfment of the olfactory bulbs was not considered by [Ashwell & Scofield \(2008:151\)](#), when they concluded that moa showed “No evidence of olfactory specialization (i.e., enlarged olfactory bulbs and increased surface area of the olfactory nasal cavity..” despite moa being well known to have the largest olfactory chambers of any ratite other than kiwi ([Worthy & Scofield 2012](#)).

**4.4.1.1.2 Trigeminal ganglia**—transmit the three divisions of the trigeminal nerve (V), and insert on the ventral surface of the mesencephalon. They are distinctive in dromornithids, in that the maxillomandibular branch (V<sub>2</sub> + V<sub>3</sub>) transmits minimally 20 mm (in *Dromornis*) rostroventrolaterally, prior to exiting the skull at the foramen n. maxillomandibularis, a single opening between the prootic and laterosphenoid bones of the skull. In the extant galloanseres assessed here, this transmission is markedly shorter, and the nerves exit the skull almost directly after separation from the ventral surface

of the mesencephalon. The extended transmission condition of the maxillomandibular branch through the skull in dromornithids, is likely to accommodate for the unusually thick trabecular bone structure forming the dromornithid neurocranium, within which the cortical bone describing the endocranial capsule ‘floats’ within a honeycomb-like trabecular matrix (e.g. Fig. A4.8I). In the extant galloanseres assessed here, and in several other galloanseres too (e.g. Chapter 5, Figs. A5.1–A5.8), the transmission of these nerves to the foramen n. maxillomandibularis is markedly shorter. Notably however, in the phasianid galliform *Gallus gallus* (see Chapter 5, Figs. A5.4M, A5.8N), there occurs transmission of the maxillomandibular nerve through the skull that, although somewhat shorter than that observed in dromornithids, is longer than observed in the other galloanseres assessed here. What is more, in the raw CT data for *G. gallus*, this condition is accompanied by trabecular matrix surrounding the endocranial capsule through which the nerves transmit (Pers. Obs. Author). Thus, an extended transmission of the maxillomandibular nerve branch, appears to be a feature of birds in which the brain does not closely approximate the cortical boundaries of the skull. In general, the morphology of the avian neurocranium does exhibit a close approximation of the brain within (e.g. Iwaniuk & Nelson 2002; Striedter 2005, 2006; Witmer et al. 2008; Picasso et al. 2009; Walsh et al. 2013; Walsh & Knoll 2018), but patterns of the brain ‘lagging behind’ the body have been recognised in Haast’s eagle (*Hieraaetus moorei*) by Scofield & Ashwell (2009), who showed the eagle’s “ten-fold” increase in body size was only accompanied by a “doubling or tripling” of endocast volume. This demonstrated lag of neuroanatomical hypertrophy accompanying rapid skeletal changes in a taxon, may relate to strong selection for body size, i.e., adaptation to a novel trophic niche, or artificial selection in the form of “stringent” human mediated selection for desirable phenotypes (e.g., as in the case of *G. gallus* [see Lawal et al. 2018, and references therein]). Consequently, as dromornithids became larger through the course of their evolution (i.e., from the cassowary-sized *D. murrayi*, to arguably the largest bird to walk the planet in *D. stirtoni* (see Worthy et al. 2016b; Handley et al. 2016), it is likely the increase in physical size of the skull, was accommodated for by an increase in trabecular bone enclosing the ‘lagging’ endocranial capsule (see also Scofield & Ashwell 2009:fig 5a). Similarly, the *G. gallus* skull used for CT-scanning in this project, was almost certainly from a domestic chicken, and may demonstrate increasing trabecular thickness in the skull, mediated by human induced selection for body size. In order to assess these observations more comprehensively, additional data in the form of wider sampling across galloanseres in particular, but across Neornithes in general is required, targeting taxa with demonstrated temporal increases in body size.

These distinctions notwithstanding, Modular Distance data results show that the length ratios of the trigeminal ganglion between dromornithids, are quite similar to, but somewhat longer than those of *A. cornuta*, and *A. semipalmata*, but that of *L. ocellata* is markedly shorter than all taxa assessed. Width ratios show that all dromornithids have wider trigeminal ganglion morphology than all extant galloanseres, with *A. cornuta* displaying the narrowest trigeminal ganglion width ratio of all taxa assessed. Modular Surface Area ratios of dromornithid trigeminal ganglia are somewhat greater

than those of the anhimid *A. cornuta*, which together are greater than that of the megapodiid *L. ocellata*, but that of the anseranatid *A. semipalmata* is the largest of all taxa assessed. Ratios for the truncated face of the maxillomandibular ( $V_2+V_3$ ) nerve, allows inference regarding the relative importance of this nerve complex to each taxon, where dromornithids have the largest ratios, followed by *A. semipalmata*, and *A. cornuta*. Overall, size-standardised ratios for the trigeminal ganglion, show that *A. cornuta*, and *A. semipalmata* essentially overlap with *D. murrayi*, and *D. planei*, and *I. woodburnei* has the smallest trigeminal complex among dromornithids. The megapodiid *L. ocellata* has the smallest trigeminal ratios across all specimens assessed.

I note that the Modular Perimeter ratio for the trigeminal complex of *L. ocellata*, show the relative area the structure describes on the ventral surface of the mesencephalon, is similar to those of the other galloanseres. However, Modular Surface area ratios for this taxon imply hypertrophy of the trigeminal ganglion, is less pronounced than in the other extant galloanseres, and much less pronounced than in dromornithids. These trends are reflected by the relatively small cross-sectional Surface Area ratio of the maxillomandibular nerve in *L. ocellata*, and suggests maxillomandibular sensory capability in the taxon is comparably reduced with regard to all other taxa assessed.

In dromornithids the glossopharyngeal (IX) and vagus (X) nerves separate somewhat caudoventrolaterally from the eminence of the proximal ganglion from the rhombencephalon surface, similar to, but somewhat further distally than the condition seen in *A. semipalmata*, to a lesser extent to that seen in *A. cornuta*, but distinct to that of *L. ocellata*. The eminence of the hypoglossal nerves (XII), which typically comprise a dorsal and ventral branch, is represented by one nerve root eminence at either side of the caudoventrolateral medulla oblongata in dromornithids, a condition distinct to those galloanseres assessed here.

**4.4.1.2 Eminentia sagittalis**—are the most distinguishing feature uniting dromornithids. They form massively hypertrophied structures that dominate the entire dorsal endocast morphology. These structures extend rostromediolaterally to effectively engulf the olfactory bulbs, and extend rostroventrally over the most rostral eminence of the rostral telencephalon, substantially overhanging the rostroventral surfaces of the brain. They extend strongly rostromediolaterally, masking the rostromedial telencephalon (see **4.4.1.3** below), and extend mediolaterally across the entire dorsal forebrain. The structure of the eminentia sagittalis in dromornithids are unlike any seen in the extant galloanseres assessed, where those of *L. ocellata*, *A. cornuta*, and *A. semipalmata* appear much hypotrophied in comparison, and occupy substantially less dorsal endocast surface area. Modular Distance ratios show that the eminentia sagittalis of all galloanseres, are substantially shorter and narrower than those of all dromornithids. Similar patterns are described by Modular Surface Area data results, which show that all ratios for extant galloanseres are substantially less than those of dromornithids. The megapodiid *L. ocellata* displays the most hypotrophied eminentia sagittalis, followed by the anseriforms *A. cornuta*, and *A. semipalmata* respectively. *Anseranas semipalmata* displays the most hypertrophied eminentia sagittalis of all extant galloanseres assessed.

It is notable however, that the rostral orientation of the eminentia sagittalis on the dorsal endocast in dromornithids, is more similar to the condition seen in the megapodiid *L. ocellata*, and anhimid *A. cornuta*, than the more caudal positioning of the eminentia sagittalis in the anseranatid *A. semipalmata* (Figs. 4.4D, 4.4H, 4.4L, 4.4P; see also Chapter 5, Figs. A5.5–A5.8).

Among taxa that were not included in these analyses, some palaeognaths display eminentia sagittalis hypertrophy. For example, Corfield et al. (2008:fig 1b B–E) figured endocasts of the extinct New Zealand (NZ) moa *Dinornis novaezealandiae* Owen, 1843, and *Anomalopteryx didiformis* (Owen, 1843), and those of extant ratites like emu (*Dromaius novaehollandiae*), and ostrich (*Struthio camelus*). Additionally, Ashwell & Scofield (2008:figs. 6g–l) figured the dorsal endocasts of several NZ moa: *D. robustus*, *A. didiformis*, *E. c. gravis*, and *Emeus crassus* (Owen, 1846) as well, all of which show eminentia sagittalis characteristics similar to those seen in dromornithids, wherein the vallecule, especially in the larger moa taxa, clearly extend rostrocaudally across the entire dorsolateral telencephalic hemisphere. These traits suggest that such characteristic hypertrophy of the eminentia sagittalis in large flightless birds (see also Craigie 1939:figs. 1-2; Martin et al. 2007:fig. 2a; Peng et al. 2010:figs. 1, 3; Picasso et al. 2011:fig 1; Walsh & Knoll 2018:fig. 5.3[1-6]), may represent a parallel convergent modification towards enhanced visual proficiency (see also 4.4.4.2.1 below). However, ratite taxa clearly show a lesser degree of hypertrophy than that seen in dromornithids. Even the oldest dromornithid cranial fossils (e.g. *D. murrayi* from the ~20 Ma sites of Riversleigh), display greater eminentia sagittalis hypertrophy, indicating a long “ghost lineage” must have existed prior to any substantive fossil evidence of dromornithids in Australia (see also Worthy et al. 2016b:19). Evidence for such, comprise trackways reported from the late Oligocene of Tasmania (Vickers-Rich 1991), postcranial remains from the late Oligocene Pwerte Marnte Marnte LF in the Northern Territory (Murray & Megirian 2006), and a mould of fossil footprints from the Eocene Redbank Plains Formation of Queensland (Vickers-Rich & Molnar 1996). Enhancement of visual proficiency through time, continued from the late Oligocene to the middle Miocene at least, as evidenced by the continued trend of rostradorsal and mediolateral hypertrophy of the dromornithid eminentia sagittalis quantified here, irrespective of taxon.

Remarkably however, eminentia sagittalis hypertrophy comparable to that seen in dromornithids, is evident in Strigiformes like the Barn owl (*Tyto alba*), and Caprimulgiformes like the Tawny frogmouth (*Podargus strigoides*; see Stingelin 1957:pl. 26; Iwaniuk & Wylie 2006:fig 2; Martin et al. 2007:fig. 2c; Corfield et al. 2008:fig. 1bK; Wylie et al. 2015:fig. 3A-B; Walsh & Knoll 2018:fig. 5.3[34-35]). These taxa are primarily crepuscular ambush predators, and have high levels of stereoscopic visual acuity (see 4.4.4.2.1 below).

**4.4.1.3 Rostral telencephalon**—evidence of the rostral telencephalon are only present rostroventrally as twin eminences ventromediolateral of the olfactory bulb, on either side of the rostromedial endocast in dromornithids (**tel.r**; Figs. 4.3B, 4.3D). It is possible that these eminences are expanded cerebrum tuber ventrolaterale structures, as evident in *A. cornuta* (Fig. 4.4I–J).

However, their interpretation as remnant rostral telencephalon eminences is favoured, as in all dromornithid taxa modelled, there exist pronounced paired eminences in this rostromedial zone that are not present to the same degree, in any avian endocast modelled nor observed in the literature (Pers. Obs. Author; see also Chapter 5, Figs. A5.5–A5.8). Further support for this, is that the positioning of these rostral eminences in dromornithids, agrees with the angle and position of rostral telencephalon eminences in extant galloanseres, when endocasts are aligned to putative “alert posture” (e.g. Witmer et al. 2003; Milner & Walsh 2009; Witmer & Ridgely 2009; Walsh et al. 2014), with reference to the horizontal positioning of the lateral semicircular duct of the vestibular organ. Additionally, the rostrocaudal transition angle of the valleculla, defining the dorsal margins of the caudal telencephalon, agree with the extension of the visible rostral eminences of the dromornithid rostral telencephalon, should the dorsolateral curve of the rostral telencephalon, not be masked by the hypertrophy of the rostromedial eminencia sagittalis. In support of this interpretation, the apparent rostral extension of the valleculla across the dorsolateral surface of moa endocasts, figured by Ashwell & Scofield (2008:figs. 5e-1, 6g-1), and Corfield et al. (2008:fig 1b D-E), and similarly in the brains of extant flightless ratites (see Craigie 1939:figs. 1-2; Martin et al. 2007:fig. 2a; Ashwell & Scofield 2008:fig 6; Corfield et al. 2008:fig 1B-C; Peng et al. 2010:figs. 1, 3; Picasso et al. 2011:fig 1; Walsh & Knoll 2018:fig. 5.3[1-6]), suggest the evolution of rostromediolaterally hypertrophied eminencia sagittalis in large flightless birds, may effectively mask rostral telencephalon morphology. As such, the dromornithid rostral telencephalon appears to have been engulfed by the rostromedial hypertrophy of the eminencia sagittalis, and appear entirely rostradorsally and rostromedially masked by the latter. The accommodation of this apparently major change in rostradorsal endocranial morphology in dromornithids, would have necessitated a somewhat dorsomedial displacement of the olfactory bulb, which I think is a possibility, as this condition is somewhat similar to that seen in moa (e.g. Ashwell & Scofield (2008:figs. 5e-1, 6g-1) and Corfield et al. (2008:fig 1b D-E).

As detailed comparisons between the dromornithid rostral telencephalon were not possible, I discuss only data derived from those extant galloanseres assessed here. Modular Distance data results show the megapodiid *L. ocellata* has the shortest and narrowest rostral telencephalon, followed by the anseriforms *A. cornuta*, and *A. semipalmata* respectively. Modular Surface Area data results describe similar patterns for these taxa, where *A. semipalmata* displays the largest Perimeter and Surface Area ratios, and the megapodiid *L. ocellata* has the most hypotrophied rostral telencephalon amongst all extant galloanseres assessed.

**4.4.1.4 Caudal telencephalon**—are strongly defined in dromornithids. Modular Distance data results show dromornithids have larger rostrocaudal length ratios than all extant galloanseres assessed. The ratio for *A. cornuta* is more similar to dromornithids, than for both *A. semipalmata*, and *L. ocellata*. Although, *A. semipalmata* and *A. cornuta* have larger dorsoventral width ratios than all dromornithids, and the width ratio for *L. ocellata* is more similar to the dromornithids in this respect.

Linear Distance data results show the ratio for overall caudal telencephalon width for *D. murrayi* are larger than all other dromornithids, is identical to *A. semipalmata*, but that of *A. cornuta* is larger still, and represents the largest caudal endocast width ratio for all taxa assessed. Modular Surface Area data results show that dromornithids have the smallest Perimeter ratios, but display larger Surface Area ratios than all extant galloanseres. These results likely describe greater mediolateral hypertrophy of dromornithid caudal telencephalon, relative to those of the extant galloansere taxa. Notably, the Surface Area ratios for *A. semipalmata* and *A. cornuta* are more similar to those of dromornithids than *L. ocellata*, which has the smallest overall Surface Area ratio of all taxa assessed.

**4.4.1.5 Mesencephalon**—in dromornithids appear somewhat indistinct, and not as well delimited as in the extant galloanseres assessed. Within the extant taxa, the megapodiid *L. ocellata* appears to display the most hypertrophied state, followed by the anseranatid *A. semipalmata*, and the mesencephalon of the anhimid *A. cornuta* appear to be the most hypotrophied. Results for Modular Distance data show that *L. ocellata* does in fact have the largest length ratio among all taxa, followed by *A. semipalmata*, and *A. cornuta*, which shares very similar length ratios with *Dromornis* species *D. murrayi*, and *D. planei*. The smallest length ratio for all taxa is that of *I. woodburnei*. Similarly, width ratios are largest in *L. ocellata*, followed by that of the dromornithid *I. woodburnei*, *A. cornuta*, *A. semipalmata*, and then by the *Dromornis* species *D. murrayi*, and *D. planei*. These results show that the taxa of largest size display the smallest overall mesencephalon dorsoventral width ratios. Modular Surface Area data results show the megapodiid *L. ocellata* has the largest overall Perimeter and Surface Area ratios of all taxa, followed by *A. semipalmata*, and that of *A. cornuta*, which shows the smallest Surface Area ratios of all taxa assessed. The distinction between Perimeter and Surface Area ratios for all galloanseres, show relatively greater mesencephalon hypertrophy in *I. woodburnei* compared with species of *Dromornis*, and greater overall hypertrophy of dromornithid mesencephalon than seen in anseriforms.

I note that although dromornithids display apparent hypotrophy of mesencephalon structures, size-standardised results show both *A. semipalmata*, and *A. cornuta* effectively have smaller mesencephalon structures than those of *I. woodburnei*, and in fact, all dromornithids have larger mesencephalon Surface Area ratios than the anhimid *A. cornuta*. Moreover, dromornithid Perimeter ratios are all smaller than those of all galloanseres, suggesting there occurs more hypertrophy, relative to total surface area of specimen endocasts, over mesencephalon surfaces in dromornithid taxa than in anseriforms (see above). These results strongly suggest that taxa which apparently display hypo- or hypertrophy of a particular structure, may in fact have comparably larger or smaller relative Surface Area ratios when size is accounted for. Therefore, caution must be exercised when directly comparing morphological structures across taxa, and deriving functional inference from such assessment, without first accounting for variation in overall size.

**4.4.1.6 Cerebellum**—in dromornithids, cerebellum margins are characteristically rostrocaudally compressed and mediolaterally expanded. In lateral aspect, they form a rostral

rostrocaudal shelf, and turn sharply ventrally in the vicinity of the dorsolateral auricula cerebelli, to meet the caudodorsal medulla spinalis at the foramen magnum. This condition is similar to that seen in *A. semipalmata*, and in *L. ocellata*, with the anseranatid showing a steeper, or more pronounced, ventral transition. However, this characteristic is not evident in the caudodorsal cerebellum of the anhimid *A. cornuta*, which displays a comparably gradual caudoventral transitional gradient. From the dorsal aspect, rostral of the foramen magnum, all extant galloanseres display rostrolateral divergence of the cerebellum margins, prior to grading into the cerebrum pars occipitalis regions of the caudal telencephalon. This condition is not evident in dromornithids which, in dorsal aspect, display more abrupt mediolateral divergence of cerebellum margins, after rostral transmission of the medulla spinalis through the foramen magnum. Where after, the dorsolateral cerebellum surfaces describe a somewhat parallel rostrocaudal transition into the cerebrum pars occipitalis regions.

Modular Distance data results show the cerebellum of dromornithids are much rostrocaudally shorter than *A. cornuta*, are less so than *A. semipalmata*, but the rostrocaudal length ratio of the *L. ocellata* cerebellum approaches that of dromornithids. Conversely, the mediolateral width ratios of the dromornithids are all greater than those extant galloanseres assessed. However, the width ratio of *A. semipalmata* approaches those of the dromornithids, in contrast to the much smaller width ratios of *A. cornuta*, and *L. ocellata*. Notably, Modular Surface Area data results show all extant galloanseres have larger Perimeter ratios than all dromornithids, although that of *A. semipalmata* approaches that of *D. murrayi*, wherein it is the largest of all dromornithids. However, Surface Area ratios for dromornithids are comparable with *A. cornuta*, are somewhat larger than that of *A. semipalmata*, and are greater than that of *L. ocellata*, which displays the smallest Surface Area ratio of all taxa. These results imply that dromornithid cerebellum hypertrophy appears to exceed that of the extant galloanseres assessed here, but ratios overlap somewhat in *I. woodburnei* and *A. cornuta*. These trends for a ‘larger than apparent’ dromornithid cerebellum, further support my contention that overall taxon size is an important aspect that must be accounted for, prior to making interspecific inference based on direct morphological comparisons.

In addition, all extant galloanseres show a more ventrally oriented foramen magnum, than do dromornithids, which appear more caudally oriented with the rostrocaudal axis of the endocasts (e.g. Figs. 4.4E, 4.4I, 4.4M vs Figs. 4.4A, 4.3A, 4.3E, 4.3I). This possibly suggests the angle of articulation of the atlas and axis vertebrae with the skull, was less acute in dromornithids, than in those extant galloanseres assessed here. These characteristics imply dromornithid cranial posture potentially differed from that of the extant galloansere taxa, in that the articulation of proximal vertebrae with the dromornithid neurocranium, was somewhat more horizontally orientated, perhaps as in dinornithiforms (see [Worthy & Holdaway 2002:163](#)). The further assessment of which lies beyond the scope of this chapter.

**4.4.1.7 Rhombencephalon**—dromornithids display somewhat flat ventral rhombencephalon surfaces rostrocaudally and mediolaterally, whereas all extant galloanseres display much ventrally

hypertrophied surfaces (**rho**; Figs. 4.4E, 4.4I, 4.4M; see also Chapter 5, Figs. A5.1–A5.8). These trends are reflected by Modular Distance data results, showing all galloansere taxa, with the exception of *L. ocellata*, display somewhat similar rhombencephalon length ratios, however, width ratios of extant galloanseres are all greater than those of dromornithids. Linear Distance ratios of the medulla oblongata, reflecting the relative width of the hindbrain, shows dromornithids have a greater ventral hindbrain width than extant galloanseres. These results support the observation (see **4.3.4.7** above) that the depth, or ventral projection of the rhombencephalon in extant galloanseres, is greater than in dromornithids (i.e., the width ratios reflect the directional ‘curve’ over the ventral rhombencephalon [see **4.2.6.2**]). Modular Surface Area data results show Perimeter ratios for dromornithids are somewhat smaller than for extant galloanseres, but Surface Area ratios for *A. cornuta*, *D. murrayi*, *A. semipalmata*, and *I. woodburnei* are similar, although *D. planei* has the largest ratio of all taxa assessed, and *L. ocellata* the least.

#### 4.4.2 Endocranial apomorphies distinguishing lineages within dromornithids

This project sought to identify apomorphic characters of the dromornithid endocranium that may prove informative in future phylogenetic assessments of the group. Recently, the Gastornithiformes clade, inclusive of dromornithids and gastornithids, was robustly supported by the analyses of [Worthy et al. \(2017a\)](#); see also [2017b](#)). However, gastornithiform relationships within galloanseres were “weakly” supported. Further phylogenetic assessment using additional cranial material and/or informative endocranial characters, may potentially contribute to clarifying relationships between dromornithids, and potentially between dromornithids and galliforms.

The eight species of dromornithids described were hypothesised to form two lineages ([Worthy et al. 2016b](#), see **4.1** above). The *Dromornis* lineage was recognised as monotypic at any one time throughout its range, and includes *Dromornis murrayi* (late Oligocene–early Miocene [~24–17 Ma]), *D. planei* (middle Miocene [15–12 Ma]), *D. stirtoni* (late Miocene [9–7 Ma]), and *D. australis* (age unknown, likely Pliocene–Pleistocene). The *Ilbandornis/Barawertornis* lineage comprises *B. tedfordi* (late Oligocene–early Miocene [~24–17 Ma]), *I. lawsoni* (middle to late Miocene [15–7 Ma]), *I. woodburnei* (middle to late Miocene [15–7 Ma]), and *Genyornis newtoni* (late Pleistocene). The placement of *G. newtoni* in the *Barawertornis/Ilbandornis* lineage, requires further testing via phylogenetic analyses incorporating cranial material of *G. newtoni*, which until recently, has not been possible, due to the paucity of suitable cranial fossils of *G. newtoni* (see [Worthy et al. 2016b](#)). However, recent discoveries of two crania from the Callabonna region of South Australia, although fragmentary, will allow further testing of the hypothesis of an increase in size of the *Barawertornis/Ilbandornis* lineage after the late Miocene, and forms the focus of ongoing work.

The examination of dromornithid endocrania here has revealed morphological features of the dromornithid brain that may provide support for the two lineage hypothesis (*sensu* [Worthy et al. 2016b](#)). I define these endocranial apomorphies below, with a focus on *Ilbandornis*.

*Ilbandornis* can be distinguished from the two species of *Dromornis* with adequate preservation for comparison (i.e. *D. planei*, and *D. murrayi*) by: **1**, in *Ilbandornis*, the medial boundaries of the eminentia sagittalis in the rostrocaudal fissura interhemispherica zone of the dorsal endocast, are more medially delimited, than in species of *Dromornis* (Figs. 4.7I, 4.7M, 4.9H–I, 4.9K–L); **2**, in *Ilbandornis*, the caudal telencephalon projects further caudally in the zone of the cerebrum pars occipitalis, than in species of *Dromornis* (Figs. 4.7K, 4.7O, 4.9G–I, 4.9J–L); **3**, in *Ilbandornis*, the caudoventral regions incorporating the arcopallium, comprising the most ventral eminence of the caudal telencephalon in the zone of the fissura subhemispherica, is notably less ventrally pronounced than in species of *Dromornis* (Figs. 4.7K–L, 4.7O–P, 4.9G, 4.9J, 4.9I, 4.9L); **4**, in *Ilbandornis*, the rostradorsal cerebellum defines a more rostrally projecting mediolateral curve than in species of *Dromornis*, which display a flatter rostral dorsomediolateral margin (Figs. 4.8J, 4.8N, 4.9H–I, 4.9K–L); **5**, in *Ilbandornis*, the caudodorsal cerebellum projects further caudally in the region of the dorsal medulla spinalis, whereas this region is mediolaterally flatter in species of *Dromornis* (Figs. 4.8I–J, 4.8M–N, 4.8L, 4.8P, 4.9H–I, 4.9K–L); **6**, in *Ilbandornis*, the entire hindbrain (rhombencephalon, medulla oblongata and metencephalon complex (cerebellum + pons), is rostrocaudally longer and mediolaterally narrower, than in species of *Dromornis* (Figs. 4.8J, 4.8N, 4.9H–I, 4.9K–L).

As to whether the traits described above are robust lineage specific apomorphies, remains to be tested with additional specimens of the putative *Ilbandornis/Barawertornis* lineage, in the form of yet to be discovered cranial specimens of *I. lawsoni* and *Barawertornis tedfordi*, and the inclusion of cranial material of *Genyornis newtoni*, the youngest member of the *Ilbandornis/Barawertornis* lineage (see [Worthy et al. 2016b](#)).

#### 4.4.3 Temporal changes in the endocranial morphology of the *Dromornis* lineage

Across the ~10 Ma period between specimens of Oligo-Miocene *D. murrayi*, and the middle Miocene *D. planei* assessed here, the orientation of the brain within the skull appears to have remained the same, despite foreshortening of the cranium. Other than regional changes in endocast shape, for example, the rostradorsal hypertrophy of the eminentia sagittalis accompanying other effects described above, the brains of these taxa are generally similar. The relatively major change in the overall size of *Dromornis* dromornithid morphology, reflected by crania of *D. murrayi* and *D. planei* figured here (Figs. 4.1A–D, A4.1A–H, A4.4A–H), and postcranial fossils described elsewhere (e.g. [Murray & Vickers-Rich 2004](#); [Worthy et al. 2016b](#)), appear to have not been substantial enough to affect changes in the position and orientation of the brain in *D. planei*, relative to that of *D. murrayi*. However, by the late Miocene, some ~6 Ma after the occurrence of *D. planei*, the cranium of the *Dromornis* lineage had become even more foreshortened and dorsoventrally deeper, as manifested in *Dromornis stirtoni* (Fig. 4.1E, see also [Worthy et al. 2016b](#)). These morphological changes appear to have indeed affected the orientation of the brain.

Concerning *D. stirtoni*, it is unfortunate that the state of preservation of specimens, prevented the level of endocast shape assessment achieved for the other dromornithids. This was primarily due to the taphonomic characteristics of the only site that preserves these giant birds (see 4.2.2 above). In turn, this limited the biological and functional inferences that potentially could have been correlated with their exceptional cranial architecture. However, I have shown from the alignment of preserved features of the *D. stirtoni* endocast models, with that of *D. planei* (see 4.2.4.3, and 4.3.3.2 above), that the brain of *D. stirtoni* does not depart greatly from typical dromornithid endocranial morphology. However, the altered endocranial alignment to ‘fit’ in the foreshortened cranium, resulted in the rostroventral endocranial surfaces in *D. stirtoni*, being rotated rostradorsally around the medial caudal telencephalon, into a more dorsally oriented position. Additionally, it appears the brain of *D. stirtoni* has experienced a measure of dorsoventral compression and mediolateral expansion, resulting in an effective reduction in the most ventral eminence of the caudal telencephalon in the area of the arcopallium. These changes in the forebrain are accompanied by a more ventrally orientated hindbrain, which may reflect a compensatory ventral rotation of the dorsoventral hindbrain complex in the species, although the ‘life position’ of the midbrain in the skull of *D. stirtoni* has not changed appreciably from that of *D. planei*. A cranium preserving a better endocranial ‘capsule’ for *D. stirtoni* would undoubtedly clarify these observations, and allow estimates of relative size and shape of various modules used here, to better characterise the endocast of the taxon.

The reasons for this unusual rotation and apparent subtle compression of the endocast, may lie in the highly derived state of cranial morphology attained by this, the largest of the dromornithids, by the late Miocene. The cranium of *D. stirtoni* is unique in that the rostrocaudal cranial length is effectively about half the cranial depth, and represents the terminal state of a concerted trend in cranial foreshortening, concomitant with an increase in bill size, of the most extreme avian cranial specialisation known (see Murray & Megirian 1998; Worthy et al. 2016b). This trend extends from the oldest known species of *Dromornis*, the Oligo-Miocene *D. murrayi*, through the middle Miocene *D. planei*, to the most derived late Miocene taxon *D. stirtoni*.

#### **4.4.4 Functional implications of dromornithid endocranial morphology**

In the following section, I summarise the main characteristics of the dromornithid brain with respect to the current understanding of functional attributes for morphological divisions of the avian brain. Hypotheses such as the mosaic model of brain evolution underpinning several inferences made below, have been previously described (e.g. Introduction, 1.5.4; Chapter 3, 3.4.1), and so will not be reiterated here. Functional mosaic correlations with endocranial morphological traits described below, which have been previously mentioned, are reiterated where relevant to maintain narrative continuity.

**4.4.4.1 Innervation**—In birds, the trigeminal nerve system comprises the medial portion carrying the ophthalmic (V<sub>1</sub>) nerve, which innervates the orbit and nasal cavity, the rostral palate and the tip of the upper bill, and forms a major sensory pathway for the skin of the head and maxillary

rostrum. The maxillary ( $V_2$ ) branch innervates the maxillary rostrum and infraorbital regions, and the mandibular ( $V_3$ ) division innervates the entire lower bill and several mandibular and interramal regions (Dubbeldam 1980; Bubień-Waluszewska 1981; Dubbeldam et al. 1981; Wild & Zeigler 1996). The trigeminal nucleus receives exclusively proprioceptive information from the descending tract, and the principal sensory nucleus of the trigeminal system (Gutiérrez-Ibáñez et al. 2009). This includes not only projections from ophthalmic ( $V_1$ ) and maxillomandibular ( $V_2+V_3$ ) nerves described above, but taste information from the tongue is conveyed, within the lingual branch of the maxillomandibular ramus, by the facial (VII) nerve to the trigeminal principal sensory nucleus, which also receives input from glossopharyngeal (IX) and hypoglossal (XII) nerves (Dubbeldam et al. 1979; Bubień-Waluszewska 1981; Wild & Zeigler 1980; Wild 1981, 1990; Dubbeldam 1998a, 1998b). The glossopharyngeal (IX) and vagus (X) nerves share the large proximal ganglion, and the glossopharyngeal components of this complex comprise somatic, “special”, and visceral afferent fibres. The “special” fibres connect with the palatine branch of the facial (VII) nerve at the cranial cervical ganglion, and are associated with sensory taste and tactile information (Dubbeldam et al. 1979; Bubień-Waluszewska 1981; Dubbeldam 1984; Arends & Dubbeldam 1984). Additionally, Dubbeldam (1992) proposed that differences in the trigeminal principal sensory nucleus, were indicative of the functional demands of specific feeding behaviours. Gutiérrez-Ibáñez et al. (2009) reported hypertrophy of the trigeminal principal sensory nucleus in species that had feeding behaviours dependent on tactile input, and that beak morphology, and the concentration of mechanoreceptors in the beak and tongue, strongly correlate with feeding behaviour. In summary, the trigeminal (V) nerve comprises the largest somatosensory cranial innervation complex, and transmits epicritic sensation from the entire facial region and mastication musculature (see Bubień-Waluszewska 1981; Wild 1987; Dubbeldam 1998b).

The morphology of dromornithid cranial innervation in the form of the maxillomandibular ( $V_2+V_3$ ), glossopharyngeal (IX), and vagus (X) nerves, and the morphometric results presented above for the trigeminal ganglion, are more similar to those anseriform taxa which use tactile feeding mechanisms, i.e., taxa employing sensory input from the beak, palate and tongue (e.g. Dubbeldam et al. 1979; Berkhoudt et al. 1981; Bubień-Waluszewska 1981; Dubbeldam 1984; Arends & Dubbeldam 1984; Wild 1987; Dubbeldam 1998b; Gutiérrez-Ibáñez et al. 2009). For example, distinct hypertrophy of the trigeminal ganglion complex is evident in grazing and filter feeding (dabbling) anseriforms (Chapter 5, Figs. A5.5–A5.7), in contrast with the relative trigeminal ganglion hypotrophy in terrestrial, omnivorous galliform taxa (Chapter 5, Fig. A5.8).

Dromornithids have extremely large, deep bills, with dorsally prominent mediolaterally compressed culmens (Murray & Megirian 1998; Murray & Vickers-Rich 2004; Worthy et al. 2016b). The herbivorous diet of dromornithids is well established (Murray & Vickers-Rich 2004, and references therein), but the musculature for the operation of the beak is “surprisingly limited”, and suggests these birds were not capable of a particularly forceful bite (Worthy et al. 2016b; *contra*

Murray & Megirian 1998:88). For example, there is no temporal fossa on the side of the cranium for insertion of mandibular musculature, which is thus limited to the fused postorbital-zygomatic process, and peculiar insertions on the orbital wall of the cranium. Moreover, the culmen, while large, has a lightly constructed osseous core that was only partially covered in rhamphotheca, highly vascularised and likely highly innervated, a combination of features conferring relatively weak biting ability (Worthy et al. 2016b). The large size of the dromornithid culmen, combined with the fact that they are not strengthened for food manipulation, suggest they were primarily used for display, and that the distinctive morphology was likely driven by sexual selection, or by thermoregulatory requisites.

Bill architecture suggests that dromornithids were likely not consuming coarse browse requiring strong bite forces, as were those of some moa (see Worthy & Holdaway 2002, and references therein). This contention can be tested by observations of the collections of gastroliths used to process such food, for example, such as those seen in moa like *Dinornis robustus*. Gastroliths are well known from *D. murrayi* (e.g. Archer et al. 1991:79, re Riversleigh D-Site specimen), and individual stones are common in Alcoota (e.g. Woodburne 1967:164; Murray & Megirian 1992:fig 8A; Murray & Vickers-Rich 2004; Pers. Obs. Author), but no individual set is available from these dromornithid taxa. However, several specimens of the Pleistocene dromornithid *Genyornis newtoni* have complete or partial gizzard stone sets, allowing total volume of gastroliths and size of stones used to be assessed, and from which inference with respect to potential diet may be ascertained (e.g. Davies 1978, 2002; Wings 2007; Fritz et al. 2011). Size-standardised ratio results for the gastrolith data set (see 4.3.5 above), show that dromornithids selected gastroliths of much smaller diameter, and accumulated them in remarkably small overall volumes, compared with *Dinornis* moa, although the dromornithids were somewhat larger birds. What is more, data for an extant emu (*Dromaius novaehollandiae*), show gastroliths selected by the Australian ratite can be remarkably large (see also Davies 1978:table 2, 2002:26). In fact, when overall body size is accounted for, emu show gastrolith size ratios larger than those of *D. robustus*, although accumulated in smaller quantities. Notably, the ‘stout-legged’ moa (*Euryapteryx curtus gravis*), displays very similar gastrolith size and gizzard mass ratios to those of *G. newtoni* (see 4.3.5 above). *E. c. gravis* moa are hypothesised to have exploited a diet of soft leaves and fruit, in dry scrubland and mosaic environments. As opposed to the generalist tree and shrub browsing *D. robustus* moa, the gizzard contents of which have been shown to comprise much coarser, low-quality fibrous leaf and twig material (e.g. Worthy 1989; Worthy & Holdaway 2002; Wood et al. 2008; Wood et al. 2013; and references therein). If the gastrolith volume and stone size preferences are representative of dromornithids in general, these results suggest the fibrosity of browse dromornithids were targeting, was likely similar to that of stout-legged moa (i.e., new growth, soft leaves, and fruit), requiring less vigorous mechanical processing in the crop (e.g. Wings 2007). Moreover, characteristics of the dromornithid visual pathways (see below), suggest these birds possessed well developed visual and tactile capabilities, affording the capability for more precise and

selective browsing abilities, likely required for the identification and selection of more specific, and less generalised food resources.

#### 4.4.4.2 Visual pathways

There are three principal visual pathways in birds: **1**, the thalamofugal pathway transmits visual signals from the retina via the mesencephalon, to the principal optic nucleus of the dorsal thalamus, and thence to the eminentia sagittalis; **2**, the tectofugal pathway transmits via the mesencephalon to the nucleus rotundas of the thalamus and proceeds to the entopallium of the caudal telencephalon; and **3**, the third visual pathway transmits via the mesencephalon through retinal recipient nuclei in the accessory optic system and pretectum, and projects to several regions of the brain, including the cerebellum (see [Wylie et al. 2009](#); [Iwaniuk et al. 2010](#); [Wylie & Iwaniuk 2012](#); [Corfield et al. 2012](#); [Wylie et al. 2015](#); and references therein; see also Introduction, **1.5.4.2**).

**4.4.4.2.1 Eminentia sagittalis**—are composed of two main regions, the larger “visual” region, located dorsally and extending caudodorsally, which receives retinal projections, and a smaller rostral somatosensory region, receiving “substantial” somatosensory and kinesthetic input ([Wild & Williams 2000](#); [Iwaniuk et al. 2008](#); see also [Wild 1987](#); [Miceli et al. 1990](#); [Deng & Wang 1992](#)). The thalamofugal pathway incorporating the eminentia sagittalis, has been shown to be primarily involved in binocular vision capability, and global stereopsis or depth perception ([Pettigrew 1986](#); [Rogers 1996](#); [Iwaniuk & Wylie 2006](#); [Iwaniuk et al. 2008](#), and references therein). [Iwaniuk et al. \(2008\)](#) showed the size of eminentia sagittalis were significantly correlated with more frontally orientated orbits, and broader binocular fields (see also [Wild et al. 2008](#)), and argued changes in the relative size of the eminentia sagittalis, suggest increases in somatosensory and motor processing capabilities (see also [Wild 1997](#); [Manger et al. 2002](#); [Jarvis et al. 2005](#); [Iwaniuk & Wylie 2006](#)). Additionally, eminentia sagittalis are hypertrophied in species that forage using tactile information from the beak ([Pettigrew & Frost 1985](#); [Iwaniuk & Wylie 2006](#); [Wylie et al. 2015](#); see also [Martin 2009](#)).

Dromornithids may have had a well-developed thalamofugal pathway, as they display particularly hypertrophied eminentia sagittalis structures. Potential indications of the kinds of adaptive selection driving dromornithid eminentia sagittalis morphology, may lie in the extraordinarily similar morphology of strigiforms such as barn owls (*Tyto alba*), and the frogmouth (*Podargus strigoides*), which have much hypertrophied eminentia sagittalis too (e.g. [Stingelin 1957:pl. 26](#); [Iwaniuk & Wylie 2006:fig 2](#); [Martin et al. 2007:fig. 2c](#); [Corfield et al. 2008:fig. 1bK](#); [Wylie et al. 2015:fig. 3A-B](#); [Walsh & Knoll 2018:fig. 5.3\[34-35\]](#)). Barn owls are nocturnal, and possess exceptional low-light visual proficiency and binocularity, or stereovision capabilities ([Pettigrew & Konishi 1976](#); [Pettigrew 1979](#); [van der Willigen et al. 1998](#), [Orlowski et al. 2012](#); [Gutiérrez-Ibáñez et al. 2013](#)). Similar specialisations typical of low-light and stereoptic visual proficiency, have been recognised in Australian caprimulgids. For example, podargid Frogmouth, and aegothelid Owlet-nightjar taxa, have highly developed visual systems ([Iwaniuk & Wylie 2006](#); [Wylie et al. 2015](#)), and are thought to possess stereoscopic vision ([Pettigrew 1986](#)). In addition, [Iwaniuk et al. \(2008\)](#) showed that the

relative size of the eminentia sagittalis was correlated with orientation of the orbits (see also [Wylie et al. 2015:fig.3E](#)). Stereoptic proficiency has been shown to facilitate accuracy in nocturnal prey capture in caprimulgid taxa ([Pettigrew 1986](#)), and spatial, or “topographical cues” associated with feeding activities in *Columba*, and *Gallus* ([Rogers 1996](#)), and corvids ([Kulemeyer et al. 2009](#); see also [Martin 2009](#)). Furthermore, it has been argued that taxa which use tactile information for foraging (see also [4.4.4.2.2](#) below), show somewhat hypertrophied rostral eminentia sagittalis structures ([Iwaniuk & Wylie 2006](#); [Wylie et al. 2015](#)), likely as the mandibular ( $V_3$ ) division of the trigeminal (V) cranial nerve, innervating the lower bill (see Introduction, [1.5.4.2.2](#), and [4.4.4.1](#) above), terminates in rostradorsal mesopallial regions of the brain (e.g. [Northcutt 1981](#); [Dubbeldam et al. 1981](#); [Pettigrew & Frost 1985](#); [Wild et al. 1985](#)). As such, the development of stereopsis in birds has been linked with the presence of well-developed eminentia sagittalis, evidence of which is proposed as compelling indications for the presence of stereoscopic vision specialities in fossil material ([Pettigrew 1986:220](#)).

Therefore, appraisal of dromornithid orbit size and orientation in the skull, may provide additional insight into the hypertrophy noted in eminentia sagittalis structures for these birds. Neurocranial material unambiguously suggests dromornithids were possessed of large, forward facing eyes in life. For example, orbit widths of 117–136 mm for specimens of *D. planei*, 128–141mm for specimens of *D. stirtoni*, and 130 mm for a specimen of *D. murrayi* were reported by [Worthy et al. \(2016b\)](#); see Table A4.4; see also Figs. A4.1, A4.4, A4.6). However, inference as to whether dromornithid retinal topography was structurally adapted (i.e., corneal diameter, cell density/type etc), for sensitivity to low light conditions, may only be made by interpretation of orbit shape and size from skeletal remains. In a large study assessing the relationship between corneal diameter, and axial length of the avian eye, [Hall & Ross \(2007\)](#) showed that species adapted to light-limited (scotopic or crepuscular) habitats, have larger corneal diameters and axial lengths, relative to those active during well-lit (photopic or diurnal) conditions. [Hall \(2008\)](#) showed there exists a close relationship between corneal diameter and axial length of the eye, and metrics describing the bony structures of the orbit were “well associated” with photic activity in birds. In support of these observations, several additional studies have shown that in nocturnal birds, eye shape increases relative to skull length. They display larger orbit diameters relative to depth, and orbits are more frontally orientated (e.g. [Iwaniuk et al. 2008, 2010](#); [Corfield et al. 2011](#), and references therein; but see also [Martin 2009](#)). Animals that exploit low-light environments, have evolved in one of two ways: **1**, by enlargement and orientation of the visual system (i.e., increasing orbit size and binocular overlap); or **2**, they develop enhanced sensitivity of somatosensory and tactile systems (e.g. [Corfield et al. 2011](#), and references therein). Among ratites, kiwi are the only nocturnal taxon, and have evolved reduced eye size and distinct endocranial morphology associated with the somatosensory and tactile systems strategy (i.e. **2.**, see [Martin et al. 2007](#); [Corfield et al. 2008](#)). All other flightless ratites are diurnal, as were the extinct NZ moa (see [Ashwell & Scofield 2008](#)), and inspection of the shape of their brains (e.g.

Craigie 1939:fig 2; Martin et al. 2007:fig. 2a-b; Ashwell & Scofield 2008:fig 6g-l; Corfield et al. 2008:fig. 1bA-E; Peng et al. 2010:figs. 1, 3; Picasso et al. 2011:fig 1; Walsh & Knoll 2018:fig. 5.3[1-6]), show rostromediolaterally hypertrophied eminentia sagittalis in these large flightless birds, which may represent evolution for enhanced visual proficiency (i.e., strategy **1** above). However, none of these diurnal ratite taxa display the massively hypertrophied state of the eminentia sagittalis, evident in dromornithid dorsal endocasts.

Martin (2009) advanced that binocular vision in birds is primarily used for the inspection of food items held in the bill, and for bill control during the process of foraging and food provision to chicks. He also argued that binocular vision in the control of locomotion is a secondary function, as spatial information may be provided by each eye independently.

Considering dromornithid cranial morphology displays large, forward facing orbits, and their dorsal endocranial morphology is dominated by the eminentia sagittalis. It is more than likely these birds adopted the strategy (i.e. **1** above) of enlargement and orientation of the visual system, whereby they developed good stereoscopic vision, were capable of accurate depth perception, and possessed enhanced visual capabilities. This would preadapt them to being specialised browsers capable of selecting individual fruit and leaves from within complex browse.

Additionally, such combined features of cranial and endocranial morphology, also raise the possibility that dromornithids were adaptively selected for low-light visual proficiency along the nocturnal-diurnal gradient (scotopic *sensu* Hall 2008; see also Garamszegi et al. 2002). However, I prefer the explanation that features of dromornithid neuro- and endocranial anatomy, are more likely associated with foraging dexterity and locomotion within complex diurnal environments.

**4.4.4.2.2 Cerebrum** (rostral and caudal telencephalon)—the nido- and mesopallial structures of the cerebrum are recognised to form a complex with “integrative” functions (see Dubbeldam 1998a, and references therein). As part of the tectofugal visual pathway (i.e. **2**; see 4.4.4.2 above), the telencephalon has been associated with a wide range of behaviours including: feeding, taste, tactile sense, taste discrimination, vocalisation, and with high levels of cognition and complex tasks (Corfield et al. 2012, and references therein). Furthermore, stereotyped species-specific behaviour (Reiner et al. 1984; Dubbeldam 1998a), pecking accuracy (Salzen et al. 1975), and the processing of visual information such as brightness, colour, and pattern discrimination (Iwaniuk et al. 2010), have been attributed to processes within the caudolateral telencephalon. Pettigrew & Frost (1985) showed the maxillary (V<sub>2</sub>) division of the trigeminal (V) cranial nerve, which innervates the upper bill (see Introduction, 1.5.4.2.2; and 4.4.4.1 above), transmits to extensive terminal fields in the region of the rostradorsal mesopallium of the cerebrum (see also Northcutt 1981). Similarly, Dubbeldam et al. (1981) showed that ascending maxillary and mandibular trigeminal projections, transmitted rostradorsally via the nucleus basalis to mesopallial terminal fields (see also Wild et al. 1985). These sensorimotor projections were related to the “detection” of food particles, particularly in low-visibility feeding in anseriforms (Berkhoudt et al. 1981), and food grasping in columbiforms (Wild et al. 1984,

1985), and passeriforms (Wild & Farabaugh 1996). Caudal telencephalon areas of the dromornithid brain are strongly hypertrophied, and suggest the tactile senses of these birds were likely well developed (for e.g., in kiwi these regions are massively hypertrophied, see Corfield et al. 2012). Collectively, these capabilities potentially facilitated interactive behaviours essential for large birds employing high levels of tactile browsing dexterity in complex mosaic environments.

**4.4.4.2.3 Mesencephalon**—form part of the visual pathway system. Hellmann et al. (2004) characterised the mesencephalon as “relay stations” for the conveyance of ascending visual output to the forebrain (see 4.4.4.2.1 above), projecting descending output to the premotor regions of the hindbrain (see 4.4.4.2.4 below), and comprise multiple cell types that are retinotopically organised, and functionally specific. So called “optic flow” (*sensu* Gibson 1954), are retinal stimuli generated by self-motion through an environment (see Wylie et al. 2018, and references therein). Optic flow stimuli are analysed by recipient nuclei in the accessory optic system and the pretectum, which serves to generate optokinetic response for the control of posture and eye movement stabilisation (Simpson 1984; Simpson et al. 1988; Giolli et al. 2006; Wylie et al. 2009, 2018; Gaede et al. 2019; and references therein). The lentiformis mesencephali, or pretectal nucleus, responds to “moving large-field visual stimuli” and controls posture and locomotion, including determining compensatory movement, and navigation through complex environments, facilitated by processes within the cerebellum (Pakan & Wylie 2006; see also Jerison 1973). The dromornithid mesencephalon, in contrast to initial appearances, are not particularly hypotrophied in comparison to those extant galloansere taxa assessed here, when size is accounted for. Bennet & Harvey (1985a) reported that the size of the mesencephalon is not correlated with either nocturnal or diurnal behaviour, further supporting my contention that functional or behavioural inference derived from comparisons of absolute mesencephalon size, must be made with appropriate caution (see 4.4.1.5 above; and Chapter 3, 3.4.3).

**4.4.4.2.4 Hindbrain**—the cerebellum has long been associated with motor integration and posture control in birds (Jerison 1973). Visual signals are projected through the third visual pathway via the retinal-recipient nuclei of the mesencephalon (see above) to the cerebellum (Lau et al. 1998; Wylie 2001; Pakan & Wylie 2006; Wylie et al. 2009), where they facilitate obstacle avoidance responses. Additionally, Pakan & Wylie (2006) suggest folia VI–VIII of the cerebellum may be involved in “steering” functions, and Iwaniuk et al. (2007) showed that VI and VII folia are hypertrophied in birds they classified as “strong fliers”.

Morphometric results for the dromornithid mid- and hindbrain, with respect to those of basal extant galloanseres, show that the shapes described by the metencephalon (cerebellum and rhombencephalon), and mesencephalon are certainly distinct. However, Modular Distance and Surface Area results show ratios for the dromornithid mid- and hindbrain overlap with extant galloanseres in several aspects, and there are few mid- and hindbrain characteristics that identify dromornithids as particularly dissimilar. The apparent visual distinction between caudal endocasts

across taxa, may lie in the particularly distinct hypertrophy of the dromornithid prosencephalon, or dorsoventral and mediolateral forebrain, several aspects of which certainly do differ from those of extant galloanseres (see **4.4.1** above). These hypertrophied forebrain characteristics give the impression that the dromornithid mid- and hindbrain is comparatively hypotrophied, but this is not well supported by results presented here.

The retention of a comparably large cerebellum, and associated mid- and hindbrain morphology in dromornithids, such as those shown by the volant galloansere taxa assessed, raises the question as to why dromornithids maintained the capacity for capable movement through complex environments, associated with third visual pathway processes in the hindbrain (see above). That these functional attributes were selected for during early dromornithid evolution is a possibility.

During the transition from the early Cenozoic through the Eocene, Australia was blanketed by predominantly warm to cool-temperate rainforest, which only began to open into scleromorphic vegetation on higher ground during the Oligocene (Martin 2006). These forests became progressively drier during the transition from the Oligocene through the late Miocene, eventuating in the establishment of scleromorphic fire-sensitive woodlands, or ‘dry jungles’, which during the Miocene became the dominant continental floras (Murray & Vickers-Rich 2004; see also Macphail 1997). Dromornithid evolution on the Australian continent has a long history, and the key characteristics of the dromornithid brain were likely assembled when they first evolved into large flightless birds, sometime during the Palaeogene. During those times, dromornithids would have occupied highly complex forested environments, where the capacity for visual proficiency, the taxon’s trophic preferences established, and capability for navigating complex environments maintained from their flighted ancestors. Dromornithids likely co-opted these traits in adapting to, and exploiting the steadily drying Australian environment through their known temporal range, traits that persisted in the last dromornithid taxon of the late Pleistocene.

The neuro- and endocranial morphology of dromornithids is unlike any seen in the evolution of birds, and represents distinct morphological adaptations to progressively changing Australian Cenozoic environments. These ‘magnificent Mihirungs’ are inimitably Australian, and like much of the idiosyncratic Australian fauna of the past, represent combinations of unique adaptations now lost.

#### **4.5 Acknowledgements**

I thank Michael Archer and Suzanne Hand, (University of NSW, Sydney), for access to *Dromornis murrayi* specimens (QM F57984, QM F57974 and QM F50412 endocast). Philippa Horton and Maya Penck, (South Australian Museum, Adelaide), for access to the ornithology collection. Adelaide Microscopy (University of Adelaide), for access to the Skyscan  $\mu$ CT instrument. Joseph Bevitt (ANSTO, Sydney), for Neutron scanning of *Dromornis planei*, and Mishelle Korlaet (SAHMRI, Adelaide), for CT-scanning *D. murrayi* and *Ilbandornis woodburnei* specimens.

## 4.6 REFERENCES

- Adams, D.C., Collyer, M.L., Kaliontzopoulou, A., 2018. *Geomorph: Software for geometric morphometric analyses*. R package version 3.0.7. <https://cran.r-project.org/package=geomorph>.
- Alexander, R.M., 1983. Allometry of the leg bones of moas (Dinornithes) and other birds. *Journal of Zoology, London* 200, 215-231.
- Angst, D., Lécuyer, C., Amiot, R., Buffetaut, E., Fourel, F., Martineau, F., Legendre, S., Abourachid, A., Herrel, A., 2014. Isotopic and anatomical evidence of an herbivorous diet in the Early Tertiary giant bird *Gastornis*. Implications for the structure of Paleocene terrestrial ecosystems. *Naturwissenschaften* 101, 313-322. doi:10.1007/s00114-00014-01158-00112.
- Archer, M., Godthelp, H., Hand, S.J., Attenborough, D., 1991. *Australia's Lost World: Riversleigh, World Heritage Site*. New Holland Publishers (Australia), Frenchs Forest, NSW. p. 264.
- Archer, M., Godthelp, H., Hand, S.J., Megirian, D., 1989. Fossil mammals of Riversleigh, northwestern Queensland: preliminary overview of biostratigraphy, correlation and environmental change. *Australian Zoologist* 25, 29-65.
- Archer, M., Hand, S.J., Godthelp, H., Creaser, P., 1997. Correlation of the Cainozoic sediments of the Riversleigh World Heritage fossil property, Queensland, Australia, In: Aguilar, J.-P., Legendre, S., Michaux, J. (Eds.), *Actes du Congrès Biochrom '97, Mémoires et travaux de l'Institut de Montpellier de l'Ecole Pratique des Hautes Etudes* 21, pp. 131-152.
- Arena, D.A., Travouillon, K.J., Beck, R.M.D., Black, K.H., Gillespie, A.K., Myers, T.J., Archer, M., Hand, S.J., 2016. Mammalian lineages and the biostratigraphy and biochronology of Cenozoic faunas from the Riversleigh World Heritage Area, Australia. *Lethaia* 49, 43-60. doi:10.1111/let.12131.
- Arends, J.J.A., Dubbeldam, J.L., 1984. The subnuclei and primary afferents of the descending trigeminal system in the mallard (*Anas platyrhynchos* L.). *Neuroscience* 13, 781-795.
- Ashwell, K.W.S., Scofield, R.P., 2008. Big birds and their brains: Paleoneurology of the New Zealand moa. *Brain, Behavior and Evolution* 71, 151-166. doi:10.1159/000111461.
- Bennett, P.M., Harvey, P.H., 1985a. Brain size, development and metabolism in birds and mammals. *Journal of Zoology* 207, 491-509.
- Berkhoudt, H., Dubbeldam, J.L., Zeilstra, S., 1981. Studies on the somatotopy of the trigeminal system in the mallard, *Anas platyrhynchos* L. IV. Tactile representation in the nucleus basalis. *Journal of Comparative Neurology* 196, 407-420.
- Boles, W.E., 2006. The Avian Fossil Record of Australia: An Overview, in: Merrick, J.R., Archer, M., Hickey, G.M., Lee, M.S.Y. (Eds.), *Evolution and Biogeography of Australasian Vertebrates*, Auscipub, Sydney, Australia, pp. 387-411.
- Bookstein, F.L., 1991. *Morphometric Tools for Landmark Data: Geometry and Biology*. Cambridge University Press, Cambridge. UK. p.435.
- Bubień-Waluszewska, A., 1981. The Cranial Nerves, in: King, A.S., McLelland, J. (Eds.), *Form and Function in Birds*. Vol. 2, Academic Press, London, pp. 385-438.
- Campbell Jr, K.E., Marcus, L., 1992. The relationship of hindlimb bone dimensions to body weight in birds, In: Campbell Jr, K.E. (Ed.), *Papers in Avian Paleontology Honoring Pierce Brodkorb, Incorporating the Proceedings of the II International Symposium of the Society of Avian*

- Paleontology and Evolution, Natural History Museum of Los Angeles County, 1988, *Natural History Museum of Los Angeles County Science Series* 36, pp. 395-412.
- Cignoni, P., Callieri, M., Corsini, M., Dellepiane, M., Ganovelli, F., Ranzuglia, G., 2008. Meshlab: an Open-Source Mesh Processing Tool, In: Scarano, V., De Chiara, R., Erra, U. (Eds.), *Proceedings of the 2008 Eurographics Italian Chapter Conference, Salerno, Italy*, pp. 129-136. ISBN 978-123-905673-905668-905675.
- Corfield, J.R., Gsell, A.C., Brunton, D., Heesy, C.P., Hall, M.I., Acosta, M.L., Iwaniuk, A.N., 2011. Anatomical specializations for nocturnality in a critically endangered parrot, the Kakapo (*Strigops habroptilus*). *PLoS ONE* 6, e22945. doi:10.1371/journal.pone.0022945.
- Corfield, J.R., Wild, J.M., Hauber, M.E., Parsons, S., Kubke, M.F., 2008. Evolution of brain size in the palaeognath lineage, with an emphasis on New Zealand ratites. *Brain, Behavior and Evolution* 71, 87-99. doi:10.1159/000111456.
- Corfield, J.R., Wild, J.M., Parsons, S., Kubke, M.F., 2012. Morphometric analysis of telencephalic structure in a variety of neognath and paleognath bird species reveals regional differences associated with specific behavioral traits. *Brain, Behavior and Evolution* 80, 181-195. doi:10.1159/000339828.
- Craigie, E.H., 1939. The cerebral cortex of *Rhea americana*. *Journal of Comparative Neurology* 70, 331-353.
- Davies, S.J.J.F., 1978. The food of emus. *Austral Ecology* 3, 411-422. doi:10.1111/j.1442-9993.1978.tb01189.x.
- Davies, S.J.J.F., 2002. *Bird families of the world: Ratites and Tinamous: Tinamidae, Rheidae, Dromaiidae, Casuariidae, Apterygidae, Struthionidae*. Oxford University Press, Oxford U.K. p. 310.
- Deng, C., Wang, B., 1992. Overlap of somatic and visual response areas in the Wulst of pigeon. *Brain Research* 582, 320-322.
- Dickinson, E.C., Remsen Jr, J.V. (Eds.), 2013. *The Howard & Moore Complete Checklist of the Birds of the World*. 4th Edition. Aves Press, Eastbourne, U.K.
- Dubbeldam, J.L., 1980. Studies on the somatotopy of the trigeminal system in the mallard, *Anas platyrhynchos* L. II. Morphology of the principal sensory nucleus. *Journal of Comparative Neurology* 191, 557-571.
- Dubbeldam, J.L., 1984. Afferent connections of nervus facialis and nervus glossopharyngeus in the pigeon (*Columba livia*) and their role in feeding behavior. *Brain, Behavior and Evolution* 24, 47-57.
- Dubbeldam, J.L., 1992. Cranial nerves and sensory centres—a matter of definition? Hypoglossal and other afferents of the avian sensory trigeminal system. *Zoologische Jahrbücher* 122, 179-186.
- Dubbeldam, J.L., 1998a. Birds, in: Nieuwenhuys, R., ten Donkelaar, H.J., Nicholson, C. (Eds.), *The Central Nervous System of Vertebrates*, Springer-Verlag, Berlin, pp. 1525-1636.
- Dubbeldam, J.L., 1998b. The sensory trigeminal system in birds: input, organization and effects of peripheral damage. A review. *Archives of Physiology and Biochemistry* 106, 338-345. doi:10.1076/apab.1106.1075.1338.4367.
- Dubbeldam, J.L., Brauch, C.S.M., Don, A., 1981. Studies on the somatotopy of the trigeminal system in the mallard, *Anas platyrhynchos* L. III. Afferents and organization of the nucleus basalis. *Journal of Comparative Neurology* 196, 391-405.

- Dubbeldam, J.L., Brus, E.R., Menken, S.B.J., Zeilstra, S., 1979. The central projections of the glossopharyngeal and vagus ganglia in the mallard, *Anas platyrhynchos* L. *Journal of Comparative Neurology* 183, 149-168. doi:110.1002/cne.901830111
- Fritz, J., Hummel, J., Kienzle, E., Wings, O., Streich, W.J., Clauss, M., 2011. Gizzard vs. teeth, it's a tie: food-processing efficiency in herbivorous birds and mammals and implications for dinosaur feeding strategies. *Paleobiology* 37, 577-586.
- Gaede, A.H., Gutierrez-Ibañez, C., Armstrong, M.S., Altshuler, D.L., Wylie, D.R.W., 2019. Pretectal projections to the oculomotor cerebellum in hummingbirds (*Calypte anna*), zebra finches (*Taeniopygia guttata*), and pigeons (*Columba livia*). *Journal of Comparative Neurology* xx, 1-15 (early view). doi:10.1002/cne.24697.
- Garamszegi, L.Z., Møller, A.P., Erritzøe, J., 2002. Coevolving avian eye size and brain size in relation to prey capture and nocturnality. *Proceedings of the Royal Society of London B: Biological Sciences* 269, 961-967.
- Gibson, J.J., 1954. The visual perception of objective motion and subjective movement. *Psychological Review* 61, 304-314. doi:310.1037/h0061885.
- Giolli, R.A., Blanks, R.H.I., Lui, F., 2006. The accessory optic system: basic organization with an update on connectivity, neurochemistry, and function. *Progress in Brain Research* 151, 407-440.
- Grellet-Tinner, G., Spooner, N.A., Handley, W.D., Worthy, T.H., 2017. The *Genyornis* egg: Response to Miller et al.'s commentary on Grellet-Tinner et al., 2016. *Quaternary Science Reviews* 161, 128-133. doi:110.1016/j.quascirev.2016.1012.1004.
- Gutiérrez-Ibañez, C., Iwaniuk, A.N., Lisney, T.J., Wylie, D.R.W., 2013. Comparative study of visual pathways in owls (Aves: Strigiformes). *Brain, Behavior and Evolution* 81, 27-39. doi:10.1159/000343810.
- Gutiérrez-Ibañez, C., Iwaniuk, A.N., Wylie, D.R.W., 2009. The independent evolution of the enlargement of the principal sensory nucleus of the trigeminal nerve in three different groups of birds. *Brain, Behavior and Evolution* 74, 280-294. doi:210.1159/000270904.
- Hall, M.I., 2008. The anatomical relationships between the avian eye, orbit and sclerotic ring: implications for inferring activity patterns in extinct birds. *Journal of Anatomy* 212, 781-794. doi:710.1111/j.1469-7580.2008.00897.x.
- Hall, M.I., Ross, C.F., 2007. Eye shape and activity pattern in birds. *Journal of Zoology* 271, 437-444. doi:410.1111/j.1469-7998.2006.00227.x.
- Handley, W.D., Chinsamy, A., Yates, A.M., Worthy, T.H., 2016. Sexual dimorphism in the late Miocene mihirung *Dromornis stirtoni* (Aves: Dromornithidae) from the Alcoota Local Fauna of central Australia. *Journal of Vertebrate Paleontology* 36, e1180298. doi:1180210.1181080/02724634.02722016.01180298.
- Hansford, J.P., Turvey, S.T., 2018. Unexpected diversity within the extinct elephant birds (Aves: Aepyornithidae) and a new identity for the world's largest bird. *Royal Society Open Science* 5, 181295. doi:181210.181098/rsos.181295.
- Hellmann, B., Güntürkün, O., Manns, M., 2004. Tectal mosaic: organization of the descending tectal projections in comparison to the ascending tectofugal pathway in the pigeon. *Journal of Comparative Neurology* 472, 395-410.

- Iwaniuk, A.N., Gutierrez-Ibañez, C., Pakan, J.M., Wylie, D.R.W., 2010. Allometric scaling of the tectofugal pathway in birds. *Brain, Behavior and Evolution* 75, 122-137. doi:110.1159/000311729.
- Iwaniuk, A.N., Heesy, C.P., Hall, M.I., 2010. Morphometrics of the eyes and orbits of the nocturnal swallow-tailed gull (*Creagrurus furcatus*). *Canadian Journal of Zoology* 88, 855-865. doi:10.1139/Z1110-1051.
- Iwaniuk, A.N., Heesy, C.P., Hall, M.I., Wylie, D.R.W., 2008. Relative Wulst volume is correlated with orbit orientation and binocular visual field in birds. *Journal of Comparative Physiology A* 194, 267-282. doi:10.1007/s00359-00007-00304-00350.
- Iwaniuk, A.N., Hurd, P.L., Wylie, D.R.W., 2007. Comparative morphology of the avian cerebellum: II. Size of folia. *Brain, Behavior and Evolution* 69, 196-219. doi:110.1159/000096987.
- Iwaniuk, A.N., Nelson, J.E., 2002. Can endocranial volume be used as an estimate of brain size in birds? *Canadian Journal of Zoology* 80, 16-23. doi:10.1139/Z11301-1204.
- Iwaniuk, A.N., Wylie, D.R.W., 2006. The evolution of stereopsis and the Wulst in caprimulgiform birds: a comparative analysis. *Journal of Comparative Physiology A* 192, 1313-1326. doi:10.1007/s00359-00006-00161-00352.
- Jarvis, E.D., Güntürkün, O., Bruce, L., Csillag, A., Karten, H., Kuenzel, W., Medina, L., Paxinos, G., Perkel, D.J., Shimizu, T., 2005. Avian brains and a new understanding of vertebrate brain evolution. *Nature Reviews Neuroscience* 6, 151-159.
- Jerison, H.J., 1973. *Evolution of the Brain and Intelligence*. Academic Press, New York.
- Kulemeyer, C., Asbahr, K., Gunz, P., Frahnert, S., Bairlein, F., 2009. Functional morphology and integration of corvid skulls—a 3D geometric morphometric approach. *Frontiers in Zoology* 6, 1-14. doi:10.1186/1742-9994-1186-1182.
- Lau, K.L., Glover, R.G., Linkenhoker, B., Wylie, D.R.W., 1998. Topographical organization of inferior olive cells projecting to translation and rotation zones in the vestibulocerebellum of pigeons. *Neuroscience* 85, 605-614.
- Lawal, R.A., Al-Atiyat, R.M., Aljumaah, R.S., Silva, P., Mwacharo, J.M., Hanotte, O., 2018. Whole-genome resequencing of red junglefowl and indigenous village chicken reveal new insights on the genome dynamics of the species. *Frontiers in Genetics* 9, 264 (17pp). doi:10.3389/fgene.2018.00264.
- Macphail, M.K., 1997. Late Neogene climates in Australia: fossil pollen-and spore-based estimates in retrospect and prospect. *Australian Journal of Botany* 45, 425-464. doi:10.1071/BT96052.
- Manger, P.R., Elston, G.N., Pettigrew, J.D., 2002. Multiple maps and activity-dependent representational plasticity in the anterior Wulst of the adult barn owl (*Tyto alba*). *European Journal of Neuroscience* 16, 743-750. doi:10.1046/j.1460-9568.2002.02119.x.
- Martin, G.R., 2009. What is binocular vision for? A birds' eye view. *Journal of Vision* 9, 1-19. doi:10.1167/1169.1111.1114.
- Martin, G.R., Wilson, K.-J., Wild, J.M., Parsons, S., Kubke, M.F., Corfield, J., 2007. Kiwi forego vision in the guidance of their nocturnal activities. *PLoS ONE* 2, e198. doi:10.1371/journal.pone.0000198.
- Martin, H.A., 2006. Cenozoic climatic change and the development of the arid vegetation in Australia. *Journal of Arid Environments* 66, 533-563. doi:10.1016/j.jaridenv.2006.1001.1009.

- Mayr, G., 2009. *Paleogene Fossil Birds*. Springer-Verlag, Berlin Heidelberg.
- Mayr, G., 2011. Cenozoic mystery birds—on the phylogenetic affinities of bony-toothed birds (Pelagornithidae). *Zoologica Scripta* 40, 448-467. doi:410.1111/j.1463-6409.2011.00484.x.
- Megirian, D., Prideaux, G.J., Murray, P.F., Smit, N., 2010. An Australian land mammal age biochronological scheme. *Paleobiology* 36, 658-671.
- Miceli, D., Marchand, L., Repérant, J., Rio, J.-P., 1990. Projections of the dorsolateral anterior complex and adjacent thalamic nuclei upon the visual Wulst in the pigeon. *Brain Research* 518, 317-323.
- Miller, G.H., Fogel, M.L., Magee, J.W., Gagan, M.K., Clarke, S.J., Johnson, B.J., 2005. Ecosystem collapse in Pleistocene Australia and a human role in megafaunal extinction. *Science* 309, 287-290.
- Milner, A.C., Walsh, S.A., 2009. Avian brain evolution: new data from Palaeogene birds (Lower Eocene) from England. *Zoological Journal of the Linnean Society* 155, 198-219.
- Murray, P., Megirian, D., Rich, T., Plane, M., Black, K., Archer, M., Hand, S.J., Vickers-Rich, P., 2000. Morphology, systematics, and evolution of the marsupial genus *Neohelos* Stirton (Diprotodontidae, Zygomaturinae). *Museums and Art Galleries of the Northern Territory Research Report* 6, 1-141.
- Murray, P.F., Megirian, D., 1992. Continuity and contrast in middle and late Miocene vertebrate communities from the Northern Territory. *The Beagle, Records of the Northern Territory Museum of Arts and Sciences* 9, 195-218.
- Murray, P.F., Megirian, D., 1998. The skull of dromornithid birds: anatomical evidence for their relationship to Anseriformes. *Records of the South Australian Museum* 31, 51-97.
- Murray, P.F., Megirian, D., 2006. The Pwerte Marnte Marnte Local Fauna: a new vertebrate assemblage of presumed Oligocene age from the Northern Territory of Australia. *Alcheringa* 30, 211-228. doi:210.1080/03115510609506864.
- Murray, P.F., Vickers-Rich, P., 2004. *Magnificent Mihirungs: The Colossal Flightless Birds of the Australian Dreamtime*. Indiana University Press, Bloomington.
- Nguyen, J.M.T., Boles, W.E., Hand, S.J., 2010. New material of *Barawertornis tedfordi*, a dromornithid bird from the Oligo-Miocene of Australia, and its phylogenetic implications. *Records of the Australian Museum* 62, 45-60.
- Northcutt, R.G., 1981. Evolution of the telencephalon in nonmammals. *Annual Review of Neuroscience* 4, 301-350.
- Olson, S.L., 1985. The Fossil Record of Birds, in: Farner, D.S., King, J.R., Parkes, K.C. (Eds.), *Avian Biology*. Vol. 8, Academic Press, New York, pp. 79-238.
- Orlowski, J., Harmening, W., Wagner, H., 2012. Night vision in barn owls: Visual acuity and contrast sensitivity under dark adaptation. *Journal of Vision* 12, 1-8.
- Pakan, J.M.P., Wylie, D.R.W., 2006. Two optic flow pathways from the pretectal nucleus lentiformis mesencephali to the cerebellum in pigeons (*Columba livia*). *Journal of Comparative Neurology* 499, 732-744. doi:710.1002/cne.21108.
- Peng, K., Feng, Y., Zhang, G., Liu, H., Song, H., 2010. Anatomical study of the brain of the African ostrich. *Turkish Journal of Veterinary and Animal Sciences* 34, 235-241. doi:210.3906/vet-0806-3919.

- Pettigrew, J.D., 1979. Binocular visual processing in the owl's telencephalon. *Proceedings of the Royal Society of London B: Biological Sciences* 204, 435-454. doi:410.1098/rspb.1979.0038.
- Pettigrew, J.D., 1986. Evolution of Binocular Vision, in: Pettigrew, J.D., Sanderson, K.J., Levick, W.R. (Eds.), *Visual Neuroscience*, Springer, New York, pp. 208-222.
- Pettigrew, J.D., Frost, B.J., 1985. A tactile fovea in the Scolopacidae? *Brain, Behavior and Evolution* 26, 185-195. doi: 110.1159/000118775.
- Pettigrew, J.D., Konishi, M., 1976. Neurons selective for orientation and binocular disparity in the visual wulst of the barn owl (*Tyto alba*). *Science* 193, 675-678. doi:610.1126/science.948741.
- Phillips, M.J., Gibb, G.C., Crimp, E.A., Penny, D., 2010. Tinamous and moa flock together: mitochondrial genome sequence analysis reveals independent losses of flight among ratites. *Systematic Biology* 59, 90-107. doi:110.1093/sysbio/syp1079.
- Picasso, M.B.J., Tambussi, C., Dozo, M.T., 2009. Neurocranial and brain anatomy of a Late Miocene eagle (Aves, Accipitridae) from Patagonia. *Journal of Vertebrate Paleontology* 29, 831-836. doi:810.1671/1039.1029.0319.
- Picasso, M.B.J., Tambussi, C.P., Degrange, F.J., 2011. Virtual reconstructions of the endocranial cavity of *Rhea americana* (Aves, Palaeognathae): Postnatal anatomical changes. *Brain, Behavior and Evolution* 76, 176-184. doi:110.1159/000321173.
- Rasband, W.S., 2018. *ImageJ*, U.S. National Institutes of Health, Bethesda, Maryland, USA. <https://imagej.nih.gov/ij/>.
- R Core Team, 2018. *R: A language and environment for statistical computing*. R Foundation for Statistical Computing, Vienna, Austria. URL: <https://www.R-project.org/>.
- Reiner, A., Davis, B.M., Brecha, N.C., Karten, H.J., 1984. The distribution of enkephalinlike immunoreactivity in the telencephalon of the adult and developing domestic chicken. *Journal of Comparative Neurology* 228, 245-262.
- Rich, P.V., 1975. Changing continental arrangements and the origin of Australia's non-passeriform continental avifauna. *Emu* 75, 97-112.
- Rich, P.V., 1979. The Dromornithidae, an extinct family of large ground birds endemic to Australia. *Bureau of National Resources, Geology and Geophysics Bulletin* 184, Canberra.
- Rogers, L., 1996. Behavioral, structural and neurochemical asymmetries in the avian brain: a model system for studying visual development and processing. *Neuroscience & Biobehavioral Reviews* 20, 487-503.
- RStudio Team, 2016. *RStudio: Integrated Development for R*, RStudio, Inc., Boston, MA URL <http://www.rstudio.com/>.
- Salzen, E.A., Parker, D.M., Williamson, A.J., 1975. A forebrain lesion preventing imprinting in domestic chicks. *Experimental Brain Research* 24, 145-157.
- Scofield, R.P., Ashwell, K.W.S., 2009. Rapid somatic expansion causes the brain to lag behind: the case of the brain and behavior of New Zealand's Haast's Eagle (*Harpagornis moorei*). *Journal of Vertebrate Paleontology* 29, 637-649.
- Simpson, J.I., 1984. The accessory optic system. *Annual Review of Neuroscience* 7, 13-41.
- Simpson, J.I., Leonard, C.S., Soodak, R.E., 1988. The accessory optic system. Analyzer of self-motion. *Annals of the New York Academy of Sciences* 545, 170-179.

- Stingelin, W., 1957. *Vergleichende Morphologische Untersuchungen am Vorderhirn der Vögel auf Cytologischer und Cytoarchitektonischer Grundlage*. Verlag Helbing & Lichtenhahn, Basel. p.123.
- Stirling, E.C., Zietz, A.H.C., 1896a. Preliminary notes on *Genyornis newtoni*: A new genus and species of fossil struthious bird found at Lake Callabonna, South Australia. *Transactions of the Royal Society of South Australia* 20, 171-211.
- Stirling, E.C., Zietz, A.H.C., 1896b. *Genyornis newtoni* - A fossil struthious bird from Lake Callabonna, South Australia: Description of the bones of the leg and foot. *Transactions of the Royal Society of South Australia* 20, 191-211.
- Stirton, R.A., Woodburne, M.O., Plane, M.D., 1967. A phylogeny of the Tertiary Diprotodontidae and its significance in correlation, in: Tertiary Diprotodontidae from Australia and New Guinea, *Bulletin of the Bureau of Mineral Resources, Geology and Geophysics* 85, Australia, pp. 149-160.
- Streidter, G.F., 2005. *Principles of brain evolution*. Sinauer Associates, Sunderland, MA.
- Striedter, G.F., 2006. Précis of principles of brain evolution. *Behavioral and Brain Sciences* 29, 1-12.
- Travouillon, K.J., Archer, M., Hand, S.J., Godthelp, H., 2006. Multivariate analyses of Cenozoic mammalian faunas from Riversleigh, northwestern Queensland. *Alcheringa Special Issue* 1, 323-349.
- Travouillon, K.J., Escarguel, G., Legendre, S., Archer, M., Hand, S.J., 2011. The use of MSR (Minimum Sample Richness) for sample assemblage comparisons. *Paleobiology* 37, 696-709.
- van der Willigen, R.F., Frost, B.J., Wagner, H., 1998. Stereoscopic depth perception in the owl. *NeuroReport* 9, 1233-1237.
- Vickers-Rich, P., 1991. The Mesozoic and Tertiary History of Birds on the Australian Plate, in: Vickers-Rich, P., Monaghan, J.M., Baird, R.F., Rich, T.H. (Eds.), *Vertebrate Palaeontology of Australasia*, Pioneer Design Studios in cooperation with the Monash University Publications Committee, Melbourne, pp. 721-808.
- Vickers-Rich, P., Molnar, R.E., 1996. The foot of a bird from the Eocene Redbank Plains Formation of Queensland, Australia. *Alcheringa* 20, 21-29.
- Walsh, S.A., Iwaniuk, A.N., Knoll, M.A., Bourdon, E., Barrett, P.M., Milner, A.C., Nudds, R.L., Abel, R.L., Sterpaio, P.D., 2013. Avian cerebellar floccular fossa size is not a proxy for flying ability in birds. *PLoS ONE* 8, e67176. doi:67110.61371/journal.pone.0067176.
- Walsh, S.A., Knoll, F., 2018. The Evolution of Avian Intelligence and Sensory Capabilities: The Fossil Evidence, in: Bruner, E., Ogihara, N., Tanabe, H.C. (Eds.), *Digital Endocasts: From Skulls to Brains*, Springer Japan, Tokyo, pp. 59-69. doi:10.1007/1978-1004-1431-56582-56586.
- Walsh, S.A., Luo, Z.-X., Barrett, P.M., 2014. Modern Imaging Techniques as a Window to Prehistoric Auditory Worlds, in: Koppl, C., Manley, G.A., Popper, A.N., Fay, R.R. (Eds.), *Insights from Comparative Hearing Research*, Springer, New York, pp. 227-261.
- Wells, R.T., Tedford, R.H., 1995. *Sthenurus* (Macropodidae: Marsupialia) from the Pleistocene of Lake Callabonna, South Australia. *Bulletin of the American Museum of Natural History* 225, 3-111.
- Wetmore, A., 1960. A classification for the birds of the world. *Smithsonian Miscellaneous Collections* 139, 1-37.

- Wild, J.M., 1981. Identification and localization of the motor nuclei and sensory projections of the glossopharyngeal, vagus, and hypoglossal nerves of the cockatoo (*Cacatua roseicapilla*), Cacatuidae. *Journal of Comparative Neurology* 203, 351-377.
- Wild, J.M., 1987. The avian somatosensory system: connections of regions of body representation in the forebrain of the pigeon. *Brain Research* 412, 205-223.
- Wild, J.M., 1990. Peripheral and central terminations of hypoglossal afferents innervating lingual tactile mechanoreceptor complexes in Fringillidae. *Journal of Comparative Neurology* 298, 157-171.
- Wild, J.M., 1997. The avian somatosensory system: the pathway from wing to wulst in a passerine (*Chloris chloris*). *Brain Research* 759, 122-134.
- Wild, J.M., Williams, M.N., 2000. Rostral wulst in passerine birds. I. Origin, course, and terminations of an avian pyramidal tract. *Journal of Comparative Neurology* 416, 429-450.
- Wild, J.M., Zeigler, H.P., 1980. Central representation and somatotopic organization of the jaw muscles within the facial and trigeminal nuclei of the pigeon (*Columba livia*). *Journal of Comparative Neurology* 192, 175-201.
- Wild, J.M., Zeigler, H.P., 1996. Central projections and somatotopic organisation of trigeminal primary afferents in pigeon (*Columba livia*). *Journal of Comparative Neurology* 368, 136-152.
- Wiley, D.F., 2006. *Landmark Editor 3.0*. Institute for Data Analysis and Visualization, University of California, Davis. <http://graphics.idav.ucdavis.edu/research/EvoMorph>.
- Wings, O., 2007. A review of gastrolith function with implications for fossil vertebrates and a revised classification. *Acta Palaeontologica Polonica* 52, 1-16.
- Witmer, L.M., Chatterjee, S., Franzosa, J., Rowe, T., 2003. Neuroanatomy of flying reptiles and implications for flight, posture and behaviour. *Nature* 425, 950-953.
- Witmer, L.M., Ridgely, R.C., 2009. New insights into the brain, braincase, and ear region of tyrannosaurs (Dinosauria, Theropoda), with implications for sensory organization and behavior. *The Anatomical Record* 292, 1266-1296. doi:1210.1002/ar.20983.
- Witmer, L.M., Ridgely, R.C., Dufeu, D.L., Semones, M.C., 2008. Using CT to Peer into the Past: 3D Visualization of the Brain and Ear Regions of Birds, Crocodiles, and Nonavian Dinosaurs, in: Endo, H., Frey, R. (Eds.), *Anatomical Imaging, Towards a New Morphology*, Springer, Tokyo, Japan, pp. 67-87.
- Wood, J.R., Rawlence, N.J., Rogers, G.M., Austin, J.J., Worthy, T.H., Cooper, A., 2008. Coprolite deposits reveal the diet and ecology of the extinct New Zealand megaherbivore moa (Aves, Dinornithiformes). *Quaternary Science Reviews* 27, 2593-2602. doi:2510.1016/j.quascirev.2008.2509.2019.
- Wood, J.R., Wilmshurst, J.M., Richardson, S.J., Rawlence, N.J., Wagstaff, S.J., Worthy, T.H., Cooper, A., 2013. Resolving lost herbivore community structure using coprolites of four sympatric moa species (Aves: Dinornithiformes). *Proceedings of the National Academy of Sciences U.S.A.* 110, 16910-16915. doi:16910.11073/pnas.1307700110.
- Woodburne, M.O., 1967. The Alcoota Fauna, central Australia: an integrated palaeontological and geological study. *Bulletin of the Bureau of Mineral Resources, Geology and Geophysics, Australia* 87, 1-187.

- Woodhead, J., Hand, S.J., Archer, M., Graham, I., Sniderman, K., Arena, D.A., Black, K.H., Godthelp, H., Creaser, P., Price, E., 2016. Developing a radiometrically-dated chronologic sequence for Neogene biotic change in Australia, from the Riversleigh World Heritage Area of Queensland. *Gondwana Research* 29, 153-167.
- Worthy, T.H., 1989. Aspects of the biology of two moa species (Aves: Dinornithiformes). *New Zealand Journal of Archaeology* 11, 77-86.
- Worthy, T.H., Degrange, F.J., Handley, W.D., Lee, M.S.Y., 2017a. The evolution of giant flightless birds and novel phylogenetic relationships for extinct fowl (Aves, Galloanseres). *Royal Society Open Science* 4, 170975. doi:170910.171098/rsos.170975.
- Worthy, T.H., Degrange, F.J., Handley, W.D., Lee, M.S.Y., 2017b. Correction to 'The evolution of giant flightless birds and novel phylogenetic relationships for extinct fowl (Aves, Galloanseres)'. *Royal Society Open Science* 4, 171621. doi:171610.171098/rsos.171621.
- Worthy, T.H., Handley, W.D., Archer, M., Hand, S.J., 2016b. The extinct flightless mihirungs (Aves, Dromornithidae): cranial anatomy, a new species, and assessment of Oligo-Miocene lineage diversity. *Journal of Vertebrate Paleontology* 36, e1031345. doi:1031340.1031080/02724634.02722015.01031345.
- Worthy, T.H., Holdaway, R.N., 2002. *The Lost World of the Moa: Prehistoric Life of New Zealand*. Indiana University Press, Bloomington, IN. p760.
- Worthy, T.H., Mitri, M., Handley, W.D., Lee, M.S.Y., Anderson, A., Sand, C., 2016a. Osteology supports a stem-Galliform affinity for the giant extinct flightless bird *Sylviornis neocaledoniae* (Sylviornithidae, Galloanseres). *PLoS ONE* 11, e0150871. doi:0150810.0151371/journal.pone.0150871.
- Worthy, T.H., Scofield, R.P., 2012. Twenty-first century advances in knowledge of the biology of moa (Aves: Dinornithiformes): a new morphological analysis and moa diagnoses revised. *New Zealand Journal of Zoology* 39, 87-153. doi:110.1080/03014223.03012012.03665060.
- Worthy, T.H., Yates, A., 2015. Connecting the thigh and foot: resolving the association of post-cranial elements in the species of *Ilbandornis* (Aves: Dromornithidae). *Alcheringa* 39, 1-21. doi:10.1080/03115518.03112015.01015818.
- Worthy, T.H., Yates, A., 2017. A review of the smaller birds from the late Miocene Alcoota Local Faunas of Australia with a description of a new species, in: Hospitaleche, C.A., Agnolin, F.L., Haidr, N., Noriega, J.I., Tambussi, C.P. (Eds.), Proceedings of the 9th International Meeting of the Society of Avian Paleontology and Evolution, Diamante (Argentina), 1-6 August 2016. *Paleontología y Evolución de las Aves, Contribuciones del Museo Argentino de Ciencias Naturales* 7, pp. 221-252.
- Wylie, D.R.W., Gutiérrez-Ibáñez, C., Gaede, A.H., Altshuler, D.L., Iwaniuk, A.N., 2018. Visual-cerebellar pathways and their roles in the control of avian flight. *Frontiers in Neuroscience* 12, 223 (10pp). doi:210.3389/fnins.2018.00223.
- Wylie, D.R.W., Gutiérrez-Ibáñez, C., Iwaniuk, A.N., 2015. Integrating brain, behavior, and phylogeny to understand the evolution of sensory systems in birds. *Frontiers in Neuroscience* 9, 281 (17pp). doi:210.3389/fnins.2015.00281.
- Wylie, D.R.W., 2001. Projections from the nucleus of the basal optic root and nucleus lentiformis mesencephali to the inferior olive in pigeons (*Columba livia*). *Journal of Comparative Neurology* 429, 502-513.

- Wylie, D.R.W., Gutiérrez-Ibáñez, C., Pakan, J.M.P., Iwaniuk, A.N., 2009. The optic tectum of birds: mapping our way to understanding visual processing. *Canadian Journal of Experimental Psychology* 63, 328-338. doi:310.1037/a0016826.
- Wylie, D.R.W., Iwaniuk, A.N., 2012. Neural Mechanisms Underlying Visual Motion Detection in Birds, in: Lazareva, O.F., Shimizu, T., Wasserman, E.A. (Eds.), *How Animals See the World: Comparative Behavior, Biology, and Evolution of Vision*, Oxford University Press, New York, pp. 289-318.
- Yates, A.M., 2013. A new species of long-necked turtle (Pleurodira: Chelidae: *Chelodina*) from the late Miocene Alcoota Local Fauna, Northern Territory, Australia. *PeerJ* 1, e170. doi:110.7717/peerj.7170.
- Yates, A.M., 2015. New craniodental remains of *Wakaleo alcootaensis* (Diprotodontia: Thylacoleonidae) a carnivorous marsupial from the late Miocene Alcoota Local Fauna of the Northern Territory, Australia. *PeerJ* 3, e1408. doi:1410.7717/peerj.1408.

## 4.7 APPENDICES

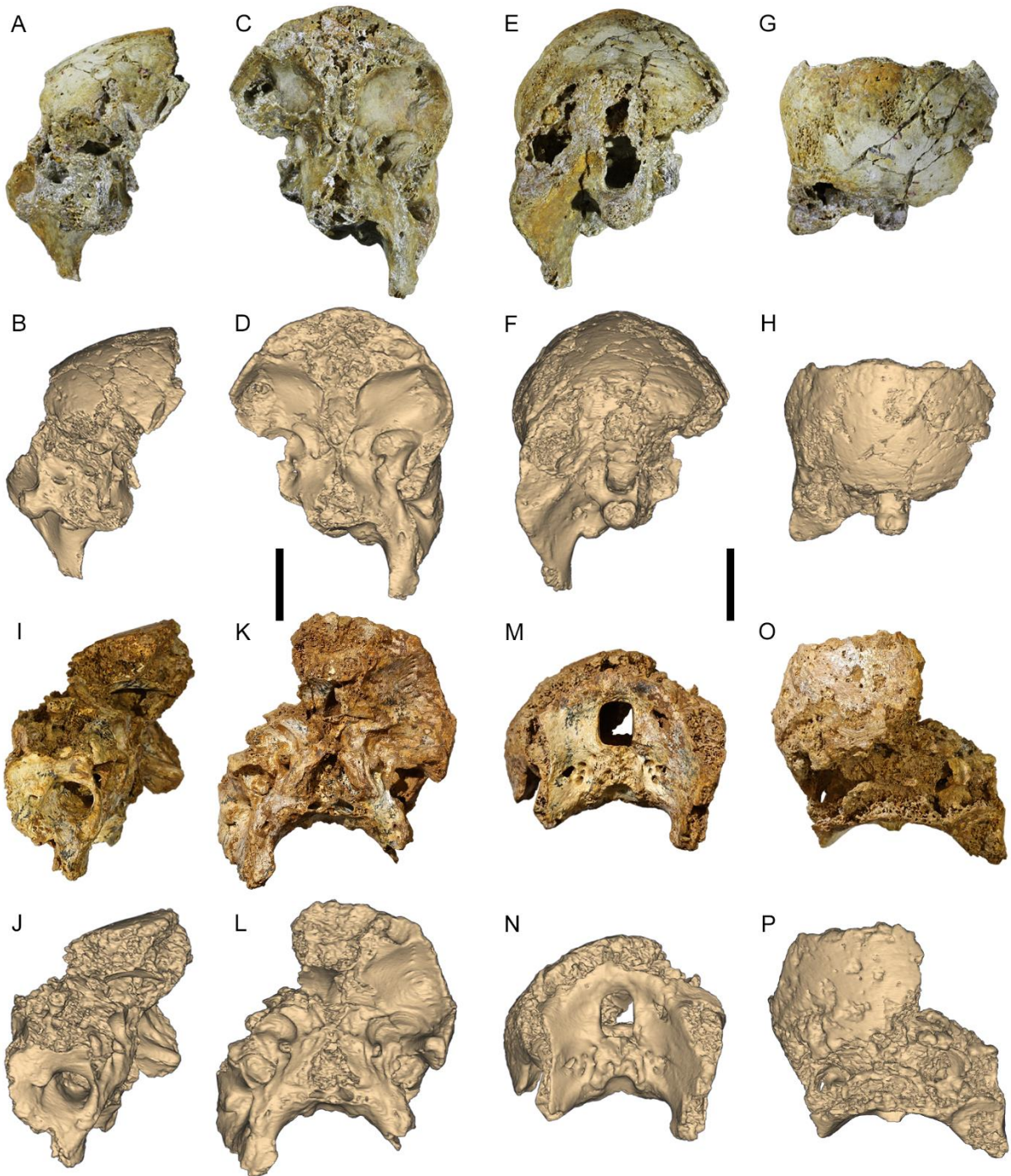


Figure A4.1. Oligo-Miocene dromornithid fossil and digital neurocrania. Riversleigh specimens *Dromornis murrayi* (QM F57984), A–H; and *D. murrayi* (QM F57974), I–P. Neurocrania are shown in photo image (A, C, E, G, I, K, M, O) and digital model (B, D, F, H, J, L, N, P) views. Digital models are derived from CT data used for the modelling of endocasts, and are arranged in the same approximate orientation as photo images of fossil specimens. **Views**, RHS lateral (A, B, I, J); rostral (C, D, K, L); caudal (E, F, M, N) and dorsal (G, H, O, P). **Abbreviations**, RHS, right hand side; **mm**, millimetres. Scale bars equal 40 mm.

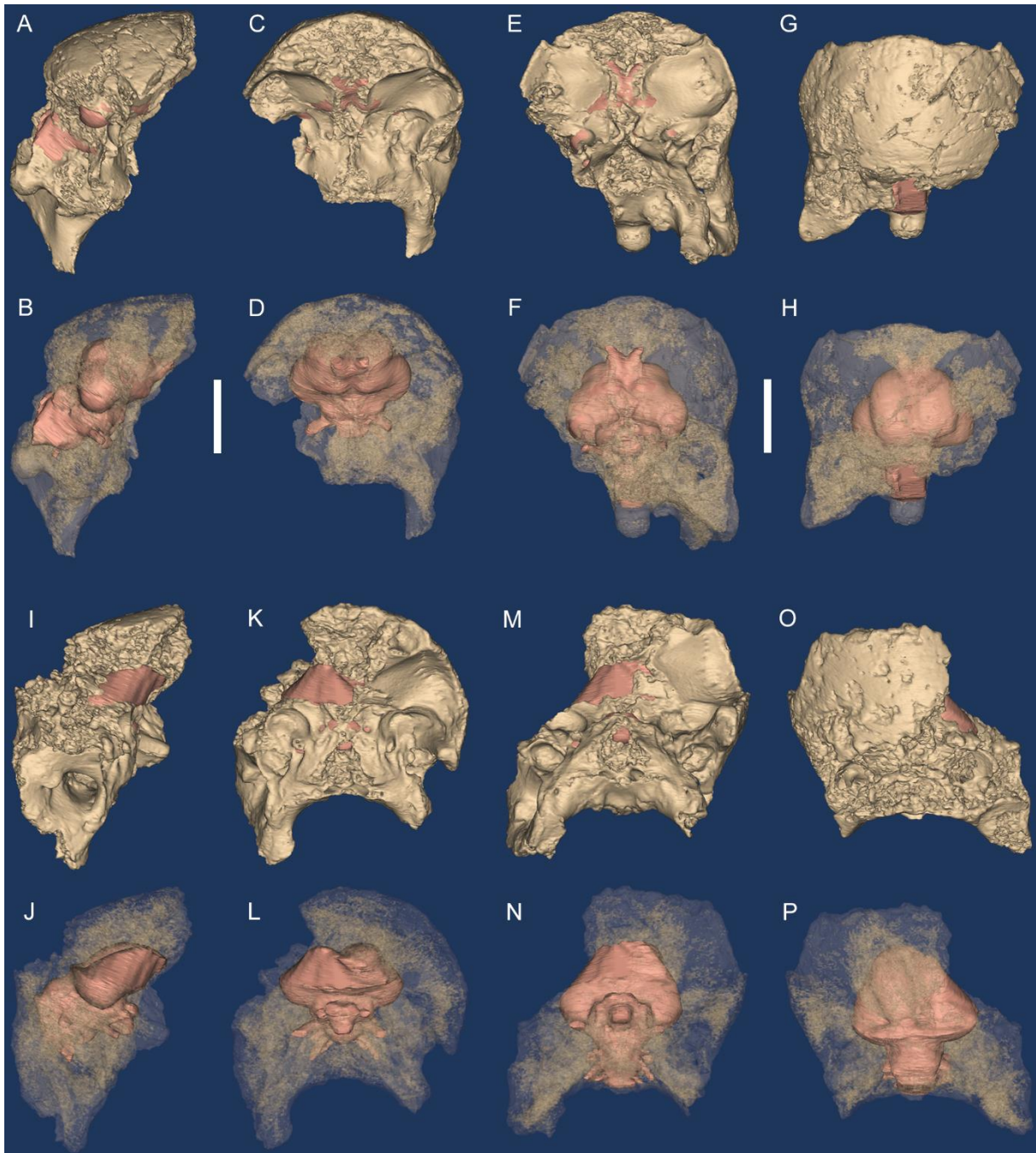


Figure A4.2. Oligo-Miocene dromornithid digital neurocrania. Riversleigh specimens *Dromornis murrayi* (QM F57984), **A–H**; and *D. murrayi* (QM F57974), **I–P**. Neurocrania are shown in solid (**A, C, E, G, I, K, M, O**) and transparent (**B, D, F, H, J, L, N, P**) views. Endocasts are shown within transparent neurocrania and indicate location within the skull. Neurocrania are orientated in approximate ‘alert posture’ with respect to the horizontal positioning of the lateral semicircular duct of the vestibular organ (semicircular ducts + cochlea), as observed in *D. planei* and *I. woodburnei* (see Fig. A4.5 and 4.4.1.3). Trigeminal nerves (**V<sub>1</sub>**, **V<sub>2</sub>**, **V<sub>3</sub>**) are truncated approximately where exiting the neurocranium. **Views**, RHS lateral (**A, B, I, J**); rostral (**C, D, K, L**); ventral (**E, F, M, N**) and dorsal (**G, H, O, P**). **Abbreviations**, **RHS**, right hand side; **mm**, millimetres. Scale bars equal 40 mm.

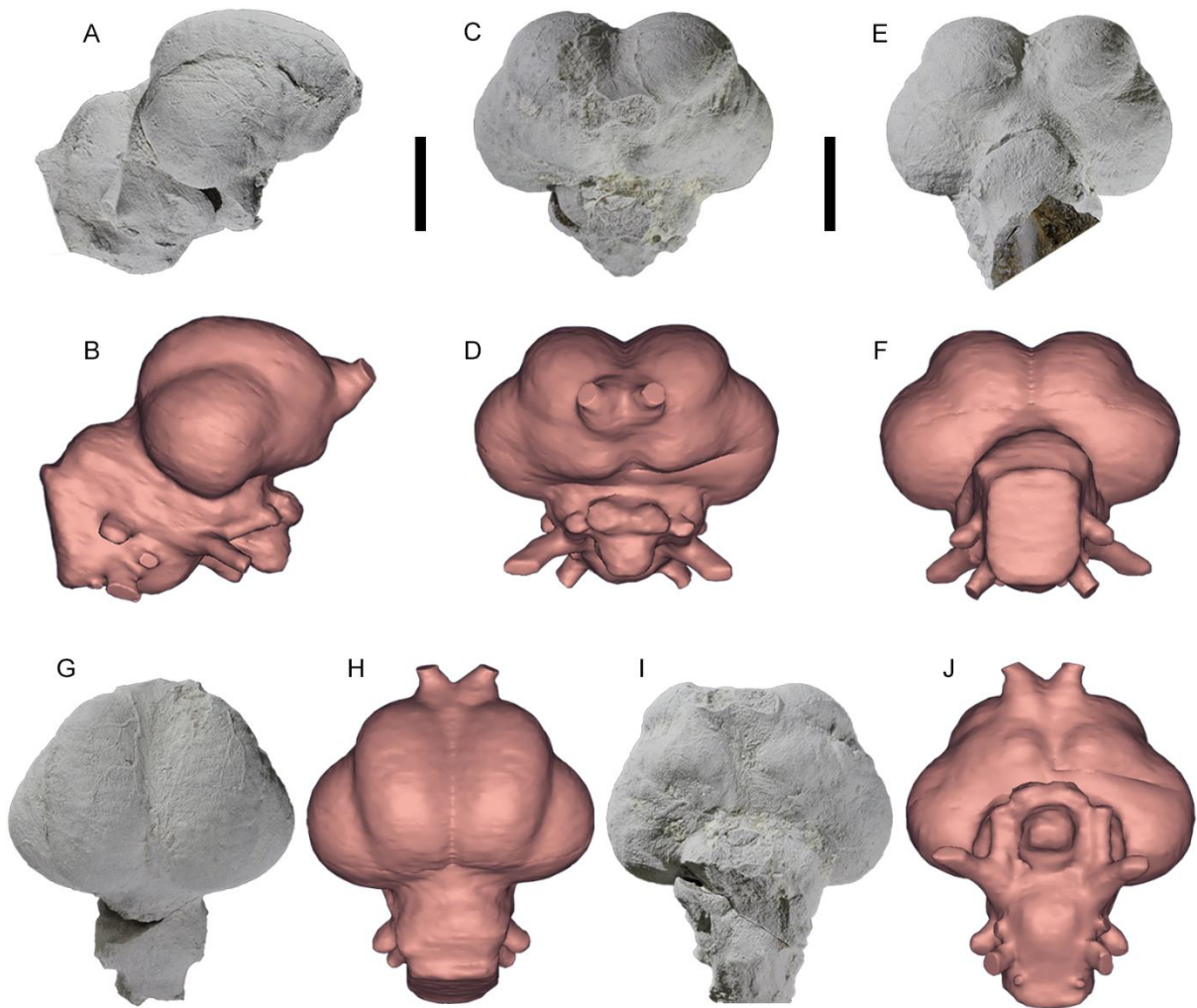


Figure A4.3. *Dromornis murrayi* fossil and digitally reconstructed endocasts. *D. murrayi* fossil endocast (QM F50412; **A, C, E, G, I**; see 4.2.1.2) has been whitened with ammonium chloride ( $\text{NH}_4\text{Cl}$ ); *D. murrayi* digital endocast (**B, D, F, H, J**) is a reconstruction of the CT-data derived from the Riversleigh specimens QM F57984 and QM F57974 (see Figs. A4.1–A4.2, A4.9; Methods 4.2.4.4). **Views.** RHS lateral (**A–B**); rostral (**C–D**); caudal (**E–F**); dorsal (**G–H**); ventral (**I–J**). **Abbreviations, mm,** millimetres. Scale bars equal 20 mm.

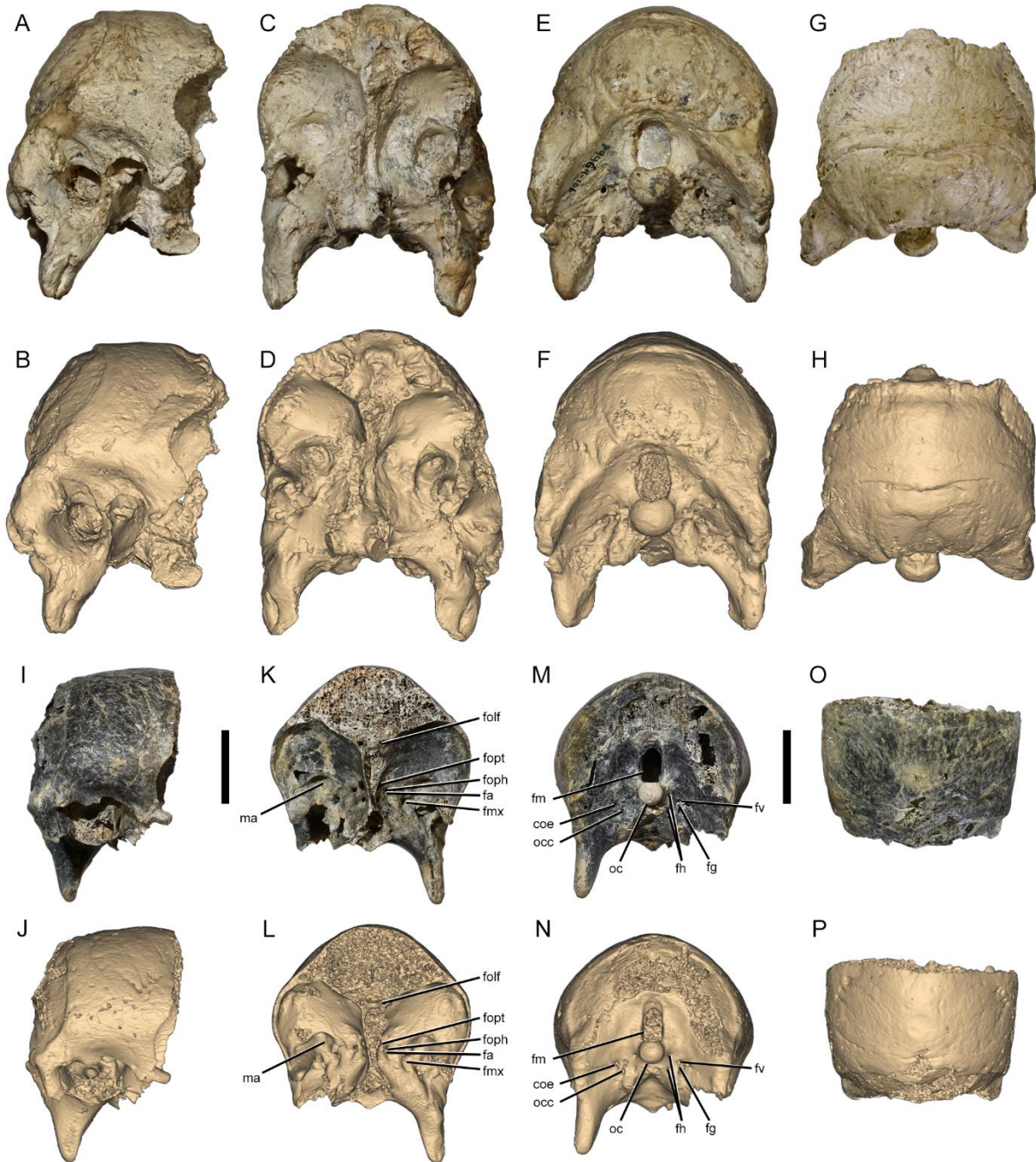


Figure A4.4. Middle Miocene dromornithid fossil and digital neurocrania. Bullock Creek Local Fauna specimens *Dromornis planei* (NTM P9464-106), **A–H**; and *Ilbandornis woodburnei* (QVM:2000:GFV:20), **I–P**. Neurocrania are shown in photo image (**A, C, E, G, I, K, M, O**) and digital model (**B, D, F, H, J, L, N, P**) views. Digital models are derived from CT data used for the modelling of endocasts, and are arranged in the same approximate orientation as photo images of fossil specimens. **Views**, RHS lateral (**A, B, I, J**); rostral (**C, D, K, L**); caudal (**E, F, M, N**) and dorsal (**G, H, O, P**). **Abbreviations**, **coe**, canalis ophthalmici externi for transmission of venae and arteria ophthalmica externa; **fa**, foramen n. abducentis (VI); **fg**, foramen n. glossopharyngeus (IX); **fh**, foramen n. hypoglossi (XII), **fm**, foramen magnum; **fmx**, foramen n. maxillomandibularis ( $V_2 + V_3$ ); **folf**, foramen n. olfactorii (I); **foph**, foramen n. ophthalmici ( $V_1$ ); **foft**, foramen opticum (II); **fv**, foramen n. vagi (X); **ma**, insertion area for m. adductor mandibulae externus medialis et superficialis; **mm**, millimetres; **oc**, condylus occipitalis; **occ**, ostium canalis carotici (VII); **RHS**, right hand side. Scale bars equal 40 mm.

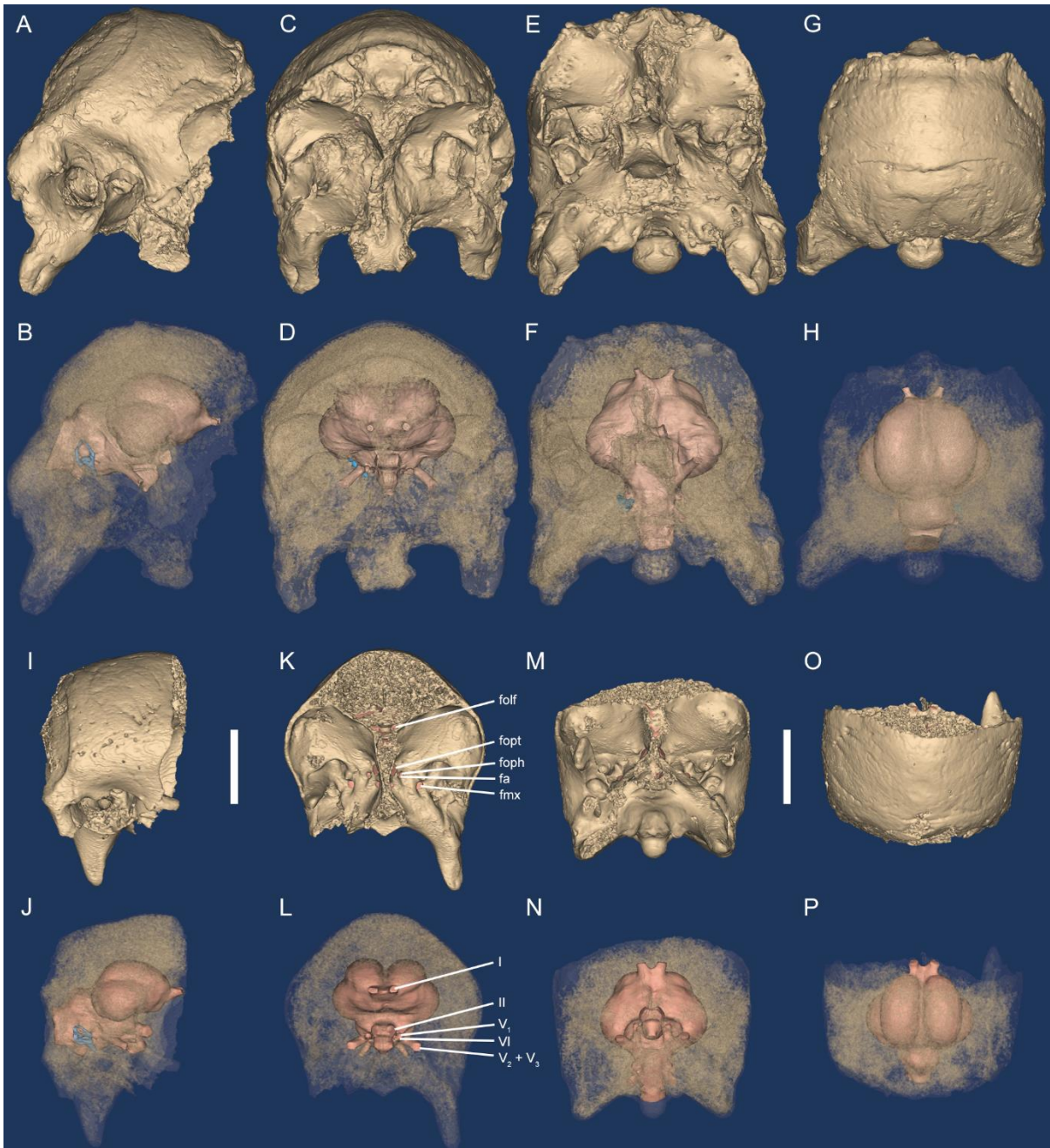


Figure A4.5. Middle Miocene dromornithid digital neurocrania. Bullock Creek Local Fauna specimens *Dromornis planei* (NTM P9464-106), **A–H**; and *Ilbandornis woodburnei* (QVM:2000:GFV:20), **I–P**. Neurocrania are shown in solid (**A, C, E, G, I, K, M, O**) and transparent (**B, D, F, H, J, L, N, P**) views. Endocasts are shown within transparent neurocrania and indicate location within the skull. Neurocrania are orientated in approximate ‘alert posture’ with respect to the horizontal positioning of the lateral semicircular duct of the vestibular organ (semicircular ducts + cochlea [blue]; see also **4.4.1.3**). Trigeminal nerves (**V<sub>1</sub>, V<sub>2</sub>, V<sub>3</sub>**) are truncated approximately where exiting the neurocranium. **Views**, RHS lateral (**A, B, I, J**); rostral (**C, D, K, L**); ventral (**E, F, M, N**) and dorsal (**G, H, O, P**). **Abbreviations**, **fa**, foramen n. abducentis; **fmx**, foramen n. maxillomandibularis; **folf**, foramen n. olfactorii; **foph**, foramen n. ophthalmici; **foft**, foramen opticum; **mm**, millimetres; **RHS**, right hand side; **I**, olfactory nerve; **II**, optic nerve; **V<sub>1</sub>**, ophthalmic nerve; **V<sub>2</sub>**, maxillary nerve; **V<sub>3</sub>**, mandibular nerve; **VI**, abducent nerve. Scale bars equal 40 mm.

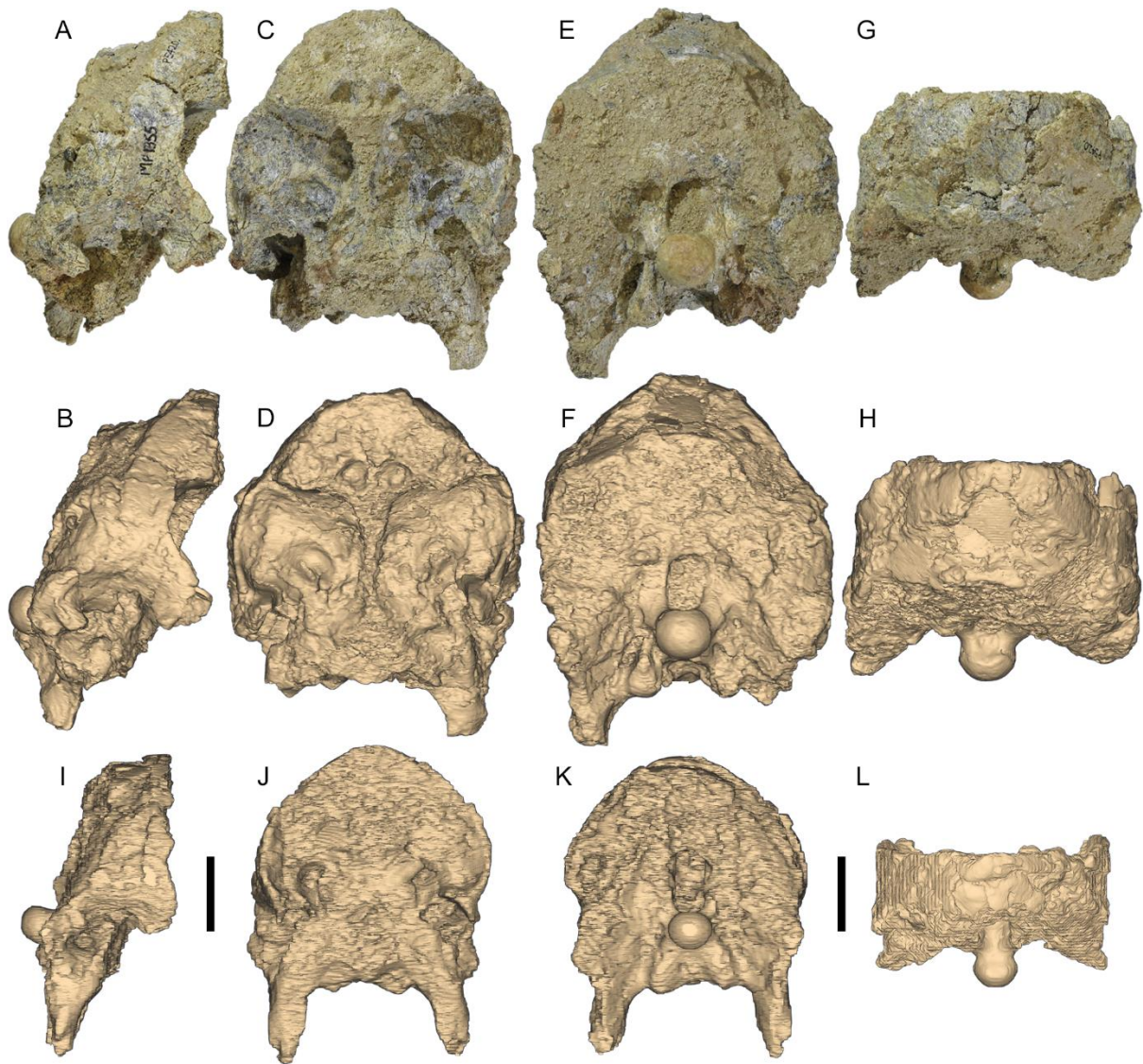


Figure A4.6. Late Miocene dromornithid fossil and digital neurocrania. Alcoota Local Fauna specimens *Dromornis stirtoni* (NTM P5420), A–H; and *D. stirtoni* (NTM P3250), I–L. Neurocrania are shown in photo image (A, C, E, G) and digital model (B, D, F, H, I–L\*) views. Digital models are derived from CT data used for the modelling of endocasts, and are arranged in the same approximate orientation as photo images of fossil specimens. **Views**, RHS lateral (A, B, I); rostral (C, D, J); caudal (E, F, K) and dorsal (G, H, L). **Abbreviations**, mm, millimetres; **RHS**, right hand side. Scale bars equal 40 mm. [Note: the neurocranium of *D. stirtoni* (NTM P3250) is represented by digital model images only (I–L), as appropriate photographs of the skeletal neurocranium were not available].

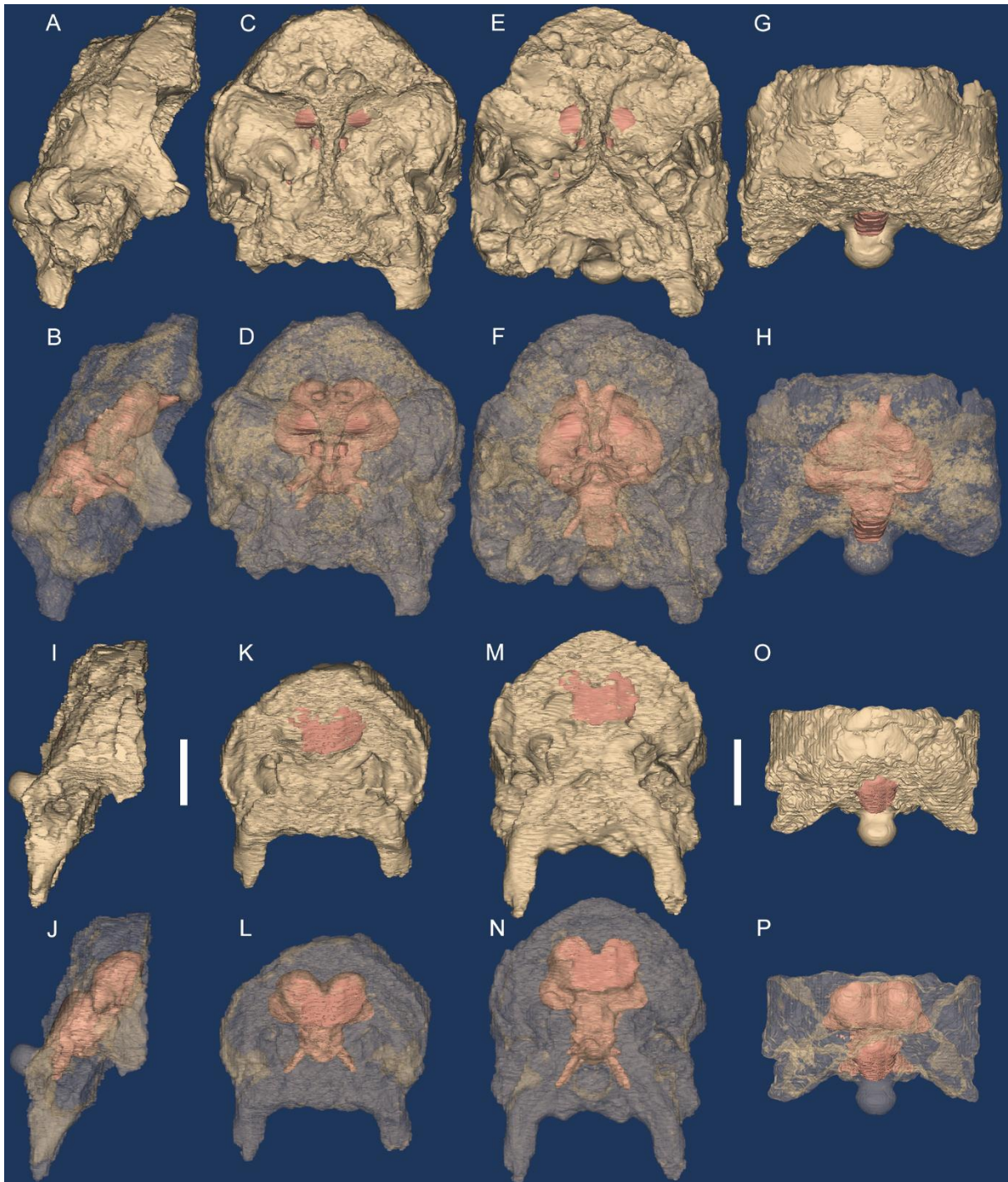


Figure A4.7. Late Miocene dromornithid digital neurocrania. Alcoota Local Fauna specimens *Dromornis stirtoni* (NTM P5420), **A–H**; and *Dromornis stirtoni* (NTM P3250), **I–P**. Neurocrania are shown in solid (**A, C, E, G, I, K, M, O**) and transparent (**B, D, F, H, J, L, N, P**) views. Endocasts are shown within transparent neurocrania and indicate location within the skull. Neurocrania are orientated in approximate ‘alert posture’ with respect to the horizontal positioning of the lateral semicircular duct of the vestibular organ (semicircular ducts + cochlea) as observed in *D. planei* and *I. woodburnei* (see Fig. A4.5 and 4.4.1.3). Views, RHS lateral (**A, B, I, J**); rostral (**C, D, K, L**); ventral (**E, F, M, N**) and dorsal (**G, H, O, P**). Abbreviations, mm, millimetres; RHS, right hand side. Scale bars equal 40 mm.

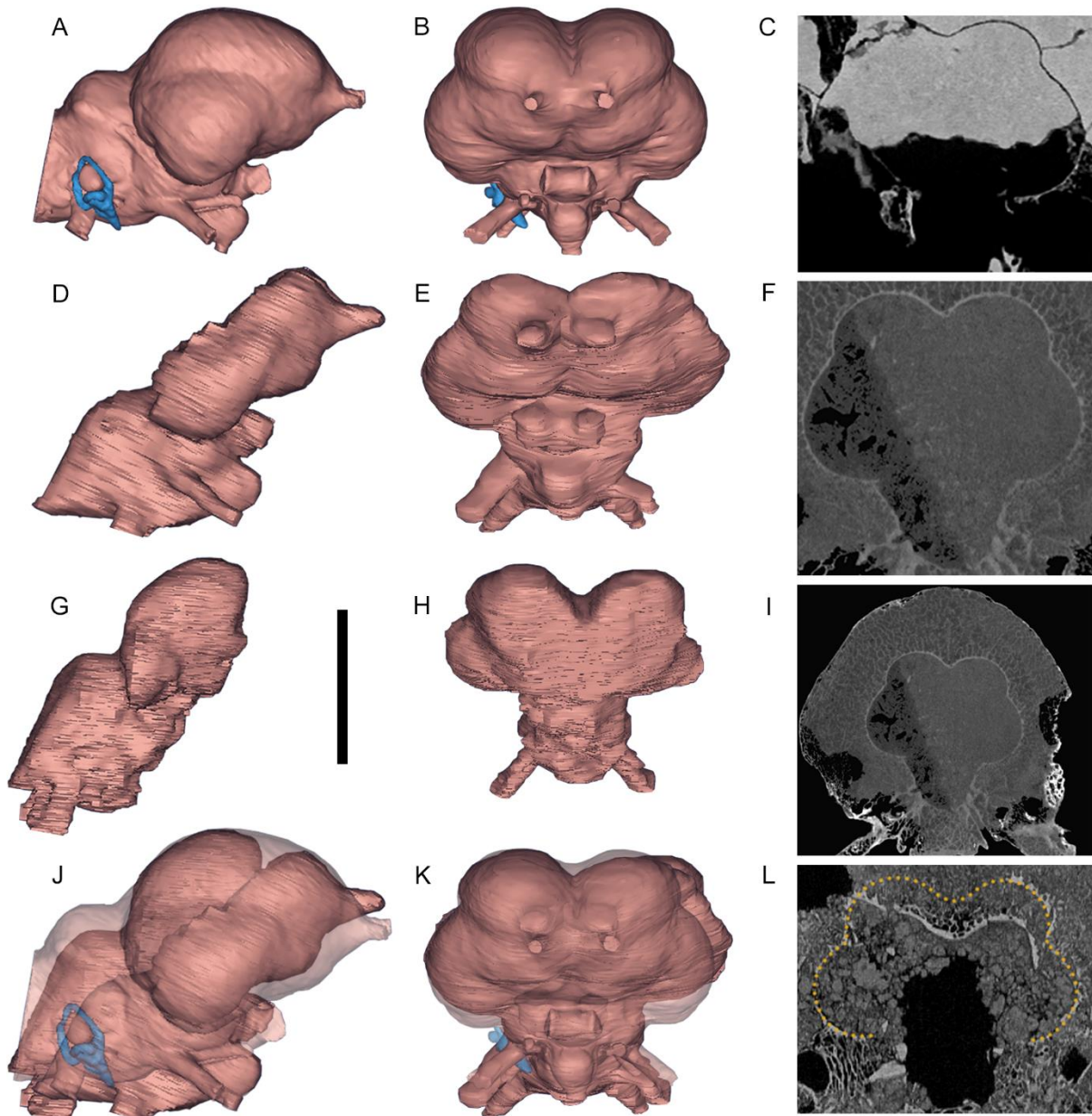


Figure A4.8. Hypothesised lateral RHS (**J**) and rostral (**K**) form of the *Dromornis stirtoni* endocast with reference to the endocast of *D. planei* (NTM P9464-106—see Methods 4.2.4.3). **A–B. Views**, Lateral RHS (**A, D, G, J**), rostral (**B, E, H, K**); mediolateral (coronal) CT-slice images, viewed from the rostrocaudal aspect, showing the profile of the eminentia sagittalis and caudal telencephalon of; **C**, *D. murrayi* (QM F57984), **F**, *D. planei* (NTM P9464-106), **I**, *D. planei* (NTM P9464-106) full cranium CT-slice showing the open-cell honeycomb-like network of the internal trabecular bone structure of the dromornithid skull, within which the endocranial cortical bone ‘capsule’ is supported (see 4.4.1.1.2), **L**, *D. stirtoni* likely endocranial profile described by yellow stippled line superimposed over a coronal CT-slice image derived from *D. stirtoni* (NTM P3250) CT data. Two incomplete *D. stirtoni* endocasts preserving the rostroventral (NTM P5420, **D**; NTM P3250, **G**) and caudodorsal (NTM P5420, **E**; NTM P3250, **H**) endocast surfaces derived from CT-data, transposed over the re-scaled lateral RHS (**A**) and rostral (**B**) endocast of *D. planei* (NTM P9464-106) and visualised at 65% opacity. **Abbreviations**, **mm**, millimetres; **RHS**, right hand side. Scale bar equals 40 mm (not applicable to CT-slice images; **C, F, I, L**).

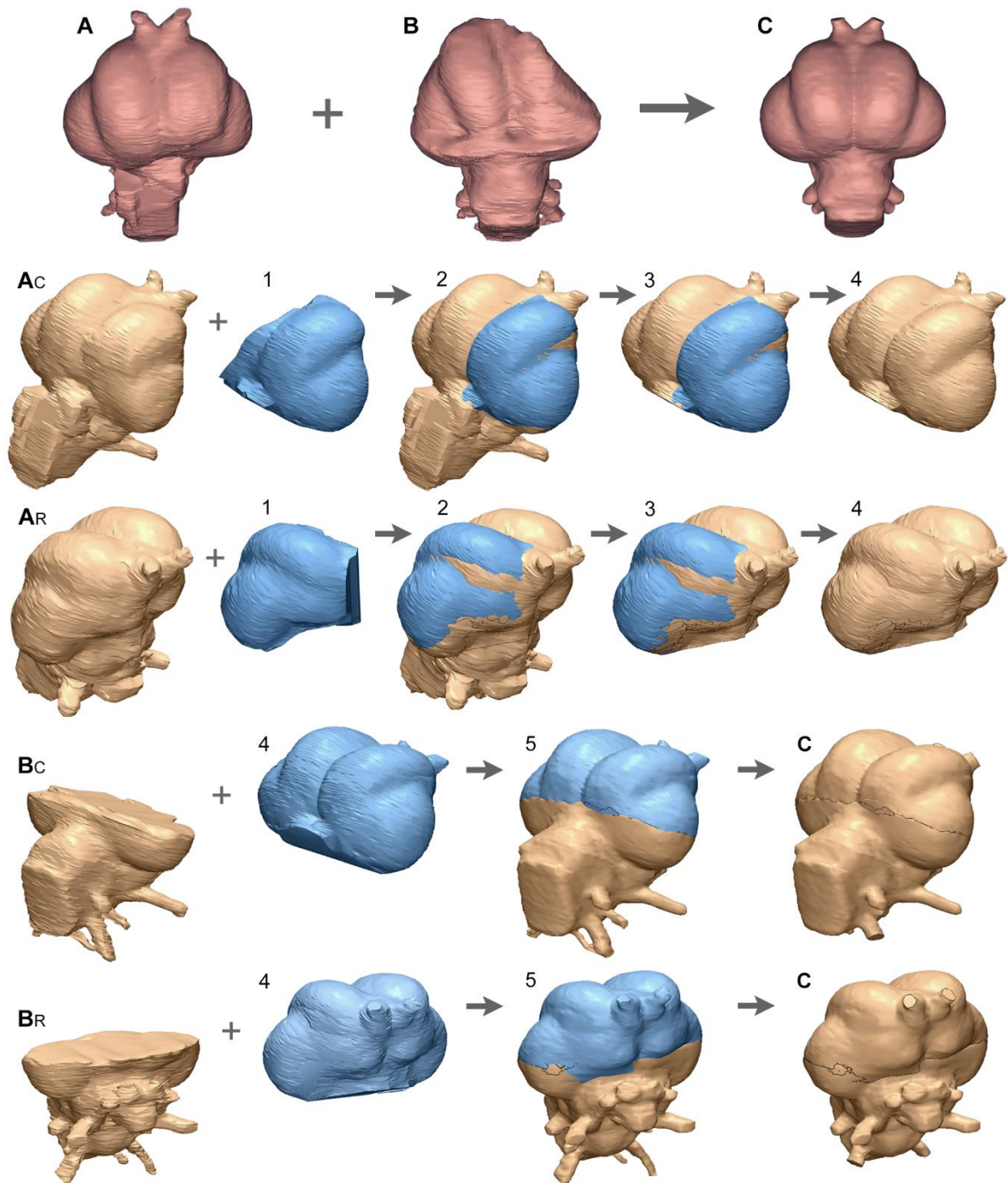


Figure A4.9. Reconstruction of the *Dromornis murrayi* endocast model. **A**, endocast of *D. murrayi* (QM F57984) preserving the dorsolateral LHS endocast surfaces (Figs. A4.2A–H); **Ac**, caudolateral and **AR**, rostralateral views of workflow for reconstruction of the dorsal endocast (**4**) based on **A**; **B**, endocast of *D. murrayi* (QM F57974) preserving the ventral endocast surfaces (Figs. A4.2I–P); **Bc**, caudolateral and **BR**, rostralateral views of workflow for reconstruction of the complete endocast (**C**) based on **4**+**B**; **C**, complete reconstructed endocast of *D. murrayi* (QM F57984 + QM F57974). **Abbreviations**, **LHS**, left hand side; **RHS**, right hand side; **1**, LHS dorsolateral mirrored model, flipped and cropped to form RHS dorsolateral surfaces; **2**, mirrored LHS model (**1**) fitted to **A**; **3**, ventral endocast surfaces are trimmed from the dorsal endocast model and; **4**, merged to form completed reconstruction of the dorsal endocast; **5**, reconstructed dorsal endocast model (**4**) fitted to dorsally trimmed ventral endocast model (**B**), the complete reconstructed endocast model is then merged, trimmed and remeshed (**C**—see Methods, 4.2.4.4).

Table A4.1. **A**, Mean Modular Distance measurement values calculated between Lm locations for each specimen (see Methods 4.2.6.2). Paired structure data (i.e., eminentia sagittalis, rostral and caudal telencephalon, mesencephalon, and trigeminal ganglion modules) were combined and mean Modular Distance values calculated; **B**, Linear Distance values calculated between two Lm locations describing gross endocast morphological distances (see Methods 4.2.6.3). **C**, size-standardised mean Modular Distance ratios calculated by dividing  $\log_{10}$  transformed mean Modular Distance values by  $\log_{10}$  transformed specimen endocast volumes. **D**, Size-standardised endocast Linear Distance ratios calculated by dividing  $\log_{10}$  transformed Linear Distance values by  $\log_{10}$  transformed endocast volumes. **Abbreviations**, **Anhima**, *Anhima cornuta* (MV B12574); **Anseranas**, *Anseranas semipalmata* (SAM B48035); **Cer L**, cerebellum length; **Cer W**, cerebellum width; **D. murrayi**; *Dromornis murrayi* reconstruction (QM F57984 + QM F57974); **D. planei**; *Dromornis planei* (NTM P9464-106); **EmSg L**, eminentia sagittalis length; **EmSg W**, eminentia sagittalis width; **Endo Vol**, endocast total volume; **I. woodburnei**; *Ilbandornis woodburnei* (QVM:2000:GFV:20); **Leipoa**, *Leipoa ocellata* (SAM B11482); **Med.Ob TW**, medulla oblongata total width; **Mes L**, mesencephalon length; **Mes W**, mesencephalon width; **Meten TH**, metencephalon total height; **mm**, millimetres; **mm<sup>3</sup>**, cubic millimetres; **Rho L**, rhombencephalon length; **Rho W**, rhombencephalon width; **Tel.c.TW**, caudal telencephalon total width; **Tel.c L**, caudal telencephalon length; **Tel.c W**, caudal telencephalon width **Tel.r L**, rostral telencephalon length **Tel.r W**, rostral telencephalon width; **Tri.g L** trigeminal ganglion length; **Tri.g W**, trigeminal ganglion width.

| <b>A. Mean Modular Distance values (mm)</b>              |         |         |           |            |           |               |
|--|---------|---------|-----------|------------|-----------|---------------|
| <b>Measurement</b>                                       | Leipoa  | Anhima  | Anseranas | D. murrayi | D. planei | I. woodburnei |
| EmSg L   | 14.52   | 19.69   | 19.64     | 55.90      | 67.65     | 51.32         |
| EmSg W   | 5.68    | 6.64    | 7.76      | 27.63      | 34.43     | 28.87         |
| Tel.r L  | 10.03   | 12.33   | 16.94     | N/A        | N/A       | N/A           |
| Tel.r W  | 5.74    | 8.10    | 11.57     | N/A        | N/A       | N/A           |
| Tel.c L  | 13.87   | 18.54   | 18.94     | 47.26      | 49.71     | 41.88         |
| Tel.c W  | 14.24   | 20.27   | 23.41     | 41.14      | 40.61     | 30.52         |
| Mes L  | 17.66   | 11.68   | 14.82     | 16.96      | 19.11     | 16.72         |
| Mes W  | 7.65    | 5.08    | 4.13      | 6.75       | 5.96      | 8.02          |
| Tri.g L  | 4.10    | 7.22    | 7.95      | 13.47      | 13.76     | 12.30         |
| Tri.g W  | 2.90    | 2.99    | 3.30      | 9.56       | 9.20      | 9.18          |
| Cer L  | 10.72   | 17.48   | 15.68     | 16.85      | 20.84     | 21.24         |
| Cer W  | 9.99    | 13.02   | 17.42     | 36.62      | 44.85     | 32.35         |
| Rho L  | 9.91    | 12.13   | 14.52     | 24.53      | 26.90     | 23.80         |
| Rho W  | 10.10   | 13.55   | 10.67     | 17.72      | 17.50     | 13.83         |
| <b>B. Linear Distance values (mm)</b>                    |         |         |           |            |           |               |
| Tel.c TW   | 22.05   | 28.93   | 31.25     | 69.79      | 72.85     | 57.52         |
| Meten TH   | 16.26   | 20.32   | 22.01     | 38.76      | 40.69     | 34.56         |
| Med.Ob TW  | 11.73   | 14.28   | 15.57     | 39.36      | 40.59     | 28.91         |
| Endo Vol (mm <sup>3</sup> )                              | 4528.73 | 8086.55 | 10904.16  | 96175.85   | 123391.24 | 61588.91      |
| <b>C. Size-standardised mean Modular Distance ratios</b> |         |         |           |            |           |               |
| EmSg L   | 0.318   | 0.331   | 0.320     | 0.351      | 0.359     | 0.357         |
| EmSg W   | 0.206   | 0.210   | 0.220     | 0.288      | 0.302     | 0.305         |
| Tel.r L  | 0.274   | 0.279   | 0.304     | N/A        | N/A       | N/A           |
| Tel.r W  | 0.207   | 0.232   | 0.263     | N/A        | N/A       | N/A           |
| Tel.c L  | 0.312   | 0.324   | 0.316     | 0.335      | 0.333     | 0.339         |
| Tel.c W  | 0.315   | 0.334   | 0.339     | 0.326      | 0.316     | 0.310         |
| Mes L  | 0.341   | 0.273   | 0.290     | 0.274      | 0.274     | 0.258         |
| Mes W  | 0.242   | 0.181   | 0.153     | 0.169      | 0.161     | 0.188         |
| Tri.g L  | 0.168   | 0.220   | 0.223     | 0.227      | 0.224     | 0.228         |
| Tri.g W  | 0.127   | 0.122   | 0.129     | 0.197      | 0.189     | 0.201         |
| Cer L  | 0.282   | 0.318   | 0.296     | 0.244      | 0.259     | 0.277         |
| Cer W  | 0.273   | 0.285   | 0.307     | 0.311      | 0.324     | 0.315         |
| Rho L  | 0.273   | 0.277   | 0.288     | 0.277      | 0.281     | 0.287         |
| Rho W  | 0.275   | 0.290   | 0.255     | 0.248      | 0.244     | 0.238         |
| <b>D. Size-standardised Linear Distance ratios</b>       |         |         |           |            |           |               |
| Tel.c TW   | 0.367   | 0.374   | 0.370     | 0.370      | 0.366     | 0.367         |
| Meten TH   | 0.331   | 0.335   | 0.333     | 0.319      | 0.316     | 0.321         |
| Med.Ob TW  | 0.293   | 0.295   | 0.295     | 0.320      | 0.316     | 0.305         |
| $\log_{10}$ Endo Vol                                     | 3.656   | 3.908   | 4.038     | 4.980      | 5.091     | 4.780         |

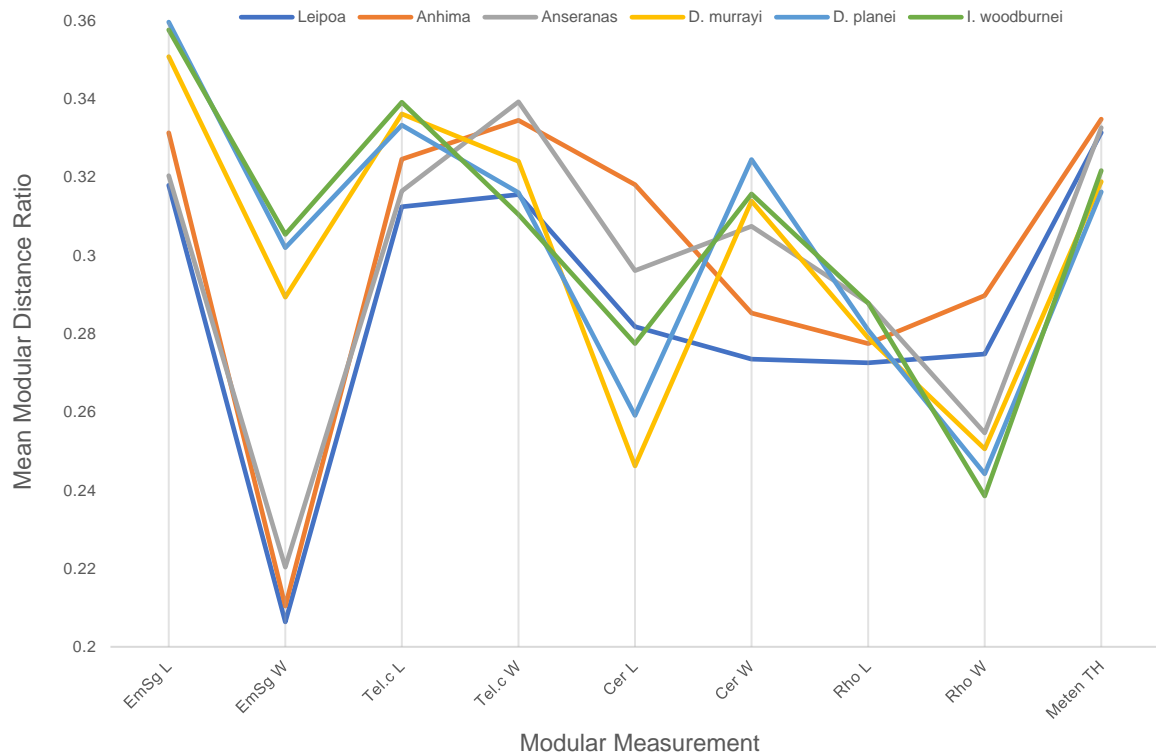


Figure A4.10. Mean Modular Distance ratios plot for all galloansere taxa. Ratios are size-standardised by dividing  $\log_{10}$  transformed mean Modular Distance values by  $\log_{10}$  transformed specimen endocast volumes (see Tables A4.1C–D; Methods, 4.2.6.2-3). **Abbreviations**, **Anhima**; *Anhima cornuta* (SAM B12574); **Anseranas**; *Anseranas semipalmata* (SAM B48035); **Cer L**, cerebellum length; **Cer W**, cerebellum width; **D. murrayi**; *Dromornis murrayi* reconstruction (QM F57984 + QM F57974); **D. planei**; *Dromornis planei* (NTM P9464-106); **EmSg L**, eminentia sagittalis length; **EmSg W**, eminentia sagittalis width; **I. woodburnei**; *Ibandornis woodburnei* (QVM:2000:GFV:20); **Leipoa**, *Leipoa ocellata* (SAM B11482); **Mes L**, mesencephalon length; **Mes W**, mesencephalon width; **Meten TH**, metencephalon total height; **Rho L**, rhombencephalon length; **Rho W**, rhombencephalon width; **Tel.c L**, caudal telencephalon length; **Tel.c W**, caudal telencephalon width.

Table A4.2. **A**, mean Modular Surface Area values computed directly from the surface of each endocast model (see Methods 4.2.6.4). **B**, mean Modular Perimeter values (mm) for the Modular Surface Areas defined and calculated in **A** (see General Methods, Fig. 2.2K: **tel.r per**); **C**, size-standardised mean Modular Surface Area ratios calculated by dividing  $\log_{10}$  transformed mean Modular Surface Area values (**A**) by  $\log_{10}$  transformed specimen endocast total Surface Area values; **D**, size-standardised mean Modular Perimeter ratios calculated by dividing  $\log_{10}$  transformed mean Modular Perimeter values (**B**) by  $\log_{10}$  transformed specimen endocast total Surface Area values. **Abbreviations**, **Anhima**, *Anhima cornuta* (MV B12574); **Anseranas**, *Anseranas semipalmata* (SAM B48035); **Cer**, cerebellum; **D. murrayi**; *Dromornis murrayi* reconstruction (QM F57984 + QM F57974); **D. planei**; *Dromornis planei* (NTM P9464-106); **EmSg**, eminentia sagittalis; **Endo Surf**, endocast total Surface Area; **I. woodburnei**; *Ilbandornis woodburnei* (QVM:2000:GFV:20); **Leipoa**, *Leipoa ocellata* (SAM B11482); **Mes**, mesencephalon; **mm**, millimetres; **mm<sup>2</sup>**, square millimetres; **Rho**, rhombencephalon; **Tel.c**, caudal telencephalon; **Tel.r**, rostral telencephalon; **Tri.g**, trigeminal ganglion; **Tri.g F**, cross-section of the maxillomandibular ( $V_2+V_3$ ) branch of the trigeminal nerve (V).

| <b>A. Mean Modular Surface Area values (mm<sup>2</sup>)</b>  |         |         |           |            |           |               |
|--|---------|---------|-----------|------------|-----------|---------------|
| <b>Module</b>  | Leipoa  | Anhima  | Anseranas | D. murrayi | D. planei | I. woodburnei |
| EmSg   | 65.71   | 90.65   | 117.40    | 1353.96    | 1851.49   | 1170.99       |
| Tel.r  | 47.39   | 82.55   | 216.04    | N/A        | N/A       | N/A           |
| Tel.c  | 133.10  | 249.41  | 297.48    | 1213.28    | 1297.48   | 852.94        |
| Mes  | 118.28  | 52.33   | 71.57     | 139.37     | 164.03    | 145.83        |
| Tri.g  | 13.44   | 22.14   | 40.23     | 132.07     | 136.50    | 102.58        |
| Tri.g F  | 1.330   | 5.110   | 6.240     | 14.540     | 13.480    | 10.430        |
| Cer  | 103.59  | 205.25  | 192.07    | 678.37     | 816.82    | 528.19        |
| Rho  | 86.91   | 136.69  | 135.38    | 394.24     | 585.79    | 290.76        |
| <b>B. Mean Modular Perimeter values (mm)</b>                 |         |         |           |            |           |               |
| EmSg   | 36.34   | 46.36   | 49.00     | 136.94     | 156.55    | 121.19        |
| Tel.r  | 31.92   | 40.04   | 61.41     | N/A        | N/A       | N/A           |
| Tel.c  | 43.09   | 54.46   | 62.93     | 107.74     | 115.18    | 96.31         |
| Mes  | 46.04   | 34.11   | 41.17     | 55.86      | 73.11     | 54.06         |
| Tri.g  | 19.58   | 24.77   | 34.80     | 53.63      | 57.45     | 48.11         |
| Tri.g F  | 5.220   | 9.510   | 10.39     | 15.92      | 15.76     | 12.74         |
| Cer  | 41.84   | 58.67   | 52.64     | 110.41     | 115.64    | 92.74         |
| Rho  | 33.91   | 43.14   | 44.92     | 73.83      | 103.38    | 63.53         |
| Endo Surf (mm <sup>2</sup> )                                 | 1682.29 | 2404.61 | 2985.52   | 13199.82   | 15874.02  | 10200.52      |
| <b>C. Size-standardised mean Modular Surface Area ratios</b> |         |         |           |            |           |               |
| EmSg   | 0.563   | 0.579   | 0.596     | 0.760      | 0.778     | 0.765         |
| Tel.r  | 0.519   | 0.567   | 0.672     | N/A        | N/A       | N/A           |
| Tel.c  | 0.658   | 0.709   | 0.712     | 0.748      | 0.741     | 0.731         |
| Mes  | 0.643   | 0.508   | 0.534     | 0.520      | 0.527     | 0.540         |
| Tri.g  | 0.350   | 0.398   | 0.462     | 0.515      | 0.508     | 0.502         |
| Tri.g F  | 0.039   | 0.210   | 0.229     | 0.282      | 0.269     | 0.254         |
| Cer  | 0.625   | 0.684   | 0.657     | 0.687      | 0.693     | 0.679         |
| Rho  | 0.601   | 0.632   | 0.613     | 0.630      | 0.659     | 0.615         |
| <b>D. Size-standardised mean Modular Perimeter ratios</b>    |         |         |           |            |           |               |
| EmSg   | 0.484   | 0.493   | 0.486     | 0.519      | 0.522     | 0.520         |
| Tel.r  | 0.466   | 0.474   | 0.515     | N/A        | N/A       | N/A           |
| Tel.c  | 0.507   | 0.513   | 0.518     | 0.493      | 0.491     | 0.495         |
| Mes  | 0.516   | 0.453   | 0.465     | 0.424      | 0.444     | 0.432         |
| Tri.g  | 0.400   | 0.412   | 0.444     | 0.420      | 0.419     | 0.420         |
| Tri.g F  | 0.223   | 0.289   | 0.293     | 0.292      | 0.285     | 0.276         |
| Cer  | 0.503   | 0.523   | 0.495     | 0.496      | 0.491     | 0.491         |
| Rho  | 0.474   | 0.484   | 0.476     | 0.453      | 0.480     | 0.450         |
| $\log_{10}$ Endo Surf  | 3.226   | 3.381   | 3.475     | 4.121      | 4.201     | 4.009         |

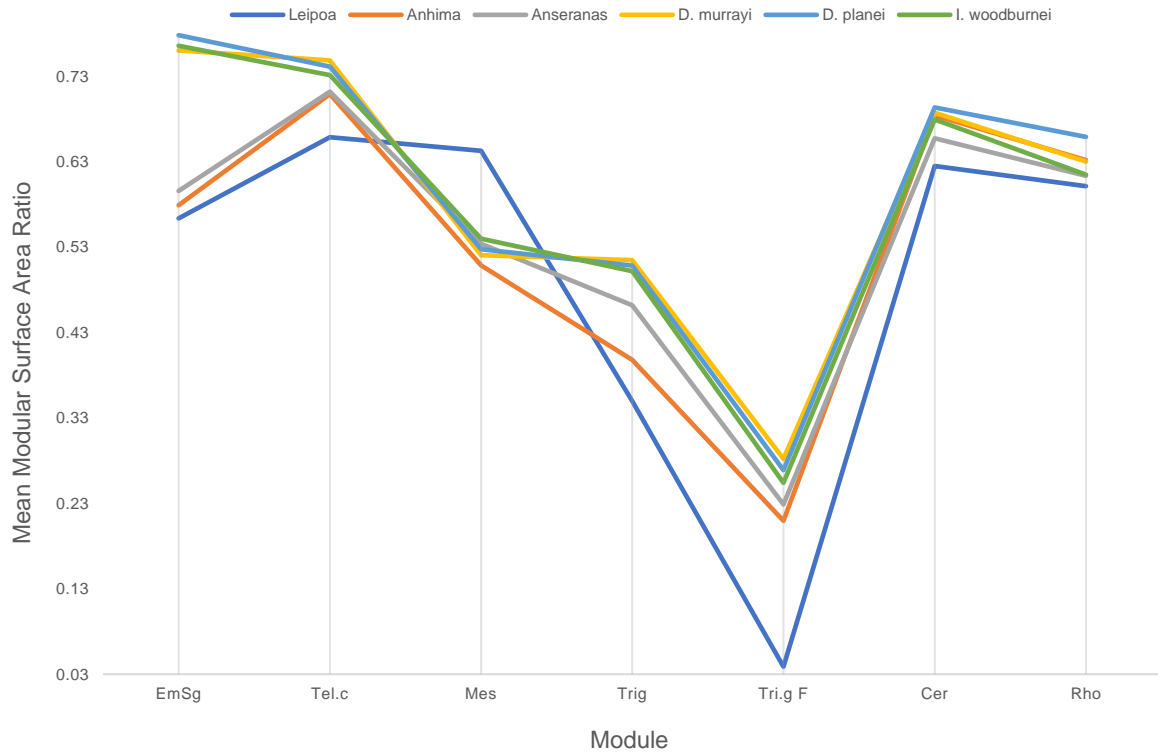


Figure A4.11. Mean Modular Surface Area ratios plot for all galloansere taxa. Size-standardised ratios are calculated by dividing  $\log_{10}$  transformed mean Modular Surface Area values by  $\log_{10}$  transformed specimen endocast total Surface Area values (see Tables A4.2C–D; Methods, 4.2.6.4).

**Abbreviations**, **Anhima**, *Anhima cornuta* (MV B12574); **Anseranas**, *Anseranas semipalmata* (SAM B48035); **Cer**, cerebellum; **D. murrayi**, *Dromornis murrayi* reconstruction (QM F57984 + QM F57974); **D. planei**, *Dromornis planei* (NTM P9464-106); **EmSg**, eminentia sagittalis; **I. woodburnei**, *Ilbandornis woodburnei* (QVM:2000:GFV:20); **Leipoa**, *Leipoa ocellata* (SAM B11482); **Mes**, mesencephalon; **Rho**, rhombencephalon; **Tel.c**, caudal telencephalon; **Tri.g**, trigeminal ganglion; **Tri.g F**, cross-section of the maxillomandibular ( $V_2+V_3$ ) branch of the trigeminal (V) nerve (see Figs. 4.4B, 4.4F, 4.4J, 4.4N).

Table A4.3. **A**, gastrolith size, gizzard mass and modal body mass by taxon for Holocene NZ palaeognath moa: *Dinornis robustus* (Owen, 1846); *Euryapteryx curtus gravis* (Owen, 1870); Australian Emu (*Dromaius novaehollandiae*) and dromornithid (*Genyornis newtoni*) taxa, for which complete gizzard data are associated. Body masses were calculated using Alexander's (1983) algorithm employing Fem L to ensure estimated mass continuity across taxa. However, the fossil specimen of *G. newtoni* (CU 2018-23) has no accompanying complete femora, therefore the mass estimation for CU 2018-23 was taken as the mean mass estimation for *G. newtoni* 'unsexed data' (n=22) from Grellet-Tinner et al. (2017:table A2); this value falls within the estimated mass range of Alexander's (1983) Fem L algorithm results for *G. newtoni* SAM 53833 (see **A** below). Gastrolith size is the narrowest width of two dimensions for each gastrolith measured (*sensu* Worthy 1989). **B**, size-standardised gastrolith size and gizzard mass ratios were calculated by dividing log<sub>10</sub> transformed gastrolith size and gizzard mass values by log<sub>10</sub> transformed specimen modal body mass values. **Abbreviations**, **BM**, modal body mass; **CB**, Callabonna; **CM**, Canterbury Museum; **CU**, Callabonna Uncatalogued, field code, Flinders University fossil collection; **FB**, Frome Basin; **Fem L**, femur length; **FUR**, Flinders University Reference collection; **g**, grams; **GM**, gizzard mass; **GS**, gastrolith size; **HH**, Honeycomb Hill Cave; **kg**, kilograms; **MC**, Maximus Cave; **mm**, millimetres; **MS**, Moonsilver Cave; **NMNZ**, National Museum of New Zealand; **No**, number; **NZ** New Zealand; **PV**, Pyramid Valley Swamp; **SAM**, South Australian Museum.

| <b>A. Taxon</b>           | <b>Catalogue No</b> | <b>Site</b>          | <b>Fem L (mm)</b> | <b>GS (mm)</b>       | <b>GM (g)</b>  | <b>BM Modal [Range] (kg)</b> |                |                     |                 |                     |
|---------------------------|---------------------|----------------------|-------------------|----------------------|----------------|------------------------------|----------------|---------------------|-----------------|---------------------|
| <i>D. robustus</i>        | NMNZ S25765         | HH ‡                 | 334               | >40 ●                | 2450           | 154.92 [132.56–181.33]       |                |                     |                 |                     |
| <i>D. robustus</i>        | CM 20118            | PV ‡                 | 390               | >40 ●                | 4380           | 255.42 [218.23–298.97]       |                |                     |                 |                     |
| <i>D. robustus</i>        | NMNZ S23654         | HH ‡                 | 303               | >40 ●                | 2310           | 113.15 [96.67–132.44]        |                |                     |                 |                     |
| <i>D. robustus</i>        | NMNZ S32678         | MS ‡                 | 324               | >40 ●                | 3080           | 140.45 [119.99–164.39]       |                |                     |                 |                     |
| <i>D. robustus</i>        | NMNZ S28225         | MC ‡                 | 265               | >40 ●                | 2090           | 73.44 [62.74–85.96]          |                |                     |                 |                     |
| <i>E. curtus gravis</i>   | NMNZ S25656         | HH ‡                 | 310               | 15 ♦                 | 630            | 121.8 [104.06–142.10]        |                |                     |                 |                     |
| <i>D. novaehollandiae</i> | FUR 163             | FB ☼                 | 223               | 21.2 (n=5) ■         | 240            | 42.09[35.96–49.26]           |                |                     |                 |                     |
| <i>G. newtoni</i>         | CU 2018-23          | CB ☼                 | –                 | 12.5 (n=5) ■         | 1270           | 219.8 *                      |                |                     |                 |                     |
| <i>G. newtoni</i>         | SAM 53833           | CB ☼                 | 355               | 15.4 (n=5) ■         | 540            | 188.59 [161.13–220.75]       |                |                     |                 |                     |
| <b>B. Taxon</b>           | <b>GS Ratio</b>     | <b>GS Ratio Mean</b> | <b>GM Ratio</b>   | <b>GM Ratio Mean</b> | <b>Log(GS)</b> | <b>Log(GS) Mean</b>          | <b>Log(GM)</b> | <b>Log(GM) Mean</b> | <b>Log (BM)</b> | <b>Log(BM) Mean</b> |
| <i>D. robustus</i>        | 0.731               |                      | 1.547             |                      | 1.602          |                              | 3.389          |                     | 2.190           |                     |
| <i>D. robustus</i>        | 0.666               |                      | 1.513             |                      | 1.602          |                              | 3.641          |                     | 2.407           |                     |
| <i>D. robustus</i>        | 0.780               | 0.756                | 1.638             | 1.620                | 1.602          | 1.602                        | 3.364          | 3.441               | 2.054           | 2.133               |
| <i>D. robustus</i>        | 0.746               |                      | 1.624             |                      | 1.602          |                              | 3.489          |                     | 2.148           |                     |
| <i>D. robustus</i>        | 0.859               |                      | 1.779             |                      | 1.602          |                              | 3.320          |                     | 1.866           |                     |
| <i>E. curtus gravis</i>   | 0.564               | 0.564                | 1.342             | 1.342                | 1.176          | 1.176                        | 2.799          | 2.799               | 2.086           | 2.086               |
| <i>D. novaehollandiae</i> | 0.817               | 0.817                | 1.465             | 1.465                | 1.326          | 1.326                        | 2.380          | 2.380               | 1.624           | 1.624               |
| <i>G. newtoni</i>         | 0.468               |                      | 1.325             |                      | 1.097          |                              | 3.104          |                     | 2.342           |                     |
| <i>G. newtoni</i>         | 0.522               | 0.495                | 1.201             | 1.263                | 1.188          | 1.142                        | 2.732          | 2.918               | 2.276           | 2.309               |

Alexander (1983) Fem L BM algorithms

Modal:  $Y/Y_o=(BM/M_o)^{0.31}$ ;  $M_o=78$ ,  $Y=Fem\ L$ ,  $Y_o=(Modal)270$

Range:  $Y/Y_o=(BM/M_o)^{0.31}$ ;  $M_o=78$ ,  $Y=Fem\ L$ ,  $Y_o=(Range)270*1.05$  [283.5];  $270/1.05$  [257.14]

\* mean mass estimation for *G. newtoni* 'unsexed data' (n=22), based on tibiotarsus least-shaft circumference from Grellet-Tinner et al. (2017:table A2); see Methods 4.2.6.5 and A above. ♦ Worthy 1989; ● Worthy & Holdaway 2002; ■ measured by Author

‡ South Island NZ site; ☼ South Australian site.

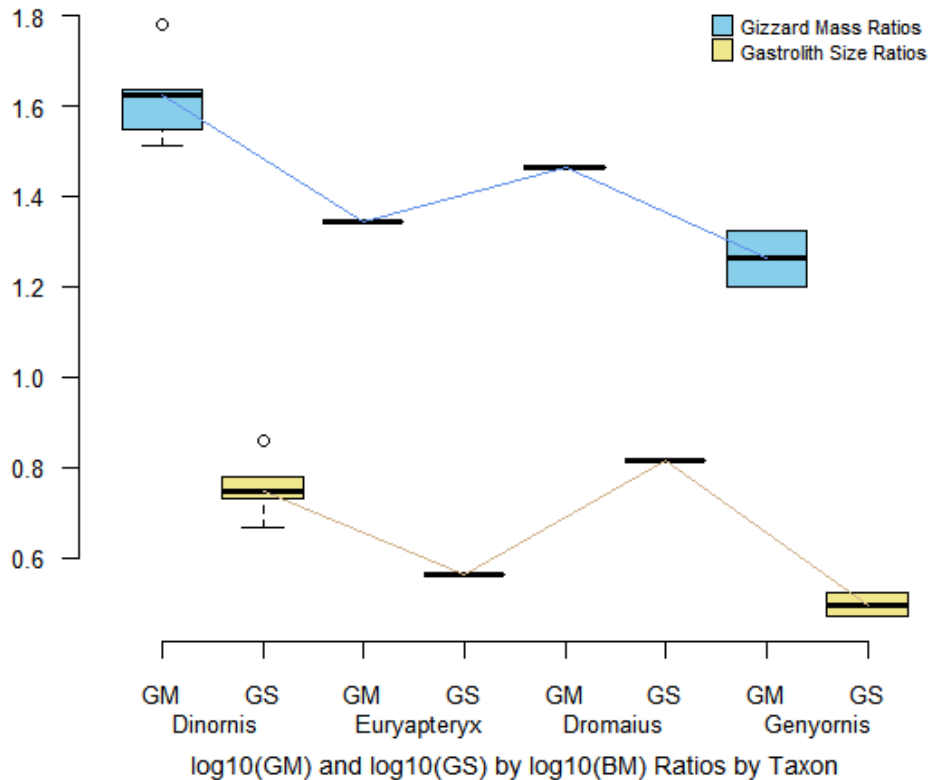


Figure A4.12. Quantile boxplots of size-standardised gizzard size ratios and gizzard mass ratios by taxon for Holocene NZ palaeognath moa (*Dinornis robustus*; n=5; *Euryapteryx curtus gravis*; n=1); Australian Emu (*Dromaius novaehollandiae*; n=1) and dromornithid (*Genyornis newtoni*; n=2) taxa, for which complete gizzard data are associated (see Table A4.3A; Methods, 4.2.6.5-6). Boxplot medians are linked to visualise distinctions between the two groups of data. Upper and lower bounds of each boxplot represent the upper and lower quartiles respectively, the horizontal line represents the median, and whiskers represent standard deviation at 1.5 IQR. *D. robustus* gizzard mass and gizzard size ratios boxplot outliers (open circles) represent the PVS specimen which falls outside 1.5 IQR. Body masses were calculated using Alexander's (1983) algorithms employing Fem L (see Table A4.3) to ensure estimated body mass continuity across taxa. However, the fossil specimen of *G. newtoni* (CB 2018-23) has no accompanying complete femora, therefore the body mass estimation for CB 2018-23 was taken as the mean body mass estimation for *G. newtoni* 'unsexed data' (n=22) from Grellet-Tinner et al. (2017:table A2); this value falls within the estimated body mass range of Alexander's (1983) Fem L algorithm results for *G. newtoni* (SAM 53833; see Table A4.3A). Gizzard size is the narrowest width of two dimensions for each gizzard measured (*sensu* Worthy 1989). Size-standardised gizzard mass and gizzard size ratios were calculated by dividing log<sub>10</sub> transformed gizzard mass and gizzard size values by log<sub>10</sub> transformed specimen modal body mass (see Table A4.3B). Full details for all specimens are given in Table A4.3. **Abbreviations**, **BM**, modal body mass; **Fem L**, femur length; **GM**, gizzard mass; **GS**, gizzard size; **IQR**, inter-quartile range (25–75%); **NZ**, New Zealand; **PVS**, Pyramid Valley Swamp.

Table A4.4. Cranial measurements (mm) of *Dromornis stirtoni* and *D. planei* from NTM collections compared with those of *D. murrayi* QM F57984. **Abbreviations**, **CranH**, height of crania from mamillar tuberosities to top of cranium; **mm**, millimetres; **NTM**, Museum of Central Australia, Alice Springs, Northern Territory, Australia. **OccW**, width of occipital condyle; **OccH**, height of occipital condyle; **OrbW**, width across the orbits; **POP**, width across the processus paroccipitalis; **QSW**, width between lateral margins of recessus quadratica; **ZFC**, width zona flexoria craniofacialis.

| <b>Taxon</b>       | <b>Catalogue no.</b> | <b>OrbW</b> | <b>POP</b> | <b>OccW</b> | <b>OccH</b> | <b>QSW</b> | <b>CranH</b> | <b>ZFC</b> |
|--------------------|----------------------|-------------|------------|-------------|-------------|------------|--------------|------------|
| <i>D. stirtoni</i> | P3250                | 127.9       | 111        | 23.4        | 20.6        | 97         | 136          | –          |
| <i>D. stirtoni</i> | P98105               | 137         | ca. 117.0  | –           | –           | 105        | –            | 105        |
| <i>D. stirtoni</i> | P3251                | –           | –          | 26.5        | 23.8        | –          | –            | –          |
| <i>D. stirtoni</i> | P9342                | 125         | ca. 93.0   | –           | –           | 96         | –            | 91         |
| <i>D. stirtoni</i> | P98106               | –           | –          | 24.3        | 21.5        | –          | –            | –          |
| <i>D. stirtoni</i> | P3249                | 141         | –          | –           | –           | 121        | 165          | –          |
| <i>D. planei</i>   | P9464-109            | 114.4       | –          | 19.9        | 19.9        | 91.1       | 105.8        | –          |
| <i>D. planei</i>   | P9464-106            | 117         | 105.5      | 24          | 22.5        | 102.5      | 115          | 84         |
| <i>D. planei</i>   | P9973.6              | 126         | –          | 23.7        | 22.4        | 92.4       | 117.7        | 89.5       |
| <i>D. planei</i>   | P9464-xx             | –           | –          | 18.4        | 15.8        | –          | –            | –          |
| <i>D. planei</i>   | P9612-1              | –           | –          | 20.8        | 18.4        | –          | –            | –          |
| <i>D. planei</i>   | P9276-4              | –           | –          | 23.1        | 22.4        | –          | –            | –          |
| <i>D. planei</i>   | P907-6               | –           | –          | 22.3        | 20.7        | –          | –            | –          |
| <i>D. planei</i>   | P9464-111            | 135.7       | –          | 22.2        | 19.7        | 108.3      | –            | –          |
| <i>D. planei</i>   | P9973-1              | –           | –          | 20.1        | 18          | –          | –            | –          |
| <i>D. murrayi</i>  | QM F57984            | 130         | –          | –           | –           | 103        | –            | –          |

'ca.' means the measurement was estimated because some of the structure was missing. Table and captions adapted from [Worthy et al. \(2016b:table 1\)](#).

## CHAPTER 5

**The phylogenetic utility of Galloansere endocranial anatomy**

## 5.1 INTRODUCTION

In preceding Chapters, I have applied geometric morphometric methods to assess endocranial transformations in Finsch's duck, and used four specimens sampled across a ~20 ky period to show directional transformations in endocast shape, associated with the transition to flightlessness. I sampled dromornithid endocranial anatomy across a ~18 Ma evolutionary transect, and along with reference to three extant galloanseres, described the characteristics of the dromornithid brain, its principle innervation, and distinctions in endocast shape between dromornithid lineages for the first time. Here, I extend this approach to the assessment of endocast shape across a clade, to ascertain the potential impact of adaptive radiation for specific niches, on the phylogenetic utility of the galloansere brain.

Galloansere taxa, including galliforms (landfowl), anseriforms (waterfowl), and gastornithiforms (dromornithids; see Introduction, **1.2**), represent several taxa occupying trophic and ecological niches which appear repeatedly across the tree (i.e., see Fig. 5.1A below). Repeated adaptations to trophic guild across the clade, allow testing of the competing hypotheses that endocranial shape reflects a systematically informative phylogenetic component, or that the shape of the avian brain is driven more by adaptation to habitat use.

Traditional methods of subjectively describing morphology, in the form of discrete or continuous characters, have long been employed in generating and testing phylogenetic hypotheses in evolutionary biology. By such means, the phylogenetic efficacy of the vertebrate cranium has been explored using parsimony based approaches (*sensu* [Camin & Sokal 1965](#); [Swofford 2003](#)). For example, in mammals, the craniofacial region of hominin taxa ([González-José et al. 2008](#)), and modern hominoids ([Lockwood et al. 2004](#); [Gilbert 2011](#)) were evaluated. The fossil crania of a Cretaceous theriiform ([Macrini et al. 2007](#)), an Eocene oreodontid ([Macrini 2009](#)), the Miocene platypus *Obdurodon* ([Macrini et al. 2006](#)), fossil and extant Caninae ([Lyras & Van der Geer 2003](#)), and the vestibular organs of extant diprotodontian taxa ([Schmelzle et al. 2007](#)) have been assessed. Additionally, endocast morphology of extant and fossil charadriiform ([Smith & Clarke 2012](#)), and sphenisciform ([Ksepka et al. 2012](#); [Proffitt et al. 2016](#)) birds were coded.

The use of anatomical shape data characterised by morphometric methods, have long been recognised as potentially phylogenetically informative, and assessed appropriately, may provide information about relationships among taxa ([Zelditch et al. 1995](#)). However, early attempts at the extension of morphometric approaches to cladistic reconstruction, have proved somewhat controversial (see [Rohlf 1998](#); [Klingenberg & Gidaszewski 2010](#), and references therein). The debate

as to the appropriate utilisation of multivariate morphometric data to estimate a well-supported phylogeny, continues to occupy the field (Klingenberg & Gidaszewski 2010). However, the testing for patterns of “phenotypic similarity” among taxa with a shared evolutionary history, termed “phylogenetic signal”, is well-supported, and is an important step in understanding the distribution of trait variation across a phylogeny (Blomberg et al. 2003; Klingenberg & Gidaszewski 2010; Adams 2014b). The concept is predicated on the observation that data derived from species sharing a hierarchical evolutionary history, are not independently distributed (Felsenstein 1985, Harvey & Pagel 1991), and that phylogenetic signal is a measure of the “statistical nonindependence” among trait values of related species (Revell et al. 2008). The most common model for assessment of phylogenetic signal, is under a Brownian motion (BM) model of evolutionary change, based on the evolutionary processes of genetic drift and forms of natural selection (e.g. Felsenstein 1988; O’Meara et al. 2006). Under a BM evolutionary model, the measure ‘K’ has an expected value of one (1) and variation of the measure, i.e.  $K > 1$ , or  $K < 1$ , provides an indication of excess or deficiency respectively, of BM “statistical dependence” across the tips of a particular phylogeny (see Ives et al. 2007:257; Revell et al. 2008:593; Münkemüller et al. 2012). However, multiple processes may produce patterns of phylogenetic signal in data, and phylogenetic signal alone is not a “direct” means of illuminating all processes involved in phenotypic diversification (Blomberg et al. 2003; Revell et al. 2008; Pennell & Harmon 2013; Adams 2014b).

An approach by which to investigate phenotypic diversification by visualisation of morphometric traits with respect to phylogenetic history, was demonstrated by Rohlf (2002), who used Lm data derived from mosquito wings, and squared-change parsimony methods (*sensu* Huey & Bennett 1987; Maddison 1991; Rohlf 2001), to estimate ancestral states across a phylogeny. Such methods were subsequently employed to explore cranial evolutionary patterns in phylomorphospace (*sensu* Sidlauskas 2008) for mammalian taxa, represented by leaf nosed bats (Wilson et al. 2016). Reptiles have formed the focus of several assessments, for example, extant and fossil snakes and lizards (Yi & Norell 2015), xenodontine snakes (Klaczko et al. 2016), western rattlesnakes (Davis et al. 2016), and an ontogenetic series of squamates (Da Silva et al. 2018). The skulls of caecilian amphibians were assessed by Sherratt et al. (2014), and neornithine birds comprised the focal taxa for the analyses of Klingenberg & Marugán-Lobón (2013), Carril et al. (2015), Marugán-Lobón et al. (2016), Tokita et al. (2016), Young et al. (2017), Bright et al. (2019), Felice & Goswami (2018), and Felice et al. (2019).

The assessment of allometric trait covariation across taxa, whilst accounting for phylogenetic non-independence of data, may take several approaches. The most commonly used of which are phylogenetic regression methods. For example, phylogenetic independent contrasts (PIC— *sensu* Felsenstein 1985; Garland et al. 1992), or phylogenetic generalised least squares (PGLS *sensu* Grafen 1989; Martins & Hansen 1997). These methods employ linear models to evaluate patterns of allometric covariation across species data within a statistical framework, while accounting for

phylogeny. PGLS methods have been extensively used across comparative biology, and morphometric data derived from both 2D and 3D Lms have been employed to assess trait variation in human teeth (Gómez-Robles et al. 2013), New World monkeys (Aristide et al. 2016), leporids (Kraatz & Sherratt 2016), and carnivorous bats and canids (Santana & Cheung 2016). Assessments using reptiles are represented by those of *Anolis* lizards (Sanger et al. 2013), squamates, including both snakes and lizards (Palci et al. 2017), basal madtsoiid snakes (Palci et al. 2018), microcephalic sea snakes (Sherratt et al. 2019), amphibolurine lizards (Gray et al. 2019), and ceratopsid dinosaurs (Maiorino et al. 2013). The interspecific ontogenetic allometry of amphibians (Sherratt et al. 2017a), trends in shell shape (Sherratt et al. 2016), and ecomorph patterns (Sherratt et al. 2017b) of pectinid scallops have been addressed. However, studies investigating phylogenetic diversity in avian cranial morphology employing PGLS methods are few, e.g., pigeon skulls (Young et al. 2017), and beak/skull shape in parrots (Bright et al. 2019).

The recognition of cerebrotype-like patterns in avian endocranial morphology led Walsh & Milner (2011a) to suggest the form of the brain, or parts thereof, may be phylogenetically informative, and Walsh & Milner (2011b) argued endocranial features may prove useful in addressing the “poor phylogenetic resolution” displayed by some avian clades. The current phylogenetic topology of galloanseres has only recently been accepted after compelling molecular support (e.g. Ericson et al. 2006; Hackett et al. 2008; Jarvis et al. 2014, and references therein; see also Introduction, 1.2). With respect to morphological attributes alone, only few cranial characters unite galloanseres, i.e., features of the basipterygoid, quadrate, and mandibular processes (Ericson 1996:199; Mayr 2009:35, 2017:107). A more recent assessment of galloanseres, including dromornithid taxa, identified only one “unique” mandibular synapomorphy, along with an “unambiguous” basipterygoid character (Worthy et al. 2017a:9) supporting the taxon. Walsh & Knoll (2011) argued that avian endocranial morphology had not been successfully “mined” for phylogenetically informative data, and the potential exists for the identification of morphological characters, derived from statistical assessment of the various divisions of the avian brain, which may compliment the demonstrably weak morphological cranial apomorphies uniting the clade.

It is apparent that avian brain morphology is linked with adaptive and functional traits (see Introduction, 1.5.4), but whether the differential hypo- or hypertrophy of one or more brain regions across a clade is consistently related to occupancy of specific trophic niches, such as diving or terrestrial grazing, or whether the shape of one or more brain regions are reflective of phylogenetic affinity, may be addressed by employing the comprehensive analytical framework of geometric morphometrics.

I combined the four endocasts of Finsch’s duck (Chapter 3), with those of three dromornithid taxa (Chapter 4), along with two endocasts of the European Oligo-Miocene duck *Mionetta blanchardi* (see Introduction, 1.4.6.2), and a broad sample of extant galloanseres, assembling a total data set comprising 34 endocasts. With the application of multi- and univariate phylogenetic regression

methods, I assessed three categories of endocast shape data, to investigate whether the modular aspect of multivariate shape, univariate surface areas, and univariate directional dimensions of morphological features represented by those data: **1**, retain phylogenetic signal; **2**, whether one or more modular brain regions hold a phylogenetic component, which may prove informative if described as traditional discrete or continuous characters; or **3**, may be employed as modular multivariate matrices for incorporation in more comprehensive cladistic assessments. Additionally, I assessed the endocast morphology of the fossil taxa, with respect to their evolutionary affinity with extant galloanseres. Given the apomorphies uniting galloanseres comprise exclusively cranial characteristics, such assessment may potentially identify characteristics of galloansere endocranial morphology to complement existing cranial apomorphies, and further clarify dromornithid affinities within the clade.

With respect to the fossils of the European Oligo-Miocene taxon *Mionetta blanchardi* (see Introduction, **1.4.6.2**) included here, [Worthy et al. \(2007\)](#) noted these ducks displayed morphological similarities with antipodean erismaturine taxa, and the taxon was recognised as a non-diving erismaturine by [Worthy & Lee \(2008\)](#). The assessment of the endocast morphology of these fossils, may afford additional insight regarding hypotheses of a Neogene erismaturine global radiation (see [Worthy et al. 2007, 2008](#); [Worthy & Lee 2008](#); [Worthy 2009](#)). Additionally, the assessment of the endocast morphology of the New Zealand duck *Chenonetta finschi*, along with an expanded data set, may shed additional light on the hypothesised sister relationship between it and the Australian wood duck *C. jubata* (e.g. [Worthy & Olson 2002](#)).

## 5.2 METHODS

### 5.2.1 Abbreviations

**5.2.1.1 Institutions**—**ANWC**, Australian National Wildlife Collection, Canberra, Australia; **ANSTO**, Australian Nuclear Science and Technology Organisation, Lucas Heights, Sydney, New South Wales, Australia; **KU**, University of Kansas Natural History Museum, Lawrence, USA; **MNHN**, Muséum National d'Histoire Naturelle, Paris, France; **NMNZ**, Museum of New Zealand Te Papa Tongarewa, Wellington, New Zealand; **NTM**, Museum of Central Australia, Alice Springs, Northern Territory, Australia; **QM**, Queensland Museum, Brisbane, Queensland, Australia; **QVM**, Queen Victoria Museum and Art Gallery, Launceston, Tasmania; **SAHMRI**, South Australian Medical and Health Research Institute, Adelaide, South Australia; **SAM**, South Australian Museum.

**5.2.1.2 Specimens**—*Anas platyrhynchos* (SAM B48742), *A. superciliosa* (SAM B38172), *A. castanea* (SAM B24479), *Lophodytes cucullatus* (SAM B47750), *Aythya australis* (SAM B33108), *Nettapus pulchellus* (SAM B45606), *Chenonetta finschi*.CR (NMNZ S.039838), *C. finschi*.HC (NMNZ S.034496), *C. finschi*.GYL2 (NMNZ S.023695), *C. finschi*.GYL3 (NMNZ S.023702), *C. jubata* (SAM B39457), *Tadorna tadornoides* (SAM B39872), *Branta canadensis* (SAM B31086),

*Anser caerulescens* (SAM B36868), *Cygnus atratus* (SAM B46123), *Cereopsis novaehollandiae* (SAM B39638), *Stictonetta naevosa* (SAM B56055), *Malacorhynchus membranaceus* (SAM B32483), *Oxyura australis* (SAM B31910), *Biziura lobata* (SAM B11405), *Mionetta blanchardi*.1 (MNHN S.G.10005), *M. blanchardi*.2 (MNHN S.G.10002), *Dendrocygna bicolor* (SAM B36869), *D. eytoni* (SAM B45769), *Anseranas semipalmata* (SAM B48035), *Anhima cornuta* (SAM B12574), *Dromornis planei* (NTM P9464-106), *D. murrayi* reconstruction (QM F57984 + QM F57974), *Ibandornis woodburnei* (QVM:2000:GFV:20), *Talegalla fuscirostris* (KU 97007), *Leipoa ocellata* (SAM B11482), *Megapodius reinwardt* (ANWC O22869), *Gallus gallus* (SAM B34041), *Ortalis vetula* (SAM B13342).

## 5.2.2 Geological and temporal data for the fossils analysed

5.2.2.1 *Chenonetta finschi*—see Chapter 3, 3.2.3

5.2.2.2 Dromornithids—see Chapter 4, 4.2.2

5.2.2.3 *Mionetta blanchardi*.1–2; Saint-Gerand-le-Puy, Oligo-Miocene, France (see Introduction, 1.4.6.2; and [Cheneval 1983](#); [Livezey & Martin 1988](#); [Mourer-Chauviré et al. 2004](#)).

5.2.3 **Nomenclature**—for anatomical nomenclature adopted in the following texts, see Introduction, 1.5.2, and Fig. 1.5.1 above.

## 5.2.4 Modelling

One of each of the following neurocrania were  $\mu$ CT scanned using the Skyscan 1076  $\mu$ CT instrument (Bruker microCT) at Adelaide Microscopy, University of Adelaide: *Anas platyrhynchos* was scanned at 17.0 micrometre ( $\mu$ m) resolution at 48 kilovolts (kV) and 169 microamps ( $\mu$ A), *A. superciliosa* was scanned at 17.0  $\mu$ m, at 49 kV and 169  $\mu$ A, *A. castanea* was scanned at 17.0  $\mu$ m, at 46 kV and 214  $\mu$ A, *Lophodytes cucullatus* was scanned at 17.0  $\mu$ m, at 40 kV and 240  $\mu$ A, *Aythya australis* was scanned at 17.0  $\mu$ m, at 49 kV and 169  $\mu$ A, *Nettapus pulchellus* was scanned at 17.0  $\mu$ m, at 41 kV and 240  $\mu$ A, *Chenonetta finschi*.CR was scanned at 17.0  $\mu$ m, at 51 kV and 192  $\mu$ A, *C. finschi*.HC was scanned at 17.0  $\mu$ m, at 70 kV and 141  $\mu$ A, *C. finschi*.GYL2 was scanned at 17.0  $\mu$ m, at 51 kV and 192  $\mu$ A, *C. finschi*.GYL3 was scanned at 17.0  $\mu$ m, at 51 kV and 192  $\mu$ A, *C. jubata* was scanned at 17.4  $\mu$ m, at 48 kV and 139  $\mu$ A, *Tadorna tadornoides* was scanned at 17.4  $\mu$ m, at 48 kV and 139  $\mu$ A, *Branta canadensis* was scanned at 34  $\mu$ m, at 100 kV and 90  $\mu$ A, *Anser caerulescens* was scanned at 34  $\mu$ m, at 100 kV and 90  $\mu$ A, *Cygnus atratus* was scanned at 34  $\mu$ m, at 100 kV and 90  $\mu$ A, *Cereopsis novaehollandiae* was scanned at 17.4  $\mu$ m, at 49 kV and 139  $\mu$ A, *Stictonetta naevosa* was scanned at 34  $\mu$ m, at 100 kV and 90  $\mu$ A, *Malacorhynchus membranaceus* was scanned at 17.0  $\mu$ m, at 49 kV and 169  $\mu$ A, *Oxyura australis* was scanned at 17.4  $\mu$ m, at 48 kV and 139  $\mu$ A, *Biziura lobata* was scanned at 34  $\mu$ m, at 100 kV and 90  $\mu$ A, *Dendrocygna bicolor* was scanned at 34  $\mu$ m, at 100 kV and 90  $\mu$ A, *D. eytoni* was scanned at 17.4  $\mu$ m, at 48 kV and 139  $\mu$ A, *Anseranas semipalmata* was

scanned at 34.8  $\mu\text{m}$ , at 100 kV and 90  $\mu\text{A}$ , *Anhima cornuta* was scanned at 34  $\mu\text{m}$ , at 100 kV and 100  $\mu\text{A}$ , *Talegalla fuscirostris* was scanned at 17.4  $\mu\text{m}$ , at 48 kV and 139  $\mu\text{A}$ , *Leipoa ocellata* was scanned at 17.4  $\mu\text{m}$ , at 48 kV and 139  $\mu\text{A}$ , *Megapodius reinwardt* was scanned at 17.3  $\mu\text{m}$ , at 49 kV and 139  $\mu\text{A}$ , *Gallus gallus* was scanned at 17.0  $\mu\text{m}$ , at 59 kV and 167  $\mu\text{A}$ , and *Ortalis vetula* was scanned at 17.3  $\mu\text{m}$ , at 48 kV and 139  $\mu\text{A}$ . Skyscan raw  $\mu\text{CT}$  acquisition data were reconstructed using NRecon v1.6.10.4 (Bruker microCT) and compressed using ImageJ v1.51w (Rasband 2018) software (see General Methods, 2.1.1).

The following neurocrania were  $\mu\text{CT}$  scanned using a Phoenix Nanotom CT instrument (Phoenix X-ray), at the Biomaterials Science Centre, University of Basel, Switzerland: *Mionetta blanchardi*.1 (MNHN S.G.10005) was scanned at 23  $\mu\text{m}$ , at 120 kV and 200  $\mu\text{A}$ , *M. blanchardi*.2 (MNHN S.G.10002) was scanned at 23  $\mu\text{m}$ , at 120 kV and 200  $\mu\text{A}$ .

Two neurocrania of *Dromornis murrayi* (QM F57984; QM F57974) and one of *Ilbandornis woodburnei* (QVM:2000:GFV:20) were medical X-ray CT-scanned using the Siemens Somatom Force CT instrument located at the SAHMRI facility in Adelaide (see General Methods, 2.1.2). The neurocranium of *D. planei* (NTM P9464-106) was scanned at the ANSTO nuclear facilities in Sydney using the DINGO neutron CT-scanning instrument located in the OPAL reactor beam hall on thermal beam HB2. (For additional details see Chapter 4, 4.2.4, and General Methods, 2.1.3).

**5.2.4.1 Three dimensional (3D) surface model construction**—was conducted using Materialise Mimics v18 software and raw 3D surface endocast \*.stl models representative of the shape of the brain were produced from reconstructed CT data. (Figs. A5.1–A5.8). These included the base and immediate stem of the major nerves passing from the brain into the neurocranium. See also General Methods, 2.1.1.

**5.2.4.2 Model reconstructions**—a single endocast surface model was compiled from CT-scan data of the two specimens of *D. murrayi* (QM F57984 + QM F57974; see Chapter 4, 4.2.4.4, Fig. A4.9; Chapter 5, Figs. A5.4C–D, A5.8C–D).

**5.2.4.3 Remeshing**—of raw 3D \*.stl surface models is required to optimise the quality of the triangles comprising the surface mesh and to reduce the physical file size of models for landmarking operations (see below). Remeshing operations were carried out in Materialise 3-matic v10 and conversion of remeshed \*.stl format 3D objects to \*.ply format was conducted in MeshLab v2016.12 (Cignoni et al. 2008).

## 5.2.5 Landmarking

Digital landmarking of 3D endocast surface models was conducted in IDAV Landmark v3.6 (Wiley 2006), using 20 fixed (type 1) and 460 semi (type 3) landmarks (*sensu* Bookstein 1991), for a total of 480. These landmarks were assigned into 13 modules for subsequent analyses (see General Methods, Fig. 2.1). The full Lm suite is described in General Methods Appendices (A2.1).

## 5.2.6 Data

For each of the three forms of data described below (i.e. Modular Lm data, Modular Distance data, and Modular Surface Area data). Two separate data sets were generated, one including dromornithids (Complete data), and one data set excluding dromornithid taxa (hereafter ‘Dromornithids-excluded data’). Each of these data sets were assessed separately using the analytical protocols described below, and results are presented so as to identify any effect the inclusion of data from the highly derived endocast morphology of these markedly divergent galloansere taxa, may have had on the assessments performed.

**5.2.6.1 Modular Lm data**—three dimensional digital shape data derived from the Modular Lm suite (see General Methods, Fig. 2.1), were used for all analytical protocols described below (see 5.2.7). Phylogenetic statistics and numerical output from each assessment are presented in text, and in Table A5.1.

**5.2.6.2 Modular Distance data**—were calculated between Lm and SIm locations for each specimen employing the ‘interlmkdist’ function in Geomorph v3.0.7 (Adams et al. 2018; see also 5.2.8 below), using raw Lm coordinate data. Modular distance measurements for the length and width of each modular structure, capturing the directional ‘curve’ over a 3D surface (i.e., eminentia sagittalis; see General Methods, 2.3.2, Figs. 2.2C–D), were calculated incorporating the distances between each SIm forming the measurement vectors. Then individual measurements between SImS were added together to form the total modular distance measurement value (see General Methods, Fig. 2.2C–D). Paired structure data (i.e., eminentia sagittalis, rostral and caudal telencephalon, mesencephalon, and trigeminal ganglion modules), were combined and mean Modular Distance data calculated (see Table A5.2). Size-standardised mean Modular Distance ratios were calculated by dividing  $\log_{10}$  transformed mean modular distance values, by  $\log_{10}$  transformed specimen endocast volume values (see General Methods, 2.3.2; Table A5.3; Fig. A5.9). For phylogenetically informed analyses (see 5.2.7.3–5.2.7.4 below), only standardised  $\log_{10}$  transformed mean Modular Distance data and  $\log_{10}$  transformed endocast volume data were used (see Tables A5.2, A5.4–A5.5). Linear Distance data (see General Methods, 2.3.2; Figs. 2.2G–I) were not used, as comparable metrics were not available for 3D Modular Lm data (see 5.2.6.1; General Methods, 2.3.1, Fig. 2.1) and Modular Surface Area data (see 5.2.6.3; General Methods, 2.3.4, Figs. 2.2J–K).

**5.2.6.3 Modular Surface Area data**—for each endocast module, as defined by the Lm modules described in General Methods Appendices (A2.1), and shown in Figs. 2.1A–D, were computed directly from the surface of each 3D endocast model using MeshLab (see General Methods, 2.3.3, Figs. 2.2J–K; Table A5.6). Mean Modular Surface Area ratio data were generated by dividing  $\log_{10}$  transformed mean surface area values, by  $\log_{10}$  transformed total endocast surface area values (see Table A5.7; Fig. A5.10). For phylogenetically informed analyses (see 5.2.7.3–5.2.7.4 below) only standardised  $\log_{10}$  transformed mean Modular Surface Area data, and  $\log_{10}$  transformed total endocast surface data were used (see Tables A5.6, A5.8–A5.9). Modular Perimeter data (General

Methods, **2.3.2**, Figs. 2.2G–I) were not used, as comparable metrics were not available for 3D Modular Lm data (see **5.2.6.1**; General Methods, **2.3.1**, Fig. 2.1), and Modular Distance data (see **5.2.6.2**; General Methods, **2.3.2**, Fig. 2.2C–D).

**5.2.6.4 Phylogenetic trees**—were assembled based on familial phylogenetic hypotheses for extant anseriforms proposed by [Donne-Goussé et al. \(2002\)](#), [Gonzalez et al. \(2009\)](#), and [Liu et al. \(2014\)](#). The composition of erismaturines (=oxyurines) was derived from [Worthy & Lee \(2008\)](#), and the relationships between species of *Chenonetta* within anatines follows [Worthy & Olson \(2002\)](#). The analyses of [Worthy et al. \(2017a\)](#) informed the placement of gastornithiforms, and galliform taxa were assigned according to [Harris et al. \(2014\)](#), and [Stein et al. \(2015\)](#). Branch lengths were by necessity set to a length of one (1), as there exists no previous molecular or morphologically based cladistic analyses comprising the full specimen data set assessed here. This was expected to have limited effect on phylogenetically informed assessments, as trees were more than 60% resolved (see [Davies et al. 2012:246](#); Fig. 5.1, and **5.2.7.3** below). Additionally, in simulation studies where branch length data have been unavailable, branch lengths for trees used were set to 1.0 (e.g. [Revell 2010:321](#)). Newick strings were generated for two specific trees, Complete and Dromornithids-excluded data respectively, using T-Rex ([Boc et al. 2012](#)). Tree topology (see Fig. 5.1; [Note: Tree topology for Dromornithids-excluded data is not shown]), was visualised using FigTree v1.4.4 ([Rambaut 2012](#)). Taxa were assigned factorial designations: **A**, Trophic Guild (seven categories for Complete data sets, six categories for Dromornithids-excluded data sets); **B**, Sub-Family/Family (10 for Complete data sets, nine for Dromornithids-excluded data sets); and **C**, Order (three for Complete data sets, two for Dromornithids-excluded data sets; see Fig. 5.1), which were used for phylogenetically informed analyses (see **5.2.7.3–5.2.7.4** below). Tree tips (see Fig. 5.1), are highlighted with taxon Trophic Guild designations (**A**) for extant anseriform and galliform taxa, derived from [Marchant & Higgins \(1990\)](#), and [Kear \(2005\)](#), and for fossil taxa from [Worthy \(1988\)](#), [Worthy & Holdaway \(2002\)](#), [Murray & Vickers-Rich \(2004\)](#), and references therein). Note: ‘Sub-Family’ factorial designations includes both Family and Sub-Family taxonomic attributes.

## 5.2.7 Analyses

All data analyses and visualisations (Figs. 5.2–5.10, A5.9–A5.11), excluding Figs. A5.12–A5.13 (Microsoft Excel v16), were conducted in R v3.5.2 ([R Core Team 2018](#)) using RStudio v1.1.456 ([RStudio Team 2016](#)). Multivariate 3D Modular Lm data were conditioned (see GPA; General Methods, **2.4.1**), and analysed using Geomorph (see also General Methods, **2.4**). Univariate Modular Distance and Surface Area data, were analysed using both Geomorph and phytools v0.6-60 ([Revell 2012](#)) packages.

**5.2.7.1 Principal Component Analysis**—PCA (see General Methods, **2.4.2**) for all data forms were performed prior to phylogenetic assessments, to assess structural patterns using the full modular response variable (see **5.2.7.4**) suite (see Figs. A5.9–A5.11). Response variables for Modular Distance

and Modular Surface Area data were standardised by  $\log_{10}$  transformation, prior to PCA using the function ‘prcomp’ (R Core Team 2018), and PCA for Modular Lm data were conducted employing the function ‘plotTangentSpace’ as implemented in Geomorph. Subsequent to PGLS assessments (see 5.2.7.4 below), PCAs for Modular Lm data response variables identified as potentially phylogenetically informative were performed (see Figs. 5.6–5.7, A5.14). To facilitate visualisation of the multivariate shape change occurring across each axis, 3D modular shape change plots, derived from PC shape residuals describing the modular shape extremes across respective axes, are given (see 5.2.7.2 below). PC Eigenvalues for respective axes for all PCA plots are given in parenthesis.

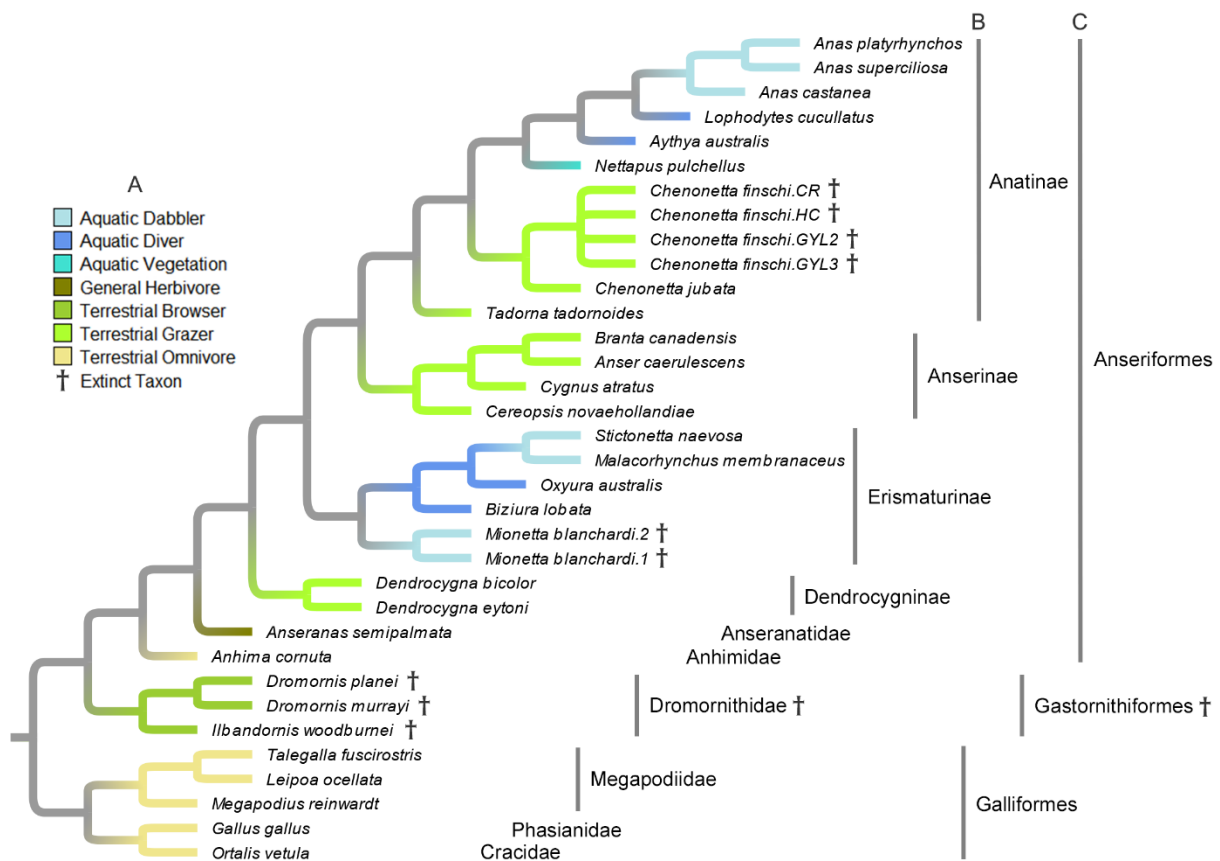


Figure 5.1. Undated phylogenetic tree topology for the Complete data sets (n=34). Root branch is Galloanseres. All tree branches were assigned to a length of one (1), and taxon assigned **A**, Trophic Guild; **B**, Sub-Family/Family; and **C**, Order designations (see 5.2.6.4) were used as factorial variables for phylogenetically informed analyses (see 5.2.7.3-4). Tree tips are highlighted with taxon Trophic Guild preferences, and fossil taxa are indicated by the † symbol (see A Legend). **Abbreviations**, **CR**, Castle Rocks Fissure; **GYL2**, Honeycomb Hill Cave, Graveyard Layer 2; **GYL3**, Honeycomb Hill Cave, Graveyard Layer 3; **HC**, Hodges Creek Cave.

**5.2.7.2 Three dimensional modular shape change plots**—are an effective method to describe 3D shape as captured by multivariate Lm data. For 3D plots associated with modular shape change across particular PCA axes (see 5.2.7.1 above, and Figs. 5.6–5.7, A5.10, A5.14), a mean modular configuration based on all specimens comprising the full data set was calculated, the modular shapes

of which are represented by grey dots with grey links. Mean modular configurations are overlain by modular shapes described by black dots with blue links, depicting modular configurations derived from PCA shape residuals, representative of the modular shape extremes across respective axes. Mean modular configurations (grey), are scaled to the same size across each axis of PCA plots presented. Taken together, these plots describe the extent and direction of modular shape change across each PC axis, with respect to the data set-mean modular configuration.

**5.2.7.3 Phylogenetic signal**—the method described by [Blomberg et al. \(2003\)](#) for the assessment of phylogenetic signal ( $K$ ) in univariate data, is based on the assessment of covariance matrices. Subsequently, a distance-based approach ( $K_{\text{mult}}$ ), structured on the statistical equivalency between covariance and distance matrices (i.e. R vs Q mode; see **5.2.7.4** below), was developed by [Adams \(2014b\)](#), for the assessment of phylogenetic signal under a BM evolutionary model in multivariate shape data. There exists several methods of assessing BM phylogenetic signal (e.g. Abouheif's  $C_{\text{mean}}$ , Moran's  $I$ , Pagel's  $\lambda$ , see [Münkemüller et al. 2012](#) for review). Although Blomberg's  $K$  methods are reasonably robust to polytomies, and lack of branch length information (see **5.2.7.4** above), and perform somewhat reliably at small sample sizes ([Münkemüller et al. 2012](#)); by means of a series of simulations, [Davies et al. \(2012:246\)](#) showed Blomberg's  $K$  estimations are progressively biased by an increasing lack of resolution within a particular tree (i.e., polytomies). However, those authors also showed a tree with a resolution of greater than 60% affected “little bias” in Blomberg's  $K$  estimations. Thus, the methods of Blomberg's  $K$ , as implemented in phytools, was selected to assess for phylogenetic signal in univariate data, and Adams'  $K_{\text{mult}}$  as implemented in Geomorph, was used for assessments across univariate and multivariate data sets, affording comparison of equivalent mathematical approaches across both data forms (see also [Adams & Collyer 2018a:25](#)).

**5.2.7.4 Phylogenetic regression and model fitting**—in simple terms, phylogenetic regression works by “parameterising” a linear model, while taking phylogenetic relationships into account. The linear model includes a response variable, evaluated with respect to one or more predictor variables, and one may specify variable interactions with one or more factorial, or categorical variables ([Adams 2014c](#); [Symonds & Blomberg 2014](#)). Phylogenetic Generalised Least Squares regression methods (covariance- and distance-PGLS; see **5.2.7.4.1-2**), were employed to evaluate patterns of evolutionary allometry in both uni- and multivariate forms of data.

The application of phylogenetic regression methods across uni- and multivariate data can be accommodated mathematically (i.e. R vs Q mode), where the statistical equivalency that exists between covariance (R) and distance (Q) based approaches, allows for the application of several procedures for which results are numerically identical (see [Rohlf 2001](#); [Adams 2014a](#), and references therein). Statistically, phylogenetic regression is an R-mode, parametric analysis, and in the case of multivariate shape data, the functionality of regression methods can be compromised by the “complexity” of the data. In other words, parametric methods require the number of variables within a

data set, to exceed the number of trait dimensions ( $n > p$ ), in order to assess significance. Traditionally, this requisite has been accommodated for by deriving univariate residuals from multivariate data, prior to application of phylogenetically informed assessments (see [Adams 2014c](#)). This “paradox” is also pertinent to the dimensionality of the linear model response variable (see **5.2.7.4.1** below), where the statistical power to detect phylogenetic patterns decreases as the dimensionality of the response variable increases. To deal with these issues, [Adams \(2014c\)](#) developed a Q-mode, or distance-based PGLS method, designed for accommodating high dimensional data under a BM model of evolution, for the identification of evolutionary patterns in multivariate data. Additionally, [Adams \(2014c\)](#) showed that in comparison with traditional covariance-PGLS methods, the multivariate method generated numerically identical statistical estimates when applied to univariate data. Thus, I applied the multivariate distance-PGLS approach as implemented in Geomorph, to both multi- and univariate data sets, employing 999 randomized residual permutation procedure (RRPP) iterations (RRPP; *sensu* [Adams & Collyer 2015](#); [Collyer et al. 2015](#); [Collyer & Adams 2018](#); [Adams & Collyer 2018b](#), and references therein; see **5.2.7.4.1** below).

In order to compare results between distance-PGLS assessments of univariate data (see above), and covariance-PGLS methods, I applied covariance-PGLS to univariate data as implemented in phytools, which is statistically equivalent with PIC “regression through origin” procedures (*sensu* [Felsenstein 1985](#); [Garland et al. 1992](#)), under a BM model of evolution (see also [Rohlf 2001](#); [Revell 2010](#), [Blomberg et al. 2012](#); [Adams 2014c](#); [Uyeda et al. 2018](#)). Factorial models were fitted under a BM evolutionary model, iterated over 999 permutations, and by maximising the restricted maximum likelihood (REML *sensu* [Smyth & Verbyla 1996](#)). I used REML methods for optimisation of PGLS assessments of univariate data, as [Ives et al. \(2007\)](#) showed REML estimates were “consistently” more precise, and “outperformed” those of maximum likelihood (ML), and estimated generalised least squares (EGLS) methods. Linear model fitting analysis of variance (ANOVA; base package ‘stats’; [R Core Team 2018](#)) statistics, were computed for each factorial assessment, yielding AIC values (Akaike Information Criterion–AIC *sensu* [Akaike 1974](#); see below), along with sigma ( $\delta$ ), F and P values.

**5.2.7.4.1 Distance-PGLS model evaluation**—within the distance-PGLS linear model fitting procedure as implemented in Geomorph, model evaluation is achieved by inspection of RRPP statistics. The framework of which allows for “proper null model” evaluation of multiple effects in factorial based models ([Collyer et al. 2015](#)). The expected covariance due to phylogeny, in the form of phylogenetically transformed residuals, are incorporated into the residual error component of a model, allowing for model evaluation accounting for the correlation between model design, and phylogenetic covariance (see [Adams 2014c](#); [Adams & Collyer 2018a, 2018b:1206](#)). Distance based ANOVA statistics were computed, i.e. Sums of Squares (SS) are estimated from full model residual values, which are then used to generate F and  $R^2$  values. z-scores, or “effect sizes”, are estimated as the standard deviation of F values in RRPP distributions, and P values, describing the probability of

finding a larger F value than observed by chance, are calculated (Adams 2014c; Adams & Collyer 2018b:1211; see also Adams & Collyer 2015; Collyer et al. 2015). Model ‘goodness of fit’ was assessed by inspection of F values, in comparison with effect size values (z-scores), with respect to  $R^2$  values of response variable regression scores (a univariate summary computed from multivariate regression coefficients, i.e., ‘shape score’ *sensu* Drake and Klingenberg 2008:72; see also Adams et al. 2013; Sherratt et al. 2019), versus predictor variables for each factorial model.

**5.2.7.4.2 Covariate-PGLS model evaluation**—with regard to univariate linear model specification and assessment, Zuur et al. (2009) advocates a process of model assessment based on hypothesis testing. In essence, after factorial model fitting, one derives ANOVA statistics from resultant regression results (see 5.2.7.4 above), and uses one of several metrics (e.g. AIC), as a measure, where the “lowest” AIC value affords an indication of which model best fits the data (see Faraway 2005:21; O’Meara et al. 2006:926; Zuur et al. 2009:61, see also Adams & Collyer 2018a:18).

**5.2.7.4.3 PGLS model development**—the benefit of distance-PGLS approaches over those of covariate-PGLS procedures, is that analytical designs incorporating ANOVA can be accommodated, as can the assessment of more complex factorial models (Pennell & Harmon 2013; Adams 2014c). This aspect became apparent after initial model fitting and assessment was conducted, using the multivariate Modular Lm data sets, and a particularly descriptive ‘multiplicative’ model (e.g.  $Y \sim Z * X$ ; where Y = response variable, Z = size variable, i.e., centroid size/endocast volume, and X = factorial variable), was developed and tested (data not shown).

While the application of this particular model to univariate data sets was possible using the function ‘procDppls’, as implemented in Geomorph (see below), when I attempted to fit the model to univariate data employing the function ‘ppls.SEy’, as implemented in phytools, I discovered the ‘multiplicative’ operator (i.e. ‘\*’) model syntax, was not supported by the ‘gls’ function (package ‘nlme’; R Core Team 2018), which underlies phytools linear model construction. (Note: \* is supported as a mathematical operator within a linear model framework, but not as a specific linear model operator). Consequently, several iterations of various ‘additive’ model structures were evaluated using phytools. Comprising model syntax (e.g.  $Y \sim Z + Z : X$ ), that is supported by the ‘gls’ functional framework, in attempts to replicate the three way factorial variable (X) interaction afforded by the multiplicative (\*) operator, when applied in the linear model developed in Geomorph. So that a valid comparison between the two PGLS methods, could be compared across univariate data sets. Unfortunately, the multiplicative model that, along with RRPP evaluation of regression residuals as implemented in Geomorph, proved instrumental in identifying the optimal ‘best fit’ factorial interactions for both multivariate and univariate data (see below), was not able to be replicated across univariate data sets employing the phytools package. Additionally, in a process of reverse testing, I applied the best fit ‘additive’ model developed in phytools (i.e.  $Y \sim Z + Z : X$ ) in Geomorph. However, this approach did not afford equivalent model fitting as was achieved by the multiplicative model (data not shown).

Consequently, the ‘multiplicative’ distance-PGLS model (i.e.  $Y \sim Z^*X$ ) as implemented in Geomorph, was applied to multivariate Modular Lm data (see Tables A5.1C–D), and univariate Modular Distance (see Tables A5.4C–D), and Modular Surface Area (see Tables A5.9C–D) data forms. Additionally, the ‘additive’ covariance-PGLS model (i.e.  $Y \sim Z+Z:X$ ), as implemented in phytools, was applied to the univariate Modular Distance (see Tables A5.5C–D), and Modular Surface Area (see Tables A5.8C–D) data forms. Although these two model forms are not directly comparable (see above), they represent the ‘best fit’ achieved between the two approaches of factorial model fitting using identical data, employing both distance-PGLS and covariance-PGLS methods.

In the following, I used multivariate Modular Lm data (**5.2.6.1**), univariate Modular Distance data (**5.2.6.2**), and univariate Modular Surface Area data (**5.2.6.3**) derived from 34 endocast reconstructions, representing 30 species of galloanseres (**5.2.4**; see also Figs. A5.1–A5.8). I performed PCA (see **5.2.7.1**) using the full modular suite for each data form, to visualise patterns of variation in morphospace (see **5.3.1**).

To test for whether variation in endocast shape retained a phylogenetic component, or was driven by adaptive features, I assessed endocranial variation described by each data form for phylogenetic signal, using both distance- and covariance-based methods under a BM evolutionary model (see **5.3.2**).

I employed distance- and covariance-based factorial model PGLS regression methods, to statistically assess for patterns of evolutionary allometry, and identify modular regions of the endocast which may prove systematically informative. In both multi- and univariate forms of data assessed here, response variables within each data set (i.e., nine total variables in multivariate Modular Lm and univariate Modular Surface Area data, and 15 in univariate Modular Distance data), were assessed by PGLS methods with respect to only one predictor variable, represented by either centroid size, endocast surface area, or endocast volume respectively. Each interaction was assessed with respect to three categorical factors (i.e. Trophic Guild, Order, and Sub-Family; see Fig 5.1). Model fitting assessment was dictated by which model form was employed (i.e., distance- or covariance-based PGLS), and model ‘best fit’ was assessed through inspection of the relevant statistics associated with either PGLS form (see **5.2.7.4.1-2**).

### 5.3 RESULTS

In these assessments, I employed multi- and univariate data forms (see **5.2.7**), derived from 34 endocast reconstructions including nine fossil taxa, representing 30 species of galloanseres. (see **5.2.4**; see also Figs. A5.1–A5.8).

### 5.3.1 Principal component analyses

PCAs were conducted on the full suite of response variables for all data forms, to initially investigate the patterns of shape variation described by multi- and univariate data in morphospace.

**5.3.1.1 Modular Lm Data**—the PCA plot (Fig. A5.9) for these data (see 5.2.7.1) shows that the combined Modular Lm suite reflect the distinction between galliforms, gastornithiforms, and anseriforms quite well at Order level (see Fig. 5.1C). However, the resolution within anseriform taxa is not well defined. For example, the anserines *Branta canadensis*, *Cygnus atratus*, and *Anser caerulescens* are clustered within anatines, and the distinction between the anseriform *Anhima cornuta* and galliforms is poor, where *A. cornuta* is more closely associated with galliforms in morphospace. The PCA plot of dorsal endocast modules (i.e., eminentia sagittalis, caudal telencephalon, and cerebellum; Fig. A5.10), shows similar patterns of taxon distribution to that shown by the PCA plot of all endocast Lm modules (Fig. A5.9). This implies that the distinctive differences in dorsal endocast morphology between these clades, as captured by these dorsal Lm modules, are driving the patterns of taxon distribution in PCA morphospace for multivariate shape data.

**5.3.1.2 Modular Distance data**—the PCA plot (Fig. A5.11) for these data (see 5.2.7.2), show that the full complement of  $\log_{10}$  transformed Modular distance metrics, when assessed together, reflect the distinction between galliforms, gastornithiforms, and anseriforms quite well, and show differentiation between anserine, anatine, and erismaturine anseriform taxa in morphospace. Notably, these data identify the anhimid within anseriforms, as previously hypothesised. They show the erismaturine *Biziura lobata* more closely associated with anserines, and *Malacorhynchus membranaceus* associated with *Mionetta blanchardi*. These patterns are like those seen in the PCA plot of Modular Surface Area data (see Fig. A5.12 and below), and in regression results for Sub-family factorial assessments of Modular Lm data (see 5.3.3.1 below; Figs. 5.4, 5.5). Results show univariate Modular Distance data, when all modules are combined, reflect a sensible distribution of taxa within PCA morphospace.

**5.3.1.3 Modular Surface Area data**—the PCA plot (Fig. A5.12) for these combined data (see 5.2.7.3), reflects the distinction between galliforms, gastornithiforms, and anseriforms well, and distribution patterns are like those seen for univariate Modular Distance data above. The PCA plot shows the distinction of anserine, anatine, and erismaturine anseriforms, and that the anhimid *A. cornuta*, and *B. lobata* are more closely associated with anserines. However, the somewhat close association of *M. membranaceus* with *M. blanchardi* was not as well defined, as was seen in the PCA plot for Modular Distance data (Fig. A5.11).

In summary, the PCA plot for the full suite of multivariate Modular Lm data, showed the least resolution for phylogenetic relationships between assessed taxa. The much disparate dorsal endocranial morphology across galloanseres, are likely driving distributions within PCA morphospace for these data. However, PCA plots of Modular Distance and Modular Surface Area data sets, reflected taxonomic distinctions between taxa well, and Modular Distance data performed somewhat

better in this regard. Notably, for both univariate data sets, *Chenonetta jubata*, *Cereopsis novaehollandiae*, *Nettapus pulchellus*, and *M. membranaceus* are found distinct from anserines and anatines, and *M. membranaceus* is more closely associated with Oligo-Miocene *M. blanchardi*.

### 5.3.2 Phylogenetic signal

Having established that taxa exhibited morphospace associations suggestive of phylogenetic relatedness, I examined this with explicit tests for phylogenetic signal in modular subsets.

Results are presented for phylogenetic signal using both Geomorph (Adam's  $K_{\text{mult}}$ ) and phytools (Blomberg's  $K$ ) methods, where Brownian motion (BM) phylogenetic signal was identified in the same module across both Complete and Dromornithids-excluded data sets, for each data form.

Note: the expected value of Blomberg's  $K$ /Adams'  $K_{\text{mult}}$  under a BM model of evolution is one (1). Therefore, variation of the Blomberg's  $K$ /Adams'  $K_{\text{mult}}$  measure, i.e.  $K > 1$ , or  $K < 1$ , provides an indication of excess or deficiency respectively, of BM "statistical dependence" across the tree topology (i.e. Fig. 5.1). Thus, a Blomberg's  $K$ /Adams'  $K_{\text{mult}}$  value closer to one (1) indicates species 'related' by the phylogenetic tree, are more similar than species drawn randomly from the tree (see [Revell et al. 2008](#); [Münkemüller et al. 2012](#)). Full results for all modules (see General Methods, Fig. 2.1) across all data forms are presented in Appendices Tables cited below.

**5.3.2.1 Modular Lm data**—assessments using Adams'  $K_{\text{mult}}$  (see Fig. 5.2A, Tables A5.1A–B), for both Complete and Dromornithids-excluded data sets, revealed that BM phylogenetic signal occurred predominately in ventral endocast modules.  $K_{\text{mult}}$  results in the following are presented for the Complete, and Dromornithids-excluded data sets respectively: mesencephalon (0.616; 0.582), trigeminal ganglion (0.482; 0.476), mesencephalon + trigeminal ganglion (0.554; 0.534), rhombencephalon (0.893; 1.059). These results show irrespective of whether Modular Lm data included dromornithids or not, phylogenetic signal was identified exclusively in the same ventral endocast Lm modules across both data sets.  $K_{\text{mult}}$  values for the Complete data set were all higher than those for the Dromornithids-excluded data set, except results for the rhombencephalon module. In fact, although the value for the rhombencephalon module in the Complete data set slightly exceeded BM, as did results for Complete Lm data caudal telencephalon module (1.047), the  $K_{\text{mult}}$  value for the caudal telencephalon module for the Dromornithids-excluded data set was substantially higher (1.163). These results suggest the inclusion of data for dromornithid taxa, somewhat improved the phylogenetic signal resolution within Modular Lm data.

**5.3.2.2 Modular Distance data**—assessments using Geomorph (Adams'  $K_{\text{mult}}$ ; see Fig. 5.2B, Tables A5.4A–B, A5.5A–B), and phytools (Blomberg's  $K$ ; see Tables A5.5A–B), reveal BM phylogenetic signal in both dorsal and ventral Distance modules. Notably, BM phylogenetic signal values recovered for both Adams'  $K_{\text{mult}}$  and Blomberg's  $K$  were identical across all Modular Distance metrics assessed (see Tables A5.4A–B, A5.5A–B). Results in the following are presented for the

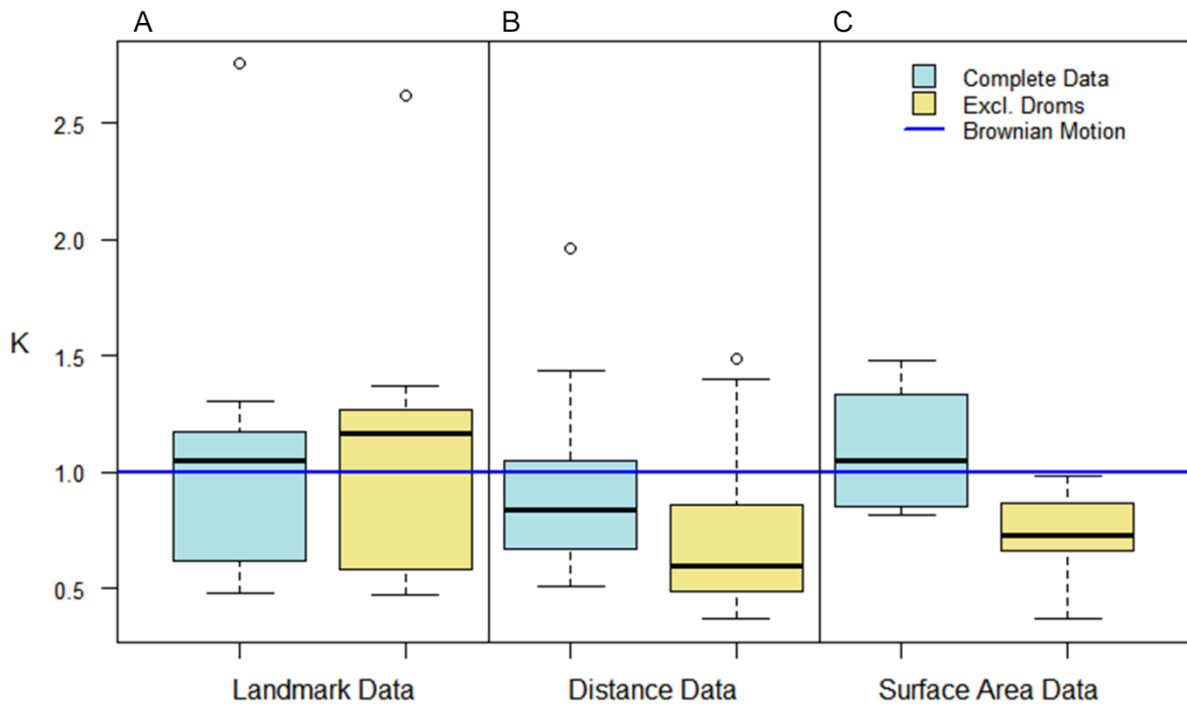


Figure 5.2. Quantile boxplots summarising phylogenetic signal ( $K_{\text{mult}}$ ) results for each data set assessed. Phylogenetic signal was assessed under Brownian motion assumptions using the Geomorph function ‘physignal’ (Adams’  $K_{\text{mult}}$  *sensu* Adams 2014b), employing the appropriate phylogenetic topologies (e.g. Fig. 5.1). **A**, Modular Lm data (see Table A5.1); **B**, Modular Distance data (see Table A5.5); **C**, Modular Surface Area data (see Table A5.8). Upper and lower bounds of each boxplot represent the upper and lower quartiles respectively, the black horizontal line represents the median, and whiskers represent standard deviation at 1.5 IQR. Pure Brownian motion evolution (i.e. 1.0) is described by the blue horizontal line. Note: phylogenetic signal ( $K$ ) results for Complete and Dromornithids-excluded univariate Modular Distance (**B**; see Table A5.5) and Modular Surface Area data sets (**C**; see Table A5.8) are identical, irrespective of the assessment function employed, so only Geomorph function ‘physignal’ results are plotted. **Abbreviations**, **Excl.**, excluding; **Droms**, dromornithids; **IQR**, inter-quartile range (25–75%); **Lm**, landmark.

Complete, and Dromornithids-excluded data sets respectively: BM phylogenetic signal was identified in eminentia sagittalis length (0.838; 0.505), eminentia sagittalis width (0.785; 0.674), telencephalon total length (0.870; 0.595), mesencephalon length (0.599; 0.480), mesencephalon width (0.509; 0.367), trigeminal ganglion length (0.592; 0.603), trigeminal ganglion width (0.902; 0.408), cerebellum width (0.709; 0.549), rhombencephalon length (0.781; 0.495), and rhombencephalon width (0.625; 0.381). These results show that Modular Distance data captures BM phylogenetic signal in the ventral zones of the endocast (mesencephalon, trigeminal ganglion, rhombencephalon), in agreement with the Modular Lm data results (see above). However, Modular Distance data results include two modules on the dorsal endocast surface (eminentia sagittalis and cerebellum), that showed BM phylogenetic signal not identified in Modular Lm data. Furthermore, it is notable that in all Distance modules, with the exception of trigeminal ganglion length, in which it differed only marginally (i.e., by around one tenth), BM phylogenetic signal was stronger in the Complete Modular Distance data set. Therefore, as in Modular Lm data results (see above), the inclusion of dromornithid taxa improved the BM phylogenetic signal resolution within Modular Distance data.

**5.3.2.3 Modular Surface Area data**—assessments using Geomorph (Adams'  $K_{mult}$ ; see Fig. 5.2C, Tables A5.8A–B, A5.9A–B), and phytools (Blomberg's  $K$ ; see Tables A5.8A–B), identify BM phylogenetic signal in both dorsal and ventral Surface Area modules. As with univariate assessments of Modular Distance data (see **5.3.2.2** above), BM phylogenetic signal values recovered for both Adams'  $K_{mult}$  and Blomberg's  $K$  were identical across all Modular Surface Area metrics assessed (see Tables A5.8 A–B, A5.9 A–B). Results in the following are presented for the Complete and Dromornithids-excluded data sets respectively: BM phylogenetic signal was identified in the rostral telencephalon (0.817; 0.987), trigeminal ganglion face (0.849; 0.662), and the rhombencephalon (0.814; 0.553) modules across both data sets. However, in the Modular Surface Area Dromornithids-excluded data set, BM phylogenetic signal was recovered for all nine modules. Considering the results for the Modular Lm data (see **5.3.2.1** above) and Modular Distance data (see **5.3.2.2** above), the identification of BM phylogenetic signal in the entire Modular Surface Area Dromornithids-excluded data set, may be not representative for the data form. The patterns in the results for Modular Lm data and Modular Distance data above, suggest that data sets inclusive of dromornithid taxa, likely improve the phylogenetic resolution within those data. Accordingly, with respect to Modular Surface Area data, it is more likely that the data set inclusive of dromornithid taxa, provides a more reasonable indication for BM phylogenetic signal inherent in those data. If this is indeed the case, BM phylogenetic signal is identified in two ventral modules, and one rostradorsal module in Modular Surface Area data. Notably, the rostral telencephalon module shows a greater BM phylogenetic signal in the Dromornithids-excluded data set. However, in the two ventral modules, the BM phylogenetic signal values for the Dromornithids-excluded data set are less than those of the Complete data set.

Results reported above for univariate Modular Distance data, and Modular Surface area data forms, where values for  $K_{mult}$  and Blomberg's  $K$  were identical, agree with the results of [Adams \(2014b:686\)](#), who recovered similarly identical estimates of BM phylogenetic signal for univariate data using  $K_{mult}$  and Blomberg's  $K$  functions in his assessments.

### 5.3.3 PGLS factorial model fitting results

**5.3.3.1 Modular Lm data**—results for 'multiplicative' distance-PGLS model fitting, as implemented in Geomorph (see **5.2.7.4** above), are summarised in Figs. 5.3A–H, and presented in Tables A5.1C–D. For the sake of brevity in the following and below, only the full interaction between each of nine modular shapes, as defined by subsets of the Modular Lm suite for each data set (i.e. response variable:  $Y$ ), are listed with the effect of the predictor variable (i.e., modular centroid size:  $Z$ ), with respect to the interaction between one of three factorial variables (i.e. Trophic Guild, Order, and Sub-Family; see Fig. 5.1 and above).

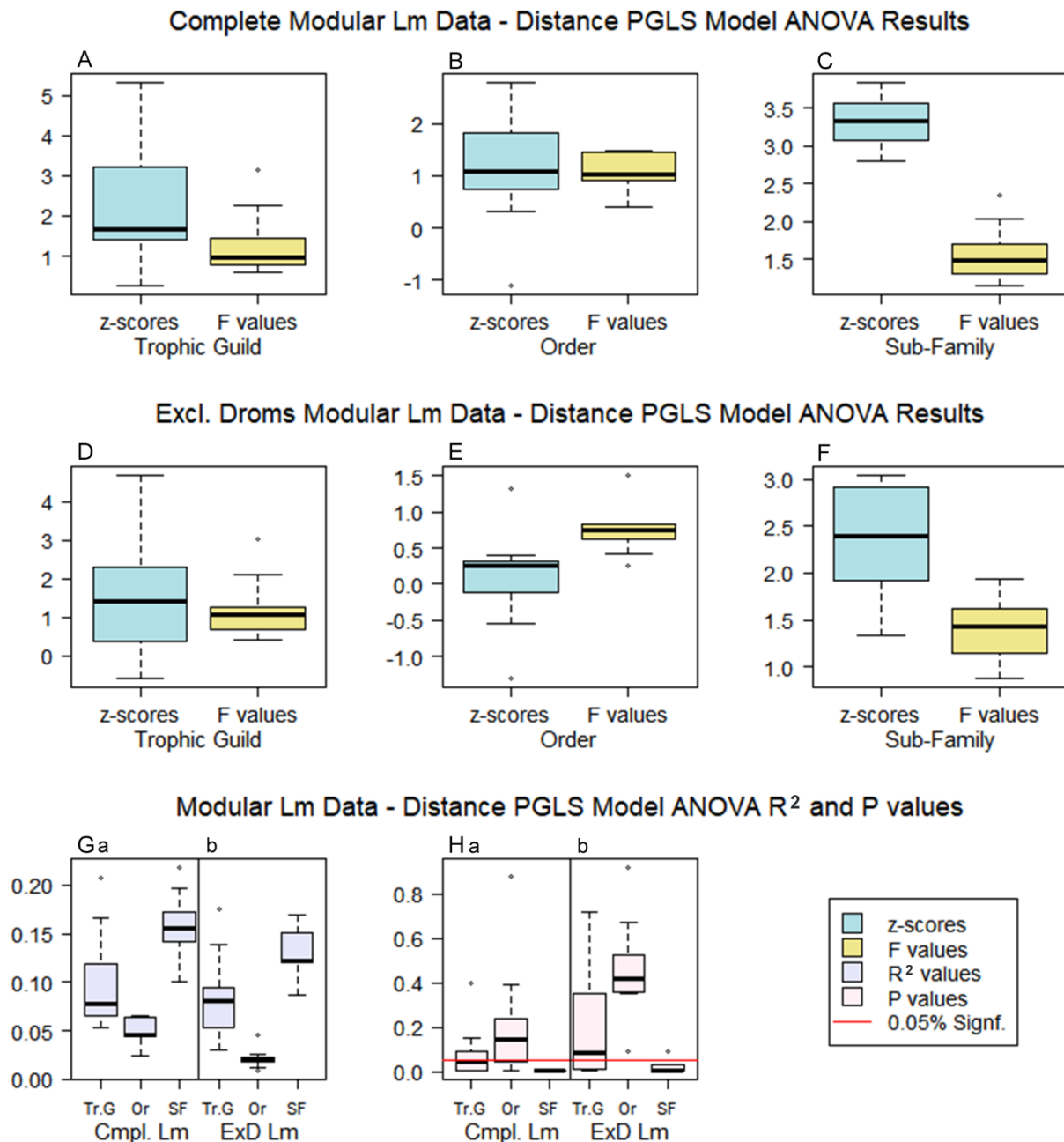


Figure 5.3. Quantile boxplots summarising Procrustes distance-PGLS model fitting results: **A–F**, z-scores (“effect size” *sensu* Collyer et al. 2015; see 5.2.7.4.1) and F values; **Ga–Gb**, R<sup>2</sup> values; and **Ha–Hb**, P values for the Complete (n=34), and Dromornithids-excluded (n=31) Modular Lm data sets respectively (see Tables A5.1C–D). Upper and lower bounds of each boxplot represent the upper and lower quartiles respectively, the black horizontal line represents the median, and whiskers represent standard deviation at 1.5 IQR. Phylogenetic trees, along with one of three factorial models: Trophic Guild, Order, or Sub-Family (see Fig. 5.1; 5.2.6.4) were fitted to each data set respectively, using the function ‘procDppls’ employing 999 RRPP permutations as implemented in Geomorph (see 5.2.7.4), and Procrustes distance ANOVA assessments of model fitting were computed. Below the horizontal red line (**H**) represents the 5% significance level. **Abbreviations**, ANOVA, analysis of variance; **Cmpl.**, Complete; **Conf.**, confidence; **Droms**, dromornithids; **Excl.**, excluding; **ExD**, Dromornithids-excluded; **IQR**, inter-quartile range (25–75%); **Lm**, landmark; **Or**, Order; **PGLS**, phylogenetic generalised least squares; **R<sup>2</sup>**, R squared; **RRPP**, randomized residual permutation procedure; **SF**, Sub-Family/Family; **Tr.G**, Trophic Guild.

### 5.3.3.1.1 Complete Modular Lm data

**5.3.3.1.1.1 Trophic guild**—factorial assessment results align reasonably well with those of modular BM phylogenetic signal identified (see above, Table A5.1A), where all modules that display BM phylogenetic signal, showed significant fitting statistics with the factorial model (mesencephalon,  $F=3.150$ ,  $P=0.001$ ; trigeminal ganglion,  $F=1.431$ ,  $P=0.002$ ; mesencephalon + trigeminal ganglion,  $F=2.256$ ,  $P=0.001$ ; rhombencephalon,  $F=0.976$ ,  $P=0.045$ ; Tables A5.1A, A5.1C). However, four of nine response variables showed non-significant factorial model fitting results (Table A5.1C, Fig. 5.3Ha). As shown in Fig. 5.3A, z-score (effect size) results for model fitting overlap with F values, and the medians between the two data are not particularly distinct.  $R^2$  values (Fig. 5.3Ga) show the widest distribution for all factorial models assessed across the Complete Modular Lm data set, and suggest the overall model fit is not most optimal.

**5.3.3.1.1.2 Order**—factorial assessment results show higher levels of model fitting non-significance for modular shape subsets, as compared with results for Trophic guild assessments (i.e., six vs four non-significant results; see Table A5.1C, Fig. 5.3Ha; and above). Additionally, mesencephalon and rhombencephalon Lm modules, within which BM phylogenetic signal was identified (Table A5.1A), showed non-significant model fitting results (0.071, 0.393, respectively; Table A5.1C). In contrast, model fitting results for trigeminal ganglion ( $F=1.423$ ,  $P=0.042$ ) and mesencephalon + trigeminal ganglion ( $F=1.458$ ,  $P=0.046$ ) response variables were significant (Table A5.1C), however, both results approached non-significant correlation with the factorial model. The summary boxplot (Fig. 5.3B) shows z-scores and F values overlap, and medians between the data are similar, suggesting overall Order factorial model fitting is less optimal than that of Trophic Guild, and  $R^2$  median results are the lowest for all models assessed (see Fig. 5.3Ga).

**5.3.3.1.1.3 Sub-Family**—factorial assessment results show no non-significant model fitting P values (see Table A5.1C, Fig. 5.3Ha), suggesting that Sub-Family explained the allometric shape variation in the Modular Lm response variable subsets reasonably well. Significant model fitting statistics were returned for all four response variables, within which BM phylogenetic signal was recognised (mesencephalon,  $F=2.354$ ,  $P=0.001$ ; trigeminal ganglion,  $F=1.694$ ,  $P=0.001$ ; mesencephalon + trigeminal ganglion,  $F=2.035$ ,  $P=0.001$ ; rhombencephalon,  $F=1.600$ ,  $P=0.045$ ; Tables A5.1A, A5.1C), although the rhombencephalon module approached non-significance. The summary boxplot (Fig. 5.3C), shows that z-scores and F values are distinct, data ranges do not overlap, and medians between the two data are widely separated.  $R^2$  values for Sub-Family factorial model fitting, for response variable modular subsets showing BM phylogenetic signal, and significant P values (see Table A5.1C, Fig. 5.3Ga), were all greater than those of Trophic Guild and Order  $R^2$  results: e.g., mesencephalon (0.218 vs 0.207 and 0.066, respectively); trigeminal ganglion (0.172 vs 0.119 and 0.064, respectively); mesencephalon + trigeminal ganglion (0.197 vs 0.167 and 0.065, respectively); and rhombencephalon (0.160 vs 0.088 and 0.042, respectively). Summary  $R^2$  boxplots (Fig. 5.3Ga), show that Sub-Family affords the highest overall range of  $R^2$  values, and although

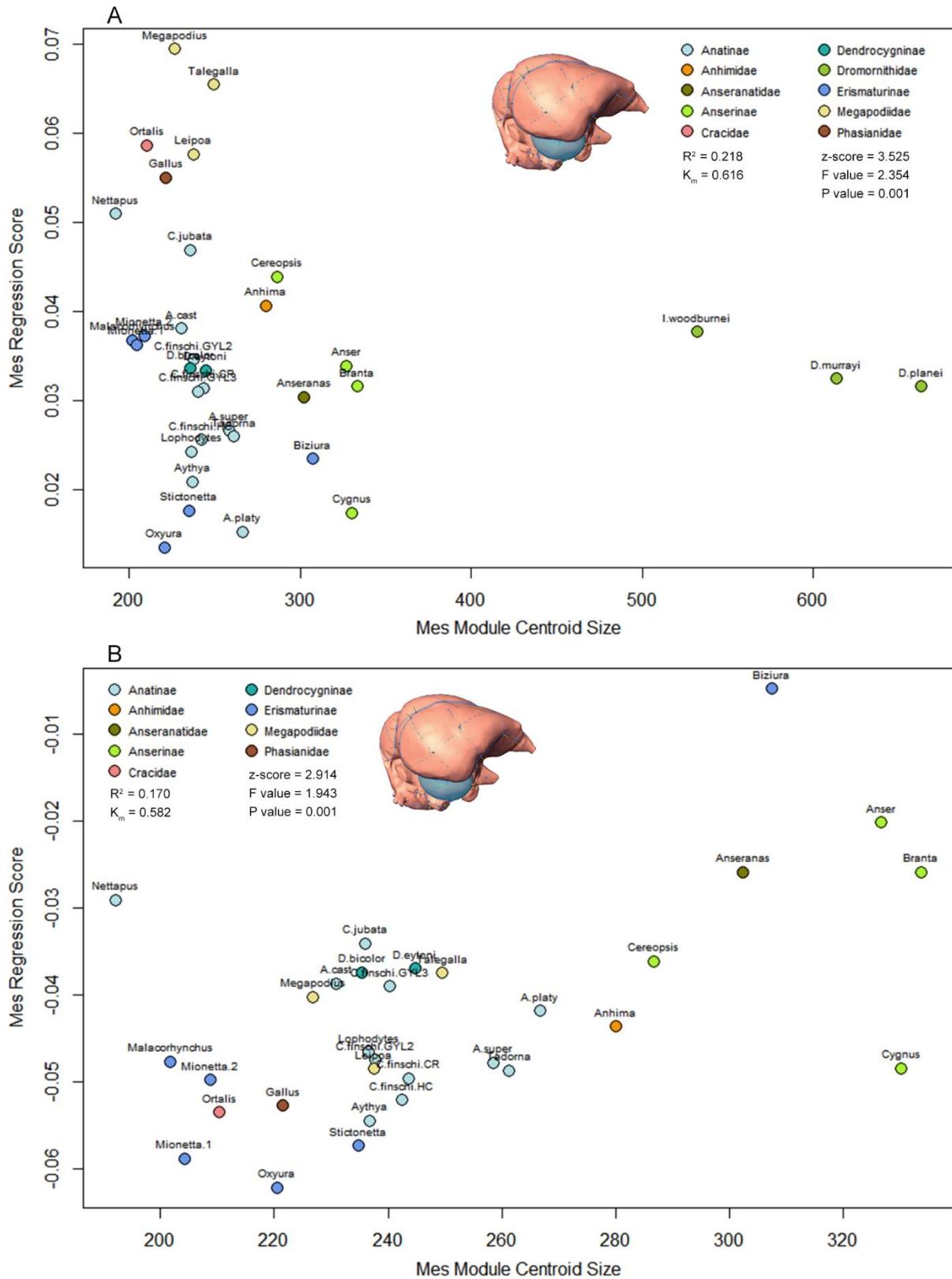


Figure 5.4. Modular Lm data sets. Mesencephalon distance PGLS Sub-Family factorial model regression plots (see Fig. 5.1), representing the allometric relationship between mesencephalon shape and size. **A**, Complete Modular Lm data. **B**, Modular Lm data Dromornithids-excluded. **Insets**, *Aythya australis* (SAM B33108) RHS lateral view, showing mesencephalon Lm modules (blue; see General Methods, Fig. 2.1). For taxon abbreviations see Tables A5.6, A5.7. **Abbreviations**,  $K_m$ , Adams'  $K_{mult}$ ; **Lm**, landmark; **Mes**, mesencephalon; **PGLS**, phylogenetic generalised least squares; **RHS**, right hand side;  $R^2$ , R squared.

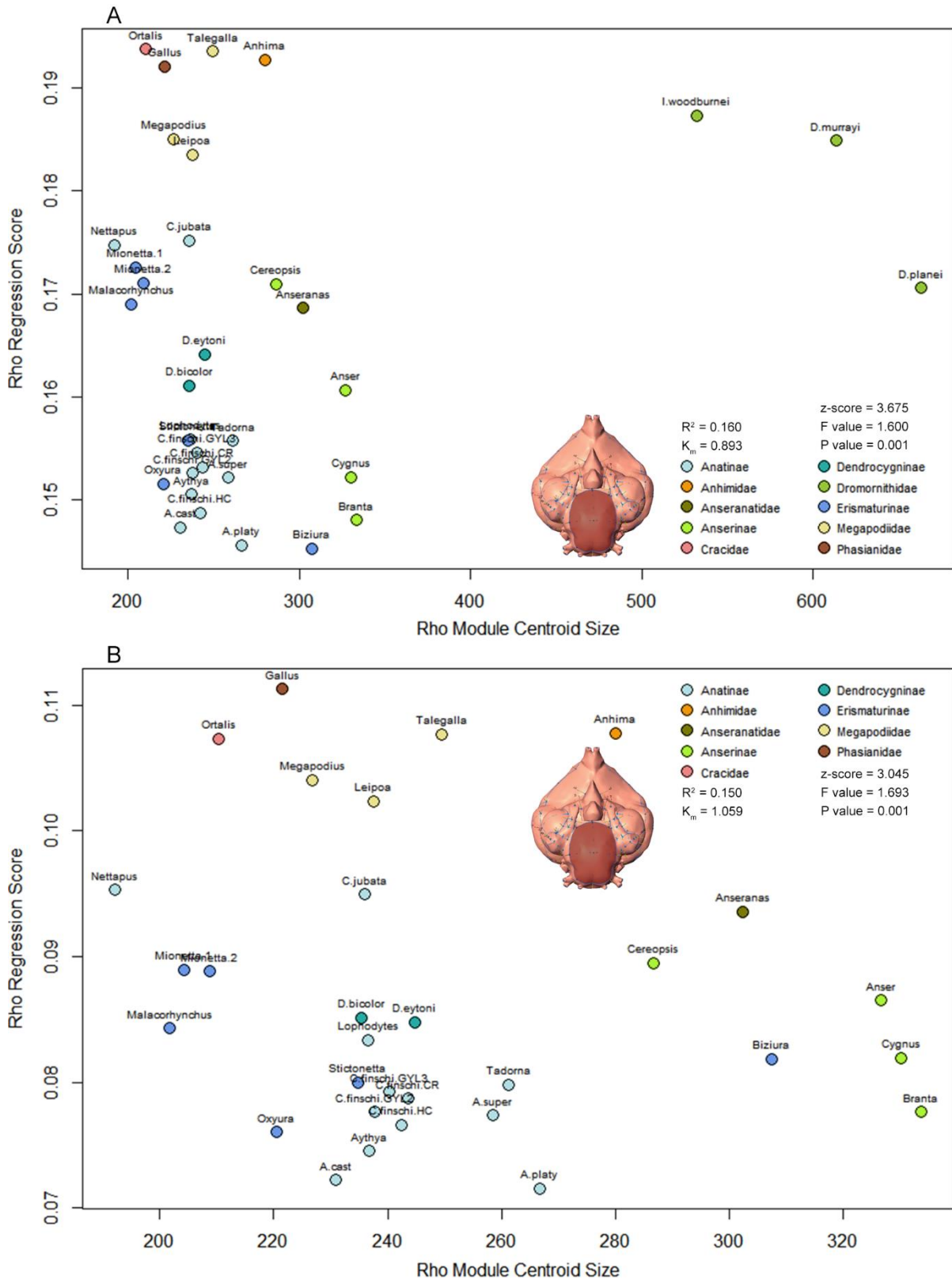


Figure 5.5. Modular Lm data sets. Rhombencephalon distance PGLS Sub-Family factorial model regression plots (see Fig. 5.1), representing the allometric relationship between rhombencephalon shape and size. **A**, Complete Modular Lm data. **B**, Modular Lm data Dromornithids-excluded. **Insets**, *Aythya australis* (SAM B33108) ventral view, showing rhombencephalon Lm module (brown; see General Methods, Fig. 2.1). For taxon abbreviations see Tables A5.6, A5.7. **Abbreviations**,  $K_m$ , Adams'  $K_{mult}$ ; **Lm**, landmark; **Rho**, rhombencephalon; **PGLS**, phylogenetic generalised least squares;  $R^2$ , R squared.

results for Trophic Guild and Sub-Family overlap somewhat, the  $R^2$  median for Sub-Family is markedly higher, than those of Trophic Guild and Order factorial models.

In summary, results show Sub-Family affords the ‘best fit’ to the Complete Modular Lm data set, followed by Trophic Guild. Of all assessments Order performed least well across these data.

### 5.3.3.1.2 Modular Lm data Dromornithids-excluded

**5.3.3.1.2.1 Trophic guild**–factorial assessment results for these data, align well with those of Trophic Guild factorial assessments of the Complete Modular Lm data set (see **5.3.3.1.1.1**, Table A5.1B), where modules identified as displaying BM phylogenetic signal, showed significant factorial model fitting statistics (mesencephalon,  $F=3.018$ ,  $P=0.001$ ; trigeminal ganglion,  $F=1.259$ ,  $P=0.009$ ; mesencephalon + trigeminal ganglion,  $F=2.113$ ,  $P=0.001$ ; Tables A5.1B, A5.1D), with the exception of the rhombencephalon Lm module, which returned a non-significant result ( $F=1.053$ ,  $P=0.082$ ; Table A5.1D). The summary boxplot (Fig. 5.3D) show z-scores overlap F values, and the medians

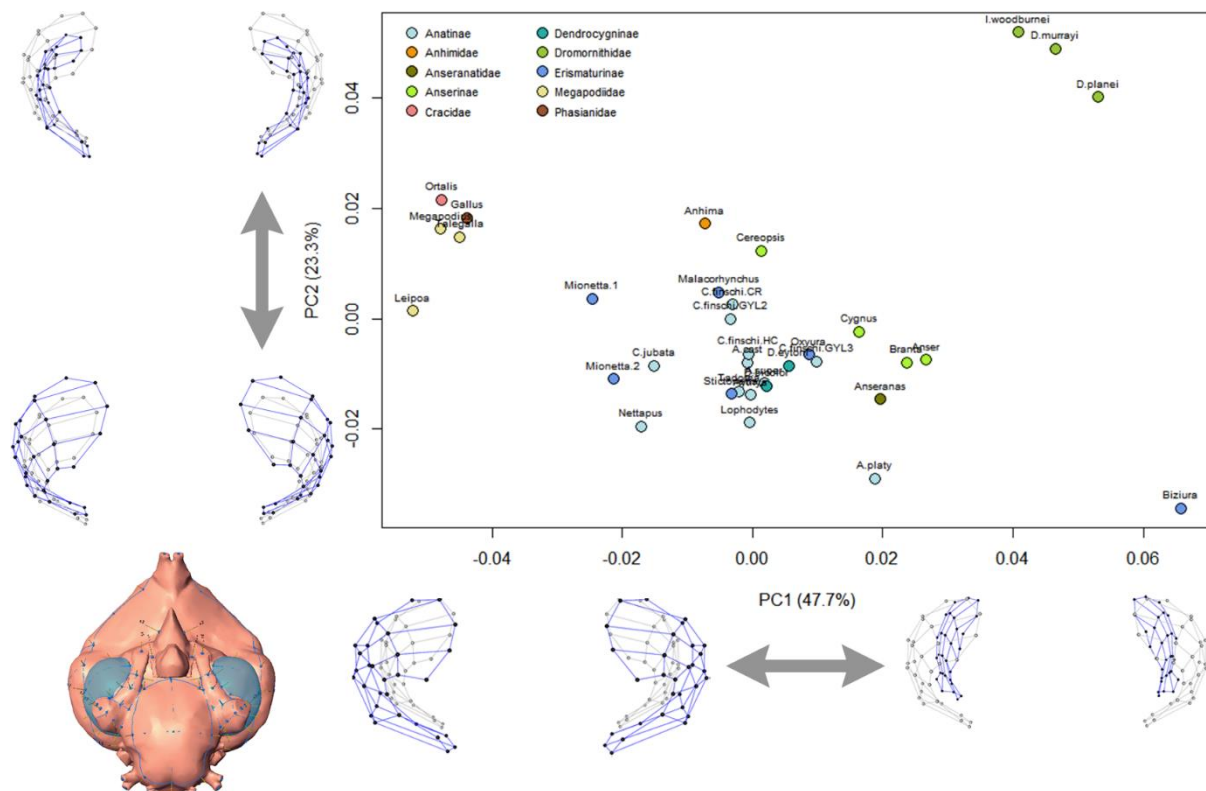


Figure 5.6. Complete Modular Lm data. PCA plot of mesencephalon Lm modules. Taxa are assigned Sub-Family factorial model colour coding (see Fig. 5.1A, Legend). **Inset.** *Aythya australis* (SAM B33108) endocast in ventral view, showing mesencephalon (blue; see General Methods, Fig. 2.1) Lm modules depicted by modular shape change plots presented across each PC axis. Modular shape change plots described by grey dots with grey links represent a mean modular configuration based on all specimens ( $n=34$ ). Mean modular configurations are overlain by modular shapes described by black dots with blue links, representing the modular shape extremes across respective PC axes. Mean modular configurations (grey) are scaled to the same size across both PC axes (see **5.2.7.2**). For taxon abbreviations see Tables A5.6, A5.7. **Abbreviations, Lm**, landmark; **PC**, Principal Component; **PCA**, Principal Component Analysis; **SAM**, South Australian Museum.

between the two data are not distinct. Data medians are less distinct than results for Complete Lm data (see Fig. 5.3A, and above), and the range of P values across the Modular Lm Dromornithids-excluded data set, was much greater than across the Complete Modular Lm data set (Fig. 5.3Hb). These results suggest the overall model fit is not particularly optimal. However,  $R^2$  summary results (Fig. 5.3Gb) for the Trophic Guild factorial model, show that the model performed somewhat better across the Dromornithids-excluded data set, as the  $R^2$  median for these data was higher than that of the Complete data set, albeit the range of  $R^2$  values was lower across these data in general.

These results imply Trophic Guild afforded a somewhat better fit across the Modular Lm Dromornithids-excluded data set overall, but Trophic Guild was less optimal in explaining the modular shape variation within the Dromornithids-excluded data set, where the P value range was larger than across all factorial models assessed (Fig. 5.3Hb).

**5.3.3.1.2.2 Order**—factorial assessment results show model fitting non-significance for all modular shape subsets, were markedly distinct from the results for Trophic Guild assessments reported (i.e., nine vs five non-significant results; see Table A5.1D, and above). The summary boxplot (see Fig. 5.3E), shows z-scores and F values overlap, and although medians between the two data are less similar than those reported for Trophic Guild assessments above, the ranges of both data lie beyond the inter-quartile range described by boxplot whiskers (i.e. 25–75%; see Fig. 5.3E). This suggests Order fit these data less well than Sub-Family (see above). Similar to the trends reported for Sub-Family assessments (see above),  $R^2$  median results for data inclusive of dromornithids (Fig. 5.3Ga), provided better factorial model fitting with respect to Order assessments, than Modular Lm Dromornithids-excluded data (Fig. 5.3Gb). These results for the assessment of Modular Lm Dromornithids-excluded data sets show Order provided the least optimal fit with these data, than any other factorial model assessed.

**5.3.3.1.2.3 Sub-Family**—factorial assessment results show only one Modular Lm subset (caudal telencephalon) non-significant model fitting P value result ( $F=0.869$ ,  $P=0.087$ ; Table A5.1D, Fig. 5.3Hb), suggesting that, with the exception of this module, Sub-Family explained the shape variation within the Modular Lm Dromornithids-excluded data set reasonably well. The summary boxplot (see Fig. 5.3F) shows that z-scores and F value medians are distinct, but data ranges overlap somewhat at the outer bounds of the inter-quartile range. Notably, medians between the two Sub-Family assessments, are more distinct than those of all other factorial assessments (see Figs. 5.3D–F, and above).  $R^2$  values for Sub-Family model fitting for response (Y) variables showing BM phylogenetic signal, and significant P values (see Table A5.1D), were greater than those of Trophic Guild and Order  $R^2$  results, i.e., trigeminal ganglion (0.120 vs 0.094 and 0.022, respectively); mesencephalon + trigeminal ganglion (0.147 vs 0.138 and 0.021, respectively); and rhombencephalon (0.150 vs 0.081 and 0.022, respectively). With the exception of  $R^2$  results for the mesencephalon module, which was somewhat better for Trophic Guild (0.170 vs 0.175 and 0.019, respectively). The  $R^2$  summary boxplot (Fig. 5.3Gb) for Sub-Family factorial model assessments, show that for the



BM phylogenetic signal was identified (see above). Results show that Trophic Guild afforded less optimal fitting, and Order showed the least resolution for all models assessed across all Modular Lm data. Plots visualising distance-PGLS Sub-Family model fitting for Complete Modular Lm and Modular Lm Dromornithids-excluded data sets respectively, are presented in the form of response variable regression scores vs predictor variable centroid size for: mesencephalon Lm modules (Figs. 5.4A–B), mesencephalon + trigeminal ganglion Lm modules (Figs. A5.13A–B), and rhombencephalon Lm modules (Figs. 5.5A–B). Using Complete Lm data, PCA plots for the mesencephalon modules (Fig. 5.6), mesencephalon and rhombencephalon modules (Fig. 5.7), and mesencephalon + trigeminal ganglion and rhombencephalon modules (Fig. A5.14), show phylogenetic differentiation between taxa are reasonably well defined in morphospace. The distribution of taxa afforded by the combination of mesencephalon and rhombencephalon modules (Fig. 5.7), is arguably the better representation of the differentiation between various Sub-Family taxonomic groups. Notably, *Malacorhynchos membranaceus*, *Chenonetta jubata*, and *Nettapus pulchellus* are associated with *Mionetta blanchardi* specimens in PCA morphospace, patterns somewhat similar to those seen in PGLS factorial model regression plots (i.e. Fig. 5.5A).

**5.3.3.2 Modular Distance data**—results for ‘multiplicative’ distance-PGLS model fitting as implemented in Geomorph (see above), are summarised in Figs. 5.8A–H and presented in Tables A5.4C–D.

#### **5.3.3.2.1 Complete Modular Distance data**

**5.3.3.2.1.1 Trophic guild**—factorial assessment results show that of the 10 modular distance metrics that displayed BM phylogenetic signal, seven showed significant statistics for the Trophic Guild model (Tables A5.4A, A5.4C). However, as shown by Fig. 5.8A, z-score results overlap with F values, and although the medians between data are somewhat distinct, the two data overlap within the upper and lower quartiles (see Fig. 5.8A), suggesting the overall factorial model fit was not optimal. The range of  $R^2$  values for Trophic Guild was the widest for all assessed data, although  $R^2$  medians were somewhat better than results for Order assessments (see Fig. 5.8Ga, and below).

**5.3.3.2.1.2 Order**—factorial assessment results show higher levels of model fitting non-significance for Modular Distance subsets, as compared with results for Trophic guild assessments (i.e., eight vs six non-significant results; see Table A5.4C, and above). The range of non-significant results for these modules is greater than any of the Complete Distance data factorial models assessed (Fig. 5.8Ha). Fewer modules (six) showed significant fitting statistics with the factorial model within which BM phylogenetic signal was identified, than was found for Trophic Guild assessments (seven; see Tables A5.4A, A5.4C, and above). The summary boxplot (see Fig. 5.8B), shows z-scores and F values overlap, and medians between the data are almost identical, suggesting overall factorial model fitting is not optimal, and is less well resolved than that of Trophic Guild (see above). The  $R^2$  median for those data show the lowest model fitting resolution for the Complete Modular Distance data set,

although only somewhat lower than those of Trophic Guild assessments (see above), and the overall range of Order  $R^2$  results was less (Fig. 5.8Ga).

**5.3.3.2.1.3 Sub-Family**–factorial assessment results show only two non-significant model fitting P values (mesencephalon width,  $F=1.943$ ,  $P=0.158$ ; and cerebellum length,  $F=0.791$ ,  $P=0.137$ ; see Table A5.4C, Fig. 5.8Ha). Of these, only one variable was found to display BM phylogenetic signal (mesencephalon width; Table A5.4A). These results suggest that of the 10 variables displaying BM phylogenetic signal, nine model fitting results for Sub-Family assessments are significant (Tables A5.4A–C, Fig. 5.8Ha). The summary boxplot (Fig. 5.8C) shows that although z-score and F value ranges for Sub-Family overlap, medians between the two data are most widely distinct, compared with the ranges for Trophic Guild and Order assessments (Figs. 5.8A–C).  $R^2$  summary boxplots show that Sub-Family returned the highest overall  $R^2$  values for all Complete Distance data assessments (Fig. 5.8Ga). These results suggest Sub-Family afforded the ‘best fit’ to the Complete Modular Distance data set of all factorial assessments.

#### **5.3.3.2.2 Modular Distance data Dromornithids-excluded**

**5.3.3.2.2.1 Trophic guild**–factorial assessment results show that of the 11 modular distance metrics that displayed BM phylogenetic signal, seven had significant P values for the fitted factorial model (Tables A5.4B, A5.4D). However, as was found for Trophic Guild factorial assessments for Complete Modular Distance data (see Fig. 5.8A, and above), z-score results for these assessments overlap with F values, medians between the two data sets are also somewhat distinct, and similarly overlap within the upper and lower quartiles (see Fig. 5.8D). The P value range for Trophic Guild assessments for Modular Distance Dromornithids-excluded data, is much wider than that of Complete Modular Distance data (Figs. 5.8H). This suggest the overall model fit is not as well resolved in the former, and that assessments of Complete Modular Distance data set showed somewhat better model fitting results. The range of  $R^2$  values (Fig. 5.8Gb, Table A5.4D), show that although the medians between the two Modular Distance data are similar, Trophic Guild  $R^2$  results for the Modular Distance Dromornithids-excluded data set, had a somewhat wider inter quartile range.

**5.3.3.2.2.2 Order**–factorial assessment results show higher levels of factorial model fitting non-significance for the Modular Distance Dromornithids-excluded data set, compared with results for Trophic Guild assessments (i.e. 11 vs seven non-significant results; see Table A5.4D). Eight variables that showed BM phylogenetic signal, returned non-significant model fitting results (Tables A5.4B, A5.4D). Additionally, fewer modules showed significant fitting statistics with Order, within which BM phylogenetic signal was identified, than was found for Trophic Guild assessments (i.e., three vs seven; Tables A5.4B, A5.4D). The summary boxplot (Fig. 5.8E), shows z-scores and F values for the Order assessment mostly overlap (excluding two outliers), and medians between the data are virtually identical. As apparent in the Trophic Guild assessments (see Fig. 5.8B and above), the range of P values for Order assessments in the Modular Distance Dromornithids-excluded data set, is wider than that of the Complete Modular Distance data set (Figs. 5.8Ha).

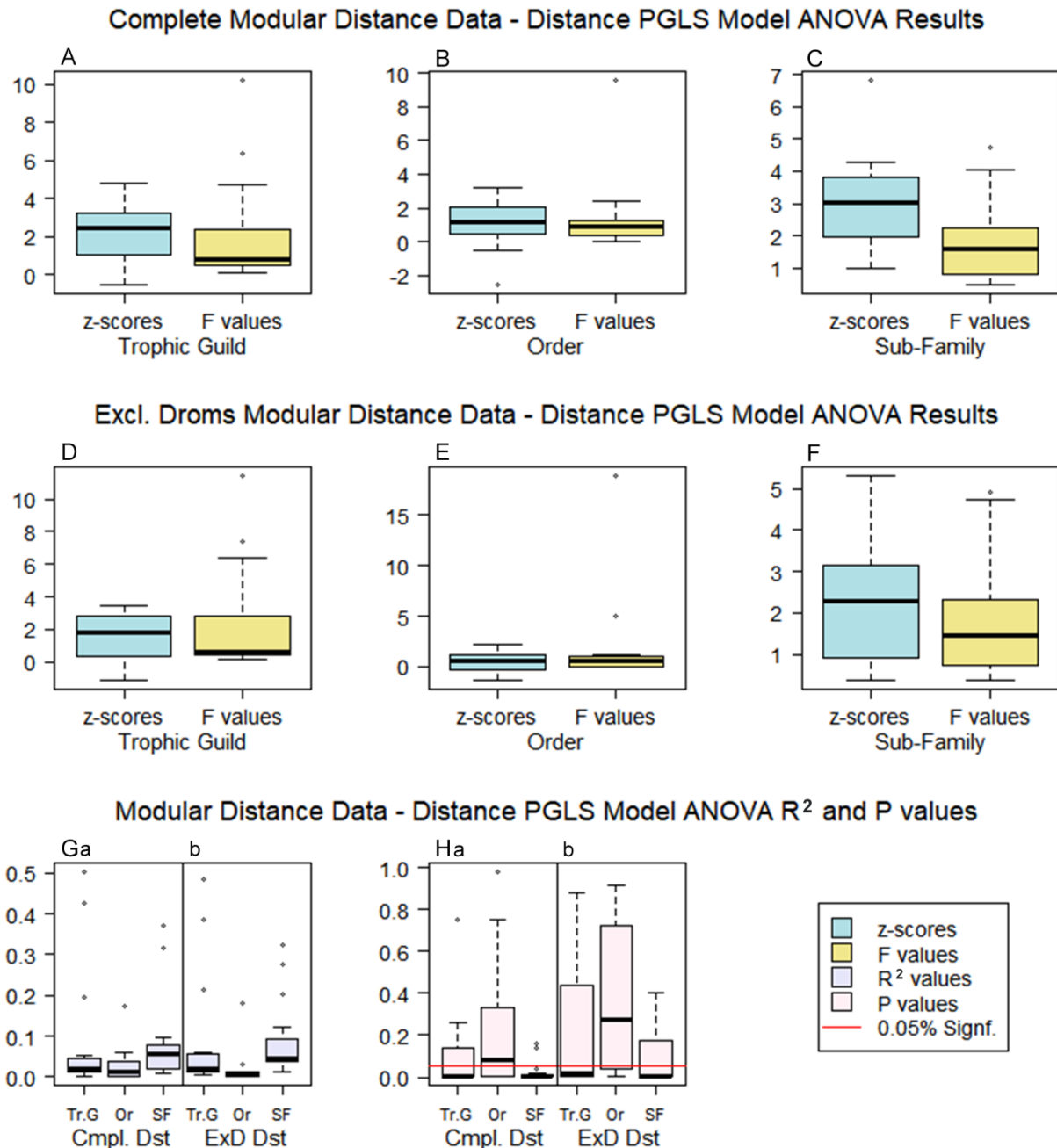


Figure 5.8. Quantile boxplots summarising Procrustes distance-PGLS model fitting results. **A–F**, z-scores (‘effect size’ *sensu* Collyer et al. 2015; see 5.2.7.4.1) and F values; **Ga–Gb**,  $R^2$  values; and **Ha–Hb**, P values for the Complete (n=34), and Dromornithids-excluded (n=31) Modular Distance data sets respectively (see Tables A5.4C–D). Upper and lower bounds of each boxplot represent the upper and lower quartiles respectively, the black horizontal line represents the median, and whiskers represent standard deviation at 1.5 IQR. Phylogenetic trees, along with one of three factorial models: Trophic Guild, Order, or Sub-Family (see Fig. 5.1; 5.2.6.4) were fitted to each data set respectively, using the function ‘procDppls’ employing 999 RRPP permutations as implemented in Geomorph (see 5.2.7.4), and Procrustes distance ANOVA assessments of model fitting were computed. Below the horizontal red line (**H**) represents the 5% significance level. **Abbreviations**, ANOVA, analysis of variance; **Cmpl.**, Complete; **Conf.**, confidence; **Droms**, dromornithids; **Excl.**, excluding; **ExD**, Dromornithids-excluded; **IQR**, inter-quartile range (25–75%); **Lm**, landmark; **Or**, Order; **PGLS**, phylogenetic generalised least squares;  **$R^2$** , R squared; **RRPP**, randomized residual permutation procedure; **SF**, Sub-Family/Family; **Tr.G**, Trophic Guild.

This suggests that overall, Order model fitting is not optimal, and is less well resolved than that of Trophic Guild and Sub-Family assessments for the Modular Distance Dromornithids-excluded data set (see Fig. 5.8Hb, and below). Additionally, the range of  $R^2$  values for Order assessments are the most narrow, and the Order  $R^2$  median are the lowest for all factorial assessments (Fig. 5.8Gb).

**5.3.3.2.2.3 Sub-Family**–factorial assessment results show five non-significant model fitting P values, including three response variables within which BM phylogenetic signal was identified (eminentia sagittalis width,  $F=0.388$ ,  $P=0.185$ ; mesencephalon width,  $F=1.889$ ,  $P=0.197$ ; and trigeminal ganglion width,  $F=0.625$ ,  $P=0.166$ ; see Tables A5.4B, A5.4D). These results suggest that of the 11 variables displaying BM phylogenetic signal, eight model fitting results for Sub-Family assessments are significant (Tables A5.4B–D). As for the Sub-Family assessments of Complete Modular Distance data, the summary boxplot (Fig. 5.8F) shows the ranges of z-scores and F values overlap, but the medians between the two data are most widely separated, compared with those of Trophic Guild and Order assessments (Figs. 5.8D–F). The range of P values is lowest among all assessments of the Modular Distance Dromornithids-excluded data sets, and the median falls well within the 5% significance level (Fig. 5.8Hb). However, the range of P values for Complete Modular Distance data, shows that both Trophic Guild and Sub-Family display better P value ranges for those data (Fig. 5.8Ha).  $R^2$  summary results show that Sub-Family had the highest median of all factorial assessments for Modular Distance Dromornithids-excluded data, but the range was less than that of Sub-Family for Complete Modular Distance data (Figs. 5.8Ga–b). These results suggest Sub-Family provided the ‘best fit’ to the Modular Distance Dromornithids-excluded data set, of all factorial assessments.

In summary, results for distance-PGLS factorial model fitting assessments employing the multiplicative model as implemented in Geomorph, shows better fitting for Complete Modular Distance data sets (see Figs. 5.8A–H, and above). The best fit for both Modular Distance data sets was Sub-family, followed by Trophic Guild and Order, respectively.

**5.3.3.3 Modular Distance data**–results for ‘additive’ covariance-PGLS factorial model fitting as implemented in phytools, are summarised in Figs. 5.9A, 5.9C, 5.9D, 5.9F and presented in Tables A5.5C–D. Note: computation of  $R^2$  values is possible for ‘lm’ or ‘glm’ linear model forms. However, assessments employing the ‘gls’ linear model framework, as implemented in phytools (Revell 2010, 2012, see also Methods 5.2.7.4), does not accommodate the calculation of  $R^2$  values, but instead affords the acquisition of AIC values, amongst other model fitment metrics. By convention, evaluation of linear model fitting through inspection of AIC values, affords identification of the ‘best fit’ of a particular model for covariance-PGLS model assessment (see 5.2.7.4.2). In order to maintain continuity with the presentation of Results (as above), this will be addressed after the description of Results for each covariance-PGLS factorial model fitting.

### 5.3.3.3.1 Complete Modular Distance data

**5.3.3.3.1.1 Trophic guild**—factorial assessment results show that of the 10 modular distance metrics that displayed BM phylogenetic signal, seven showed non-significant model fitting P values, and only three showed significant statistics for the fitted factorial model (telencephalon total length,  $F=2.894$ ,  $P=0.027$ ; mesencephalon length,  $F=2.756$ ,  $P=0.033$ ; and rhombencephalon width,  $F=3.683$ ,  $P=0.009$ ; Tables A5.5A, A5.5C). The degree of non-significance in the Trophic Guild model fitting, is shown well by the summary boxplot (Fig. 5.9Ca), where the P value median is well above the 5% significance level, and the range extends through to 0.998 (mesencephalon width).

**5.3.3.3.1.2 Order**—as was shown for Order factorial assessments using distance-PGLS methods (see Table A5.4C, and 5.3.3.2.1.2 above), results for Order assessments using covariance-PGLS methods, show higher levels of model fitting non-significance for Complete Modular Distance data response variables, as compared with results for Trophic Guild assessments (i.e. 12 vs 11 non-significant results; see Table A5.5C, and above). Additionally, only two modules (trigeminal ganglion length,  $F=3.450$ ,  $P=0.045$ ; rhombencephalon width,  $F=4.080$ ,  $P=0.027$ ), showed significant fitting statistics for Order, within which BM phylogenetic signal was identified (Tables A5.5A, A5.5C). Rhombencephalon width was the only response variable (of 15) common between Trophic Guild, and Order factorial models, that showed significant model fitting. As shown by the P value summary boxplot (Fig. 5.9Cb), the Order P values extend widely, the median is well above the 5% significance level, and is higher than that of Trophic Guild for the Complete Modular Distance data set (Fig. 5.9Ca).

**5.3.3.3.1.3 Sub-Family**—factorial assessment results show 11 non-significant model fitting results, of which only trigeminal ganglion length ( $F=2.439$ ,  $P=0.041$ ; Table A5.5C) and rhombencephalon width ( $F=3.006$ ,  $P=0.016$ ; Table A5.5C), within which BM phylogenetic signal was identified (Table A5.5A), showed significant model fitting statistics for Sub-Family. These results match those of the Order factorial model fitting for the Complete Modular Distance data sets (see above). However, although the number of variables returning non-significant model fitting results for Sub-Family was similar to that of Order (11 vs 12; Table A5.5C), the range of non-significant P values for Sub-Family was the widest for all factorial models assessed across the Complete Distance data set (Fig. 5.9Cc).

The boxplot summarising AIC values for Trophic Guild, Order and Sub-Family factorial model fitting across the Complete Modular Distance data set (Fig. 5.9A), shows that Order has the lowest AIC median. Although the upper quartile overlaps somewhat with the lower quartiles of Trophic Guild AIC results, the range of the Order AIC values are notably lower than those of both the Trophic Guild, and Sub-Family model AIC values. Additionally, AIC values for Sub-Family are the highest of all three factorial models, followed by Trophic Guild, and Order (Fig. 5.9A). Thus, with respect to AIC model selection criteria (see 5.2.7.4.2), Order has the most optimal fit with the Complete Distance data set.

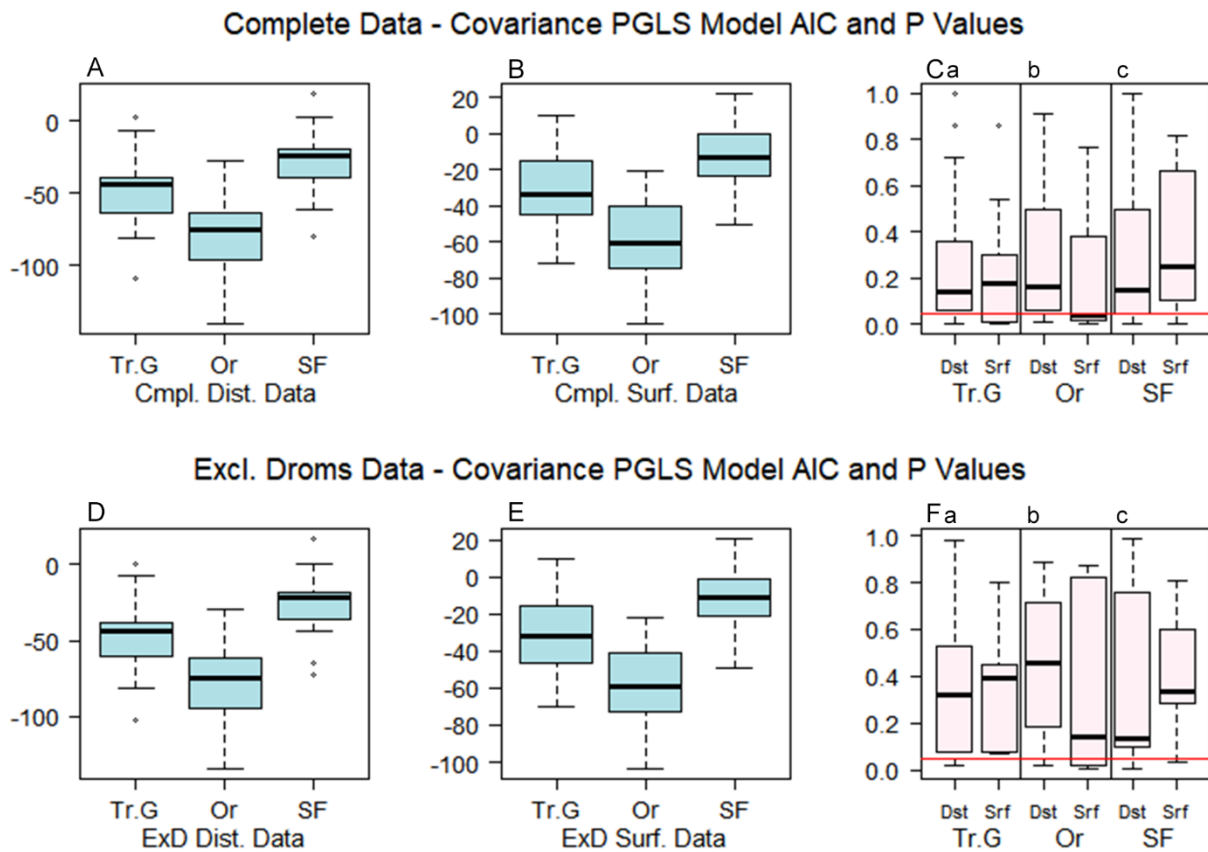


Figure 5.9. Quantile boxplots summarizing covariance-PGLS model fitting results. **A–B, D–E**, AIC and **C, F**, P values for the Complete (**A–C**;  $n=34$ ), and Dromornithids-excluded (**D–F**;  $n=31$ ) univariate datasets. **A**, Complete Modular Distance data (see Table A5.5C); **B**, Complete Modular Surface Area data (see Table A5.8C); **Ca–Cc**, Complete data sets P values (see Tables A5.5C, A5.8C); **D**, Modular Distance data Dromornithids-excluded (see Table A5.5D); **E**, Modular Surface Area data Dromornithids-excluded (see Table A5.8D); **Fa–Fc**, Dromornithids-excluded data sets P values (see Tables A5.5D, A5.8D). Upper and lower bounds of each boxplot represent the upper and lower quartiles respectively, the black horizontal line represents the median, and whiskers represent standard deviation at 1.5 IQR. Phylogenetic trees, along with one of three factorial models: Trophic Guild, Order, or Sub-Family (see Fig. 5.1; **5.2.6.4**) were fitted to each data set respectively, using the function ‘*pgls.SEy*’ as implemented in *phytools*, and model fitting was optimised using REML employing 999 permutations (see **5.2.7.4**). ANOVA assessments of each model fitting were conducted using the R base package ‘*stats*’ (R Core Team 2018), where AIC and P values were computed for each fitted model. Below the horizontal red line (**C, F**) represents the 5% significance level **Abbreviations**, AIC, Akaike Information Criterion values (*sensu* Akaike 1974); **Compl.**, Complete; **Dist.**, Modular Distance; **Droms**, dromornithids; **Dst**, Modular Distance data; **Excl.**, excluding; **ExD**, Dromornithids-excluded; **IQR**, inter-quartile range (25–75%); **Lm**, landmark; **Or**, Order; **PGLS**, Phylogenetic partial least squares; **REML**, restricted maximum likelihood (see **5.2.7.4**); **R<sup>2</sup>**, R squared; **SF**, Sub-Family/Family; **Srf**, Modular Surface Area data; **Surf.**, Modular Surface Area; **Tr.G**, Trophic Guild.

### 5.3.3.3.2 Modular Distance data Dromornithids-excluded

**5.3.3.3.2.1 Trophic guild**–factorial assessment results show that of the 11 Modular Distance metrics that displayed BM phylogenetic signal, nine showed non-significant model fitting results, and only two response variables within which BM phylogenetic signal was identified, showed significant statistics for Trophic Guild (telencephalon total length,  $F=3.154$ ,  $P=0.025$ ; and mesencephalon length,

$F=2.999$ ,  $P=0.031$ ; see Tables A5.5B, A5.5D). The degree of non-significance in Trophic Guild, is shown well by the summary boxplot (Fig. 5.9Fa), where the median is well above the 5% significance level, as are the lower quartiles, and the range of non-significant P values extends through to 0.983 (mesencephalon width; Table A5.5D). Results are somewhat similar to those seen in factorial model assessments of Complete Distance data (see above). Although, one additional response variable, within which BM phylogenetic signal was identified, returned a non-significant model fitting result (rhombencephalon width,  $F=2.335$ ,  $P=0.073$ ; Table A5.5D) in Trophic Guild assessments for the Modular Distance Dromornithids-excluded data set.

**5.3.3.3.2.2 Order**—as for the results of Order and Trophic Guild factorial assessments in Complete Modular Distance data sets (see above), Modular Distance Dromornithids-excluded data sets show a higher level of non-significant assessments for Order (i.e. 12 vs 11, respectively, see Table A5.5C; and 14 vs 12, respectively; see Table A5.5D, and above). Additionally, only one module (rostral telencephalon width,  $F=6.136$ ,  $P=0.020$ ; Table A5.5D), showed significant model fitting statistics for Order, across Modular Distance Dromornithids-excluded data sets. However, BM phylogenetic signal was not identified in this particular module (Tables A5.5B, A5.5D). As shown by the P value summary boxplot (Fig. 5.9Cb), Order P values extend widely, the median is well above the 5% significance level, and comprises the highest P value median result for all factorial model assessments for Modular Distance data sets (see also below).

**5.3.3.3.2.3 Sub-Family**—factorial assessment results show 13 non-significant model fitting P values, of which rostral telencephalon width ( $F=5.286$ ,  $P=0.001$ ; Table A5.5D), and caudal telencephalon width ( $F=3.579$ ,  $P=0.009$ ; Table A5.5D) showed significant model fitting statistics for Sub-Family. However, BM phylogenetic signal was identified only in the caudal telencephalon width module (Table A5.5B). Although the number of variables returning non-significant model fitting results for Sub-Family, was somewhat similar to that of Order (13 vs 14; Table A5.5D), the range of non-significant P values for Sub-Family assessment of Modular Distance Dromornithids-excluded data sets, was the widest for all factorial models assessed across both Modular Distance data sets, and the P value median was the lowest (Fig. 5.9Cc). The boxplot summarising AIC values for Trophic Guild, Order and Sub-Family model fitting across the Modular Distance Dromornithids-excluded data set (Fig. 5.9D), shows remarkable similarity to AIC results for the Complete Modular Distance data set described above (see Fig. 5.9A), and shows Order has the lowest AIC median, and the upper quartile overlaps somewhat with the lower quartiles of Trophic Guild AIC results. The range of Order AIC values are notably lower than both Trophic Guild and Sub-Family AIC values. Additionally, AIC values for Sub-Family are the highest of all three factorial models, followed by Trophic Guild and Order (Fig. 5.9D). Thus, with respect to AIC model selection criteria, Order is identified as affording the most optimal fit with the Modular Distance Dromornithids-excluded data sets.

In summary, results for covariance-PGLS factorial model fitting assessments of Modular Distance data sets, employing the ‘additive’ model as implemented in phytools, and with respect to

AIC model selection criteria, identify Order as affording the most optimal fit with these data, followed by Trophic guild, and Sub-Family respectively.

**5.3.3.4 Modular Surface Area data**—results for ‘additive’ covariance-PGLS factorial model fitting as implemented in phytools, are summarised in Figs. 5.9B–C, 5.9E–F and presented in Tables A5.8C–D.

#### **5.3.3.4.1 Complete Modular Surface Area data**

**5.3.3.4.1.1 Trophic guild**—factorial assessment results show that of the three Surface Area modules that displayed BM phylogenetic signal, two showed non-significant factorial model fitting P values (trigeminal ganglion face,  $F=0.416$ ,  $P=0.862$ ; rhombencephalon,  $F=2.060$ ,  $P=0.093$ ; Table A5.8C), and only one showed significant statistics for the fitted model (rostral telencephalon,  $F=3.885$ ,  $P=0.007$ ; Table A5.8C). The degree of non-significance in Trophic Guild model fitting, is shown well by the summary boxplot for Complete Modular Surface Area data sets (Fig. 5.9Ca), where the median is well above the 5% significance level, and the range extends through to 0.862 (trigeminal ganglion face; see Table A5.8C, and above).

**5.3.3.4.1.2 Order**—factorial assessments show higher levels of model fitting significance for Complete Modular Surface Area response variables, as compared with results for Trophic Guild assessments (i.e. three vs six non-significant results; see Table A5.8C, and above). Additionally, all three Surface Area modules within which BM phylogenetic signal was identified (Table A5.8A), showed significant fitting statistics for the Order factorial model (rostral telencephalon,  $F=9.248$ ,  $P=0.001$ ; trigeminal ganglion face,  $F=3.908$ ,  $P=0.031$ ; rhombencephalon,  $F=4.482$ ,  $P=0.020$ ; Table A5.8C). Rostral telencephalon was the only response variable (of nine), common between Trophic Guild and Order models, that showed significant model fitting (Table A5.8C). As shown by the P value summary boxplot (Fig. 5.9Cb), Order P values extend widely, but the P value median for Order is the only median which falls below the 5% significance level with respect to all assessments of Modular Surface Area data sets (see Fig. 5.9C).

**5.3.3.4.1.3 Sub-Family**—factorial assessment results show seven non-significant model fitting P values. The rostral telencephalon module was the only Complete Surface Area response variable showing significant model fitting statistics for the Sub-Family model ( $F=3.662$ ,  $P=0.006$ ), within which BM phylogenetic signal was identified (Tables A5.8A, A5.8C). These results match those of Trophic Guild fitting for the Complete Surface Area data sets (see above). However, although the number of variables returning non-significant model fitting results for Sub-Family, was similar to that of Trophic Guild (i.e. seven vs six; Table A5.8C), the interquartile range of non-significant P values for Sub-Family, was the widest for all factorial models assessed across the Complete Surface Area data set (Fig. 5.9Cc).

The boxplot summarising AIC values for Trophic Guild, Order and Sub-Family factorial model fitting across the Complete Modular Surface Area data set (Fig. 5.9B), shows that Order had the lowest AIC median, and although the upper quartile overlaps somewhat with the lower quartiles of

Trophic Guild AIC results, the range of Order AIC values are notably lower than both those of the Trophic Guild, and Sub-Family AIC values. Additionally, AIC values for Sub-Family are the highest of all three factorial models, followed by Trophic Guild, and Order (Fig. 5.9B). These results show similar patterns to those seen for the Complete Modular Distance data set (see Fig. 5.9A, and above). However, the interquartile ranges for both Trophic Guild and Sub-Family, are greater in the Complete Modular Surface Area data set (Fig. 5.9B). Thus, with respect to AIC model selection criteria, Order is identified as affording the most optimal fit with the Complete Surface Areas data set.

#### **5.3.3.4.2 Modular Surface Area data Dromornithids-excluded**

**5.3.3.4.2.1 Trophic guild**—factorial assessment results show that of the nine Modular Surface Area response variables that displayed BM phylogenetic signal, all showed non-significant P values (Tables A5.8B, A5.8D). The degree of non-significance in Trophic Guild fitting is shown well by the summary boxplot (Fig. 5.9Fa), where the median is well above the 5% significance level, and no P values fall below the 5% significance level. Results for the Surface Area Dromornithids-excluded data sets, were somewhat worse than those of the Complete Surface Area factorial assessments (see above), which displayed one significant model fitting result, with no modules showing significant fit with Trophic Guild (Tables A5.8C, A5.8D).

**5.3.3.4.2.2 Order**—as was shown for Order assessments across the Complete Modular Surface Area data set (see above), there were fewer non-significant assessments for Order in the Modular Surface Area Dromornithids-excluded data set (i.e., nine vs six, respectively; see Table A5.8D, and above). Additionally, three Modular Surface Area response variables (rostral telencephalon,  $F=8.740$ ,  $P=0.006$ ; total telencephalon,  $F=5.966$ ,  $P=0.021$ ; mesencephalon,  $F=5.857$ ,  $P=0.022$ ; Table A5.8D), showed significant fitting statistics for the Order model across Modular Surface Area Dromornithids-excluded data sets, wherein BM phylogenetic signal was identified (Tables A5.8B, A5.8D). As shown by the P value summary boxplot (Fig. 5.9Fb), Order P values extend widely, but although the median is above the 5% significance level, it is the lowest of all factorial model assessments for Modular Surface Area data sets (see also below).

**5.3.3.4.2.3 Sub-Family**—factorial assessment results show eight non-significant model fitting P values, of which rostral telencephalon ( $F=2.637$ ,  $P=0.036$ ; Table A5.8D) was the only response variable which showed significant model fitting statistics for Sub-Family. Although the range of non-significant P values for Sub-Family was narrower than that of Order, the P value median was markedly higher (Figs. 5.9Fb–c). Additionally, the P value median for the Sub-Family assessment, was somewhat lower than shown by the Trophic Guild assessment, although across the Modular Surface Area Dromornithids-excluded data set, both factorial assessments showed similar ranges of non-significance (Fig. 5.9Cc).

The boxplot summarising AIC values for Trophic Guild, Order, and Sub-Family factorial model fitting across the Modular Distance Dromornithids-excluded data set (Fig. 5.9E), shows remarkable similarity to AIC results for the Complete Modular Surface Area data sets described

above (see Fig. 5.9B). Results show Order has the lowest AIC median, and the upper quartile overlaps somewhat with the lower quartiles of Trophic Guild AIC results. AIC values for Sub-Family are the highest of all three factorial models, followed by Trophic Guild, and Order (Fig. 5.9E). Thus, with respect to AIC model selection criteria, Order is identified as affording the most optimal fit with the Modular Surface Area Dromornithids-excluded data set.

In summary, results for covariance-PGLS factorial model fitting assessments of Modular Surface Area data sets, employing the ‘additive’ model as implemented in phytools, and with respect to AIC model selection criteria, identify Order as affording the most optimal fit with these data, followed by Trophic guild, and Sub-Family models respectively.

**5.3.3.5 Modular Surface Area data**—results for ‘multiplicative’ distance-PGLS factorial model fitting as implemented in Geomorph, are summarised in Figs. 5.10A–H and presented in Tables A5.9C–D.

#### **5.3.3.5.1 Complete Modular Surface Area data**

**5.3.3.5.1.1 Trophic guild**—factorial assessment results show four non-significant fitting results, and of the three Modular Surface Area response variables that displayed BM phylogenetic signal, two showed significant statistics for Trophic Guild (rostral telencephalon,  $F=2.060$ ,  $P=0.001$ ; rhombencephalon,  $F=2.661$ ,  $P=0.001$ ; Tables A5.9A, A5.9C). However, as shown by Fig. 5.10A, z-score results overlap entirely with F values, and although the medians between data are somewhat distinct (see Fig. 5.10A), suggesting the overall factorial model fit is not optimal. The upper and lower quartile range of  $R^2$  values for Trophic Guild was the widest for all Complete Surface Area data assessed, although Trophic Guild  $R^2$  medians were somewhat better than results for Order (see Fig. 5.10Ga, and below).

**5.3.3.5.1.2 Order**—factorial assessment results show identical model fitting non-significance for Complete Modular Surface Area response variables, compared with results for Trophic Guild (i.e., four; see Table A5.9C, and above). The P value range of non-significant results for these response variables, are greater than any of the Complete Surface Area data assessed (Fig. 5.10Ha). Results for Order show significant fitting results for the same Surface Area response variables as was found for Trophic Guild (i.e. rostral telencephalon,  $F=1.478$ ,  $P=0.003$ ; rhombencephalon,  $F=2.227$ ,  $P=0.001$ ; Tables A5.9A, A5.9C). The summary boxplot (see Fig. 5.10B), shows z-scores and F values overlap, although medians between data are somewhat distinct. Overall, Order model fitting is least optimal, as Order  $R^2$  values are the lowest for the Complete Modular Surface Area data set (Fig. 5.10Ga).

**5.3.3.5.1.3 Sub-Family**—factorial assessment results show only one non-significant P value (mesencephalon,  $F=0.179$ ,  $P=0.810$ ; see Table A5.9C, Fig. 5.10Ha). These results suggest that of the three response variables displaying BM phylogenetic signal, all results for Sub-Family are significant (i.e. rostral telencephalon,  $F=1.504$ ,  $P=0.001$ ; trigeminal ganglion face,  $F=1.210$ ,  $P=0.044$ ; rhombencephalon,  $F=2.280$ ,  $P=0.001$ ; Tables A5.9A–C).

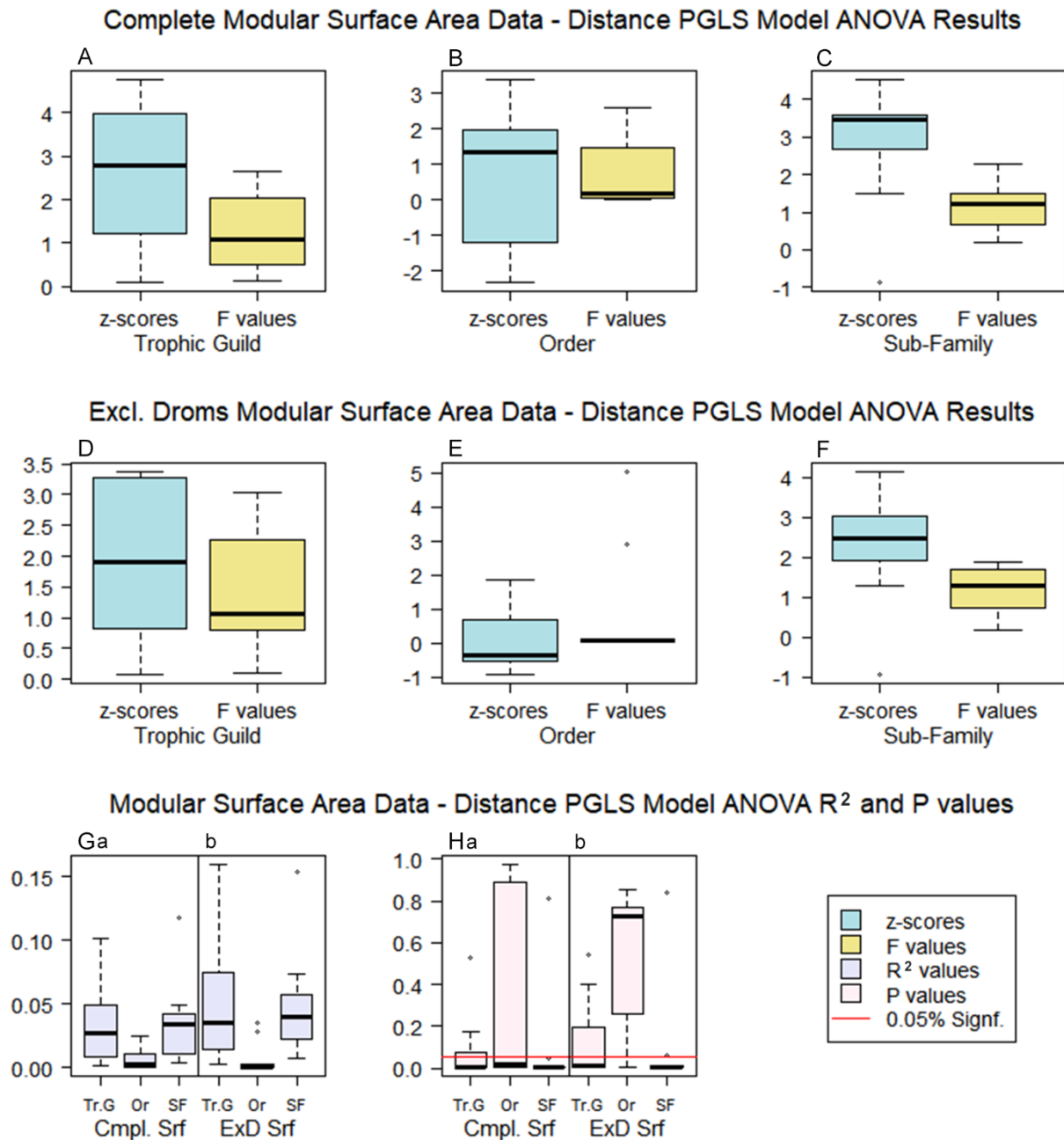


Figure 5.10. Quantile boxplots summarising Procrustes distance-PGLS model fitting results. **A–F**, z-scores (‘effect size’ *sensu* Collyer et al. 2015; see 5.2.7.4.1) and F values; **Ga–Gb**, R<sup>2</sup> values; and **Ha–Hb**, P values for the Complete (n=34), and Dromornithids-excluded (n=31) Modular Surface Area data sets respectively (see Tables A5.8C–D). Upper and lower bounds of each boxplot represent the upper and lower quartiles respectively, the black horizontal line represents the median, and whiskers represent standard deviation at 1.5 IQR. Phylogenetic trees, along with one of three factorial models: Trophic Guild, Order, or Sub-Family (see Fig. 5.1; 5.2.6.4) were fitted to each data set respectively, using the function ‘procDppls’ employing 999 RRPP permutations as implemented in Geomorph (see 5.2.7.4), and Procrustes distance ANOVA assessments of model fitting were computed. Below the horizontal red line (**H**) represents the 5% significance level. **Abbreviations**, ANOVA, analysis of variance; **Cmpl.**, Complete; **Conf.**, confidence; **Droms**, dromornithids; **Excl.**, excluding; **ExD**, Dromornithids-excluded; **IQR**, inter-quartile range (25–75%); **Lm**, landmark; **Or**, Order; **PGLS**, phylogenetic generalised least squares; **R<sup>2</sup>**, R squared; **RRPP**, randomized residual permutation procedure (see 5.2.7.4); **SF**, Sub-Family/Family; **Tr.G**, Trophic Guild.

The summary boxplot (Fig. 5.10C), shows that although z-score and F value ranges for Sub-Family overlap somewhat across the outer quartiles, medians between the two data are most widely distinct, compared with the ranges for Trophic Guild and Order (Figs. 5.10A–C).  $R^2$  boxplots show that Sub-Family returned the highest overall  $R^2$  median for all Complete Surface Area data factorial assessments (Fig. 5.10Ga). These results suggest Sub-Family afforded the ‘best fit’ to the Complete Modular Surface Area data set of all factorial assessments.

### **5.3.3.5.2 Modular Surface Area data Dromornithids-excluded**

**5.3.3.5.2.1 Trophic guild**–factorial assessment results show four non-significant model fitting results, and of the nine Modular Surface Area response variables that displayed BM phylogenetic signal, five were significant for Trophic Guild (*eminentia sagittalis*,  $F=2.743$ ,  $P=0.001$ ; rostral telencephalon,  $F=3.028$ ,  $P=0.001$ ; total telencephalon,  $F=0.803$ ,  $P=0.001$ ; trigeminal ganglion,  $F=1.056$ ,  $P=0.01$ ; rhombencephalon,  $F=2.227$ ,  $P=0.001$ ; Tables A5.9B, A5.9D). However, as shown by Fig. 5.10B, z-score results overlap entirely with F values, although the medians between data are somewhat distinct (see Fig. 5.10B). Similar to what was seen in Trophic Guild for Complete Surface Area data sets (Fig. 5.10A), this pattern suggests the overall factorial model fit is not optimal. The range of  $R^2$  values for Trophic Guild was the widest for all Surface Area data assessed, although the  $R^2$  median for these data were somewhat better than for Trophic Guild for the Complete Surface Area data set (see Figs. 5.10Ga–b, and above).

**5.3.3.5.2.2 Order**–factorial assessment results show a higher level of non-significance for Modular Surface Area response variables, compared with results for Trophic Guild (i.e., seven vs four; see Table A5.9C, and above). The range of non-significant results for these response variables, is far greater than any of the Surface Area Dromornithids-excluded data set factorial models assessed (Fig. 5.10Hb), and approaches that seen in Order of the Complete Surface Area data set (see Figs. 5.10Ha–b, and above). Notably, the P value median for Order is the highest across Modular Surface Area data sets assessed (see Figs. 5.10Ha–b). Results for Order are significant for only two Surface Area response variables (*eminentia sagittalis*,  $F=5.025$ ,  $P=0.001$ ; rostral telencephalon,  $F=2.901$ ,  $P=0.001$ ; Table A5.9C). The summary boxplot (Fig. 5.10E), shows z-scores and F value medians are more similar than all other factorial models assessed (see Figs. 5.10D–F), and suggest overall model fitting is least optimal for Order.  $R^2$  values for these data show they are the lowest for the Modular Surface Area Dromornithids-excluded data set (Fig. 5.10Gb).

**5.3.3.5.2.3 Sub-Family**–factorial assessment results show two non-significant model fitting P values (mesencephalon,  $F=0.187$ ,  $P=0.842$ ; trigeminal ganglion face,  $F=1.459$ ,  $P=0.059$ ; Table A5.9D; Fig. 5.10Hb). These results suggest that of the nine response variables displaying BM phylogenetic signal, seven model fitting results for Sub-Family assessments are significant (i.e. *eminentia sagittalis*,  $F=0.710$ ,  $P=0.009$ ; rostral telencephalon,  $F=1.861$ ,  $P=0.001$ ; caudal telencephalon,  $F=0.636$ ,  $P=0.009$ ; total telencephalon,  $F=0.946$ ,  $P=0.001$ ; trigeminal ganglion,  $F=1.294$ ,  $P=0.002$ ; cerebellum,  $F=1.680$ ,  $P=0.001$ ; rhombencephalon,  $F=1.867$ ,  $P=0.001$ ; Tables

A5.9B, A5.9D). The summary boxplot (Fig. 5.10F) shows that although z-score and F value ranges for Sub-Family overlap somewhat across the outer quartiles, and ranges overlap to a lesser degree than all factorial model assessments for Modular Surface Area Dromornithids-excluded data (Figs. 5.10D–F). The medians between Sub-Family are not particularly distinct from those of Trophic Guild (Figs. 5.10A–C), but  $R^2$  boxplots show that Sub-Family returned the highest overall  $R^2$  median for all Complete Surface Area data factorial assessments (Figs. 5.10Ga–b). These results suggest Sub-Family afforded the ‘best fit’ to the Modular Surface Area Dromornithids-excluded data set of all factorial assessments, followed by Trophic Guild, and Order respectively.

In summary, for all distance-PGLS factorial model fitting assessments of Modular Surface Area data sets employing the ‘multiplicative’ model as implemented in Geomorph, better fitting results were identified for Dromornithids-excluded data (see Figs. 5.10A–H, 5.10G, and above). Sub-Family best fit both Modular Surface Area data sets, followed by Trophic Guild, and Order factorial models respectively.

## 5.4 DISCUSSION

In this project, the aims were to assess three categories of endocast shape data, and investigate whether the modular aspect of multivariate shape, univariate surface areas, and univariate directional dimensions of morphological features represented by those data: **1**, retain phylogenetic signal; **2**, whether one or more modular brain regions hold a phylogenetic component, which may prove informative if described as traditional discrete or continuous characters; or **3**, may be employed as modular multivariate matrices for incorporation in more comprehensive cladistic assessments.

I used three forms of data derived from 34 endocast reconstructions, representing 30 species of galloanseres, including nine fossil taxa. These data comprised 22 species of anseriforms (including two fossil taxa: *Mionetta blanchardi* and *Chenonetta finschi*), three species of extinct gastornithiforms (*Dromornis* and *Ibandornis* taxa), and five species of extant galliforms (see Fig. 5.1). The approach employed here, using groups, or modules of semilandmarks to define morphology, was used by Wiley et al. (2005) to delimit discrete divisions of Old World monkey skulls, and ‘morph’ them to target specimens. A similar method was used by Gunz & Mitteroecker (2013:fig. 4) to demonstrate sliding semilandmarks on curves and surfaces of primate skulls. Other studies have adopted similar approaches. For example, Aristide et al. (2016) assessed New World monkey brains, Parr et al. (2016) characterised the neurocranial and mandibular morphology of dingoes, and Felice & Goswami (2018) assessed neornithine neurocrania in a similar manner. I used discrete Lm modules to compare endocast shape differences between individuals or taxa, allowing the quantification of these differences in a way not previously attained for birds.

Initial PCA visualisations of multivariate Modular Lm data, univariate Modular Distance data, and univariate Surface Area data describing endocast morphology, were suggestive of

phylogenetically informative patterns to some degree. However, PCA plots for multivariate Modular Lm data were indicative of functional signal in the dorsal endocast. To test whether variation in endocast shape retained a phylogenetic component (e.g. Walsh & Milner 2011a, 2011b), or was driven by adaptive features (e.g. Dubbeldam 1998a; Barton & Harvey 2000; Iwaniuk et al. 2008; Corfield et al. 2012, 2015a; and references therein), I assessed endocranial variation described by those data for phylogenetic signal, using both distance- and covariance-based methods under a BM evolutionary model, and identified phylogenetic signal predominantly in ventral endocast modules. I employed distance- and covariance-based factorial model PGLS regression methods, to statistically assess for patterns of evolutionary allometry, and identified modular regions of the ventral endocast which may prove systematically informative.

In the following I discuss the utility of the three forms of data, from least to most potentially phylogenetically informative, in order to identify where future analyses might concentrate efforts. This is contrary to the order of results presented above, but facilitates better narrative continuity.

#### **5.4.1 Modular Surface Area Data**

**5.4.1.1 Covariance-PGLS**—factorial model fitting assessments of Modular Surface Area data sets employing the ‘additive’ model as implemented in phytools, identified Order as affording the most optimal fit with these data, followed by Trophic guild, and Sub-Family respectively. These results showed similar patterns to those of the Modular Distance data sets using covariance-PGLS methods (see 5.4.2.1 below), in that there were high levels of non-significance across both Modular Surface Area data sets. This implies that the ‘additive’ linear model fitted, was not effectively differentiating between fine scale endocast morphological differences, and distinctions between taxa described by the Trophic Guild and Sub-Family factorial designations (i.e., where trophic preferences appear repeatedly across the tree; see Fig. 5.1).

**5.4.1.2 Distance-PGLS**—factorial model fitting assessments of Modular Surface Area data sets employing the ‘multiplicative’ model as implemented in Geomorph, showed better model fitting results for Modular Surface Area Dromornithids-excluded data. The Sub-Family factorial model best fit both Modular Surface Area data sets, followed by Trophic Guild and Order respectively. The factorial model fitting results for Modular Surface Area data, represent the only occasion where the Dromornithids-excluded data set produced better model fitting results (see also 5.4.4 below). BM phylogenetic signal was identified in all response variables within the Modular Surface Area Dromornithids-excluded data set, as opposed to only in three response variables in the Complete Modular Surface Area data set. This likely contributed to a higher level of significant model fitting results in the Dromornithids-excluded data set. However, the difference was minimal, as the Complete Modular Surface Area data set showed only one non-significant fitting result, compared with two from the Dromornithids-excluded data set.

## 5.4.2 Modular Distance data

**5.4.2.1 Covariance-PGLS**—factorial model fitting assessments of Modular Distance data sets employing the ‘additive’ model as implemented in phytools, identified Order as affording the most optimal fit for both Modular Distance data sets, followed by Trophic guild and Sub-Family respectively. There were high levels of non-significance across both Complete and Dromornithids-excluded data sets, implying that the fitted linear model was not effectively differentiating between fine scale endocast morphological distinctions between taxa described by the Trophic Guild and Sub-Family factorial designations.

**5.4.2.2 Distance-PGLS**—factorial model fitting assessments of Modular Distance data sets employing the ‘multiplicative’ distance-PGLS model as implemented in Geomorph, show that Sub-Family provided the most optimal fit across both Complete and Dromornithids-excluded data sets, followed by Trophic Guild and Order respectively. Factorial model fitting was better resolved for the Complete Distance data set. In both Modular Distance data sets, there was incongruity with eminentia sagittalis width and length metrics showing BM phylogenetic signal, which also showed disparate results (i.e., significant for Complete data, and non-significant for Dromornithids-excluded data). Additionally, the only dorsal endocast distance metric that showed continuity with BM phylogenetic signal, and significant factorial model fitting results across both Modular Distance data sets, was telencephalon total length. However, common to both Modular Distance data sets, was the prevalence of BM phylogenetic signal identified in ventral endocast distance metrics (i.e., mesencephalon, trigeminal ganglion, and rhombencephalon). Significant Sub-Family model fitting statistics were associated with these modules, with the exception of mesencephalon width in the Dromornithids-excluded data set. It is notable however, that the RRPP informed distance-PGLS factorial assessments of univariate Modular Distance data, show results which concur with multivariate Modular Lm data assessments (see 5.4.3 below), in that the Sub-Family factorial model was shown to optimally fit both Modular Distance data sets, and Modular Surface Area data sets (see 5.4.1.2 above).

## 5.4.3 Modular Lm Data

**5.4.3.1 Distance-PGLS**—factorial model fitting assessments of Modular Lm data sets employing the ‘multiplicative’ model as implemented in Geomorph, show Sub-Family provided the most optimal fit across both Complete and Dromornithids-excluded data sets, followed by Trophic Guild and Order respectively. Moreover, Sub-Family returned significant model fitting statistics for all response variables in the Complete Lm data set. BM phylogenetic signal was identified in the mesencephalon, trigeminal ganglion, mesencephalon + trigeminal ganglion, and rhombencephalon Lm modules. Notably, these subsets of the Modular Lm suite are located exclusively on the ventral endocast (see Figs. 5.4–5.5). BM phylogenetic signal results for the dorsal endocast, are all greater than one (i.e.  $K_{\text{mult}} > 1$ ), especially that of the dorsal cerebellum, and suggest that deviation from a steady, or continuous state of character evolution, as defined by the BM evolutionary model, is likely

indicative of functionally driven morphology in these dorsal endocast modules (see also **1.5.4**). This observation is supported by PCA plots for the Complete Modular Lm data set (Figs. A5.9, A5.10), where the distribution of taxa in morphospace using all response variables (Fig. A5.9), is similar to that using only dorsal endocast response variables (Fig. A5.10). This suggests that the distinctive differences in dorsal endocast morphology between galloansere taxa, as captured by dorsal Lm modules, are driving patterns of taxa distribution in PCA morphospace for multivariate shape data, and ‘overwhelming’ the more subtle phylogenetically informative effect of ventral endocast shape. These data support my earlier contention that the variation observed in dorsal endocast shape, as described by the eminentia sagittalis, rostral and caudal telencephalon, and cerebellum Lm modules, are likely related to trophic and behavioural attributes (see Chapter 3, **3.4.3**, and Chapter 4, **4.4.4**). This hypothesis is further supported by the distribution of taxa in PCA morphospace, for ventral Lm modules identified as potentially phylogenetically informative (see Figs. 5.6–5.7, A5.14), where the distinction between Sub-Family/Family taxonomic designations of taxa are much more clearly differentiated. This is particularly so for the combination of mesencephalon and rhombencephalon Lm modules (Fig. 5.7), which arguably present the most sensible taxonomic distribution of taxa. [Catalano & Torres \(2017\)](#) recommended that combining informative Lm modules in cladistic assessments may improve phylogenetic resolution, and the results of these assessments suggest this may be the case (e.g. Fig. 5.7; see also **5.4.5** below). The identification of BM phylogenetic signal only in ventral endocast Lm modules, also supports the distinction between multivariate shape and univariate forms of data. This is likely as the greater level of information conveyed by the multivariate modular Lm configurations, likely facilitated the differentiation of functional from phylogenetically informative attributes in endocast shape, as described by the Modular Lm suite (see General Methods, Fig. 2.1).

#### **5.4.4 Efficiency of data set types**

The utility of univariate data as a source for generating phylogenetically informative ‘characters’ for use in cladistic assessments, depends entirely on the means by which potentially informative metrics are assessed and identified. For example, by means of covariate-PGLS assessments, the Order factorial model was identified as ‘best fit’ for both Modular Distance and Modular Surface Area data sets. However, there were disparate results for the number of significant variables between Complete and Dromornithids-excluded data, within which BM phylogenetic signal was identified, across both data forms (e.g., two vs none of 15 response variables, and two vs three of nine response variables, respectively). Of these variables, rostral telencephalon metrics were the only common response variable across these data forms. I have argued that the shape of the dorsal endocast, is likely dominated by functional signal (see **5.4.3.1** above; and also **1.5.4**). I also suggest factorial model fitting, using covariance-PGLS methods, performed poorly in differentiating between functional and potentially phylogenetically informative endocranial morphology, as described by univariate data forms. While it is likely that the linear model employed here may not be most optimal,

and that a more descriptive model may potentially be developed to assess these data more efficiently. It is clear that model fitment results for covariance-PGLS assessments for both Modular Surface Area (see 5.4.1.1), and Modular Distance data sets (see 5.4.2.1), agree with the observations of Adams & Collyer (2018a), who noted AIC-based approaches display high levels of model misspecification that can exceed 50%.

Conversely, results for distance-PGLS factorial model fitting assessments, employing the ‘multiplicative’ model as implemented in Geomorph, showed complimentary factorial model fitting results across all forms of data assessed. In assessments of univariate Modular Surface Area and Modular Distance data sets, the Sub-Family factorial model was identified as ‘best fitting’ those data forms, and agreed with factorial model fitting results for multivariate Lm data sets. What is more, the response variables identified as potentially phylogenetically informative in univariate Complete Modular Distance and Complete Surface Area data sets, agreed with those identified in both multivariate Lm data sets. The only exceptions were one response variable in the Complete Modular Surface Area data (rostral telencephalon), and several in the Dromornithids-excluded data set, within which BM phylogenetic signal was found in all nine response variables. With regard to this, the distance-PGLS factorial model fitting results for Modular Surface Area data, represent the only occasion where the Dromornithids-excluded data set produced better model fitting results. However, given the trends described above, that Complete data sets for all data forms consistently afford better results for BM phylogenetic signal and factorial model fitting, suggests that the high frequency of BM phylogenetic signal identified in the Surface Area Dromornithids-excluded data set, may be representative of type 1 errors (i.e., false positives). This is supported by results showing that the low resolution of the univariate Modular Surface Area data, contributed to affect the least conclusive model fitting results for all data sets assessed employing distance-PGLS models, followed by univariate Modular Distance data. However, with respect to the morphological information conveyed by these data forms, RRPP procedures, employed as part of distance-PGLS factorial model assessments, appear to have capably differentiated between Trophic Guild and Sub-Family factorial assignments. Together these results show that the distance-PGLS approach, incorporating RRPP procedures as implemented in Geomorph, is clearly the superior factorial model assessment method. Although optimised for multivariate data, distance-PGLS performed better than the alternative, and optimised the limited morphological information conveyed by univariate data.

The PCA plots utilising all response variables for univariate data sets (Figs. A5.11, A5.12), are likely representative of the potential phylogenetic utility of these data forms. The Complete Modular Distance data PCA plot (Fig. A5.11), shows somewhat better discrimination of taxa in morphospace, than does the PCA plot for Complete Modular Surface Area data (Fig. A5.12). However, both data distinguish taxa remarkably well, and suggest that a combination of univariate metrics, appropriately ‘vetted’ by distance-PGLS methods, and applied in a similar fashion to that

argued above for multivariate Lm data (i.e., *sensu* Catalano & Torres 2017), may prove systematically informative, and contribute to future cladistic assessments (see 5.4.5 below).

In these assessments, I have shown that morphological information conveyed by the multivariate Modular Lm data sets, comprise the most potentially useful phylogenetically informative data form. These high-dimensional data clearly capture functional attributes of the dorsal endocast, represented by the lack of phylogenetic structure in the PCA plot for the eminentia sagittalis, caudal telencephalon, and cerebellum Lm modules (Fig. A5.10; see also 1.5.4). In contrast, PCA plots for mesencephalon and rhombencephalon Lm modules, identified as potentially phylogenetically informative (Figs. 5.6–5.7, A5.14), show phylogenetically correlated distribution patterns in morphospace, and most strongly so in the combination of mesencephalon and rhombencephalon Lm modules (Fig. 5.7).

Although all assessments identify the trigeminal ganglion, and metrics thereof (see above), as potentially phylogenetically informative, the combination of the mesencephalon and trigeminal ganglion modules, which were used to capture the entire ventral surface of the mesencephalon structure, show less resolution in morphospace for all clades in the PCA plot for these data (Fig. A5.14). The trigeminal ganglion is recognised as the largest somatosensory cranial innervation complex, involved in sensory reception for the entire facial region and mastication musculature (Bubień-Waluszewska 1981; Wild 1987; Dubbeldam 1998b; see also Introduction, 1.5.4.1), and is associated with functional demands of specific feeding behaviours linked with afferent receptive centres within the rostradorsal mesopallium (e.g. Berkhoudt et al. 1981; Dubbeldam et al. 1981; Northcutt 1981; Wild et al. 1984, 1985; Pettigrew & Frost 1985; Wild & Farabaugh 1996; see also Introduction, 1.5.4.2.2). However, I point out that the actual ‘footprint’ of the trigeminal ganglion complex on the ventral surface of the mesencephalon, is somewhat similar across taxa, but the differential hyper- or hypotrophy of the structure is distinctive between taxa using tactile feeding mechanisms like anseriforms, compared with the generalist omnivores within galliforms (Figs. A5.5–A5.8). The reasons as to why the trigeminal ganglion complex presents results as described above, is not currently clear, and further testing is required to determine whether the trigeminal ganglion comprises a phylogenetically informative structure.

#### 5.4.5 Cladistic assessment of modular brain regions

PGLS results show that the ventral rhombencephalon and mesencephalon endocast modules, as defined by the Modular Lm configurations used here, likely represent phylogenetically informative modular zones of the avian endocast. It appears then, that data derived from these Modular Lm configurations, Modular Distances, and to a lesser degree Modular Surface Areas, may prove cladistically informative, and afford additional taxonomic differentiation of avian taxa if incorporated in the form of shape matrices (i.e. Modular Lm coordinates), as continuous characters (Modular univariate metrics, or ratios thereof, e.g. Tables A5.3, A5.7), or described as traditional discrete

characters, for inclusion within more comprehensive parsimony, ML or Bayesian forms of cladistic analyses (e.g. [Ronquist et al. 2009](#); [Pennell & Harmon 2013](#); [Garamszegi 2014](#); [Lee & Palci 2015](#); [Harmon 2019](#); and references therein).

In order to test these hypotheses, and that of [Klingenberg & Gidaszewski \(2010:247\)](#) for example, who argued shape data may not be appropriate for inferring phylogenies; an appropriate set of molecular data, along with morphological characters, is required to be assembled for the taxa included in these analyses. Then, analyses run with, and without univariate data derived continuous characters, to ascertain whether those data improve the resolution of resultant phylogenetic topologies. At very least, if the resolution of subsequent analyses are improved, those univariate data may augment the amount of phylogenetically informative continuous morphological characters available (e.g. [Wiens 2004](#)). However, results for Modular Lm data showed the best promise for cladistic utility. At this point in time, phylogenetic analyses incorporating 3D Lm configurations are only possible using the package TNT v1.5 ([Goloboff & Catalano 2016](#)). This package allows for incorporation of matrices of 3D Lm coordinates, along with standard characters, in a parsimony-based framework (see also [Catalano et al. 2010](#)), affording resolution of optimal trees for “large-sized” Lm data sets. However, it is important to note that the Lm modules identified as potentially phylogenetically informative in these analyses, are composed exclusively of Type III Lms, as defined by [Palci & Lee \(2019:3\)](#); see also [Bookstein 1991](#)), and those authors suggest Type III Lm configurations constitute “weak levels of anatomical correspondence”. What is more, the paired nature of the mesencephalon Lm configurations (i.e., both left and right hand side Modular Lm configurations were incorporated in Modular Lm data analyses), constitute statistically ‘non-independent’ modules, which are effectively “correlated via bilateral symmetry”. The effect of which may “profoundly” influence the estimation of evolutionary rates (see [Palci & Lee 2019:9](#)).

Accordingly, in order to properly understand and appropriately condition those data, so as to justify their inclusion in any future cladistic assessments, further testing and accommodation of several recommendations proposed by [Palci & Lee \(2019\)](#) and [Catalano & Torres \(2017\)](#) are required. For example, Modular Lm configurations should be assessed via phylogenetic 2B-PLS assessments to ascertain integration levels (i.e., distinctness) with other Lm modules comprising the Modular Lm suite (*sensu* [Klaczko et al. 2016](#); [Sherratt et al. 2017b](#)). Investigations should consider the potential use of phylogenetically conditioned regression or PCA residuals as input data (*sensu* [Sherratt et al. 2017a](#); [Bright et al. 2019](#)), as opposed to Procrustes aligned coordinates. Correction for “bilateral redundancy” may be accommodated by excluding Lm coordinates from one side of bilateral configurations after Procrustes alignment (*sensu* [Palci & Lee 2019](#)), and these data should be tested on so called “low-level phylogenetic relationships” ([Palci & Lee 2019:11](#)), where morphological variation is not particularly distinct (see also [Catalano et al. 2010:548](#); i.e., for the same reasons I initially established two data sets: one including, and one excluding the highly derived dromornithid taxa). [Catalano & Torres \(2017\)](#) recognised there existed a relationship between the number of

distinct Lm configurations included in a cladistic assessment, and resultant topological correspondence. Thus, all appropriately conditioned Modular Lm configurations showing significant Sub-Family factorial model fitting results, should be included together in subsequent cladistic assessments employing TNT software.

#### 5.4.6 Fossil taxa and other things

With respect to the fossil taxa included in these assessments, it is notable that the Oligo-Miocene taxon *Mionetta blanchardi* associates remarkably closely with *Malacorhynchus membranaceus* in all PGLS regression plots for mesencephalon (Figs. 5.4A–B), and rhombencephalon (Figs. 5.5A–B) Lm modules, and also in the PCA plot for the same (Fig. 5.7). These results support hypotheses of a close relationship between these taxa by [Worthy et al. \(2007\)](#), who noted close similarities in features of the coracoid, and [Worthy & Lee \(2008\)](#) and [Worthy \(2009\)](#) who proposed the taxa were basal in the erismaturine clade. However, although [Worthy & Lee \(2008\)](#) advocated a position “close to *Anas*” within Anatinae for *Nettapus pulchellus* (i.e., see Fig. 5.1), results of the present analyses suggest a more basal position for *N. pulchellus* may be more likely, e.g., similar to that proposed by the molecular analyses of [Sraml et al. \(1996\)](#). Additionally, there has been much contention regarding the systematic affinities of the Australian wood duck *Chenonetta jubata*. For example, the taxon has been variously assigned to Anatini ([Livezey 1986:743](#)), along with *N. pulchellus* in the supergenus *Chenonetta* ([Livezey 1991:485](#)), in the Subtribe Nettapodina, also with *N. pulchellus* ([Livezey 1997:476](#)), and erected to generic rank in Anatinae by [Worthy & Olson \(2002:14\)](#). It is beyond the scope of this project to resolve the affinities of *C. jubata*, as a comprehensive combined molecular and morphological assessment would likely be required to properly investigate the systematic uncertainties surrounding the taxon. However, it is notable that the close affinity of *C. jubata* with *N. pulchellus* advocated by [Livezey \(1991, 1997\)](#), was not supported by [Sraml et al. \(1996\)](#); see also [Sorenson et al. 1999](#)), but *N. pulchellus* and *C. jubata* are found closely associated, in all forms of morphological assessment here (see Figs. 5.4A, 5.5A, 5.6, 5.7). Furthermore, I suggest that the close morphological associations noted here between *Mionetta blanchardi*, and the extant taxa *Malacorhynchus membranaceus*, *Nettapus pulchellus*, and *Chenonetta jubata*, may be indicative of the hypothesised Oligo-Miocene through Miocene basal erismaturine global radiation. This is represented by the fossil taxa *Mionetta* in the Northern Hemisphere, and *Pinpanetta*, *Tirarinetta*, *Awengkere* (see Introduction, **1.4.7.1**), *Manuherikia*, and *Dunstanetta* (see Introduction, **1.4.7.2**) in the Australasian Southern Hemisphere (see [Worthy et al. 2007](#); [Worthy 2008](#); [Worthy & Lee 2008](#); [Worthy et al. 2008](#); [Worthy 2009](#); [Worthy & Yates 2017](#)). The extant taxa *M. membranaceus*, *N. pulchellus*, and *C. jubata* (and potentially *Stictonetta naevosa* too), may represent relictual remnants of this ancient waterfowl radiation ([Worthy 2009](#)), and ventral endocast morphometric data may prove informative, if used in future combined analyses investigating these relationships.

A notable characteristic with respect to the positioning of *C. finschi* specimens in both regression and PCA plots for morphometric data, is the distinction between *C. jubata* and *C. finschi* (see Figs. 5.4–5.7). The endocasts of these taxa are quite different (Figs. A5.1, A5.2, A5.5, A5.6), and display morphological dissimilarities recognised early in this work (see Chapter 3, 3.3.2.1). In the present analyses, I included *C. finschi* fossils along with *C. jubata* in a much larger data set, and results suggest there is no close similarity between the endocast morphology of *C. finschi* and that of *C. jubata*, as sister-taxa status might predict (e.g. [Worthy & Olson 2002](#)). In fact, the endocast morphology of *C. finschi* conforms much more strongly with those of other anatines, than does that of *C. jubata* (see Figs. 5.4A, 5.5A, 5.6, 5.7; and above). [Worthy & Olson \(2002:10\)](#) recognised several “uniquely shared” skeletal characters between *C. finschi* and *C. jubata*, and the taxa were long suspected to be congeneric (e.g. [Oliver 1930, 1955](#)). Yet, the possibility exists that the several synapomorphies identified by [Worthy & Olson \(2002:14\)](#) in the synonymy of *C. finschi*, are functional adaptations to terrestrial grazing, as the shape of the *C. finschi* brain characterised here suggests the taxon is more closely associated with extant anatines. These observations suggest there may be a case for the systematic reassessment of *C. finschi*, with respect to the validity of the monotypic genus *Euryanas* [Oliver, 1930](#), previously erected for it within Anatinae, now synonymised with *Chenonetta* (see [Worthy & Olson 2002](#)). Such assessment is not impossible, as fossil remains of *C. finschi* are a common component of many Late Pleistocene and Holocene sites of New Zealand, and museum collections comprise many thousands of bones ([Worthy & Olson 2002](#), and references therein; [Pers. Obs. Author](#)). An ancient DNA assessment including both *C. finschi* and *C. jubata* is long overdue, and the combination of molecular data along with these and other morphological data, may clarify the affinities of *C. finschi* one way or the other.

With respect to dromornithid taxa, the endocranial distinctions between them and other galloansere taxa is somewhat striking, affecting a positioning of dromornithid taxa outside of either galliform or anseriform morphospace in all assessment plotting (e.g. Figs. 5.4A, 5.5A, 5.6, 5.7). The distinctions between dromornithid endocast morphology, with respect to those of basal galloanseres, has previously been treated more comprehensively (see Chapter 4, 4.4.1), and will not be reiterated at length here. However, the inclusion of dromornithid taxa in the more comprehensive data set assessed here, allowed for recognition that, apart from the highly derived and hypertrophied nature of dromornithid eminentia sagittalis morphology, the rostral positioning of the dromornithid eminentia sagittalis on the dorsal endocast, conforms more closely to the position of the eminentia sagittalis seen in galliform taxa. This condition is distinct to the more caudal positioning of the eminentia sagittalis in anseriform taxa, such that the caudal margins of the eminentia sagittalis overlap the rostradorsal eminence of the cerebellum, when viewed from the lateral aspect (e.g. Figs. A5.1–A5.4). These morphological trends are apparent in dorsal endocast views too (see Figs. A5.5–A5.8). This caudal condition is evident in both anseriform and pelecyaniform taxa (e.g. [Stingelin 1957:pl. 29](#); [Ebinger 1995:fig. 1a-b](#); [Kalisinska 2005:figs. 1.1, 1.2](#); [Kawabe et al. 2010:fig 1](#); [2013:fig. 2](#); [2014:fig. 4](#); see

also Proffitt et al. 2016:fig. 3). Such characteristics are clearly described by the PC1 shape change plots for dorsal endocast Lm modules (x-axis; Fig. A5.10), where the galliform condition, i.e., of more rostrally orientated eminentia sagittalis structures, is depicted particularly well with respect to the more caudal positioning evident in anseriform taxa assessed here. The distinctive rostral versus caudal positioning of eminentia sagittalis structures across avian taxa has long been recognised. For example, Stingelin (1957) proposed the more rostral positioning of the eminentia sagittalis is a primitive, or “lower” form, as he termed it, and is evident in sphenisciforms (e.g. Ksepka et al. 2012; Paulina-Carabajal et al. 2014:fig 5; Kawabe et al. 2014:fig 5; Tambussi et al. 2015:fig 7; Proffitt et al. 2016:fig 3), ratites (e.g. Craigie 1939:figs. 1-2; Martin et al. 2007:fig. 2a; Ashwell & Scofield 2008:figs. 6g-l; Corfield et al. 2008:fig 1B-E; Peng et al. 2010:figs. 1, 3; Picasso et al. 2011:fig 1), and in several neornithine taxa (e.g. Stingelin 1957:pls. 23-27; Corfield et al. 2008:fig. 1bL; Picasso et al. 2009:fig 5; Kawabe et al. 2010:fig 1; Walsh & Milner 2011a:figs. 11.3D-G; Smith & Clarke 2012:figs. 2-3, 8-11; Wylie et al. 2015:figs. 3A-C; Walsh & Knoll 2018:fig. 5.3). Therefore, this ‘primitive’ condition is evident in taxa other than galliforms, and if not independently derived in all these lineages, may be plesiomorphic for neornithines (see also Introduction, 1.1).

Additionally, I note that although dromornithids plot outside of the galloansere morphospace, they are aligned more closely with, and overlap the galliform morphospace along the negative x-axis more so, than they do across the morphospace occupied by all anseriforms along the positive x-axis (Fig. A5.10). This morphological trend was noted in Chapter 4 (see 4.4.1.2), and is now distinguished more comprehensively using a larger data set. Furthermore, I suggest that derivation of the distinctive dromornithid eminentia sagittalis morphology from the galliform condition, is arguably more ‘parsimonious’ than from the more caudally positioned anseriform condition, and this is suggestive of dromornithid origins more closely aligned with basal galliform taxa, as proposed by Worthy et al. (2017a:13, see also 2017b), and *contra* Murray & Vickers-Rich (2004).

The musk duck *Biziura lobata* is a particularly anomalous taxon in general, exhibiting several autapomorphic behavioural and skeletal characters (i.e., extreme sexual size dimorphism, lekking behaviour, and distinctive anatomy; see McCracken 1999; McCracken et al. 1999, 2000a, 2000b). Although morphological assessments have recognised the taxon in Erismaturinae (e.g. Livezey 1997, Worthy & Lee 2008; and references therein), several molecular and behavioural analyses (e.g. Sraml et al. 1996; McCracken et al. 1999; De Mendoza 2019; and references therein) have suggested it is likely not an erismaturine. In fact, McCracken & Sorenson (2005) specifically excluded the taxon from their molecular assessment of stiff-tailed ducks for these reasons (for an alternative point of view see Worthy 2009:439-440). In these analyses, *B. lobata* was recovered in univariate assessments (e.g. Figs. A5.11, A5.12), and in regressions of ventral endocast Modular Lm data (e.g. Figs. 5.4, 5.5), as most closely associated with anserines. I note, however, that Livezey (1997:464) categorised *B. lobata* as “bizarre”, a term which certainly applies to the morphology of the *B. lobata* brain visualised here. The Modular Lm suite developed to capture the endocranial divisions of the galloansere brain (e.g.

General Methods, Fig. 2.1), was initially based on common endocranial morphology observed across as many galloanseres possible, either previously modelled, or in published literature. However, no visualisations of *B. lobata* brains were available at the time (to my knowledge). Thus, it was with some surprise I discovered that the Modular Lm suite, appropriately structured for all taxa assessed herein, was not particularly suitable to capture the truly ‘bizarre’ ventral endocast morphology displayed by *B. lobata*. For example, (galloansere condition in parenthesis), the trigeminal ganglion of *B. lobata* inserts on the caudal surface of the mesencephalon (inserts ventrally), the eminence of the V<sub>2</sub> and V<sub>3</sub> cranial nerves are laterally orientated (rostrolaterally), the V<sub>1</sub> cranial nerve inserts into the ventromedial mesencephalon (does not insert), and does not comprise a continuous part of the trigeminal ganglion as a whole (as in all galloanseres; see Figs. A5.3C, A5.7D). Thus, the effective application of the mesencephalon and trigeminal ganglion Lm modules to the morphology of *Biziura lobata*, was essentially compromised. What is more, not only is the overall mesencephalon condition in *B. lobata* distinct from all galloanseres, it is distinct from any neornithine brain observed (Pers. Obs. Author). Therefore, results of anserine affinity for *B. lobata* reported here, must be considered with appropriate caution.

Similarly, the molecular assessments of [Sraml et al. \(1996\)](#), and [McCracken et al. \(1999\)](#); see also [De Mendoza 2019](#)) suggested *B. lobata* is not an erismaturine, or even closely related. Those authors argued diving is a secondarily evolved trait, and is morphologically convergent on other erismaturine taxa. [McCracken et al. \(1999, 2000b\)](#) suggested *B. lobata* is ecologically convergent with the Northern Hemisphere eiders (e.g. *Polysticta* and *Somateria* spp.), and Southern Hemisphere Steamer ducks (e.g. *Tachyeres* spp.), and that in the Australasian region, *B. lobata* occupies the “otherwise unoccupied” niche filled by large-bodied diving ducks elsewhere. *Biziura lobata* is highly sexually dimorphic, with males and females not overlapping in body mass, a characteristic that has facilitated intraspecific trophic niche divergence. For example, the male bill size is 15–22% larger than in females, delivers strong bite forces, and is used for crushing hard-shelled prey inaccessible to females (see [McCracken 1999](#); [McCracken et al. 2000b](#)). For the purposes of this study, I selected skulls that were clearly mature adult males where possible, consequently the *B. lobata* skull scanned and modelled is a large and robust male. The possibility exists that given the trend for intraspecific behavioural, trophic, and body size divergences in the taxon, female *B. lobata* may display endocranial morphology distinct to that seen in the males, and warrants further investigation, as the above morphological distinctions are unknown elsewhere in anseriforms to my knowledge. Additionally, given the extraordinary ventral endocast morphology in these ducks, a unique opportunity exists to assess how intraspecific neuroanatomy may correlate with behavioural and morphological distinctions within a single taxon. This may be achieved by brain sectioning assessments (e.g. [Iwaniuk & Wylie 2007](#); [Gutiérrez-Ibáñez et al. 2009](#); [Wylie et al. 2015](#)), whereby using photomicrographic methods, the arrangement of neuroanatomical sensory systems in the taxon may be better defined, and assessed with respect to several biological attributes.

## 5.5 CONCLUSIONS

In these assessments, I have employed multi- and univariate data forms, derived from 34 endocast reconstructions including nine fossil taxa, representing 30 species of galloanseres. The approach of using multiple Lm modules to define and allow independent comparison of shape change across distinct regions of the endocast between galloansere taxa, has afforded appreciation of the degree of differential hyper- or hypotrophy between individual zones of the galloansere brain. The evaluation of endocast shape, has allowed the relative importance of changes in the various areas of the brain to be considered systematically. By means of PCA and phylogenetically informed regression methods, I assessed and visualised patterns of endocast morphological variation across the clade. By employing both distance- and covariance-based methods under a BM evolutionary model, I showed that multivariate Modular Lm data was the most effective phylogenetically informative data form, followed by univariate Distance, and Surface Area data respectively. These Modular Lm data facilitated the identification of phylogenetic signal, and significant evolutionary correlations with Sub-Family taxonomic designations across the galloanseres evaluated. The existence of significant phylogenetic signal in the ventral mesencephalon and rhombencephalon regions of the avian endocast, is potentially phylogenetically informative if employed appropriately, along with traditional continuous and discrete data forms, in future cladistic assessments. Moreover, I have demonstrated over the course of this project, that the shape of the avian dorsal endocast, is likely driven more by functional requisites of trophic niche and habitat use. Additionally, the statistical assessment of patterns of evolutionary allometry within these data, have revealed evolutionary correlations between fossil taxa and putative extant relatives, and identified directions for future research into these relationships.

## 5.6 Acknowledgements

I thank Vanesa De Pietri and R. Paul Scofield (Museum of Canterbury, Christchurch, New Zealand) for access to *Mionetta blanchardi* CT data, and Georg Schulz (University of Basel, Switzerland) and Loic Costeur (Natural History Museum Basel, Switzerland), for their assistance in scanning the MNHN specimens. I also thank Alan J. D. Tennyson (Te Papa Museum, Wellington, New Zealand), for access to *Chenonetta finschi* specimens. Michael Archer and Suzanne Hand (University of NSW, Sydney), for access to *D. murrayi* specimens. Philippa Horton and Maya Penck (South Australian Museum, Adelaide), for access to the ornithology collection. Adelaide Microscopy, (University of Adelaide), for access to the Skyscan  $\mu$ CT instrument. Joseph Bevitt (ANSTO, Sydney), for Neutron scanning of *Dromornis planei*, and Mishelle Korlaet (SAHMRI, Adelaide), for CT scanning *D. murrayi* and *Ilbandornis woodburnei* specimens.

## 5.7 REFERENCES

- Adams, D.C., 2014a. Quantifying and comparing phylogenetic evolutionary rates for shape and other high-dimensional phenotypic data. *Systematic Biology* 63, 166-177. doi:110.1093/sysbio/syt1105.
- Adams, D.C., 2014b. A generalized K statistic for estimating phylogenetic signal from shape and other high-dimensional multivariate data. *Systematic Biology* 63, 685-697. doi:610.1093/sysbio/syu1030.
- Adams, D.C., 2014c. A method for assessing phylogenetic least squares models for shape and other high-dimensional multivariate data. *Evolution* 68, 2675-2688. doi:2610.1111/evo.12463.
- Adams, D.C., Collyer, M.L., 2015. Permutation tests for phylogenetic comparative analyses of high-dimensional shape data: what you shuffle matters. *Evolution* 69, 823-829. doi:810.1111/evo.12596.
- Adams, D.C., Collyer, M.L., 2018a. Multivariate phylogenetic comparative methods: evaluations, comparisons, and recommendations. *Systematic Biology* 67, 14-31. doi:10.1093/sysbio/syx1055.
- Adams, D.C., Collyer, M.L., 2018b. Phylogenetic ANOVA: Group-clade aggregation, biological challenges, and a refined permutation procedure. *Evolution* 72, 1204-1215. doi:1210.1111/evo.13492.
- Adams, D.C., Collyer, M.L., Kaliontzopoulou, A., 2018. *Geomorph: Software for geometric morphometric analyses*. R package version 3.0.7. <https://cran.r-project.org/package=geomorph>.
- Adams, D.C., Rohlf, F.J., Slice, D.E., 2013. A field comes of age: geometric morphometrics in the 21st century. *Hystrix* 24, 7-14. doi:10.4404/hystrix-4424.4401-6283.
- Akaike, H., 1974. A New Look at the Statistical Model Identification, in: Parzen, E., Tanabe, K., Kitagawa, G. (Eds.), *Selected Papers of Hirotugu Akaike*. Springer Series in Statistics, Springer Science & Business Media, New York, pp. 215-222.
- Aristide, L., dos Reis, S.F., Machado, A.C., Lima, I., Lopes, R.T., Perez, S.I., 2016. Brain shape convergence in the adaptive radiation of New World monkeys. *Proceedings of the National Academy of Sciences USA* 113, 2158-2163. doi:2110.1073/pnas.1514473113.
- Ashwell, K.W.S., Scofield, R.P., 2008. Big birds and their brains: Paleoneurology of the New Zealand moa. *Brain, Behavior and Evolution* 71, 151-166. doi:110.1159/000111461.
- Barton, R.A., Harvey, P.H., 2000. Mosaic evolution of brain structure in mammals. *Nature* 405, 1055-1058.
- Berkhoudt, H., Dubbeldam, J.L., Zeilstra, S., 1981. Studies on the somatotopy of the trigeminal system in the mallard, *Anas platyrhynchos* L. IV. Tactile representation in the nucleus basalis. *Journal of Comparative Neurology* 196, 407-420.
- Blomberg, S.P., Garland Jr, T., Ives, A.R., 2003. Testing for phylogenetic signal in comparative data: behavioral traits are more labile. *Evolution* 57, 717-745.
- Blomberg, S.P., Lefevre, J.G., Wells, J.A., Waterhouse, M., 2012. Independent contrasts and PGLS regression estimators are equivalent. *Systematic Biology* 61, 382-391. doi:310.1093/sysbio/syr1118.

- Boc, A., Diallo, A.B., Makarenkov, V., 2012. T-REX: a web server for inferring, validating and visualizing phylogenetic trees and networks. *Nucleic Acids Research* 40, W573-W579. doi:510.1093/nar/gks1485.
- Bookstein, F.L., 1991. *Morphometric Tools for Landmark Data: Geometry and Biology*. Cambridge University Press, Cambridge. UK. p.435.
- Bright, J.A., Marugán-Lobón, J., Rayfield, E.J., Cobb, S.N., 2019. The multifactorial nature of beak and skull shape evolution in parrots and cockatoos (Psittaciformes). *BMC Evolutionary Biology* 19, 104. doi:110.1186/s12862-12019-11432-12861.
- Bubień-Waluszewska, A., 1981. The Cranial Nerves, in: King, A.S., McLelland, J. (Eds.), *Form and Function in Birds*. Vol. 2, Academic Press, London, pp. 385-438.
- Camin, J.H., Sokal, R.R., 1965. A method for deducing branching sequences in phylogeny. *Evolution* 19, 311-326.
- Carril, J., Tambussi, C.P., Degrange, F.J., Benitez Saldivar, M.J., Picasso, M.B.J., 2015. Comparative brain morphology of Neotropical parrots (Aves, Psittaciformes) inferred from virtual 3D endocasts. *Journal of Anatomy* 229, 239-251. doi:210.1111/joa.12325.
- Catalano, S.A., Goloboff, P.A., Giannini, N.P., 2010. Phylogenetic morphometrics (I): the use of landmark data in a phylogenetic framework. *Cladistics* 26, 539-549. doi:510.1111/j.1096-0031.2010.00302.x.
- Catalano, S.A., Torres, A., 2017. Phylogenetic inference based on landmark data in 41 empirical data sets. *Zoologica Scripta* 46, 1-11. doi:10.1111/zsc.12186.
- Cheneval, J., 1983. Les Anatidae (Aves, Anseriformes) du gisement aquitain de Saint-Gérard-le-Puy (Allier, France), In: Buffetaut, E., Mazin, J.M., Salmon, E. (Eds.), *Actes du Symposium Paléontologique Georges Cuvier, Ville de Montbéliard, Montbéliard, France, 1982*, pp. 85-97.
- Cignoni, P., Callieri, M., Corsini, M., Dellepiane, M., Ganovelli, F., Ranzuglia, G., 2008. Meshlab: an open-source mesh processing tool, In: Scarano, V., De Chiara, R., Erra, U. (Eds.), *Proceedings of the 2008 Eurographics Italian Chapter Conference, Salerno, Italy*, pp. 129-136. ISBN 978-123-905673-905668-905675.
- Collyer, M.L., Adams, D.C., 2018. RRPP: An R package for fitting linear models to high-dimensional data using residual randomization. *Methods in Ecology and Evolution* 9, 1772-1779. doi:1710.1111/2041-1210X.13029.
- Collyer, M.L., Sekora, D.J., Adams, D.C., 2015. A method for analysis of phenotypic change for phenotypes described by high-dimensional data. *Heredity* 115, 357-365. doi:310.1038/hdy.2014.1075.
- Corfield, J.R., Long, B., Krilow, J.M., Wylie, D.R.W., Iwaniuk, A.N., 2015. A unique cellular scaling rule in the avian auditory system. *Brain Structure and Function* 9, 102-120. doi:110.1007/s00429-00015-01064-00421.
- Corfield, J.R., Wild, J.M., Hauber, M.E., Parsons, S., Kubke, M.F., 2008. Evolution of brain size in the palaeognath lineage, with an emphasis on New Zealand ratites. *Brain, Behavior and Evolution* 71, 87-99. doi:10.1159/000111456.
- Corfield, J.R., Wild, J.M., Parsons, S., Kubke, M.F., 2012. Morphometric analysis of telencephalic structure in a variety of neognath and paleognath bird species reveals regional differences associated with specific behavioral traits. *Brain, Behavior and Evolution* 80, 181-195. doi:110.1159/000339828.

- Craigie, E.H., 1939. The cerebral cortex of *Rhea americana*. *Journal of Comparative Neurology* 70, 331-353.
- Da Silva, F.O., Fabre, A.-C., Savriama, Y., Ollonen, J., Mahlow, K., Herrel, A., Müller, J., Di-Poï, N., 2018. The ecological origins of snakes as revealed by skull evolution. *Nature Communications* 9, 376. doi:310.1038/s41467-41017-02788-41463.
- Davies, T.J., Kraft, N.J.B., Salamin, N., Wolkovich, E.M., 2012. Incompletely resolved phylogenetic trees inflate estimates of phylogenetic conservatism. *Ecology* 93, 242-247. doi:210.1890/1811-1360.1891.
- Davis, M.A., Douglas, M.R., Collyer, M.L., Douglas, M.E., 2016. Deconstructing a species-complex: geometric morphometric and molecular analyses define species in the Western Rattlesnake (*Crotalus viridis*). *PLoS ONE* 11, e0146166. doi:0146110.0141371/journal.pone.0146166.
- De Mendoza, R.S., 2019. Phylogenetic relationships of the Early Miocene diving and flightless duck *Cayaoa bruneti* (Aves, Anatidae) from Patagonia: homology or convergence? *Papers in Palaeontology* (early view) xx, 1-9. doi:10.1002/spp1002.1268.
- Donne-Goussé, C., Laudet, V., Hänni, C., 2002. A molecular phylogeny of anseriformes [sic] based on mitochondrial DNA analysis. *Molecular Phylogenetics and Evolution* 23, 339-356. doi:310.1016/S1055-7903(1002)00019-00012.
- Drake, A.G., Klingenberg, C.P., 2008. The pace of morphological change: historical transformation of skull shape in St Bernard dogs. *Proceedings of the Royal Society of London B: Biological Sciences* 275, 71-76. doi:10.1098/rspb.2007.1169.
- Dubbeldam, J.L., 1998a. Birds, in: Nieuwenhuys, R., ten Donkelaar, H.J., Nicholson, C. (Eds.), *The Central Nervous System of Vertebrates*, Springer-Verlag, Berlin, pp. 1525-1636.
- Dubbeldam, J.L., 1998b. The sensory trigeminal system in birds: input, organization and effects of peripheral damage. A review. *Archives of Physiology and Biochemistry* 106, 338-345. doi:310.1076/apab.1106.1075.1338.4367.
- Dubbeldam, J.L., Brauch, C.S.M., Don, A., 1981. Studies on the somatotopy of the trigeminal system in the mallard, *Anas platyrhynchos* L. III. Afferents and organization of the nucleus basalis. *Journal of Comparative Neurology* 196, 391-405.
- Ebinger, P., 1995. Domestication and plasticity of brain organization in mallards (*Anas platyrhynchos*). *Brain, Behavior and Evolution* 45, 286-300.
- Ericson, P.G.P., 1996. The skeletal evidence for a sister-group relationship of anseriform and galliform birds: a critical evaluation. *Journal of Avian Biology* 27, 195-202.
- Ericson, P.G.P., Anderson, C.L., Britton, T., Elzanowski, A., Johansson, U.S., Källersjö, M., Ohlson, J.I., Parsons, T.J., Zuccon, D., Mayr, G., 2006. Diversification of Neoaves: integration of molecular sequence data and fossils. *Biology Letters* 2, 543-547. doi:510.1098/rsbl.2006.0523.
- Faraway, J.J., 2005. *Extending the Linear Model with R: Generalized Linear, Mixed Effects and Nonparametric Regression Models*. 1st Edition. Chapman & Hall/CRC, New York. p.312.
- Felice, R.N., Goswami, A., 2018. Developmental origins of mosaic evolution in the avian cranium. *Proceedings of the National Academy of Sciences USA* 115, 555-560. doi:510.1073/pnas.1716437115.

- Felice, R.N., Tobias, J.A., Pigot, A.L., Goswami, A., 2019. Dietary niche and the evolution of cranial morphology in birds. *Proceedings of the Royal Society of London. Series B: Biological Sciences* 286, 20182677. doi:20182610.20181098/rspb.20182018.20182677.
- Felsenstein, J., 1985. Confidence limits on phylogenies: an approach using the bootstrap. *Evolution* 39, 783-791.
- Felsenstein, J., 1988. Phylogenies and quantitative characters. *Annual Review of Ecology and Systematics* 19, 445-471.
- Garamszegi, L.Z., 2014. *Modern Phylogenetic Comparative Methods and their Application in Evolutionary Biology*. Springer-Verlag, Berlin.
- Garland Jr, T., Harvey, P.H., Ives, A.R., 1992. Procedures for the analysis of comparative data using phylogenetically independent contrasts. *Systematic Biology* 41, 18-32.
- Gilbert, C.C., 2011. Phylogenetic analysis of the African papionin basicranium using 3-D geometric morphometrics: The need for improved methods to account for allometric effects. *American Journal of Physical Anthropology* 144, 60-71. doi:10.1002/ajpa.21370.
- Goloboff, P.A., Catalano, S.A., 2016. TNT version 1.5, including a full implementation of phylogenetic morphometrics. *Cladistics* 32, 221-238. doi:210.1111/cla.12160.
- Gómez-Robles, A., de Castro, J.M.B., Arsuaga, J.-L., Carbonell, E., Polly, P.D., 2013. No known hominin species matches the expected dental morphology of the last common ancestor of Neanderthals and modern humans. *Proceedings of the National Academy of Sciences USA* 110, 18196-18201. doi:18110.11073/pnas.1302653110.
- Gonzalez, J., Düttmann, H., Wink, M., 2009. Phylogenetic relationships based on two mitochondrial genes and hybridization patterns in Anatidae. *Journal of Zoology* 279, 310-318. 318. doi:310.1111/j.1469-7998.2009.00622.x.
- González-José, R., Escapa, I., Neves, W.A., Cúneo, R., Pucciarelli, H.M., 2008. Cladistic analysis of continuous modularized traits provides phylogenetic signals in *Homo* evolution. *Nature* 453, 775-779. doi:710.1038/nature06891.
- Grafen, A., 1989. The phylogenetic regression. *Philosophical Transactions of the Royal Society of London. B, Biological Sciences* 326, 119-157.
- Gray, J.A., Sherratt, E., Hutchinson, M.N., Jones, M.E.H., 2019. Changes in ontogenetic patterns facilitate diversification in skull shape of Australian agamid lizards. *BMC Evolutionary Biology* 19, 1-10. doi:10.1186/s12862-12018-11335-12866.
- Gunz, P., Mitteroecker, P., 2013. Semilandmarks: a method for quantifying curves and surfaces. *Hystrix* 24, 103-109. doi:110.4404/hystrix-4424.4401-6292.
- Gutiérrez-Ibáñez, C., Iwaniuk, A.N., Wylie, D.R.W., 2009. The independent evolution of the enlargement of the principal sensory nucleus of the trigeminal nerve in three different groups of birds. *Brain, Behavior and Evolution* 74, 280-294. doi:210.1159/000270904.
- Hackett, S.J., Kimball, R.T., Reddy, S., Bowie, R.C.K., Braun, E.L., Braun, M.J., Chojnowski, J.L., Cox, W.A., Han, K.-L., Harshman, J., Huddleston, C.J., Marks, B.D., Miglia, K.J., Moore, W.S., Sheldon, F.H., Steadman, D.W., Witt, C.C., Yuri, T., 2008. A phylogenomic study of birds reveals their evolutionary history. *Science* 320, 1763-1768. doi: 1710.1126/science.1157704.
- Harmon, L.J., 2019. *Phylogenetic Comparative Methods*. p.234. <https://open.umn.edu/opentextbooks/textbooks/phylogenetic-comparative-methods>.

- Harris, R.B., Birks, S.M., Leaché, A.D., 2014. Incubator birds: biogeographical origins and evolution of underground nesting in megapodes (Galliformes: Megapodiidae). *Journal of Biogeography* 41, 2045-2056. doi:2010.1111/jbi.12357.
- Harvey, P.H., Pagel, M.D., 1991. *The Comparative Method in Evolutionary Biology*. Oxford University Press, Oxford, UK. p.239.
- Huey, R.B., Bennett, A.F., 1987. Phylogenetic studies of coadaptation: preferred temperatures versus optimal performance temperatures of lizards. *Evolution* 41, 1098-1115.
- Ives, A.R., Midford, P.E., Garland Jr, T., 2007. Within-species variation and measurement error in phylogenetic comparative methods. *Systematic Biology* 56, 252-270. doi:210.1080/10635150701313830.
- Iwaniuk, A.N., Heesy, C.P., Hall, M.I., Wylie, D.R.W., 2008. Relative wulst volume is correlated with orbit orientation and binocular visual field in birds. *Journal of Comparative Physiology A* 194, 267-282. doi:210.1007/s00359-00007-00304-00350.
- Iwaniuk, A.N., Wylie, D.R.W., 2007. Neural specialization for hovering in hummingbirds: Hypertrophy of the pretectal nucleus lentiformis mesencephali. *Journal of Comparative Neurology* 500, 211-221.
- Jarvis, E.D., Mirarab, S., Aberer, A.J., Li, B., Houde, P., Li, C., Ho, S.Y., Faircloth, B.C., Nabholz, B., Howard, J.T., et al., 2014. Whole-genome analyses resolve early branches in the tree of life of modern birds. *Science* 346, 1320-1331.
- Kalisińska, E., 2005. Anseriform brain and Its parts versus taxonomic and ecological categories. *Brain, Behavior and Evolution* 65, 244-261. doi:210.1159/000084315.
- Kawabe, S., Ando, T., Endo, H., 2014. Enigmatic affinity in the brain morphology between ptopterids and penguins, with a comprehensive comparison among water birds. *Zoological Journal of the Linnean Society* 170, 467-493. doi:410.1111/zoj.12072.
- Kawabe, S., Shimokawa, T., Miki, H., Okamoto, T., Matsuda, S., 2010. A simple and accurate method for estimating the brain volume of birds: Possible application in paleoneurology. *Brain, Behavior and Evolution* 74, 295-301. doi:210.1159/000270906.
- Kawabe, S., Shimokawa, T., Miki, H., Okamoto, T., Matsuda, S., Itou, T., Koie, H., Kitagawa, M., Sakai, T., Hosojima, M., 2013. Relationship between brain volume and brain width in mammals and birds. *Paleontological Research* 17, 282-293. doi:210.2517/1342-8144-2517.2513.2282.
- Kear, J., 2005. *Bird Families of the World: Ducks, Geese and Swans*, Vols 1 and 2. Oxford University Press, Oxford, U.K.
- Klaczko, J., Sherratt, E., Setz, E.Z.F., 2016. Are diet preferences associated to skulls shape diversification in xenodontine snakes? *PLoS ONE* 11, e0148375. doi:0148310.0141371/journal.pone.0148375.
- Klingenberg, C.P., Gidaszewski, N.A., 2010. Testing and quantifying phylogenetic signals and homoplasy in morphometric data. *Systematic Biology* 59, 245-261. doi:210.1093/sysbio/syp1106.
- Klingenberg, C.P., Marugán-Lobón, J., 2013. Evolutionary covariation in geometric morphometric data: analyzing integration, modularity, and allometry in a phylogenetic context. *Systematic Biology* 62, 591-610. doi:510.1093/sysbio/syt1025.

- Kraatz, B., Sherratt, E., 2016. Evolutionary morphology of the rabbit skull. *PeerJ* 4, e2453. doi:2410.7717/peerj.2453.
- Ksepka, D.T., Balanoff, A.M., Walsh, S., Revan, A., Ho, A., 2012. Evolution of the brain and sensory organs in Sphenisciformes: new data from the stem penguin *Parapterodytes antarcticus*. *Zoological Journal of the Linnean Society* 166, 202-219. doi:210.1111/j.1096-3642.2012.00835.x.
- Lee, M.S.Y., Palci, A., 2015. Morphological phylogenetics in the genomic age. *Current Biology* 25, R922-R929. doi:910.1016/j.cub.2015.1007.1009.
- Liu, G., Zhou, L., Li, B., Zhang, L., 2014. The complete mitochondrial genome of *Aix galericulata* and *Tadorna ferruginea*: Bearings on their phylogenetic position in the Anseriformes. *PLoS ONE* 9, e109701. doi:109710.101371/journal.pone.0109701.
- Livezey, B.C., 1986. A phylogenetic analysis of recent anseriform genera using morphological characters. *Auk* 103, 737-754.
- Livezey, B.C., 1991. A phylogenetic analysis and classification of recent dabbling ducks (Tribe Anatini) based on comparative morphology. *Auk* 108, 471-507.
- Livezey, B.C., 1997. A phylogenetic classification of waterfowl (Aves: Anseriformes), including selected fossil species. *Annals of the Carnegie Museum* 66, 457-496.
- Livezey, B.C., Martin, L.D., 1988. The systematic position of the Miocene anatid *Anas*[?] *blanchardi* Milne-Edwards. *Journal of Vertebrate Paleontology* 8, 196-211.
- Lockwood, C.A., Kimbel, W.H., Lynch, J.M., 2004. Morphometrics and hominoid phylogeny: support for a chimpanzee–human clade and differentiation among great ape subspecies. *Proceedings of the National Academy of Sciences USA* 101, 4356-4360. doi:4310.1073/pnas.0306235101.
- Lyras, G.A., Van Der Geer, A.A.E., 2003. External brain anatomy in relation to the phylogeny of Caninae (Carnivora: Canidae). *Zoological Journal of the Linnean Society* 138, 505-522.
- Macrini, T.E., 2009. Description of a digital cranial endocast of *Bathygenys reevesi* (Merycoidodontidae; Oreodontoidea) and implications for apomorphy-based diagnosis of isolated, natural endocasts. *Journal of Vertebrate Paleontology* 29, 1199-1211.
- Macrini, T.E., Rougier, G.W., Rowe, T., 2007. Description of a cranial endocast from the fossil mammal *Vincelestes neuquenianus* (Theriiformes) and its relevance to the evolution of endocranial characters in therians. *Anatomical Record* 290, 875-892. doi:810.1002/ar.20551.
- Macrini, T.E., Rowe, T., Archer, M., 2006. Description of a cranial endocast from a fossil platypus, *Obdurodon dicksoni* (Monotremata, Ornithorhynchidae), and the relevance of endocranial characters to monotreme monophyly. *Journal of Morphology* 267, 1000-1015. doi:1010.1002/jmor.10452.
- Maddison, W.P., 1991. Squared-change parsimony reconstructions of ancestral states for continuous-valued characters on a phylogenetic tree. *Systematic Biology* 40, 304-314.
- Maiorino, L., Farke, A.A., Piras, P., Ryan, M.J., Terris, K.M., Kotsakis, T., 2013. The evolution of squamosal shape in ceratopsid dinosaurs (Dinosauria, Ornithischia). *Journal of Vertebrate Paleontology* 33, 1385-1393.
- Marchant, S., Higgins, P.J., 1990. *Handbook of Australian, New Zealand and Antarctic birds*, Vols 1A and 1B. Oxford University Press, Melbourne, Australia.

- Martin, G.R., Wilson, K.-J., Wild, J.M., Parsons, S., Kubke, M.F., Corfield, J., 2007. Kiwi forego vision in the guidance of their nocturnal activities. *PLoS ONE* 2, e198. doi:110.1371/journal.pone.0000198.
- Martins, E.P., Hansen, T.F., 1997. Phylogenies and the comparative method: a general approach to incorporating phylogenetic information into the analysis of interspecific data. *American Naturalist* 149, 646-667.
- Marugán-Lobón, J., Watanabe, A., Kawabe, S., 2016. Studying avian encephalization with geometric morphometrics. *Journal of Anatomy* 229, 191-203. doi:110.1111/joa.12476.
- Mayr, G., 2009. *Paleogene Fossil Birds*. Springer-Verlag, Berlin Heidelberg.
- Mayr, G., 2017. *Avian Evolution: The Fossil Record of Birds and its Paleobiological Significance*. John Wiley & Sons, Chichester. UK. pp 293.
- McCracken, K.G., 1999. Systematics, ecology, and social biology of the Musk Duck (*Biziura lobata*) of Australia, PhD Dissertation, *Louisiana State University*, Baton Rouge, Louisiana.
- McCracken, K.G., Afton, A.D., Paton, D.C., 2000a. Nest and eggs of Musk Ducks *Biziura lobata* at Murray Lagoon, Cape Gantheaume Conservation Park, Kangaroo Island, South Australia. *South Australian Ornithologist* 33, 65-70.
- McCracken, K.G., Harshman, J., McClellan, D.A., Afton, A.D., 1999. Data set incongruence and correlated character evolution: an example of functional convergence in the hind-limbs of stiff-tail diving ducks. *Systematic Biology* 48, 683-714.
- McCracken, K.G., Paton, D.C., Afton, A.D., 2000b. Sexual size dimorphism of the Musk Duck. *Wilson Bulletin* 112, 457-466.
- McCracken, K.G., Sorenson, M.D., 2005. Is homoplasy or lineage sorting the source of incongruent mtDNA and nuclear gene trees in the stiff-tailed ducks (*Nomonyx-Oxyura*)? *Systematic Biology* 54, 35-55. doi:10.1080/10635150590910249.
- Mourer-Chauviré, C., Berthet, D., Hugueney, M., 2004. The late Oligocene birds of the Créchy quarry (Allier, France), with a description of two new genera (Aves: Pelecaniformes: Phalacrocoracidae, and Anseriformes: Anseranatidae). *Senckenbergiana Lethaea* 84, 303-315.
- Münkemüller, T., Lavergne, S., Bzeznik, B., Dray, S., Jombart, T., Schiffers, K., Thuiller, W., 2012. How to measure and test phylogenetic signal. *Methods in Ecology and Evolution* 3, 743-756. doi:710.1111/j.2041-1210X.2012.00196.x.
- Murray, P.F., Vickers-Rich, P., 2004. *Magnificent Mhirungs: The Colossal Flightless Birds of the Australian Dreamtime*. Indiana University Press, Bloomington.
- Northcutt, R.G., 1981. Evolution of the telencephalon in nonmammals. *Annual Review of Neuroscience* 4, 301-350.
- Oliver, W.R.B., 1930. *New Zealand Birds*. 1st Edition. Fine Arts NZ, Wellington.
- Oliver, W.R.B., 1955. *New Zealand Birds*. 2nd Edition. A. H. & A. W. Reed, Wellington.
- O'Meara, B.C., Ané, C., Sanderson, M.J., Wainwright, P.C., 2006. Testing for different rates of continuous trait evolution using likelihood. *Evolution* 60, 922-933.
- Palci, A., Hutchinson, M.N., Caldwell, M.W., Lee, M.S.Y., 2017. The morphology of the inner ear of squamate reptiles and its bearing on the origin of snakes. *Royal Society Open Science* 4, 170685. doi:170610.171098/rsos.170685.

- Palci, A., Hutchinson, M.N., Caldwell, M.W., Scanlon, J.D., Lee, M.S.Y., 2018. Palaeoecological inferences for the fossil Australian snakes *Yurlunggur* and *Wonambi* (Serpentes, Madtsoiidae). *Royal Society Open Science* 5, 172012. doi:172010.171098/rsos.172012.
- Palci, A., Lee, M.S.Y., 2019. Geometric morphometrics, homology and cladistics: review and recommendations. *Cladistics* 35, 230-242. doi:210.1111/cla.12340.
- Parr, W.C.H., Wilson, L.A.B., Wroe, S., Colman, N.J., Crowther, M.S., Letnic, M., 2016. Cranial shape and the modularity of hybridization in dingoes and dogs; hybridization does not spell the end for native morphology. *Evolutionary Biology* 43, 171-187. doi:110.1007/s11692-11016-19371-x.
- Paulina-Carabajal, A., Acosta-Hospitaleche, C., Yury-Yáñez, R.E., 2014. Endocranial morphology of *Pygoscelis calderensis* (Aves, Spheniscidae) from the Neogene of Chile and remarks on brain morphology in modern *Pygoscelis*. *Historical Biology* 27, 571-582. doi:510.1080/08912963.08912014.08898067.
- Peng, K., Feng, Y., Zhang, G., Liu, H., Song, H., 2010. Anatomical study of the brain of the African ostrich. *Turkish Journal of Veterinary and Animal Sciences* 34, 235-241. doi:210.3906/vet-0806-3919.
- Pennell, M.W., Harmon, L.J., 2013. An integrative view of phylogenetic comparative methods: connections to population genetics, community ecology, and paleobiology. *Annals of the New York Academy of Sciences* 1289, 90-105. doi:110.1111/nyas.12157.
- Pettigrew, J.D., Frost, B.J., 1985. A tactile fovea in the Scolopacidae? *Brain, Behavior and Evolution* 26, 185-195. doi:110.1159/000118775.
- Picasso, M.B.J., Tambussi, C., Dozo, M.T., 2009. Neurocranial and brain anatomy of a Late Miocene eagle (Aves, Accipitridae) from Patagonia. *Journal of Vertebrate Paleontology* 29, 831-836. doi:810.1671/1039.1029.0319.
- Picasso, M.B.J., Tambussi, C.P., Degrange, F.J., 2011. Virtual reconstructions of the endocranial cavity of *Rhea americana* (Aves, Palaeognathae): Postnatal anatomical changes. *Brain, Behavior and Evolution* 76, 176-184. doi:110.1159/000321173.
- Proffitt, J.V., Clarke, J.A., Scofield, R.P., 2016. Novel insights into early neuroanatomical evolution in penguins from the oldest described penguin brain endocast. *Journal of Anatomy* 229, 228-238. doi:210.1111/joa.12447.
- Rambaut, A., 2012. *FigTree v1. 4*. Computer program distributed by the author, website: <http://tree.bio.ed.ac.uk/software/figtree/>.
- Rasband, W.S., 2018. *ImageJ*, U.S. National Institutes of Health, Bethesda, Maryland, USA. <https://imagej.nih.gov/ij/>.
- R Core Team, 2018. *R: A language and environment for statistical computing*. R Foundation for Statistical Computing, Vienna, Austria. URL: <https://www.R-project.org/>.
- Revell, L.J., 2010. Phylogenetic signal and linear regression on species data. *Methods in Ecology and Evolution* 1, 319-329, doi:310.1111/j.2041-1210X.2010.00044.x.
- Revell, L.J., 2012. phytools: an R package for phylogenetic comparative biology (and other things). *Methods in Ecology and Evolution* 3, 217-223. doi:210.1071/MU05027 00158-04197/05005/030217.
- Revell, L.J., Harmon, L.J., Collar, D.C., 2008. Phylogenetic signal, evolutionary process, and rate. *Systematic Biology* 57, 591-601. doi:510.1080/10635150802302427.

- Rohlf, F.J., 1998. On applications of geometric morphometrics to studies of ontogeny and phylogeny. *Systematic Biology* 47, 147-158.
- Rohlf, F.J., 2001. Geometric interpretations of comparative methods for the analysis of continuous variables. *Evolution* 55, 2143-2160.
- Rohlf, F.J., 2002. Geometric Morphometrics and Phylogeny, in: Macleod, N., Forey, P.L. (Eds.), *Morphology, Shape, and Phylogeny*, Taylor and Francis, London, pp. 175-193.
- Ronquist, F., van der Mark, P., Huelsenbeck, J.P., 2009. Bayesian Phylogenetic Analysis using MrBayes, in: Lemey, P., Salemi, M., Vandamme, A.M. (Eds.), *The Phylogenetic Handbook: A Practical Approach to Phylogenetic Analysis and Hypothesis Testing*, Cambridge University Press, Cambridge, pp. 210-266.
- RStudio Team, 2016. *RStudio: Integrated Development for R*, RStudio, Inc., Boston, MA URL <http://www.rstudio.com/>.
- Sanger, T.J., Sherratt, E., McGlothlin, J.W., Brodie III, E.D., Losos, J.B., Abzhanov, A., 2013. Convergent evolution of sexual dimorphism in skull shape using distinct developmental strategies. *Evolution* 67, 2180-2193. doi:2110.1111/evo.12100.
- Santana, S.E., Cheung, E., 2016. Go big or go fish: morphological specializations in carnivorous bats. *Proceedings of the Royal Society B: Biological Sciences* 283, 20160615. doi:20160610.20161098/rspb.20162016.20160615.
- Schmelzle, T., Sánchez-Villagra, M.R., Maier, W., 2007. Vestibular labyrinth diversity in diprotodontian marsupial mammals. *Mammal Study* 32, 83-97.
- Sherratt, E., Alejandrino, A., Kraemer, A.C., Serb, J.M., Adams, D.C., 2016. Trends in the sand: directional evolution in the shell shape of recessing scallops (Bivalvia: Pectinidae). *Evolution* 70, 2061-2073. doi:2010.1111/evo.12995.
- Sherratt, E., Gower, D.J., Klingenberg, C.P., Wilkinson, M., 2014. Evolution of cranial shape in caecilians (Amphibia: Gymnophiona). *Evolutionary Biology* 41, 528-545. doi:510.1007/s11692-11014-19287-11692.
- Sherratt, E., Sanders, K.L., Watson, A., Hutchinson, M.N., Lee, M.S.Y., Palci, A., 2019. Heterochronic shifts mediate ecomorphological convergence in skull shape of microcephalic sea snakes. *Integrative and Comparative Biology*, 1-9. doi:10.1093/icb/icz1033.
- Sherratt, E., Serb, J.M., Adams, D.C., 2017b. Rates of morphological evolution, asymmetry and morphological integration of shell shape in scallops. *BMC evolutionary biology* 17, 248. doi:210.1186/s12862-12017-11098-12865.
- Sherratt, E., Vidal-García, M., Anstis, M., Keogh, J.S., 2017a. Adult frogs and tadpoles have different macroevolutionary patterns across the Australian continent. *Nature Ecology & Evolution* 1, 1385-1391. doi:1310.1038/s41559-41017-40268-41556.
- Sidlauskas, B., 2008. Continuous and arrested morphological diversification in sister clades of characiform fishes: a phylomorphospace approach. *Evolution* 62, 3135-3156. doi:3110.1111/j.1558-5646.2008.00519.x.
- Smith, N.A., Clarke, J.A., 2012. Endocranial anatomy of the Charadriiformes: sensory system variation and the evolution of wing-propelled diving. *PLoS ONE* 7, e49584. doi:49510.41371/journal.pone.0049584.

- Smyth, G.K., Verbyla, A.P., 1996. A conditional likelihood approach to residual maximum likelihood estimation in generalized linear models. *Journal of the Royal Statistical Society: Series B (Methodological)* 58, 565-572.
- Sorenson, M.D., Cooper, A., Paxinos, E.E., Quinn, T.W., James, H.F., Olson, S.L., Fleischer, R.C., 1999. Relationships of the extinct moa-nalos, flightless Hawaiian waterfowl, based on ancient DNA. *Proceedings of the Royal Society of London. Series B: Biological Sciences* 266, 2187-2193.
- Sraml, M., Christidis, L., Easteal, S., Horn, P., Collet, C., 1996. Molecular relationships within Australasian waterfowl (Anseriformes). *Australian Journal of Zoology* 44, 47-58.
- Stein, R.W., Brown, J.W., Mooers, A.Ø., 2015. A molecular genetic time scale demonstrates Cretaceous origins and multiple diversification rate shifts within the order Galliformes (Aves). *Molecular Phylogenetics and Evolution* 92, 155-164. doi:110.1016/j.ympev.2015.1006.1005.
- Stingelin, W., 1957. *Vergleichende Morphologische Untersuchungen am Vorderhirn der Vögel auf Cytologischer und Cytoarchitektonischer Grundlage*. Verlag Helbing & Lichtenhahn, Basel. p.123.
- Swofford, D.L., 2003. *PAUP\*. Phylogenetic analysis using parsimony (\* and other methods)*. Version 4.0b10. Sunderland, MA: Sinauer Associates Inc.
- Symonds, M.R.E., Blomberg, S.P., 2014. A Primer on Phylogenetic Generalised Least Squares, in: Garamszegi, L.Z. (Ed.), *Modern Phylogenetic Comparative Methods and their Application in Evolutionary Biology*, Springer-Verlag, Berlin, pp. 105-130.
- Tambussi, C.P., Degrange, F.J., Ksepka, D.T., 2015. Endocranial anatomy of Antarctic Eocene stem penguins: implications for sensory system evolution in Sphenisciformes (Aves). *Journal of Vertebrate Paleontology* 35, e981635. doi:981610.981080/02724634.02722015.02981635.
- Tokita, M., Yano, W., James, H.F., Abzhanov, A., 2017. Cranial shape evolution in adaptive radiations of birds: comparative morphometrics of Darwin's finches and Hawaiian honeycreepers. *Philosophical Transactions of the Royal Society B: Biological Sciences* 372, 20150481. doi:20150410.20151098/rstb.20152015.20150481.
- Uyeda, J.C., Zenil-Ferguson, R., Pennell, M.W., 2018. Rethinking phylogenetic comparative methods. *Systematic Biology* 67, 1091-1109. doi:1010.1093/sysbio/syy1031.
- Walsh, S., Milner, A., 2011a. Evolution of the Avian Brain and Senses, in: Dyke, G., Kaiser, G. (Eds.), *Living Dinosaurs: The Evolutionary History of Modern Birds*, Wiley, Chichester, pp. 282-305.
- Walsh, S., Milner, A., 2011b. *Halcyornis toliapicus* (Aves: Lower Eocene, England) indicates advanced neuromorphology in Mesozoic Neornithes. *Journal of Systematic Palaeontology* 9, 173-181. doi:110.1080/14772019.14772010.14513703.
- Walsh, S.A., Knoll, F., 2018. The Evolution of Avian Intelligence and Sensory Capabilities: The Fossil Evidence, in: Bruner, E., Ogiwara, N., Tanabe, H.C. (Eds.), *Digital Endocasts: From Skulls to Brains*, Springer Japan, Tokyo, pp. 59-69. doi:10.1007/1978-1004-1431-56582-56586.
- Walsh, S.A., Knoll, M.A., 2011. Directions in palaeoneurology. *Special Papers in Palaeontology* 86, 263-279. doi:210.1111/j.1475-4983.2011.01085.x.
- Wiens, J.J., 2004. The role of morphological data in phylogeny reconstruction. *Systematic Biology* 53, 653-661. doi:650.1080/10635150490472959.

- Wild, J.M., 1987. The avian somatosensory system: connections of regions of body representation in the forebrain of the pigeon. *Brain Research* 412, 205-223.
- Wild, J.M., Arends, J.J.A., Zeigler, H.P., 1984. A trigeminal sensorimotor circuit for pecking, grasping and feeding in the pigeon (*Columba livia*). *Brain Research* 300, 146-151.
- Wild, J.M., Arends, J.J.A., Zeigler, H.P., 1985. Telencephalic connections of the trigeminal system in the pigeon (*Columba livia*): a trigeminal sensorimotor circuit. *Journal of Comparative Neurology* 234, 441-464.
- Wild, J.M., Farabaugh, S.M., 1996. Organization of afferent and efferent projections of the nucleus basalis prosencephali in a passerine, *Taeniopygia guttata*. *Journal of Comparative Neurology* 365, 306-328.
- Wiley, D.F., 2006. *Landmark Editor 3.0*. Institute for Data Analysis and Visualization, University of California, Davis. <http://graphics.idav.ucdavis.edu/research/EvoMorph>.
- Wiley, D.F., Amenta, N., Alcantara, D.A., Ghosh, D., Kil, Y.J., Delson, E., Harcourt-Smith, W., Rohlf, F.J., St John, K., Hamann, B., 2005. Evolutionary Morphing, in *Proceedings of IEEE Visualization 2005, IEEE*, pp. 431-438.
- Wilson, L.A.B., Hand, S.J., López-Aguirre, C., Archer, M., Black, K.H., Beck, R.M.D., Armstrong, K.N., Wroe, S., 2016. Cranial shape variation and phylogenetic relationships of extinct and extant Old World leaf-nosed bats. *Alcheringa* 40, 509-524. doi:10.1080/03115518.2016.112016.01196434.
- Worthy, T.H., 1988. Loss of flight ability in the extinct New Zealand duck *Euryanas finschi*. *Journal of Zoology, London* 215, 619-628.
- Worthy, T.H., 2008. Pliocene waterfowl (Aves: Anseriformes) from South Australia and a new genus and species. *Emu* 108, 153-165.
- Worthy, T.H., 2009. Descriptions and phylogenetic relationships of two new genera and four new species of Oligo-Miocene waterfowl (Aves: Anatidae) from Australia. *Zoological Journal of the Linnean Society* 156, 411-454.
- Worthy, T.H., Degrange, F.J., Handley, W.D., Lee, M.S.Y., 2017a. The evolution of giant flightless birds and novel phylogenetic relationships for extinct fowl (Aves, Galloanseres). *Royal Society Open Science* 4, 170975. doi:10.1098/rsos.170975.
- Worthy, T.H., Degrange, F.J., Handley, W.D., Lee, M.S.Y., 2017b. Correction to 'The evolution of giant flightless birds and novel phylogenetic relationships for extinct fowl (Aves, Galloanseres)'. *Royal Society Open Science* 4, 171621. doi:10.1098/rsos.171621.
- Worthy, T.H., Holdaway, R.N., 2002. *The Lost World of the Moa: Prehistoric Life of New Zealand*. Indiana University Press, Bloomington, IN. p760.
- Worthy, T.H., Lee, M.S.Y., 2008. Affinities of Miocene waterfowl (Anatidae: *Manuherikia*, *Dunstanetta* and *Miotadorna*) from the St Bathans Fauna, New Zealand. *Palaeontology* 51, 677-708. doi: 10.1111/j.1475-4983.2008.00778.x.
- Worthy, T.H., Olson, S.L., 2002. Relationships, adaptations, and habits of the extinct duck '*Euryanas finschi*'. *Notornis* 49, 1-17.
- Worthy, T.H., Tennyson, A.J.D., Hand, S.J., Scofield, R.P., 2008. A new species of the diving duck *Manuherikia* and evidence for geese (Aves: Anatidae: Anserinae) in the St Bathans Fauna (Early Miocene), New Zealand. *Journal of the Royal Society of New Zealand* 38, 97-114.

- Worthy, T.H., Tennyson, A.J.D., Jones, C., McNamara, J.A., Douglas, B.J., 2007. Miocene waterfowl and other birds from Central Otago, New Zealand. *Journal of Systematic Palaeontology* 5, 1-39. doi:10.1017/S1477201906001957.
- Worthy, T.H., Yates, A., 2017. A review of the smaller birds from the late Miocene Alcoota Local Faunas of Australia with a description of a new species, In: Hospitaleche, C.A., Agnolin, F.L., Haidr, N., Noriega, J.I., Tambussi, C.P. (Eds.), Proceedings of the 9th International Meeting of the Society of Avian Paleontology and Evolution, Diamante (Argentina), 1-6 August 2016. *Paleontología y Evolución de las Aves, Contribuciones del Museo Argentino de Ciencias Naturales* 7, pp. 221-252.
- Wylie, D.R.W., Gutiérrez-Ibáñez, C., Iwaniuk, A.N., 2015. Integrating brain, behavior, and phylogeny to understand the evolution of sensory systems in birds. *Frontiers in Neuroscience* 9, 281 (217pp). doi:210.3389/fnins.2015.00281.
- Yi, H., Norell, M.A., 2015. The burrowing origin of modern snakes. *Science Advances* 1, e1500743. doi:1500710.1501126/sciadv.1500743.
- Young, N.M., Linde-Medina, M., Fondon III, J.W., Hallgrímsson, B., Marcucio, R.S., 2017. Craniofacial diversification in the domestic pigeon and the evolution of the avian skull. *Nature Ecology & Evolution* 1, 0095. doi:0010.1038/s41559-41017-40095.
- Zelditch, M.L., Fink, W.L., Swiderski, D.L., 1995. Morphometrics, homology, and phylogenetics: quantified characters as synapomorphies. *Systematic Biology* 44, 179-189. doi:110.1093/sysbio/1044.1092.1179.
- Zuur, A., Ieno, E.N., Walker, N., Saveliev, A.A., Smith, G.M., 2009. *Mixed Effects Models and Extensions in Ecology with R*. Springer Science & Business Media LLC, New York. p.574.

## 5.8 APPENDICES

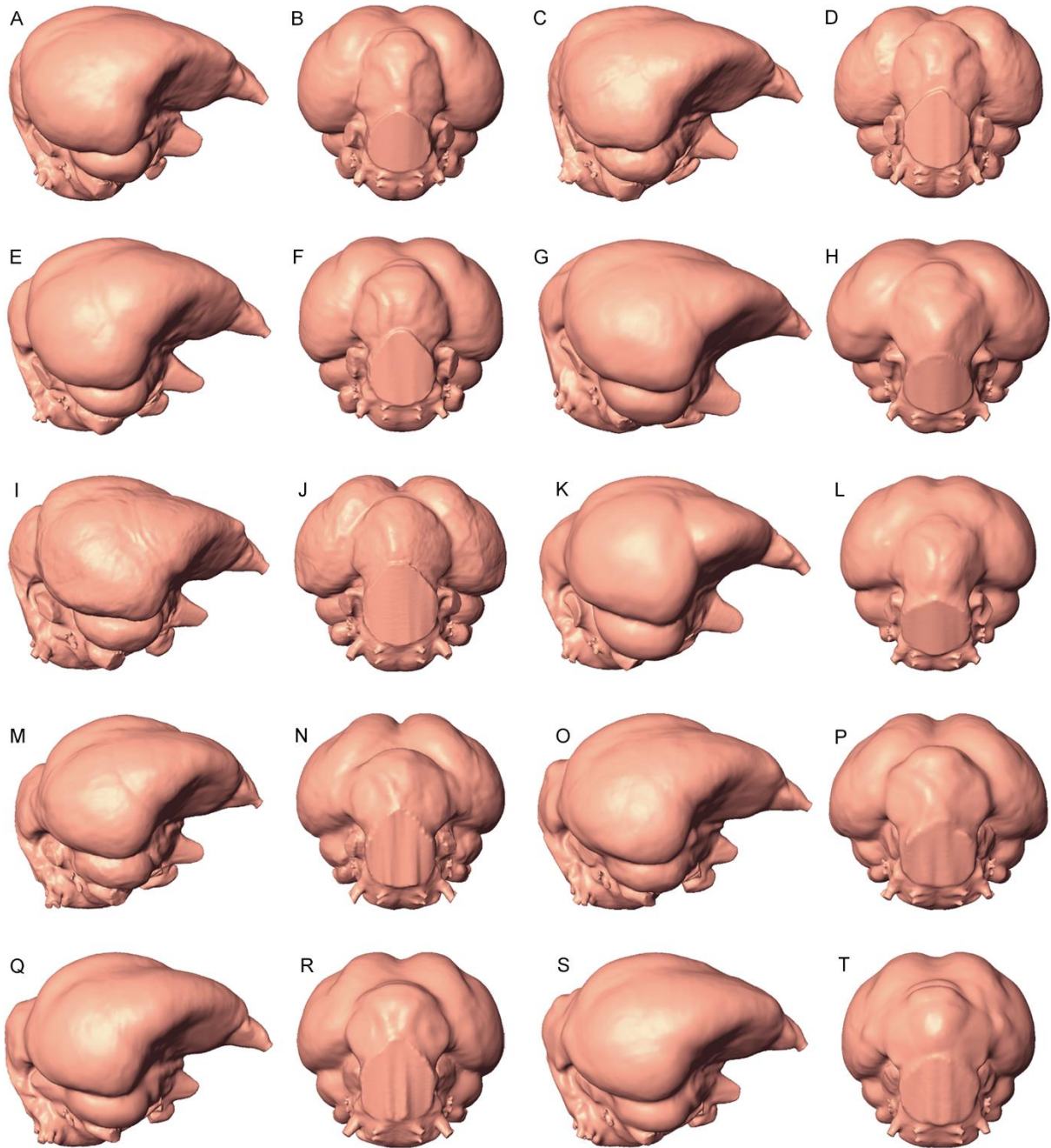


Figure A5.1. Anatine endocasts viewed from the RHS lateral (A, C, E, G, I, K, M, O, Q, S), and caudal (B, D, F, H, J, L, N, P, R, T) aspect, and presented in descending topological order (see Fig. 5.1). Endocast views are scaled to a common dorsoventral height, and are not representative of actual inter- and intraspecific size. A–B, *Anas platyrhynchos* (SAM B48742); C–D, *A. superciliosa* (SAM B38172); E–F, *A. castanea* (SAM B24479); G–H, *Lophodytes cucullatus* (SAM B47750); I–J, *Aythya australis* (SAM B33108); K–L, *Nettapus pulchellus* (SAM B45606); M–N, *Chenonetta finschi*.CR (NMNZ S.039838); O–P, *C. finschi*.HC (NMNZ S.034496); Q–R, *C. finschi*.GYL2 (NMNZ S.023695); S–T, *C. finschi*.GYL3 (NMNZ S.023702). **Abbreviations**, CR, Castle Rocks Fissure; GYL2, Honeycomb Hill Cave, Graveyard Layer 2; GYL3, Honeycomb Hill Cave, Graveyard Layer 3; HC, Hodges Creek Cave; NMNZ, Museum of New Zealand Te Papa; RHS, right hand side; SAM, South Australian Museum.

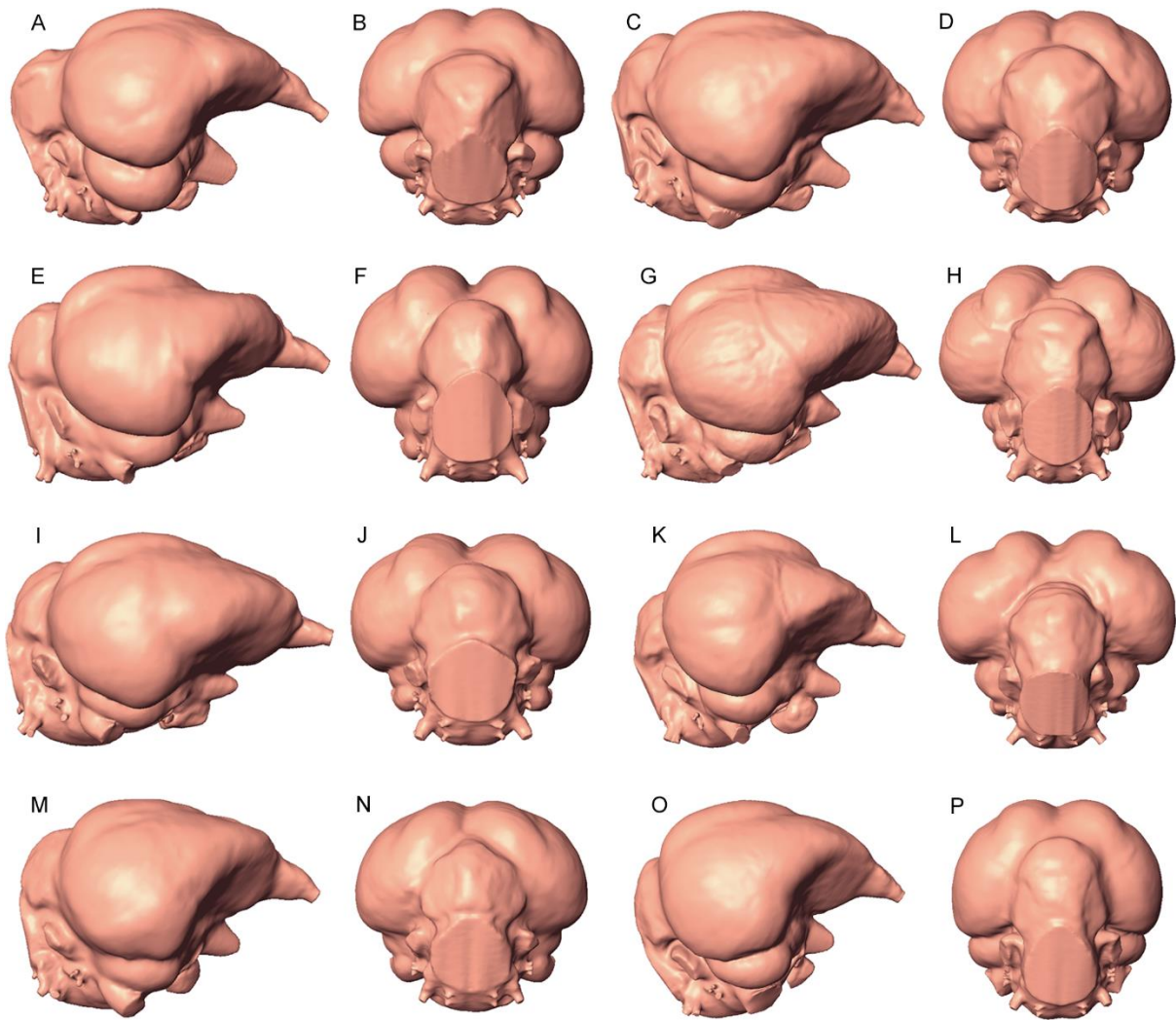


Figure A5.2. Anseriform endocasts viewed from the RHS lateral (A, C, E, G, I, K, M, O), and caudal (B, D, F, H, J, L, N, P) aspect, and presented in descending topological order (see Fig. 5.1). Endocast views are scaled to a common dorsoventral height, and are not representative of actual inter- and intraspecific size. A–B, *C. jubata* (SAM B39457); C–D, *Tadorna tadornoides* (SAM B39872); E–F, *Branta canadensis* (SAM B31086); G–H, *Anser caerulescens* (SAM B36868); I–J, *Cygnus atratus* (SAM B46123); K–L, *Cereopsis novaehollandiae* (SAM B39638); M–N, *Stictonetta naevosa* (SAM B56055); O–P, *Malacorhynchus membranaceus* (SAM B32483). **Abbreviations**, RHS, right hand side; SAM, South Australian Museum.

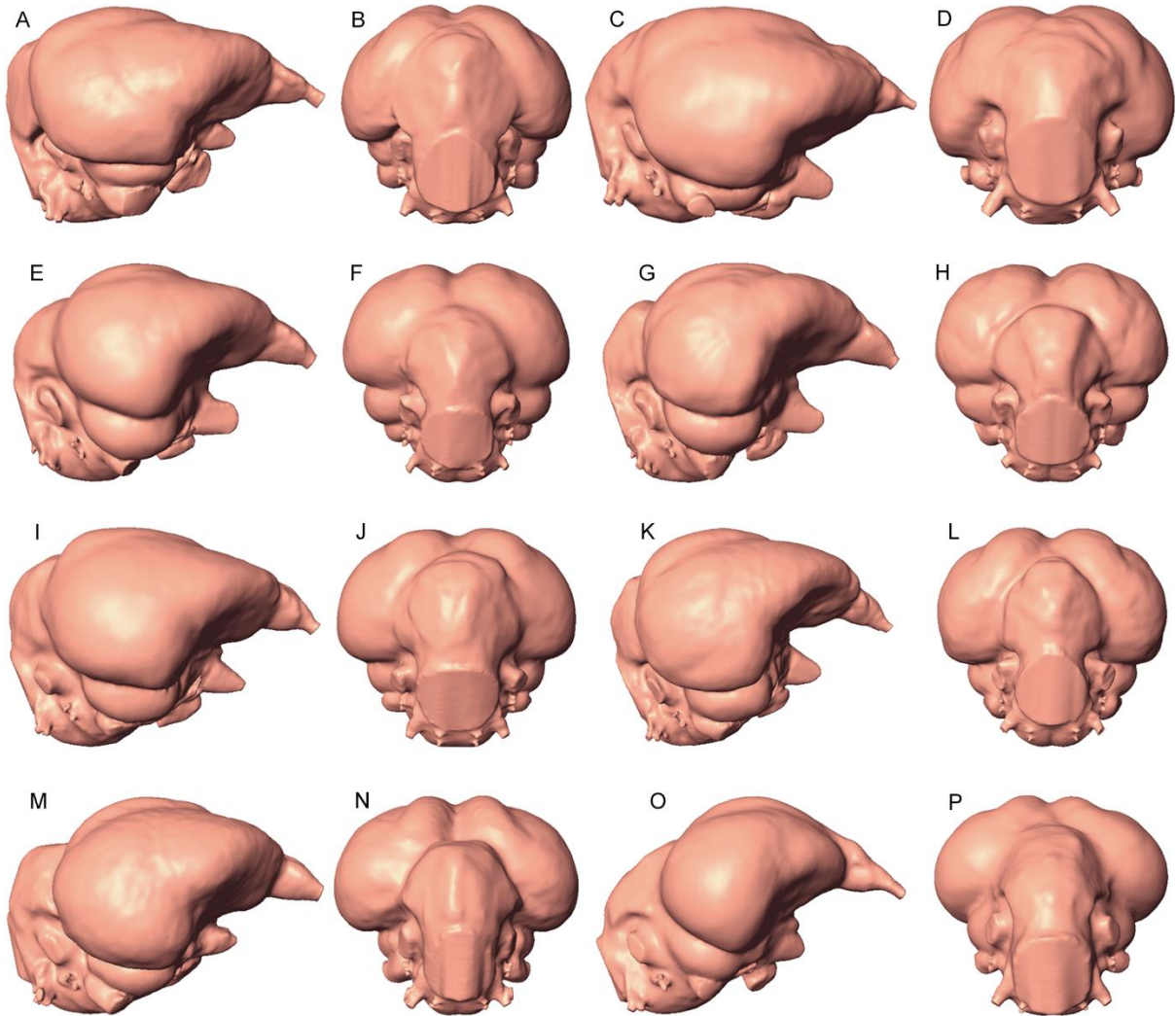


Figure A5.3. Anseriform endocasts viewed from the RHS lateral (**A, C, E, G, I, K, M, O**), and caudal (**B, D, F, H, J, L, N, P**) aspect, and presented in descending topological order (see Fig. 5.1). Endocast views are scaled to a common dorsoventral height, and are not representative of actual inter- and intraspecific size. **A–B**, *Oxyura australis* (SAM B31910); **C–D**, *Biziura lobata* (SAM B11405); **E–F**, *Mionetta blanchardi.2* (MNHN S.G.10002); **G–H**, *M. blanchardi.1* (MNHN S.G.10005); **I–J**, *Dendrocygna bicolor* (SAM B36869); **K–L**, *D. eytoni* (SAM B45769); **M–N**, *Anseranas semipalmata* (SAM B48035); **O–P**, *Anhima cornuta* (SAM B12574). **Abbreviations**, **RHS**, right hand side; **MNHN**, Muséum National d'Histoire Naturelle, Paris, France; **SAM**, South Australian Museum.

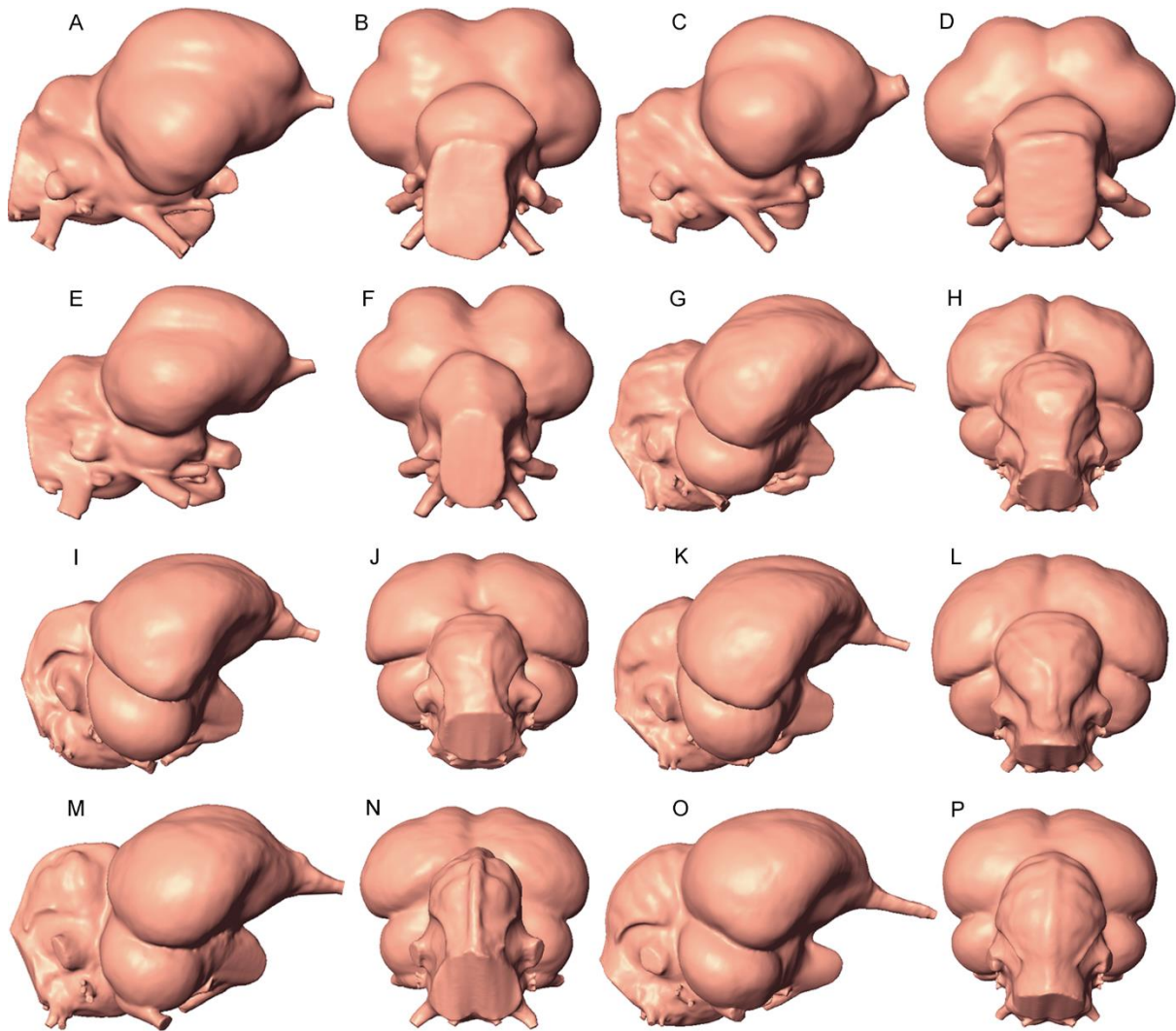


Figure A5.4. Galloansere endocasts viewed from the RHS lateral (A, C, E, G, I, K, M, O), and caudal (B, D, F, H, J, L, N, P) aspect, and presented in descending topological order (see Fig. 5.1). Endocast views are scaled to a common dorsoventral height, and are not representative of actual inter- and intraspecific size. A–B, *Dromornis planei* (NTM P9464-106); C–D, *D. murrayi* reconstruction (QM F57984 + QM F57974); E–F, *Ilbandornis woodburnei* (QVM:2000:GFV:20); G–H, *Talegalla fuscirostris* (KU 97007); I–J, *Leipoa ocellata* (SAM B11482); K–L, *Megapodius reinwardt* (ANWC O22869); M–N, *Gallus gallus* (SAM B34041); O–P, *Ortalis vetula* (SAM B13342). Note: dromornithid lateral endocasts (A, C, E) are scaled to a common dorsoventral height (dorsal eminencia sagittalis to ventral rhombencephalon). However, dromornithid caudal views (B, D, F) are presented at a smaller scale in order to fit the plate. Similarly, the olfactory (I) nerve of *G. gallus* (M) has been cropped to fit the plate; the full rostral extension of the (I) nerve in *G. gallus* is shown in Fig. A5.8M–N. **Abbreviations**, ANWC, Australian National Wildlife Collection, Canberra, Australia; **cm**, centimetres; **KU**, University of Kansas Natural History Museum, Lawrence, USA; **NTM**, Museum of Central Australia, Alice Springs, Northern Territory, Australia, **QM**, Queensland Museum, Brisbane, Queensland, Australia; **QVM**, Queen Victoria Museum and Art Gallery, Launceston, Tasmania; **RHS**, right hand side; **SAM**, South Australian Museum.

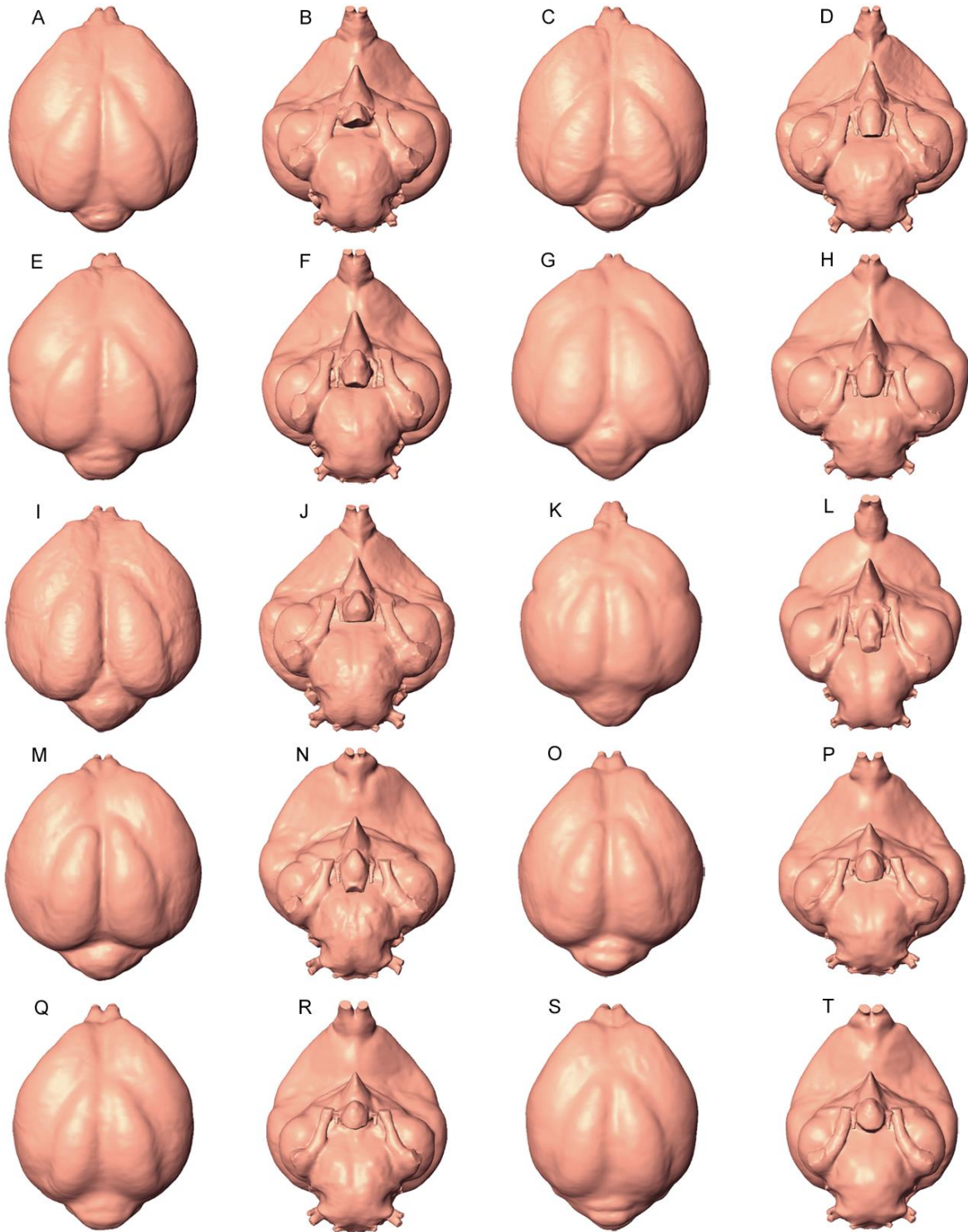


Figure A5.5. Anatine endocasts viewed from the dorsal (A, C, E, G, I, K, M, O, Q, S), and ventral (B, D, F, H, J, L, N, P, R, T) aspect, and presented in descending topological order (see Fig. 5.1). Endocasts are scaled to a common rostrocaudal length, and ventral views are scaled to taxon specific mediolateral endocast width. Thus, endocasts are not representative of actual inter- and intraspecific size. **A–B**, *Anas platyrhynchos* (SAM B48742); **C–D**, *A. superciliosa* (SAM B38172); **E–F**, *A. castanea* (SAM B24479); **G–H**, *Lophodytes cucullatus* (SAM B47750); **I–J**, *Aythya australis* (SAM B33108); **K–L**, *Nettapus pulchellus* (SAM B45606); **M–N**, *Chenonetta finschi*.CR (NMNZ S.039838); **O–P**, *C. finschi*.HC (NMNZ S.034496); **Q–R**, *C. finschi*.GYL2 (NMNZ S.023695); **S–T**, *C. finschi*.GYL3 (NMNZ S.023702).

**Abbreviations**, CR, Castle Rocks Fissure; GYL2, Honeycomb Hill Cave, Graveyard Layer 2; GYL3, Honeycomb Hill Cave, Graveyard Layer 3; HC, Hodges Creek Cave; NMNZ, Museum of New Zealand Te Papa; RHS, right hand side; SAM, South Australian Museum.

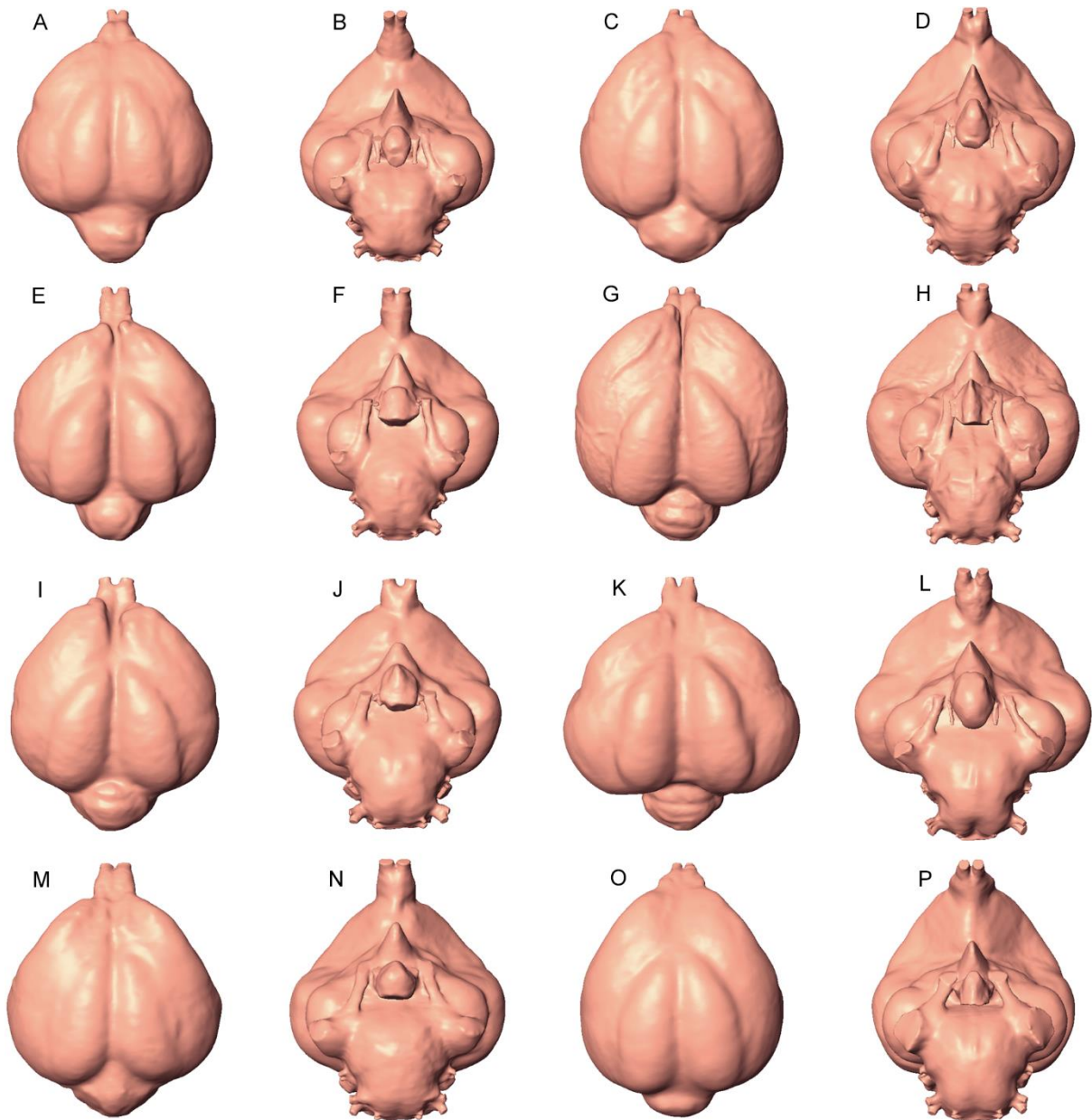


Figure A5.6. Anseriform endocasts viewed from the dorsal (A, C, E, G, I, K, M, O), and ventral (B, D, F, H, J, L, N, P) aspect, and presented in descending topological order (see Fig. 5.1). Endocasts are scaled to a common rostrocaudal length, and ventral views are scaled to taxon specific mediolateral endocast width. Thus, endocasts are not representative of actual inter- and intraspecific size. **A–B**, *C. jubata* (SAM B39457); **C–D**, *Tadorna tadornoides* (SAM B39872); **E–F**, *Branta canadensis* (SAM B31086); **G–H**, *Anser caerulescens* (SAM B36868); **I–J**, *Cygnus atratus* (SAM B46123); **K–L**, *Cereopsis novaehollandiae* (SAM B39638); **M–N**, *Stictonetta naevosa* (SAM B56055); **O–P**, *Malacorhynchus membranaceus* (SAM B32483). **Abbreviations**, **RHS**, right hand side; **SAM**, South Australian Museum.

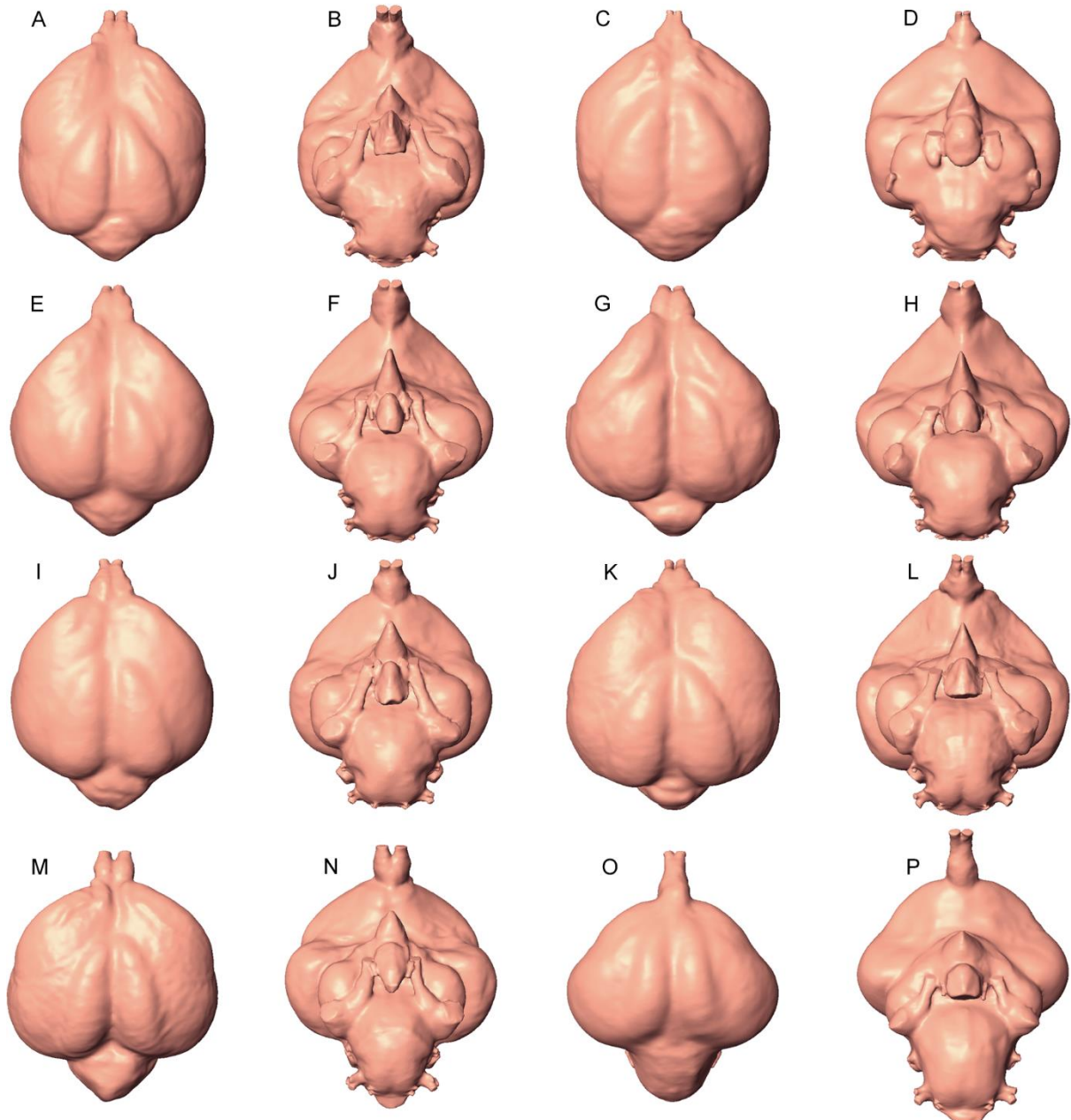


Figure A5.7. Anseriform endocasts viewed from the dorsal (A, C, E, G, I, K, M, O), and ventral (B, D, F, H, J, L, N, P) aspect, and presented in descending topological order (see Fig. 5.1). Endocasts are scaled to a common rostrocaudal length, and ventral views are scaled to taxon specific mediolateral endocast width. Thus, endocasts are not representative of actual inter- and intraspecific size. A–B, *Oxyura australis* (SAM B31910); C–D, *Biziura lobata* (SAM B11405); E–F, *Mionetta blanchardi.2* (MNHN S.G.10002); G–H, *M. blanchardi.1* (MNHN S.G.10005); I–J, *Dendrocygna bicolor* (SAM B36869); K–L, *D. eytoni* (SAM B45769); M–N, *Anseranas semipalmata* (SAM B48035); O–P, *Anhima cornuta* (SAM B12574). **Abbreviations**, RHS, right hand side; MNHN, Muséum National d'Histoire Naturelle, Paris, France; SAM, South Australian Museum.

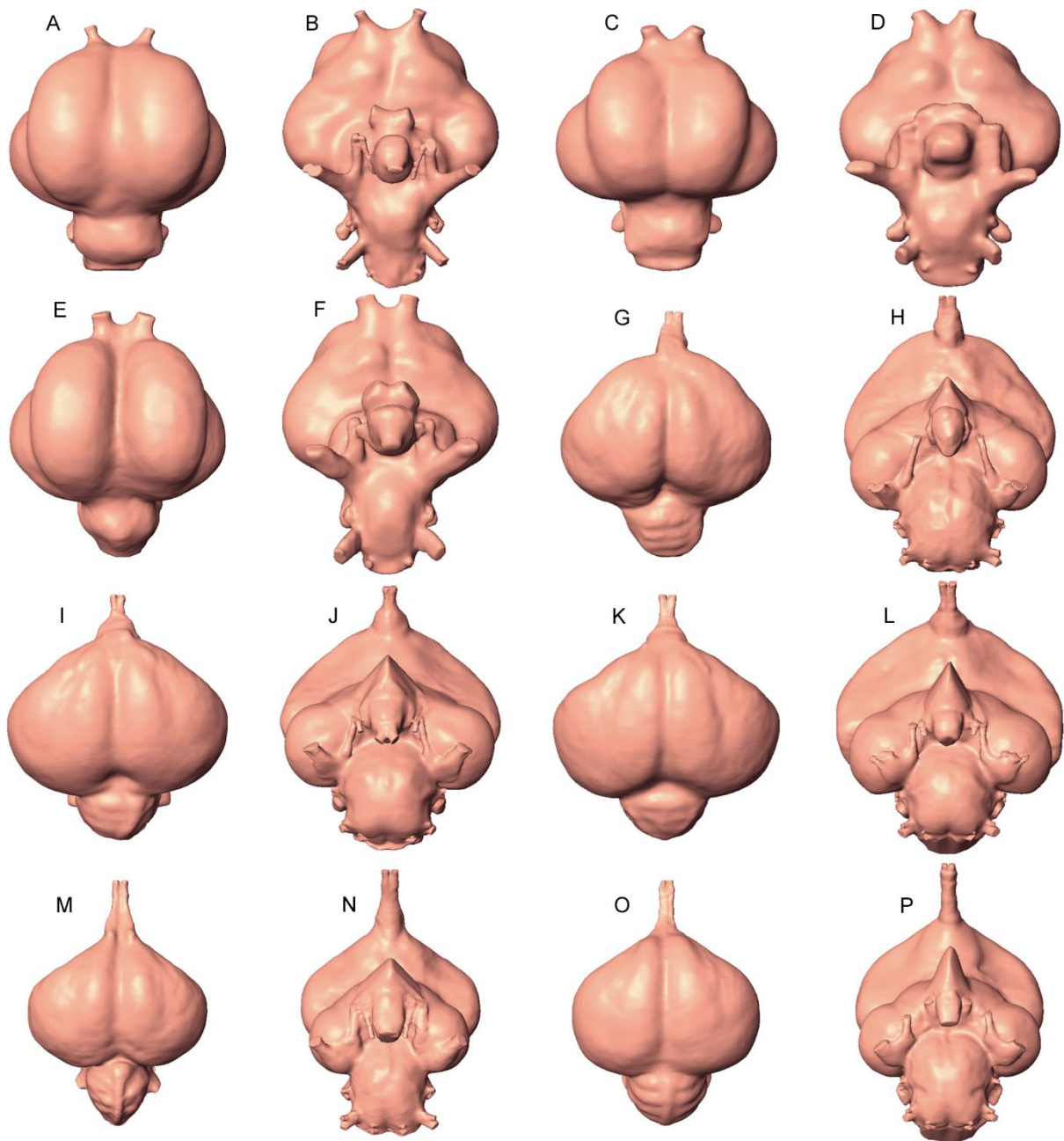


Figure A5.8. Galloansere endocasts viewed from the dorsal (A, C, E, G, I, K, M, O), and ventral (B, D, F, H, J, L, N, P) aspect, and presented in descending topological order (see Fig. 5.1). Endocasts are scaled to a common rostrocaudal length, and ventral views are scaled to taxon specific mediolateral endocast width. Thus, endocasts are not representative of actual inter- and intraspecific size. **A–B**, *Dromornis planei* (NTM P9464-106); **C–D**, *D. murrayi* reconstruction (QM F57984 + QM F57974); **E–F**, *Ibandornis woodburnei* (QVM:2000:GFV:20); **G–H**, *Talegalla fuscirostris* (KU 97007); **I–J**, *Leipoa ocellata* (SAM B11482); **K–L**, *Megapodius reinwardt* (ANWC O22869); **M–N**, *Gallus gallus* (SAM B34041); **O–P**, *Ortalis vetula* (SAM B13342). **Abbreviations**, ANWC, Australian National Wildlife Collection, Canberra, Australia; **KU**, University of Kansas Natural History Museum, Lawrence, USA; **NTM**, Museum of Central Australia, Alice Springs, Northern Territory, Australia, **QM**, Queensland Museum, Brisbane, Queensland, Australia; **QVM**, Queen Victoria Museum and Art Gallery, Launceston, Tasmania; **RHS**, right hand side; **SAM**, South Australian Museum.



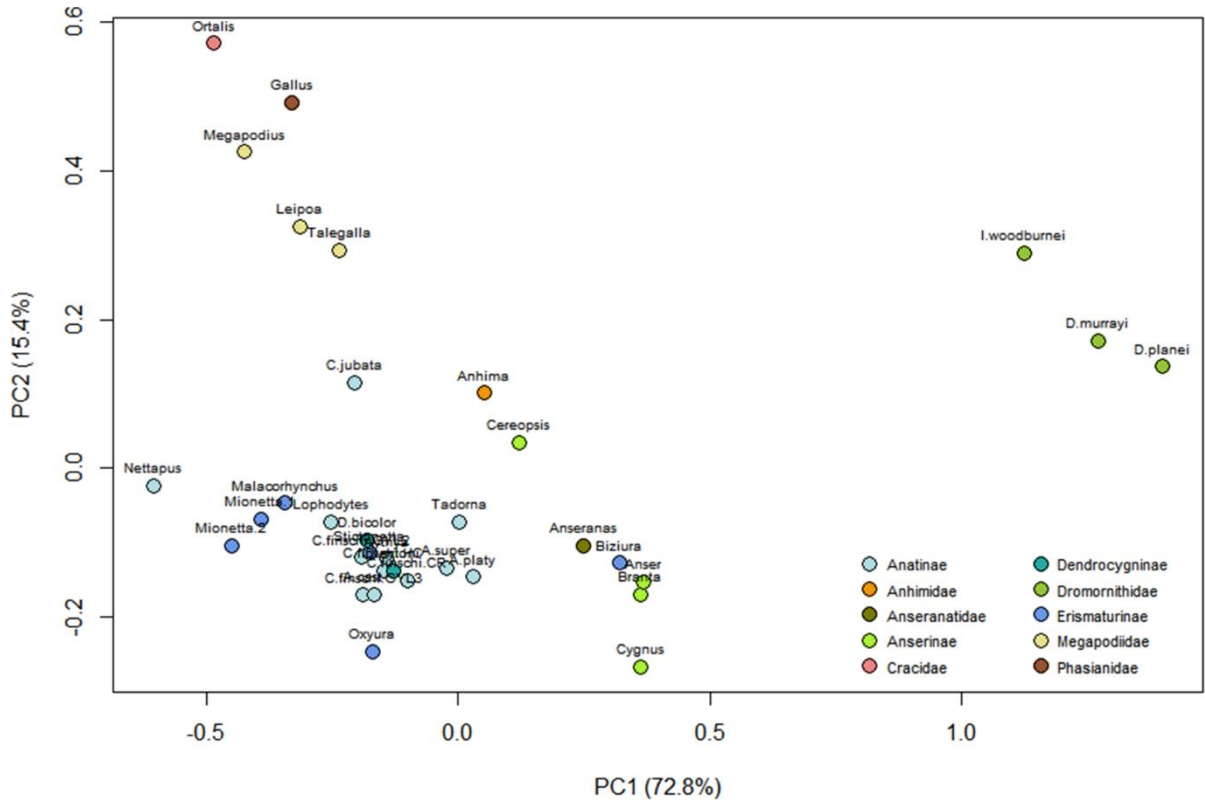


Figure A5.11. Complete Modular Distance data. PCA plot of all Distance modules used as response variables for phylogenetic assessments. Taxa are assigned Sub-Family factorial model colour coding (see Fig. 5.1A, Legend). For taxon abbreviations see Tables A5.6, A5.7.

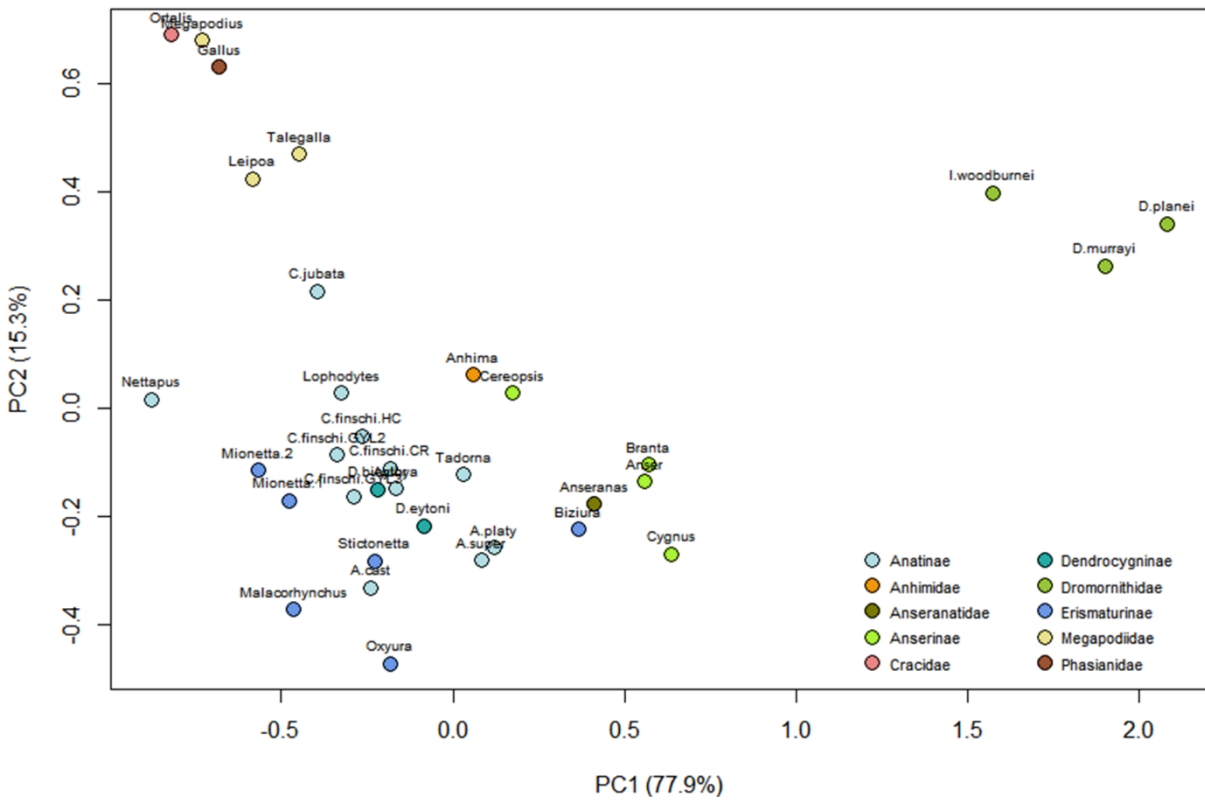


Figure A5.12. Complete Modular Surface Area data. PCA plot of all Surface Area modules used as response variables for phylogenetic assessments. Taxa are assigned Sub-Family factorial model colour coding (see Fig. 5.1A, Legend). For taxon abbreviations see Tables A5.6, A5.7.

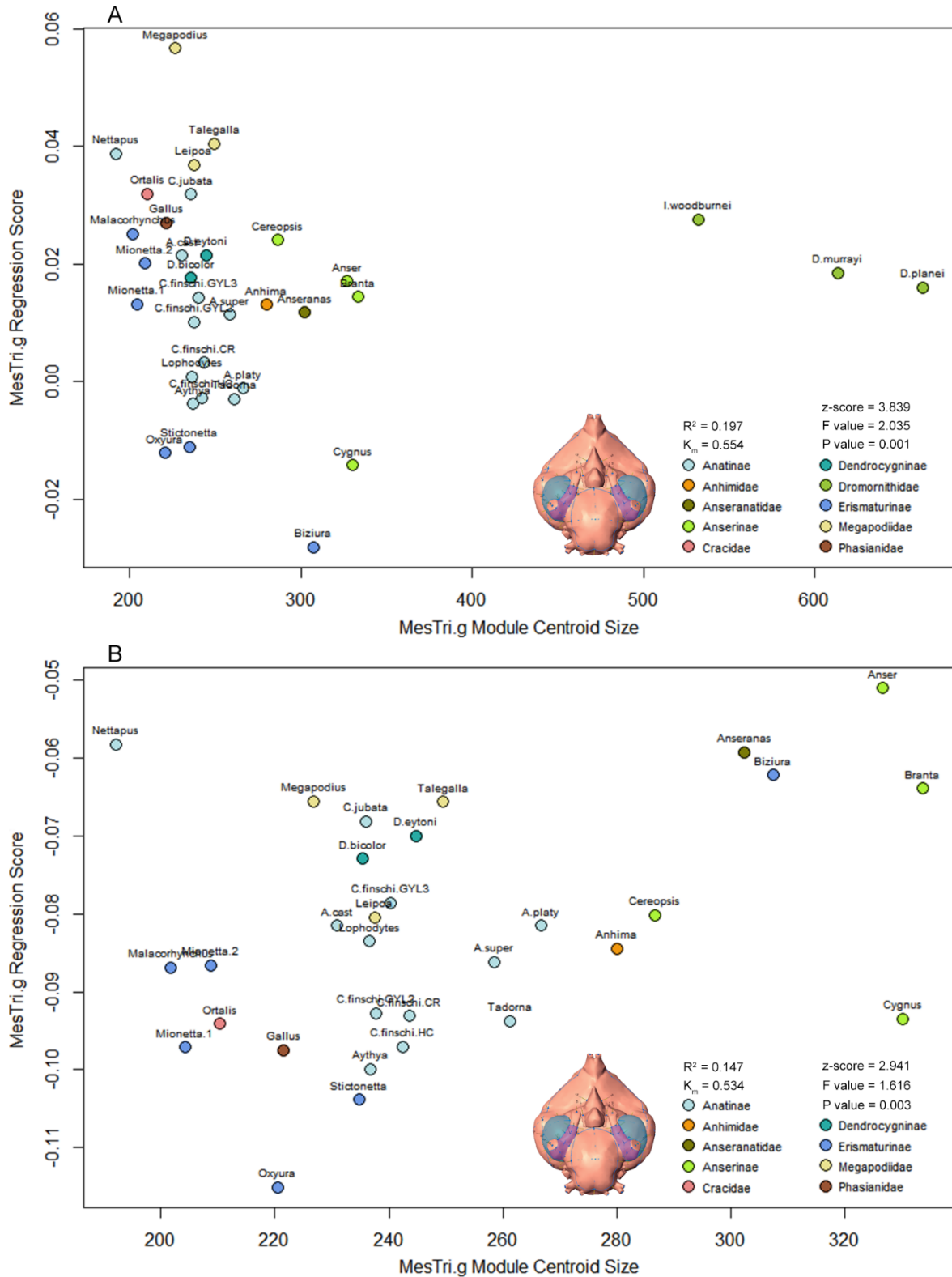


Figure A5.13. Modular Lm data. Mesencephalon + trigeminal ganglion distance-PGLS Sub-Family factorial model regression plots (see Fig. 5.1) representing the allometric relationship between mesencephalon + trigeminal ganglion shape and size. **A**, Complete Modular Lm data. **B**, Modular Lm data Dromornithids-excluded. **Insets**, *Aythya australis* (SAM B33108) ventral view, showing mesencephalon (blue) and trigeminal ganglion (purple) Lm modules (see Fig. 2.1). For taxon abbreviations see Tables A5.6, A5.7. **Abbreviations**,  $K_m$ , Adams'  $K_{mult}$ ; **Lm**, landmark; **MesTri.g**, mesencephalon + trigeminal ganglion; **PGLS**, phylogenetic generalised least squares;  $R^2$ , R squared; **Tri.g**, trigeminal ganglion.

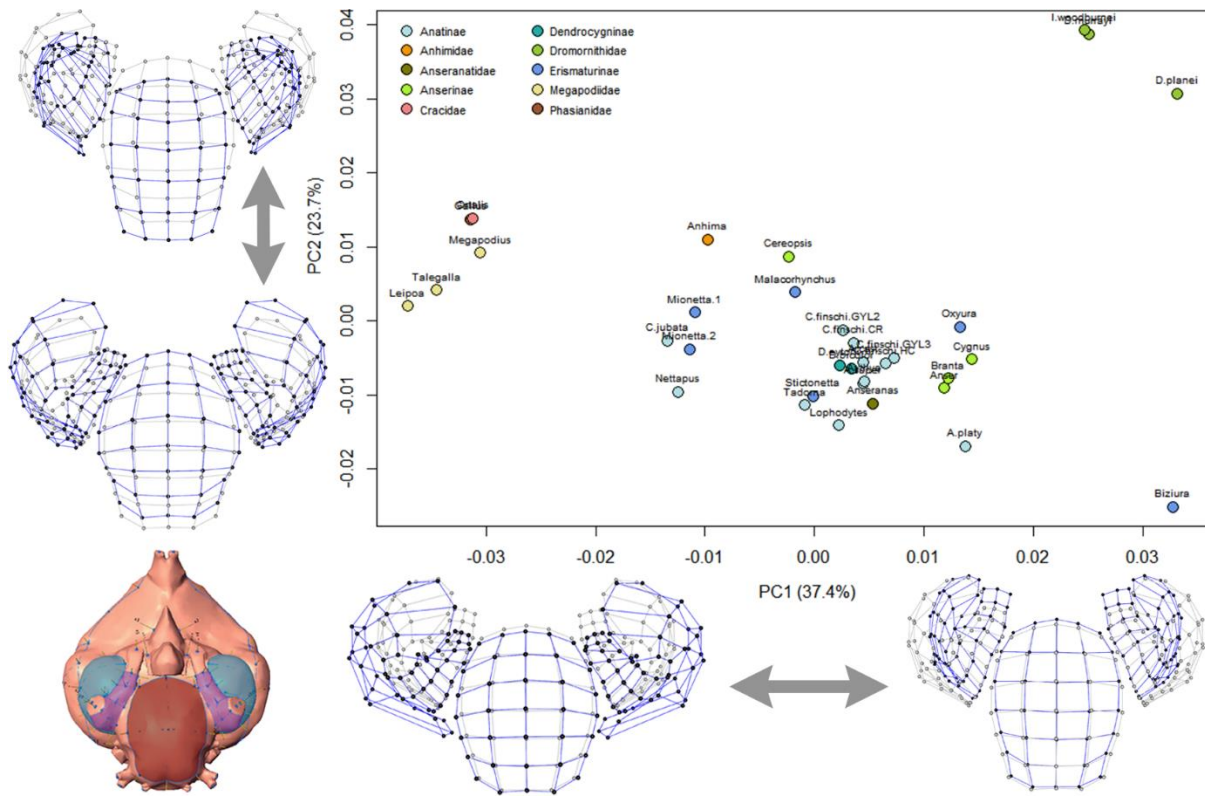


Figure A5.14. Complete Modular Lm data. PCA plot of mesencephalon, trigeminal ganglion and rhombencephalon Lm modules. Taxa are assigned Sub-Family factorial model colour coding (see Fig. 5.1A, Legend). **Inset.** *Aythya australis* (SAM B33108) endocast in ventral view, showing mesencephalon (blue), trigeminal ganglion (purple) and rhombencephalon (brown; see Fig. 2.1) Lm modules depicted by modular shape change plots presented across each PC axis. Modular shape change plots described by grey dots with grey links represent a mean modular configuration based on all specimens ( $n=34$ ). Mean modular configurations are overlain by modular shapes described by black dots with blue links, representing the modular shape extremes across respective PC axes. Mean modular configurations (grey) are scaled to the same size across both PC axes (see 5.2.7.2). For taxon abbreviations see Tables A5.6, A5.7. **Abbreviations, Lm**, landmark; **PC**, Principal Component; **PCA**, Principal Component Analysis; **SAM**, South Australian Museum.

Table A5.1. Modular Lm data: Phylogenetic signal and multivariate Procrustes distance-ANOVA PGLS factorial model fitting results for the Complete (**A**, **C**; n=34) and Dromornithids-excluded (**B**, **D**; n=31) data sets. **A–B**, phylogenetic signal assessed under Brownian motion assumptions for each endocast module conducted using the Geomorph function ‘physignal’ and Lm modules showing phylogenetic signal are highlighted green. **C–D**, model fitting conducted using the function ‘procDppls’ employing 999 RRPP permutations as implemented in Geomorph. Procrustes distance-ANOVA statistics are given for each of three categorical (Trophic Guild, Order, and Sub-Family) fitted model factors (see **5.2.7.4**), where non-significant results are highlighted pink. **Abbreviations**, ANOVA, analysis of variance; **Cer**, cerebellum; **Csize**, centroid size; **EmSg**, eminentia sagittalis; **K<sub>m</sub>**, Adams’ K<sub>mult</sub>; **Lm**, landmark; **Mes**, mesencephalon; **MesTri.g**, mesencephalon plus trigeminal ganglion Lm modules; **MShp**, modular shape; **PGLS**, phylogenetic generalised least squares; **Phylo.**, phylogenetic; **Rho**, rhombencephalon; **RRPP**, randomized residual permutation procedure; **SSq**, sum of squares; **Sub.Fam**, Sub-Family/Family; **Tel.c**, caudal telencephalon; **Tel.r**, rostral telencephalon; **Telen**, complete telencephalon; **Tr.Guild**, trophic guild; **Tri.g**, trigeminal ganglion; **X**, factorial variable; one of three categorical model factors: Trophic Guild, Order or Sub-Family (see Fig. 5.1; **5.2.6.4**); **Y**, response variable; one of nine endocast Lm modules (see **MShp**).

| A. Phylo. Signal  |                |         | C. Complete Modular Lm data: PGLS model = Y ~ Csize * X               |       |                |         |         |         |             |       |                |         |         |         |                |       |                |         |         |         |
|-------------------|----------------|---------|---|-------|----------------|---------|---------|---------|-------------|-------|----------------|---------|---------|---------|----------------|-------|----------------|---------|---------|---------|
| Modules<br>Y=MShp | Geomorph       |         | X = Trophic Guild   |       |                |         | ANOVA   |         | X = Order   |       |                |         | ANOVA   |         | X = Sub-Family |       |                |         | ANOVA   |         |
|                   | K <sub>m</sub> | P value | Effect  | SSq   | R <sup>2</sup> | z-score | F value | P value | Effect      | SSq   | R <sup>2</sup> | z-score | F value | P value | Effect         | SSq   | R <sup>2</sup> | z-score | F value | P value |
| EmSg              | 1.098          | 0.001   | Csize:Tr.Guild  | 0.002 | 0.068          | 3.224   | 1.038   | 0.001   | Csize:Order | 0.001 | 0.053          | 2.791   | 1.489   | 0.001   | Csize:Sub.Fam  | 0.003 | 0.101          | 3.238   | 1.146   | 0.002   |
| Tel.r             | 1.308          | 0.001   | Csize:Tr.Guild  | 0.002 | 0.078          | 1.432   | 0.877   | 0.091   | Csize:Order | 0.001 | 0.044          | 0.743   | 0.923   | 0.235   | Csize:Sub.Fam  | 0.005 | 0.155          | 2.880   | 1.387   | 0.002   |
| Tel.c             | 1.047          | 0.001   | Csize:Tr.Guild  | 0.002 | 0.053          | 1.054   | 0.665   | 0.153   | Csize:Order | 0.001 | 0.045          | 1.086   | 1.018   | 0.146   | Csize:Sub.Fam  | 0.004 | 0.128          | 2.793   | 1.249   | 0.002   |
| Telen             | 1.173          | 0.001   | Csize:Tr.Guild  | 0.004 | 0.065          | 1.413   | 0.773   | 0.09    | Csize:Order | 0.003 | 0.045          | 0.987   | 0.971   | 0.177   | Csize:Sub.Fam  | 0.009 | 0.141          | 3.074   | 1.319   | 0.002   |
| Mes               | 0.616          | 0.001   | Csize:Tr.Guild  | 0.004 | 0.207          | 5.327   | 3.150   | 0.001   | Csize:Order | 0.001 | 0.066          | 1.762   | 1.488   | 0.071   | Csize:Sub.Fam  | 0.004 | 0.218          | 3.525   | 2.354   | 0.001   |
| Tri.g             | 0.482          | 0.001   | Csize:Tr.Guild  | 0.002 | 0.119          | 2.995   | 1.431   | 0.002   | Csize:Order | 0.001 | 0.064          | 1.814   | 1.423   | 0.042   | Csize:Sub.Fam  | 0.003 | 0.172          | 3.563   | 1.694   | 0.001   |
| MesTri.g          | 0.554          | 0.001   | Csize:Tr.Guild  | 0.005 | 0.167          | 4.974   | 2.256   | 0.001   | Csize:Order | 0.002 | 0.065          | 1.919   | 1.458   | 0.046   | Csize:Sub.Fam  | 0.006 | 0.197          | 3.839   | 2.035   | 0.001   |
| Cer               | 2.755          | 0.001   | Csize:Tr.Guild  | 0.001 | 0.055          | 0.249   | 0.605   | 0.397   | Csize:Order | 0.000 | 0.024          | -1.120  | 0.397   | 0.877   | Csize:Sub.Fam  | 0.002 | 0.142          | 3.334   | 1.479   | 0.001   |
| Rho               | 0.893          | 0.001   | Csize:Tr.Guild  | 0.000 | 0.088          | 1.660   | 0.976   | 0.045   | Csize:Order | 0.000 | 0.042          | 0.325   | 0.811   | 0.393   | Csize:Sub.Fam  | 0.001 | 0.160          | 3.675   | 1.600   | 0.001   |
| B. Phylo. Signal  |                |         | D. Modular Lm data Dromornithids-excluded: PGLS model = Y ~ Csize * X |       |                |         |         |         |             |       |                |         |         |         |                |       |                |         |         |         |
| Modules           | K <sub>m</sub> |         | X = Trophic Guild   |       |                |         | ANOVA   |         | X = Order   |       |                |         | ANOVA   |         | X = Sub-Family |       |                |         | ANOVA   |         |
|                   | K <sub>m</sub> | P value | Effect  | SSq   | R <sup>2</sup> | z-score | F value | P value | Effect      | SSq   | R <sup>2</sup> | z-score | F value | P value | Effect         | SSq   | R <sup>2</sup> | z-score | F value | P value |
| EmSg              | 1.369          | 0.001   | Csize:Tr.Guild  | 0.001 | 0.091          | 1.886   | 1.145   | 0.024   | Csize:Order | 0.001 | 0.045          | 1.312   | 1.506   | 0.092   | Csize:Sub.Fam  | 0.002 | 0.114          | 1.770   | 1.019   | 0.03    |
| Tel.r             | 1.267          | 0.001   | Csize:Tr.Guild  | 0.002 | 0.077          | 0.923   | 0.917   | 0.173   | Csize:Order | 0.001 | 0.025          | 0.254   | 0.830   | 0.414   | Csize:Sub.Fam  | 0.004 | 0.162          | 2.125   | 1.432   | 0.013   |
| Tel.c             | 1.163          | 0.001   | Csize:Tr.Guild  | 0.001 | 0.031          | -0.596  | 0.418   | 0.719   | Csize:Order | 0.000 | 0.011          | -0.542  | 0.418   | 0.673   | Csize:Sub.Fam  | 0.002 | 0.087          | 1.335   | 0.869   | 0.087   |
| Telen             | 1.212          | 0.001   | Csize:Tr.Guild  | 0.003 | 0.052          | 0.362   | 0.669   | 0.351   | Csize:Order | 0.001 | 0.018          | -0.123  | 0.623   | 0.522   | Csize:Sub.Fam  | 0.006 | 0.122          | 1.920   | 1.151   | 0.032   |
| Mes               | 0.582          | 0.001   | Csize:Tr.Guild  | 0.003 | 0.175          | 4.686   | 3.018   | 0.001   | Csize:Order | 0.000 | 0.019          | 0.283   | 0.742   | 0.356   | Csize:Sub.Fam  | 0.003 | 0.170          | 2.914   | 1.943   | 0.001   |
| Tri.g             | 0.476          | 0.001   | Csize:Tr.Guild  | 0.001 | 0.094          | 2.286   | 1.259   | 0.009   | Csize:Order | 0.000 | 0.022          | 0.393   | 0.832   | 0.371   | Csize:Sub.Fam  | 0.001 | 0.120          | 2.393   | 1.254   | 0.005   |
| MesTri.g          | 0.534          | 0.001   | Csize:Tr.Guild  | 0.004 | 0.138          | 4.254   | 2.113   | 0.001   | Csize:Order | 0.001 | 0.021          | 0.314   | 0.783   | 0.353   | Csize:Sub.Fam  | 0.004 | 0.147          | 2.941   | 1.616   | 0.003   |
| Cer               | 2.618          | 0.001   | Csize:Tr.Guild  | 0.001 | 0.048          | 0.306   | 0.648   | 0.36    | Csize:Order | 0.000 | 0.008          | -1.311  | 0.252   | 0.918   | Csize:Sub.Fam  | 0.002 | 0.120          | 2.922   | 1.445   | 0.001   |
| Rho               | 1.059          | 0.001   | Csize:Tr.Guild  | 0.000 | 0.081          | 1.407   | 1.053   | 0.082   | Csize:Order | 0.000 | 0.022          | 0.151   | 0.749   | 0.463   | Csize:Sub.Fam  | 0.001 | 0.150          | 3.045   | 1.693   | 0.001   |

Table A5.2. Modular Distance values (mm) for the Complete (n=34) data set. Taxa are arranged in descending topological order (see Fig. 5.1). **Abbreviations**, **Cer L**, cerebellum length; **Cer W**, cerebellum width; **EmSg L**, eminentia sagittalis length; **EmSg W**, eminentia sagittalis width; **Mes L**, mesencephalon length; **Mes W**, mesencephalon width; **mm**, millimetres; **mm<sup>3</sup>**, cubic millimetres; **Rho L**, rhombencephalon length; **Rho W**, rhombencephalon width; **Tel.c L**, caudal telencephalon length; **Tel.c W**, caudal telencephalon width; **Tel.r L**, rostral telencephalon length; **Tel.r W**, rostral telencephalon width; **Telen L**, total telencephalon length; **Tri.g L**, trigeminal ganglion length; **Tri.g W**, trigeminal ganglion width; **Vol**, endocast volume (mm<sup>3</sup>). For taxon abbreviations see Tables A5.6, A5.7.

| Taxon                  | Vol       | EmSg L | EmSg W | Tel.r L | Tel.r W | Tel.c L | Tel.c W | Telen L | Mes L | Mes W | Tri.g L | Tri.g W | Cer L | Cer W | Rho L | Rho W |
|------------------------|-----------|--------|--------|---------|---------|---------|---------|---------|-------|-------|---------|---------|-------|-------|-------|-------|
| <i>A. platy</i>        | 7197.62   | 22.14  | 9.03   | 17.99   | 8.97    | 12.21   | 16.26   | 30.20   | 14.56 | 5.51  | 9.28    | 2.40    | 11.21 | 14.72 | 14.23 | 9.21  |
| <i>A. super</i>        | 6375.13   | 20.23  | 8.97   | 16.44   | 8.95    | 11.49   | 15.08   | 27.93   | 15.29 | 5.18  | 9.22    | 2.69    | 10.27 | 13.90 | 12.93 | 9.18  |
| <i>A. cast</i>         | 4710.47   | 17.00  | 7.29   | 15.65   | 8.57    | 9.98    | 13.99   | 25.64   | 13.32 | 4.74  | 7.97    | 2.42    | 8.65  | 13.13 | 11.87 | 9.34  |
| <i>Lophodytes</i>      | 4861.23   | 19.30  | 8.47   | 13.19   | 7.01    | 12.43   | 13.58   | 25.61   | 13.24 | 4.34  | 6.88    | 1.75    | 10.28 | 11.49 | 9.73  | 8.63  |
| <i>Aythya</i>          | 5070.56   | 18.33  | 8.23   | 13.78   | 8.01    | 11.17   | 14.83   | 24.95   | 14.08 | 4.46  | 8.11    | 2.43    | 8.28  | 14.32 | 12.31 | 8.97  |
| <i>Nettapus</i>        | 2701.19   | 12.93  | 5.58   | 8.17    | 7.42    | 11.50   | 12.03   | 19.67   | 12.19 | 4.92  | 5.71    | 1.31    | 7.93  | 10.29 | 8.20  | 6.21  |
| <i>C. finschi.CR</i>   | 5470.17   | 20.01  | 8.76   | 15.55   | 8.47    | 11.14   | 13.96   | 26.69   | 13.24 | 4.19  | 7.58    | 2.52    | 9.37  | 15.38 | 11.11 | 9.31  |
| <i>C. finschi.HC</i>   | 5473.45   | 20.25  | 8.86   | 14.96   | 8.22    | 11.15   | 13.65   | 26.11   | 12.73 | 4.27  | 7.08    | 2.18    | 10.22 | 14.11 | 10.77 | 8.98  |
| <i>C. finschi.GYL2</i> | 5129.47   | 18.61  | 8.29   | 15.16   | 8.22    | 10.75   | 13.14   | 25.90   | 12.91 | 4.95  | 6.57    | 2.36    | 8.45  | 13.75 | 10.93 | 8.69  |
| <i>C. finschi.GYL3</i> | 5318.97   | 19.23  | 8.63   | 15.51   | 8.49    | 10.27   | 13.27   | 25.78   | 11.92 | 4.39  | 7.07    | 2.13    | 10.11 | 15.09 | 10.93 | 8.75  |
| <i>C. jubata</i>       | 4806.77   | 16.92  | 7.61   | 10.36   | 7.08    | 14.59   | 14.46   | 24.95   | 15.41 | 6.64  | 5.91    | 2.10    | 10.75 | 15.05 | 10.53 | 8.65  |
| <i>Tadorna</i>         | 6696.64   | 19.52  | 8.47   | 15.23   | 8.34    | 13.19   | 15.61   | 28.42   | 14.66 | 4.51  | 8.52    | 2.99    | 11.63 | 14.84 | 13.33 | 9.78  |
| <i>Branta</i>          | 14310.75  | 25.80  | 13.43  | 21.08   | 11.37   | 16.94   | 21.69   | 38.02   | 15.67 | 4.59  | 9.63    | 3.09    | 12.79 | 18.54 | 16.85 | 11.55 |
| <i>Anser</i>           | 13627.95  | 26.34  | 12.07  | 21.56   | 12.28   | 17.57   | 21.14   | 39.13   | 15.75 | 6.16  | 10.43   | 2.68    | 15.45 | 19.31 | 16.18 | 11.45 |
| <i>Cygnus</i>          | 14142.86  | 24.79  | 11.41  | 20.90   | 13.06   | 16.01   | 20.14   | 36.90   | 15.42 | 2.86  | 10.71   | 3.64    | 14.45 | 19.63 | 15.84 | 12.54 |
| <i>Cereopsis</i>       | 8841.18   | 22.20  | 10.07  | 14.78   | 8.78    | 17.86   | 19.26   | 32.64   | 14.77 | 6.23  | 6.94    | 2.55    | 13.22 | 16.27 | 13.17 | 11.03 |
| <i>Stictonetta</i>     | 4879.81   | 16.65  | 7.67   | 13.31   | 7.80    | 11.41   | 13.61   | 24.72   | 12.73 | 3.52  | 8.70    | 3.01    | 9.62  | 11.45 | 11.99 | 8.80  |
| <i>Malacorhynchus</i>  | 3100.25   | 15.32  | 7.66   | 12.10   | 6.37    | 9.96    | 12.13   | 22.05   | 11.58 | 4.30  | 7.01    | 2.68    | 8.16  | 11.43 | 9.93  | 6.66  |
| <i>Oxyura</i>          | 4320.38   | 16.06  | 6.91   | 14.17   | 9.93    | 9.36    | 13.97   | 23.53   | 12.08 | 2.50  | 8.38    | 3.22    | 11.33 | 13.66 | 11.07 | 8.97  |
| <i>Biziura</i>         | 11436.29  | 24.59  | 11.72  | 20.13   | 10.93   | 13.14   | 17.47   | 33.27   | 6.92  | 7.72  | 12.99   | 4.72    | 14.60 | 16.98 | 12.98 | 11.95 |
| <i>Mionetta.2</i>      | 3438.02   | 13.29  | 5.88   | 12.34   | 7.70    | 9.62    | 12.60   | 21.96   | 13.32 | 4.79  | 6.04    | 1.64    | 10.03 | 10.51 | 10.40 | 8.16  |
| <i>Mionetta.1</i>      | 3098.34   | 14.52  | 6.58   | 12.10   | 6.29    | 10.10   | 11.46   | 22.20   | 12.51 | 4.33  | 7.16    | 1.95    | 9.46  | 11.83 | 10.42 | 8.00  |
| <i>D. bicolor</i>      | 5102.09   | 15.89  | 7.40   | 12.10   | 8.80    | 12.81   | 14.95   | 24.90   | 12.12 | 4.27  | 7.31    | 1.95    | 12.44 | 15.46 | 11.42 | 9.05  |
| <i>D. eytoni</i>       | 5512.83   | 17.42  | 8.09   | 14.45   | 9.01    | 13.07   | 15.15   | 27.51   | 13.38 | 4.55  | 8.55    | 2.04    | 11.15 | 13.58 | 11.72 | 8.49  |
| <i>Anseranas</i>       | 10881.35  | 21.12  | 8.99   | 17.73   | 11.93   | 17.52   | 22.18   | 35.25   | 15.87 | 4.85  | 9.60    | 3.32    | 15.27 | 17.55 | 14.54 | 10.03 |
| <i>Anhima</i>          | 8031.85   | 19.71  | 8.00   | 10.37   | 8.13    | 17.30   | 18.43   | 27.66   | 13.37 | 4.67  | 7.95    | 3.03    | 17.53 | 13.63 | 13.64 | 12.39 |
| <i>D. planei</i>       | 122859.93 | 67.65  | 34.43  | N/A     | N/A     | 49.71   | 40.61   | N/A     | 19.11 | 5.96  | 13.76   | 9.20    | 20.85 | 45.99 | 26.82 | 18.02 |
| <i>D. murrayi</i>      | 95577.71  | 55.90  | 27.63  | N/A     | N/A     | 47.26   | 41.14   | N/A     | 16.96 | 6.75  | 13.47   | 9.56    | 17.79 | 37.87 | 25.65 | 18.19 |
| <i>I. woodburnei</i>   | 60289.34  | 51.32  | 28.87  | N/A     | N/A     | 41.88   | 30.52   | N/A     | 16.72 | 8.02  | 12.30   | 9.18    | 21.24 | 33.21 | 23.47 | 13.83 |
| <i>Talegalla</i>       | 5168.22   | 15.98  | 6.77   | 8.12    | 5.71    | 16.25   | 13.55   | 24.37   | 16.78 | 7.48  | 5.70    | 2.31    | 13.74 | 13.85 | 11.24 | 9.17  |
| <i>Leipoa</i>          | 4519.27   | 14.51  | 5.88   | 9.59    | 5.45    | 12.75   | 13.40   | 22.34   | 18.25 | 7.81  | 4.32    | 3.76    | 10.95 | 9.91  | 10.71 | 9.51  |
| <i>Megapodius</i>      | 3944.34   | 16.26  | 6.74   | 7.16    | 3.82    | 15.51   | 13.34   | 22.67   | 16.91 | 6.56  | 4.66    | 2.41    | 13.68 | 8.56  | 8.91  | 6.96  |
| <i>Gallus</i>          | 3733.84   | 13.72  | 5.84   | 5.59    | 4.02    | 15.46   | 12.91   | 21.06   | 15.08 | 5.98  | 5.96    | 4.83    | 12.73 | 10.71 | 9.69  | 7.66  |
| <i>Ortalis</i>         | 3210.97   | 15.56  | 6.17   | 6.04    | 2.14    | 15.12   | 11.62   | 21.16   | 13.57 | 6.44  | 4.46    | 2.54    | 12.21 | 11.77 | 9.04  | 8.44  |

Table A5.3. Modular Distance ratios for the Complete (n=34) data set. Taxa are arranged in descending topological order (see Fig. 5.1). **Abbreviations**, **Cer L**, cerebellum length; **Cer W**, cerebellum width; **EmSg L**, eminentia sagittalis length; **EmSg W**, eminentia sagittalis width; **Mes L**, mesencephalon length; **Mes W**, mesencephalon width; **Rho L**, rhombencephalon length; **Rho W**, rhombencephalon width; **Tel.c L**, caudal telencephalon length; **Tel.c W**, caudal telencephalon width; **Tel.r L**, rostral telencephalon length; **Tel.r W**, rostral telencephalon width; **Telen L**, total telencephalon length; **Tri.g L**, trigeminal ganglion length; **Tri.g W**, trigeminal ganglion width. For taxon abbreviations see Tables A5.6, A5.7.

| Taxon                  | EmSg L | EmSg W | Tel.r L | Tel.r W | Tel.c L | Tel.c W | Telen L | Mes L | Mes W | Tri.g L | Tri.g W | Cer L | Cer W | Rho L | Rho W |
|------------------------|--------|--------|---------|---------|---------|---------|---------|-------|-------|---------|---------|-------|-------|-------|-------|
| <i>A. platy</i>        | 0.349  | 0.248  | 0.325   | 0.247   | 0.282   | 0.314   | 0.384   | 0.302 | 0.192 | 0.251   | 0.098   | 0.272 | 0.303 | 0.299 | 0.250 |
| <i>A. super</i>        | 0.343  | 0.250  | 0.320   | 0.250   | 0.279   | 0.310   | 0.380   | 0.311 | 0.188 | 0.254   | 0.113   | 0.266 | 0.300 | 0.292 | 0.253 |
| <i>A. cast</i>         | 0.335  | 0.235  | 0.325   | 0.254   | 0.272   | 0.312   | 0.384   | 0.306 | 0.184 | 0.245   | 0.104   | 0.255 | 0.304 | 0.293 | 0.264 |
| <i>Lophodytes</i>      | 0.349  | 0.252  | 0.304   | 0.229   | 0.297   | 0.307   | 0.382   | 0.304 | 0.173 | 0.227   | 0.066   | 0.274 | 0.288 | 0.268 | 0.254 |
| <i>Aythya</i>          | 0.341  | 0.247  | 0.307   | 0.244   | 0.283   | 0.316   | 0.377   | 0.310 | 0.175 | 0.245   | 0.104   | 0.248 | 0.312 | 0.294 | 0.257 |
| <i>Nettapus</i>        | 0.324  | 0.218  | 0.266   | 0.254   | 0.309   | 0.315   | 0.377   | 0.316 | 0.202 | 0.221   | 0.034   | 0.262 | 0.295 | 0.266 | 0.231 |
| <i>C. finschi.CR</i>   | 0.348  | 0.252  | 0.319   | 0.248   | 0.280   | 0.306   | 0.382   | 0.300 | 0.166 | 0.235   | 0.107   | 0.260 | 0.318 | 0.280 | 0.259 |
| <i>C. finschi.HC</i>   | 0.349  | 0.253  | 0.314   | 0.245   | 0.280   | 0.304   | 0.379   | 0.296 | 0.169 | 0.227   | 0.091   | 0.270 | 0.307 | 0.276 | 0.255 |
| <i>C. finschi.GYL2</i> | 0.342  | 0.248  | 0.318   | 0.247   | 0.278   | 0.302   | 0.381   | 0.299 | 0.187 | 0.220   | 0.100   | 0.250 | 0.307 | 0.280 | 0.253 |
| <i>C. finschi.GYL3</i> | 0.345  | 0.251  | 0.320   | 0.249   | 0.272   | 0.301   | 0.379   | 0.289 | 0.173 | 0.228   | 0.088   | 0.270 | 0.316 | 0.279 | 0.253 |
| <i>C. jubata</i>       | 0.334  | 0.239  | 0.276   | 0.231   | 0.316   | 0.315   | 0.379   | 0.323 | 0.223 | 0.210   | 0.088   | 0.280 | 0.320 | 0.278 | 0.255 |
| <i>Tadorna</i>         | 0.337  | 0.243  | 0.309   | 0.241   | 0.293   | 0.312   | 0.380   | 0.305 | 0.171 | 0.243   | 0.124   | 0.279 | 0.306 | 0.294 | 0.259 |
| <i>Branta</i>          | 0.340  | 0.271  | 0.319   | 0.254   | 0.296   | 0.322   | 0.380   | 0.288 | 0.159 | 0.237   | 0.118   | 0.266 | 0.305 | 0.295 | 0.256 |
| <i>Anser</i>           | 0.344  | 0.262  | 0.323   | 0.263   | 0.301   | 0.321   | 0.385   | 0.290 | 0.191 | 0.246   | 0.104   | 0.288 | 0.311 | 0.292 | 0.256 |
| <i>Cygnus</i>          | 0.336  | 0.255  | 0.318   | 0.269   | 0.290   | 0.314   | 0.378   | 0.286 | 0.110 | 0.248   | 0.135   | 0.279 | 0.311 | 0.289 | 0.265 |
| <i>Cereopsis</i>       | 0.341  | 0.254  | 0.296   | 0.239   | 0.317   | 0.326   | 0.384   | 0.296 | 0.201 | 0.213   | 0.103   | 0.284 | 0.307 | 0.284 | 0.264 |
| <i>Stictonetta</i>     | 0.331  | 0.240  | 0.305   | 0.242   | 0.287   | 0.307   | 0.378   | 0.300 | 0.148 | 0.255   | 0.130   | 0.267 | 0.287 | 0.292 | 0.256 |
| <i>Malacorhynchus</i>  | 0.340  | 0.253  | 0.310   | 0.230   | 0.286   | 0.310   | 0.385   | 0.305 | 0.181 | 0.242   | 0.122   | 0.261 | 0.303 | 0.285 | 0.236 |
| <i>Oxyura</i>          | 0.332  | 0.231  | 0.317   | 0.274   | 0.267   | 0.315   | 0.377   | 0.298 | 0.109 | 0.254   | 0.140   | 0.290 | 0.312 | 0.287 | 0.262 |
| <i>Biziura</i>         | 0.343  | 0.263  | 0.321   | 0.256   | 0.276   | 0.306   | 0.375   | 0.207 | 0.219 | 0.274   | 0.166   | 0.287 | 0.303 | 0.274 | 0.265 |
| <i>Mionetta.2</i>      | 0.318  | 0.218  | 0.309   | 0.251   | 0.278   | 0.311   | 0.379   | 0.318 | 0.193 | 0.221   | 0.061   | 0.283 | 0.289 | 0.288 | 0.258 |
| <i>Mionetta.1</i>      | 0.333  | 0.234  | 0.310   | 0.229   | 0.288   | 0.303   | 0.386   | 0.314 | 0.182 | 0.245   | 0.083   | 0.279 | 0.307 | 0.292 | 0.259 |
| <i>D. bicolor</i>      | 0.324  | 0.234  | 0.292   | 0.255   | 0.299   | 0.317   | 0.377   | 0.292 | 0.170 | 0.233   | 0.078   | 0.295 | 0.321 | 0.285 | 0.258 |
| <i>D. eytoni</i>       | 0.332  | 0.243  | 0.310   | 0.255   | 0.298   | 0.316   | 0.385   | 0.301 | 0.176 | 0.249   | 0.083   | 0.280 | 0.303 | 0.286 | 0.248 |
| <i>Anseranas</i>       | 0.328  | 0.236  | 0.309   | 0.267   | 0.308   | 0.333   | 0.383   | 0.297 | 0.170 | 0.243   | 0.129   | 0.293 | 0.308 | 0.288 | 0.248 |
| <i>Anhima</i>          | 0.332  | 0.231  | 0.260   | 0.233   | 0.317   | 0.324   | 0.369   | 0.288 | 0.171 | 0.231   | 0.123   | 0.319 | 0.291 | 0.291 | 0.280 |
| <i>D. planei</i>       | 0.360  | 0.302  | N/A     | N/A     | 0.333   | 0.316   | N/A     | 0.252 | 0.152 | 0.224   | 0.189   | 0.259 | 0.327 | 0.281 | 0.247 |
| <i>D. murrayi</i>      | 0.351  | 0.289  | N/A     | N/A     | 0.336   | 0.324   | N/A     | 0.247 | 0.167 | 0.227   | 0.197   | 0.251 | 0.317 | 0.283 | 0.253 |
| <i>I. woodburnei</i>   | 0.358  | 0.306  | N/A     | N/A     | 0.339   | 0.311   | N/A     | 0.256 | 0.189 | 0.228   | 0.201   | 0.278 | 0.318 | 0.287 | 0.239 |
| <i>Talegalla</i>       | 0.324  | 0.224  | 0.245   | 0.204   | 0.326   | 0.305   | 0.373   | 0.330 | 0.235 | 0.204   | 0.098   | 0.306 | 0.307 | 0.283 | 0.259 |
| <i>Leipoa</i>          | 0.318  | 0.210  | 0.269   | 0.201   | 0.302   | 0.308   | 0.369   | 0.345 | 0.244 | 0.174   | 0.157   | 0.284 | 0.272 | 0.282 | 0.268 |
| <i>Megapodius</i>      | 0.337  | 0.230  | 0.238   | 0.162   | 0.331   | 0.313   | 0.377   | 0.342 | 0.227 | 0.186   | 0.106   | 0.316 | 0.259 | 0.264 | 0.234 |
| <i>Gallus</i>          | 0.318  | 0.215  | 0.209   | 0.169   | 0.333   | 0.311   | 0.370   | 0.330 | 0.217 | 0.217   | 0.191   | 0.309 | 0.288 | 0.276 | 0.247 |
| <i>Ortalis</i>         | 0.340  | 0.225  | 0.223   | 0.094   | 0.336   | 0.304   | 0.378   | 0.323 | 0.231 | 0.185   | 0.116   | 0.310 | 0.305 | 0.273 | 0.264 |

Table A5.4. Modular Distance data: Phylogenetic signal and multivariate Procrustes distance-ANOVA PGLS factorial model fitting results for the Complete (A, C; n=34) and Dromornithids-excluded (B, D; n=31) data sets. **A**, phylogenetic signal assessed under Brownian motion assumptions for each endocast module conducted using the Geomorph function ‘physignal’ and Modular Distances showing phylogenetic signal are highlighted green. **B**, Model fitting conducted using the function ‘procDppls’ employing 999 RRPP permutations as implemented in Geomorph. Procrustes distance-ANOVA statistics are given for each of three categorical (Trophic Guild, Order, and Sub-Family) fitted model factors (see 5.2.7.4), where non-significant results are highlighted pink. **Abbreviations**, ANOVA, analysis of variance; **Cer L**, cerebellum length; **Cer W**, cerebellum width; **EmSg L**, eminentia sagittalis length; **EmSg W**, eminentia sagittalis width; **K<sub>m</sub>**, Adams’ K<sub>mult</sub>; **MDist**, modular distance measurement; **Mes L**, mesencephalon length; **Mes W**, mesencephalon width; **PGLS**, phylogenetic generalised least squares; **Phylo.**, phylogenetic; **R<sup>2</sup>**, r squared; **Rho L**, rhombencephalon length; **Rho W**, rhombencephalon width; **RRPP**, randomized residual permutation procedure; **SSq**, sum of squares; **Sub.Fam**, Sub-Family/Family; **Tel.c L**, caudal telencephalon length; **Tel.c W**, caudal telencephalon width; **Tel.r L**, rostral telencephalon length; **Tel.r W**, rostral telencephalon width; **Telen L**, total telencephalon length; **Tr.Guild**, trophic guild; **Tri.g L**, trigeminal ganglion length; **Tri.g W**, trigeminal ganglion width; **Vol**, endocast volume; **X**, factorial variable; one of three categorical model factors: Trophic Guild, Order or Sub-Family (see Fig. 5.1; 5.2.6.4); **Y**, response variable; one of 14 modular endocast distance measurements (see also MDist).

| A. Phylo. Signal   |                |         | C. Complete Modular Distance data: PGLS model = log <sub>10</sub> (Y) ~ log <sub>10</sub> (Vol) * X               |       |                |         |         |         |                               |       |                |         |         |         |                                 |       |                |         |         |         |
|--------------------|----------------|---------|---|-------|----------------|---------|---------|---------|-------------------------------|-------|----------------|---------|---------|---------|---------------------------------|-------|----------------|---------|---------|---------|
| Modules<br>Y=MDist | Geomorph       |         | X = Trophic Guild   |       |                |         | ANOVA   |         | X = Order                     |       |                |         | ANOVA   |         | X = Sub-Family                  |       |                |         | ANOVA   |         |
|                    | K <sub>m</sub> | P value | Effect  | SSq   | R <sup>2</sup> | z-score | F value | P value | Effect                        | SSq   | R <sup>2</sup> | z-score | F value | P value | Effect                          | SSq   | R <sup>2</sup> | z-score | F value | P value |
| EmSg L             | 0.838          | 0.001   | log <sub>10</sub> (Vol):Tr.Guild  | 0.001 | 0.007          | 2.899   | 0.544   | 0.001   | log <sub>10</sub> (Vol):Order | 0.002 | 0.013          | 3.159   | 2.410   | 0.001   | log <sub>10</sub> (Vol):Sub.Fam | 0.002 | 0.015          | 4.265   | 1.085   | 0.001   |
| EmSg W             | 0.785          | 0.001   | log <sub>10</sub> (Vol):Tr.Guild  | 0.004 | 0.021          | 3.809   | 1.642   | 0.001   | log <sub>10</sub> (Vol):Order | 0.001 | 0.007          | 2.202   | 0.981   | 0.001   | log <sub>10</sub> (Vol):Sub.Fam | 0.002 | 0.010          | 2.317   | 0.462   | 0.003   |
| Tel R.L            | 1.036          | 0.001   | log <sub>10</sub> (Vol):Tr.Guild  | 0.002 | 0.010          | 1.312   | 0.369   | 0.072   | log <sub>10</sub> (Vol):Order | 0.000 | 0.002          | -0.497  | 0.090   | 0.719   | log <sub>10</sub> (Vol):Sub.Fam | 0.009 | 0.052          | 3.265   | 1.629   | 0.001   |
| Tel.r W            | 1.107          | 0.001   | log <sub>10</sub> (Vol):Tr.Guild  | 0.034 | 0.194          | 2.681   | 4.755   | 0.001   | log <sub>10</sub> (Vol):Order | 0.031 | 0.172          | 2.696   | 9.591   | 0.001   | log <sub>10</sub> (Vol):Sub.Fam | 0.010 | 0.055          | 3.010   | 1.584   | 0.002   |
| Tel.c L            | 1.963          | 0.001   | log <sub>10</sub> (Vol):Tr.Guild  | 0.000 | 0.004          | -0.577  | 0.103   | 0.751   | log <sub>10</sub> (Vol):Order | 0.000 | 0.000          | -2.600  | 0.005   | 0.979   | log <sub>10</sub> (Vol):Sub.Fam | 0.003 | 0.028          | 1.602   | 0.584   | 0.041   |
| Tel.c W            | 1.060          | 0.001   | log <sub>10</sub> (Vol):Tr.Guild  | 0.001 | 0.012          | 3.399   | 0.996   | 0.001   | log <sub>10</sub> (Vol):Order | 0.000 | 0.001          | 1.173   | 0.227   | 0.083   | log <sub>10</sub> (Vol):Sub.Fam | 0.001 | 0.010          | 3.514   | 0.795   | 0.001   |
| Telen L            | 0.870          | 0.001   | log <sub>10</sub> (Vol):Tr.Guild  | 0.000 | 0.002          | 4.812   | 0.664   | 0.001   | log <sub>10</sub> (Vol):Order | 0.000 | 0.002          | 3.052   | 0.893   | 0.001   | log <sub>10</sub> (Vol):Sub.Fam | 0.001 | 0.009          | 6.819   | 2.526   | 0.001   |
| Mes L              | 0.599          | 0.002   | log <sub>10</sub> (Vol):Tr.Guild  | 0.026 | 0.425          | 3.034   | 10.240  | 0.001   | log <sub>10</sub> (Vol):Order | 0.004 | 0.059          | 0.507   | 0.926   | 0.258   | log <sub>10</sub> (Vol):Sub.Fam | 0.023 | 0.372          | 1.830   | 4.716   | 0.019   |
| Mes W              | 0.509          | 0.002   | log <sub>10</sub> (Vol):Tr.Guild  | 0.095 | 0.503          | 2.415   | 6.392   | 0.007   | log <sub>10</sub> (Vol):Order | 0.010 | 0.053          | 0.403   | 0.867   | 0.404   | log <sub>10</sub> (Vol):Sub.Fam | 0.060 | 0.317          | 0.985   | 1.943   | 0.158   |
| Tri.g L            | 0.592          | 0.003   | log <sub>10</sub> (Vol):Tr.Guild  | 0.005 | 0.035          | 1.676   | 0.834   | 0.015   | log <sub>10</sub> (Vol):Order | 0.004 | 0.026          | 1.629   | 1.375   | 0.009   | log <sub>10</sub> (Vol):Sub.Fam | 0.008 | 0.057          | 3.276   | 1.587   | 0.001   |
| Tri.g W            | 0.902          | 0.001   | log <sub>10</sub> (Vol):Tr.Guild  | 0.012 | 0.039          | 0.685   | 0.575   | 0.261   | log <sub>10</sub> (Vol):Order | 0.010 | 0.032          | 1.109   | 1.130   | 0.099   | log <sub>10</sub> (Vol):Sub.Fam | 0.019 | 0.063          | 2.112   | 1.081   | 0.005   |
| Cer L              | 1.439          | 0.001   | log <sub>10</sub> (Vol):Tr.Guild  | 0.004 | 0.053          | 1.156   | 0.828   | 0.106   | log <sub>10</sub> (Vol):Order | 0.004 | 0.046          | 1.263   | 1.401   | 0.052   | log <sub>10</sub> (Vol):Sub.Fam | 0.006 | 0.077          | 1.051   | 0.791   | 0.137   |
| Cer W              | 0.709          | 0.001   | log <sub>10</sub> (Vol):Tr.Guild  | 0.002 | 0.013          | 0.946   | 0.363   | 0.176   | log <sub>10</sub> (Vol):Order | 0.001 | 0.008          | 1.035   | 0.525   | 0.11    | log <sub>10</sub> (Vol):Sub.Fam | 0.015 | 0.097          | 4.097   | 4.055   | 0.001   |
| Rho L              | 0.781          | 0.001   | log <sub>10</sub> (Vol):Tr.Guild  | 0.004 | 0.041          | 4.356   | 3.017   | 0.001   | log <sub>10</sub> (Vol):Order | 0.001 | 0.011          | 1.853   | 1.086   | 0.002   | log <sub>10</sub> (Vol):Sub.Fam | 0.007 | 0.077          | 4.291   | 3.552   | 0.001   |
| Rho W              | 0.625          | 0.002   | log <sub>10</sub> (Vol):Tr.Guild  | 0.001 | 0.012          | 0.931   | 0.340   | 0.166   | log <sub>10</sub> (Vol):Order | 0.000 | 0.002          | -0.564  | 0.075   | 0.754   | log <sub>10</sub> (Vol):Sub.Fam | 0.003 | 0.031          | 2.389   | 0.831   | 0.002   |
| B. Phylo. Signal   |                |         | D. Modular Distance data Dromornithids-excluded: PGLS model = log <sub>10</sub> (Y) ~ log <sub>10</sub> (Vol) * X |       |                |         |         |         |                               |       |                |         |         |         |                                 |       |                |         |         |         |
| Y=MDist            | K <sub>m</sub> |         | Effect  |       |                |         | ANOVA   |         | Effect                        |       |                |         | ANOVA   |         | Effect                          |       |                |         | ANOVA   |         |
|                    | K <sub>m</sub> | P value | Effect  | SSq   | R <sup>2</sup> | z-score | F value | P value | Effect                        | SSq   | R <sup>2</sup> | z-score | F value | P value | Effect                          | SSq   | R <sup>2</sup> | z-score | F value | P value |
| EmSg L             | 0.505          | 0.006   | log <sub>10</sub> (Vol):Tr.Guild  | 0.001 | 0.016          | 1.758   | 0.691   | 0.017   | log <sub>10</sub> (Vol):Order | 0.002 | 0.032          | 2.080   | 5.067   | 0.001   | log <sub>10</sub> (Vol):Sub.Fam | 0.002 | 0.036          | 3.173   | 1.457   | 0.001   |
| EmSg W             | 0.674          | 0.002   | log <sub>10</sub> (Vol):Tr.Guild  | 0.004 | 0.055          | 2.629   | 2.292   | 0.001   | log <sub>10</sub> (Vol):Order | 0.001 | 0.011          | 1.228   | 1.209   | 0.034   | log <sub>10</sub> (Vol):Sub.Fam | 0.001 | 0.018          | 0.908   | 0.388   | 0.185   |
| Tel R.L            | 1.487          | 0.001   | log <sub>10</sub> (Vol):Tr.Guild  | 0.002 | 0.013          | 1.043   | 0.451   | 0.136   | log <sub>10</sub> (Vol):Order | 0.000 | 0.001          | -0.428  | 0.038   | 0.738   | log <sub>10</sub> (Vol):Sub.Fam | 0.009 | 0.065          | 2.688   | 1.872   | 0.001   |
| Tel.r W            | 1.038          | 0.001   | log <sub>10</sub> (Vol):Tr.Guild  | 0.036 | 0.213          | 2.703   | 6.347   | 0.001   | log <sub>10</sub> (Vol):Order | 0.031 | 0.182          | 2.265   | 18.93   | 0.001   | log <sub>10</sub> (Vol):Sub.Fam | 0.010 | 0.057          | 2.951   | 1.930   | 0.003   |
| Tel.c L            | 1.400          | 0.001   | log <sub>10</sub> (Vol):Tr.Guild  | 0.000 | 0.009          | -1.163  | 0.131   | 0.879   | log <sub>10</sub> (Vol):Order | 0.000 | 0.000          | -1.390  | 0.009   | 0.91    | log <sub>10</sub> (Vol):Sub.Fam | 0.003 | 0.067          | 0.563   | 0.668   | 0.317   |
| Tel.c W            | 0.633          | 0.003   | log <sub>10</sub> (Vol):Tr.Guild  | 0.001 | 0.022          | 3.146   | 1.637   | 0.001   | log <sub>10</sub> (Vol):Order | 0.000 | 0.000          | -0.280  | 0.024   | 0.705   | log <sub>10</sub> (Vol):Sub.Fam | 0.001 | 0.011          | 3.326   | 0.775   | 0.001   |
| Telen L            | 0.595          | 0.004   | log <sub>10</sub> (Vol):Tr.Guild  | 0.000 | 0.004          | 2.967   | 0.621   | 0.001   | log <sub>10</sub> (Vol):Order | 0.000 | 0.002          | 1.439   | 0.655   | 0.004   | log <sub>10</sub> (Vol):Sub.Fam | 0.001 | 0.019          | 5.319   | 2.733   | 0.001   |
| Mes L              | 0.480          | 0.041   | log <sub>10</sub> (Vol):Tr.Guild  | 0.022 | 0.384          | 2.917   | 11.428  | 0.002   | log <sub>10</sub> (Vol):Order | 0.002 | 0.029          | 0.611   | 0.837   | 0.25    | log <sub>10</sub> (Vol):Sub.Fam | 0.019 | 0.325          | 1.758   | 4.725   | 0.034   |
| Mes W              | 0.367          | 0.087   | log <sub>10</sub> (Vol):Tr.Guild  | 0.086 | 0.486          | 2.286   | 7.374   | 0.002   | log <sub>10</sub> (Vol):Order | 0.000 | 0.000          | -1.406  | 0.006   | 0.917   | log <sub>10</sub> (Vol):Sub.Fam | 0.049 | 0.277          | 0.852   | 1.889   | 0.197   |
| Tri.g L            | 0.603          | 0.002   | log <sub>10</sub> (Vol):Tr.Guild  | 0.001 | 0.010          | 0.157   | 0.245   | 0.486   | log <sub>10</sub> (Vol):Order | 0.001 | 0.011          | 0.905   | 0.879   | 0.119   | log <sub>10</sub> (Vol):Sub.Fam | 0.004 | 0.037          | 2.268   | 0.977   | 0.005   |
| Tri.g W            | 0.408          | 0.045   | log <sub>10</sub> (Vol):Tr.Guild  | 0.007 | 0.035          | 0.231   | 0.467   | 0.467   | log <sub>10</sub> (Vol):Order | 0.001 | 0.005          | 0.104   | 0.225   | 0.545   | log <sub>10</sub> (Vol):Sub.Fam | 0.009 | 0.044          | 0.897   | 0.625   | 0.166   |
| Cer L              | 1.276          | 0.001   | log <sub>10</sub> (Vol):Tr.Guild  | 0.001 | 0.020          | 0.365   | 0.389   | 0.404   | log <sub>10</sub> (Vol):Order | 0.000 | 0.001          | -0.417  | 0.050   | 0.752   | log <sub>10</sub> (Vol):Sub.Fam | 0.003 | 0.039          | 0.358   | 0.458   | 0.4     |
| Cer W              | 0.549          | 0.01    | log <sub>10</sub> (Vol):Tr.Guild  | 0.001 | 0.015          | -0.186  | 0.254   | 0.633   | log <sub>10</sub> (Vol):Order | 0.001 | 0.011          | 0.656   | 0.611   | 0.275   | log <sub>10</sub> (Vol):Sub.Fam | 0.015 | 0.204          | 3.137   | 4.926   | 0.001   |
| Rho L              | 0.495          | 0.016   | log <sub>10</sub> (Vol):Tr.Guild  | 0.003 | 0.061          | 3.426   | 3.354   | 0.001   | log <sub>10</sub> (Vol):Order | 0.000 | 0.010          | 1.180   | 1.018   | 0.05    | log <sub>10</sub> (Vol):Sub.Fam | 0.006 | 0.122          | 3.296   | 3.857   | 0.001   |
| Rho W              | 0.381          | 0.068   | log <sub>10</sub> (Vol):Tr.Guild  | 0.001 | 0.019          | 1.295   | 0.612   | 0.07    | log <sub>10</sub> (Vol):Order | 0.000 | 0.002          | 0.104   | 0.129   | 0.563   | log <sub>10</sub> (Vol):Sub.Fam | 0.003 | 0.040          | 2.189   | 1.095   | 0.007   |

Table A5.5. Modular Distance data: Phylogenetic signal and univariate covariance-ANOVA PGLS factorial model fitting results for the Complete (A, C; n=34) and Dromornithids-excluded (B, D; n=31) data sets. A, phylogenetic signal assessed under Brownian motion assumptions for each distance measurement conducted using Geomorph ‘physignal’ and phytools ‘phylosig’ functions, and Modular Distances showing phylogenetic signal are highlighted green. C–D, model fitting conducted using the function ‘pgls.SEy’ employing 999 permutations as implemented in phytools. Covariance-ANOVA statistics for each of three categorical (Trophic Guild, Order, and Sub-Family) fitted model factors (see 5.2.7.4) are given, where non-significant results are highlighted pink. **Abbreviations**, AIC, Akaike information criterion; ANOVA, analysis of variance; **Cer L**, cerebellum length; **Cer W**, cerebellum width; **EmSg L**, eminentia sagittalis length; **EmSg W**, eminentia sagittalis width; **K<sub>B</sub>**, Blomberg’s K; **K<sub>m</sub>**, Adams’ K<sub>mult</sub>; **MDist**, modular distance measurement; **Mes L**, mesencephalon length; **Mes W**, mesencephalon width; **PGLS**, phylogenetic generalised least squares; **Phylo.**, phylogenetic; **Rho L**, rhombencephalon length; **Rho W**, rhombencephalon width;  $\delta$ , sigma; **Sub.Fam**, Sub-Family/Family; **Tel.c L**, caudal telencephalon length; **Tel.c W**, caudal telencephalon width; **Tel.r L**, rostral telencephalon length; **Tel.r W**, rostral telencephalon width; **Telen L**, total telencephalon length; **Tr.Guild**, trophic guild; **Tri.g L**, trigeminal ganglion length; **Tri.g W**, trigeminal ganglion width; **Vol**; endocast volume; **X**, factorial variable; one of three categorical model factors: Trophic Guild, Order or Sub-Family (see Fig. 5.1; 5.2.6.4); **Y**, response variable; one of 14 modular endocast distance measurements (see also MDist).

| A. Phylo. Signal   |                |         |                |         | C. Complete Modular Distance data: PGLS model = $\log_{10}(Y) \sim \log_{10}(\text{Vol}) + \log_{10}(\text{Vol}) : X$               |          |                                  |         |         |          |          |                               |           |         |          |         |                                 |         |         |          |             |        |         |         |       |  |  |  |
|--------------------|----------------|---------|----------------|---------|---|----------|----------------------------------|---------|---------|----------|----------|-------------------------------|-----------|---------|----------|---------|---------------------------------|---------|---------|----------|-------------|--------|---------|---------|-------|--|--|--|
| Modules<br>Y=MDist | Geomorph       |         | phytools       |         | X = Trophic Guild   |          |                                  |         | ANOVA   |          |          |                               | X = Order |         |          |         | ANOVA                           |         |         |          | X = Sub.Fam |        |         |         | ANOVA |  |  |  |
|                    | K <sub>m</sub> | P value | K <sub>B</sub> | P value | $\delta$  | AIC      | Effect                           | F value | P value | $\delta$ | AIC      | Effect                        | F value   | P value | $\delta$ | AIC     | Effect                          | F value | P value | $\delta$ | AIC         | Effect | F value | P value |       |  |  |  |
| EmSg L             | 0.838          | 0.001   | 0.838          | 0.002   | 0.001   | -66.570  | log <sub>10</sub> (Vol):Tr.Guild | 0.843   | 0.549   | 0.001    | -103.113 | log <sub>10</sub> (Vol):Order | 0.710     | 0.500   | 0.001    | -46.113 | log <sub>10</sub> (Vol):Sub.Fam | 1.204   | 0.339   |          |             |        |         |         |       |  |  |  |
| EmSg W             | 0.785          | 0.001   | 0.785          | 0.002   | 0.001   | -54.574  | log <sub>10</sub> (Vol):Tr.Guild | 1.884   | 0.122   | 0.001    | -88.107  | log <sub>10</sub> (Vol):Order | 3.151     | 0.057   | 0.002    | -30.294 | log <sub>10</sub> (Vol):Sub.Fam | 1.045   | 0.436   |          |             |        |         |         |       |  |  |  |
| Tel.r L            | 1.036          | 0.001   | 1.036          | 0.001   | 0.001   | -43.663  | log <sub>10</sub> (Vol):Tr.Guild | 4.086   | 0.005   | 0.002    | -66.218  | log <sub>10</sub> (Vol):Order | 3.030     | 0.063   | 0.002    | -21.215 | log <sub>10</sub> (Vol):Sub.Fam | 2.444   | 0.040   |          |             |        |         |         |       |  |  |  |
| Tel.r W            | 1.107          | 0.001   | 1.107          | 0.001   | 0.002   | -19.047  | log <sub>10</sub> (Vol):Tr.Guild | 1.673   | 0.168   | 0.002    | -51.613  | log <sub>10</sub> (Vol):Order | 5.371     | 0.010   | 0.002    | -18.846 | log <sub>10</sub> (Vol):Sub.Fam | 5.737   | 0.000   |          |             |        |         |         |       |  |  |  |
| Tel.c L            | 1.963          | 0.001   | 1.963          | 0.001   | 0.001   | -46.863  | log <sub>10</sub> (Vol):Tr.Guild | 2.104   | 0.087   | 0.001    | -77.501  | log <sub>10</sub> (Vol):Order | 2.753     | 0.080   | 0.002    | -24.544 | log <sub>10</sub> (Vol):Sub.Fam | 1.350   | 0.266   |          |             |        |         |         |       |  |  |  |
| Tel.c W            | 1.060          | 0.001   | 1.060          | 0.001   | 0.001   | -81.265  | log <sub>10</sub> (Vol):Tr.Guild | 1.693   | 0.163   | 0.001    | -117.709 | log <sub>10</sub> (Vol):Order | 1.906     | 0.166   | 0.001    | -61.342 | log <sub>10</sub> (Vol):Sub.Fam | 2.267   | 0.055   |          |             |        |         |         |       |  |  |  |
| Telen L            | 0.870          | 0.001   | 0.870          | 0.001   | 0.001   | -108.905 | log <sub>10</sub> (Vol):Tr.Guild | 2.894   | 0.027   | 0.000    | -140.753 | log <sub>10</sub> (Vol):Order | 0.098     | 0.907   | 0.001    | -79.530 | log <sub>10</sub> (Vol):Sub.Fam | 1.850   | 0.113   |          |             |        |         |         |       |  |  |  |
| Mes L              | 0.599          | 0.002   | 0.599          | 0.001   | 0.002   | -37.622  | log <sub>10</sub> (Vol):Tr.Guild | 2.756   | 0.033   | 0.002    | -60.754  | log <sub>10</sub> (Vol):Order | 0.962     | 0.394   | 0.003    | -16.377 | log <sub>10</sub> (Vol):Sub.Fam | 1.748   | 0.135   |          |             |        |         |         |       |  |  |  |
| Mes W              | 0.509          | 0.002   | 0.509          | 0.002   | 0.003   | 2.865    | log <sub>10</sub> (Vol):Tr.Guild | 0.079   | 0.998   | 0.003    | -27.611  | log <sub>10</sub> (Vol):Order | 0.618     | 0.546   | 0.005    | 19.124  | log <sub>10</sub> (Vol):Sub.Fam | 0.159   | 0.996   |          |             |        |         |         |       |  |  |  |
| Tri.g L            | 0.592          | 0.003   | 0.592          | 0.002   | 0.001   | -39.604  | log <sub>10</sub> (Vol):Tr.Guild | 1.697   | 0.162   | 0.001    | -72.242  | log <sub>10</sub> (Vol):Order | 3.450     | 0.045   | 0.002    | -25.281 | log <sub>10</sub> (Vol):Sub.Fam | 2.439   | 0.041   |          |             |        |         |         |       |  |  |  |
| Tri.g W            | 0.902          | 0.001   | 0.902          | 0.001   | 0.003   | -6.248   | log <sub>10</sub> (Vol):Tr.Guild | 0.424   | 0.857   | 0.003    | -36.041  | log <sub>10</sub> (Vol):Order | 0.708     | 0.501   | 0.002    | 2.496   | log <sub>10</sub> (Vol):Sub.Fam | 1.693   | 0.148   |          |             |        |         |         |       |  |  |  |
| Cer L              | 1.439          | 0.001   | 1.439          | 0.001   | 0.001   | -42.282  | log <sub>10</sub> (Vol):Tr.Guild | 1.791   | 0.140   | 0.001    | -73.170  | log <sub>10</sub> (Vol):Order | 2.435     | 0.105   | 0.002    | -18.644 | log <sub>10</sub> (Vol):Sub.Fam | 0.873   | 0.562   |          |             |        |         |         |       |  |  |  |
| Cer W              | 0.709          | 0.001   | 0.709          | 0.001   | 0.001   | -41.451  | log <sub>10</sub> (Vol):Tr.Guild | 0.609   | 0.721   | 0.001    | -75.117  | log <sub>10</sub> (Vol):Order | 0.501     | 0.611   | 0.002    | -21.658 | log <sub>10</sub> (Vol):Sub.Fam | 0.702   | 0.701   |          |             |        |         |         |       |  |  |  |
| Rho L              | 0.781          | 0.001   | 0.781          | 0.002   | 0.001   | -72.121  | log <sub>10</sub> (Vol):Tr.Guild | 2.071   | 0.092   | 0.001    | -103.366 | log <sub>10</sub> (Vol):Order | 0.833     | 0.445   | 0.001    | -39.163 | log <sub>10</sub> (Vol):Sub.Fam | 0.222   | 0.988   |          |             |        |         |         |       |  |  |  |
| Rho W              | 0.625          | 0.002   | 0.625          | 0.001   | 0.001   | -59.504  | log <sub>10</sub> (Vol):Tr.Guild | 3.683   | 0.009   | 0.001    | -87.666  | log <sub>10</sub> (Vol):Order | 4.080     | 0.027   | 0.001    | -38.805 | log <sub>10</sub> (Vol):Sub.Fam | 3.006   | 0.016   |          |             |        |         |         |       |  |  |  |
| B. Phylo. Signal   |                |         |                |         | D. Modular Distance data Dromornithids-excluded: PGLS model = $\log_{10}(Y) \sim \log_{10}(\text{Vol}) + \log_{10}(\text{Vol}) : X$ |          |                                  |         |         |          |          |                               |           |         |          |         |                                 |         |         |          |             |        |         |         |       |  |  |  |
| Y=MDist            | K <sub>m</sub> |         | K <sub>B</sub> |         | $\delta$  |          |                                  |         | ANOVA   |          |          |                               | $\delta$  |         |          |         | ANOVA                           |         |         |          |             |        |         |         |       |  |  |  |
|                    | P value        | P value | P value        | P value | AIC   | Effect   | F-value                          | p-value | AIC     | Effect   | F-value  | p-value                       | AIC       | Effect  | F-value  | p-value | AIC                             | Effect  | F-value | p-value  |             |        |         |         |       |  |  |  |
| EmSg L             | 0.505          | 0.006   | 0.505          | 0.013   | 0.001   | -64.107  | log <sub>10</sub> (Vol):Tr.Guild | 0.754   | 0.592   | 0.001    | -100.426 | log <sub>10</sub> (Vol):Order | 0.112     | 0.740   | 0.001    | -43.501 | log <sub>10</sub> (Vol):Sub.Fam | 1.203   | 0.344   |          |             |        |         |         |       |  |  |  |
| EmSg W             | 0.674          | 0.002   | 0.674          | 0.001   | 0.001   | -55.824  | log <sub>10</sub> (Vol):Tr.Guild | 1.015   | 0.430   | 0.001    | -89.441  | log <sub>10</sub> (Vol):Order | 0.078     | 0.782   | 0.001    | -31.439 | log <sub>10</sub> (Vol):Sub.Fam | 0.562   | 0.797   |          |             |        |         |         |       |  |  |  |
| Tel.r L            | 1.487          | 0.001   | 1.487          | 0.001   | 0.002   | -41.086  | log <sub>10</sub> (Vol):Tr.Guild | 3.432   | 0.018   | 0.002    | -64.181  | log <sub>10</sub> (Vol):Order | 1.798     | 0.191   | 0.002    | -18.807 | log <sub>10</sub> (Vol):Sub.Fam | 1.943   | 0.106   |          |             |        |         |         |       |  |  |  |
| Tel.r W            | 1.038          | 0.001   | 1.038          | 0.001   | 0.003   | -17.809  | log <sub>10</sub> (Vol):Tr.Guild | 0.978   | 0.451   | 0.003    | -50.741  | log <sub>10</sub> (Vol):Order | 6.136     | 0.020   | 0.001    | -17.406 | log <sub>10</sub> (Vol):Sub.Fam | 5.286   | 0.001   |          |             |        |         |         |       |  |  |  |
| Tel.c L            | 1.400          | 0.001   | 1.400          | 0.001   | 0.001   | -43.932  | log <sub>10</sub> (Vol):Tr.Guild | 1.298   | 0.298   | 0.002    | -74.518  | log <sub>10</sub> (Vol):Order | 0.361     | 0.553   | 0.002    | -21.578 | log <sub>10</sub> (Vol):Sub.Fam | 0.805   | 0.606   |          |             |        |         |         |       |  |  |  |
| Tel.c W            | 0.633          | 0.003   | 0.633          | 0.004   | 0.001   | -81.334  | log <sub>10</sub> (Vol):Tr.Guild | 2.045   | 0.108   | 0.001    | -117.926 | log <sub>10</sub> (Vol):Order | 3.578     | 0.069   | 0.000    | -64.325 | log <sub>10</sub> (Vol):Sub.Fam | 3.579   | 0.009   |          |             |        |         |         |       |  |  |  |
| Telen L            | 0.595          | 0.004   | 0.595          | 0.007   | 0.000   | -102.164 | log <sub>10</sub> (Vol):Tr.Guild | 3.154   | 0.025   | 0.001    | -134.719 | log <sub>10</sub> (Vol):Order | 0.061     | 0.807   | 0.000    | -72.805 | log <sub>10</sub> (Vol):Sub.Fam | 1.907   | 0.113   |          |             |        |         |         |       |  |  |  |
| Mes L              | 0.480          | 0.041   | 0.480          | 0.033   | 0.002   | -37.454  | log <sub>10</sub> (Vol):Tr.Guild | 2.999   | 0.031   | 0.002    | -59.871  | log <sub>10</sub> (Vol):Order | 0.156     | 0.696   | 0.002    | -16.134 | log <sub>10</sub> (Vol):Sub.Fam | 1.808   | 0.132   |          |             |        |         |         |       |  |  |  |
| Mes W              | 0.367          | 0.087   | 0.367          | 0.09    | 0.004   | 0.853    | log <sub>10</sub> (Vol):Tr.Guild | 0.133   | 0.983   | 0.004    | -29.655  | log <sub>10</sub> (Vol):Order | 1.867     | 0.183   | 0.004    | 16.908  | log <sub>10</sub> (Vol):Sub.Fam | 0.243   | 0.977   |          |             |        |         |         |       |  |  |  |
| Tri.g L            | 0.603          | 0.002   | 0.603          | 0.002   | 0.004   | -38.818  | log <sub>10</sub> (Vol):Tr.Guild | 0.960   | 0.461   | 0.002    | -70.828  | log <sub>10</sub> (Vol):Order | 1.057     | 0.313   | 0.001    | -24.363 | log <sub>10</sub> (Vol):Sub.Fam | 1.952   | 0.105   |          |             |        |         |         |       |  |  |  |
| Tri.g W            | 0.408          | 0.045   | 0.408          | 0.057   | 0.003   | -7.355   | log <sub>10</sub> (Vol):Tr.Guild | 0.458   | 0.804   | 0.004    | -37.728  | log <sub>10</sub> (Vol):Order | 2.169     | 0.152   | 0.002    | 0.589   | log <sub>10</sub> (Vol):Sub.Fam | 2.099   | 0.083   |          |             |        |         |         |       |  |  |  |
| Cer L              | 1.276          | 0.001   | 1.276          | 0.001   | 0.002   | -44.500  | log <sub>10</sub> (Vol):Tr.Guild | 1.247   | 0.319   | 0.002    | -75.078  | log <sub>10</sub> (Vol):Order | 0.019     | 0.890   | 0.006    | -20.532 | log <sub>10</sub> (Vol):Sub.Fam | 0.535   | 0.817   |          |             |        |         |         |       |  |  |  |
| Cer W              | 0.549          | 0.01    | 0.549          | 0.01    | 0.002   | -39.972  | log <sub>10</sub> (Vol):Tr.Guild | 0.609   | 0.694   | 0.002    | -73.135  | log <sub>10</sub> (Vol):Order | 0.241     | 0.628   | 0.002    | -19.707 | log <sub>10</sub> (Vol):Sub.Fam | 0.657   | 0.722   |          |             |        |         |         |       |  |  |  |
| Rho L              | 0.495          | 0.016   | 0.495          | 0.012   | 0.001   | -68.212  | log <sub>10</sub> (Vol):Tr.Guild | 2.256   | 0.081   | 0.001    | -99.540  | log <sub>10</sub> (Vol):Order | 1.164     | 0.290   | 0.001    | -35.685 | log <sub>10</sub> (Vol):Sub.Fam | 0.200   | 0.988   |          |             |        |         |         |       |  |  |  |
| Rho W              | 0.381          | 0.068   | 0.381          | 0.062   | 0.001   | -57.009  | log <sub>10</sub> (Vol):Tr.Guild | 2.335   | 0.073   | 0.001    | -85.580  | log <sub>10</sub> (Vol):Order | 0.568     | 0.457   | 0.001    | -36.534 | log <sub>10</sub> (Vol):Sub.Fam | 2.118   | 0.080   |          |             |        |         |         |       |  |  |  |

Table A5.6. Modular Surface Area values (mm<sup>2</sup>) for the Complete (n=34) data set. Taxa are arranged in descending topological order (see Fig. 5.1). **Abbreviations.** *A. cast*, *Anas castanea*; *A. platy*, *Anas platyrhynchos*; *A. super*, *Anas superciliosa*; *Anhima*, *Anhima cornuta*; *Anser*, *Anser caerulescens*; *Anseranas*, *Anseranas semipalmata*; *Aythya*, *Aythya australis*; *Biziura*, *Biziura lobata*; *Branta*, *Branta canadensis*; *C. jubata*, *Chenonetta jubata*; *C. finschi.CR*, *Chenonetta finschi* Castle Rocks Fissure; *C. finschi.GYL2*, *Chenonetta finschi* Honeycomb Hill Cave Graveyard Layer 2; *C. finschi.GYL3*, *Chenonetta finschi* Honeycomb Hill Cave Graveyard Layer 3; *C. finschi.HC*, *Chenonetta finschi* Hodges Creek Cave; **Cer**, cerebellum; *Cereopsis*, *Cereopsis novaehollandiae*; *Cygnus*, *Cygnus atratus*; *D. bicolor*, *Dendrocygna bicolor*; *D. eytoni*, *Dendrocygna eytoni*; *D. murrayi*, *Dromornis murrayi* reconstruction; *D. planei*, *Dromornis planei*; **EmSg**, eminentia sagittalis; *Gallus*, *Gallus gallus*; *I. woodburnei*, *Ibandornis woodburnei*; *Leipoa*, *Leipoa ocellata*; *Lophodytes*, *Lophodytes cucullatus*; *Malacorhynchus*, *Malacorhynchus membranaceus*; *Megapodius*, *Megapodius reinwardt*; **Mes** mesencephalon; *Mionetta.1*, *Mionetta blanchardi.1*; *Mionetta.2*, *Mionetta blanchardi.2*; **mm<sup>2</sup>**, square millimetres; *Nettapus*, *Nettapus pulchellus*; *Ortalis*, *Ortalis vetula*; *Oxyura*, *Oxyura australis*; **Rho**, rhombencephalon; *Stictonetta*, *Stictonetta naevosa*; *Tadorna*, *Tadorna tadornoides*; *Talegalla*, *Talegalla fuscirostris*; **Tel.c**, caudal telencephalon; **Tel.r**, rostral telencephalon; **Telen**, complete telencephalon, **Tri.g**, trigeminal ganglion, **Tri.g F**, cross-section of the maxillomandibular (V2+V3) branch of the trigeminal nerve (V); **TSurf**, total endocast surface area (mm<sup>2</sup>).

| Taxon                  | TSurf    | EmSg    | Tel.r  | Tel.c   | Telen  | Mes    | Tri.g  | Tri.g F | Cer    | Rho    |
|------------------------|----------|---------|--------|---------|--------|--------|--------|---------|--------|--------|
| <i>A. platy</i>        | 2190.13  | 128.16  | 182.22 | 164.79  | 347.01 | 64.73  | 26.94  | 5.56    | 114.86 | 112.25 |
| <i>A. super</i>        | 2090.82  | 121.90  | 160.12 | 144.39  | 304.51 | 69.08  | 25.30  | 7.00    | 109.73 | 106.45 |
| <i>A. cast</i>         | 1691.20  | 81.58   | 154.64 | 118.17  | 272.81 | 50.91  | 20.33  | 4.60    | 85.50  | 77.71  |
| <i>Lophodytes</i>      | 1686.49  | 115.77  | 99.37  | 125.41  | 224.78 | 64.04  | 16.09  | 2.15    | 93.62  | 81.04  |
| <i>Aythya</i>          | 1795.11  | 100.58  | 126.69 | 133.28  | 259.97 | 61.08  | 23.58  | 3.48    | 87.98  | 99.46  |
| <i>Nettapus</i>        | 1140.81  | 47.16   | 61.81  | 109.23  | 171.04 | 54.73  | 8.35   | 1.98    | 62.18  | 48.41  |
| <i>C. finschi.CR</i>   | 1841.28  | 117.31  | 137.27 | 128.04  | 265.31 | 55.56  | 21.87  | 2.66    | 108.11 | 80.63  |
| <i>C. finschi.HC</i>   | 1821.77  | 103.91  | 130.10 | 138.46  | 268.56 | 49.94  | 20.57  | 1.95    | 107.51 | 81.72  |
| <i>C. finschi.GYL2</i> | 1749.56  | 99.52   | 139.51 | 118.77  | 258.27 | 56.07  | 18.08  | 1.86    | 90.86  | 81.71  |
| <i>C. finschi.GYL3</i> | 1752.50  | 100.09  | 140.43 | 115.91  | 256.34 | 47.69  | 17.70  | 2.63    | 111.98 | 73.07  |
| <i>C. jubata</i>       | 1742.97  | 79.25   | 82.40  | 170.72  | 253.12 | 81.31  | 13.66  | 1.70    | 125.25 | 79.07  |
| <i>Tadorna</i>         | 2109.16  | 106.66  | 125.26 | 170.91  | 296.18 | 61.63  | 24.58  | 5.08    | 140.68 | 108.34 |
| <i>Branta</i>          | 3594.54  | 231.63  | 255.54 | 316.87  | 572.41 | 82.49  | 36.33  | 5.02    | 188.86 | 152.96 |
| <i>Anser</i>           | 3546.49  | 206.88  | 299.55 | 281.95  | 581.49 | 89.35  | 33.71  | 4.92    | 225.71 | 149.99 |
| <i>Cygnus</i>          | 3456.09  | 203.52  | 307.00 | 273.61  | 580.61 | 61.99  | 43.81  | 6.58    | 207.63 | 183.20 |
| <i>Cereopsis</i>       | 2643.49  | 144.48  | 131.72 | 250.88  | 382.60 | 78.12  | 21.38  | 4.22    | 160.04 | 128.11 |
| <i>Stictonetta</i>     | 1691.43  | 83.29   | 112.08 | 120.02  | 232.11 | 41.04  | 27.03  | 4.76    | 79.17  | 87.81  |
| <i>Malacorhynchus</i>  | 1272.32  | 73.18   | 90.50  | 86.39   | 176.88 | 40.14  | 13.55  | 7.17    | 74.35  | 58.55  |
| <i>Oxyura</i>          | 1585.30  | 81.53   | 138.37 | 101.16  | 239.53 | 29.49  | 24.12  | 7.23    | 104.65 | 80.79  |
| <i>Biziura</i>         | 2894.77  | 196.72  | 218.03 | 210.20  | 428.24 | 44.26  | 33.72  | 4.87    | 190.61 | 124.14 |
| <i>Mionetta.2</i>      | 1383.98  | 50.68   | 91.90  | 109.14  | 201.04 | 57.40  | 13.29  | 2.92    | 85.01  | 75.22  |
| <i>Mionetta.1</i>      | 1299.36  | 61.99   | 83.02  | 92.90   | 175.92 | 51.43  | 17.33  | 4.02    | 86.14  | 73.07  |
| <i>D. bicolor</i>      | 1730.58  | 81.22   | 119.50 | 147.56  | 267.06 | 52.64  | 15.82  | 4.24    | 134.58 | 79.82  |
| <i>D. eytoni</i>       | 1890.76  | 98.58   | 141.80 | 161.63  | 303.44 | 57.59  | 20.49  | 5.01    | 107.15 | 89.39  |
| <i>Anseranas</i>       | 2985.52  | 117.40  | 216.04 | 297.48  | 513.52 | 71.57  | 40.23  | 6.24    | 192.07 | 135.38 |
| <i>Anhima</i>          | 2404.61  | 90.65   | 82.55  | 249.41  | 331.96 | 52.33  | 22.14  | 5.11    | 205.25 | 136.69 |
| <i>D. planei</i>       | 15874.02 | 1851.49 | N/A    | 1297.48 | N/A    | 164.03 | 136.50 | 13.48   | 816.82 | 585.79 |
| <i>D. murrayi</i>      | 13199.82 | 1353.96 | N/A    | 1213.28 | N/A    | 139.37 | 132.07 | 14.54   | 678.37 | 394.24 |
| <i>I. woodburnei</i>   | 10200.52 | 1170.99 | N/A    | 852.94  | N/A    | 145.83 | 102.58 | 10.43   | 528.19 | 290.76 |
| <i>Talegalla</i>       | 1855.50  | 68.41   | 48.84  | 177.71  | 226.55 | 101.62 | 14.03  | 1.44    | 163.04 | 85.87  |
| <i>Leipoa</i>          | 1682.29  | 65.71   | 47.39  | 133.10  | 180.49 | 118.28 | 13.44  | 1.33    | 103.59 | 86.91  |
| <i>Megapodius</i>      | 1528.97  | 69.72   | 22.19  | 166.01  | 188.20 | 97.34  | 11.84  | 1.14    | 115.25 | 58.36  |
| <i>Gallus</i>          | 1544.33  | 58.50   | 19.62  | 144.52  | 164.14 | 78.90  | 20.73  | 1.34    | 124.10 | 63.21  |
| <i>Ortalis</i>         | 1322.41  | 62.67   | 15.89  | 127.39  | 143.28 | 75.10  | 11.84  | 1.24    | 127.21 | 61.10  |

Table A5.7. Modular Surface Area ratios for the Complete (n=34) data set. Taxa are arranged in descending topological order (see Fig. 5.1). **Abbreviations**, **A. cast**, *Anas castanea*; **A. platy**, *Anas platyrhynchos*; **A. super**, *Anas superciliosa*; **Anhima**, *Anhima cornuta*; **Anser**, *Anser caerulescens*; **Anseranas**, *Anseranas semipalmata*; **Aythya**, *Aythya australis*; **Biziura**, *Biziura lobata*; **Branta**, *Branta canadensis*; **C. jubata**, *Chenonetta jubata*; **C.finschi.CR**, *Chenonetta finschi* Castle Rocks Fissure; **C.finschi.GYL2**, *Chenonetta finschi* Honeycomb Hill Cave Graveyard Layer 2; **C.finschi.GYL3**, *Chenonetta finschi* Honeycomb Hill Cave Graveyard Layer 3; **C.finschi.HC**, *Chenonetta finschi* Hodges Creek Cave; **Cer**, cerebellum; **Cereopsis**, *Cereopsis novaehollandiae*; **Cygnus**, *Cygnus atratus*; **D. bicolor**, *Dendrocygna bicolor*; **D. eytoni**, *Dendrocygna eytoni*; **D. murrayi**, *Dromornis murrayi* reconstruction; **D. planei**, *Dromornis planei*; **EmSg**, eminentia sagittalis; **Gallus**, *Gallus gallus*; **I. woodburnei**, *Ibandornis woodburnei*; **Leipoa**, *Leipoa ocellata*; **Lophodytes**, *Lophodytes cucullatus*; **Malacorhynchus**, *Malacorhynchus membranaceus*; **Megapodius**, *Megapodius reinwardt*; **Mes** mesencephalon; **Mionetta.1**, *Mionetta blanchardi*.1; **Mionetta.2**, *Mionetta blanchardi*.2; **Nettapus**, *Nettapus pulchellus*; **Ortalis**, *Ortalis vetula*; **Oxyura**, *Oxyura australis*; **Rho**, rhombencephalon; **Stictonetta**, *Stictonetta naevosa*; **Tadorna**, *Tadorna tadornoides*; **Talegalla**, *Talegalla fuscirostris*; **Tel.c**, caudal telencephalon; **Tel.r**, rostral telencephalon; **Telen**, complete telencephalon, **Tri.g**, trigeminal ganglion, **Tri.g F**, cross-section of the maxillomandibular (V2+V3) branch of the trigeminal nerve (V).

| Taxon                  | EmSg  | Tel.r | Tel.c | Telen | Mes   | Tri.g | Tri.g F | Cer   | Rho   |
|------------------------|-------|-------|-------|-------|-------|-------|---------|-------|-------|
| <i>A. platy</i>        | 0.631 | 0.677 | 0.664 | 0.760 | 0.542 | 0.428 | 0.223   | 0.617 | 0.614 |
| <i>A. super</i>        | 0.628 | 0.664 | 0.650 | 0.748 | 0.554 | 0.423 | 0.254   | 0.614 | 0.611 |
| <i>A. cast</i>         | 0.592 | 0.678 | 0.642 | 0.755 | 0.529 | 0.405 | 0.205   | 0.598 | 0.586 |
| <i>Lophodytes</i>      | 0.639 | 0.619 | 0.650 | 0.729 | 0.560 | 0.374 | 0.103   | 0.611 | 0.591 |
| <i>Aythya</i>          | 0.615 | 0.646 | 0.653 | 0.742 | 0.549 | 0.422 | 0.166   | 0.598 | 0.614 |
| <i>Nettapus</i>        | 0.547 | 0.586 | 0.667 | 0.730 | 0.569 | 0.302 | 0.097   | 0.587 | 0.551 |
| <i>C. finschi.CR</i>   | 0.634 | 0.655 | 0.645 | 0.742 | 0.534 | 0.410 | 0.130   | 0.623 | 0.584 |
| <i>C. finschi.HC</i>   | 0.619 | 0.648 | 0.657 | 0.745 | 0.521 | 0.403 | 0.089   | 0.623 | 0.587 |
| <i>C. finschi.GYL2</i> | 0.616 | 0.661 | 0.640 | 0.744 | 0.539 | 0.388 | 0.083   | 0.604 | 0.590 |
| <i>C. finschi.GYL3</i> | 0.617 | 0.662 | 0.636 | 0.743 | 0.517 | 0.385 | 0.130   | 0.632 | 0.575 |
| <i>C. jubata</i>       | 0.586 | 0.591 | 0.689 | 0.741 | 0.589 | 0.350 | 0.071   | 0.647 | 0.586 |
| <i>Tadorna</i>         | 0.610 | 0.631 | 0.672 | 0.744 | 0.538 | 0.418 | 0.212   | 0.646 | 0.612 |
| <i>Branta</i>          | 0.665 | 0.677 | 0.703 | 0.776 | 0.539 | 0.439 | 0.197   | 0.640 | 0.614 |
| <i>Anser</i>           | 0.652 | 0.698 | 0.690 | 0.779 | 0.550 | 0.430 | 0.195   | 0.663 | 0.613 |
| <i>Cygnus</i>          | 0.652 | 0.703 | 0.689 | 0.781 | 0.507 | 0.464 | 0.231   | 0.655 | 0.639 |
| <i>Cereopsis</i>       | 0.631 | 0.619 | 0.701 | 0.755 | 0.553 | 0.389 | 0.183   | 0.644 | 0.616 |
| <i>Stictonetta</i>     | 0.595 | 0.635 | 0.644 | 0.733 | 0.500 | 0.444 | 0.210   | 0.588 | 0.602 |
| <i>Malacorhynchus</i>  | 0.601 | 0.630 | 0.624 | 0.724 | 0.517 | 0.365 | 0.275   | 0.603 | 0.569 |
| <i>Oxyura</i>          | 0.597 | 0.669 | 0.627 | 0.744 | 0.459 | 0.432 | 0.268   | 0.631 | 0.596 |
| <i>Biziura</i>         | 0.663 | 0.676 | 0.671 | 0.760 | 0.475 | 0.441 | 0.199   | 0.659 | 0.605 |
| <i>Mionetta.2</i>      | 0.543 | 0.625 | 0.649 | 0.733 | 0.560 | 0.358 | 0.148   | 0.614 | 0.597 |
| <i>Mionetta.1</i>      | 0.576 | 0.616 | 0.632 | 0.721 | 0.550 | 0.398 | 0.194   | 0.622 | 0.599 |
| <i>D. bicolor</i>      | 0.590 | 0.642 | 0.670 | 0.749 | 0.532 | 0.370 | 0.194   | 0.657 | 0.587 |
| <i>D. eytoni</i>       | 0.608 | 0.657 | 0.674 | 0.758 | 0.537 | 0.400 | 0.214   | 0.620 | 0.596 |
| <i>Anseranas</i>       | 0.596 | 0.672 | 0.712 | 0.780 | 0.534 | 0.462 | 0.229   | 0.657 | 0.613 |
| <i>Anhima</i>          | 0.579 | 0.567 | 0.709 | 0.746 | 0.508 | 0.398 | 0.210   | 0.684 | 0.632 |
| <i>D. planei</i>       | 0.778 | N/A   | 0.741 | N/A   | 0.527 | 0.508 | 0.269   | 0.693 | 0.659 |
| <i>D. murrayi</i>      | 0.760 | N/A   | 0.748 | N/A   | 0.520 | 0.515 | 0.282   | 0.687 | 0.630 |
| <i>I. woodburnei</i>   | 0.765 | N/A   | 0.731 | N/A   | 0.540 | 0.502 | 0.254   | 0.679 | 0.615 |
| <i>Talegalla</i>       | 0.561 | 0.517 | 0.688 | 0.721 | 0.614 | 0.351 | 0.048   | 0.677 | 0.592 |
| <i>Leipoa</i>          | 0.563 | 0.519 | 0.658 | 0.699 | 0.643 | 0.350 | 0.039   | 0.625 | 0.601 |
| <i>Megapodius</i>      | 0.579 | 0.423 | 0.697 | 0.714 | 0.624 | 0.337 | 0.017   | 0.647 | 0.555 |
| <i>Gallus</i>          | 0.554 | 0.405 | 0.677 | 0.695 | 0.595 | 0.413 | 0.040   | 0.657 | 0.565 |
| <i>Ortalis</i>         | 0.576 | 0.385 | 0.674 | 0.691 | 0.601 | 0.344 | 0.030   | 0.674 | 0.572 |

Table A5.8. Modular Surface Area data: Phylogenetic signal and univariate covariance-ANOVA PGLS factorial model fitting results for the Complete (n=34; **A, C**) and Dromornithids-excluded (n=31; **B, D**) data sets. **A–B**, phylogenetic signal assessed under Brownian motion assumptions for each endocast module conducted using Geomorph ‘physignal’ and phytools ‘phylosig’ functions, and Modular Surface Areas showing phylogenetic signal are highlighted green. **C–D**, Model fitting conducted using the function ‘ppls.SEy’ employing 999 permutations as implemented in phytools. Covariance-ANOVA statistics for each of three categorical (Trophic Guild, Order, and Sub-Family) fitted model factors (see 5.2.7.4) are given, where non-significant results are highlighted pink. **Abbreviations**, AIC, Akaike information criterion; ANOVA, analysis of variance; **Cer**, cerebellum; **EmSg**, eminentia sagittalis; **K<sub>B</sub>**, Blomberg’s K; **K<sub>m</sub>**, Adams’ K<sub>mult</sub>; **MSurf**, modular surface area; **Mes**, mesencephalon; **PGLS**, phylogenetic generalised least squares; **Phylo**, phylogenetic; **Rho**, rhombencephalon; **δ**, sigma; **Sub.Fam**, Sub-Family/Family; **Surf.**, surface; **Tel.c**, caudal telencephalon; **Tel.r**, rostral telencephalon; **Telen**, complete telencephalon; **Tr.Guild**, trophic guild; **Tri.g**, trigeminal ganglion; **Tri.g F**, cross-section of the maxillomandibular (**V2+V3**) branch of the trigeminal nerve (**V**); **TSurf**, total endocast surface area; **X**, factorial variable; one of three categorical model factors: Trophic Guild, Order or Sub-Family (see Fig. 5.1; 5.2.6.4); **Y**, response variable; one of nine modular endocast surface area measurements (see also **MSurf**).

| A. Phylo. Signal   |                |         |                |         | C. Complete Modular Surface Area data: PGLS model = log <sub>10</sub> (Y) ~ log <sub>10</sub> (TSurf) + log <sub>10</sub> (TSurf) : X               |         |                                    |         |         |           |         |                                 |         |         |                |         |                                   |         |         |
|--------------------|----------------|---------|----------------|---------|---|---------|------------------------------------|---------|---------|-----------|---------|---------------------------------|---------|---------|----------------|---------|-----------------------------------|---------|---------|
| Modules<br>Y=MSurf | Geomorph       |         | phytools       |         | X = Trophic Guild   |         |                                    |         |         | X = Order |         |                                 |         |         | X = Sub-Family |         |                                   |         |         |
|                    | K <sub>m</sub> | P value | K <sub>B</sub> | P value | δ   | AIC     | Effect                             | F value | P value | δ         | AIC     | Effect                          | F value | P value | δ              | AIC     | Effect                            | F value | P value |
| <b>EmSg</b>        | 1.047          | 0.001   | 1.047          | 0.002   | 0.002   | -37.05  | log <sub>10</sub> (TSurf):Tr.Guild | 3.451   | 0.012   | 0.002     | -60.41  | log <sub>10</sub> (TSurf):Order | 3.648   | 0.038   | 0.002          | -15.533 | log <sub>10</sub> (TSurf):Sub.Fam | 1.884   | 0.106   |
| <b>Tel.r</b>       | 0.817          | 0.001   | 0.817          | 0.001   | 0.003   | -8.64   | log <sub>10</sub> (TSurf):Tr.Guild | 3.885   | 0.007   | 0.004     | -33.87  | log <sub>10</sub> (TSurf):Order | 9.248   | 0.001   | 0.002          | 3.103   | log <sub>10</sub> (TSurf):Sub.Fam | 3.662   | 0.006   |
| <b>Tel.c</b>       | 1.367          | 0.001   | 1.367          | 0.001   | 0.002   | -47.92  | log <sub>10</sub> (TSurf):Tr.Guild | 1.624   | 0.181   | 0.002     | -74.97  | log <sub>10</sub> (TSurf):Order | 0.269   | 0.766   | 0.002          | -23.172 | log <sub>10</sub> (TSurf):Sub.Fam | 0.563   | 0.813   |
| <b>Telen</b>       | 1.032          | 0.001   | 1.032          | 0.001   | 0.001   | -72.01  | log <sub>10</sub> (TSurf):Tr.Guild | 4.432   | 0.003   | 0.001     | -105.71 | log <sub>10</sub> (TSurf):Order | 9.780   | 0.001   | 0.001          | -50.603 | log <sub>10</sub> (TSurf):Sub.Fam | 3.432   | 0.008   |
| <b>Mes</b>         | 1.481          | 0.001   | 1.481          | 0.001   | 0.003   | -19.84  | log <sub>10</sub> (TSurf):Tr.Guild | 0.856   | 0.539   | 0.002     | -52.82  | log <sub>10</sub> (TSurf):Order | 3.712   | 0.036   | 0.002          | -6.884  | log <sub>10</sub> (TSurf):Sub.Fam | 1.383   | 0.252   |
| <b>Tri.g</b>       | 1.073          | 0.001   | 1.073          | 0.002   | 0.002   | -15.50  | log <sub>10</sub> (TSurf):Tr.Guild | 1.341   | 0.275   | 0.003     | -40.43  | log <sub>10</sub> (TSurf):Order | 1.002   | 0.379   | 0.002          | -0.699  | log <sub>10</sub> (TSurf):Sub.Fam | 1.334   | 0.274   |
| <b>Tri.g F</b>     | 0.849          | 0.001   | 0.849          | 0.002   | 0.004   | 10.34   | log <sub>10</sub> (TSurf):Tr.Guild | 0.416   | 0.862   | 0.003     | -20.96  | log <sub>10</sub> (TSurf):Order | 3.908   | 0.031   | 0.004          | 22.091  | log <sub>10</sub> (TSurf):Sub.Fam | 0.710   | 0.694   |
| <b>Cer</b>         | 1.331          | 0.001   | 1.331          | 0.001   | 0.003   | -33.88  | log <sub>10</sub> (TSurf):Tr.Guild | 1.280   | 0.301   | 0.002     | -61.68  | log <sub>10</sub> (TSurf):Order | 0.849   | 0.438   | 0.003          | -13.458 | log <sub>10</sub> (TSurf):Sub.Fam | 0.749   | 0.662   |
| <b>Rho</b>         | 0.814          | 0.001   | 0.814          | 0.001   | 0.002   | -45.32  | log <sub>10</sub> (TSurf):Tr.Guild | 2.060   | 0.093   | 0.001     | -77.16  | log <sub>10</sub> (TSurf):Order | 4.482   | 0.020   | 0.002          | -24.718 | log <sub>10</sub> (TSurf):Sub.Fam | 1.400   | 0.245   |
| B. Phylo. Signal   |                |         |                |         | D. Modular Surface Area data Dromornithids-excluded: PGLS model = log <sub>10</sub> (Y) ~ log <sub>10</sub> (TSurf) + log <sub>10</sub> (TSurf) : X |         |                                    |         |         |           |         |                                 |         |         |                |         |                                   |         |         |
| Modules<br>Y=MSurf | Geomorph       |         | phytools       |         | X = Trophic Guild   |         |                                    |         |         | X = Order |         |                                 |         |         | X = Sub-Family |         |                                   |         |         |
|                    | K <sub>m</sub> | P value | K <sub>B</sub> | P value | δ   | AIC     | Effect                             | F value | P value | δ         | AIC     | Effect                          | F value | P value | δ              | AIC     | Effect                            | F value | P value |
| <b>EmSg</b>        | 0.732          | 0.003   | 0.732          | 0.001   | 0.002   | -35.558 | log <sub>10</sub> (TSurf):Tr.Guild | 2.278   | 0.079   | 0.002     | -59.26  | log <sub>10</sub> (TSurf):Order | 0.574   | 0.455   | 0.002          | -14.597 | log <sub>10</sub> (TSurf):Sub.Fam | 1.220   | 0.335   |
| <b>Tel.r</b>       | 0.987          | 0.001   | 0.987          | 0.002   | 0.003   | -8.184  | log <sub>10</sub> (TSurf):Tr.Guild | 2.320   | 0.075   | 0.004     | -34.20  | log <sub>10</sub> (TSurf):Order | 8.740   | 0.006   | 0.004          | 2.890   | log <sub>10</sub> (TSurf):Sub.Fam | 2.637   | 0.036   |
| <b>Tel.c</b>       | 0.867          | 0.002   | 0.867          | 0.002   | 0.001   | -46.024 | log <sub>10</sub> (TSurf):Tr.Guild | 1.806   | 0.150   | 0.001     | -72.86  | log <sub>10</sub> (TSurf):Order | 0.031   | 0.861   | 0.002          | -21.135 | log <sub>10</sub> (TSurf):Sub.Fam | 0.543   | 0.811   |
| <b>Telen</b>       | 0.676          | 0.004   | 0.676          | 0.003   | 0.001   | -70.199 | log <sub>10</sub> (TSurf):Tr.Guild | 2.422   | 0.065   | 0.001     | -103.95 | log <sub>10</sub> (TSurf):Order | 5.966   | 0.021   | 0.001          | -48.973 | log <sub>10</sub> (TSurf):Sub.Fam | 2.136   | 0.078   |
| <b>Mes</b>         | 0.917          | 0.001   | 0.916          | 0.001   | 0.003   | -18.260 | log <sub>10</sub> (TSurf):Tr.Guild | 0.547   | 0.739   | 0.003     | -51.68  | log <sub>10</sub> (TSurf):Order | 5.857   | 0.022   | 0.003          | -5.898  | log <sub>10</sub> (TSurf):Sub.Fam | 1.322   | 0.286   |
| <b>Tri.g</b>       | 0.374          | 0.061   | 0.374          | 0.079   | 0.002   | -15.807 | log <sub>10</sub> (TSurf):Tr.Guild | 1.052   | 0.411   | 0.004     | -41.03  | log <sub>10</sub> (TSurf):Order | 0.052   | 0.821   | 0.002          | -1.340  | log <sub>10</sub> (TSurf):Sub.Fam | 1.226   | 0.332   |
| <b>Tri.g F</b>     | 0.662          | 0.001   | 0.662          | 0.005   | 0.004   | 9.876   | log <sub>10</sub> (TSurf):Tr.Guild | 0.467   | 0.797   | 0.004     | -21.89  | log <sub>10</sub> (TSurf):Order | 9.159   | 0.005   | 0.005          | 20.731  | log <sub>10</sub> (TSurf):Sub.Fam | 0.908   | 0.529   |
| <b>Cer</b>         | 0.814          | 0.002   | 0.814          | 0.002   | 0.002   | -31.799 | log <sub>10</sub> (TSurf):Tr.Guild | 1.094   | 0.389   | 0.002     | -59.46  | log <sub>10</sub> (TSurf):Order | 0.026   | 0.872   | 0.002          | -11.373 | log <sub>10</sub> (TSurf):Sub.Fam | 0.587   | 0.777   |
| <b>Rho</b>         | 0.553          | 0.008   | 0.553          | 0.015   | 0.001   | -47.037 | log <sub>10</sub> (TSurf):Tr.Guild | 0.988   | 0.446   | 0.001     | -79.97  | log <sub>10</sub> (TSurf):Order | 2.341   | 0.137   | 0.001          | -26.515 | log <sub>10</sub> (TSurf):Sub.Fam | 0.813   | 0.600   |

Table A5.9. Modular Surface Area data: Phylogenetic signal and multivariate Procrustes distance-ANOVA PGLS factorial model fitting results for the Complete (**A, C**; n=34) and Dromornithids-excluded (**B, D**; n=31) data sets. **A–B**, phylogenetic signal assessed under Brownian motion assumptions for each endocast module conducted using the Geomorph function ‘physignal’ and Modular Surface Areas showing phylogenetic signal are highlighted green. **C–D**, Model fitting conducted using the function ‘procDppls’ employing 999 RRPP permutations as implemented in Geomorph. Procrustes distance-ANOVA statistics are given for each of three categorical (Trophic Guild, Order, and Sub-Family) fitted model factors (see 5.2.7.4), where non-significant results are highlighted pink. **Abbreviations**, ANOVA, analysis of variance; **Cer**, cerebellum; **EmSg**, eminentia sagittalis; **K<sub>m</sub>**, Adams’ K<sub>mult</sub>; **MSurf**, modular surface area; **Mes**, mesencephalon; **PGLS**, phylogenetic generalised least squares; **Phylo.**, phylogenetic; **Rho**, rhombencephalon; **RRPP**, randomized residual permutation procedure; **Sub.Fam**, Sub-Family/Family; **Tel.c**, caudal telencephalon; **Tel.r**, rostral telencephalon; **Telen**, complete telencephalon; **Tr.Guild**, trophic guild; **Tri.g**, trigeminal ganglion; **Tri.g F**, cross-section of the maxillomandibular (V2+V3) branch of the trigeminal nerve (V); **TSurf**, total endocast surface area; **X**, factorial variable; one of three categorical model factors: Trophic Guild, Order or Sub-Family (see Fig. 5.1; 5.2.6.4); **Y**, response variable; one of nine modular endocast surface area measurements (see also **MSurf**).

| A. Phylo. Signal   |                |         | C. Complete Modular Surface Area data: PGLS model = log <sub>10</sub> (Y) ~ log <sub>10</sub> (TSurf) * X               |       |                |         |         |         |             |       |                |         |         |         |                |       |                |         |         |         |
|--------------------|----------------|---------|---|-------|----------------|---------|---------|---------|-------------|-------|----------------|---------|---------|---------|----------------|-------|----------------|---------|---------|---------|
| Modules<br>Y=MSurf | Geomorph       |         | X = Trophic Guild   |       |                |         | ANOVA   |         | X = Order   |       |                |         | ANOVA   |         | X = Sub-Family |       |                |         | ANOVA   |         |
|                    | K <sub>m</sub> | P value | Effect  | SSq   | R <sup>2</sup> | z-score | F value | P value | Effect      | SSq   | R <sup>2</sup> | z-score | F value | P value | Effect         | SSq   | R <sup>2</sup> | z-score | F value | P value |
| <b>EmSg</b>        | 1.047          | 0.001   | TSurf:Tr.Guild  | 0.012 | 0.014          | 4.763   | 2.037   | 0.001   | TSurf:Order | 0.009 | 0.011          | 3.379   | 2.585   | 0.001   | TSurf:Sub.Fam  | 0.007 | 0.008          | 3.447   | 0.663   | 0.001   |
| <b>Tel.r</b>       | 0.817          | 0.001   | TSurf:Tr.Guild  | 0.033 | 0.058          | 3.147   | 2.060   | 0.001   | TSurf:Order | 0.014 | 0.025          | 1.949   | 1.478   | 0.003   | TSurf:Sub.Fam  | 0.028 | 0.050          | 3.214   | 1.504   | 0.001   |
| <b>Tel.c</b>       | 1.367          | 0.001   | TSurf:Tr.Guild  | 0.001 | 0.002          | 0.898   | 0.121   | 0.177   | TSurf:Order | 0.000 | 0.000          | 0.133   | 0.067   | 0.513   | TSurf:Sub.Fam  | 0.004 | 0.010          | 2.676   | 0.513   | 0.002   |
| <b>Telen</b>       | 1.032          | 0.001   | TSurf:Tr.Guild  | 0.001 | 0.003          | 3.994   | 0.582   | 0.001   | TSurf:Order | 0.000 | 0.000          | 1.648   | 0.166   | 0.008   | TSurf:Sub.Fam  | 0.001 | 0.004          | 4.529   | 0.669   | 0.001   |
| <b>Mes</b>         | 1.481          | 0.001   | TSurf:Tr.Guild  | 0.007 | 0.050          | 0.084   | 0.517   | 0.528   | TSurf:Order | 0.000 | 0.002          | -1.205  | 0.059   | 0.893   | TSurf:Sub.Fam  | 0.003 | 0.021          | -0.883  | 0.179   | 0.810   |
| <b>Tri.g</b>       | 1.073          | 0.001   | TSurf:Tr.Guild  | 0.016 | 0.028          | 2.793   | 1.077   | 0.001   | TSurf:Order | 0.006 | 0.011          | 1.346   | 0.750   | 0.015   | TSurf:Sub.Fam  | 0.024 | 0.042          | 3.591   | 1.488   | 0.001   |
| <b>Tri.g F</b>     | 0.849          | 0.001   | TSurf:Tr.Guild  | 0.048 | 0.102          | 1.226   | 1.251   | 0.072   | TSurf:Order | 0.000 | 0.000          | -2.341  | 0.013   | 0.975   | TSurf:Sub.Fam  | 0.056 | 0.118          | 1.484   | 1.210   | 0.044   |
| <b>Cer</b>         | 1.331          | 0.001   | TSurf:Tr.Guild  | 0.003 | 0.009          | 1.290   | 0.344   | 0.065   | TSurf:Order | 0.000 | 0.000          | -1.327  | 0.019   | 0.903   | TSurf:Sub.Fam  | 0.014 | 0.042          | 3.470   | 1.425   | 0.001   |
| <b>Rho</b>         | 0.814          | 0.001   | TSurf:Tr.Guild  | 0.010 | 0.030          | 4.243   | 2.661   | 0.001   | TSurf:Order | 0.005 | 0.015          | 2.844   | 2.227   | 0.001   | TSurf:Sub.Fam  | 0.011 | 0.034          | 4.290   | 2.280   | 0.001   |
| B. Phylo. Signal   |                |         | D. Modular Surface Area data Dromornithids-excluded: PGLS model = log <sub>10</sub> (Y) ~ log <sub>10</sub> (TSurf) * X |       |                |         |         |         |             |       |                |         |         |         |                |       |                |         |         |         |
| Y=MSurf            | K <sub>m</sub> |         | Effect  |       |                |         | ANOVA   |         | Effect      |       |                |         | ANOVA   |         | Effect         |       |                |         | ANOVA   |         |
|                    | P value        |         | Effect  | SSq   | R <sup>2</sup> | z-score | F value | P value | Effect      | SSq   | R <sup>2</sup> | z-score | F value | P value | Effect         | SSq   | R <sup>2</sup> | z-score | F value | P value |
| <b>EmSg</b>        | 0.732          | 0.003   | TSurf:Tr.Guild  | 0.012 | 0.045          | 3.315   | 2.743   | 0.001   | TSurf:Order | 0.009 | 0.035          | 1.844   | 5.025   | 0.001   | TSurf:Sub.Fam  | 0.006 | 0.023          | 1.980   | 0.710   | 0.009   |
| <b>Tel.r</b>       | 0.987          | 0.001   | TSurf:Tr.Guild  | 0.037 | 0.075          | 2.827   | 3.028   | 0.001   | TSurf:Order | 0.014 | 0.028          | 1.539   | 2.901   | 0.001   | TSurf:Sub.Fam  | 0.028 | 0.057          | 3.022   | 1.861   | 0.001   |
| <b>Tel.c</b>       | 0.867          | 0.002   | TSurf:Tr.Guild  | 0.000 | 0.002          | 0.070   | 0.112   | 0.543   | TSurf:Order | 0.000 | 0.001          | 0.079   | 0.070   | 0.571   | TSurf:Sub.Fam  | 0.004 | 0.022          | 1.913   | 0.636   | 0.009   |
| <b>Telen</b>       | 0.676          | 0.004   | TSurf:Tr.Guild  | 0.001 | 0.005          | 3.373   | 0.803   | 0.001   | TSurf:Order | 0.000 | 0.000          | 0.695   | 0.091   | 0.261   | TSurf:Sub.Fam  | 0.001 | 0.008          | 4.135   | 0.946   | 0.001   |
| <b>Mes</b>         | 0.917          | 0.001   | TSurf:Tr.Guild  | 0.009 | 0.094          | 0.324   | 0.858   | 0.40    | TSurf:Order | 0.000 | 0.003          | -0.384  | 0.108   | 0.729   | TSurf:Sub.Fam  | 0.003 | 0.027          | -0.951  | 0.187   | 0.842   |
| <b>Tri.g</b>       | 0.374          | 0.061   | TSurf:Tr.Guild  | 0.012 | 0.034          | 1.902   | 1.056   | 0.01    | TSurf:Order | 0.000 | 0.000          | -0.547  | 0.033   | 0.766   | TSurf:Sub.Fam  | 0.018 | 0.049          | 2.518   | 1.294   | 0.002   |
| <b>Tri.g F</b>     | 0.662          | 0.001   | TSurf:Tr.Guild  | 0.058 | 0.160          | 1.304   | 1.943   | 0.053   | TSurf:Order | 0.000 | 0.001          | -0.945  | 0.023   | 0.857   | TSurf:Sub.Fam  | 0.056 | 0.153          | 1.296   | 1.459   | 0.059   |
| <b>Cer</b>         | 0.814          | 0.002   | TSurf:Tr.Guild  | 0.003 | 0.015          | 0.835   | 0.426   | 0.198   | TSurf:Order | 0.000 | 0.000          | -0.463  | 0.031   | 0.758   | TSurf:Sub.Fam  | 0.014 | 0.073          | 2.477   | 1.680   | 0.001   |
| <b>Rho</b>         | 0.553          | 0.008   | TSurf:Tr.Guild  | 0.006 | 0.035          | 3.275   | 2.277   | 0.001   | TSurf:Order | 0.000 | 0.000          | -0.907  | 0.007   | 0.844   | TSurf:Sub.Fam  | 0.007 | 0.040          | 3.412   | 1.867   | 0.001   |

## CHAPTER 6

## SUMMARY AND CONCLUSIONS

In this study, the application of CT scanning technologies allowed the construction of model endocasts representing the brain anatomy of fossil birds and kin. Geometric information described by multivariate coordinates of anatomical landmarks, combined with univariate measurements derived from those data, were employed to characterise morphological shape distinctions between galloanseres across diverse temporal scales, with the objective of addressing three main aims: **1**, assess morphological changes over short time scales; **2**, characterise endocranial morphology relating to lineage evolution through time; and **3**, assess whether brain morphology retains a phylogenetically informative component across a diverse avian clade, or whether adaptation to habitat is overwhelming in endocranial structure. Three case studies examined these aims by quantifying transformations in endocast shape. In **1**, over a timescale of thousands of years, I assessed endocast morphological changes associated with loss of volancy in Finsch's duck (see Chapter 3, and **6.2** below). In **2**, reflecting millions of years of change, I characterised endocast morphology and lineage evolution of three species of dromornithids [Note; four species were assessed, but only three endocasts were landmarked, and so more thoroughly evaluated], (see Chapter 4, and **6.3** below). In **3**, I assessed brain shape and how it relates to phylogeny and adaptive signal across the diverse avian clade Galloanseres, which includes waterfowl (Anseriformes), where specialist divers and grazers repeatedly appear in the family tree, dromornithids (Gastornithiformes), which were terrestrial browsers, and landfowl (Galliformes), which are exclusively terrestrial omnivores (see Chapter 5, and **6.4** below).

I used two suites of Modular Lms to characterise endocast shape in these assessments. For the Finsch's duck assessment (see **6.2** below), I first developed a Modular Lm suite comprising 14 modules, each capturing a distinct zone of the brain (see Chapter 3, Appendices, **A3.8.1**). Based on results from these assessments, a second refined Modular Lm suite, incorporating 13 individual Lm modules, was employed for the categorisation and assessment of endocast shape in the remaining two data chapters (see Chapter 2 Appendices, **A2.1**).

I developed these individual Modular Lm suites to allow for comparisons of discrete zones of the avian endocast, as it is well established that overall brain shape is dictated by independent hyper- or hypotrophy of individual brain regions (e.g. [Barton et al. 1995, 2003](#); [Barton & Harvey 2000](#); [Whiting & Barton 2003](#); and references therein), known as the 'mosaic' model of brain evolution (*sensu* [Barton & Harvey 2000](#); see Introduction, **1.5.4**). I was interested in identifying where, and to what degree, covariation and differential hyper- or hypotrophy between individual zones, or parts, of the brain was occurring. As it has been shown that particular brain nuclei share greater levels of neuronal connectivity associated with specific functions, and that distinctions in the shape of parts of

the brain, are somewhat reflective of functional specialisation (e.g. [Dubbeldam 1998a](#); [Barton & Harvey 2000](#); [Iwaniuk et al. 2008](#); [Corfield et al. 2012, 2015a](#); and references therein).

Morphological integration is the correlation between traits, and assessment of the degree of trait correlation, as described by the Modular Lm suite, may inform how endocranial shape is influenced by common developmental pathways or by functional adaptation (e.g. [Klingenberg 2009](#); [Adams & Felice 2014](#); [Adams 2016](#)). I tested for morphological integration across the full Modular Lm suite by means of Modularity analyses (see Chapter 3, [3.2.7.2](#)), which showed that the degree of covariation between modules was less than that found within modules (i.e., characteristic of a more modular structure, where modules vary independently of one another). Assessments of the degree of pairwise modular covariation were conducted using Two-Block Partial Least Squares analyses (2B-PLS, *sensu* [Rohlf & Corti 2000](#); see also [Bookstein et al. 2003](#); [Adams & Felice 2014](#); and Chapter 3, [3.2.7.3](#)), which showed that some modules were clearly more closely integrated than others. These assessments also showed that the morphological modules comprising the Modular Lm suite were independent, and robustly defined.

### **6.1 Limitations of, and modifications to the Modular Lm suite**

The quality of data derived from the Modular Lm suite developed here (i.e. Chapter 3, Appendices, [A3.8.1](#), Fig. A3.1), was dependent on the consistent placement of modular Lm patches on surfaces that do not include particularly well-defined boundaries, or borders between different brain structures. I argued that modules with better delimited margins, could be those most consistently defined, and so more reliably detect trends in endocast shape change. These most easily defined modules included: eminentia sagittalis, rostral telencephalon, caudal telencephalon, mesencephalon, cerebellum, and rhombencephalon. Additionally, I recommended the exclusion of the olfactory and orbits modules, as they were not well morphologically delimited, and recognised that it was an oversight in the Chapter 3 analyses to remove, or ‘segment out’ from the final models employed, the trigeminal ganglia (V) complexes inserting on the ventral surfaces of the mesencephalon (see **tri.g**, Introduction, Fig. 1.5.1C, and below). Trigeminal ganglia represent the largest somatosensory cranial innervation complexes (e.g. [Dubbeldam et al. 1979](#); [Bubień-Waluszewska 1981](#); [Wild & Zeigler 1980](#); [Wild 1981, 1990](#); [Dubbeldam 1998a, 1998b](#); and Introduction, [1.5.4.1](#)), and so the assessment of trigeminal ganglia shape would have allowed additional functional insight into levels of sensory input from the beak, palate and tongue (e.g. [Gutiérrez-Ibáñez et al. 2009](#)), specific feeding behaviours (e.g. [Dubbeldam 1992](#)), and cerebral afferent terminal fields associated with these nerves (e.g. Introduction, [1.5.4.2.2](#)). Consequently, a refined Modular Lm suite was established, incorporating trigeminal ganglia modules, and excluding the orbit and olfactory modules (see General Methods Appendices, [A2.1](#), Fig. 2.1), for application in subsequent assessments (Chapters 4, [6.3](#) and 5, [6.4](#) below).

Overall, during this project, the use of discrete Lm modules to compare endocast shape differences between individuals or taxa, allowed the quantification of these differences in a way not previously attained for birds. The approach demonstrated by [Wiley et al. \(2005\)](#) for delimiting discrete divisions of Old World monkey neurocrania, using groups, or modules, of semilandmarks has been applied, for example, to demonstrate the process of sliding semilandmarks on curves and surfaces of primate skulls by [Gunz & Mitteroecker \(2013:fig. 4\)](#), in the assessment of the brains of New World monkeys ([Aristide et al. 2016](#)), the neurocranial and mandibular morphology of dingoes ([Parr et al. 2016](#)), and also in [Felice & Goswami's \(2018\)](#) assessment of mosaic evolution in neornithine neurocrania. However, until now, comparisons of 3D fossil avian brains have been largely subjective, and based on visual inspection of whole endocasts (e.g. [Ashwell & Scofield 2008](#); [Corfield et al. 2008](#); [Scofield & Ashwell 2009](#); [Walsh & Knoll 2011](#); [Walsh & Milner 2011a, 2011b](#); [Smith & Clarke 2012](#); [Ksepka et al. 2012](#); [Paulina-Carabajal et al. 2014](#); [Tambussi et al. 2015](#); [Proffitt et al. 2016](#); [Walsh et al. 2016](#)), or by using Lms placed on extremities, eminences and junctions between divisions of the brain (e.g. [Kawabe et al. 2013b, 2014, 2015](#); [Carril et al. 2015](#); [Marugán-Lobón et al. 2016](#)). The approach used here allowed for the first time, appreciation of the degree of differential hyper- or hypotrophy between individual zones of the fossil avian brain. The evaluation of these morphological patterns, allowed the relative importance of changes in various areas of the brain to be considered systematically, and with respect to the current understanding of the functional attributes of avian neuroanatomy.

## 6.2 Endocranial morphology associated with loss of volancy in Finsch's duck

Previous work on fossils of *Chenonetta finschi* has shown there was a 10% reduction in the size of forelimb and pectoral girdle elements, relative to body size, based on femur length, over a ~20 kys period, revealing a rapid transition to flightlessness in the taxon (e.g. [Worthy 1988, 1997](#); [Watanabe 2017](#)). I used four *C. finschi* endocasts, sourced from key time periods across a radiocarbon dated temporal sequence, documenting the transition to flightlessness. Assessment of all modules sought directional change through time, that may have been correlated with the postcranial morphological changes. All data forms identified a similar trend of hypertrophy of the orbits, eminentia sagittalis, and mediolateral caudal telencephalon Lm modules, along with hypotrophy of the hindbrain in Finsch's duck across the temporal sequence. I suggested that those morphological changes were potentially related to increasing reliance on a visually accurate, tactile terrestrial grazing mode of life, and to the diminishing requisites of 3D spatial awareness as the taxon became progressively flightless.

Results showed that *C. finschi* likely transitioned into a flightless terrestrial grazing niche, remarkably rapidly in the post-glacial Holocene period (*sensu* [Worthy 1988, 1997](#); [Watanabe 2017](#)), facilitated by the increase of more abundant shrubland, and increasingly stable food resources (e.g. [Worthy 1988:625](#)). The marked changes identified in postcranial elements of *C. finschi* by [Worthy](#)

(1988, 1997), were accompanied by only comparatively small changes in its brain over the same period. However, this was not unexpected, as the pattern of the brain ‘lagging behind’ rapid postcranial anatomical changes has been recognised before, such as for Haast’s eagle (see [Scofield & Ashwell 2009](#)). So, I would predict that in the numerous cases where flightless insular forms have developed over short geological timescales, such as for *Anas* teals in the NZ subantarctic (see [Livezey 1990](#)), or rails (Rallidae; see [Olson 1973](#); [Livezey 2003](#)), that the overt features related to flightlessness, will be greater than any concomitant changes in endocranial morphology.

In hindsight, this first analysis of Finsch’s Duck may have been improved if the more refined second modular suite developed for Chapters 4 and 5 was applied to the problem (e.g. General Methods Appendices, **A2.1**; Fig. 2.1; and above), especially if this also included modules capturing the trigeminal ganglia on the ventral mesencephalon (see **6.1** above). Additionally, while constrained by availability, it would be desirable to increase the sample size by minimally one specimen per dated site; this is not possible, however, for the oldest population (Honeycomb Hill Cave L3), as only one cranium is known. This would allow better characterisation of the intraspecific variation for individual time periods, and thus better assess the trends found across the ~20 kys period. In addition, I recommend that such a refined analysis should be accompanied by linear data collected from specimen neurocranial orbits (*sensu* [Hall & Ross 2007](#); [Hall 2008](#)). Nevertheless, this study identified a series of directional changes over time in the endocast of Finsch’s duck, and future investigations into transitions associated with flightlessness could look for similar patterns, employing the techniques developed herein.

### **6.3 Endocranial morphology and lineage evolution of three species of dromornithids**

Dromornithid neurocranial anatomy has previously been comprehensively described (e.g. [Murray & Megirian 1998](#); [Murray & Vickers-Rich 2004](#); [Worthy et al. 2016b](#)), but there existed no information regarding the variation in specific shape and size of the dromornithid brain, across the two lineages hypothesised by [Worthy et al. \(2016b\)](#).

The digital reconstruction from medical CT data of a composite endocast for the Oligo-Miocene *Dromornis murrayi*, derived from two incomplete fossil skulls (Chapter 4, **4.2.4.4**; Fig. A4.9), allowed the assessment of the endocast shape of this species for the first time. Similarly, the first digital reconstruction of the brain of the middle Miocene *Dromornis planei*, was extracted from within a dense limestone matrix by Neutron CT scanning technology. These endocasts were compared to each other, and to that of the middle Miocene *Ibandornis woodburnei*, from the second hypothesised dromornithid lineage. A third *Dromornis* species, *D. stirtoni*, from the late Miocene, was represented by more poorly preserved specimens. Endocast models were therefore incomplete, but allowed the alignment of 2D preserved features with those of *D. planei*. This enabled assessment of endocranial changes associated with the extreme neurocranial foreshortening across the *Dromornis* lineage recognised by [Worthy et al. \(2016b\)](#).

Those assessments showed that neurocranial foreshortening had resulted in rostroventral endocranial surfaces in *D. stirtoni*, rotating rostr dorsally around the medial caudal telencephalon into a more dorsally oriented position. This was accompanied by a more ventrally orientated hindbrain in *D. stirtoni*, possibly reflecting a compensatory ventral rotation of the dorsoventral hindbrain complex. However, the ‘life position’ of the midbrain in the skull of *D. stirtoni*, had not changed appreciably from that of *D. planei*.

Overall, dromornithids differed markedly from basal galloanseres in the shape of the rostr dorsals regions of the endocast. In caudolateral regions of the cerebrum, dromornithids were more similar to the anseriforms *Anseranas semipalmata* and *Anhima cornuta*, than the galliform megapodiid *Leipoa ocellata*. All sampled galloanseres showed greater ventral projection of the rhombencephalon regions of the ventral hindbrain than dromornithids, but in most hindbrain ratios, dromornithids and galloanseres overlap.

The two lineage hypothesis (i.e. *Dromornis* and *Ilbandornis/Barawertornis* lineages *sensu* [Worthy et al. 2016b](#)) was supported by minimally five endocast apomorphies, namely: **1**, in *Ilbandornis*, the medial boundaries of the eminentia sagittalis in the rostrocaudal fissura interhemispherica zone of the dorsal endocast, are more medially delimited, i.e., closer together, than in species of *Dromornis*; **2**, in *Ilbandornis*, the caudal telencephalon projects further caudally in the zone of the cerebrum pars occipitalis, than in species of *Dromornis*; **3**, in *Ilbandornis*, the caudoventral regions incorporating the arcopallium, comprising the most ventral eminence of the caudal telencephalon in the zone of the fissura subhemispherica, is notably less ventrally pronounced, than in species of *Dromornis*; **4**, the projection of rostr dorsals and caudodorsal cerebellum margins is greater in *Ilbandornis*, than in species of *Dromornis*; and **5**, the overall hindbrain is rostrocaudally longer, and mediolaterally narrower in *Ilbandornis*, than in species of *Dromornis*.

Interpreted with data from associated gastrolith sets as a proxy for diet, I inferred functional interpretations from endocast shape that suggested dromornithids were highly specialised herbivores, possessed stereoscopic depth perception, and had well-developed visual proficiency associated with foraging dexterity and locomotion. Taken together, results suggested dromornithids likely targeted a soft browse (i.e., new growth, soft leaves and fruit) trophic niche in complex, mosaic vegetative environments.

The endocast reconstructions presented herein, revealed the oldest dromornithid *D. murrayi* (~20 Ma) likely possessed reasonable olfactory capabilities. The olfactory bulb visible is somewhat hypertrophied, comparable with the anseriform *A. semipalmata*, and distinctly larger than that of the galliform *L. ocellata*. Those assessments also showed that there appears to have been no reduction in the size of the dromornithid olfactory bulb across the temporal sequence. This conclusion is reached despite apparent reduction in dorsal aspect, as from the ventral aspect, the lateral margins of the organ transitions into the rostroventral endocast, without reduction in mediolateral width. It appears that progressive hypertrophy of eminentia sagittalis structures, have dorsally-engulfed the olfactory bulbs,

so reducing their visibility. This condition potentially occurs in all moa species, which show the largest skeletal olfactory chambers of all ratites (e.g. [Worthy & Scofield 2012](#)), and moa display rostr dorsally hypertrophied eminentia sagittalis structures too (see [Ashwell & Scofield 2008:fig 6g-l](#); [Corfield et al. 2008:fig. 1bD-E](#)), which effectively mask the olfactory bulb from the dorsal aspect. However, engulfment of the olfactory bulbs was not considered by [Ashwell & Scofield \(2008:151\)](#). Therefore, the potential exists for future comparisons of dromornithid and moa olfactory capacity by means of CT scanning rostral skull regions, and volumetric assessment of their respective olfactory chambers. The olfactory chamber in moa is in the ethmoid capsule rostral to the orbits, and so within the cranium (see [Worthy & Scofield 2012](#)), but in dromornithids, with the foreshortened crania, these will likely be in the large complex rostrum. Such rostra are known, but are as yet unstudied. These evaluations should also potentially include an endocast assessment between taxa, because as with dromornithids, moa may display evidence of the extent of the olfactory bulb. Such is suggested to some degree by the ventral views of endocasts for *Dinornis novaezealandiae* and *Anomalopteryx didiformis* (see [Corfield et al. 2008:figs. 1D-E](#); [Ashwell & Scofield 2008:figs. 6e-i](#)).

The comparisons herein (see Chapter 4, [4.4.1.2](#); and Chapter 5, [5.4.6](#)), showed that in dromornithids, the eminentia sagittalis was positioned relatively rostr dorsally, more similar to the condition seen in galliforms, and distinct to that seen in anseriforms, which are more caudally orientated. This aspect of dromornithid endocranial morphology has potential phylogenetic implications, that are discussed along with other morphological correlations between fossil and extant taxa recognised in Chapter 5 assessments (see [6.4](#) below).

In future, it will be desirable to assess whether the morphological differences from species of *Dromornis* revealed in *Ilbandornis woodburnei* are robust lineage specific traits. Yet to be discovered cranial specimens of *I. lawsoni* and *Barawertornis tedfordi* are required for this. Additionally, such evaluation should include cranial material of *Genyornis newtoni*, the youngest member of the putative *Ilbandornis/Barawertornis* lineage (*sensu* [Worthy et al. 2016b](#)). This is now possible following the recent discovery of cranial material from Lake Callabonna in South Australia.

During this project, I scanned neurocrania of *Dromornis stirtoni*, *D. murrayi* and *Ilbandornis woodburnei* using medical CT technology, that afforded resolutions of between 240-320  $\mu\text{m}$ . The  $\sim 95$   $\mu\text{m}$  resolution of the *D. planei* Neutron CT data, provided substantially more morphological information, than was afforded by medical CT data, and so I suggest that future scanning of dromornithid neurocrania should be conducted at a maximum of 100  $\mu\text{m}$  resolution. Although the reconstructed scan data for dromornithid specimens at  $\sim 100$   $\mu\text{m}$  requires significant computing power, and are cumbersome to segment, the quality of resultant data derived from such endocast models, are worth the effort, and yield more precise data.

#### 6.4 Assessment of how brain shape relates to phylogeny and ecology across galloanseres

I extended the geometric morphometric approach to the assessment of endocast shape across a clade (Chapter 5), to ascertain the potential impact of adaptive radiation for specific niches, on the phylogenetic utility of the galloansere brain. It is apparent that avian brain morphology is linked with adaptive and functional traits (see Introduction, **1.5.4**), but whether the differential hypo- or hypertrophy of one or more brain regions across a clade, is consistently related to occupancy of specific trophic niches, such as diving or terrestrial grazing, or whether the shape of one or more brain regions are reflective of phylogenetic affinity, remained to be assessed.

I combined the four endocasts of Finsch's duck (Chapter 3, **6.2** above), with those of three dromornithid taxa (Chapter 4, **6.3** above), along with two endocasts of the European Oligo-Miocene duck *Mionetta blanchardi*, and a broad sample of extant galloanseres, assembling a total data set of 34 endocasts (see Chapter 5 Appendices, Figs. A5.1–A5.8). By means of multi- and univariate Phylogenetic Generalized Least Squares (PGLS) factorial model regression methods, I assessed three categories of endocast data, to investigate whether morphological features represented by those data; **1**, retained phylogenetic signal; **2**, whether one or more modular brain regions hold a phylogenetic component, which may prove informative if described as traditional discrete or continuous characters, or used as modular multivariate matrices, for incorporation in more comprehensive cladistic assessments; and **3**, at the same time this allowed evaluation of the endocranial morphology of several fossil taxa, with respect to their evolutionary affinity with extant galloanseres.

These analyses demonstrated that morphological information conveyed by the multivariate Modular Lm data sets, comprised the most potentially useful phylogenetically informative data form. PGLS results showed that the ventral rhombencephalon and mesencephalon Lm modules, likely represented phylogenetically informative modular zones of the avian endocast. Data derived from Modular Lm configurations, Modular Distances, and to a lesser degree, Modular Surface Areas, was identified as potentially cladistically informative. Those data may afford additional taxonomic differentiation of avian taxa, if incorporated in the form of shape matrices (i.e. Modular Lm coordinates), as continuous characters (Modular univariate metrics or ratios thereof), or described as traditional discrete characters, for inclusion within more comprehensive parsimony, ML or Bayesian forms of cladistic analyses (e.g. [Ronquist et al. 2009](#); [Pennell & Harmon 2013](#); [Garamszegi 2014](#); [Lee & Palci 2015](#); [Harmon 2019](#), and references therein).

In order to test these hypotheses, and that of [Klingenberg & Gidaszewski \(2010:247\)](#) for example, who argued shape data may not be appropriate for inferring phylogenies; an appropriate set of molecular data, along with morphological characters, are required to be assembled for the taxa included in these analyses. Then, analyses run with, and without continuous characters derived from univariate data, to ascertain whether those data improve the resolution of resultant phylogenetic topologies. Results for Modular Lm data showed the best promise for cladistic utility. At this point in time, phylogenetic analyses incorporating 3D Lm configurations, are only possible using the package

TNT v1.5 (Goloboff & Catalano 2016; see also Catalano et al. 2010) in a parsimony framework. However, it is important to note that the Lm modules identified as potentially phylogenetically informative in these analyses are composed exclusively of type III Lms, as defined by Palci & Lee (2019:3; see also Bookstein 1991), and those authors suggest type III Lm configurations constitute “weak levels of anatomical correspondence”. What is more, both LHS and RHS Modular Lm configurations incorporated in Modular Lm data analyses, constitute statistically ‘non-independent’ modules, which are effectively “correlated via bilateral symmetry”. The effect of which may influence the estimation of evolutionary rates (see Palci & Lee 2019:9).

Accordingly, several recommendations proposed by Palci & Lee (2019) and Catalano & Torres (2017) are required. For example, Modular Lm configurations should be assessed via phylogenetic 2B-PLS assessments to ascertain integration levels (i.e., distinctness), with other Lm modules comprising the Modular Lm suite (*sensu* Klaczko et al. 2016; Sherratt et al. 2017b). Investigations should consider the potential use of phylogenetically conditioned regression or PCA residuals as input data (*sensu* Sherratt et al. 2017a; Bright et al. 2019), as opposed to Procrustes aligned coordinates. Corrections for “bilateral redundancy” may be accommodated, by excluding Lm coordinates from one side of bilateral configurations after Procrustes alignment (*sensu* Palci & Lee 2019), and those data should be tested on so called “low-level phylogenetic relationships” (see Palci & Lee 2019:11), where morphological variation is not particularly distinct (see also Catalano et al. 2010:548). Catalano & Torres (2017) recognised there existed a relationship between the number of distinct Lm configurations included in a cladistic assessment, and the resultant topological correspondence. Thus, all appropriately conditioned Modular Lm configurations showing significant Sub-Family factorial model fitting results, should be included together along with assembled molecular data and morphological characters, in cladistic assessments employing TNT software.

## 6.5 Evolutionary correlations of fossil and extant taxa

The data sets assembled for the first two projects, were reasonably limited (i.e. Chapter 3 used five specimens, and Chapter 4 used six). This was primarily a result of specimen availability, i.e., all available dromornithid crania were assessed, and further exemplars of the older Finsch’s duck population do not exist. In addition, limitations relating to scanning costs, and time constraints involved with the extraction of appropriate endocasts from those CT data, limited what could be achieved in this project. The full 34 specimen data set used for Chapter 5, was only available after years of data collection and meticulous modelling. Consequently, appropriate comparisons of how *C. finschi*, dromornithid and *M. blanchardi* fossil endocasts compared across the broader sampling of galloanseres, was only able to be appreciated once the full data set was available and assessed in Chapter 5.

In the first assessment of *Chenonetta finschi* (Chapter 3, 6.2 above), it was recognised that the endocast morphology of the four specimens of *C. finschi*, were quite dissimilar to that of *C. jubata*,

which is the species identified as its sister-taxon by [Worthy & Olson \(2002\)](#). The differences between the species, is far greater than shown by the whole intraspecific variation observed in *C. finschi*. The inclusion of *Chenonetta* specimens in the expanded data set used for phylogenetic regression assessments (Chapter 5, **6.4** above), afforded the opportunity to reassess morphological correlations between *C. finschi* and *C. jubata*, with respect to a broader sample of galloanseres. Results from these analyses suggested there were distinct differences between the endocasts of *Chenonetta* specimens, more so than might be predicted by the sister-taxa status between them (see [Worthy & Olson 2002](#)). Notably, these comparisons reveal that the endocast morphology of *C. finschi* was more similar to that of other anatines such as *Anas* spp., *Tadorna*, or dendrocygnines (e.g. Chapter 5, Figs. 5.5–5.8) than to *C. jubata*, which was more closely associated with *Malacorhynchus membranaceus* and *Nettapus pulchellus* (see also below). These observations raise the possibility that the postcranial synapomorphies recognised by [Worthy & Olson \(2002\)](#) in the synonymy of *C. finschi*, may represent convergent functional adaptations to terrestrial grazing. Accordingly, further assessment of the relationships of species currently placed in *Chenonetta* taxonomy is required, and if the differences found here are supported, resurrection of the genus *Euryanas* may be justified for *C. finschi*. It is notable that as yet, the relationships of *C. finschi* have not been assessed in any DNA analysis of waterfowl. Existing molecular phylogenies (e.g. [Sraml et al. 1996](#); [Johnson & Sorenson 1999](#); [Sorenson et al. 1999](#); [Donne-Goussé et al. 2002](#); [McCracken & Sorenson 2005](#); [Eo et al. 2009](#); [Gonzalez et al. 2009](#); [Robertson & Goldstein 2012](#)), have not included a suitably comprehensive suite of taxa to assess the relationships of all Australian waterfowl, and I suggest that such an analysis needs to include *C. finschi*.

The distinction between dromornithids and all other taxa, was recognised across all data sets (see above), with dromornithids positioned outside of either galliform or anseriform morphospace in all assessment plots in the expanded data sets (n=34) for Chapter 5 assessments (e.g. Figs. 5.5A, 5.6A, 5.7, 5.8). Apart from the highly derived and hypertrophied nature of dromornithid eminentia sagittalis morphology, it was recognised (see Chapter 4, **4.4.1.2** and Chapter 5, **5.4.6**) that the more rostradorsal condition of the dromornithid eminentia sagittalis, is more similar to the condition seen in galliforms, and is distinct to that seen in anseriforms, wherein it is more caudally orientated (e.g. [Stingelin 1957:pl. 29](#); [Ebinger 1995:fig. 1a-b](#); [Kalisińska 2005:figs. 1.1, 1.2](#); [Kawabe et al. 2010:fig 1, 2013a:fig. 2, 2014:fig. 4](#); see also [Proffitt et al. 2016:fig. 3](#)). This results in the caudal margins of the anseriform eminentia sagittalis overlapping the rostradorsal eminence of the cerebellum, when viewed from the lateral aspect (see also Chapter 4, Fig 4.4; Chapter 5, Figs. A5.1–A5.4). These distinctions are evident in dorsal endocast views too (Chapter 4, Fig. 4.4; Chapter 5, Figs. A5.5–A5.8), and clearly described by Chapter 5 PC1 shape change plots for dorsal endocast Lm modules. For example, x-axis; Fig. A5.10, where the galliform condition of more rostrally orientated eminentia sagittalis structures is depicted particularly well, with respect to the more caudal positioning evident in anseriform taxa.

The distinctive rostral versus caudal positioning of eminentia sagittalis structures across avian taxa has long been recognised. For example, [Stingelin \(1957\)](#) proposed the more rostral positioning of the eminentia sagittalis is a primitive, or “lower” form, as he termed it, and is evident in sphenisciforms (e.g. [Ksepka et al. 2012](#); [Paulina-Carabajal et al. 2014:fig 5](#); [Kawabe et al. 2014:fig 5](#); [Tambussi et al. 2015:fig 7](#); [Proffitt et al. 2016:fig 3](#)), ratites (e.g. [Craigie 1939:figs. 1-2](#); [Martin et al. 2007:fig. 2a](#); [Ashwell & Scofield 2008:figs. 6g-l](#); [Corfield et al. 2008:fig 1B-E](#); [Peng et al. 2010:figs. 1, 3](#); [Picasso et al. 2011:fig 1](#)), and in several neornithine taxa (e.g. [Stingelin 1957:pls. 23-27](#); [Corfield et al. 2008:fig. 1bL](#); [Picasso et al. 2009:fig 5](#); [Kawabe et al. 2010:fig 1](#); [Walsh & Milner 2011a:figs. 11.3D-G](#); [Smith & Clarke 2012:figs. 2-3, 8-11](#); [Wylie et al. 2015:figs. 3A-C](#); [Walsh & Knoll 2018:fig. 5.3](#)). Therefore, this ‘primitive’ condition is evident in taxa other than galliforms, and if not independently derived in all these lineages, may be plesiomorphic for neornithines.

Additionally, I note that although dromornithids plot outside of the galloansere morphospace (e.g. Chapter 5, Fig. A5.10), they are aligned more closely with, and overlap the galliform morphospace along the negative x-axis more so, than they do across the morphospace occupied by all anseriforms along the positive x-axis. Furthermore, I suggest that derivation of the distinctive dromornithid eminentia sagittalis condition from the galliform condition, is arguably more ‘parsimonious’ than from the more caudally positioned anseriform condition, and is suggestive of dromornithid origins more closely aligned with basal galliform taxa, as proposed by [Worthy et al. \(2017b:13, see also 2017c\)](#), and *contra* [Murray & Vickers-Rich \(2004\)](#).

*Mionetta blanchardi* is a common early Oligo-Miocene erismaturine from Europe ([Livezey & Martin 1988](#); [Worthy 2009](#)). It is notable that *M. blanchardi* associates remarkably closely with *Malacorhynchus membranaceus* in all PGLS regression plots for mesencephalon (Chapter 5, Figs. 5.5A–B), and rhombencephalon (Chapter 5, Figs. 5.6A–B) Lm modules, and also in the PCA plot for the same modules (Chapter 5, Fig. 5.8). These results support hypotheses of a close relationship between these taxa by [Worthy et al. \(2007\)](#), [Worthy & Lee \(2008\)](#) and [Worthy \(2009\)](#) who proposed the taxa were basal in the erismaturine clade. The close morphological associations noted here between *M. blanchardi*, and the extant taxa *M. membranaceus*, *Nettapus pulchellus*, and *Chenonetta jubata*, may be indicative of the hypothesised Oligo-Miocene through Miocene basal erismaturine global radiation. This is represented by the fossil taxa *Mionetta* in the Northern Hemisphere, and *Pinpanetta*, *Tirarinetta*, *Awengkere* (see Introduction, **1.4.7.1**), *Manuherikia*, and *Dunstanetta* (see Introduction, **1.4.7.2**) in the Australasian Southern Hemisphere (see [Worthy et al. 2007](#); [Worthy 2008](#); [Worthy & Lee 2008](#); [Worthy et al. 2008b](#); [Worthy 2009](#); [Worthy & Yates 2017](#)). The extant taxa *M. membranaceus*, (and potentially *Stictonetta naevosa* too), may represent relictual remnants of this ancient waterfowl radiation ([Worthy 2009](#); see also the molecular assessments of [Sraml et al. 1996](#); [Eo et al. 2009](#); [Gonzalez et al. 2009](#)).

The relationships of some extant Australasian anatids have as yet not been robustly constrained by analyses of comprehensive molecular data. Notably, *Nettapus pulchellus* is one such

taxon. [Worthy & Lee \(2008\)](#) and [Worthy \(2009\)](#) advocated a position “close to *Anas*” within Anatinae based on morphological data. However, results of the present analyses suggested a more basal position for *N. pulchellus* may be more likely, consistent with the very limited molecular data available (e.g. [Sraml et al. 1996](#); [Eo et al. 2009](#)). Additionally, there has been much contention regarding the affinities of the Australian wood duck *Chenonetta jubata*, which is usually placed relatively basal in Anatinae as now defined ([Donne-Goussé et al. 2002](#); [Gonzalez et al. 2009](#); [Robertson & Goldstein 2012](#)). On morphological data, the taxon has been variously assigned to Anatini ([Livezey 1986:743](#)), along with *N. pulchellus* in the supergenus *Chenonetta* ([Livezey 1991:485](#)), and in the Subtribe Nettapodina, also with *N. pulchellus* ([Livezey 1997a:476](#)). The close affinity of *C. jubata* with *N. pulchellus* advocated by [Livezey \(1991, 1997a\)](#), was not supported by the limited molecular data of [Sraml et al. \(1996](#); see also [Sorenson et al. 1999](#)), but *N. pulchellus* and *C. jubata* were found closely associated in all forms of morphological assessment here (see Chapter 5, Figs. 5.5A, 5.6A, 5.7, 5.8). These morphological correlations between *C. jubata* and *N. pulchellus*, warrant further assessment including postcranial and endocranial morphological characters, and substantial new molecular data, as the affinities of the taxa appear unresolved.

The musk duck *Biziura lobata* exhibits several autapomorphic behavioural and skeletal characteristics (e.g. [McCracken 1999](#); [McCracken et al. 1999, 2000a, 2000b](#)). Although morphological assessments have recognised the taxon in Erismaturinae (formerly Oxyurinae, e.g. [Livezey 1997a](#); [Worthy & Lee 2008](#); and references therein), previous molecular and behavioural analyses (e.g. [Sraml et al. 1996](#); [McCracken et al. 1999](#); [De Mendoza 2019](#); and references therein), have suggested it is likely not an erismaturine. In fact, [De Mendoza’s \(2019\)](#) assessment of neurocranial characters alone recovered *B. lobata* as a basal taxon, and sister to all Anatidae, although in their total data set, *Biziura* was found to be the sister species to *Thalassornis*. [De Mendoza \(2019:8\)](#) argued that as homoplastic diving characters compromise morphological topologies (e.g. [Worthy & Lee 2008](#)), cranial characters provide a topology “closer” to that of molecular assessments. [Livezey \(1997a:464\)](#) categorised *B. lobata* as “bizarre”, a term which certainly applies to the morphology of the *B. lobata* brain. The Modular Lm suite used here (e.g. Introduction, Fig. 2.1), developed to capture discrete morphological divisions of the galloansere brain, was not appropriate to describe the truly ‘bizarre’ ventral endocast morphology displayed by *B. lobata* (see Chapter 5, [5.4.6](#), for comprehensive discussion of this). Not only is the overall mesencephalon condition in *B. lobata* distinct from all galloanseres, it is distinct from any neornithine brain observed ([Pers. Obs. Author](#)).

*Biziura lobata* is highly sexually dimorphic, with males and females not overlapping in body mass, a characteristic that has facilitated intraspecific trophic niche divergence (see [McCracken 1999](#); [McCracken et al. 2000b](#)). Given the extraordinary ventral endocranial morphology in these ducks, a unique opportunity exists to assess how intraspecific neuroanatomy may correlate with behavioural and morphological distinctions within a single taxon. This may be achieved by brain sectioning assessments (e.g. [Iwaniuk & Wylie 2007](#); [Gutiérrez-Ibáñez et al. 2009](#); [Wylie et al. 2015](#)). In addition,

it is curious as to why assessments including both postcranial, neuro- and endocranial morphological characterisations of highly dimorphic, and trophically divergent lekking species have not yet been universally conducted. Many avian taxa display such characteristics. For example, several galliform phasianid taxa (e.g. *Tetrao tetrax*, *T. urogallus*, *Centrocercus* spp., *Tympanuchus* spp.), the trochilidid hummingbird (*Phaethornis guy*), the otidid bustard (*Tetrax tetrax*), passerines (e.g. *Paradisaea* spp., and *Lipaugus vociferans*), and the only parrot that displays lekking behaviour (*Strigops habroptila*), may potentially be assessed in this manner. The literature abounds with assessments of lekking behaviour in birds (e.g. Pruettt-Jones & Pruettt-Jones 1990; Gibson et al. 1991; Gibson 1996; Jiguet et al. 2000; and references therein), to name but a few. However, to my knowledge, the assessment of skeletal distinctions between highly dimorphic, trophically divergent lekking taxa, have not been approached appropriately. This appears to be an oversight, and a potentially productive direction for future research.

## 6.6 CONCLUSION

The approach of using multiple Lm modules to define and allow independent comparison of shape change across distinct endocast regions between galloansere taxa, has afforded appreciation of the degree of differential hyper- or hypotrophy between individual zones of the galloansere brain. The evaluation of endocast shape has allowed the relative importance of changes in the various areas of the brain to be considered systematically. This shows that ventral endocast regions likely convey greater levels of phylogenetic information than dorsal regions, that the shapes of the dorsal regions of the brain are more functionally constrained, and likely reflect homoplastic trends for convergent functional adaptation to trophic niche and habitat use.

## CHAPTER 7

## GENERAL REFERENCES

- Acosta Hospitaleche, C., Gelfo, J.N., 2015. New Antarctic findings of Upper Cretaceous and lower Eocene loons (Aves: Gaviiformes). *Annales de Paléontologie* 101, 315-324. doi:310.1016/j.annpal.2015.1010.1002.
- Adams, D.C., 2016. Evaluating modularity in morphometric data: challenges with the RV coefficient and a new test measure. *Methods in Ecology and Evolution* 7, 565-572. doi: 510.1111/2041-1210X.12511.
- Adams, D.C., Collyer, M.L., 2016. On the comparison of the strength of morphological integration across morphometric datasets. *Evolution* 70, 2623-2631. doi:2610.1111/evo.13045.
- Adams, D.C., Collyer, M.L., Kaliontzopoulou, A., 2018. *Geomorph: Software for geometric morphometric analyses*. R package version 3.0.7. <https://cran.r-project.org/package=geomorph>.
- Adams, D.C., Felice, R., 2014. Assessing phylogenetic morphological integration and trait covariation in morphometric data using evolutionary covariance matrices. *PLoS ONE* 9, e94335. doi:94310.91371/journal.pone.0094335.
- Adams, D.C., Rohlf, F.J., Slice, D.E., 2004. Geometric morphometrics: ten years of progress following the 'revolution'. *Italian Journal of Zoology* 71, 5-16. doi:10.1080/11250000409356545.
- Adams, D.C., Rohlf, F.J., Slice, D.E., 2013. A field comes of age: geometric morphometrics in the 21st century. *Hystrix* 24, 7-14. doi:10.4404/hystrix-4424.4401-6283.
- Agnolín, F.L., Egli, F.B., Chatterjee, S., Marsà, J.A.G., Novas, F.E., 2017. Vegaviidae, a new clade of southern diving birds that survived the K/T boundary. *The Science of Nature* 104, 87. doi:10.1007/s00114-00017-01508-y.
- Allen, J., Gosden, C., Jones, R., White, J.P., 1988. Pleistocene dates for the human occupation of New Ireland, Northern Melanesia. *Nature* 331, 707-709.
- Allen, J., Gosden, C., White, J.P., 1989. Human Pleistocene adaptations in the tropical island Pacific: recent evidence from New Ireland, a Greater Australian outlier. *Antiquity* 63, 548-561. doi:510.1017/S0003598X00076547.
- Allentoft, M.E., Heller, R., Oskam, C.L., Lorenzen, E.D., Hale, M.L., Gilbert, M.T.P., Jacomb, C., Holdaway, R.N., Bunce, M., 2014. Extinct New Zealand megafauna were not in decline before human colonization. *Proceedings of the National Academy of Sciences USA* 111, 4922-4927. doi: 4910.1073/pnas.1314972111.
- Alvarenga, H.M.F., 1988. Ave fóssil (Gruiformes: Rallidae) dos folhelhos da Bacia de Taubaté, estado de São Paulo, Brasil. *Anais da Academia Brasileira de Ciências* 60, 321-328.
- Alvarenga, H.M.F., 1999. A fossil screamer (Anseriformes: Anhimidae) from the middle Tertiary of Southeastern Brazil, in: Olson, S.L. (Ed.), *Avian Paleontology at the Close of the 20th Century*. Proceedings of the 4th International Meeting of the Society of Avian Paleontology and Evolution, Washington, D.C., 4-7 June 1996, *Smithsonian Contributions to Paleobiology* 89, pp. 223-230.

- Alvarez, R., 1977. A Pleistocene avifauna from Jalisco, Mexico. *Contributions from the Museum of Paleontology* 24, 205-220.
- Alvarez, R., Olson, S.L., 1978. A new merganser from the Miocene of Virginia (Aves: Anatidae). *Proceedings of the Biological Society of Washington* 91, 522-532.
- Anderson, A., Sand, C., Petchey, F., Worthy, T.H., 2010. Faunal extinction and human habitation in New Caledonia: initial results and implications of new research at the Pindai Caves. *Journal of Pacific Archaeology* 1, 89-109.
- Andors, A.V., 1991. Paleobiology and relationships of the giant groundbird *Diatryma* (Aves: Gastornithiformes), Acta XX Congressus Internationalis Ornithologici, New Zealand *Ornithological Congress Trust Board*, Wellington, pp. 563-571.
- Andors, A.V., 1992. Reappraisal of the Eocene groundbird *Diatryma* (Aves: Anserimorphae), In: Campbell Jr, K.E. (Ed.), Papers in Avian Paleontology Honoring Pierce Brodkorb, Incorporating the Proceedings of the II International Symposium of the Society of Avian Paleontology and Evolution, Natural History Museum of Los Angeles County, 1988, *Natural History Museum of Los Angeles County Science Series* 36, pp. 109-125.
- Angst, D., Buffetaut, E., 2013. The first mandible of *Gastornis* Hébert, 1855 (Aves, Gastornithidae) from the Thanetian (Paleocene) of Mont-de-Berru (France). *Revue de Paléobiologie* 32, 423-432.
- Angst, D., Lécuyer, C., Amiot, R., Buffetaut, E., Fourel, F., Martineau, F., Legendre, S., Abourachid, A., Herrel, A., 2014. Isotopic and anatomical evidence of an herbivorous diet in the Early Tertiary giant bird *Gastornis*. Implications for the structure of Paleocene terrestrial ecosystems. *Naturwissenschaften* 101, 313-322. doi:310.1007/s00114-00014-01158-00112.
- Arends, J.J.A., Dubbeldam, J.L., 1984. The subnuclei and primary afferents of the descending trigeminal system in the mallard (*Anas platyrhynchos* L.). *Neuroscience* 13, 781-795.
- Aristide, L., dos Reis, S.F., Machado, A.C., Lima, I., Lopes, R.T., Perez, S.I., 2016. Brain shape convergence in the adaptive radiation of New World monkeys. *Proceedings of the National Academy of Sciences USA* 113, 2158-2163. doi:2110.1073/pnas.1514473113.
- Armstrong, E., 1983. Relative brain size and metabolism in mammals. *Science* 220, 1302-1304.
- Ashwell, K.W.S., Scofield, R.P., 2008. Big birds and their brains: Paleoneurology of the New Zealand moa. *Brain, Behavior and Evolution* 71, 151-166. doi:110.1159/000111461.
- Aslanova, S.M., Burčák-Abramovič, N.I., 1968. A fossil swan from the Maykopian series of Azerbaydzhan. *Acta Zoologica Cracoviensia* 14, 325-338.
- Baird, R.F., 1991. The dingo as a possible factor in the disappearance of *Gallinula mortierii* from the Australian mainland. *Emu* 91, 121-122.
- Balanoff, A.M., Bever, G.S., Rowe, T.B., Norell, M.A., 2013. Evolutionary origins of the avian brain. *Nature* 501, 93-96. doi:10.1038/nature12424.
- Ballmann, P., 1969. Die vögel aus der altburdigalen spaltenfüllung von Wintershof (West) bei eichstätt in Bayern. *Zitteliana* 1, 5-60.
- Balouet, J.C., 1984. Les étranges fossiles de Nouvelle-Calédonie. *La Recherche* 15, 390-392.
- Balouet, J.C., 1987. Extinctions des vertébrés terrestres de Nouvelle-Calédonie. *Mémoires de la Société Géologique de France* 150, 177-183.
- Balouet, J.C., Olson, S.L., 1989 Fossil birds from late Quaternary deposits in New Caledonia. *Smithsonian Contributions to Zoology* 469, pp.38.

- Barton, R.A., Aggleton, J.P., Grenyer, R., 2003. Evolutionary coherence of the mammalian amygdala. *Proceedings of the Royal Society of London B: Biological Sciences* 270, 539-543. doi:510.1098/rspb.2002.2276.
- Barton, R.A., Harvey, P.H., 2000. Mosaic evolution of brain structure in mammals. *Nature* 405, 1055-1058.
- Barton, R.A., Purvis, A., Harvey, P.H., 1995. Evolutionary radiation of visual and olfactory brain systems in primates, bats and insectivores. *Philosophical Transactions of the Royal Society of London B: Biological Sciences* 348, 381-392.
- Baumel, J.J., King, A.S., Breazile, J.E., Evans, H.E., Vanden Berge, J.C., 1993. Handbook of avian anatomy: Nomina anatomica avium. 2nd edition. *Publications of the Nuttall Ornithological Club* 23, Cambridge, Massachusetts, USA.
- Becker, J.J., 1987. The fossil birds of the late Miocene and early Pliocene of Florida. 1. Geology, correlation, and systematic overview, in: Mourer-Chauviré, C. (Ed.), l'Évolution des Oiseaux d'Après le Temoignage des Fossils, *Documents du Laboratoire Geologique de Lyon* 99, pp. 159-171.
- Beddard, F.E., 1898. *The Structure and Classification of Birds*. Longmans, Green, and Company, London. p.548.
- Bennett, P.M., Harvey, P.H., 1985. Relative brain size and ecology in birds. *Journal of Zoology* 207, 151-169.
- Benson, R.D., 1999. *Presbyornis isoni* and other late Paleocene birds from North Dakota, in: Olson, S.L. (Ed.), Avian Paleontology at the Close of the 20th Century. Proceedings of the 4th International Meeting of the Society of Avian Paleontology and Evolution, Washington, D.C., 4-7 June 1996, *Smithsonian Contributions to Paleobiology* 89, pp. 253-259.
- Berkhoudt, H., Dubbeldam, J.L., Zeilstra, S., 1981. Studies on the somatotopy of the trigeminal system in the mallard, *Anas platyrhynchos* L. IV. Tactile representation in the nucleus basalis. *Journal of Comparative Neurology* 196, 407-420.
- Bickart, K.J., 1990. Part I: The birds of the late Miocene-early Pliocene Big Sandy Formation, Mohave County, Arizona. *Ornithological Monographs* 44, 1-72.
- Bocheński, Z., 1997. List of European fossil bird species. *Acta Zoologica Cracoviensia* 40, 293-333.
- Bock, W.J., 1963. The cranial evidence for ratite affinities, In: Sibley, C.G. (Ed.), Proceedings of the XIII International Ornithological Congress. Baton Rouge, LA, *American Ornithologists' Union*, Washington D.C, pp. 39-54.
- Boeuf, O., Mourer-Chauviré, C., 1992. Les oiseaux des gisements d'âge pliocène supérieur de Chilhac, Haute-Loire, France. *Comptes rendus de l'Académie des sciences de Paris* 314 (Série II), 1091-1096.
- Boev, Z., 1998. Fossil birds of Dorkovo-an Early Pliocene site in the Rhodope Mts.(Southern Bulgaria). *Geologica Balcanica* 28, 53-60.
- Boev, Z., 2000. *Cygnus verae* sp. n. (Anseriformes: Anatidae) from the Early Pliocene of Sofia (Bulgaria). *Acta Zoologica Cracoviensia* 43, 185-192.
- Boev, Z., 2002a. Fossil record and disappearance of peafowl (*Pavo Linnaeus*) from the Balkan Peninsula and Europe (Aves: Phasianidae). *Historia Naturalis Bulgarica* 14, 109-115.

- Boev, Z., 2002b. Neogene avifauna of Bulgaria, In: Zhou, Z., Zhang, F. (Eds.), Proceedings of the 5th symposium of the Society of Avian Paleontology and Evolution, Beijing, 1-4 June 2000, *Science Press*, Beijing, pp. 29-40.
- Boev, Z.N., Koufos, G.D., 2006. The late Miocene vertebrate locality of Perivolaki, Thessaly, Greece 2. Aves. *Palaeontographica Abteilung A* 276, 11-22.
- Boles, W.E., 1997. Riversleigh birds as palaeoenvironmental indicators. *Memoirs of the Queensland Museum* 41, 241-246.
- Boles, W.E., 2006. The Avian Fossil Record of Australia: An Overview, in: Merrick, J.R., Archer, M., Hickey, G.M., Lee, M.S.Y. (Eds.), *Evolution and Biogeography of Australasian Vertebrates*, Auscipub, Sydney, Australia, pp. 387-411.
- Boles, W.E., 2008. Systematics of the fossil Australian giant megapodes *Progura* (Aves: Megapodiidae). *Oryctos* 7, 195-215.
- Boles, W.E., Ivison, T.J., 1999. A new genus of dwarf megapode (Galliformes: Megapodiidae) from the Late Oligocene of Central Australia, In: Olson, S.L. (Ed.), Avian Paleontology at the Close of the 20th Century: Proceedings of the 4th International Meeting of the Society of Avian Paleontology and Evolution, Washington D.C., 4-7 June 1996, *Smithsonian Contributions to Paleobiology* 89, pp. 199-206.
- Boles, W.E., Mackness, B., 1994. Birds from the Bluff Downs Local Fauna, Allingham Formation, Queensland. *Records of the South Australian Museum* 27, 139-149.
- Bookstein, F.L., 1986. Size and shape spaces for landmark data in two dimensions. *Statistical Science* 1, 181-242.
- Bookstein, F.L., 1989. Principal warps: Thin-plate splines and the decomposition of deformations. *IEEE Transactions on Pattern Analysis and Machine Intelligence* 11, 567-585.
- Bookstein, F.L., 1991. *Morphometric Tools for Landmark Data: Geometry and Biology*. Cambridge University Press, Cambridge. UK. p.435.
- Bookstein, F.L., 1997a. Landmark methods for forms without landmarks: morphometrics of group differences in outline shape. *Medical Image Analysis* 1, 225-243.
- Bookstein, F.L., 1997b. Shape and the information in medical images: A decade of the morphometric synthesis. *Computer Vision and Image Understanding* 2, 97-118. doi:110.1006/cviu.1997.0607.
- Bookstein, F.L., Gunz, P., Mitteroecker, P., Prossinger, H., Schaefer, K., Seidler, H., 2003. Cranial integration in *Homo*: singular warps analysis of the midsagittal plane in ontogeny and evolution. *Journal of Human Evolution* 44, 167-187. doi:110.1016/S0047-2484(1002)00201-00204.
- Bourdon, E., Mourer-Chauviré, C., Laurent, Y., 2016. Early Eocene birds from La Borie, southern France. *Acta Palaeontologica Polonica* 61, 175-190.
- Brennan, P.L.R., Birkhead, T.R., Zyskowski, K., Van Der Waag, J., Prum, R.O., 2008. Independent evolutionary reductions of the phallus in basal birds. *Journal of Avian Biology* 39, 487-492. doi:410.1111/j.2008.0908-8857.04610.x.
- Bright, J.A., Marugán-Lobón, J., Rayfield, E.J., Cobb, S.N., 2019. The multifactorial nature of beak and skull shape evolution in parrots and cockatoos (Psittaciformes). *BMC Evolutionary Biology* 19, 104. doi:110.1186/s12862-12019-11432-12861.
- Brodkorb, P., 1954. A chachalaca from the Miocene of Florida. *Wilson Bulletin* 66, 180-183.

- Brodkorb, P., 1958a. Fossil birds from Idaho. *Wilson Bulletin* 70, 237-242.
- Brodkorb, P., 1958b. Birds from the middle Pliocene of McKay, Oregon. *Condor* 60, 252-255.
- Brodkorb, P., 1962. The systematic position of two Oligocene birds from Belgium. *Auk* 79, 706-707.
- Brodkorb, P., 1964. Catalogue of fossil birds, Part 2 (Anseriformes through Galliformes). *Bulletin of the Florida State Museum Biological Sciences* 8, 201-335.
- Brodkorb, P., 1967. Catalogue of fossil birds: Part 3 (Ralliformes, Ichthyornithiformes, Charadriiformes). *Bulletin of the Florida State Museum Biological Sciences* 2, 106-220.
- Brodkorb, P., 1978. Catalogue of fossil birds, Part 5 (Passeriformes). *Bulletin of the Florida State Museum Biological Sciences* 23, 139-228.
- Brown, J., Rest, J., Garcia-Moreno, J., Sorenson, M., Mindell, D., 2008. Strong mitochondrial DNA support for a Cretaceous origin of modern avian lineages. *BMC Biology* 6, 6. doi: 10.1186/1741-7007-1186-1186.
- Brunet, J., 1970. Oiseaux de l'Eocène supérieur du bassin de Paris. *Annales De Paleontologie* 56, 3-57.
- Brusatte, S.L., Muir, A., Young, M.T., Walsh, S., Steel, L., Witmer, L.M., 2016. The braincase and neurosensory anatomy of an Early Jurassic marine crocodylomorph: implications for crocodylian sinus evolution and sensory transitions. *Anatomical Record* 299, 1511-1530. doi:1510.1002/ar.23462.
- Brush, A.H., 1976. Waterfowl feather proteins: analysis of use in taxonomic studies. *Journal of Zoology* 179, 467-498.
- Bubień-Waluszewska, A., 1981. The Cranial Nerves, in: King, A.S., McLelland, J. (Eds.), *Form and Function in Birds*. Vol. 2, Academic Press, London, pp. 385-438.
- Buchholtz, E.A., Seyfarth, E.-A., 1999. The gospel of the fossil brain: Tilly Edinger and the science of paleoneurology. *Brain Research Bulletin* 48, 351-361.
- Buffetaut, E., 1997. New remains of the giant bird *Gastornis* from the Upper Paleocene of the eastern Paris Basin and the relationships between *Gastornis* and *Diatryma*. *Neues Jahrbuch für Geologie und Paläontologie* 3, 179-190.
- Buffetaut, E., 2004. Footprints of giant birds from the Upper Eocene of the Paris Basin: an ichnological enigma. *Ichnos* 11, 357-362. doi:10.1080/10420940490442287.
- Buffetaut, E., 2008. First evidence of the giant bird *Gastornis* from southern Europe: a tibiotarsus from the Lower Eocene of Saint-Papoul (Aude, southern France). *Oryctos* 7, 75-82.
- Buffetaut, E., 2013. The giant bird *Gastornis* in Asia: A revision of *Zhongyuanus xichuanensis* Hou, 1980, from the Early Eocene of China. *Paleontological Journal* 47, 1302-1307. doi:1310.1134/S0031030113110051.
- Burčák-Abramovič, N.I., Gadziev, D.V., 1978. *Anser eldaricus* sp. nova from the Upper Sarmatian Hipparion fauna of Eldar. *Acta Zoologica Cracoviensia* 23, 67-78.
- Burish, M.J., Kueh, H.Y., Wang, S.S.H., 2004. Brain architecture and social complexity in modern and ancient birds. *Brain, Behavior and Evolution* 63, 107-124. doi:110.1159/000075674.
- Burleigh, J.G., Kimball, R.T., Braun, E.L., 2015. Building the avian tree of life using a large-scale, sparse supermatrix. *Molecular Phylogenetics and Evolution* 84, 53-63. doi:10.1016/j.ympev.2014.1012.1003.

- Callaghan, D., Harshman, J., 2005. Taxonomy and Systematics, in: Kear, J. (Ed.), *Ducks, Geese and Swans*. 2 Volumes. 908 pp, Oxford University Press, Oxford, UK, pp. 14-26.
- Cardini, A., Loy, A., 2013. On growth and form in the “computer era”: from geometric to biological morphometrics. *Hystrix* 24, 1-5. doi:10.4404/hystrix-4424.4401-8749.
- Carezzano, F., Bee-de-Speroni, N., 1995. Composición volumétrica encefálica e índices cerebrales en tres aves de ambiente acuático (Ardeidae, Podicipedidae, Rallidae). *Facena* 11, 75-83.
- Carril, J., Tambussi, C.P., Degrange, F.J., Benitez Saldivar, M.J., Picasso, M.B.J., 2015. Comparative brain morphology of Neotropical parrots (Aves, Psittaciformes) inferred from virtual 3D endocasts. *Journal of Anatomy* 229, 239-251. doi:210.1111/joa.12325.
- Catalano, S.A., Goloboff, P.A., Giannini, N.P., 2010. Phylogenetic morphometrics (I): the use of landmark data in a phylogenetic framework. *Cladistics* 26, 539-549. doi:510.1111/j.1096-0031.2010.00302.x.
- Catalano, S.A., Torres, A., 2017. Phylogenetic inference based on landmark data in 41 empirical data sets. *Zoologica Scripta* 46, 1-11. doi:10.1111/zsc.12186.
- Chakraborty, M., Walløe, S., Nedergaard, S., Fridel, E.E., Dabelsteen, T., Pakkenberg, B., Bertelsen, M.F., Dorresteijn, G.M., Brauth, S.E., Durand, S.E., Jarvis, E.D., 2015. Core and shell song systems unique to the parrot brain. *PLoS ONE* 10, e0118496. doi:0118410.0111371/journal.pone.0118496.
- Charvet, C.J., Striedter, G.F., Finlay, B.L., 2011. Evo-devo and brain scaling: candidate developmental mechanisms for variation and constancy in vertebrate brain evolution. *Brain, Behavior and Evolution* 78, 248-257. doi:210.3389/fnana.2011.00004.
- Chatterjee, S., 2002. The morphology and systematics of *Polarornis*, a Cretaceous loon (Aves: Gaviidae) from Antarctica, In: Zhou, Z., Zhang, F. (Eds.), Proceedings of the 5th Symposium of the Society of Avian Paleontology and Evolution, Beijing, 1-4 June 2000, *Science Press*, Beijing, China, pp. 125-155.
- Cheneval, J., 1983. Les Anatidae (Aves, Anseriformes) du gisement aquitain de Saint-Gérard-le-Puy (Allier, France), In: Buffetaut, E., Mazin, J.M., Salmon, E. (Eds.), Actes du Symposium Paléontologique Georges Cuvier, Ville de Montbéliard, Montbéliard, France, 1982, pp. 85-97.
- Cheneval, J., 1984. Les oiseaux aquatiques (Gaviiformes a Anseriformes) du gisement aquitain de Saint-Gérard-le-Puy (Allier, France). Révision systématique. *Palaeovertebrata* 14, 33-115.
- Cheneval, J., 1987. Les Anatidae (Aves, Anseriformes) du Miocène de France. Révision systématique et évolution, In: Mourer-Chauviré, C. (Ed.), l'Évolution des Oiseaux d'Après le Temoignage des Fossils, *Documents du Laboratoire Géologique de Lyon*, pp. 137-157.
- Cheneval, J., Ginsburg, L., Mourer-Chauviré, C., Ratanasthien, B., 1991. The Miocene avifauna of the Li Mae Long locality, Thailand: systematics and paleoecology. *Journal of Southeast Asian Earth Sciences* 6, 117-126.
- Christidis, L., Boles, W.E., 2008. *Systematics and Taxonomy of Australian Birds*. CSIRO Publishing, Collingwood, Victoria, Australia. p.277.
- Cignoni, P., Callieri, M., Corsini, M., Dellepiane, M., Ganovelli, F., Ranzuglia, G., 2008. *Meshlab: an open-source mesh processing tool*, In: Scarano, V., De Chiara, R., Erra, U. (Eds.), Proceedings of the 2008 Eurographics Italian Chapter Conference, Salerno, Italy, pp. 129-136. ISBN 978-123-905673-905668-905675.

- Claramunt, S., Cracraft, J., 2015. A new time tree reveals Earth history's imprint on the evolution of modern birds. *Science Advances* 1, e1501005, doi:1501010.1501126/sciadv.1501005.
- Clark, D.A., Mitra, P.P., Wang, S.S.-H., 2001. Scalable architecture in mammalian brains. *Nature* 411, 189-193.
- Clarke, J.A., 2004. Morphology, phylogenetic taxonomy, and systematics of *Ichthyornis* and *Apatornis* (Avialae: Ornithurae). *Bulletin of the American Museum of Natural History* 286, 1-179.
- Clarke, J.A., Chatterjee, S., Li, Z., Riede, T., Agnolin, F., Goller, F., Isasi, M.P., Martinioni, D.R., Mussel, F.J., Novas, F.E., 2016. Fossil evidence of the avian vocal organ from the Mesozoic. *Nature* 538, 502-505. doi:510.1038/nature19852.
- Clarke, J.A., Norell, M.A., 2004. New avialan remains and a review of the known avifauna from the Late Cretaceous Nemegt Formation of Mongolia. *American Museum Novitates* 3447, 1-12.
- Clarke, J.A., Tambussi, C.P., Noriega, J.I., Erickson, G.M., Ketchum, R.A., 2005. Definitive fossil evidence for the extant avian radiation in the Cretaceous. *Nature* 433, 305-308.
- Cockerell, T.D.A., 1923. The supposed plumage of the Eocene bird *Diatryma*. *American Museum Novitates* 62, 1-4.
- Condon, H.T., 1975. *Checklist of the Birds of Australia, Part I. Non-Passerines*. Royal Australasian Ornithologists Union, Melbourne, p 311.
- Cooper, A., Penny, D., 1997. Mass survival of birds across the Cretaceous-Tertiary boundary: molecular evidence. *Science* 275, 1109-1113.
- Cooper, R.A., Millener, P.R., 1993. The New Zealand biota: historical background and new research. *Trends in Ecology and Evolution* 8, 429-433.
- Cope, E.D., 1876. On a gigantic bird from the Eocene of New Mexico. *Proceedings of the Academy of Natural Sciences of Philadelphia* 28, 10-11.
- Corfield, J.R., Gsell, A.C., Brunton, D., Heesy, C.P., Hall, M.I., Acosta, M.L., Iwaniuk, A.N., 2011. Anatomical specializations for nocturnality in a critically endangered parrot, the Kakapo (*Strigops habroptilus*). *PLoS ONE* 6, e22945. doi:22910.21371/journal.pone.0022945.
- Corfield, J.R., Long, B., Krilow, J.M., Wylie, D.R.W., Iwaniuk, A.N., 2015a. A unique cellular scaling rule in the avian auditory system. *Brain Structure and Function* 9, 102-120. doi:110.1007/s00429-00015-01064-00421.
- Corfield, J.R., Price, K., Iwaniuk, A.N., Gutierrez-Ibañez, C., Birkhead, T., Wylie, D.R.W., 2015b. Diversity in olfactory bulb size in birds reflects allometry, ecology, and phylogeny. *Frontiers in Neuroanatomy* 9, 102. doi: 110.3389/fnana.2015.00102.
- Corfield, J.R., Wild, J.M., Hauber, M.E., Parsons, S., Kubke, M.F., 2008. Evolution of brain size in the palaeognath lineage, with an emphasis on New Zealand ratites. *Brain, Behavior and Evolution* 71, 87-99. doi:10.1159/000111456.
- Corfield, J.R., Wild, J.M., Parsons, S., Kubke, M.F., 2012. Morphometric analysis of telencephalic structure in a variety of neognath and paleognath bird species reveals regional differences associated with specific behavioral traits. *Brain, Behavior and Evolution* 80, 181-195. doi:110.1159/000339828.
- Cox, W.A., Kimball, R.T., Braun, E.L., Klicka, J., 2007. Phylogenetic position of the New World quail (Odontophoridae): eight nuclear loci and three mitochondrial regions contradict morphology and the Sibley-Ahlquist tapestry. *Auk* 124, 71-84.

- Cracraft, J., 1973. Systematics and evolution of the Gruiformes (class Aves). Phylogeny of the suborder Grues. *Bulletin of the American Museum of Natural History* 151, 1-128.
- Cracraft, J., 1974. Phylogeny and evolution of the ratite birds. *Ibis* 116, 494-521.
- Cracraft, J., 1981. Toward a phylogenetic classification of the recent birds of the world (Class Aves). *Auk* 98, 681-714.
- Cracraft, J., 1985. Monophyly and phylogenetic relationships of the Pelecaniformes: a numerical cladistic analysis. *Auk* 102, 834-853.
- Cracraft, J., 2001. Avian evolution, Gondwana biogeography and the Cretaceous–Tertiary mass extinction event. *Proceedings of the Royal Society of London. Series B: Biological Sciences* 268, 459-469. doi:410.1098/rspb.2000.1368.
- Cracraft, J., Barker, F.K., Braun, M., Harshman, J., Dyke, G.J., Feinstein, J., Stanley, S., Cibois, A., Schikler, P., Beresford, P., García-Moreno, J., Sorenson, M.D., Yuri, T., Mindell, D.P., 2004. Phylogenetic Relationships among Modern Birds (Neornithes): Towards an Avian Tree of Life, in: Cracraft, J., Donoghue, M. (Eds.), *Assembling the Tree of Life*, Oxford University Press, New York, pp. 468-489.
- Cracraft, J., Clarke, J.A., 2001. The basal clades of modern birds, new perspectives on the origin and early evolution of birds. Proceedings of the international symposium in honor of John H. Ostrom, *Peabody Museum of Natural History*, New Haven CT, pp. 143-152.
- Craigie, E.H., 1939. The cerebral cortex of *Rhea americana*. *Journal of Comparative Neurology* 70, 331-353.
- Crowe, T.M., 1978. The evolution of Guinea-fowl (Galliformes, Phasianidae, Numidinae): taxonomy, phylogeny, speciation and biogeography. *Annals of the South African Museum* 76, 43-136.
- Crowe, T.M., Bowie, R.C.K., Bloomer, P., Mandiwana, T.G., Hedderson, T.A.J., Randi, E., Pereira, S.L., Wakeling, J., 2006. Phylogenetics, biogeography and classification of, and character evolution in, gamebirds (Aves: Galliformes): effects of character exclusion, data partitioning and missing data. *Cladistics* 22, 495-532. doi:410.1111/j.1096-0031.2006.00120.x.
- Crowe, T.M., Short, L.L., 1992. A new gallinaceous bird from the Oligocene of Nebraska, with comments on the phylogenetic position of the Gallinuloididae, In: Campbell Jr, K.E. (Ed.), *Papers in Avian Paleontology Honoring Pierce Brodkorb, Incorporating the Proceedings of the II International Symposium of the Society of Avian Paleontology and Evolution, Natural History Museum of Los Angeles County, 1988, Natural History Museum of Los Angeles County Science Series* 36, pp. 179-185.
- Davis, J.C., 2002. *Statistics and Data Analysis in Geology*, 3rd Edition. John Wiley & Sons, New York. p. 638, New York.
- De Mendoza, R.S., 2019. Phylogenetic relationships of the Early Miocene diving and flightless duck *Cayaoa bruneti* (Aves, Anatidae) from Patagonia: homology or convergence? *Papers in Palaeontology* xx, 1-9. doi:10.1002/spp1002.1268.
- De Pietri, V.L., Scofield, R.P., Hand, S.J., Tennyson, A.J.D., Worthy, T.H., 2016b. Sheathbill-like birds (Charadriiformes: Chionoidea) from the Oligocene and Miocene of Australasia. *Journal of the Royal Society of New Zealand* 46, 1-19. doi:10.1080/03036758.03032016.01194297.
- De Pietri, V.L., Scofield, R.P., Tennyson, A.J., Hand, S.J., Worthy, T.H., 2016a. Wading a lost southern connection: Miocene fossils from New Zealand reveal a new lineage of shorebirds (Charadriiformes) linking Gondwanan avifaunas. *Journal of Systematic Palaeontology* 14, 603-616. doi:610.1080/14772019.14772015.11087064.

- De Pietri, V.L., Scofield, R.P., Tennyson, A.J.D., Hand, S.J., Worthy, T.H., 2017. The Diversity of Early Miocene Pigeons (Columbidae) in New Zealand, in: Hospitaleche, C.A., Agnolin, F.L., Haidr, N., Noriega, J.I., Tambussi, C.P. (Eds.), Proceedings of the 9th International Meeting of the Society of Avian Paleontology and Evolution, Diamante (Argentina), 1-6 August 2016. *Paleontología y Evolución de las Aves, Contribuciones del Museo Argentino de Ciencias Naturales* 7, pp. 49-68.
- De Pietri, V.L., Scofield, R.P., Zelenkov, N., Boles, W.E., Worthy, T.H., 2016c. The unexpected survival of an ancient lineage of anseriform birds into the Neogene of Australia: the youngest record of Presbyornithidae. *Royal Society Open Science* 3, 150635. doi:150610.151098/rsos.150635.
- De Vis, C.W., 1888. Australian ancestry of the crowned pigeon of New Guinea. *Proceedings of the Royal Society of Queensland* 5, 127-131.
- de Winter, W., Oxnard, C.E., 2001. Evolutionary radiations and convergences in the structural organization of mammalian brains. *Nature* 409, 710-714.
- Dekker, R.W.R.J., 2007. Distribution and Speciation of Megapodes (Megapodiidae) and Subsequent Development of their Breeding, in: Renema, W. (Ed.), *Biogeography, Time, and Place: Distributions, Barriers, and Islands. Topics In Geobiology*, vol 29, Springer, Dordrecht, pp. 93-102. doi:110.1007/1978-1001-4020-6374-1009\_1003.
- Delacour, J., 1964. *The Waterfowl of the World*. Volume 4. Country Life Limited, London.
- Delacour, J., Mayr, E., 1945. The family Anatidae. *Wilson Bulletin* 57, 3-55.
- Deng, C., Wang, B., 1992. Overlap of somatic and visual response areas in the wulst of pigeon. *Brain Research* 582, 320-322.
- Depéret, C., 1890. Les animaux Pliocènes du Roussillon. Mémoires de la Société géologique de France. *Paléontologie* 3, 1-198.
- Dickinson, E.C., Remsen Jr, J.V. (Eds.), 2013. *The Howard & Moore Complete Checklist of the Birds of the World*. 4th Edition. Aves Press, Eastbourne, U.K.
- Dollo, L., 1883. Note sur la présence du *Gastornis edwardsii* Lemoine dans l'assise inférieure de l'étage landénien à Mesvin, près Mons. *Bulletin du Musée Royal d'Histoire Naturelle de Belgique* 2, 297-305.
- Domínguez Alonso, P., Milner, A.C., Ketcham, R.A., Cookson, M.J., Rowe, T.B., 2004. The avian nature of the brain and inner ear of *Archaeopteryx*. *Nature* 430, 666-669.
- Donne-Goussé, C., Laudet, V., Hänni, C., 2002. A molecular phylogeny of anseriformes [sic] based on mitochondrial DNA analysis. *Molecular Phylogenetics and Evolution* 23, 339-356. doi:310.1016/S1055-7903(1002)00019-00012.
- Doré, J.-C., Ojasoo, T., Thireau, M., 2002. Using the volumetric indices of telencephalic structures to distinguish Salamandridae and Plethodontidae: Comparison of three statistical methods. *Journal of Theoretical Biology* 214, 427-439. doi:410.1006/jtbi.2001.2467.
- Douglas, B.J., 1986. Lignite resources of Central Otago (Manuherikia Group of Central Otago, New Zealand: stratigraphy, depositional environments, lignite resource assessment and exploration models). *New Zealand Energy Research and Development Committee Publication*, 2 Volumes. 104 p.
- Douglas, B.J., Lindqvist, J.K., Fordyce, R.E., Campbell, J.D., 1981. Early Miocene terrestrial vertebrates from Central Otago. *Geological Society of New Zealand Newsletter* 53, 17.

- Dryden, I.L., Mardia, K.V., 1993. Multivariate shape analysis. *Sankhyā* 55, 460-480.
- Dryden, I.L., Mardia, K.V., 1998. *Statistical Shape Analysis*. Wiley, Chichester. p. 347.
- Dubbeldam, J.L., 1980. Studies on the somatotopy of the trigeminal system in the mallard, *Anas platyrhynchos* L. II. Morphology of the principal sensory nucleus. *Journal of Comparative Neurology* 191, 557-571.
- Dubbeldam, J.L., 1984. Afferent connections of nervus facialis and nervus glossopharyngeus in the pigeon (*Columba livia*) and their role in feeding behavior. *Brain, Behavior and Evolution* 24, 47-57.
- Dubbeldam, J.L., 1992. Cranial nerves and sensory centres—a matter of definition? Hypoglossal and other afferents of the avian sensory trigeminal system. *Zoologische Jahrbücher* 122, 179-186.
- Dubbeldam, J.L., 1998a. Birds, in: Nieuwenhuys, R., ten Donkelaar, H.J., Nicholson, C. (Eds.), *The Central Nervous System of Vertebrates*, Springer-Verlag, Berlin, pp. 1525-1636.
- Dubbeldam, J.L., 1998b. The sensory trigeminal system in birds: input, organization and effects of peripheral damage. A review. *Archives of Physiology and Biochemistry* 106, 338-345. doi:310.1076/apab.1106.1075.1338.4367.
- Dubbeldam, J.L., Brauch, C.S.M., Don, A., 1981. Studies on the somatotopy of the trigeminal system in the mallard, *Anas platyrhynchos* L. III. Afferents and organization of the nucleus basalis. *Journal of Comparative Neurology* 196, 391-405.
- Dubbeldam, J.L., Brus, E.R., Menken, S.B.J., Zeilstra, S., 1979. The central projections of the glossopharyngeal and vagus ganglia in the mallard, *Anas platyrhynchos* L. *Journal of Comparative Neurology* 183, 149-168. doi:110.1002/cne.901830111.
- Dubbeldam, J.L., Visser, A.M., 1987. The organization of the nucleus basalis–neostriatum complex of the mallard (*Anas platyrhynchos* L.) and its connections with the archistriatum and the paleostriatum complex. *Neuroscience* 21, 487-517.
- Dughi, R., Sirugue, F., 1959. Sur des fragments de coquilles d'oeufs fossiles de l'Eocène de Basse-Provence. *Comptes Rendus Hebdomadaires des Séances de l'Académie des Sciences* 249, 959-961.
- Dyke, G.J., 2001. The fossil waterfowl (Aves: Anseriformes) from the Eocene of England. *American Museum Novitates* 3354, 1-15.
- Dyke, G.J., 2003a. Review of Cenozoic Birds of the World. Part 1: Europe by Jiří Mlíkovský 2002 *Journal of Vertebrate Paleontology* 23, 258.
- Dyke, G.J., 2003b. The phylogenetic position of *Gallinuloides* Eastman (Aves: Galliformes) from the Tertiary of North America. *Zootaxa* 199, 1-10.
- Dyke, G.J., Crowe, T.M., 2008. Avian paleontology: opinions and quasi-phenetics versus characters and cladistics. *Cladistics* 24, 77-81. doi:10.1111/j.1096-0031.2007.00188.x.
- Dyke, G.J., Gulas, B.E., 2002. The fossil galliform bird *Paraortygoides* from the Lower Eocene of the United Kingdom. *American Museum Novitates*, 1-14.
- Dyke, G.J., Gulas, B.E., Crowe, T.M., 2003. Suprageneric relationships of galliform birds (Aves, Galliformes): a cladistic analysis of morphological characters. *Zoological Journal of the Linnean Society* 137, 227-244.
- Dzerzhinsky, F.Y., 1995. Evidence for common ancestry of the Galliformes and Anseriformes. *Courier Forschungsinstitut Senckenberg* 181, 325-336.

- Eastman, C.R., 1905. Fossil avian remains from Armissan. *Memoirs of the Carnegie Museum* 2, 131-138.
- Ebinger, P., 1995. Domestication and plasticity of brain organization in mallards (*Anas platyrhynchos*). *Brain, Behavior and Evolution* 45, 286-300.
- Emery, N.J., Clayton, N.S., 2004. Comparing the Complex Cognition of Birds and Primates, in: Rogers, L.J., Kaplan, G. (Eds.), *Comparative Vertebrate Cognition. Developments in Primatology: Progress and Prospects*, Kluwer Academic Publishers, Dordrecht, pp. 3-55.
- Emery, N.J., Clayton, N.S., 2005. Evolution of the avian brain and intelligence. *Current Biology* 15, R946-R950.
- Emslie, S.D., 1992. Two new late Blancan avifaunas from Florida and the extinction of wetland birds in the Plio-Pleistocene, in: Campbell Jr., K.E. (Ed.), *Papers in Avian Paleontology Honoring Pierce Brodkorb, Incorporating the Proceedings of the II International Symposium of the Society of Avian Paleontology and Evolution*, Natural History Museum of Los Angeles County, 1988, *Natural History Museum of Los Angeles County Science Series* 36, pp. 249-269.
- Eo, S.H., Bininda-Emonds, O.R.P., Carroll, J.P., 2009. A phylogenetic supertree of the fowls (Galloanserae, Aves). *Zoologica Scripta* 38, 465-481. doi:410.1111/j.1463-6409.2008.00382.x.
- Ericson, P.G.P., 1996. The skeletal evidence for a sister-group relationship of anseriform and galliform birds: a critical evaluation. *Journal of Avian Biology* 27, 195-202.
- Ericson, P.G.P., 1997. Systematic relationships of the Palaeogene family Presbyornithidae (Aves: Anseriformes). *Zoological Journal of the Linnean Society* 121, 429-483.
- Ericson, P.G.P., 2000. Systematic revision, skeletal anatomy, and paleoecology of the New World early Tertiary Presbyornithidae (Aves: Anseriformes). *Paleo-Bios* 20, 1-23.
- Ericson, P.G.P., Anderson, C.L., Britton, T., Elzanowski, A., Johansson, U.S., Källersjö, M., Ohlson, J.I., Parsons, T.J., Zuccon, D., Mayr, G., 2006. Diversification of Neoaves: integration of molecular sequence data and fossils. *Biology Letters* 2, 543-547. doi:510.1098/rsbl.2006.0523.
- Fabre-Taxy, S., Touraine, F., 1960. Gisements d'oeufs d'oiseaux de très grande taille dans l'Éocène de Provence. *Comptes Rendus Hebdomadaires Des Seances De l'Academie Des Sciences* 250, 3870-3871.
- Fain, M.G., Houde, P., 2004. Parallel radiations in the primary clades of birds. *Evolution* 58, 2558-2573.
- Fain, M.G., Houde, P., 2007. Multilocus perspectives on the monophyly and phylogeny of the order Charadriiformes (Aves). *BMC Evolutionary Biology* 7, 35. doi:10.1186/1471-2148-1187-1135.
- Falla, R.A., 1953. The Australian element in the avifauna of New Zealand. *Emu* 53, 36-46.
- Feduccia, A., 1999. *The Origin and Evolution of Birds*, 2nd Edition. Yale University Press, New Haven, Connecticut.
- Feduccia, A., 2014. Avian extinction at the end of the Cretaceous: Assessing the magnitude and subsequent explosive radiation. *Cretaceous Research* 50, 1-15.

- Felice, R.N., Goswami, A., 2018. Developmental origins of mosaic evolution in the avian cranium. *Proceedings of the National Academy of Sciences USA* 115, 555-560. doi:10.1073/pnas.1716437115.
- Finlay, B.L., Darlington, R.B., 1995. Linked regularities in the development and evolution of mammalian brains. *Science* 268, 1578-1584.
- Finlay, B.L., Darlington, R.B., Nicastro, N., 2001. Developmental structure in brain evolution. *Behavioral and Brain Sciences* 24, 263-278.
- Fischer, K., 1962. Der riesenlaufvogel *Diatryma* aus der Eozänen braunkohle des geiseltales. *Hallesches Jahrbuch für Mitteldeutsche Erdgeschichte* 4, 26-33.
- Fischer, K., 1978. Neue reste des riesenlaufvogels *Diatryma* aus dem Eozän des geisteltales bei Halle (DDR). *Mitteilungen aus dem Zoologischen Museum Berlin* 54, 33-144.
- Fischer, K., 1990. Der hühnervogel *Pirortyx major* (Gaillard, 1939) aus dem marinen Mitteloligozän bei Leipzig (DDR). *Mitteilungen aus dem Zoologischen Museum Berlin* 66, 133-136.
- Fischer, K., 2003. Weitere vogelknochen von *Diomedeoides* (Diomedeoididae, Procellariiformes) und *Paraortyx* (Paraortygidae, Galliformes) aus dem Unteroligozän des weißelsterbeckens bei Leipzig (Sachsen). *Mauritiana* 18, 387-395.
- Fleming, C.A., 1962. History of the New Zealand land bird fauna. *Notornis* 9, 270-274.
- Fleming, C.A., 1979. *The Geological History of New Zealand and its Life*. Auckland University Press and Oxford University Press. pp 141
- Fordyce, R.E., 1991. A New Look at the Fossil Vertebrate Record of New Zealand, in: Rich, P.V., Monaghan, J.M., Baird, R.F., Rich, T.H. (Eds.), *Vertebrate Palaeontology of Australasia*, Pioneer Design Studios in cooperation with the Monash University Publications Committee, Melbourne pp. 1191-1316.
- Franklin, D.C., Garnett, S.T., Luck, G.W., Gutierrez-Ibañez, C., Iwaniuk, A.N., 2014. Relative brain size in Australian birds. *Emu* 114, 160-170. doi:110.1071/MU13034.
- Franzosa, J.W., 2004. *Evolution of the Brain in Theropoda (Dinosauria)*. PhD Dissertation, The University of Texas, Austin, p. 316.
- Frith, H.J., 1967. *Waterfowl in Australia*. A.H. & A.W. Reed, Sydney. 328 pp.
- Fuchs, R., Winkler, H., Bingman, V.P., Ross, J.D., Bernroider, G., 2014. Brain geometry and its relation to migratory behavior in birds. *Journal of Advanced Neuroscience Research* 1, 1-9.
- Gaede, A.H., Gutierrez-Ibañez, C., Armstrong, M.S., Altshuler, D.L., Wylie, D.R.W., 2019. Pretectal projections to the oculomotor cerebellum in hummingbirds (*Calypte anna*), zebra finches (*Taeniopygia guttata*), and pigeons (*Columba livia*). *Journal of Comparative Neurology* 527, 2644-2658. doi:2610.1002/cne.24697.
- Garamszegi, L.Z., 2014. *Modern Phylogenetic Comparative Methods and their Application in Evolutionary Biology*. Springer-Verlag, Berlin.
- Gibson, J.J., 1954. The visual perception of objective motion and subjective movement. *Psychological Review* 61, 304-314. doi:310.1037/h0061885.
- Gibson, R.M., 1996. Female choice in sage grouse: the roles of attraction and active comparison. *Behavioral Ecology and Sociobiology* 39, 55-59. doi: 10.1007/s002650050266.
- Gibson, R.M., Bradbury, J.W., Vehrencamp, S.L., 1991. Mate choice in lekking sage grouse revisited: the roles of vocal display, female site fidelity, and copying. *Behavioral Ecology* 2, 165-180. doi: 110.1093/beheco/1092.1092.1165.

- Gill, B.J., Bell, B.D., Chambers, G.K., Medway, D.G., Palma, R.L., Scofield, R.P., Tennyson, A.J.D., Worthy, T.H., 2010. *Checklist of the Birds of New Zealand, Norfolk and Macquarie Islands, and the Ross Dependency, Antarctica*. 4th Edition. Te Papa Press, Wellington, NZ.
- Giolli, R.A., Blanks, R.H.I., Lui, F., 2006. The accessory optic system: basic organization with an update on connectivity, neurochemistry, and function. *Progress in Brain Research* 151, 407-440.
- Göhlich, U.B., Mourer-Chauviré, C., 2005. Revision of the phasianids (Aves, Galliformes) from the Lower Miocene of Saint-Gérand-le-Puy (Allier, France). *Palaeontology* 48, 1331-1350.
- Goloboff, P.A., Catalano, S.A., 2016. TNT version 1.5, including a full implementation of phylogenetic morphometrics. *Cladistics* 32, 221-238. doi:210.1111/cla.12160.
- Gonzalez, J., Düttmann, H., Wink, M., 2009. Phylogenetic relationships based on two mitochondrial genes and hybridization patterns in Anatidae. *Journal of Zoology* 279, 310-318. 318. doi:310.1111/j.1469-7998.2009.00622.x.
- Gower, J.C., 1975. Generalized Procrustes analysis. *Psychometrika* 40, 33-51. doi:10.1007/BF02291478.
- Grande, L., 1980. Paleontology of the Green River Formation, with a review of the fish fauna. *Bulletin of the Geological survey of Wyoming* 63, Laramie, Wyoming.
- Groth, J.G., Barrowclough, G.F., 1999. Basal divergences in birds and the phylogenetic utility of the nuclear RAG-1 gene. *Molecular Phylogenetics and Evolution* 12, 115-123.
- Gulas-Wroblewski, B.E., Wroblewski, A.F.J., 2003. A crown-group galliform bird from the Middle Eocene Bridger Formation of Wyoming. *Palaeontology* 46, 1269-1280.
- Gunz, P., Mitteroecker, P., 2013. Semilandmarks: a method for quantifying curves and surfaces. *Hystrix* 24, 103-109. doi:110.4404/hystrix-4424.4401-6292.
- Gunz, P., Mitteroecker, P., Bookstein, F.L., 2005. Semilandmarks in Three Dimensions, in: Slice, D.E. (Ed.), *Modern Morphometrics in Physical Anthropology*, Kluwer Academic/Plenum Publishers, New York, pp. 73-98.
- Gutiérrez-Ibáñez, C., Iwaniuk, A.N., Wylie, D.R.W., 2009. The independent evolution of the enlargement of the principal sensory nucleus of the trigeminal nerve in three different groups of birds. *Brain, Behavior and Evolution* 74, 280-294. doi:210.1159/000270904.
- Hackett, S.J., Kimball, R.T., Reddy, S., Bowie, R.C.K., Braun, E.L., Braun, M.J., Chojnowski, J.L., Cox, W.A., Han, K.-L., Harshman, J., Huddleston, C.J., Marks, B.D., Miglia, K.J., Moore, W.S., Sheldon, F.H., Steadman, D.W., Witt, C.C., Yuri, T., 2008. A phylogenomic study of birds reveals their evolutionary history. *Science* 320, 1763-1768. doi:1710.1126/science.1157704.
- Hall, M.I., 2008. The anatomical relationships between the avian eye, orbit and sclerotic ring: implications for inferring activity patterns in extinct birds. *Journal of Anatomy* 212, 781-794. doi:710.1111/j.1469-7580.2008.00897.x.
- Hall, M.I., Ross, C.F., 2007. Eye shape and activity pattern in birds. *Journal of Zoology* 271, 437-444. doi:410.1111/j.1469-7998.2006.00227.x.
- Harmon, L.J., 2019. *Phylogenetic Comparative Methods*. p.234. <https://open.umn.edu/opentextbooks/textbooks/phylogenetic-comparative-methods>.

- Harris, R.B., Birks, S.M., Leaché, A.D., 2014. Incubator birds: biogeographical origins and evolution of underground nesting in megapodes (Galliformes: Megapodiidae). *Journal of Biogeography* 41, 2045-2056. doi:2010.1111/jbi.12357.
- Harrison, C.J.O., Walker, C.A., 1976. Birds of the British upper Eocene. *Zoological Journal of the Linnean Society* 59, 323-351.
- Harrison, C.J.O., Walker, C.A., 1979. Birds of the British Lower Oligocene, in: Harrison, C.J.O., Walker, C.A. (Eds.), *Studies in Tertiary Avian Paleontology, Tertiary Research Special Paper 5*, pp. 29-43.
- Harrison, C.J.O., Walker, C.A., 1982. Fossil birds from the Upper Miocene of northern Pakistan. *Tertiary Research* 4, 53-69.
- Harrison, G.L., McLenachan, P.A., Phillips, M.J., Slack, K.E., Cooper, A., Penny, D., 2004. Four new avian mitochondrial genomes help get to basic evolutionary questions in the late Cretaceous. *Molecular Biology and Evolution* 21, 974-983. doi:10.1093/molbev/msh1065.
- Harshman, J., 2007. Classification and Phylogeny of Birds, in: Jamieson, B.G.M. (Ed.), *Reproductive Biology and Phylogeny of Birds. Part A. Phylogeny, Morphology, Hormones, Fertilization*, Science Publishers, Enfield, NH, USA, pp. 1-35.
- Healy, S.D., Rowe, C., 2007. A critique of comparative studies of brain size. *Proceedings of the Royal Society of London B: Biological Sciences* 274, 453-464. doi:10.1098/rspb.2006.3748.
- Heizmann, E.P.J., Hesse, A., 1995. Die mittelmiozänen vogel-und säugetierfaunen des Nördlinger Ries (MN6) und des Steinheimer Beckens (MN7)-ein vergleich, In: Peters, D.S. (Ed.), *Acta Palaeornithologica, Courier Forschungsinstitut Senckenberg* 181, pp. 171-185.
- Hellmann, B., Güntürkün, O., Manns, M., 2004. Tectal mosaic: organization of the descending tectal projections in comparison to the ascending tectofugal pathway in the pigeon. *Journal of Comparative Neurology* 472, 395-410.
- Hodos, W., Campbell, C.B.G., 1969. Scala Naturae: Why there is no theory in comparative psychology. *Psychological Review* 76, 337-350.
- Holdaway, R.N., 1989. New Zealand's pre-human avifauna and its vulnerability. *New Zealand Journal of Ecology* 12, 11-25.
- Hope, S., 2002. The Mesozoic Radiation of Neornithes, in: Chiappe, L.M., Witmer, L.M. (Eds.), *Mesozoic Birds: Above the Heads of Dinosaurs*, University of California Press, Berkeley, pp. 339-388.
- Hosner, P.A., Braun, E.L., Kimball, R.T., 2015. Land connectivity changes and global cooling shaped the colonization history and diversification of New World quail (Aves: Galliformes: Odontophoridae). *Journal of Biogeography* 42, 1883-1895.
- Howard, H., 1955. New records and a new species of *Chendytes*, an extinct genus of diving geese. *Condor* 57, 135-143.
- Howard, H., 1964a. Fossil Anseriformes, in: Delacour, J. (Ed.), *The Waterfowl of the World*, Country Life Ltd, London, United Kingdom., pp. 233-326.
- Howard, H., 1964b. Further discoveries concerning the flightless" diving geese" of the genus *Chendytes*. *Condor* 66, 372-376.
- Howard, H., 1992. New records of middle Miocene anseriform birds from Kern County, California, in: Campbell Jr., K.E. (Ed.), *Papers in Avian Paleontology Honoring Pierce Brodkorb, Incorporating the Proceedings of the II International Symposium of the Society of Avian*

- Paleontology and Evolution, Natural History Museum of Los Angeles County, 1988, *Natural History Museum of Los Angeles County Science Series* 36, pp. 231-237.
- Huber, R., Van Staaden, M., Kaufman, L., Liem, K., 1997. Microhabitat use, trophic patterns, and the evolution of brain structure in African cichlids. *Brain, Behavior and Evolution* 50, 167-182. doi:110.1159/000113330.
- Hunt, G.R., 2000. Human-like, population-level specialization in the manufacture of pandanus tools by New Caledonian crows *Corvus moneduloides*. *Proceedings of the Royal Society of London. Series B: Biological Sciences* 267, 403-413.
- Irwin, G., Worthy, T.H., Best, S., Hawkins, S., Carpenter, J., Matararaba, S., 2011. Further investigations at the Naigani Lapita site (VL 21/5), Fiji: excavation, radiocarbon dating and palaeofaunal extinction. *Journal of Pacific Archaeology* 2, 66-78.
- Iwaniuk, A.N., 2004. Brood parasitism and brain size in cuckoos: a cautionary tale on the use of modern comparative methods. *International Journal of Comparative Psychology* 17, 17-33.
- Iwaniuk, A.N., Dean, K.M., Nelson, J.E., 2004a. A mosaic pattern characterizes the evolution of the avian brain. *Proceedings of the Royal Society of London B: Biological Sciences* 271, S148-S151. doi:110.1098/rsbl.2003.0127.
- Iwaniuk, A.N., Dean, K.M., Nelson, J.E., 2005. Interspecific allometry of the brain and brain regions in parrots (Psittaciformes): comparisons with other birds and primates. *Brain, Behavior and Evolution* 65, 40-59. doi:10.1159/000081110.
- Iwaniuk, A.N., Gutierrez-Ibañez, C., Pakan, J.M.P., Wylie, D.R.W., 2010. Allometric scaling of the tectofugal pathway in birds. *Brain, Behavior and Evolution* 75, 122-137. doi:110.1159/000311729.
- Iwaniuk, A.N., Heesy, C.P., Hall, M.I., Wylie, D.R.W., 2008. Relative wulst volume is correlated with orbit orientation and binocular visual field in birds. *Journal of Comparative Physiology A* 194, 267-282. doi:210.1007/s00359-00007-00304-00350.
- Iwaniuk, A.N., Hurd, P.L., 2005. The evolution of cerebrotypes in birds. *Brain, Behavior and Evolution* 65, 215-230. doi:210.1159/000084313.
- Iwaniuk, A.N., Hurd, P.L., Wylie, D.R.W., 2007. Comparative morphology of the avian cerebellum: II. Size of folia. *Brain, Behavior and Evolution* 69, 196-219. doi:110.1159/000096987.
- Iwaniuk, A.N., Nelson, J.E., 2001. A comparative analysis of relative brain size in waterfowl (Anseriformes). *Brain, Behavior and Evolution* 57, 87-97.
- Iwaniuk, A.N., Nelson, J.E., 2002. Can endocranial volume be used as an estimate of brain size in birds? *Canadian Journal of Zoology* 80, 16-23. doi:10.1139/Z11301-1204.
- Iwaniuk, A.N., Nelson, J.E., 2003. Developmental differences are correlated with relative brain size in birds: a comparative analysis. *Canadian Journal of Zoology* 81, 1913-1928. doi:1910.1139/Z1903-1190.
- Iwaniuk, A.N., Nelson, J.E., James, H.F., Olson, S.L., 2004b. A comparative test of the correlated evolution of flightlessness and relative brain size in birds. *Journal of Zoology* 263, 317-327. doi:310.1017/S0952836904005308.
- Iwaniuk, A.N., Wylie, D.R.W., 2007. Neural specialization for hovering in hummingbirds: Hypertrophy of the pretectal nucleus lentiformis mesencephali. *Journal of Comparative Neurology* 500, 211-221.

- Iwaniuk, A.N., Wylie, D.R.W., 2006. The evolution of stereopsis and the wulst in caprimulgiform birds: a comparative analysis. *Journal of Comparative Physiology A* 192, 1313-1326. doi:1310.1007/s00359-00006-00161-00352.
- Jacobs, B.F., Kingston, J.D., Jacobs, L.L., 1999. The origin of grass-dominated ecosystems. *Annals of the Missouri Botanical Garden*, 590-643.
- Jarvis, E.D., Güntürkün, O., Bruce, L., Csillag, A., Karten, H., Kuenzel, W., Medina, L., Paxinos, G., Perkel, D.J., Shimizu, T., 2005. Avian brains and a new understanding of vertebrate brain evolution. *Nature Reviews Neuroscience* 6, 151-159.
- Jarvis, E.D., Mirarab, S., Aberer, A.J., Li, B., Houde, P., Li, C., Ho, S.Y., Faircloth, B.C., Nabholz, B., Howard, J.T., et.al., 2014. Whole-genome analyses resolve early branches in the tree of life of modern birds. *Science* 346, 1320-1331.
- Jerison, H.J., 1973. *Evolution of the Brain and Intelligence*. Academic Press, New York.
- Jerison, H.J., 1991. Brain size and the evolution of mind, James Arthur lecture series on the evolution of the human brain, *American Museum of Natural History* 59, p. 99.
- Jetz, W., Thomas, G., Joy, J., Hartmann, K., Mooers, A.Ø., 2012. The global diversity of birds in space and time. *Nature* 491, 444-448.
- Jiguet, F., Arroyo, B., Bretagnolle, V., 2000. Lek mating systems: a case study in the Little Bustard *Tetrax tetrax*. *Behavioural Processes* 51, 63-82.
- Johnsgard, P.A., 1968. *Waterfowl; their Biology and Natural History*. University of Nebraska Press, Lincoln Nebraska.
- Johnson, K.P., Sorenson, M.D., 1999. Phylogeny and biogeography of dabbling ducks (genus: *Anas*): a comparison of molecular and morphological evidence. *Auk* 116, 792-805.
- Jolliffe, I.T., 2002. *Principal Component Analysis*. 2nd Edition. Springer-Verlag, New York. pp 487.
- Jones, D.N., Dekker, W.R.J., Roselaar, C.S., 1995. *Bird Families of the World: The Megapodes, Megapodiidae*. Oxford University Press, Oxford. U.K.
- Kalisińska, E., 2005. Anseriform brain and Its parts versus taxonomic and ecological categories. *Brain, Behavior and Evolution* 65, 244-261. doi:210.1159/000084315.
- Kawabe, S., Ando, T., Endo, H., 2014. Enigmatic affinity in the brain morphology between plotopterids and penguins, with a comprehensive comparison among water birds. *Zoological Journal of the Linnean Society* 170, 467-493. doi:410.1111/zoj.12072.
- Kawabe, S., Matsuda, S., Tsunekawa, N., Endo, H., 2015. Ontogenetic shape change in the chicken brain: implications for paleontology. *PLoS ONE* 10, e0129939. doi:0129910.0121371/journal.pone.0129939.
- Kawabe, S., Shimokawa, T., Miki, H., Matsuda, S., Endo, H., 2013b. Variation in avian brain shape: relationship with size and orbital shape. *Journal of Anatomy* 223, 495-508. doi:410.1111/joa.12109.
- Kawabe, S., Shimokawa, T., Miki, H., Okamoto, T., Matsuda, S., 2010. A simple and accurate method for estimating the brain volume of birds: Possible application in paleoneurology. *Brain, Behavior and Evolution* 74, 295-301. doi:210.1159/000270906.
- Kawabe, S., Shimokawa, T., Miki, H., Okamoto, T., Matsuda, S., Itou, T., Koie, H., Kitagawa, M., Sakai, T., Hosojima, M., 2013a. Relationship between brain volume and brain width in mammals and birds. *Paleontological Research* 17, 282-293. doi:210.2517/1342-8144-2517.2513.2282.

- Kear, J., 2005. *Bird Families of the World: Ducks, Geese and Swans*, Vols 1 and 2. Oxford University Press, Oxford, U.K.
- Kendall, D.G., 1984. Shape manifolds, procrustean metrics, and complex projective spaces. *Bulletin of the London Mathematical Society* 16, 81-121.
- Kennedy, M., Spencer, H.G., 2000. Phylogeny, biogeography, and taxonomy of Australasian teals. *Auk* 117, 154-163.
- Kessler, E., Hír, J., 2009. A new anserid [sic] species from the Neogene of Hungary. *Fragmenta Palaeontologica Hungarica* 27, 97-101.
- Klaczko, J., Sherratt, E., Setz, E.Z.F., 2016. Are diet preferences associated to skulls shape diversification in xenodontine snakes? *PLoS ONE* 11, e0148375. doi:10.1371/journal.pone.0148375.
- Klingenberg, C.P., 1996. Multivariate Allometry, in: Marcus, L.F., Corti, M., Loy, A., Naylor, G.J.P., Slice, D.E. (Eds.), *Advances in Morphometrics*, Springer, New York, pp. 23-49.
- Klingenberg, C.P., 2009. Morphometric integration and modularity in configurations of landmarks: tools for evaluating a priori hypotheses. *Evolution and Development* 11, 405-421.
- Klingenberg, C.P., Gidaszewski, N.A., 2010. Testing and quantifying phylogenetic signals and homoplasy in morphometric data. *Systematic Biology* 59, 245-261. doi:10.1093/sysbio/syp1106.
- Kriegs, J.O., Matzke, A., Churakov, G., Kuritzin, A., Mayr, G., Brosius, J., Schmitz, J., 2007. Waves of genomic hitchhikers shed light on the evolution of gamebirds (Aves: Galliformes). *BMC Evolutionary Biology* 7, 190. doi:10.1186/1471-2148-1187-1190.
- Ksepka, D., Clarke, J.A., 2015. Phylogenetically vetted and stratigraphically constrained fossil calibrations within Aves. *Palaeontologia Electronica* 18.1.3FC, 1-25. doi:10.26879/26373.
- Ksepka, D.T., 2009. Broken gears in the avian molecular clock: new phylogenetic analyses support stem galliform status for *Gallinuloides wyomingensis* and rallid affinities for *Amitabha urbsinterdictensis*. *Cladistics* 25, 173-197. doi:10.1111/j.1096-0031.2009.00250.x.
- Ksepka, D.T., Balanoff, A.M., Walsh, S., Revan, A., Ho, A., 2012. Evolution of the brain and sensory organs in Sphenisciformes: new data from the stem penguin *Paraptendytes antarcticus*. *Zoological Journal of the Linnean Society* 166, 202-219. doi:10.1111/j.1096-3642.2012.00835.x.
- Kulemeyer, C., Asbahr, K., Gunz, P., Frahnert, S., Bairlein, F., 2009. Functional morphology and integration of corvid skulls—a 3D geometric morphometric approach. *Frontiers in Zoology* 6, 1-14. doi:10.1186/1742-9994-1186-1182.
- Kurochkin, E.N., 1968. New Oligocene birds from Kazakhstan. *Paleontological Journal* 1, 92-101.
- Kurochkin, E.N., Dyke, G.J., Karhu, A.A., 2002. A new presbyornithid bird (Aves, Anseriformes) from the Late Cretaceous of southern Mongolia. *American Museum Novitates* 3386, 1-11.
- Lambrecht, K., 1933. *Handbuch der Palaeornithologie*. Gebrüder Borntraeger, Berlin.
- Lapointe, F.-J., Baron, G., Legendre, P., 1999. Encephalization, adaptation and evolution of Chiroptera: a statistical analysis with further evidence for bat monophyly. *Brain, Behavior and Evolution* 54, 119-126.
- Lau, K.L., Glover, R.G., Linkenhoker, B., Wylie, D.R.W., 1998. Topographical organization of inferior olive cells projecting to translation and rotation zones in the vestibulocerebellum of pigeons. *Neuroscience* 85, 605-614.

- Lee, M.S.Y., Cau, A., Naish, D., Dyke, G.J., 2014. Morphological clocks in paleontology, and a mid-Cretaceous origin of crown Aves. *Systematic Biology* 63, 442-449. doi:410.1093/sysbio/syt1110.
- Lee, M.S.Y., Palci, A., 2015. Morphological phylogenetics in the genomic age. *Current Biology* 25, R922-R929. doi:910.1016/j.cub.2015.1007.1009.
- Lefebvre, L., Reader, S.M., Sol, D., 2004. Brains, innovations and evolution in birds and primates. *Brain, Behavior and Evolution* 63, 233-246. doi:210.1159/000076784.
- Legendre, P., Lapointe, F.-J., Casgrain, P., 1994. Modeling brain evolution from behavior: a permutational regression approach. *Evolution* 48, 1487-1499.
- Lindow, B.E.K., Dyke, G.J., 2007. A small galliform bird from the Lower Eocene Fur Formation, northwestern Denmark. *Bulletin of the Geological Society of Denmark* 55, 59-63.
- Liu, G., Zhou, L., Li, B., Zhang, L., 2014. The complete mitochondrial genome of *Aix galericulata* and *Tadorna ferruginea*: Bearings on their phylogenetic position in the Anseriformes. *PLoS ONE* 9, e109701. doi:109710.101371/journal.pone.0109701.
- Livezey, B.C., 1986. A phylogenetic analysis of recent anseriform genera using morphological characters. *Auk* 103, 737-754.
- Livezey, B.C., 1989. Phylogenetic relationships and incipient flightlessness of the extinct Auckland Islands Merganser. *Wilson Bulletin* 101, 410-435.
- Livezey, B.C., 1990. Evolutionary morphology of flightlessness in the Auckland Islands Teal. *Condor* 92, 639-673.
- Livezey, B.C., 1991. A phylogenetic analysis and classification of recent dabbling ducks (Tribe Anatini) based on comparative morphology. *Auk* 108, 471-507.
- Livezey, B.C., 1993. Morphology of flightlessness in *Chendytes*, fossil seaducks (Anatidae: Mergini) of coastal California. *Journal of Vertebrate Paleontology* 13, 185-199.
- Livezey, B.C., 1996. A phylogenetic analysis of geese and swans (Anseriformes: Anserinae), including selected fossil species. *Systematic Biology* 45, 415-450.
- Livezey, B.C., 1997a. A phylogenetic classification of waterfowl (Aves: Anseriformes), including selected fossil species. *Annals of the Carnegie Museum* 66, 457-496.
- Livezey, B.C., 1997b. A phylogenetic analysis of basal Anseriformes, the fossil *Presbyornis*, and the interordinal relationships of waterfowl. *Zoological Journal of the Linnean Society* 121, 361-428.
- Livezey, B.C., 2003. Evolution of flightlessness in rails (Gruiformes, Rallidae): Phylogenetic, ecomorphological, and ontogenetic perspectives. *Ornithological Monographs* 53, 1-654.
- Livezey, B.C., Martin, L.D., 1988. The systematic position of the Miocene anatid *Anas*[?] *blanchardi* Milne-Edwards. *Journal of Vertebrate Paleontology* 8, 196-211.
- Livezey, B.C., Zusi, R.L., 2001. Higher-order phylogenetics of modern Aves based on comparative anatomy. *Netherlands Journal of Zoology* 51, 179-205.
- Livezey, B.C., Zusi, R.L., 2007. Higher-order phylogeny of modern birds (Theropoda, Aves: Neornithes) based on comparative anatomy. II. Analysis and discussion. *Zoological Journal of the Linnean Society* 149, 1-95.
- Longman, H.A., 1945. Fossil vertebrates from Gore Quarries. *Memoirs of the Queensland Museum* 12, 164.

- Louchart, A., Vignaud, P., Likius, A., Mackaye, H.T., Brunet, M., 2005. A new swan (Aves: Anatidae) in Africa, from the latest Miocene of Chad and Libya. *Journal of Vertebrate Paleontology* 25, 384-392.
- Lydekker, R., 1891. Catalogue of the fossil birds in the British Museum (Natural History). *British Museum of Natural History*, London.
- Madsen, C.S., McHugh, K.P., de Kloet, S.W.R., 1988. A partial classification of waterfowl (Anatidae) based on single-copy DNA. *Auk* 105, 452-459.
- Manger, P.R., Elston, G.N., Pettigrew, J.D., 2002. Multiple maps and activity-dependent representational plasticity in the anterior wulst of the adult barn owl (*Tyto alba*). *European Journal of Neuroscience* 16, 743-750. doi:710.1046/j.1460-9568.2002.02119.x.
- Marchant, S., Higgins, P.J., 1990. *Handbook of Australian, New Zealand and Antarctic birds*, Vols 1A and 1B. Oxford University Press, Melbourne, Australia.
- Marshall, B., Allen, J., 1991. Excavations at Panakiwuk Cave, New Ireland, in: Allen, J., Gosden, C. (Eds.), Report of the Lapita Homeland Project, National Museum of Australia. *Occasional Papers Prehistory*, Canberra, pp. 59-91.
- Martin, G.R., 2009. What is binocular vision for? A birds' eye view. *Journal of Vision* 9, 1-19. doi:10.1167/1169.1111.1114.
- Martin, G.R., Wilson, K.-J., Wild, J.M., Parsons, S., Kubke, M.F., Corfield, J., 2007. Kiwi forego vision in the guidance of their nocturnal activities. *PLoS ONE* 2, e198. doi:110.1371/journal.pone.0000198.
- Martin, L.D., 1992. The status of the late Paleocene birds *Gastornis* and *Remiornis*, In: Campbell Jr, K.E. (Ed.), Papers in Avian Paleontology Honoring Pierce Brodkorb, Incorporating the Proceedings of the II International Symposium of the Society of Avian Paleontology and Evolution, Natural History Museum of Los Angeles County, 1988, *Natural History Museum of Los Angeles County Science Series* 36, pp. 97-108.
- Martin, L.D., Mengel, R.M., 1980. A new goose from the late Pliocene of Nebraska with notes on variability and proportions in some recent geese, in: Campbell Jr., K.E. (Ed.), Papers in Avian Paleontology honouring Hildegard Howard, Natural History Museum of Los Angeles County, *Contributions in Science* 330, pp. 75-85.
- Martin, L.D., Tate, J., 1970. A new turkey from the Pliocene of Nebraska. *Wilson Bulletin* 82, 214-218.
- Marugán-Lobón, J., 2010. Combining Shape Data and Traditional Measurements with the 2B-PLS: Testing the Covariation Between Avian Brain Size and Cranial Shape Variation as an Example, in: Elewa, A.M.T. (Ed.), *Morphometrics for Nonmorphometricians*, Springer-Verlag, Berlin, pp. 179-190.
- Marugán-Lobón, J., Buscalioni, Á.D., 2004. Geometric morphometrics in macroevolution: morphological diversity of the skull in modern avian forms in contrast to some theropod dinosaurs, in: Elewa, A.M.T. (Ed.), *Morphometrics: Applications in Biology and Paleontology*, Springer-Verlag, Berlin, pp. 157-173.
- Marugán-Lobón, J., Buscalioni, Á.D., 2006. Avian skull morphological evolution: exploring exo-and endocranial covariation with two-block partial least squares. *Zoology* 109, 217-230. doi:210.1016/j.zool.2006.1003.1005.
- Marugán-Lobón, J., Buscalioni, Á.D., 2009. New insight on the anatomy and architecture of the avian neurocranium. *Anatomical Record* 292, 364-370. doi:310.1002/ar.20865.

- Marugán-Lobón, J., Watanabe, A., Kawabe, S., 2016. Studying avian encephalization with geometric morphometrics. *Journal of Anatomy* 229, 191-203. doi:110.1111/joa.12476.
- Mather, E.K., Tennyson, A.J.D., Scofield, R.P., De Pietri, V.L., Hand, S.J., Archer, M., Handley, W.D., Worthy, T.H., 2019. Flightless rails (Aves: Rallidae) from the early Miocene St Bathans Fauna, Otago, New Zealand. *Journal of Systematic Palaeontology* 17, 423-449. doi:410.1080/14772019.14772018.11432710.
- Matthew, W.D., Granger, W., 1917. The skeleton of *Diatryma*, a gigantic bird from the lower Eocene of Wyoming. *Bulletin of the American Natural History Museum* 37, 307-326.
- Mayr, E., 1938. Birds collected during the Whitney South Sea Expedition. XXXIX. Notes on New Guinea birds, IV. *American Museum Novitates* 1006, 1-16.
- Mayr, G., 2000. A new basal galliform bird from the Middle Eocene of Messel (Hessen, Germany). *Senckenbergiana Lethaea* 80, 45-57.
- Mayr, G., 2004. A partial skeleton of a new fossil loon (Aves, Gaviiformes) from the early Oligocene of Germany with preserved stomach content. *Journal of Ornithology* 145, 281-286. doi:210.1007/s10336-10004-10050-10339.
- Mayr, G., 2005. The Paleogene fossil record of birds in Europe. *Biological Reviews* 80, 515-542. doi:510.1017/S1464793105006779.
- Mayr, G., 2006. New specimens of the early Eocene stem group galliform *Paraortygoides* (Gallinuloididae), with comments on the evolution of a crop in the stem lineage of Galliformes. *Journal of Ornithology* 147, 31-37. doi:10.1007/s10336-10005-10006-10338.
- Mayr, G., 2007a. The birds from the Paleocene fissure filling of Walbeck (Germany). *Journal of Vertebrate Paleontology* 27, 394-408.
- Mayr, G., 2007b. New specimens of Eocene stem-group psittaciform birds may shed light on the affinities of the first named fossil bird, *Halcyornis toliapicus* Koenig, 1825. *Neues Jahrbuch für Geologie und Paläontologie-Abhandlungen* 244, 207-213.
- Mayr, G., 2008a. Avian higher-level phylogeny: well-supported clades and what we can learn from a phylogenetic analysis of 2954 morphological characters. *Journal of Zoological Systematics and Evolutionary Research* 46, 63-72. doi:10.1111/j.1439-0469.2007.00433.x.
- Mayr, G., 2008b. The fossil record of galliform birds: comments on Crowe et al.(2006). *Cladistics* 24, 74-76. doi:10.1111/j.1096-0031.2007.00170.x.
- Mayr, G., 2008c. Phylogenetic affinities and morphology of the late Eocene anseriform bird *Romainvillia stehlini* Lebedinsky, 1927. *Neues Jahrbuch für Geologie und Paläontologie-Abhandlungen* 248, 365-380. doi:310.1127 /0077-1177 1149/2008/0248-0365.
- Mayr, G., 2009. *Paleogene Fossil Birds*. Springer-Verlag, Berlin Heidelberg.
- Mayr, G., 2011a. Metaves, Mirandornithes, Strisores and other novelties—a critical review of the higher-level phylogeny of neornithine birds. *Journal of Zoological Systematics and Evolutionary Research* 49, 58-76. doi: 10.1111/j.1439-0469.2010.00586.x.
- Mayr, G., 2013. The age of the crown group of passerine birds and its evolutionary significance—molecular calibrations versus the fossil record. *Systematics and Biodiversity* 11, 7-13. doi:10.1080/14772000.14772013.14765521.
- Mayr, G., 2015. Variations in the hypotarsus morphology of birds and their evolutionary significance. *Acta Zoologica* 97, 196-210. doi:110.1111/azo.12117.

- Mayr, G., 2017. *Avian Evolution: The Fossil Record of Birds and its Paleobiological Significance*. John Wiley & Sons, Chichester. UK. pp 293.
- Mayr, G., Clarke, J., 2003. The deep divergences of neornithine birds: a phylogenetic analysis of morphological characters. *Cladistics* 19, 527-553 doi:10.1016/j.cladistics.2003.1010.1003.
- Mayr, G., De Pietri, V.L., 2013. A goose-sized anseriform bird from the late Oligocene of France: the youngest record and largest species of Romainvilliinae. *Paläontologische Zeitschrift* 87, 423-430. doi: 10.1007/s12542-12013-10165-12545.
- Mayr, G., De Pietri, V.L., Scofield, R.P., Worthy, T.H., 2018. On the taxonomic composition and phylogenetic affinities of the recently proposed clade Vegaviidae Agnolín et al., 2017–neornithine birds from the Upper Cretaceous of the Southern Hemisphere. *Cretaceous Research* 86, 178-185. doi:10.1016/j.cretres.2018.1002.1013.
- Mayr, G., Poschmann, M., Wuttke, M., 2006. A nearly complete skeleton of the fossil galliform bird *Palaeortyx* from the late Oligocene of Germany. *Acta Ornithologica* 41, 129-135.
- Mayr, G., Scofield, R.P., 2014. First diagnosable non-sphenisciform bird from the early Paleocene of New Zealand. *Journal of the Royal Society of New Zealand* 44, 48-56. doi:10.1080/03036758.03032013.03863788.
- Mayr, G., Smith, R., 2001. Ducks, rails, and limicoline waders (Aves: Anseriformes, Gruiformes, Charadriiformes) from the lowermost Oligocene of Belgium. *Geobios* 34, 547-561.
- Mayr, G., Weidig, I., 2004. The Early Eocene bird *Gallinuloides wyomingensis*-a stem group representative of Galliformes. *Acta Palaeontologica Polonica* 49, 211-217.
- McCracken, K.G., 1999. Systematics, ecology, and social biology of the Musk Duck (*Biziura lobata*) of Australia, PhD Dissertation, *Louisiana State University*, Baton Rouge, Louisiana.
- McCracken, K.G., Afton, A.D., Paton, D.C., 2000a. Nest and eggs of Musk Ducks *Biziura lobata* at Murray Lagoon, Cape Gantheaume Conservation Park, Kangaroo Island, South Australia. *South Australian Ornithologist* 33, 65-70.
- McCracken, K.G., Harshman, J., McClellan, D.A., Afton, A.D., 1999. Data set incongruence and correlated character evolution: an example of functional convergence in the hind-limbs of stiff-tail diving ducks. *Systematic Biology* 48, 683-714.
- McCracken, K.G., Paton, D.C., Afton, A.D., 2000b. Sexual size dimorphism of the Musk Duck. *Wilson Bulletin* 112, 457-466.
- McCracken, K.G., Sorenson, M.D., 2005. Is homoplasy or lineage sorting the source of incongruent mtDNA and nuclear gene trees in the stiff-tailed ducks (Nomonyx-Oxyura)? *Systematic Biology* 54, 35-55. doi:10.1080/10635150590910249.
- McNamara, G.C., 1990. The Wyandotte Local Fauna: a new, dated, Pleistocene vertebrate fauna from northern Queensland. *Memoirs of the Queensland Museum* 28, 285-297.
- Mehlhorn, J., Hunt, G.R., Gray, R.D., Rehkämper, G., Güntürkün, O., 2010. Tool-making New Caledonian crows have large associative brain areas. *Brain, Behavior and Evolution* 75, 63-70. doi:10.1159/000295151.
- Miceli, D., Marchand, L., Repérant, J., Rio, J.-P., 1990. Projections of the dorsolateral anterior complex and adjacent thalamic nuclei upon the visual wulst in the pigeon. *Brain Research* 518, 317-323.
- Millener, P.R., 1991. The Quaternary Avifauna of New Zealand, in: Vickers-Rich, P., Monaghan, J.M., Baird, R.F., Rich, T.H. (Eds.), *Vertebrate Palaeontology of Australasia*, Pioneer Design

- Studios in cooperation with the Monash University Publications Committee, Melbourne, pp. 1317-1344
- Miller, A.H., 1948. The whistling swan in the Upper Pliocene of Idaho. *Condor* 50, 132.
- Miller, A.H., Compton, L.V., 1939. Two fossil birds from the lower Miocene of South Dakota. *Condor* 41, 153-156.
- Miller, L., 1925. *Chendytes*, a diving goose from the California Pleistocene. *Condor* 27, 145-147.
- Miller, L., 1930. A fossil goose from the Ricardo Pliocene. *Condor* 32, 208-209.
- Miller, L., 1944. Some Pliocene birds from Oregon and Idaho. *Condor* 46, 25-32.
- Miller, L., 1952. The avifauna of the Barstow Miocene of California. *Condor* 54, 296-301.
- Miller, L., 1961. Birds from the Miocene of Sharktooth Hill, California. *Condor* 63, 399-402.
- Miller, L., Mitchell, E.D., Lipps, J.H., 1961. New light on the flightless goose, *Chendytes lawi*. *Los Angeles County Museum of Natural History Contributions in Science* 43, 3-11.
- Milne-Edwards, A., (1867-1871). *Recherches Anatomiques et Paléontologiques pour Servir à L'histoire des Oiseaux Fossiles de la France*. Masson, Paris: Vol. 1, 472 pp., 96 pls; Vol. 2, 627 pp., pls 97-200.
- Milne-Edwards, A., 1891. Sur les oiseaux fossiles des dépôts éocènes de phosphate de chaux du Sud de la France. *C R Second Congress Ornithologie International*, 60-80.
- Milner, A.C., Walsh, S.A., 2009. Avian brain evolution: new data from Palaeogene birds (Lower Eocene) from England. *Zoological Journal of the Linnean Society* 155, 198-219.
- Mitchell, K.J., Llamas, B., Soubrier, J., Rawlence, N.J., Worthy, T.H., Wood, J.R., Lee, M.S.Y., Cooper, A., 2014b. Ancient DNA reveals elephant birds and kiwi are sister taxa and clarifies ratite bird evolution. *Science* 344, 898-900. doi:810.1126/science.1251981.
- Mitchell, K.J., Wood, J.R., Scofield, R.P., Llamas, B., Cooper, A., 2014a. Ancient mitochondrial genome reveals unsuspected taxonomic affinity of the extinct Chatham duck (*Pachyanas chathamica*) and resolves divergence times for New Zealand and sub-Antarctic brown teals. *Molecular Phylogenetics and Evolution* 70, 420-428. doi:410.1016/j.ympev.2013.1008.1017.
- Mitteroecker, P., Gunz, P., 2009. Advances in geometric morphometrics. *Evolutionary Biology* 36, 235-247. doi:210.1007/s11692-11009-19055-x.
- Mlíkovský, J., 1982. Taxonomische identität der *Anas submajor* Jánossy, 1979 (Aves: Anseriformes) aus dem Oberpliozän ungarms. *Vestnik Československe Spolecnosti Zoologicke* 46, 199-202.
- Mlíkovský, J., 1992. The present state of knowledge of the Tertiary birds of Central Europe, in: Campbell Jr, K.E. (Ed.), *Studies in Avian Paleontology Honoring Pierce Brodkorb. Incorporating the Proceedings of the II International Symposium of the Society of Avian Paleontology and Evolution, Natural History Museum of Los Angeles County, 1988, Natural History Museum of Los Angeles County, Sciences Series* 36, pp. 433-458.
- Mlíkovský, J., 1998. Vertebrates from the Early Miocene lignite deposits of the opencast mine Oberdorf (Western Styrian Basin, Austria): 4. Aves. *Annalen des Naturhistorischen Museums Wien A* 99, 39-42.
- Mlíkovský, J., 2002. *Cenozoic Birds of the World. Part 1: Europe*. Ninox Press, Prague.
- Mlíkovský, J., Švec, P., 1986. Review of the tertiary waterfowl (Aves: Anseridae) of Asia. *Vestnik Československe Spolecnosti Zoologicke* 50, 249-272.

- Montgomerie, R., Briskie, J.V., 2007. Anatomy and Evolution of Copulatory Structures, in: Jamieson, B.G.M. (Ed.), *Reproductive Biology and Phylogeny of Birds*, Science Publishers, Enfield, pp. 115-148.
- Mourer-Chauviré, C., 1988. Le gisement du Bretou (Phosphorites du Quercy, Tarn-et-Garonne, France) et sa faune de vertébrés de l'Eocène supérieur. II oiseaux. *Palaeontographica Abteilung A* 205, 29-50.
- Mourer-Chauviré, C., 1989. A peafowl from the Pliocene of Perpignan, France. *Palaeontology* 32, 439-446.
- Mourer-Chauviré, C., 1992. The Galliformes (Aves) from the phosphorites du Quercy (France): Systematics and biostratigraphy, In: Campbell Jr, K.E. (Ed.), *Papers in Avian Paleontology Honoring Pierce Brodkorb, Incorporating the Proceedings of the II International Symposium of the Society of Avian Paleontology and Evolution*, Natural History Museum of Los Angeles County, 1988, *Natural History Museum of Los Angeles County Science Series* 36, pp. 67-95.
- Mourer-Chauviré, C., 2000. A new species of *Ameripodius* (Aves: Galliformes: Quercymegapodiidae) from the lower Miocene of France. *Palaeontology* 43, 481-493.
- Mourer-Chauviré, C., 2004. Review of: Cenozoic Birds of the World, Part 1: Europe. *Auk* 121, 623-627.
- Mourer-Chauviré, C., 2006. The avifauna of the Eocene and Oligocene phosphorites du Quercy (France): an updated list. *Strata* 13, 135-149.
- Mourer-Chauviré, C., 2008. Birds (Aves) from the early Miocene of the Northern Sperrgebiet, Namibia. *Memoirs of the Geological Survey Namibia* 20, 147-167.
- Mourer-Chauviré, C., Balouet, J.C., 2005. Description of the skull of the genus *Sylviornis* Poplin, 1980 (Aves, Galliformes, Sylviornithidae new family), a giant extinct bird from the Holocene of New Caledonia, In: Alcover, J.A., Bover, P. (Eds.), *Proceedings of the International Symposium "Insular Vertebrate Evolution: the Palaeontological Approach"*, *Monografies de la Societat d'Història Natural de les Balears* 12, pp. 205-218.
- Mourer-Chauviré, C., Berthet, D., Hugueney, M., 2004. The late Oligocene birds of the Créchy quarry (Allier, France), with a description of two new genera (Aves: Pelecaniformes: Phalacrocoracidae, and Anseriformes: Anseranatidae). *Senckenbergiana Lethaea* 84, 303-315.
- Mourer-Chauviré, C., Marshall, L.G., de Muizon, C., Sigé, B., 1983. Les Gruiformes (Aves) des phosphorites du Quercy (France): 1, sous-ordre Cariamae (Cariamidae et Phorusrhacidae): Systématique et biostratigraphie. *Palaeovertebrata* 13, 83-143.
- Mourer-Chauviré, C., Pickford, M., Senut, B., 2011. The first Palaeogene galliform from Africa. *Journal of Ornithology* 152, 617-622. doi:610.1007/s10336-10010-10630-10339.
- Murray, P.F., Megirian, D., 1998. The skull of dromornithid birds: anatomical evidence for their relationship to Anseriformes. *Records of the South Australian Museum* 31, 51-97.
- Murray, P.F., Vickers-Rich, P., 2004. *Magnificent Mhirungs: The Colossal Flightless Birds of the Australian Dreamtime*. Indiana University Press, Bloomington.
- Nealen, P.M., Ricklefs, R.E., 2001. Early diversification of the avian brain: body relationship. *Journal of Zoology* 253, 391-404.
- Noriega, J.I., 1995. The avifauna from the "Mesopotamian" (Ituzaingó Formation: Upper Miocene) of Entre Ríos Province, Argentina. *Courier Forschungsinstitut Senckenberg* 181, 141-148.

- Noriega, J.I., Tambussi, C.P., 1995. A Late Cretaceous Presbyornithidae (Aves: Anseriformes) from Vega Island, Antarctic Peninsula: Palcobiogeographic implications. *Ameghiniana* 32, 57-61.
- Noriega, J.I., Tambussi, C.P., Cozzuol, M.A., 2008. New material of *Cayaoa bruneti* Tonni, an early Miocene anseriform (Aves) from Patagonia, Argentina. *Neues Jahrbuch für Geologie und Paläontologie-Abhandlungen* 249, 271-280. doi:210.1127/0077-7749/2008/0249-0271.
- Northcote, E.M., 1992. Swans (*Cygnus*) and cranes (*Grus*) from the Maltese Pleistocene, in: Campbell Jr., K.E. (Ed.), Papers in Avian Paleontology Honoring Pierce Brodkorb, Incorporating the Proceedings of the II International Symposium of the Society of Avian Paleontology and Evolution, Natural History Museum of Los Angeles County, 1988, *Natural History Museum of Los Angeles County Science Series* 36, pp. 285-291.
- Northcutt, R.G., 1981. Evolution of the telencephalon in nonmammals. *Annual Review of Neuroscience* 4, 301-350.
- Northcutt, R.G., 2001. Changing views of brain evolution. *Brain Research Bulletin* 55, 663-674.
- Olkowicz, S., Kocourek, M., Lučan, R.K., Porteš, M., Fitch, W.T., Herculano-Houzel, S., Němec, P., 2016. Birds have primate-like numbers of neurons in the forebrain. *Proceedings of the National Academy of Sciences USA* 113, 7255-7260. doi:7210.1073/pnas.1517131113.
- Olson, S.L., 1973. Evolution of the rails of the South Atlantic islands (Aves: Rallidae). *Smithsonian Contributions to Zoology* 152, 1-53.
- Olson, S.L., 1974. Telecrex restudied: a small Eocene guineafowl. *Wilson Bulletin*, 246-250.
- Olson, S.L., 1977a. The identity of the fossil ducks described from Australia by CW De Vis. *Emu* 77, 127-131.
- Olson, S.L., 1977b. Notes on subfossil Anatidae from New Zealand, including a new species of pink-eared duck *Malacorhynchus*. *Emu* 77, 132-135.
- Olson, S.L., 1985. The Fossil Record of Birds, in: Farner, D.S., King, J.R., Parkes, K.C. (Eds.), *Avian Biology*. Vol. 8, Academic Press, New York, pp. 79-238.
- Olson, S.L., 1994. A giant *Presbyornis* (Aves: Anseriformes) and other birds from the Paleocene Aquia Formation of Maryland and Virginia. *Proceedings of the Biological Society of Washington* 107, 429-435.
- Olson, S.L., 1999. The anseriform relationships of *Anatalavis* Olson and Parris (Anseranatidae), with a new species from the Lower Eocene London Clay, in: Olson, S.L. (Ed.), Avian paleontology at the close of the 20th century: Proceedings of the 4th international meeting of the Society of Avian Paleontology and Evolution. Washington, D.C., 4-7 June 1996, *Smithsonian Contributions to Paleobiology* 89, pp. 231-243.
- Olson, S.L., 2013. Hawaii's first fossil bird: history, geological age, and taxonomic status of the extinct goose *Geochen rhuax* Wetmore (Aves: Anatidae). *Proceedings of the Biological Society of Washington* 126, 161-168.
- Olson, S.L., Farrand Jr, J., 1974. *Rhegminornis* restudied: a tiny Miocene turkey. *Wilson Bulletin* 86, 114-120.
- Olson, S.L., Feduccia, A., 1980. *Presbyornis* and the origin of the Anseriformes (Aves: Charadriomorphae). *Smithsonian Contributions to Zoology* 323, 1-24.
- Olson, S.L., James, H.F., 1991. Descriptions of thirty-two new species of birds from the Hawaiian Islands: Part I. Non-Passeriformes. *Ornithological Monographs* 45, 1-88.

- Olson, S.L., Jouventin, P., 1996. A new species of small flightless duck from Amsterdam Island, southern Indian Ocean (Anatidae: *Anas*). *Condor* 98, 1-9.
- Olson, S.L., Parris, D.C., 1987. The Cretaceous birds of New Jersey. *Smithsonian Contributions to Paleobiology* 63, 1-22.
- Olson, S.L., Rasmussen, P.C., 2001. Miocene and Pliocene Birds from the Lee Creek Mine; North Carolina. *Smithsonian Contributions to Paleobiology* 90, 233-365.
- Olson, S.L., Wetmore, A., 1976. Preliminary diagnoses of two extraordinary new genera of birds from Pleistocene deposits in the Hawaiian Islands. *Proceedings of the Biological Society of Washington* 89, 247-258.
- Pakan, J.M.P., Wylie, D.R.W., 2006. Two optic flow pathways from the pretectal nucleus lentiformis mesencephali to the cerebellum in pigeons (*Columba livia*). *Journal of Comparative Neurology* 499, 732-744. doi:10.1002/cne.21108.
- Palci, A., Lee, M.S.Y., 2019. Geometric morphometrics, homology and cladistics: review and recommendations. *Cladistics* 35, 230-242. doi:10.1111/cla.12340.
- Parkes, K.C., Clark, G.A., Jr., 1966. An additional character linking ratites and tinamous, and an interpretation of their monophyly. *Condor* 68, 459-471.
- Parr, W.C.H., Wilson, L.A.B., Wroe, S., Colman, N.J., Crowther, M.S., Letnic, M., 2016. Cranial shape and the modularity of hybridization in dingoes and dogs; hybridization does not spell the end for native morphology. *Evolutionary Biology* 43, 171-187. doi:10.1007/s11692-11016-19371-x.
- Parris, D.C., Hope, S., 2002. New interpretations of the birds from the Navesink and Hornerstown Formations, New Jersey, USA (Aves: Neornithes), in: Zhou, Z., Zhang, F. (Eds.), Proceedings of the 5th Symposium of the Society of Avian Paleontology and Evolution, Beijing, 1-4 June 2000, *Science Press*, Beijing, pp. 113-124.
- Patterson, J., Lockley, M.G., 2004. A probable *Diatryma* track from the Eocene of Washington: an intriguing case of controversy and skepticism. *Ichnos* 11, 341-347. doi:10.1080/10420940490442278.
- Paulina-Carabajal, A., Acosta-Hospitaleche, C., Yury-Yáñez, R.E., 2014. Endocranial morphology of *Pygoscelis calderensis* (Aves, Spheniscidae) from the Neogene of Chile and remarks on brain morphology in modern *Pygoscelis*. *Historical Biology* 27, 571-582. doi:10.1080/08912963.08912014.08898067.
- Peng, K., Feng, Y., Zhang, G., Liu, H., Song, H., 2010. Anatomical study of the brain of the African ostrich. *Turkish Journal of Veterinary and Animal Sciences* 34, 235-241. doi:10.3906/vet-0806-3919.
- Pennell, M.W., Harmon, L.J., 2013. An integrative view of phylogenetic comparative methods: connections to population genetics, community ecology, and paleobiology. *Annals of the New York Academy of Sciences* 1289, 90-105. doi:10.1111/nyas.12157.
- Pepperberg, I.M., 1999. *The Alex Studies: Cognitive and Communicative Abilities of Grey Parrots*. Harvard University Press, Cambridge, MA.
- Pepperberg, I.M., 2002. Cognitive and communicative abilities of grey parrots. *Current Directions in Psychological Science* 11, 83-87.

- Pereira, S.L., Baker, A.J., 2006. A molecular timescale for galliform birds accounting for uncertainty in time estimates and heterogeneity of rates of DNA substitutions across lineages and sites. *Molecular Phylogenetics and Evolution* 38, 499-509. doi:410.1016/j.ympev.2005.1007.1007.
- Pereira, S.L., Baker, A.J., Wajntal, A., 2002. Combined nuclear and mitochondrial DNA sequences resolve generic relationships within the Cracidae (Galliformes, Aves). *Systematic Biology* 51, 946-958. doi:910.1080/10635150290156051.
- Peters, D.S., 1988. Die Messel-Vögel—eine Landvogelfauna, in: Schaal, S., Ziegler, W. (Eds.), *Messel—ein Schaufenster in die Geschichte der Erde und des Lebens*, Kramer, Frankfurt, Germany, pp. 135-151.
- Peters, D.S., 1991. Zoogeographical relationships of the Eocene avifauna from Messel (Germany), In: Bell, B.D., Cossee, R.O., Flux, J.E.C., Heather, B.D., Hitchmough, R.A., Robertson, C.J.R., Williams, M.J. (Eds.), *Acta XX Congressus Internationalis Ornithologici*, New Zealand *Ornithological Congress Trust Board, Christchurch*, Christchurch, pp. 572-577.
- Pettigrew, J.D., 1986. Evolution of Binocular Vision, in: Pettigrew, J.D., Sanderson, K.J., Levick, W.R. (Eds.), *Visual Neuroscience*, Springer, New York, pp. 208-222.
- Pettigrew, J.D., Frost, B.J., 1985. A tactile fovea in the Scolopacidae? *Brain, Behavior and Evolution* 26, 185-195. doi: 110.1159/000118775.
- Phillips, M.J., Gibb, G.C., Crimp, E.A., Penny, D., 2010. Tinamous and moa flock together: mitochondrial genome sequence analysis reveals independent losses of flight among ratites. *Systematic Biology* 59, 90-107. doi:110.1093/sysbio/syp1079.
- Picasso, M.B.J., Tambussi, C., Dozo, M.T., 2009. Neurocranial and brain anatomy of a Late Miocene eagle (Aves, Accipitridae) from Patagonia. *Journal of Vertebrate Paleontology* 29, 831-836. doi:810.1671/1039.1029.0319.
- Picasso, M.B.J., Tambussi, C.P., Degrange, F.J., 2011. Virtual reconstructions of the endocranial cavity of *Rhea americana* (Aves, Palaeognathae): Postnatal anatomical changes. *Brain, Behavior and Evolution* 76, 176-184. doi:110.1159/000321173.
- Pledge, N.S., Tedford, R.H., 1990. Vertebrate fossils, in: Tyler, M.J., Twidale, C.R., Davies, M., Wells, C.B. (Eds.), *Natural History of the North East Deserts*, *Occasional Publications of the Royal Society of South Australia* 6, pp. 199-209.
- Poe, S., Chubb, A.L., 2004. Birds in a bush: five genes indicate explosive evolution of avian orders. *Evolution* 58, 404-415.
- Pole, M., Douglas, B., Mason, G., 2003. The terrestrial Miocene biota of southern New Zealand. *Journal of the Royal Society of New Zealand* 33, 415-426. doi:410.1080/03014223.03012003.09517737.
- Poplin, F., 1980. *Sylviornis neocaledoniae* n. g., n. sp. (Aves), ratite éteint de la Nouvelle-Calédonie. *Comptes Rendus de l'Académie des Sciences de Paris, Série D*, 691-694.
- Poplin, F., Mourer-Chauviré, C., 1985. *Sylviornis neocaledoniae* (Aves, Galliformes, Megapodiidae), oiseau géant éteint de l'Ile des Pins (Nouvelle-Calédonie). *Geobios* 18, 73-97.
- Poplin, F., Mourer-Chauviré, C., Evin, J., 1983. Position systématique et datation de *Sylviornis neocaledoniae*, mégapode géant (Aves, Galliformes, Megapodiidae) éteint de la Nouvelle-Calédonie. *Comptes Rendus des Séances de l'Académie des Sciences. Série II T.* 297, 301-304.

- Proffitt, J.V., Clarke, J.A., Scofield, R.P., 2016. Novel insights into early neuroanatomical evolution in penguins from the oldest described penguin brain endocast. *Journal of Anatomy* 229, 228-238. doi:210.1111/joa.12447.
- Pruett-Jones, S.G., Pruett-Jones, M.A., 1990. Sexual selection through female choice in Lawes' Parotia, a lek-mating bird of paradise. *Evolution* 44, 486-501.
- Prum, R.O., Berv, J.S., Dornburg, A., Field, D.J., Townsend, J.P., Lemmon, E.M., Lemmon, A.R., 2015. A comprehensive phylogeny of birds (Aves) using targeted next-generation DNA sequencing. *Nature* 526, 569-573.
- Pulvertaft, T.C.R., 1999. "Paleocene" or "Palaeocene". *Bulletin of the Geological Society of Denmark* 46, p.52.
- R Core Team, 2018. *R: A language and environment for statistical computing*. R Foundation for Statistical Computing, Vienna, Austria. URL: <https://www.R-project.org/>.
- Rasband, W.S., 2018. *ImageJ*, U.S. National Institutes of Health, Bethesda, Maryland, USA. <https://imagej.nih.gov/ij/>.
- Reiner, A., 2009. Avian evolution: from Darwin's finches to a new way of thinking about avian forebrain organization and behavioural capabilities. *Biology Letters* 5, 122-124. doi:110.1098/rsbl.2008.0473.
- Reiner, A., Davis, B.M., Brecha, N.C., Karten, H.J., 1984. The distribution of enkephalinlike immunoreactivity in the telencephalon of the adult and developing domestic chicken. *Journal of Comparative Neurology* 228, 245-262.
- Reiner, A., Yamamoto, K., Karten, H.J., 2005. Organization and evolution of the avian forebrain. *Anatomical Record A* 287, 1080-1102. doi:1010.1002/ar.a.20253.
- Rich, P.V., Van Tets, G.F., 1982. Fossil Birds of Australia and New Guinea: Their Biogeographic, Phylogenetic and Biostratigraphic Input, in: Rich, P.V., Thompson, E.M. (Eds.), *The Fossil Vertebrate Record of Australasia*, Monash University Offset printing Unit, Clayton, Victoria, Australia, pp. 235-384.
- Rich, T.H., Archer, M., Hand, S.J., Godthelp, H., Muirhead, J., Pledge, N.S., Flannery, T.F., Woodburne, M.O., Case, J.A., Tedford, R.H., Lundelius Jr, E.L., Rich, L.S.V., Whitelaw, M.J., Kemp, A., Vickers-Rich, P., 1991. Australian Mesozoic and Tertiary Terrestrial Mammal Localities, in: Vickers-Rich, P., Monaghan, J.M., Baird, R.F., Rich, T.H. (Eds.), *Vertebrate Palaeontology of Australasia*, Pioneer Design Studios in cooperation with the Monash University Publications Committee, Melbourne, pp. 1005-1070.
- Ridet, J.M., Bauchot, R., 1991. Analyse quantitative de l'encéphale des téléostéens: caractères évolutifs et adaptatifs de l'encéphalisation. III. Analyse multivariée des indices encéphaliques. *Journal für Hirnforschung* 32, 439-449.
- Robertson, B.C., Goldstien, S.J., 2012. Phylogenetic affinities of the New Zealand blue duck (*Hymenolaimus malacorhynchos*). *Notornis* 59, 49-59.
- Rogers, L., 1996. Behavioral, structural and neurochemical asymmetries in the avian brain: a model system for studying visual development and processing. *Neuroscience & Biobehavioral Reviews* 20, 487-503.
- Rohlf, F.J., 1990. Morphometrics. *Annual Review of Ecology and Systematics* 21, 299-316.

- Rohlf, F.J., 1993. Relative warp analysis and an example of its application to mosquito wings, In: Marcus, L.F., Bello, E., García-Valdecasas, A. (Eds.), *Contributions to Morphometrics, Monografías del Museo Nacional de Ciencias Naturales*, CSIC, Madrid, pp. 131-158.
- Rohlf, F.J., 1999. Shape statistics: Procrustes superimpositions and tangent spaces. *Journal of Classification* 16, 197-223.
- Rohlf, F.J., Corti, M., 2000. Use of two-block partial least-squares to study covariation in shape. *Systematic Biology* 49, 740-753.
- Rohlf, F.J., Marcus, L.F., 1993. A revolution in morphometrics. *Trends in Ecology & Evolution* 8, 129-132.
- Rohlf, F.J., Slice, D., 1990. Extensions of the Procrustes method for the optimal superimposition of landmarks. *Systematic Biology* 39, 40-59.
- Ronquist, F., van der Mark, P., Huelsenbeck, J.P., 2009. Bayesian Phylogenetic Analysis using MrBayes, in: Lemey, P., Salemi, M., Vandamme, A.M. (Eds.), *The Phylogenetic Handbook: A Practical Approach to Phylogenetic Analysis and Hypothesis Testing*, Cambridge University Press, Cambridge, pp. 210-266.
- RStudio Team, 2016. *RStudio: Integrated Development for R*, RStudio, Inc., Boston, MA URL <http://www.rstudio.com/>.
- Salzen, E.A., Parker, D.M., Williamson, A.J., 1975. A forebrain lesion preventing imprinting in domestic chicks. *Experimental Brain Research* 24, 145-157.
- Sayol, F., Lefebvre, L., Sol, D., 2016. Relative brain size and its relation with the associative pallium in birds. *Brain, Behavior and Evolution* 87, 69-77. doi:10.1159/000444670.
- Schaub, S., 1945. Bemerkungen zum typus von *Taoperdix keltica* Eastman. *Eclogae Geologicae Helvetiae* 38, 616-621.
- Scofield, R.P., Ashwell, K.W.S., 2009. Rapid somatic expansion causes the brain to lag behind: the case of the brain and behavior of New Zealand's Haast's Eagle (*Harpagornis moorei*). *Journal of Vertebrate Paleontology* 29, 637-649.
- Scofield, R.P., Worthy, T.H., Tennyson, A.J.D., 2010. A heron (Aves: Ardeidae) from the early Miocene St Bathans fauna of southern New Zealand. *Records of the Australian Museum* 62, 89-104. doi:110.3853/j.0067-1975.3862.2010.1542.
- Sherratt, E., Serb, J.M., Adams, D.C., 2017b. Rates of morphological evolution, asymmetry and morphological integration of shell shape in scallops. *BMC evolutionary biology* 17, 248. doi:210.1186/s12862-12017-11098-12865.
- Sherratt, E., Vidal-García, M., Anstis, M., Keogh, J.S., 2017a. Adult frogs and tadpoles have different macroevolutionary patterns across the Australian continent. *Nature Ecology & Evolution* 1, 1385-1391. doi:1310.1038/s41559-41017-40268-41556.
- Short, L.L., 1970. A new anseriform genus and species from the Nebraska Pliocene. *Auk* 87, 537-543.
- Shufeldt, R.W., 1909. *Osteology of Birds*. University of the State of New York, Albany NY.
- Shute, E., Prideaux, G.J., Worthy, T.H., 2017. Taxonomic review of the late Cenozoic megapodes (Galliformes: Megapodiidae) of Australia. *Royal Society Open Science* 4, 170233. doi:170210.171098/rsos.170233.
- Sibley, C.G., Ahlquist, J.E., 1990. *Phylogeny and Classification of Birds: A Study in Molecular Evolution*. Yale University Press, New Haven.

- Sibley, C.G., Ahlquist, J.E., Monroe Jr, B.L., 1988. A classification of the living birds of the world based on DNA-DNA hybridization studies. *Auk* 105, 409-423.
- Simonetta, A.M., 1963. Cinesi e morfologia del cranio negli uccelli non passeriformi. Studio su varie tendenze evolutive. Part 1. *Archivio Zoologico Italiano* 48, 53-135.
- Simpson, J.I., 1984. The accessory optic system. *Annual Review of Neuroscience* 7, 13-41.
- Simpson, J.I., Leonard, C.S., Soodak, R.E., 1988. The accessory optic system. Analyzer of self-motion. *Annals of the New York Academy of Sciences* 545, 170-179.
- Slice, D.E., 2005. *Modern Morphometrics in Physical Anthropology*. Springer Science & Business Media.
- Slice, D.E., 2007. Geometric morphometrics. *Annual Review of Anthropology* 36, 261-281. doi:210.1146/annurev.anthro.1134.081804.120613.
- Smith, N.A., Clarke, J.A., 2012. Endocranial anatomy of the Charadriiformes: sensory system variation and the evolution of wing-propelled diving. *PLoS ONE* 7, e49584. doi:49510.41371/journal.pone.0049584.
- Sol, D., Garcia, N., Iwaniuk, A., Davis, K., Meade, A., Boyle, W.A., Székely, T., 2010. Evolutionary divergence in brain size between migratory and resident birds. *PLoS ONE* 5, e9617-e9617. doi:9610.1371/journal.pone.0009617.
- Sorenson, M.D., Cooper, A., Paxinos, E.E., Quinn, T.W., James, H.F., Olson, S.L., Fleischer, R.C., 1999. Relationships of the extinct moa-nalos, flightless Hawaiian waterfowl, based on ancient DNA. *Proceedings of the Royal Society of London. Series B: Biological Sciences* 266, 2187-2193.
- Sorenson, M.D., Oneal, E., García-Moreno, J., Mindell, D.P., 2003. More taxa, more characters: the hoatzin problem is still unresolved. *Molecular Biology and Evolution* 20, 1484-1498. doi:1410.1093/molbev/msg1157.
- Sraml, M., Christidis, L., Easteal, S., Horn, P., Collet, C., 1996. Molecular relationships within Australasian waterfowl (Anseriformes). *Australian Journal of Zoology* 44, 47-58.
- Steadman, D.W., 1980. A review of the osteology and paleontology of turkeys (Aves: Meleagridinae), In: Campbell Jr, K.E. (Ed.), *Papers in Avian Paleontology Honoring Hildegard Howard, Natural History Museum of Los Angeles County, Contributions in Science* 330, pp. 131-207.
- Steadman, D.W., 1989. New species and records of birds (Aves: Megapodiidae, Columbidae) from an archeological site on Lifuka, Tonga. *Proceedings of the Biological Society of Washington* 102, 537-552.
- Steadman, D.W., 1991. The identity and taxonomic status of *Megapodius stairi* and *M. burnabyi* (Aves: Megapodiidae). *Proceedings of the Biological Society of Washington* 104, 870-877.
- Steadman, D.W., 1993. Biogeography of Tongan birds before and after human impact. *Proceedings of the National Academy of Sciences USA* 90, 818-822.
- Steadman, D.W., 1994. Bird bones from the To'aga site: prehistoric loss of seabirds and megapodes. *Contributions of the University of California Archaeological Research Facility* 51, 217-228.
- Steadman, D.W., 1995. Prehistoric extinctions of Pacific island birds: biodiversity meets zooarchaeology. *Science* 267, 1123-1131.
- Steadman, D.W., 1999. The biogeography and extinction of megapodes in Oceania. *Proceedings of the Third International Megapode Symposium. Zoologische Verhandlungen* 327, 7-22.

- Steadman, D.W., White, J.P., Allen, J., 1999. Prehistoric birds from New Ireland, Papua New Guinea: extinctions on a large Melanesian island. *Proceedings of the National Academy of Sciences USA* 96, 2563-2568.
- Steadman, D.W., Worthy, T.H., Anderson, A.J., Walter, R., 2000. New species and records of birds from prehistoric sites on Niue, Southwest Pacific. *Wilson Bulletin* 112, 165-304.
- Stein, R.W., Brown, J.W., Mooers, A.Ø., 2015. A molecular genetic time scale demonstrates Cretaceous origins and multiple diversification rate shifts within the order Galliformes (Aves). *Molecular Phylogenetics and Evolution* 92, 155-164. doi:110.1016/j.ympev.2015.1006.1005.
- Stephan, H., Frahm, H., Baron, G., 1981. New and revised data on volumes of brain structures in insectivores and primates. *Folia Primatologica* 35, 1-29.
- Stidham, T.A., 2015. Re-description and phylogenetic assessment of the Late Miocene ducks *Aythya shihuibas* and *Anas* sp.(Aves: Anseriformes) from Lufeng, Yunnan, China. *Vertebrata Palasiatica* 53, 335-349.
- Stidham, T.A., Zelenkov, N.V., 2017. North American–Asian aquatic bird dispersal in the Miocene: evidence from a new species of diving duck (Anseriformes: Anatidae) from North America (Nevada) with affinities to Mongolian taxa. *Alcheringa* 41, 222-230. doi:210.1080/03115518.03112016.01224439.
- Stingelin, W., 1957. *Vergleichende Morphologische Untersuchungen am Vorderhirn der Vögel auf Cytologischer und Cytoarchitektonischer Grundlage*. Verlag Helbing & Lichtenhahn, Basel. p.123.
- Stirton, R.A., Tedford, R.H., Miller, A.H., 1961. Cenozoic stratigraphy and vertebrate paleontology of the Tirari Desert, South Australia. *Records of the South Australian Museum* 14, 19-61.
- Striedter, G.F., 2005. *Principles of Brain Evolution*. Sinauer Associates, Sunderland, MA.
- Striedter, G.F., 2006. Précis of principles of brain evolution. *Behavioral and Brain Sciences* 29, 1-12.
- Sutherland, R., 1999. Basement geology and tectonic development of the greater New Zealand region: an interpretation from regional magnetic data. *Tectonophysics* 308, 341-362.
- Tambussi, C.P., Degrange, F.J., De Mendoza, R.S., Sferco, E., Santillana, S., 2019. A stem anseriform from the early Palaeocene of Antarctica provides new key evidence in the early evolution of waterfowl. *Zoological Journal of the Linnean Society* xx, 1-28.
- Tambussi, C.P., Degrange, F.J., Ksepka, D.T., 2015. Endocranial anatomy of Antarctic Eocene stem penguins: implications for sensory system evolution in Sphenisciformes (Aves). *Journal of Vertebrate Paleontology* 35, e981635. doi:981610.981080/02724634.02722015.02981635.
- Tedford, R.H., Wells, R.T., 1990. Pleistocene deposits and fossil vertebrates from the “Dead Heart of Australia”. *Memoirs of the Queensland Museum* 28, 263-284.
- Tennyson, A.J.D., 2010. The origin and history of New Zealand’s terrestrial vertebrates. *New Zealand Journal of Ecology* 34, 6-27.
- Tennyson, A.J.D., Worthy, T.H., Jones, C.M., Scofield, R.P., Hand, S.J., 2010. Moa’s Ark: Miocene fossils reveal the great antiquity of moa (Aves: Dinornithiformes) in Zealandia. *Records of the Australian Museum* 62, 105-114. doi:110.3853/j.0067-1975.3862.2010.1546.
- Tonni, E.P., 1979. Un nuevo anseriforme de sedimentos marinos terciarios de Chubut, Argentina. *Hornero* 12, 11-15.
- Tordoff, H.B., 1951. A quail from the Oligocene of Colorado. *Condor* 53, 203-204.

- Tordoff, H.B., Macdonald, J., 1957. A new bird (family Cracidae) from the early Oligocene of South Dakota. *Auk* 74, 174-184.
- Touraine, F., 1960. Oeufs d'oiseaux de très grande taille dans l'Eocène inférieur de Provence. *Bulletin de la Société géologique de France* 7, 783-789.
- Van Beneden, P.-J., 1872. Oiseaux de l'argile rupelienne et du crag d'Anvers. *Journal de Zoologie* 1, 284-288.
- Van Beneden, P.-J., 1873. Paléontologie des Vertébrés, in: van Bemmelen, E. (Ed.), *Patria Belgica* (Encyclopédie Nationale), Bruylant-Christophe, Brussels, pp. 353-376.
- van Tets, G.F., 1974. A revision of the fossil Megapodiidae (Aves), including a description of a new species of *Progura* De Vis. *Transactions of the Royal Society of South Australia* 98, 213-224.
- van Tets, G.F., 1984. A Checklist of Extinct Fossil Australasian Birds, in: Archer, M., Clayton, G. (Eds.), *Vertebrate Zoogeography & Evolution in Australasia*, Hesperian Press, Carlisle, pp. 469-475.
- van Tets, G.F., 1985. *Progura gallinacea* The Australian Giant Megapode, in: Rich, P.V., Van Tets, G.F. (Eds.), *Kadimakara: Extinct Vertebrates of Australia*, Pioneer Design Studio, Victoria, Australia, pp. 195-199.
- van Tets, G.F., Rich, P.V., 1990. An evaluation of De Vis' fossil birds. *Memoirs of the Queensland Museum* 28, 165-168.
- van Tets, G.F., Smith, M.J., 1974. Small fossil vertebrates from Victoria Cave, Naracoorte, South Australia. III. Birds (Aves). *Transactions of the Royal Society of South Australia* 98, 225-227.
- van Tuinen, M., Dyke, G.J., 2004. Calibration of galliform molecular clocks using multiple fossils and genetic partitions. *Molecular Phylogenetics and Evolution* 30, 74-86. doi:10.1016/S1055-7903(1003)00164-00167.
- van Tuinen, M., Hedges, S.B., 2001. Calibration of avian molecular clocks. *Molecular Biology and Evolution* 18, 206-213.
- van Tuinen, M., Hedges, S.B., 2004. The effect of external and internal fossil calibrations on the avian evolutionary timescale. *Journal of Paleontology* 78, 45-50.
- van Tuinen, M., Stidham, T.A., Hadly, E.A., 2006. Tempo and mode of modern bird evolution observed with large-scale taxonomic sampling. *Historical Biology* 18, 205-221. doi:10.1080/08912960600641174.
- Vickers-Rich, P., 1991. The Mesozoic and Tertiary History of Birds on the Australian Plate, in: Vickers-Rich, P., Monaghan, J.M., Baird, R.F., Rich, T.H. (Eds.), *Vertebrate Palaeontology of Australasia*, Pioneer Design Studios in cooperation with the Monash University Publications Committee, Melbourne, pp. 721-808.
- Villatte, J., 1966. Découverte de fragments de coquilles d'oeufs d'oiseaux dans l'Eocène inférieur de l'Aude. *Comptes Rendus Sommaires de la Société Géologique de France*, 345-346.
- Wagner, H.-J., 2001a. Sensory brain areas in mesopelagic fishes. *Brain, Behavior and Evolution* 57, 117-133.
- Wagner, H.-J., 2001b. Brain areas in abyssal demersal fishes. *Brain, Behavior and Evolution* 57, 301-316.
- Walsh, S., Milner, A., 2011a. Evolution of the Avian Brain and Senses, in: Dyke, G., Kaiser, G. (Eds.), *Living Dinosaurs: The Evolutionary History of Modern Birds*, Wiley, Chichester, pp. 282-305.

- Walsh, S., Milner, A., 2011b. *Halcyornis toliapicus* (Aves: Lower Eocene, England) indicates advanced neuromorphology in Mesozoic Neornithes. *Journal of Systematic Palaeontology* 9, 173-181. doi:110.1080/14772019.14772010.14513703.
- Walsh, S.A., Iwaniuk, A.N., Knoll, M.A., Bourdon, E., Barrett, P.M., Milner, A.C., Nudds, R.L., Abel, R.L., Sterpaio, P.D., 2013. Avian cerebellar floccular fossa size is not a proxy for flying ability in birds. *PLoS ONE* 8, e67176. doi:67110.61371/journal.pone.0067176.
- Walsh, S.A., Knoll, F., 2018. The Evolution of Avian Intelligence and Sensory Capabilities: The Fossil Evidence, in: Bruner, E., Ogihara, N., Tanabe, H.C. (Eds.), *Digital Endocasts: From Skulls to Brains*, Springer Japan, Tokyo, pp. 59-69. doi:10.1007/978-1004-1431-56582-56586.
- Walsh, S.A., Knoll, M.A., 2011. Directions in palaeoneurology. *Special Papers in Palaeontology* 86, 263-279. doi:210.1111/j.1475-4983.2011.01085.x.
- Walsh, S.A., Milner, A.C., Bourdon, E., 2016. A reappraisal of *Cerebavis cenomanica* (Aves, Ornithurae), from Melovodka, Russia. *Journal of Anatomy* 229, 215-227. doi:210.1111/joa.12406.
- Wang, N., Kimball, R.T., Braun, E.L., Liang, B., Zhang, Z., 2013. Assessing phylogenetic relationships among Galliformes: a multigene phylogeny with expanded taxon sampling in Phasianidae. *PLoS ONE* 8, e64312. doi:64310.61371/journal.pone.0064312.
- Wang, N., Kimball, R.T., Braun, E.L., Liang, B., Zhang, Z., 2016. Ancestral range reconstruction of Galliformes: the effects of topology and taxon sampling. *Journal of Biogeography* 44, 122-135. doi:110.1111/jbi.12782.
- Ward, B.J., Day, L.B., Wilkening, S.R., Wylie, D.R.W., Saucier, D.M., Iwaniuk, A.N., 2012. Hummingbirds have a greatly enlarged hippocampal formation. *Biology Letters* 8, 657-659. doi:610.1098/rsbl.2011.1180.
- Watanabe, J., 2017. Quantitative discrimination of flightlessness in fossil Anatidae from skeletal proportions. *Auk* 134, 672-695.
- Weidig, I., 2010. New birds from the lower Eocene Green River Formation, North America. *Records of the Australian Museum* 62, 29-44. doi:10.3853/j.0067-1975.3862.2010.1544.
- Weir, A.A.S., Chappell, J., Kacelnik, A., 2002. Shaping of hooks in New Caledonian crows. *Science* 297, 981.
- Wetmore, A., 1930. The supposed plumage of the Eocene *Diatryma*. *Auk* 47, 579-580.
- Wetmore, A., 1938. A fossil duck from the Eocene of Utah. *Journal of Paleontology* 12, 280-283.
- Wetmore, A., 1943. Remains of a swan from the Miocene of Arizona. *Condor* 45, 120.
- Wetmore, A., 1956. A fossil guan from the Oligocene of South Dakota. *Condor* 58, 234-235.
- White, C.M.N., Bruce, M.D., 1986. The birds of Wallacea (Sulawesi, the Moluccas & Lesser Sunda Islands, Indonesia): An annotated check-List. No. 7. *British Ornithologists' Union*, London.
- White, J.P., Flannery, T.F., O'Brien, R., Hancock, R.V., Pavlish, L., 1991. The Balof shelters, New Ireland, in: Allen, J., Gosden, C. (Eds.), Report of the Lapita Homeland Project, National Museum of Australia. *Occasional Papers Prehistory*, Canberra, pp. 46-58.
- Whiting, B.A., Barton, R.A., 2003. The evolution of the cortico-cerebellar complex in primates: anatomical connections predict patterns of correlated evolution. *Journal of Human Evolution* 44, 3-10. doi:10.1016/S0047-2484(1002)00162-00168.

- Wild, J.M., 1981. Identification and localization of the motor nuclei and sensory projections of the glossopharyngeal, vagus, and hypoglossal nerves of the cockatoo (*Cacatua roseicapilla*), Cacatuidae. *Journal of Comparative Neurology* 203, 351-377.
- Wild, J.M., 1987. The avian somatosensory system: connections of regions of body representation in the forebrain of the pigeon. *Brain Research* 412, 205-223.
- Wild, J.M., 1990. Peripheral and central terminations of hypoglossal afferents innervating lingual tactile mechanoreceptor complexes in Fringillidae. *Journal of Comparative Neurology* 298, 157-171.
- Wild, J.M., 1997. The avian somatosensory system: the pathway from wing to wulst in a passerine (*Chloris chloris*). *Brain Research* 759, 122-134.
- Wild, J.M., Arends, J.J.A., Zeigler, H.P., 1984. A trigeminal sensorimotor circuit for pecking, grasping and feeding in the pigeon (*Columba livia*). *Brain Research* 300, 146-151.
- Wild, J.M., Arends, J.J.A., Zeigler, H.P., 1985. Telencephalic connections of the trigeminal system in the pigeon (*Columba livia*): a trigeminal sensorimotor circuit. *Journal of Comparative Neurology* 234, 441-464.
- Wild, J.M., Farabaugh, S.M., 1996. Organization of afferent and efferent projections of the nucleus basalis prosencephali in a passerine, *Taeniopygia guttata*. *Journal of Comparative Neurology* 365, 306-328.
- Wild, J.M., Kubke, M.F., Peña, J.L., 2008. A pathway for predation in the brain of the barn owl (*Tyto alba*): projections of the gracile nucleus to the “claw area” of the rostral wulst via the dorsal thalamus. *Journal of Comparative Neurology* 509, 156-166. doi:110.1002/cne.21731.
- Wild, J.M., Williams, M.N., 2000. Rostral wulst in passerine birds. I. Origin, course, and terminations of an avian pyramidal tract. *Journal of Comparative Neurology* 416, 429-450.
- Wild, J.M., Zeigler, H.P., 1980. Central representation and somatotopic organization of the jaw muscles within the facial and trigeminal nuclei of the pigeon (*Columba livia*). *Journal of Comparative Neurology* 192, 175-201.
- Wild, J.M., Zeigler, H.P., 1996. Central projections and somatotopic organisation of trigeminal primary afferents in pigeon (*Columba livia*). *Journal of Comparative Neurology* 368, 136-152.
- Wiley, D.F., 2006. *Landmark Editor 3.0*. Institute for Data Analysis and Visualization, University of California, Davis. <http://graphics.idav.ucdavis.edu/research/EvoMorph>.
- Wiley, D.F., Amenta, N., Alcantara, D.A., Ghosh, D., Kil, Y.J., Delson, E., Harcourt-Smith, W., Rohlf, F.J., St John, K., Hamann, B., 2005. Evolutionary Morphing, in *Proceedings of IEEE Visualization 2005, IEEE*, pp. 431-438.
- Williams, M., 2015. Size and flight capability of *Anas chathamica*, an extinct duck from Chatham Island, New Zealand. *Wildfowl* 65, 75-99.
- Williams, M., Tennyson, A.J.D., Sim, D., 2014. Island differentiation of New Zealand’s extinct mergansers (Anatidae: Mergini), with description of a new species from Chatham Island. *Wildfowl* 64, 3–34.
- Witmer, L.M., Ridgely, R.C., Dufeu, D.L., Semones, M.C., 2008. Using CT to Peer into the Past: 3D Visualization of the Brain and Ear Regions of Birds, Crocodiles, and Nonavian Dinosaurs, in: Endo, H., Frey, R. (Eds.), *Anatomical Imaging, Towards a New Morphology*, Springer, Tokyo, Japan, pp. 67-87.

- Witmer, L.M., Rose, K.D., 1991. Biomechanics of the jaw apparatus of the gigantic Eocene bird *Diatryma*: implications for diet and mode of life. *Paleobiology*, 95-120.
- Wood, J.R., De Pietri, V.L., 2015. Next-generation paleornithology: Technological and methodological advances allow new insights into the evolutionary and ecological histories of living birds. *Auk* 132, 486-506. doi:410.1642/AUK-1614-1257.1641.
- Woodburne, M.O., Macfadden, B.J., Case, J.A., Springer, M.S., Pledge, N.S., Power, J.D., Woodburne, J.M., Springer, K.B., 1994. Land mammal biostratigraphy and magnetostratigraphy of the Etadunna Formation (late Oligocene) of South Australia. *Journal of Vertebrate Paleontology* 13, 483-515.
- Woolfenden, G.E., 1961. Postcranial osteology of the waterfowl. *Bulletin of the Florida State Museum Biological Sciences* 6, 1-129.
- Worthy, T.H., 1988. Loss of flight ability in the extinct New Zealand duck *Euryanas finschi*. *Journal of Zoology, London* 215, 619-628.
- Worthy, T.H., 1997. Fossil deposits in the Hodges Creek Cave System, on the northern foothills of Mt Arthur, Nelson. South Island, New Zealand. *Notornis* 44, 111-108.
- Worthy, T.H., 2000. The fossil megapodes (Aves: Megapodiidae) of Fiji with descriptions of a new genus and two new species. *Journal of the Royal Society of New Zealand* 30, 337-364.
- Worthy, T.H., 2002. The youngest giant: discovery and significance of the remains of a giant moa (*Dinornis giganteus*) near Turangi, in central North Island, New Zealand. *Journal of The Royal Society of New Zealand* 32, 183-187.
- Worthy, T.H., 2005. A new species of *Oxyura* (Aves: Anatidae) from the New Zealand Holocene. *Memoirs of the Queensland Museum* 51, 259-275.
- Worthy, T.H., 2008. Pliocene waterfowl (Aves: Anseriformes) from South Australia and a new genus and species. *Emu* 108, 153-165.
- Worthy, T.H., 2009. Descriptions and phylogenetic relationships of two new genera and four new species of Oligo-Miocene waterfowl (Aves: Anatidae) from Australia. *Zoological Journal of the Linnean Society* 156, 411-454.
- Worthy, T.H., Anderson, A.J., Molnar, R.E., 1999. Megafaunal expression in a land without mammals-the first fossil faunas from terrestrial deposits in Fiji (Vertebrata: Amphibia, Reptilia, Aves). *Senckenbergiana Biologica* 79, 237-242.
- Worthy, T.H., De Pietri, V.L., Scofield, R.P., 2017a. Recent advances in avian palaeobiology in New Zealand with implications for understanding New Zealand's geological, climatic and evolutionary histories. *New Zealand Journal of Zoology* 43, 1-35. doi:10.1080/03014223.03012017.01307235.
- Worthy, T.H., Degrange, F.J., Handley, W.D., Lee, M.S.Y., 2017b. The evolution of giant flightless birds and novel phylogenetic relationships for extinct fowl (Aves, Galloanseres). *Royal Society Open Science* 4, 170975. doi:170910.171098/rsos.170975.
- Worthy, T.H., Degrange, F.J., Handley, W.D., Lee, M.S.Y., 2017c. Correction to 'The evolution of giant flightless birds and novel phylogenetic relationships for extinct fowl (Aves, Galloanseres)'. *Royal Society Open Science* 4, 171621. doi:171610.171098/rsos.171621.
- Worthy, T.H., Hand, S.J., Archer, M., Scofield, R.P., De Pietri, V.L., 2019. Evidence for a giant parrot from the Early Miocene of New Zealand. *Biology Letters* 15, 20190467. doi:20190410.20191098/rsbl.20192019.20190467.

- Worthy, T.H., Hand, S.J., Nguyen, J.M., Tennyson, A.J., Worthy, J.P., Scofield, R.P., Boles, W.E., Archer, M., 2010a. Biogeographical and phylogenetic implications of an early Miocene wren (Aves: Passeriformes: Acanthisittidae) from New Zealand. *Journal of Vertebrate Paleontology* 30, 479-498. doi:10.1080/02724631003618033.
- Worthy, T.H., Hand, S.J., Worthy, J.P., Tennyson, A.J.D., Scofield, R.P., 2009. A large fruit pigeon (Columbidae) from the Early Miocene of New Zealand. *Auk* 126, 649-656. doi:10.1525/auk.2009.08244.
- Worthy, T.H., Handley, W.D., Archer, M., Hand, S.J., 2016b. The extinct flightless mihirungs (Aves, Dromornithidae): cranial anatomy, a new species, and assessment of Oligo-Miocene lineage diversity. *Journal of Vertebrate Paleontology* 36, e1031345. doi:10.1031340.1031080/02724634.02722015.01031345.
- Worthy, T.H., Hawkins, S., Bedford, S., Spriggs, M., 2015. Avifauna from the Teouma Lapita Site, Efate Island, Vanuatu, including a New Genus and Species of Megapode. *Pacific Science* 69, 205-254. doi:10.2984/2969.2982.2986.
- Worthy, T.H., Holdaway, R.N., 2002. *The Lost World of the Moa: Prehistoric Life of New Zealand*. Indiana University Press, Bloomington, IN. p760.
- Worthy, T.H., Holdaway, R.N., Sorenson, M.D., Cooper, A.C., 1997. Description of the first complete skeleton of the extinct New Zealand goose *Cnemiornis calcitrans* (Aves: Anatidae), and a reassessment of the relationships of *Cnemiornis*. *Journal of Zoology* 243, 695-723.
- Worthy, T.H., Lee, M.S.Y., 2008. Affinities of Miocene waterfowl (Anatidae: *Manuherikia*, *Dunstanetta* and *Miotadorna*) from the St Bathans Fauna, New Zealand. *Palaeontology* 51, 677-708. doi: 10.1111/j.1475-4983.2008.00778.x.
- Worthy, T.H., Mitri, M., Handley, W.D., Lee, M.S.Y., Anderson, A., Sand, C., 2016a. Osteology supports a stem-Galliform affinity for the giant extinct flightless bird *Sylviornis neocaledoniae* (Sylviornithidae, Galloanseres). *PLoS ONE* 11, e0150871. doi:10.1371/journal.pone.0150871.
- Worthy, T.H., Olson, S.L., 2002. Relationships, adaptations, and habits of the extinct duck '*Euryanas finschi*'. *Notornis* 49, 1-17.
- Worthy, T.H., Olson, S.L., Thierry, S., 2008a. A reassessment of the fossil goose *Anser scaldii* Lambrecht, 1933 (Aves: Anatidae). *Bulletin of the British Ornithologists' Club* 128, 228-232.
- Worthy, T.H., Pledge, N.S., 2007. A shelduck (Anatidae: Tadorna) from the Pliocene of south Australia. *Transactions of the Royal Society of South Australia* 131, 107-115.
- Worthy, T.H., Scanlon, J.D., 2009. An Oligo-Miocene Magpie Goose (Aves: Anseranatidae) from Riversleigh, Northwestern Queensland, Australia. *Journal of Vertebrate Paleontology* 29, 205-211.
- Worthy, T.H., Scofield, R.P., 2012. Twenty-first century advances in knowledge of the biology of moa (Aves: Dinornithiformes): a new morphological analysis and moa diagnoses revised. *New Zealand Journal of Zoology* 39, 87-153. doi:10.1080/03014223.03012012.03665060.
- Worthy, T.H., Tennyson, A.J.D., Archer, M., Scofield, R.P., 2010b. First Record of *Palaelodus* (Aves: Phoenicopteriformes) from New Zealand. *Records of the Australian Museum* 62, 77-88. doi:10.3853/j.0067-1975.3862.2010.1545.
- Worthy, T.H., Tennyson, A.J.D., Hand, S.J., Scofield, R.P., 2008b. A new species of the diving duck *Manuherikia* and evidence for geese (Aves: Anatidae: Anserinae) in the St Bathans Fauna (Early Miocene), New Zealand. *Journal of the Royal Society of New Zealand* 38, 97-114.

- Worthy, T.H., Tennyson, A.J.D., Jones, C., McNamara, J.A., Douglas, B.J., 2007. Miocene waterfowl and other birds from Central Otago, New Zealand. *Journal of Systematic Palaeontology* 5, 1-39. doi:10.1017/S1477201906001957.
- Worthy, T.H., Tennyson, A.J.D., Scofield, R.P., 2011a. Fossils reveal an early Miocene presence of the aberrant gruiform Aves: Aptornithidae in New Zealand. *Journal of Ornithology* 152, 669-680. doi: 610.1007/s10336-10011-10649-10336.
- Worthy, T.H., Tennyson, A.J.D., Scofield, R.P., 2011b. An early Miocene diversity of parrots (Aves, Strigopidae, Nestorinae) from New Zealand. *Journal of Vertebrate Paleontology* 31, 1102-1116. doi:1110.1080/02724634.02722011.02595857.
- Worthy, T.H., Worthy, J.P., Tennyson, A.J.D., 2013b. Miocene Fossils Show that kiwi (*Apteryx*, Apterygidae) are Probably Not Phyletic Dwarves, in: Göhlich, U.B., Kroh, A. (Eds.), Paleornithological Research 2013. Proceedings of the 8th International Meeting of the Society of Avian Paleontology and Evolution, *Naturhistorisches Museum, Wien*, pp. 63-80.
- Worthy, T.H., Worthy, J.P., Tennyson, A.J.D., Scofield, R.P., 2013a. A bittern (Aves: Ardeidae) from the early Miocene of New Zealand. *Paleontological Journal* 47, 1331-1343. doi:1310.1134/S0031030113110154.
- Worthy, T.H., Yates, A., 2017. A review of the smaller birds from the late Miocene Alcoota Local Faunas of Australia with a description of a new species, In: Hospitaleche, C.A., Agnolin, F.L., Haidr, N., Noriega, J.I., Tambussi, C.P. (Eds.), Proceedings of the 9th International Meeting of the Society of Avian Paleontology and Evolution, Diamante (Argentina), 1-6 August 2016. Paleontología y Evolución de las Aves, *Contribuciones del Museo Argentino de Ciencias Naturales* 7, pp. 221-252.
- Wylie, D.R.W., Gutiérrez-Ibáñez, C., Gaede, A.H., Altshuler, D.L., Iwaniuk, A.N., 2018. Visual-cerebellar pathways and their roles in the control of avian flight. *Frontiers in Neuroscience* 12, 223. doi:210.3389/fnins.2018.00223.
- Wylie, D.R.W., Gutiérrez-Ibáñez, C., Iwaniuk, A.N., 2015. Integrating brain, behavior, and phylogeny to understand the evolution of sensory systems in birds. *Frontiers in Neuroscience* 9, 281 (217pp). doi:210.3389/fnins.2015.00281.
- Wylie, D.R.W., 2001. Projections from the nucleus of the basal optic root and nucleus lentiformis mesencephali to the inferior olive in pigeons (*Columba livia*). *Journal of Comparative Neurology* 429, 502-513.
- Wylie, D.R.W., Gutiérrez-Ibáñez, C., Pakan, J.M.P., Iwaniuk, A.N., 2009. The optic tectum of birds: mapping our way to understanding visual processing. *Canadian Journal of Experimental Psychology* 63, 328-338. doi:310.1037/a0016826.
- Wylie, D.R.W., Iwaniuk, A.N., 2012. Neural Mechanisms Underlying Visual Motion Detection in Birds, in: Lazareva, O.F., Shimizu, T., Wasserman, E.A. (Eds.), *How Animals See the World: Comparative Behavior, Biology, and Evolution of Vision*, Oxford University Press, New York, pp. 289-318.
- Zelditch, M.L., Swiderski, D.L., Sheets, H.D., Fink, W.L., 2004. *Geometric Morphometrics for Biologists: A Primer*. Elsevier Academic Press, California USA. p443.
- Zelenitsky, D.K., Therrien, F., Ridgely, R.C., McGee, A.R., Witmer, L.M., 2011. Evolution of olfaction in non-avian theropod dinosaurs and birds. *Proceedings of the Royal Society B: Biological Sciences* 278, 3625-3634. doi:3610.1098/rspb.2011.0238.

- Zelenkov, N.V., 2011. Diving ducks from the Middle Miocene of western Mongolia. *Paleontological Journal* 45, 191-199. doi:110.1134/S0031030111020195.
- Zelenkov, N.V., 2012a. A new duck from the middle Miocene of Mongolia, with comments on Miocene evolution of ducks. *Paleontological Journal* 46, 520-530. doi:510.1134/S0031030112050139.
- Zelenkov, N.V., 2012b. Neogene geese and ducks (Aves: Anatidae) from localities of the Great Lakes Depression, western Mongolia. *Paleontological Journal* 46, 607-619. doi:610.1134/S0031030112060123.
- Zelenkov, N.V., 2013. New finds and revised taxa of Early Pliocene birds from Western Mongolia, In: Göhlich, U.B., Kroh, A. (Eds.), *Paleornithological Research 2013. Proceedings of the 8th International Meeting of the Society of Avian Paleontology and Evolution*, Verlag *Naturhistorisches Museum*, Wien, pp. 153-170.
- Zelenkov, N.V., 2016a. Revision of non-passeriform birds from Polgárdi (Hungary, Late Miocene): 1. Anseriformes. *Paleontological Journal* 50, 514-517. doi: 510.1134/S0031030116050142.
- Zelenkov, N.V., 2016b. Revision of non-passeriform birds from Polgárdi (Hungary, Late Miocene): 2. Galliformes. *Paleontological Journal* 50, 623-634. doi:610.1134/S0031030116060162.
- Zelenkov, N.V., 2018. The earliest Asian duck (Anseriformes: *Romainvillia*) and the origin of Anatidae, *Doklady Biological Sciences* 483, pp. 225-227. doi:210.1134/S0012496618060030.
- Zelenkov, N.V., Kurochkin, E.N., 2009a. Neogene phasianids (Aves: Phasianidae) of Central Asia: 1. Genus *Tologuica* gen. nov. *Paleontological Journal* 43, 208-215.
- Zelenkov, N.V., Kurochkin, E.N., 2009b. Neogene phasianids (Aves: Phasianidae) of Central Asia: 2. Genera *Perdix*, *Plioperdix*, and *Bantamyx*. *Paleontological Journal* 43, 318-325.
- Zelenkov, N.V., Kurochkin, E.N., 2010. Neogene phasianids (Aves: Phasianidae) of Central Asia: 3. Genera *Lophogallus* gen. nov. and *Syrmaticus*. *Paleontological Journal* 44, 328-336.
- Zelenkov, N.V., Kurochkin, E.N., 2012. Dabbling ducks (Aves: Anatidae) from the middle Miocene of Mongolia. *Paleontological Journal* 46, 421-429.
- Zelenkov, N.V., Kurochkin, E.N., 2014. Two new waterfowl species (Aves: Anseriformes) from the Upper Pleistocene of Yakutia: The first extinct species of Quaternary birds from Russia. *Paleontological Journal* 48, 645-654. doi:610.1134/S0031030114060161.
- Zelenkov, N.V., Panteleyev, A.V., 2014. Three bird taxa (Aves: Anatidae, Phasianidae, Scolopacidae) from the late Miocene of the Sea of Azov (southwestern Russia). *Paläontologische Zeitschrift* 89, 515-527. doi:510.1007/s12542-12014-10238-12540.
- Zelenkov, N.V., Stidham, T.A., 2018. Possible filter-feeding in the extinct *Presbyornis* and the evolution of Anseriformes (Aves). *Zoological Journal* 97, 943-956. doi:910.1134/S0044513418080159.